MODELLING OF TSUNAMI GENERATED BY THE MOTION OF A RIGID BLOCK ALONG A HORIZONTAL BOUNDARY

A thesis submitted in partial fulfilment of the

requirements for the degree of

Doctor of Philosophy in Civil Engineering

in the

University of Canterbury

by

Colin Whittaker

2013

Abstract

Tsunami are a very dangerous natural hazard, as highlighted in recent years by the Indian Ocean Tsunami of 2004 and the Japan Tsunami of 2011. In the last decade, tsunami have claimed hundreds of thousands of lives, and caused billions of dollars in damage around the world. The hazard posed to coastal communities by tsunami is expected to increase in the future, due to population growth, intensification of coastal development and sea level rise due to climate change.

Tsunami may be generated by a number of different source mechanisms. One such source mechanism is a submarine landslide, which can occur in a number of marine environments containing significant sediment accumulation on a sloping seafloor. The high amplitudes and rapid celerities of landslide-generated tsunami make them very dangerous to communities in the vicinity of the landslide, although these waves do not possess the potential for transoceanic devastation.

The objectives of this research project are to carry out a series of two-dimensional physical experiments investigating the waves generated by a rigid block landslide moving along a horizontal boundary. The use of a horizontal boundary has the advantage that waves propagating in the offshore and onshore directions may be measured (unlike previous studies using sloping boundaries). The landslide motion is provided by a mechanical system, allowing testing of a broad range of motion, and isolation of the wavemaking properties of different phases of landslide motion.

Experiments are carried out in a 14.66 m long flume, with width 0.25 m and working depth 0.50 m. A false floor installed in the flume provides the sliding surface for the landslide motion, and houses the mechanical system. A series of preliminary particle tracking velocimetry experiments confirm the ability of the mechanical system to achieve its velocity targets to within 5% or better, depending on the parameters of the landslide motion. Full spatial and temporal resolution of the wave field is achieved using a laser-induced fluorescence technique to identify the air-water interface to sub-pixel accuracy. The measurements obtained using laser-induced fluorescence are validated against measurements from a resistance wave gauge, with sub-millimetre agreement. In an additional experiment, the particle tracking velocimetry technique provides measurements of the subsurface velocity field.

The landslide motion during all experiments consists of an initial period of constant

acceleration, followed by a period of constant velocity, followed by a deceleration to rest (at the same rate as the initial acceleration). The landslide acceleration generates two dispersive packets of waves, travelling in the offshore and onshore directions. The offshore-propagating wave packet contains a leading crest and the onshore-propagating wave packet contains a leading trough, with both waves approaching the shallow water limit. A free surface depression forms above the landslide during its constant-velocity motion, and its amplitude may be predicted to within approximately 20% using standard hydraulic theory (considering a frame of reference moving with the landslide). The offshore-propagating waves passing over the landslide cause the amplitude of this depression to fluctuate over time. The deceleration of the landslide generates two additional packets of waves with the opposite polarity to the waves generated by the landslide acceleration.

The full spatial and temporal resolution of the generated wave field allows the calculation of the potential energy within the wave field. Additionally, the energy (and mass) within the onshore- and offshore-propagating wave packets may be estimated by calculating these quantities within the onshore and offshore regions of the experimental domain. The wave packets generated by the initial landslide acceleration transport positive mass in the offshore direction, and negative mass in the onshore direction. This mass transport is balanced by the waves generated during the deceleration of the landslide.

The nondimensional landslide acceleration, landslide Froude number and submergence depth are varied during the physical experiments. The landslide Froude number has the greatest effect on the behaviour of the generated wave field. At low Froude numbers, the wave field is dominated by the waves generated by the acceleration and deceleration of the landslide. As the Froude number increases, the onshore-propagating waves become negligible in amplitude compared to the offshore-propagating waves. Additionally, the free surface depression increases in amplitude and a group of short-wavelength waves become trapped behind the landslide. These waves exhibit highly nonlinear behaviour at landslide Froude numbers greater than 0.5.

The simple experimental geometry allows comparison between the measured wave fields with the predictions of three mathematical models. Two inviscid-irrotational models, differing in their treatment of the bottom boundary condition, provide comparisons over the entire parameter space. These models under-predict the amplitudes of the generated waves, and fail to correctly predict the ongoing interaction between the landslide and the offshore-propagating waves. The inclusion of bottom boundary nonlinearity improves the predictions of the amplitude of the leading waves, and the potential energy within the wave field. However, both of the inviscid models do not predict the extent of wave trapping behaviour behind the landslide observed in the experiments.

A viscous model, formulated in the DNS solver Gerris, improves the predictions of wave trapping (and amplitude in general) in one experiment. Although the model still under-predicts the amplitudes of the generated waves, it correctly predicts the amplification of the waves behind the landslide during its constant-velocity motion. The failure of the inviscid models to predict the amplitudes of these waves can be mostly attributed to the linearised free surface condition used by both models. The presence of the turbulent wake may also have a secondary effect on these predictions.

An extension of the linear inviscid-irrotational model to three dimensions allows the effect of the landslide width on the amplitudes of the generated waves to be determined. As the width increases, the behaviour of the waves approaches the two-dimensional limiting case.

Acknowledgements

This work was funded by a PhD scholarship from the Department of Civil and Natural Resources Engineering, at the University of Canterbury.

Great thanks must be given to my principal supervisor, Roger Nokes, for his instrumental role in this project. Without his guidance and support, this thesis could not have been written. It has been a pleasure to work alongside him on this project, and his attitudes towards both teaching and research are inspirational. I have also been grateful for the opportunity to work alongside my associate supervisors, Mark Davidson and Pedro Lee, and am grateful for their assistance with this project.

The technical staff in the Department of Civil and Natural Resources Engineering at the University of Canterbury have devoted significant time and expertise to this project. I am particularly grateful to the staff of the Fluid Mechanics Laboratory, Ian Sheppard, Alan Stokes and Kevin Wines, for their help in the experimental phase of this project. Thanks to Mike Weavers, for his assistance with the motion control system, and to John Koolos for his input. Peter Coursey and Shaun Cosgrove also assisted with various aspects of the physical experiments, and their work is appreciated. Thanks also to Emily Lane of NIWA for her assistance with the Gerris model.

I have been fortunate to conduct PhD research within the Department of Civil and Natural Resources Engineering at the University of Canterbury. The administrative support from Alan Jolliffe and Elizabeth Ackermann, and the excellent attitudes of every academic staff member towards students, have made my project a very rewarding experience. The fluid mechanics research group within this department has provided an excellent forum for the discussion and critique of ideas, and I have benefited greatly from interactions with the postgraduate and undergraduate students within this group. Thanks also to Sarah Delavan for her advice and encouragement during her time in New Zealand, Sarah Hoffman for her valuable perspective, and to my fellow postgraduates for contributing to an excellent work environment.

Finally, I could not have completed this project without the support and encouragement of my family and friends. Thanks to my parents for their constant support and understanding, to my flatmates for their tolerance, and to my friends for their sense of humour.

Contents

List of Figures

List of Tables

List of symbols

For clarity, the list of symbols is divided into several different sections. The first list defines the symbols used throughout the current study, as these are the symbols required to interpret the experimental and numerical results. The next two lists relate to the additional symbols used in the development of the experimental method, and in the formulation of the various numerical models. However, it should be noted that these lists only contain those symbols not already defined in the first list, and should be read in conjunction with the first list to provide a complete list of symbols for chapters 4 and 5. The final lists relate to symbols used by different authors within the literature. These lists refers to the different papers to avoid confusion, since many previous studies used different symbols to define their variables (for example the fluid depth has been defined as D, h and d by different authors).

Although the symbol λ is used as the nondimensional landslide acceleration throughout the majority of the thesis, it is also briefly used in chapter 7 as the wavelength of the generated waves. This is the more conventional definition for this symbol, and this is clearly stated when used. Unless explicitly stated otherwise, the symbol λ refers to the nondimensional landslide acceleration only. This is partly justified by the use of k as the length scale associated with the generated waves throughout the model formulation in chapter 5.

Experimental and numerical model results

a_0	Initial landslide acceleration
c_g	Wave group speed
c_p	Wave phase speed
D	Fluid depth
$\frac{dx_0(t)}{dt}$	Landslide velocity
$\frac{d^2x_0(t)}{dt^2}$	Landslide acceleration
$E_K(t)$	Kinetic energy contained within the velocity field
$E_P(t)$	Potential energy contained within the wave field
Fr	Landslide Froude number
g	Gravitational acceleration
H	Wave height
h_b	Landslide thickness
k	Wavenumber (this becomes a vector with components k_x and k_z in 3D simulations)
L_b	Landslide length
$P(x, y, t)$	Fluid pressure
$p(x, y, t)$	Modified fluid pressure (from hydrostatic)
Re	Reynolds number
t	Time
t_1	Time of motion change from constant acceleration to constant velocity
t_2	Time of motion change from constant velocity to constant deceleration
t_3	Time of motion change from constant deceleration to rest
$u(x, y, t)$	Horizontal fluid velocity
u_t	Landslide terminal velocity
$v(x, y, t)$	Vertical fluid velocity
W_b	Landslide width (only used in 3D simulations)
x	Longitudinal spatial coordinate
$x_0(t)$	Landslide centre of mass position
y	Vertical spatial coordinate
z	Lateral spatial coordinate (only used in 3D simulations)
Δ_P	Error in predictions by the numerical models
δ	Boundary layer thickness
ϵ	Nonlinearity coefficient used by Le Mehaute (1976)
$\eta(x, t)$	Free surface elevation ($\eta(x, z, t)$ in 3D simulations)
λ	Nondimensional landslide acceleration. This symbol is also used in chapter 7 as the wavelength of the generated waves (this is stated clearly when used)
μ	Coefficient used by Le Mehaute (1976) to determine depth regime
ν	Fluid viscosity
ρ	Fluid density
σ	Nondimensional landslide width (only used in 3D simulations)
τ	Nondimensional fluid depth

Two-dimensional experimental method

a_{RMS}	RMS error in landslide acceleration
d_{RMS}	RMS error in landslide deceleration
$I(x, y, t)$	Pixel intensity, used in LIF processing
I_0	Background (air) intensity used in LIF processing
I_1	Intensity at lower end of air-water interface, used in LIF processing
I_t	Threshold intensity used to determine free surface location, used in LIF processing
$P(t)$	Laser power
p_I	Intensity gradient in air-water interface, used in LIF processing
p_W	Intensity gradient below the water surface, used in LIF processing
$u(t)$	Landslide velocity
u_{RMS}	RMS error in landslide velocity
x	Landslide displacement. Also used as horizontal spatial coordinate in LIF and PTV processing
y	Vertical spatial coordinate
y_0	Vertical location of pixel at top of air-water interface, used in LIF processing
y_1	Vertical location of pixel at bottom of air-water interface, used in LIF processing
y_a, y_b	Vertical locations of pixels adjacent to free surface location, used in LIF processing
$\eta(x, t)$	Free surface location, used in LIF processing

Numerical model formulation

A	Landslide shape amplification factor
$a(k,t)$	Spectral coefficient in the assumed solution for the velocity potential ($a(k_x,k_z,t)$ in 3D simulations)
$b(k,t)$	Spectral coefficient in the assumed solution for the velocity potential ($b(k_x,k_z,t)$ in 3D simulations)
C_1, C_2	Temporary variables representing the spectral coefficient $c(k,t)$ and its derivative
$c(k,t)$	Spectral coefficient in the assumed solution for the free surface elevation ($c(k_x,k_z,t)$ in 3D simulations)
$D(k)$	Variable representing the dispersion relation ($D(k_x,k_z)$ in 3D simulations)
$F(k,t)$	Temporary variable used to describe the contribution of the landslide velocity to the wave forcing ($F(k_x,k_z,t)$ in 3D simulations)
$f(\theta(x,t))$	Landslide shape function ($f(\theta(x,t),z)$ in 3D simulations)
$G(k,t)$	Forcing function ($G(k_x,k_z,t)$ in 3D simulations)
L	Arbitrary length scale, either taking the value of D or L_b (or W_b in 3D simulations)
$p(k)$	Landslide shape coefficients ($p(k_x)$ and $q(k_z)$ in 3D simulations)
ST	Surface tension
$y_b(x,t)$	Bottom boundary ($y_b(x,z,t)$ in 3D simulations)
α	Nondimensional landslide length
ϵ	Temporary variable used to describe the contribution of the landslide position to the wave forcing
$\theta(x,t)$	Longitudinal spatial coordinate relative to the landslide centre of mass position ($\theta(x,z,t)$ in 3D simulations)
ξ	Nondimensional channel depth (scaled by the landslide thickness)
$\phi(x,y,t)$	Velocity potential ($\phi(x,y,z,t)$ in 3D simulations)
$\varphi(k,x,t)$	Temporary variable used to describe a travelling wave ($\varphi(k_x,k_z,x,z,t)$ in 3D simulations)
ω	Angular frequency of generated waves

Literature review - landslide failure mechanisms

c'	Effective cohesion, from Hampton *et al.* (1996)
F	Farboschung (term describing landslide mobility), from Locat & Lee (2002)
ΔH	Elevation difference between the slide crest and the tip of the debris, from Locat & Lee (2002)
h	Flow thickness, from Locat & Lee (2002)
h_i	Initial height of the submerged mass, from Locat & Lee (2002)
L	Runout distance, from Locat & Lee (2002)
u	Pore water pressure, from Hampton *et al.* (1996)
σ	Normal stress to failure plane, from Hampton *et al.* (1996)
τ_f	Shear strength of material, from Hampton *et al.* (1996)
ϕ'	Friction angle of sediment, from Hampton *et al.* (1996)

Literature review - mathematical framework of landslide tsunami models

$b(x,t)$	Bottom boundary
$D(x)$	Fluid depth
$\mathbf{F}$	Body force term
$f(t)$	Time-dependent forcing term on RHS of Bernoulli equation
h	Landslide thickness
L	Landslide length
P	Fluid pressure
P_a	Atmospheric pressure
$S = \alpha/\beta$	Stokes number, where α is a nondimensional wave amplitude, and β is a nondimensional channel depth
$\mathbf{u}$	Fluid velocity vector
u'	Depth-averaged fluid velocity
u_b	Velocity of bottom boundary
α	Slope angle
η_0	Characteristic tsunami amplitude
λ_0	Characteristic tsunami wavelength
ν	Fluid viscosity
Ω	Potential force function, assuming a conservative body force
ω	Fluid vorticity

Literature review - previous mathematical models

a_0	Initial landslide acceleration, from Sue *et al.* (2011)
b	Landslide length, from Watts *et al.* (2005) and Grilli & Watts (1999)
D	Landslide thickness, from Jiang & Leblond (1994)
d	Fluid depth, from Watts *et al.* (2005) , Grilli & Watts (1999) and Sue *et al.* (2011). Also used as the landslide thickness in Liu *et al.* (2003)
H	Maximum wave height, from Murty (2003)
h	Channel depth, from Grilli & Watts (1999) and Lynett & Liu (2005)
h_1	Shelf depth, from Jiang & Leblond (1994)
h_2	Channel depth, from Jiang & Leblond (1994)
h_b	Landslide thickness, from Sue *et al.* (2011)
k	Wavenumber, from Guyenne & Grilli (2006) and Lynett & Liu (2005)
L_b	Landslide length, from Sue *et al.* (2011)
l	Landslide length, from Liu *et al.* (2003)
R	Radius of curvature of slump failure surface, from Watts *et al.* (2005)
T	Landslide thickness, from Watts *et al.* (2005)
V	Landslide volume, from Murty (2003)
x_0	Landslide centre of mass position, from Sue *et al.* (2011)
α	Landslide shape variable, from Tinti *et al.* (2001)
Γ_b	Bottom boundary, from Grilli & Watts (1999)
Γ_f	Free surface boundary, from Grilli & Watts (1999)
Γ_{r1}	Sloping surface boundary, from Grilli & Watts (1999)
Γ_{r2}	Reflective offshore boundary, from Grilli & Watts (1999)
γ	Landslide specific density, from Watts *et al.* (2005)
γ_{ref}	Reference landslide specific density, from Watts *et al.* (2005)
ζ	Wave amplitude, from Tinti *et al.* (2001)
η	Wave amplitude, from Sue *et al.* (2011) and Jiang & Leblond (1994)
$\eta_{0,2D}$	Characteristic two-dimensional tsunami amplitude, from Watts *et al.* (2005)
$\eta_{0,3D}$	Characteristic three-dimensional tsunami amplitude, from Watts *et al.* (2005)
θ	Slope angle, from Watts *et al.* (2005), Sue *et al.* (2011), Grilli & Watts (1999) and Jiang & Leblond (1994)
μ	Landslide aspect ratio, from Liu *et al.* (2003). Also used as the (mud) landslide density in Jiang & LeBlond (1992)
$\Delta\Phi$	Angular displacement along failure surface, from Watts *et al.* (2005)

Literature review - previous physical experiments

a	Wave amplitude, from Watts (2000)
b	Horizontal projection of landslide length, from Watts (2000)
d	Initial landslide submergence depth, from Watts (2000). Also used as the channel depth by Enet & Grilli (2007)
d_{ref}	Reference depth, from Enet & Grilli (2007)
h	Channel depth, from Watts (2000) and Panizzo *et al.* (2002)
t_0	Duration of landslide acceleration, from Watts (2000)
U	Ursell parameter, from Watts (2000)
w	Channel width, from Panizzo *et al.* (2002)
β	Length of curved section of overflow structure, from Panizzo *et al.* (2002)
δ	Landslide block thickness, from Panizzo *et al.* (2002)
λ	Wavelength, from Watts (2000). Also used as the landslide block length by Panizzo *et al.* (2002)

Chapter 1

Introduction

1.1 Tsunami, a coastal hazard

A tsunami, defined as an impulsively driven water wave, is a significant hazard to communities and associated infrastructure in coastal areas. These waves are characterised by their large wavelengths, long periods and extremely high wave celerities. Although the amplitude of a tsunami is small in the deep ocean, the wave amplitude increases rapidly due to wave shoaling and geometric focussing as the wave approaches the shore. This led to the origin of the word tsunami, which is the Japanese word meaning 'harbour wave', since such waves could be undetected by ships at sea, yet cause significant amounts of damage on reaching a harbour.

New Zealand is an island nation located in a seismically active region of the world. This puts coastal areas of the country at risk from locally-generated tsunami waves. A seismic event in South America or elsewhere in the Pacific Ocean also has the capacity to generate a tsunami which could affect New Zealand. As such, an improved understanding of tsunami waves is important to allow New Zealand (and other at-risk countries) to be better prepared for their occurrence.

1.2 Types of tsunami

Tsunami are classified by their source mechanism, which can be a coseismic displacement of the seafloor, a subaerial or submarine landslide, an underwater volcanic eruption or a bolide (cometary) impact. Tsunami waves caused by coseismic displacement of the seafloor typically have very long wavelengths, but small initial amplitudes. This is because an underwater fault rupture has an associated vertical scale of only a few metres, but a horizontal scale of hundreds, if not thousands, of kilometres (Synolakis *et al.*, 2002). This means that the waves are less affected by frequency dispersion, giving them the ability to cross oceans without significant attenuation. An example of

this type of tsunami is the Boxing Day tsunami of December 26, 2004, which claimed over 240,000 lives in Indonesia, Thailand and Sri Lanka. Landslide-generated tsunami have higher amplitudes and shorter wavelengths by comparison, since the vertical scale of a submarine mass failure can be up to 100m, while its associated horizontal scale is usually less than 100km (Synolakis *et al.*, 2002). Such high-amplitude waves are very dangerous in the immediate vicinity of the landslide, since their location and high speed leave little evacuation time for nearby communities. They do not, however, possess the same potential for transoceanic devastation as a tsunami generated by underwater fault rupture. Since tsunamigenic landslides can themselves be triggered by earthquakes, sometimes the two source mechanisms are difficult to distinguish.

Research concerning tsunami can be broadly divided into the categories of prediction, replication and observation. Predictive models estimate wave properties for a particular forcing scenario, and can be used to improve warning systems and mitigation strategies for coastal communities. These models often are calibrated by laboratory experiments to check predictions against a small-scale idealised case. Field observations can compare model behaviour to full-scale events, and can be used to assess the effectiveness of warning systems and coastal defence measures.

1.3 Description of project

This study investigates the generation and propagation of waves generated by a submarine landslide, and the dependence of wave properties on the landslide motion and initial submergence depth. The landslide is modelled as a solid block moving along a horizontal bottom boundary, with motion controlled by a mechanical system. The use of a horizontal bottom boundary allows the properties of both onshore- and offshore-propagating waves to be measured, and the mechanical system enables the testing of a broader range of motion than has been previously possible in such experiments. Although this experimental geometry is not representative of field situations, it allows the properties of onshore-propagating waves to be investigated without the interference of a slope. Since the continental slopes down which such landslides move are often shallow (1° to 10°), the tests can yield results which are reasonable in a local sense. Two-dimensional experiments are carried out in a long flume to allow sufficient distance for waves to propagate.

The laser-induced fluorescence (LIF) technique described in Sue (2007) provides measurements of the spatial and temporal variations in free surface levels during the experiments. The particle tracking velocimetry (PTV) technique also provides spatial and temporal resolution of the subsurface velocities imparted to the fluid by the landslide motion, to investigate the transfer of energy from the moving landslide to the generated waves.

The amplitudes of the experimentally measured waves, as well as the potential energy within the wave field, are compared to the predictions of three numerical models. Two of the models are based on inviscid-irrotational flow theory, and the final model is a viscous model. One of the inviscid-irrotational models assumes a linear bottom boundary, and is solved in a semi-analytical manner by a spectral decomposition of wave modes (following the work of Sue (2007)). The second inviscid-irrotational model includes the full nonlinear bottom boundary condition, and is solved using a boundary element method (BEM). Comparisons between the predictions of the three models and the experimental results allows the applicability of the model assumptions to the physical problem to be tested.

The effect of an added lateral dimension on the landslide-generated waves is investigated by extending the linear inviscid model to three dimensions. A series of preliminary simulations compare the waves generated by the infinite landslide width assumed in the two-dimensional model to a series of finite landslide widths.

1.4 Outline of thesis chapters

Chapter 2 reviews the literature on landslides as a tsunami source mechanism, and previous research to investigate tsunami generated in this manner. Previous work is divided into post-tsunami studies, numerical simulations and physical experiments. Following this review, the objectives of this study are discussed in detail in chapter 3.

Chapter 4 lists the aims of the two-dimensional experiments. The chapter includes the experimental setup and a detailed description of the mechanical system used to control landslide motion. The chapter describes a series of initial particle tracking velocimetry (PTV) experiments used to test the repeatability of the landslide motion over a range of parameters. The chapter also provides a description of the flow visualisation techniques used within this study, as well as the image capture and post-processing procedures associated with each technique.

Chapter 5 gives details of the formulation of the numerical models used in this project. The chapter describes the model domain, the assumptions used in the model formulation, and the solution of the governing equations. The semi-analytical solution method employed in the linear inviscid model is discussed, providing solutions for the free surface wave amplitudes, the subsurface fluid velocities and the subsurface pressure field. The chapter also discusses the application of the nonlinear inviscid model (published in Sue *et al.* (2011)) to the geometry used in the current project, and the formulation of the problem within the viscous DNS solver Gerris. The extension of the free surface solution of the linear inviscid model to three dimensions is discussed, so that waves generated by a finite-width landslide may propagate in two horizontal directions.

Chapter 6 presents the nondimensional framework used to interpret the results of the physical experiments, and compare these to the predictions of the different numerical models. This chapter also gives details of the parameter space investigated during the physical experiments and the model simulations. The three nondimensional parameters varied during the experiments were the landslide acceleration, Froude number and submergence depth.

Chapter 7 shows the results of the two-dimensional LIF experiments, and describes the parametric dependence of the generated wave properties. The chapter describes the potential energy within the wave field, and compares the potential energy and mass within the onshore and offshore regions of the wave field. The chapter also investigates the nonlinear behaviour of a group of waves at higher landslide Froude numbers.

Chapter 8 compares the model predictions to the experimental measurements, and investigates the dependence of these predictions on the parameters of landslide motion. The effect of the model assumptions on their predictive abilities are determined by comparing the surface wave properties predicted by the models to the experimental measurements.

Chapter 9 presents the results of a series of preliminary simulations carried out using the extended linear inviscid-irrotational model. The effect of the landslide width on the generated waves is described, and future applications of the model are discussed.

Chapter 10 presents the conclusions of this project, including the ability of the numerical models to predict the waves generated by the motion of the submarine landslide. Suggestions for future work are also provided in this chapter.

Chapter 2

Literature review

2.1 Overview

The destructive nature of tsunami has been highlighted by the Indian Ocean tsunami of December 26, 2004 (Lay *et al.*, 2005), and the Japan tsunami of March 11, 2011 (Goto *et al.*, 2011). These extreme events, combined with a more connected global community, have increased international awareness of tsunami as a dangerous coastal hazard. Global sea level rise due to climate change has the potential to further increase the risk of inundation for low-lying coastal areas.

Landslides are one of the most common generation mechanisms for tsunami, although at times this source mechanism can be unclear due to seismic triggering of the landslide itself, as discussed in Synolakis *et al.* (2002). The threat of landslide-generated tsunami is not limited to coastal communities, as landslides can generate destructive waves in alpine lakes (Carvalho & Carmo, 2007; Anselmetti & Bussmann, 2010). Section 2.2 of this literature review describes the general properties of a tsunamigenic landslide, in terms of the environments prone to submarine landsliding, the failure mechanisms of submerged sediments and the post-failure motion of a landslide. Within this review, the term *landslide* is taken to refer generically to a submarine mass failure of any kind, while the terms *flow*, *slump*, and *slide* refer to particular types of mass failure, based on their post-failure motion.

Many tsunami events require field investigations to determine their source mechanism, physical processes, or how near-shore conditions (such as shoaling or wave focussing due to local bathymetry) affect the generated waves. Section 2.3 discusses historical tsunami events, and the field surveys and modelling used to gain an improved understanding of these events. Field surveys help to determine the source mechanism of the tsunami, the properties of the generated waves (where available), and quantitative measurements of the impact of the tsunami on the coastline.

The goal of much tsunami-related research is the ability to accurately forecast the

properties of tsunami waves, given the characteristics of the tsunami source (such as the size and location of a submarine landslide). Section 2.4 presents a framework for the formulation of any mathematical tsunami model, including consideration of the problem domain, boundary conditions, landslide and ambient fluid. The framework includes the different levels of approximation used for the generated waves, and a discussion on the compromise between the model's ability to provide realistic prdictions and its computational efficiency.

Section 2.5 discusses the mathematical models used to simulate tsunami generated by submarine landslides. The simplest mathematical models in the past have used empirical equations derived from relationships between properties of the wave forcing and amplitudes of generated waves (often from data collected from field events or laboratory studies). More advanced models either use analytical solutions to idealised problems, or numerical solutions for more complex problem formulations. Improvements in computing technology have enabled the development of numerical models which can use realistic bathymetry or solve the full equations of motion directly with fewer simplifying assumptions.

Although mathematical models are able to simulate events at field scales, laboratory experiments into landslide-generated tsunami provide an important tool for the validation of such models. The essential aspects of a laboratory experiment are that it provides a reasonable approximation to a tsunami wave (some experiments model the generation mechanism itself, while others use wave-makers to generate an appropriate wave spectrum), and that properties of the generated waves can be measured accurately. A key requirement in any physical experiment is repeatability, so that multiple repetitions of the same experiment yield the same results to within a suitable measurement tolerance. Section 2.6 contains a summary of previous physical models used to validate numerical models or replicate historical events.

An important outcome of tsunami-related research is the ability to assess the tsunami hazard for a particular location, so that coastal communities are able to effectively mitigate the hazard. In the interests of reducing fatalities caused by tsunami events, hazard mitigation is best achieved with an emphasis on community involvement, by raising awareness of the hazard and encouraging community participation in evacuation plans and tsunami drills. Section 2.7 discusses some of the methods used to assess the likelihood of a tsunami event, and describes initiatives used to improve education and community participation in hazard mitigation.

2.2 Submarine landslides as a tsunami source mechanism

2.2.1 Submarine landslide hazard

Certain submarine environments are known to be susceptible to landsliding, with conditions including the rapid accumulation of sediment, a sloping seafloor, and environmental stresses or forcing mechanisms (Hampton *et al.*, 1996). Environments where deposition is significantly larger than erosion are more prone to landsliding, since the sediment may be deposited in an unstable manner. A sloping seafloor ensures that gravity acts as a destabilising force on the sediment mass, and environmental stresses may be present in locations with extreme tidal ranges, large waves, or dissolved gases. Locations with an abundance of fine-grained sediments appear to be more susceptible to slope failure than those which receive mainly coarse-grained sediments (Masson *et al.*, 2006). The oceanic environments which meet these criteria, and hence have high susceptibility to landsliding, are fjords, active river deltas on the continental margin, the open continental slope, and oceanic volcanic islands and ridges. Since landslides can be triggered by seismic activity (explained further in section 2.2.3), if such environments exist in a region of high seismicity then the likelihood of a tsunamigenic landslide is increased. Although the regions at risk from landsliding can be identified relatively easily using these criteria, the forecasting of specific landslide events is still unattainable at our current level of understanding (Masson *et al.*, 2006).

2.2.2 Landslide classification

In the broadest sense, a landslide is the failure of a mass of rocks and sediment along a rupture surface, followed by the downslope motion of that mass. Although the failure of a slope can be due to a variety of contributing factors, the essential features of a landslide are the displaced mass (and volume) of material, and the characteristics of the failure surface (Hampton *et al.*, 1996). Classification of landslides is concerned with three key areas: the properties of the (undisturbed) sediment, the failure mechanism, and the post-failure motion of the sediment (Locat & Lee, 2002). The water depth above the sea floor and the angle of the slope, along which the submerged mass moves, may also be used to classify landslides (Masson *et al.*, 2006).

A submarine landslide (a landslide initiated below the water surface) behaves differently to a subaerial landslide (a landslide initiated above the water surface), partly due to the lack of an impact on the water body in the submarine case. Due to the availability of sediment in a submarine environment, submarine landslides tend to have much larger volumes than subaerial landslides (Blasio, 2011; Hampton *et al.*, 1996).

This has important implications for tsunami generation, as the size of the generated waves tend to scale with the volume of displaced sediment (Sue, 2007). The type of sediment can also differ between subaerial and submarine mass failures, with submarine mass failures tending to comprise finer-grained sediments, such as clays or sands that have been transported to the continental shelf by rivers or glaciers (Blasio, 2011). Subaerial landslides occur on steeper slopes than submarine landslides. The presence of an ambient fluid affects both the failure mechanism of the mass, and the motion of the mass after failure has occurred (water as an ambient fluid tends to increase the mobility of landslides). For this reason, the gravitational force on submarine landslides is relatively weak compared to a subaerial slide (due to the gentler slopes in submarine environments), however a submarine slide will generally contain a much larger volume of sediment, and run out over greater distances, than a subaerial slide.

The slide material can be classified by its component materials, its dimensions and its location. If available from geotechnical investigations (methods used in these investigations are summarised in Locat & Lee, 2002), a grain size distribution can be used to classify the type of landslide material. The water content, solid concentration and cohesive or granular structure of the slide material can be used to classify the mass motion, as shown in figure 2.1, from Locat & Lee (2002).

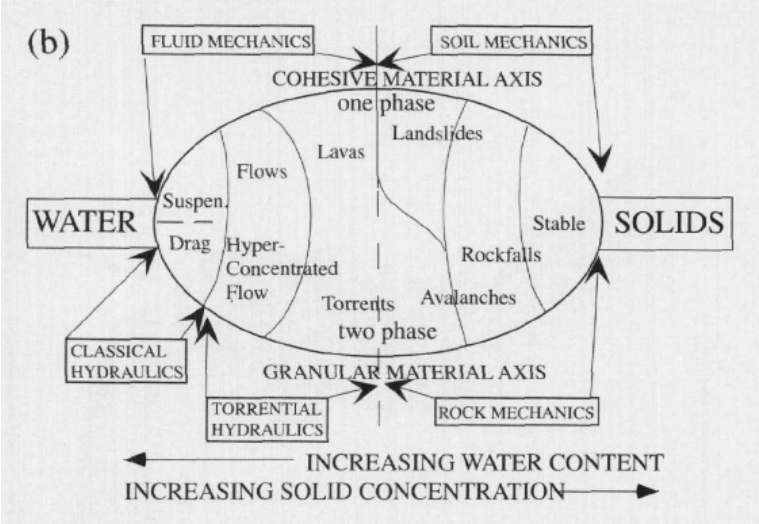

Figure 2.1: Classification of submarine mass movements, from Locat & Lee (2002).

The volume, area, length and thickness of the landslide are often estimated using the results of bathymetric surveys and seismic reflection surveys after an event has occurred. The landslide geometry can be deduced from the location of the scarp(s) and the toe of the displaced mass. If failure is retrogressive (a series of failures that propagate upslope) then there may be multiple scarps present for a single mass failure. Recognition of these features can be problematic for historical mass failures, as the features will become harder to identify after being subjected to long-term geological

effects. It may also be difficult to distinguish traces of submarine landslides from bathymetric features caused by other submarine processes, such as submarine dune formation (Hampton *et al.*, 1996).

2.2.3 Failure mechanisms

Due to the differences between submarine and subaerial landslides (discussed in the previous section), the physical mechanisms by which submerged masses fail are usually different to the physical mechanisms causing the failure of subaerial masses. The failure of submarine slopes can usually be attributed to a combination of geological factors and external factors. Human factors may also contribute to slope failure, as in the case of construction work leading to the slope failure at Nice Airport (Ioualalen *et al.*, 2010). As such, it is difficult to make general statements about the failure mechanism of a submerged mass, since the specific factors will vary depending on the submarine environment, and also between different failure events.

Mechanically, a slope will fail when the sum of the stresses on the slope material, acting with the gravitational force to destabilise the slope, exceeds the (stabilising) frictional strength of the material (Locat & Lee, 2002). The combination of factors reducing the strength of the slope material and factors increasing stress on the slope material is summarised in figure 2.2, from Hampton *et al.* (1996). The Mohr-Coulomb failure criterion is generally used to define the shear strength of a soil,

$$\tau_f = c' + (\sigma - u) \tan \phi' \tag{2.1}$$

where τ_f is the shear strength of the material, c' is the effective cohesion, ϕ' is the friction angle, σ is the normal stress to the failure surface and u is the pore water pressure (Hampton *et al.*, 1996).

Hampton *et al.* (1996) show that, for a semi-infinte inclined slope, the angle of slope declination at failure will be equal to the friction angle of the sediment. Slopes subject to large amounts of wave or earthquake loading will tend to a certain angle of declination, called the angle of repose (this will be shallower than the static angle of repose under gravity loading only).

Both earthquakes and storm waves tend to apply shear stress to the sediment mass in a cyclic fashion, and as such the pore water pressure generated by the loading may not be able to fully dissipate between cycles, leading to an undrained-type failure condition. If, however, pore water pressure is able to dissipate between loadings, the sediment may actually exhibit an increase in its frictional strength (Locat & Lee, 2002). Excess pore water pressure may also be caused by gas hydrate disassociation (referred to as 'Gas' in figure 2.2) under certain changes to temperature and/or pressure. During periods of decreased sea level in the glacial cycle, the lowered pressures may lead to

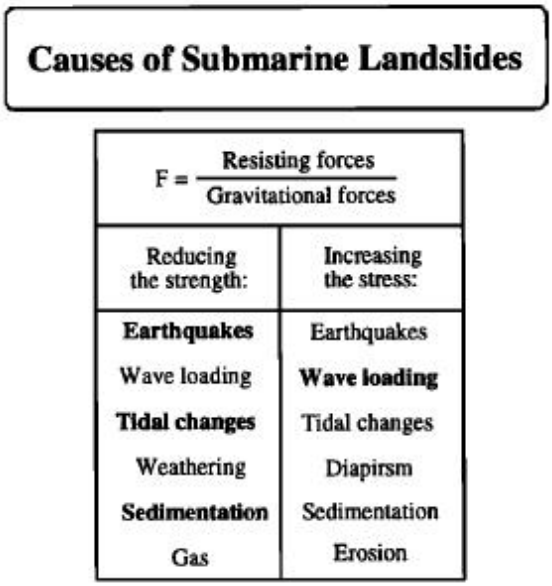

Figure 2.2: Causes of submarine landslides, from Hampton *et al.* (1996). Processes in bold type are considered to be relatively more significant.

relatively more frequent failures of this kind. Thus, the effect of sea level rise due to climate change may actually increase slope stability based on the contribution of gas hydrate disassociation alone.

Sediment failure can also be defined as disintegrative or nondisintegrative. In the case of a nondisintegrative failure, failure occurs due to soil deformations (such as those induced by an earthquake), but the post-failure deformations are relatively small. A disintegrative failure occurs when the loading reduces the soil strength to less than the downslope static force due to gravity. In this case, a large amount of deformation occurs after the failure of the slope, and sediment will move as a liquid, or flow (see 2.2.4).

2.2.4 Post-failure motion characteristics

The post-failure motion of the submerged mass is governed by the local bathymetry (providing a geometric constraint on the landslide motion), the properties of the slide material and the nature of the failure plane. If a landslide were to occur in a canyon or channel, the mass would run out over a much larger distance than if motion was not constrained by the canyon walls. Very mobile sediment failures are classified as flows, since the sediment essentially behaves as a fluid during its motion. Sediment material can flow depending on the excess of porosity over a critical value, the water content of the sediment and whether the failure was disintegrative or nondisintegrative. A disintegrative failure occurs under contractive behaviour, if positive excess pore pressure exists within the soil, and a nondisintegrative failure occurs under dilative

behaviour, if negative excess pore pressure exists within the soil. Disintegrative failures are more likely to lead to mobile mass flows (Hampton *et al.*, 1996).

Landslides which do not mobilise into flows can move as (translational) slides or (rotational) slumps, depending on the nature of the failure plane. A failure plane which is concave outward will cause a rotational motion of the submerged mass, while a failure plane which is linear will cause the mass to translate along the failure plane. The mobility of a particular landslide can be considered in terms of the retrogression of the failure, the run-out distance of the failed mass and the elevation difference between the crest of the slide and the end of the debris flow, as shown in figure 2.3 (from Locat & Lee, 2002). A term commonly used to describe landslide mobility is the Farboschung, defined as

$$F = \Delta H / L \tag{2.2}$$

where ΔH is the elevation difference between the slide crest and the tip of the debris, and L is the run-out distance, including the slope regression (see figure 2.3).

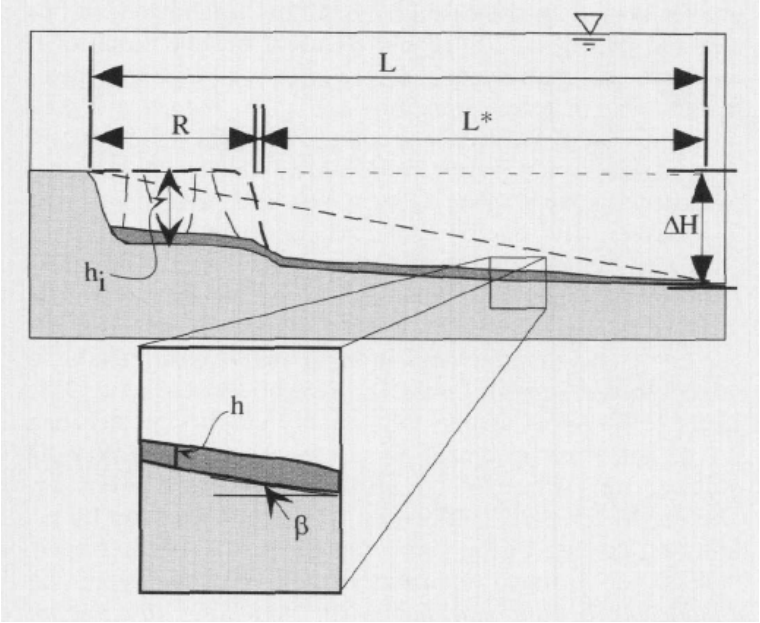

Figure 2.3: Geometric description of slide mobility, where h is flow thickness, h_i is the height of the initial mass, and β is the slope angle. From Locat & Lee (2002).

The forces acting on a moving submerged landslide are summarised in figure 2.4 (from Locat & Lee, 2002). Erosion of slope material and deposition of slide material occur along the failure and run-out slope due to basal shear. Hydroplaning of the landslide front causes lifting of the frontal lobe, resulting in the development of a more well-defined front to the landslide. Slide material at the top of the moving landslide mixes with the ambient water, creating a large turbidity current which spreads behind the slide.

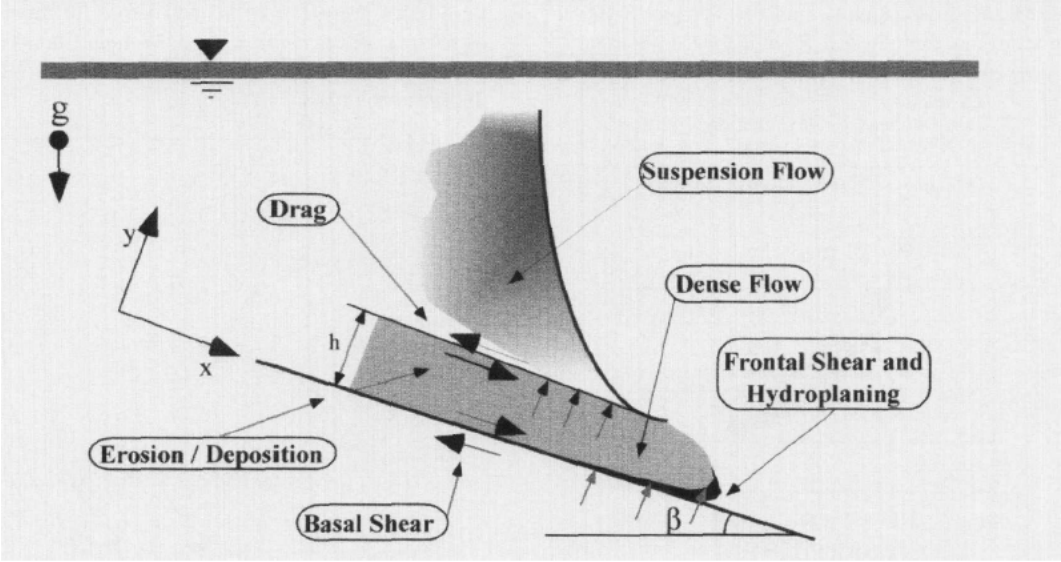

Figure 2.4: Forces acting on a submerged landslide during its motion, from Locat & Lee (2002).

The reduction of shearing resistance at the landslide front due to hydroplaning has been postulated to be one of the factors contributing to the much greater run-out distances of submarine slides, compared to subaerial slides. The suspension flow can also continue to move as a turbidity current after the dense part of the landslide has come to rest, resulting in a long run-out distance.

In summary, submarine mass failures can mobilise far greater volumes of (finer-grained) sediment, and move greater distances, than subaerial slides. Submarine slides also tend to occur on shallower slopes, and under different failure mechanisms. The build-up of excess pore water pressure (which can be due to earthquake or wave loading) is an important factor in the failure mechanism of a submarine sediment mass. Sloping submarine environments with high sediment deposition rates and the presence of environmental loadings are the most susceptible to mass failures. Future coastal developments in such areas need to account for the high likelihood of mass failures and resulting tsunami waves.

2.3 Historical landslide-generated tsunami and post-tsunami studies

Throughout history, landslide-generated tsunami have claimed thousands of lives and caused millions of dollars of economic loss. The landslide source mechanism of such tsunami has been discussed in section 2.2. This section focuses on the events themselves, and any field investigations which were undertaken following the events. Post-tsunami studies are an important aspect of tsunami-related research, as they provide field data

for calibration of numerical predictions. Lessons learned from these investigations can also improve hazard mitigation systems (discussed in section 2.7).

Field investigations after the occurrence of a landslide-generated tsunami (or tsunami in general) seek to gather information about the tsunami source mechanism and the properties of the waves themselves. Data gathered can vary, depending on the objectives of the study, and are often used in subsequent modelling of the event. Each historical landslide-generated tsunami included in this section is described, followed by a discussion of the objectives, methods and findings of the field investigations. Where appropriate, this discussion includes the application of numerical modelling to the event, and any future work or ongoing issues.

2.3.1 Mona Passage, 1918

On October 11, 1918, a magnitude 7.5 earthquake in the Mona Passage (between Puerto Rico and the Dominican Republic) was followed by a tsunami which claimed approximately 100 lives and caused over $4 million in damages. The increased population and development in the region since that time means that economic and human losses would be much more severe if such an event were to occur again.

Reid & Taber (1919) undertook a field investigation shortly after the earthquake to quantify the timing of the waves, runup levels and damage caused. They found that two underwater telegraph cables were ruptured during the event, and were buried for several kilometres under sedimentary debris. The tsunami evidenced itself as a leading depression wave, although the timing reported varied considerably depending on the location of the witness.

Initially the tsunami was assumed to be caused by the rupture of the Mona Canyon Fault. Modelling of this tsunami generation scenario led to good agreement with observed tsunami arrival times, but not with the observed wave runup and polarity (the model predicted a small leading crest followed by a large trough, rather than the observed leading trough).

Lopez-Venegas *et al.* (2008) used multibeam bathymetry data to identify an escarpment, possibly caused by a mass failure in the earthquake event, with an excavation volume of approximately 10 km^3. They compared observed runup and inundation values to a simulated rotational submarine landslide tsunami source using the COULWAVE package. The model predicted wave arrival times to within ± 1 minute, except at Mayagüez. At this location, the model predicted an arrival time 18 minutes after the earthquake, however eyewitness records state that the wave arrived 25 minutes after the earthquake. The model over-predicted the run-up levels, with an average over-prediction of 1.5 m, or 33%. The rupture of the submarine telegraph cables supports a combined source mechanism of a fault rupture and submarine landslide.

2.3.2 Tafjord, Norway, 1934

On April 7, 1934, a large quantity of rock slid into the Tafjord, in Western Norway. The fjord itself is approximately 9 km long, 1 km wide and 200 m deep. The gneiss rock slide, with an estimated volume of 1-1.5 million m^3, generated waves within the fjord that caused 41 deaths in the nearby villages. Runup levels exceeded 10 m in some locations near to the village of Tafjord (the innermost village on the fjord), and exceeded 30 m in some locations (for example, across the fjord from the slide impact location). Eyewitness accounts describe the village of Tafjord being hit by three large waves, separated by intervals of 3 to 5 minutes.

The long time intervals between the large waves has been attributed to wave reflections and the generation of cross-fjord seiche modes (from numerical modelling work by Harbitz *et al.*, 1993). This also supports observations that the sea within the fjord did not calm until approximately 8 hours after the occurrence of the landslide. The trapping of energy within the fjord was attributed to the generation of seiche modes in the cross-fjord direction, as well as wave reflection by a bend in the fjord.

2.3.3 Lituya Bay, 1958

One of the most notable landslide-generated tsunami in recent times occurred in Lituya Bay, Alaska, see Figure 2.5. An earthquake (Mw 8.3) on 10 July 1958 triggered a subaerial landslide which plunged into the Gilbert Inlet. The slide had an estimated initial elevation of 915 m, a slope of 40°, a density of 2.7 t/m^3, and an estimated volume of 30.6 million m^3 (Fritz *et al.*, 2009). The landslide was assumed to be prismatic in shape, and composed of amphibole and biotite schist (Weiss *et al.*, 2009). This landslide created a giant tsunami with a resulting runup of 524 m, which is the highest wave runup in recorded history. Since this event occurred in a relatively unpopulated area of Alaska, no casualties were recorded despite the extreme nature of the event. Due to the isolation of the bay, post-tsunami studies were only able to deduce runup levels based on the trim lines of the trees caused by the waves.

Large waves are estimated to have occurred within Lituya Bay about five times in the past two centuries (Fritz *et al.*, 2009). The material and steepness of the slopes, climate and seismicity of the region are all contributing factors to the frequency of large waves within the bay. Fritz *et al.* (2009) investigated whether similar runup values could be obtained in physical experiments. Numerical simulations and physical model studies of this event carried out by Fritz *et al.* (2009) and Weiss *et al.* (2009) are described in more detail in sections 2.5 and 2.6.

Figure 2.5: Satellite image of Lituya Bay showing 1958 tsunami, from Weiss *et al.* (2009)

2.3.4 Resurrection Bay, 1964

On 28 March, 1964, a magnitude 9.2 earthquake occurred in the Prince William Sound, Alaska, about 150 km northeast of the town of Seward. The earthquake was followed by a tsunami, which caused 122 of the 131 casualties associated with the earthquake. In addition to generating a large tsunami, the earthquake triggered over twenty tsunamigenic subaerial and submarine landslides in the region. These local tsunami were estimated to account for approximately 76% of the total tsunami casualties (Suleimani *et al.*, 2009). The high casualty rate from the local tsunami is due to the short times available for warning or evacuation before the waves impacted the shoreline.

Post-event geological investigations and eyewitness interviews suggested the submarine slope failures, triggered by the earthquake, were the source of the local tsunami that caused most of the damage to the town of Seward. Bathymetric data and subbottom profiles of Resurrection Bay (Lee *et al.*, 2006) also provided evidence of significant amounts of submarine sliding. The total volume of slide material was estimated to be approximately 211 million m^3 (Suleimani *et al.*, 2009). Although the dynamic forces induced by the earthquake were the primary triggering mechanism for the slope failures, factors such as the low tidal level at the time of the earthquake, high artesian pressure within the aquifers of the river deltas and shoreline development may have also contributed to the slope failures.

Suleimani *et al.* (2009) carried out numerical modelling of this event to recreate the sequence of tsunami waves observed in Resurrection Bay, and to test the hypothesis that the local tsunami were produced by a number of different slope failures. A three-

dimensional model of a viscous underwater slide with full interactions between the deforming slide and the waves it generated was adopted for this case (discussed in more detail in section 2.5). The model was initially proposed by Jiang & Leblond (1994). The model used the long wave approximation for water waves and the deforming slide. The slide was assumed to be a viscous incompressible fluid. Although the long wave approximation could be inaccurate for steep slopes, studies of the validity of the long wave approximation for slopes greater than 10° (Rabinovich *et al.*, 2003) suggested that the possible error arising from the use of this approximation for the slopes in this study (which ranged from 10° to 20°) was around 10%. The numerical experiment consisted of three steps. First, the slides closest to the town of Seward were modelled separately, then the three slides were modelled together, and finally all ten slides in the vicinity were modelled together. The combination of the three closest slides reproduced the timing of the maximum wave height at the town of Seward, obtaining a wave of 7 m height arriving 100 s after the earthquake (eyewitnesses described a wave of height 6-8 m, arriving 1.5-2 minutes after the earthquake). The more distant slides had a greater effect on the waves arriving at Fourth of July Creek (a small creek on the opposite side of Resurrection Bay to the town of Seward).

The numerical modelling and bathymetric surveys undertaken after the 1964 event were of particular importance, since the future tsunami hazard due to submarine landslides is very high for Resurrection Bay. The probability of future tsunami is attributed to the high accumulation rates (approximately 1.5 cm/year, from Suleimani *et al.*, 2009) of fine-grained sediments at the head of the fjord. Future sediment failures may occur due to earthquake shaking or other undrained-type failures, such as extreme low tides or construction activities.

2.3.5 Nice Airport, 1979

On October 16, 1979, a submarine mass failure occurred in the Ligurian Sea near Nice (Ioualalen *et al.*, 2010). This sudden failure occurred at shallow water depth, and within minutes the extension of Nice Airport slid into the sea. Following this, the coastline was impacted by a series of waves, of approximately 3 m in height. A total of ten lives were lost in this event, nine on the sliding masses at the airport and one at a subsequently-inundated beach 10 km away. No earthquake was reported at the time of the event. Available information on the tsunami was limited to eyewitness accounts of the timing and amplitude of the waves as they impacted the shoreline.

Klaucke & Cochonat (1999) present results of a detailed investigation of the seafloor in the area using deep-towed side-scan sonar imagery, collected in a cruise in 1986. Three different failure types were identified from the gathered data. These failure types, which depended on the location examined, were superficial slumping, deep-

seated failure, and gullying of the canyon walls. Each failure type was associated with a particular depositional setting, triggering mechanism, and frequency, allowing the hazard potential of each event to be determined. Deep-seated failures were found to have a high tsunami hazard potential.

Ioualalen *et al.* (2010) modelled this tsunami as the result of two phases of submarine mass failure using the GEOWAVE software package (Watts *et al.*, 2003). The first was the shallow-depth failure (possibly due to construction activities), and the second was a deeper failure (at a depth of approximately 800 m). When the two slides were considered separately (after confirming that dispersive effects were relatively unimportant for the study), they accounted for a significant part of the event, although not its entirety. The study investigated focusing of wave energy due to local bathymetry, and identified the region's susceptibility to future submarine mass failures.

2.3.6 Skagway Harbour, 1994

On November 3, 1994, an underwater landslide in Skagway Harbour (contained within Taiya Inlet, Alaska) caused a large-amplitude oscillatory wave group within the harbour which lasted for approximately one hour. An analog tidal gauge on the west side of the harbour recorded waves of crest-trough heights of 2 m, with periods of approximately 3 minutes. Eyewitness accounts reported that the wave heights were 5-6 m in Taiya Inlet, and 9-11 m at the shoreline. The discrepancy between these two reported wave heights can be explained by the nonlinear response of the tidal gauge at short periods (Kulikov *et al.*, 1996). The landslide and tsunami caused over $20 million in damage (Rabinovich *et al.*, 1999), and killed one dock worker. Much of the wave energy was trapped in the harbour due to the large variation in depth between the harbour and Taiya Inlet.

The slope failure occurred beneath the Pacific and Arctic Railway and Navigation Company dock (a finding supported by a geomorphologic study of the harbour Rabinovich *et al.*, 1999), and was likely caused by excess pore water pressure in the slope sediments at the extreme low tide level. Other explanations of the tsunami source included a distant coseismic source, or slope failures within Taiya Inlet which propagated into Skagway Harbour. Waves generated by a distant tsunami source would have dispersed before entering the harbour, however no dispersion was evident in the recorded waves within the harbour (additionally, no tsunamigenic earthquakes occurred within Alaska, western Canada or the Pacific Ocean on or near this date). The landslide in the harbour generated waves which formed a cross-inlet seiche in the Taiya Inlet and excited resonance within the harbour itself, explaining the long duration and lack of dispersion of these waves. An estimation of eigenoscillations of the harbour found that the first mode corresponded to a period of 3.19 minutes, which is very close to the 3

minute recorded wave period. Combined with the data from the tidal gauge, Kulikov *et al.* (1996) used these findings to discount the possibility that the waves within the harbour were caused by a distant source or a local seismic source.

Theoretical estimates of wave height, using the method of Murty (2003), showed that the landslide was a failure of the entire area beneath the Pacific and Arctic Railway and Navigation Company dock (Kulikov *et al.*, 1996). This discounted another possible explanation that the tsunami was generated by a failure of the the area opposite the site of a new wharf construction, as the dimensions of the suggested failure zone would generate waves of approximately 2 m amplitude, instead of the observed amplitude of 6 m. Numerical simulations, conducted using the model of Jiang & Leblond (1994), also supported these conclusions, as they reproduced the general form of the waves recorded by the tidal gauge (Rabinovich *et al.*, 1999). However, the predicted waves had a lower amplitude than the observed waves (with differences as large as 50% at times), and had an average period approximately 20 s smaller than the observed waves.

2.3.7 Sissano Lagoon, 1998

The Sissano Lagoon, Papua New Guinea, tsunami of 17 July 1998 has caused some confusion in the classification of its source mechanism. Following a magnitude 7.1 earthquake, a tsunami with waves over 10 m in height devastated a 40 km stretch of coastline. A photograph of the aftermath of the tsunami is shown in figure 2.6, from Lynett *et al.* (2003). The waves caused approximately 2200 casualties in the area. The first survey of the area found one location where the wave heights were up to 15 m, with flow velocities overland of up to 15 m/s (Imamura & Hashi, 2003). Field surveys, described in Lynett *et al.* (2003), also give detailed data on runup levels in the area. Distant tidal gauges located in Japan recorded wave heights not exceeding 20 cm (Synolakis *et al.*, 2002), showing that the tsunami exhibited geographical concentration. Satake & Tanioka (2003) determined that both the earthquake source and an additional local source (such as a submarine slump) were necessary to reproduce the near-field and far-field tsunami amplitudes.

A field investigation was carried out to locate the earthquake faults and possible locations of underwater landslides, using the SEABEAM 2112 multibeam bathymetric survey system (Matsumoto & Tappin, 2003). Piston core samples were obtained at four different stations to deduce the possibility of the occurrence of turbidity currents caused by underwater landslides. After this initial survey, two additional surveys were carried out using remotely-operated vehicles to gain additional visual observations and geological data within the study area. The upper slope of a large-scale underwater mass slump was identified from the results of these cruises (Matsumoto & Tappin, 2003), and this slump was determined to be large enough to generate the locally-concentrated

waves observed during the tsunami event.

Figure 2.6: Photograph of destruction caused by 1998 Sissano Lagoon tsunami, from Lynett *et al.* (2003)

To complement field observations of runup and eyewitness accounts of timing, many numerical models have been used to investigate the interactions between the submarine source and the generated waves. Heinrich *et al.* (2001) studied this event using a numerical model based on the nonlinear shallow water equations. The submarine mass failure was modelled separately as the flow of a viscous fluid, and as a fluid-like flow of cohesionless granular material. The shallow water model was validated by comparison with a more complicated Navier-Stokes model. The granular model for the landslide performed better than the viscous fluid model at reproducing the observed runups. Issues with the model included the uncertainty concerning the initial position and volume of the slump, and the applicability of the numerical model for modelling a slump-type failure.

Synolakis *et al.* (2002) studied the post-tsunami seismic, land, bathymetric and hydroacoustic surveys to determine the origin of the tsunami. They modelled the source of the tsunami as a coseismic displacement of the seafloor and compared the magnitude and timing of the tsunami runup with a slump source. The coseismic source was modelled numerically by translating the vertical displacement of the seafloor directly to the free surface. The numerical model solved the nonlinear shallow water equations and could simulate overland flow. Considering the extreme runup levels observed in Sissano Lagoon (up to 16 m in some locations), the coesismic source did not produce waves capable of generating these runup levels (maximum amplitudes generated were approximately 1 m). The slump source predicted wave amplitudes up to 11 m in some locations, and provided closer agreement with the spatial distribution of runup, and the timing of wave attack on the shoreline. The maximum error in wave impact time

using the slump source was approximately 3 min, while the coseismic source incorrectly predicted the time of the tsunami impact by approximately 12 min.

Imamura & Hashi (2003) used detailed bathymetric data to investigate the source mechanism by separately modelling the fault and slump tsunami sources. The numerical model included full treatment of runup and used the ray method to determine energy concentration within the Sissano Lagoon. The numerical model results showed that both a fault and slump source were necessary to explain the far-field tsunami observed in Japan and the distribution of runup heights in Sissano Lagoon. This agrees with the findings of an analytical study by Novikova *et al.* (2005). Results were used to estimate the approximate volume (between 4 and 8 billion m^3) and location of the slump.

2.3.8 İzmit Bay, 1999

On 17 August 1999, a magnitude 7.4 earthquake in İzmit Bay, Turkey, occurred on the northern strand of the North Anatolian Fault Zone at a depth of 17 km, causing right-lateral strike-slip movement on the fault (Altinok *et al.*, 2001). This earthquake was responsible for approximately 17,000 casualties. A number of historical earthquakes have occurred on this fault, however in many cases the ground motion was primarily horizontal, and so did not cause a tsunami. In the 1999 event, the earthquake generated a tsunami possessing wave heights of 1-2 m throughout the bay. However, disproportionally large waves, of approximately 15 m height, were observed in the town of Değirmendere (Tinti *et al.*, 2006). Since no tide gauges were located in İzmit Bay, tsunami data were gathered through field expeditions and eyewitness interviews. These large waves were generated when a segment of coast, approximately 300 m long and 75 m wide and containing several buildings, slid into the sea. Tinti *et al.* (2006) estimated the volume of the failed mass to be approximately 5.18 million m^3, and carried out a stability analysis on the slope to determine that the failure was initiated by seismic loading, although the coseismic tsunami may have also had a triggering effect.

Numerical modelling of this event inferred runup heights from the maximum water elevations calculated at the vertical coast, a reasonable approximation in most cases (Tinti *et al.*, 2006). The numerical model used a shallow-water formulation to solve the (nonlinear) inviscid-incompressible Navier-Stokes equations using a finite element method. This modelling confirmed that the strike-slip fault system, even when combined with the contributions from the normal fault system, led to tsunami waves of 1-3 m. Only a combined tsunami source (coseismic seafloor displacement and local slope failure) was able to reproduce these wave heights, as well as the extreme waves observed at Değirmendere. The timing of the wave impacts on the shoreline was also well reproduced by the model.

2.3.9 Switzerland, 1806

Landslides can also cause large waves in lakes and reservoirs, meaning that this hazard can be important even for landlocked countries. In 1806, a devastating landslide occurred on the Southern slopes of Rossberg mountain, Switzerland and caused 457 casualties. The eastern part of the landslide impacted on Lake Lauerz, causing waves of approximately 15 m height.

Anselmetti & Bussmann (2010) used sediment cores and reflection seismic profiles to show that the waves were not generated by the rockfall itself, but by the collapse of swamp material at the edge of the lake. The swamp material at the edge of the lake was loaded by accumulated rock mass from the landslide, leading to gravity spreading-induced lateral displacement of the deposits into the lake basin. This means that the 1806 event cannot be easily classified as a subaerial landslide, partially or completely submerged landslide-induced tsunami, since the waves were caused by the collapse of swamp material which was in turn triggered by the landslide. This has implications for the assessment of tsunami hazard from landslides, since a landslide impacting near to a water body can still indirectly cause a tsunami, depending on the stability of sediments at the edge of the water body.

2.4 Mathematical framework of tsunami models

2.4.1 Mathematical modelling objectives

Before describing mathematical models used in previous studies of landslide-generated tsunami, it is convenient to present the mathematical framework within which such models are developed. A goal of tsunami-related research is the ability to use mathematical equations to predict the properties of waves generated by a perturbation to the seafloor (which can be a rupture of an underwater fault or a moving landslide). Although the wave amplitude is usually the primary output of these models, other properties may also be of interest. In a model of one-dimensional wave propagation, other possible outputs include the wavelengths and associated phase and group velocities in the generated spectrum of waves, or the distance the waves run up on a beach. In a model of two-dimensional propagation, the lateral location of maximum wave amplitude may be of the most interest, since this may not necessarily be located on the axis of landslide motion. The potential energy within the wave field and kinetic energy of water particles beneath the free surface can also provide insights into the efficiency of energy exchange between the landslide and the wave field.

Often the motion of the landslide itself is an output of a mathematical model, depending on how the landslide is simulated. If the landslide is modelled as a solid block, then the motion of the landslide centre of mass will need to be prescribed, and

may include the effects of drag and added mass. If the landslide is modelled as a fluid, then the time-dependent landslide shape may affect the evolution of the wave field. The run-out distance of the landslide is also important to consider for fluid landslides.

The key differences between mathematical tsunami models are how they model the landslide, the level of simplification they adopt in their treatment of the governing equations of fluid motion (and the associated boundary conditions) and the method by which they solve these equations. Section 2.4.2 describes the problem domain in general terms, including the treatment of the different boundaries. Section 2.4.3 describes the different mathematical representations of the landslide, and how these affect the solution method used within the model. Section 2.4.4 describes the different approximations used to model the generated waves. This section includes a description of the appropriate governing equations, boundary conditions, and solution methods used to solve water wave problems under that approximation. Since a variety of solution methods exist for a particular problem, the list of solution methods is not exhaustive, and further details are included in the summaries of previous mathematical model studies in section 2.5.

2.4.2 Problem domain

For simplicity, the mathematical model framework discussed in this section will consider two-dimensional models only, so that wave propagation will be limited to one horizontal dimension. Some previous model studies have investigated the effect of an added lateral dimension on the wave properties, see section 2.5. Since different landslide models will be discussed in section 2.4.3, for simplicity the landslides illustrated in this section are all solid block landslides, moving along an impermeable bottom boundary. Within this section, the offshore direction is defined as the direction of landslide motion, and the onshore direction is defined as the opposite direction to the landslide motion (since not all problem domains contain a shoreline).

The treatment of the bottom boundary is an important decision in the formulation of a tsunami model. This section contains three simple bottom boundary configurations, although many others are possible. In figure 2.7, the bottom boundary is horizontal, and of infinite length. In this case, the landslide cannot move under the influence of gravity (unless slumping along a curved failure surface), and so a time-dependent motion must be prescribed to the landslide.

Figure 2.8 shows a bottom boundary of constant slope α and infinite length, along which the landslide moves. Although the landslide approximations are discussed in the next section, they will also affect the form of the bottom boundary. A solid landslide may form part of the bottom boundary, while a fluid landslide may simply be located on the bottom boundary before commencing its motion. The fluid depth also needs to

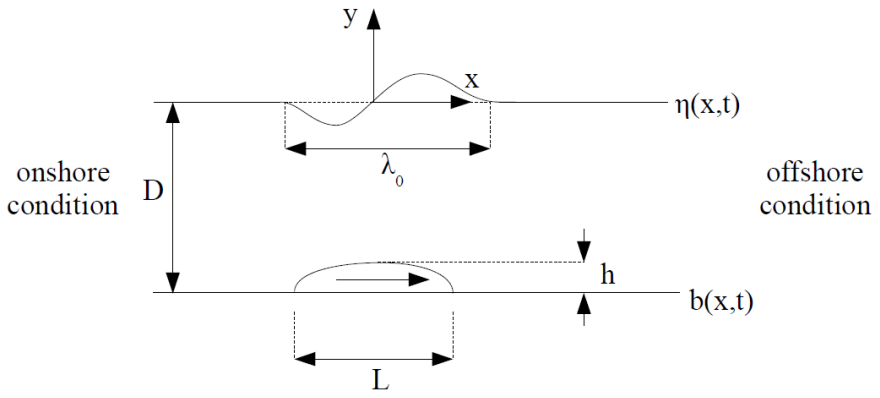

Figure 2.7: Horizontal boundary used in a mathematical tsunami model.

be accounted for in determining the wave-making capability of a given landslide, since wave amplitude decreases as fluid depth increases.

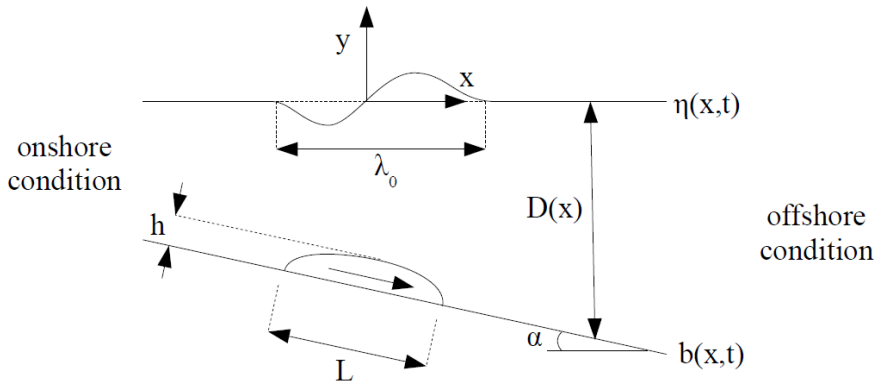

Figure 2.8: Sloping boundary used in a mathematical tsunami model.

Figure 2.9 shows a bottom boundary containing a sloping surface at angle α, with a transition to a horizontal bottom boundary. This transition can be sharp, as shown in figure 2.9, or it can be smooth to avoid unrealistic perturbations to the landslide motion.

Obviously the three bottom boundaries listed above are not the only possible options, as any impermeable surface could be used as a valid bottom boundary. However, many mathematical tsunami models used in previous studies have used one of these bottom boundaries, since they are simple representations of a continental slope. A simple bottom boundary representation may lead to a more straightforward mathematical formulation of a tsunami model, unless the model aims to simulate waves over a bathymetry representative of a field situation. The selection of a bottom boundary within a model domain should consider the physical situation being modelled, the ease of discretisation of the bottom boundary in a numerical model, the motion of the landslide over the boundary, and the complexity of the boundary geometry.

The treatment of the lateral boundaries in the problem domain must also be consi-

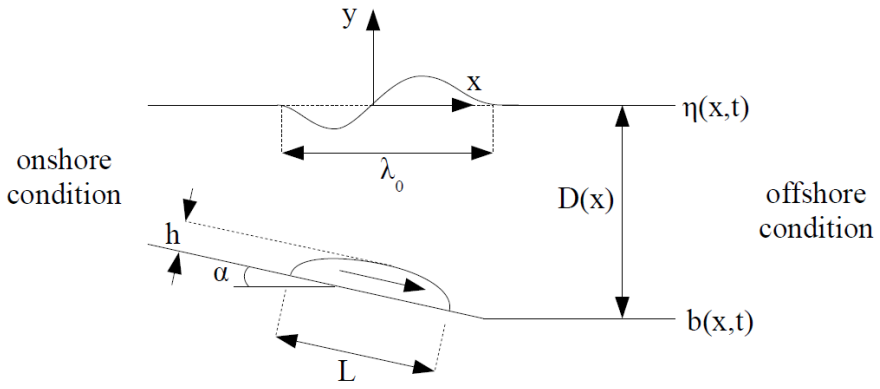

Figure 2.9: Boundary containing a transition from a slope to a horizontal boundary, used in a mathematical tsunami model.

dered. In a model with a horizontal bottom boundary (shown in figure 2.7), the onshore and offshore conditions may be the same. However, if a sloping bottom boundary is used (shown in figure 2.8), or a bottom boundary containing a slope and a transition to a horizontal bottom boundary (shown in figure 2.9), then the onshore condition may also include wave shoaling and runup. In the case where runup is of interest, this can be simply determined using a vertical wall at an appropriate horizontal location, or by continuing the sloping boundary above the free surface to simulate a sloping beach. A model incorporating a beach will need to account for wetting and drying of the boundary due to runup of onshore-propagating waves.

If the model is assumed to extend infinitely in the offshore direction, then waves reaching the offshore boundary will simply propagate out of the domain. However, this may not be practical for all models, and an absorbing boundary condition may be required, to stop waves being reflected back into the domain. Of course, a vertical wall or sloping beach could also be used as an offshore boundary, to simulate tsunami runup in an enclosed domain (such as the 2D simulations of the Lituya Bay landslide-generated tsunami, see Fritz *et al.*, 2009).

Mathematically, the problem domain is most easily represented using Cartesian coordinates, although polar coordinates may be a better choice for simulations of radial wave propagation in two horizontal dimensions (not considered in this section). In the three example domains illustrated in figures 2.7 to 2.9, the origin of the coordinate system is on the undisturbed free surface, above the initial location of the landslide center of mass. The landslide has a length L, and thickness h, and moves in the positive x-direction. The fluid depth is $D(x)$, and is constant for the case of a horizontal bottom boundary. This bottom boundary is defined as $b(x,t)$.

The free surface elevation is defined as $\eta(x,t)$. The initial condition of a landslide-generated tsunami model is usually $\eta(x,0) = 0$. As an aside, previous studies of coseismic tsunami have used a free surface displacement as an initial condition, where

the free surface displacement is equal to the displacement of the underwater fault. Such an approach assumes that the displacement of the fault can be immediately transferred to the free surface, due to the short time-scale over which fault rupture occurs, and compressibility effects are generally ignored. For inclusion of compressibility effects in a coseismic tsunami model, see Gisler (2008). Waves generated by a landslide tsunami can be considered to have a characteristic amplitude η_0, and a characteristic wavelength λ_0. The relative size of these terms can be used to simplify the model formulation, as explained in section 2.4.4.

2.4.3 Landslide approximations

In field situations, the landslide material, failure mechanism and post-failure motion are all extremely complex (see section 2.2). In order to mathematically model a submarine landslide, approximations must be made regarding all of these landslide properties. These approximations are interdependent, since the approximation used for the landslide material will affect how the mass fails (if failure is simulated within the model, as discussed later in this section), and how the mass moves after failure. The tsunamigenic potential of a model landslide also depends greatly on these factors, since the landslide material will also affect the energy exchange between the landslide and its generated wave field.

The majority of previous studies have modelled the landslide as a solid block, moving down a sloping boundary under the influence of gravity. Details of these mathematical models are provided in 2.5. The use of a solid block is a gross simplification of reality, but is used to approximate the shape and volume of the dense landslide material (see figure 2.4). This approximation ignores the multiple factors contributing to landslide deformation during motion, such as erosion, deposition, hydroplaning and drag forces. Since the entire volume of the landslide is treated as a solid, the waves generated by a solid block landslide will have larger amplitudes than those generated by a granular landslide of equal size, although the granular slide may run out over a longer distance. Because of this, mathematical models using a solid block landslide can be considered conservative if used as part of a tsunami warning system, since they will tend to over-predict the amplitudes of generated waves. A major advantage of a solid block landslide model is that this approximation allows direct comparison between model predictions and experimental measurements. This is because most previous experimental studies (see section 2.6) have modelled the landslide as a solid block, due to difficulties in replicating landslide grain size distributions at laboratory scales.

A solid block landslide can be incorporated into a mathematical model as part of a time-dependent bottom boundary, $b(x,t)$. In this case, the landslide motion may be prescribed completely as a suitable velocity profile (possibly using displacement data

recorded during experiments). Depending on the approximations made regarding the fluid flow around the landslide, drag forces may be calculated by the model (if a viscous ambient fluid is assumed), or these can be prescribed as retarding forces acting on the landslide during motion.

The landslide can also be modelled as a fluid flow, where the landslide is assumed to be a fluid with greater density than the ambient water. In this case, the model will simulate the landslide-generated tsunami as the free surface waves caused by flow within a two-fluid mixture, where the landslide fluid is used to approximate the flow of dense material only. The suspension flow of less dense material (see figure 2.4) can be simulated using a three-fluid mixture, where the landslide consists of two fluids of different densities. If the landslide is modelled as a fluid flow, this removes the need for a time-dependent bottom boundary condition within the model. Additionally, since the fluid can deform during motion, model results should be less sensitive to the initial choice of landslide shape.

Previous mathematical models using a dense fluid flow approximation for the landslide have typically assumed that the landslide fluid is incompressible, with a much higher viscosity than water. This limits the Reynolds number of the fluid approximating the landslide during its down-slope motion, since a high-Reynolds number flow would become turbulent. This condition may place an upper limit on the angle of the sloping bottom boundary. The assumption of a low-Reynolds number fluid flow limits the landslide deformation during motion, to approximate the motion of dense landslide material in a field situation. If the suspension flow is included as a separate fluid from the dense flow, then this can be modelled as an ideal (inviscid and incompressible) fluid.

Some previous studies have modelled the landslide as a Bingham fluid (see section 2.5 for details), in order to include a failure-type condition on the mass flow. A Bingham fluid does not deform from its initial stationary condition until a yield stress is exceeded, after which motion is driven by the excess of stress over the yield stress. In reality, the failure of a submerged mass depends on a variety of factors that act to either increase stress on the sediment or decrease its strength. After failure, the flow may undergo some deformation before exhibiting flow-like behaviour. However, these failure conditions are too complicated to be incorporated into a mathematical tsunami model, and in general the failure of a submerged mass is implicitly used as an initial condition to the model.

In more advanced models, the landslide may be modelled as a granular material, containing an appropriate distribution of sediment sizes. In this case, the landslide motion will be governed by the equations of soil mechanics, which physically represent the interactions between sediment particles in the landslide, and between the landslide and the ambient fluid.

2.4.4 Fluid flow approximations

Many different approximations are available for the subsurface fluid flow, and the free surface waves, generated by the motion of a submarine landslide. The level of approximation used will determine the governing equations, the mathematical form of the boundary conditions, and to an extent the numerical or analytical solution method employed by the model.

Some of the approximations made relate to the properties of the fluid, or the nature of the landslide-induced flow. For example, the fluid may be assumed to be viscous or inviscid, and fluid flow may be assumed to be rotational or irrotational. Compressibility effects are negligible for flow generated by a submarine landslide, and hence the fluid is assumed to be incompressible in all cases. Other approximations relate to the relative size of the characteristic tsunami amplitude (η_0), characteristic tsunami wavelength (λ_0), and the fluid depth (D). These approximations allow certain terms within the governing equations and boundary conditions to be neglected, and may change the location where a condition is applied (such as the linear approximation, see below).

Each of the approximations described in this section simplifies the formulation of a tsunami model, at some cost to the model's ability to accurately describe the physics of the problem. More severe approximations allow formulation of simple, computationally inexpensive models. Models with fewer simplifying assumptions may be complex and computationally expensive, but are more representative of reality. This section briefly describes the physical reasoning behind the most common approximations made within landslide-generated tsunami models, and states the governing equations and boundary conditions arising from each approximation.

Viscous fluid

Under the incompressible assumption, the fluid may be assumed to be viscous. This allows a model to simulate viscous drag on the landslide, the creation (and separation) of a boundary layer on the landslide and the subsequent wake behind the landslide. The boundary layer may be laminar or turbulent, depending on the velocity of the landslide. Turbulent effects are retained in the model, providing a mechanism for the dissipation of energy within the flow field. The governing equations for a viscous fluid are the equation of mass conservation (called the continuity equation) and the equations of momentum conservation (the Navier-Stokes equations). The continuity equation is stated in vector form as

$$\nabla \cdot \mathbf{u} = 0, \tag{2.3}$$

where $\mathbf{x} = (x, y)$ and $\mathbf{u} = (u, v)$ is the fluid velocity. In two-dimensional Cartesian coordinates, this becomes

$$\frac{\partial u}{\partial x} + \frac{\partial v}{\partial y} = 0. \tag{2.4}$$

The Navier-Stokes equations in vector form are

$$\frac{D\mathbf{u}}{Dt} = -\frac{1}{\rho}\nabla P + \mathbf{F} + \nu\nabla^2\mathbf{u}, \tag{2.5}$$

and in rectangular Cartesian form as

$$\frac{Du}{Dt} = -\frac{1}{\rho}\frac{\partial P}{\partial x} + F_x + \nu\left(\frac{\partial^2 u}{\partial x^2} + \frac{\partial^2 v}{\partial y^2}\right), \tag{2.6a}$$

$$\frac{Dv}{Dt} = -\frac{1}{\rho}\frac{\partial P}{\partial y} + F_y + \nu\left(\frac{\partial^2 u}{\partial x^2} + \frac{\partial^2 v}{\partial y^2}\right), \tag{2.6b}$$

where P is the fluid pressure, $\mathbf{F}$ is the body force term, t is time, and ν is the kinematic viscosity of the fluid. The material derivative, $\frac{D}{Dt}$, is defined according to

$$\frac{D}{Dt} \equiv \frac{\partial}{\partial t} + \mathbf{u}\cdot\nabla. \tag{2.7}$$

In the case of a viscous fluid, the condition on the bottom boundary is the no-slip condition. In the case of a stationary bottom boundary, the no-slip condition is

$$u = v = 0 \quad \text{on } y = b(x), \tag{2.8}$$

where the bottom boundary is $b(x)$. If the bottom boundary is moving with horizontal velocity u_b, then the no-slip condition becomes

$$u = u_b \qquad \text{on } y = b(x,t), \tag{2.9a}$$

$$v = \frac{\partial b}{\partial t} + u\frac{\partial b}{\partial x} \qquad \text{on } y = b(x,t). \tag{2.9b}$$

The kinematic condition requires that fluid particles on the free surface must move with the free surface,

$$v = \frac{\partial \eta}{\partial t} + u\frac{\partial \eta}{\partial x} \quad \text{on } y = \eta\,(x,t)\,. \tag{2.10}$$

The other free surface condition for a viscous fluid requires that the normal and tangential stresses on the free surface are known. In a two-dimensional domain, only one tangential condition is required. The normal and tangential stress conditions are therefore

$$P - 2\mu\left[\left(\frac{\partial\eta}{\partial x}\right)^2\frac{\partial u}{\partial x} - \frac{\partial\eta}{\partial x}\left(\frac{\partial u}{\partial y}+\frac{\partial v}{\partial x}\right)+\frac{\partial v}{\partial y}\right] / \left[1+\left(\frac{\partial\eta}{\partial x}\right)^2\right] = P_a \quad \text{on } y=\eta(x,t), \tag{2.11}$$

$$2\left(\frac{\partial\eta}{\partial x}\right)^2\left(\frac{\partial u}{\partial x}-\frac{\partial v}{\partial y}\right)+\left[\left(\frac{\partial\eta}{\partial x}\right)^2-1\right]\left[\frac{\partial\eta}{\partial x}\left(\frac{\partial u}{\partial y}+\frac{\partial v}{\partial x}\right)\right]=0 \quad \text{on } y=\eta(x,t). \tag{2.12}$$

In the case of a viscous fluid, the solution method used to solve the governing equations subject to the boundary conditions largely depends on the treatment of turbulence within the model. If turbulent scales are fully resolved, then the Navier-Stokes equations must be solved directly in a direct numerical simulation (DNS), while if only large eddy sizes are resolved then a large eddy simulation (LES) model would be appropriate. Reynolds averaging is problematic for landslide-generated flows, since the flows are highly time-dependent.

Inviscid fluid

Under the assumption that inertial forces are more important than viscous forces (or that $Re \equiv \frac{uD}{\nu} \gg 1$), the fluid can be assumed to be inviscid. In this case, viscous stresses within the fluid and at the boundaries are neglected. This means that boundary layers are no longer resolved by the model, and energy is not dissipated by turbulence within the flow field. Under this assumption, the Navier-Stokes equations reduce to the Euler equations. In vector form, these equations are:

$$\frac{D\mathbf{u}}{Dt} = -\frac{1}{\rho}\nabla P + \mathbf{F}, \tag{2.13}$$

where the equivalent rectangular Cartesian form is

$$\frac{Du}{Dt} = -\frac{1}{\rho}\frac{\partial P}{\partial x} + F_x, \tag{2.14a}$$

$$\frac{Dv}{Dt} = -\frac{1}{\rho}\frac{\partial P}{\partial y} + F_y. \tag{2.14b}$$

Assuming that the body force is conservative, $\mathbf{F}$ can be expressed as the gradient of a potential function $\mathbf{F} = -\nabla\Omega$, with $\Omega = gy$, where g is the gravitational acceleration.

Under the inviscid approximation, the no-slip condition is no longer applicable on the bottom boundary (since no viscous stresses exist within the fluid). This bottom boundary condition is replaced by the condition of flow tangency, where the component

of fluid velocity normal to the boundary must be equal to the velocity of that boundary (or that the normal fluid velocity relative to the boundary is zero). In this case, the condition on the normal fluid velocity at the boundary is the same as for a viscous fluid, however there is no condition on the fluid velocity tangential to the boundary. The condition for a stationary boundary is

$$v = 0 \quad \text{on } y = b\,(x)\,, \tag{2.15}$$

and the condition for a moving boundary is

$$v = \frac{\partial b}{\partial t} + u\frac{\partial b}{\partial x} \quad \text{on } y = b\,(x,t)\,. \tag{2.16}$$

The two free surface conditions for an inviscid fluid are known as the kinematic condition and the dynamic condition. As in the viscous case, the kinematic condition requires that fluid particles on the free surface must move with the free surface,

$$v = \frac{\partial \eta}{\partial t} + u\frac{\partial \eta}{\partial x} \quad \text{on } y = \eta\,(x,t)\,. \tag{2.17}$$

The dynamic condition for an inviscid fluid simply requires that the pressure is prescribed on the free surface of the fluid. If the atmospheric pressure is P_a, then

$$P = P_a \quad \text{on } y = \eta\,(x,t)\,. \tag{2.18}$$

Under the inviscid approximation, the Euler equations are solved, subject to the boundary conditions. If the equations are solved numerically, the domain may be discretised using a finite difference or finite element model.

Irrotational flow

If the fluid is assumed to be inviscid, flow may also be assumed to be irrotational (where $\omega = \nabla \times \mathbf{u} = 0$). In this case, the velocity vector $\mathbf{u}$ can be expressed as the gradient of a potential function, called the velocity potential, ϕ,

$$\mathbf{u} = \nabla\phi. \tag{2.19}$$

The components of the velocity vector may now be determined using the continuity equation alone, subject to appropriate boundary conditions. The new form of the continuity equation is Laplace's equation for the velocity potential, stated in vector form as

$$\nabla^2\phi = 0, \tag{2.20}$$

and in rectangular Cartesian form as

$$\frac{\partial^2 \phi}{\partial x^2} + \frac{\partial^2 \phi}{\partial y^2} = 0. \tag{2.21}$$

Under the assumption of irrotationality, the Euler equations reduce to Bernoulli's equation for an (unsteady) inviscid-irrotational fluid flow, solved for the fluid pressure, P.

$$\frac{\partial \phi}{\partial t} + \frac{1}{2}\mathbf{u} \cdot \mathbf{u} + \frac{P}{\rho} + \Omega = C. \tag{2.22}$$

The boundary conditions for an inviscid-irrotational fluid flow are the same as those for an inviscid fluid with rotation. However, these boundary conditions may still be expressed in a different form under the irrotational assumption, since the velocity vector can now be expressed as the gradient of the velocity potential, ϕ. The condition for a stationary bottom boundary becomes

$$\frac{\partial \phi}{\partial y} = 0 \quad \text{on } y = b\left(x\right), \tag{2.23}$$

and the corresponding equation for a moving bottom boundary becomes

$$\frac{\partial \phi}{\partial y} = \frac{\partial \phi}{\partial x}\frac{\partial b}{\partial x} + \frac{\partial b}{\partial t} \quad \text{on } y = b\left(x, t\right). \tag{2.24}$$

The kinematic condition for an inviscid-irrotational fluid flow is

$$\frac{\partial \phi}{\partial y} = \frac{\partial \eta}{\partial t} + \frac{\partial \phi}{\partial x}\frac{\partial \eta}{\partial x} \quad \text{on } y = \eta\left(x, t\right). \tag{2.25}$$

The dynamic condition for an inviscid-irrotational fluid flow can be expressed in terms of a pressure modified from the hydrostatic, defined as

$$p = P - \rho g y + P_a. \tag{2.26}$$

Combined with Bernoulli's equation for the pressure within an inviscid-irrotational fluid flow, this provides a dynamic boundary condition on the free surface,

$$\frac{\partial \phi}{\partial t} + \frac{1}{2}\mathbf{u} \cdot \mathbf{u} + g\eta = 0 \quad \text{on } y = \eta\left(x, t\right). \tag{2.27}$$

A model formulated using the inviscid-irrotational approximation will typically solve Laplace's equation, subject to suitable boundary conditions, for the velocity potential, ϕ, obtaining the entire velocity field within the fluid. Bernoulli's equation may be subsequently solved for the pressure field within the fluid. Analytical solutions may be available for this problem, depending on any further simplifications made (discussed in the following sections).

Linear approximation

The linear approximation states that the characteristic wave amplitude, η_0, is much smaller than both the depth of the fluid and the characteristic wavelength λ_0, i.e. $\eta_0 \ll D$ and $\eta_0 \ll \lambda_0$. In this case, all nonlinear terms within the governing equations and boundary conditions are neglected. Under the linear approximation, the modified Euler equations (for an inviscid fluid) are stated in vector form as

$$\frac{\partial \mathbf{u}}{\partial t} = -\frac{1}{\rho}\nabla P + \mathbf{F}, \tag{2.28}$$

and the Bernoulli equation (for an inviscid-irrotational fluid flow) becomes

$$\frac{\partial \phi}{\partial t} + \frac{P}{\rho} + \Omega = f(t). \tag{2.29}$$

Nonlinear terms are also neglected in the boundary conditions on the free surface. The free surface conditions may now be applied to the undisturbed free surface ($y = 0$), rather than the free surface itself ($y = \eta(x,t)$). The linear kinematic free surface condition for an inviscid fluid is

$$v = \frac{\partial \eta}{\partial t} \quad \text{on } y = 0, \tag{2.30}$$

and under the additional assumption of flow irrotationality this becomes

$$\frac{\partial \phi}{\partial y} = \frac{\partial \eta}{\partial t} \quad \text{on } y = 0. \tag{2.31}$$

The dynamic condition for an inviscid-irrotational flow, under the linear approximation, again uses the modified pressure from the hydrostatic, to obtain

$$\frac{\partial \phi}{\partial t} + g\eta = 0 \quad \text{on } y = 0. \tag{2.32}$$

Shallow water/long wave approximation

The shallow water approximation (also called the long wave approximation) states that the water depth is very small compared to the characteristic wavelength of the generated waves, $D \ll \lambda_0$. This approximation thus assumes that vertical motions within the fluid are negligible, and may be neglected. In this case, nonlinear terms are retained, but the fluid pressure is assumed to be hydrostatic. Therefore, under the long wave assumption, the Euler equations can be written as the shallow water equations,

$$\frac{Du}{Dt} = -\frac{\partial P}{\partial x} + F_x, \tag{2.33a}$$

$$\frac{\partial P}{\partial y} = F_y. \tag{2.33b}$$

The kinematic condition on the free surface is unchanged under the long wave/shallow water approximation.

Shallow water wave theory assumes that all generated waves are long waves, and therefore propagate at the shallow-water phase velocity,

$$c_p = \sqrt{gD}. \tag{2.34}$$

This phase velocity exhibits no dependence on the wavenumber of the waves, and as such, dispersive effects are neglected in shallow water models.

Linear shallow water approximation

If the linear and shallow water/long wave approximations are combined, then the characteristic wave amplitude (η_0) is assumed to be very much smaller than both the depth (D) and the characteristic wavelength (λ_0), and the characteristic wavelength is assumed to be much larger than the depth. Under this combined approximation, the Euler equations are stated as

$$\frac{\partial u}{\partial t} = -\frac{\partial P}{\partial x} + F_x, \tag{2.35a}$$

$$\frac{\partial P}{\partial y} = F_y. \tag{2.35b}$$

Under the linear shallow water approximation, the kinematic condition is unchanged from equation 2.30 (or equation 2.31 in the case of irrotational flow). The dynamic condition on the free surface under the linear shallow water approximation is now

$$\frac{\partial \phi}{\partial t} + g\eta = 0 \quad \text{on } y = 0. \tag{2.36}$$

Boussinesq approximation

If both dispersive and nonlinear effects are to be included in the model, a different assumption is the Boussinesq approximation, which states that the Stokes number of the waves is approximately 1. The Stokes number is defined as

$$S = \frac{\alpha}{\beta}, \tag{2.37}$$

where $\alpha = \eta/D$ is a nondimensional wave amplitude, and $\beta = D^2/\lambda_0^2$ is a nondimensional measure of the channel depth, relative to the wavelength.

The Stokes number is implicitly assumed to be large in the formulation of the shallow water equations. The Boussinesq approximation requires the retention of all terms that are at most linear in α or β, which are defined in the numerator and denominator of equation 2.37. The classical Boussinesq equations are obtained by using a depth-averaged velocity, defined as

$$u' = \int_{-D}^{\eta} u \; dy. \tag{2.38}$$

The Boussinesq equations arising from these approximations are

$$\frac{\partial u}{\partial t} + u\frac{\partial u}{\partial x} + g\frac{\partial \eta}{\partial x} - \frac{1}{3}D^2\frac{\partial^3 u}{\partial t \partial x^2} = 0, \tag{2.39}$$

$$\frac{\partial \eta}{\partial x} + \frac{\partial}{\partial x}\left[u(D+\eta)\right] = 0. \tag{2.40}$$

2.4.5 Summary

This section has presented a mathematical framework for the formulation of a mathematical model to simulate landslide-generated tsunami. In the selection of a problem domain, it is important to consider the shape of the bottom boundary, and the conditions at the lateral boundaries of the model. The landslide can be modelled as a solid block (expressed mathematically as a time-dependent bottom boundary), as a viscous fluid (with an ideal fluid to represent the suspension flow, if desired), or as a more complex granular flow.

The fluid within a mathematical model can either be assumed to be viscous or inviscid, where the inviscid case also leads to irrotationality of the flow by Kelvin's circulation theorem. The inviscid and irrotational approximations allow simpler formulation of the mathematical problem, however they are more limited in their ability to reflect the physics of a problem. Several different assumptions can also be made regarding the amplitude and wavelength of the generated waves, including the linear approximation, the shallow water approximation and the Boussinesq approximation. Each of these limits the behaviour able to be modelled effectively, but allows simplifications to the governing equations and boundary conditions of the problem.

The approximations used in the formulation of the model will affect its computational method (and associated computational cost), and whether results can be applied to

field situations. Mathematical models used in previous studies of landslide-generated tsunami are described in the next section.

2.5 Previous mathematical models of landslide-generated tsunami

Since the Sissano Lagoon tsunami of 1998, and the more devastating Boxing Day tsunami of 2004, much effort has gone into the mathematical modelling of tsunami in an effort to predict the properties of these waves, how they travel and especially how they interact with the shoreline. When a seismic event occurs, data are sent to a tsunami warning centre where use of a calibrated numerical model allows appropriate warnings to be issued to areas at risk of inundation (Gisler, 2008). The three phases of tsunami modelling are the generation phase, the wave propagation phase, and the runup/inundation phase. These phases are often modelled separately.

If untested or unrealistic models are used as part of a tsunami mitigation plan, this can lead to errors resulting in lives lost or unnecessary evacuations. Synolakis *et al.* (2008) recommended standards for approval of tsunami models used in such mitigation plans. The categories of testing are basic hydrodynamic considerations, benchmarking (analytical, numerical and field tests), scientific evaluations and operational evaluations. These ensure that models used by coastal authorities are robust and their methods are defensible.

Mathematical models used in previous studies may be classified into several different categories, based on the assumptions underpinning the model itself. Since a variety of solution methods can be used to solve a given problem, it is more convenient to classify models based on these assumptions and the equations solved, rather than the solution method used. Each model is described in terms of its goals, the problem domain, the governing equations and boundary conditions, the solution method, and the findings of the mathematical investigation. Limitations of the models and ongoing work are discussed as appropriate. Note that some of the mathematical models discussed use different notation to that presented in section 2.4. As such, any diagrams of problem domains provided in this section are intended for illustrative purposes only, and equations/symbols may not be consistent with those used in the remainder of this thesis.

The first models considered are empirical equations, which relate the properties of a generated wave to the properties of the wave forcing. These are generally the simplest models, and rely on large amounts of either laboratory or field data to generate robust equations. Generated wave properties of interest are usually the wave height and/or runup, while forcing factors include the landslide size and material, the slope angle, the

submergence depth, and the presence of any lateral boundaries. Due to the complex interaction between the landslide and the generated waves, it is difficult to obtain an equation which can adequately account for all of these factors. Often empirical models are based on the assumption that wave properties depend on a limited number of these forcing factors, allowing formulation of simple equations.

The second group of models considered are linear analytical and numerical models. These models use the linear assumption (discussed in section 2.4.4), and therefore are limited in the range of amplitudes they can successfully model. For this reason, such models will usually consider only the generation and propagation phases of wave motion, since they cannot realistically model the shoaling, breaking and runup of waves on a shoreline.

The third group of models described are nonlinear analytical and numerical models. Since these models do not invoke the linear assumption, they are not limited in the wave amplitude that they can effectively simulate. Often such models will instead use the long wave/shallow water approximation. Others may invoke the Boussinesq approximation, or they may solve the Navier-Stokes equations using a suitable treatment of turbulence. Turbulence can be accounted for within numerical models either by direct solution of the Navier-Stokes equations for large eddy sizes only (called Large Eddy Simulations, or LES), or by direct solution the Navier-Stokes equations for all eddy scales (called Direct Numerical Simulations, or DNS). As a general rule, a model containing fewer simplifying assumptions will be more computationally expensive. Nonlinear models are further divided into those which deal only with one-dimensional wave propagation (leading to a 2D domain, discussed in section 2.5), and those which model two-dimensional wave propagation (leading to a 3D domain, discussed in 2.5). In the case where both 1D propagation and 2D propagation are considered, the model is classified based on the focus of the study.

Empirical equations for generated wave amplitude and runup

Murty (2003) used historical field data and numerical results to determine a regression curve fit between the volume of a submarine landslide (V), in millions of m^3, and the maximum height of the tsunami waves generated by this landslide (H), in m. Factors not considered in the study include the water depth above the landslide, the slope angle, the run-out distance of the landslide, properties of the slide material, the location of the maximum wave height, and the time and velocity of landslide motion. However, the simple relationship was determined on the reasoning that the volume of a landslide was the most important parameter in determining the amplitude of generated waves (since no volume would obviously lead to a zero wave amplitude). The relationship from this regression curve fit, determined from a total of eleven historical slide events, was

$$H = 0.3945V \tag{2.41}$$

To check the validity of equation 2.41, Murty determined values of V and H from six numerical model studies, including Rabinovich *et al.* (1999). The level of agreement between the empirical equation (from the observed historical data) and the results of six numerical simulations was reasonably poor. In particular, many numerical models predicted lower wave amplitudes than the empirical equation at high landslide volumes. Reasons for these discrepancies were not discussed, but are likely due to a combination of the factors neglected by this simple equation.

Watts *et al.* (2005) derived predictive empirical equations for the characteristic amplitude of a tsunami generated by submarine mass failure. The aim of these empirical equations was for use as a first warning, order-of-magnitude, assessment on the expected wave properties generated by a mass failure in situations where time did not permit the use of numerical modelling tools. The characteristic amplitude was selected to be the maximum free surface depression above the initial location of the submerged mass. The study considered both translation failures (slides) and rotational failures (slumps). The empirical equation calculated the characteristic tsunami amplitude depending on the distance of landslide motion, the slope angle, the landslide thickness, the submergence depth and the specific density of landslide material. The equation was derived using the results of a two-dimensional, fully nonlinear potential flow model (described in section 2.5). For slides, the predictive equation for the characteristic 2D tsunami amplitude ($\eta_{0,2D}$), for the case where the specific gravity is equal to a reference specific density ($\gamma = \gamma_{ref} = 1.85$), is

$$\eta_{0,2D} \simeq 0.0286T\left(1 - 0.750\sin\theta\right)\left(\frac{b\sin\theta}{d}\right)^{1.25} \tag{2.42}$$

where T is the landslide thickness, θ is the slope angle, b is the landslide length, and d is the fluid depth. It is noted that the lower bound on submergence depths simulated was $d/b > 0.06$ to avoid wave breaking and other nonlinear phenomena. Therefore, the predictive equations should be used with caution at shallow submergences. The equivalent predictive equation for the characteristic (2D) tsunami amplitude generated by a slump is

$$\eta_{0,2D} \simeq 0.0654T\left(\sin\theta\right)^{0.25}\left(\frac{b}{d}\right)^{1.25}\left(\frac{R}{b}\right)^{0.37}\left(\Delta\Phi\right)^{1.39} \tag{2.43}$$

where R is the radius of curvature of the failure surface, and $\Delta\Phi$ is the angular displacement along the failure surface. A simple expression was determined to allow extension of the predictive equation to 3D submarine mass failures, stated as

$$\frac{\eta_{0,3D}}{\eta_{0,2D}} = \left(1 + 15.5\sqrt{\frac{d}{b\sin\theta}}\right) \simeq 0.065\sqrt{\frac{b\sin\theta}{d}} \tag{2.44}$$

$$\frac{\eta_{0,3D}}{\eta_{0,2D}} = \left(1 + 2.06\sqrt{\frac{d}{b}}\right) \tag{2.45}$$

where the expression in equation 2.44 was derived for a slide, and in equation 2.45 for a slump.

The derived equations were applied to four case studies of historical tsunami events. The predicted characteristic tsunami amplitudes in the three-dimensional model were used as a predictor of the maximum runup for each case study. These predictions were shown to be within several metres of observed runup levels, however uncertainties in some of the contributing parameters limited the applicability of the equations to the case studies. One possible limitation of the empirical equations is the choice of location for the characteristic tsunami amplitude (above the initial location of the submerged mass). This location may only be appropriate for steep slopes and high landslide accelerations. For milder slopes, the contribution of the landslide terminal velocity may become more important than that of the initial acceleration in determining the tsunami amplitude, and the maximum amplitude is likely to occur some distance away from the initial failure location.

Linear analytical and numerical models

Harbitz *et al.* (1993) simulated landslide-generated waves in fjords using a numerical model based on the linear shallow water equations. The goal of the study was to simulate waves generated by a landslide, as applied to the Tafjord (Norway) event of April 7, 1934. This case study was selected due to the large number of recorded runup heights, allowing comparison of the model with field data. The model solved the linear shallow water equations, and modelled the slide as a solid object which changed the elevation of the bottom boundary in a time-dependent manner. Shear stress between the landslide and the fluid was demonstrated to be unimportant for this event compared to the total water displacement by the landslide. An explicit finite-difference technique solved the governing equations on a staggered grid. The simulation domain size ensured that radiation from the domain boundary did not affect the wave field for the duration of the simulation. The shoreline was modelled as an impermeable wall, and runup values were compared to field measurements from the 1934 event. The study investigated the dependence of model results on the geometry and motion of the landslide. Wave reflection and the generation of seiche modes in the cross-fjord direction accounted for the occurrence of several large waves in the 1934

event. The numerical model generally performed well at reproducing the runup heights measured in the field, especially considering the inherent inaccuracies in obtaining field measurements of runup.

Liu *et al.* (2003) derived analytical solutions for the propagation of forced waves along a constant-sloping beach. The forced linear shallow water equations were solved for the case of a rigid slide moving with a constant acceleration. An initial check of the analytical solution was conducted by directly integrating the equations, with good agreement. The model results were then compared to a numerical solution of the nonlinear shallow water wave equations, solved using a finite difference scheme (Lynett & Liu, 2005). The offshore wave height and shape agreed well between the analytical and numerical models (to within <1%), however as time progressed the predicted and measured waves became out of phase near the shoreline. When the shoreline slope, $\tan\beta$, was much greater than the landslide aspect ratio, μ, the analytical solutions provided an accurate representation of the physics of wave generation by a submarine landslide. The aspect ratio is defined as $\mu = d/l$, where d is the landslide thickness and l is the landslide length.

Didenkulova *et al.* (2011) investigated the resonant behaviour of tsunami waves generated by a submarine landslide in a two-dimensional numerical study. Resonance occurs when a generated wave moves at the same speed as its forcing, and is also observed in waves generated by atmospheric disturbances (referred to as the Proudman resonance, see Vennell, 2009). In the case of a tsunami generated by a submarine landslide, this corresponds to a landslide Froude number of unity. Resonant phenomena lead to interesting behaviour within the generated tsunami waves. However, a Froude number close to unity is not representative of most field situations, where waves tend to travel much more rapidly than the landslide.

In this investigation, the governing equations were chosen to be the linear shallow water equations. The fluid depth was assumed to vary slowly in the offshore direction, and onshore-propagating waves were not considered in the study (since these would not exhibit any resonant effects). The equations were solved analytically, and subcritical, critical and supercritical landslide velocities were considered in the study. Nonlinear effects and dispersive effects were found to play a minor role in the properties of the long waves, and as such the approximate solutions determined can be considered valid for long tsunami waves generated by an underwater landslide. The study considered separate cases where the landslide volume could be fixed or variable, and where the landslide velocity could be fixed or variable.

Renzi & Sammarco (2010) carried out an analytical investigation of the propagation of landslide-generated tsunami around a conical island, in conjunction with physical experiments by Di Risio *et al.* (2009a). The model solved the linear shallow water equations in a cylindrical polar coordinate system. The landslide was modelled as a

solid block with an elliptic plan view and a Gaussian section, and the slope of the conical island was assumed to be linear (see figure 2.10).

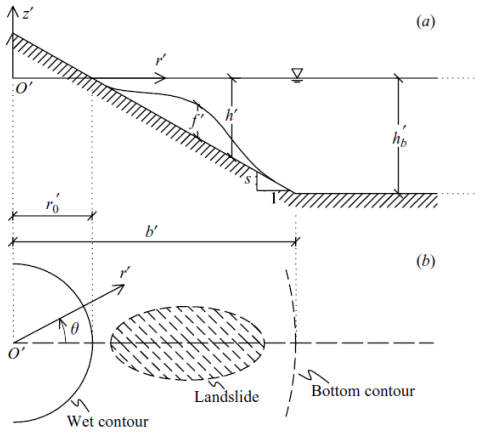

Figure 2.10: Problem domain used by Renzi & Sammarco (2010)

The solution process required the matching of the near-field (propagation on the sloping island flank) and far-field (propagation over the constant-depth domain away from the island) around the perimeter of the slope base. Satisfactory prediction was exhibited for the amplitude, timing, shape, runup and rundown of the waves, based on the comparisons between experimental and analytical wave time series at several locations around the perimeter of the island. Differences were due to dispersive effects in the experiments (not included in the analytical model), and the shape of the slide used in the experiments (since the shape used in the analytical model was much smoother).

Sue *et al.* (2011) details the development of a two-dimensional boundary element method (BEM) model, based on inviscid-irrotational theory, to investigate the waves generated by a solid block landslide moving down a 15° slope under the influence of gravity. The simulation domain, which includes definitions of the variables used in the model, is shown in figure 2.11. The BEM model solved Laplace's equation, subject to appropriate boundary conditions, on the boundaries of the domain shown in figure 2.11. The landslide motion consisted of a period of constant acceleration, followed by a period of constant deceleration (of lower magnitude than the initial acceleration) to rest.

A series of two-dimensional laboratory experiments validated the model (discussed in 2.6), and maximum crest and trough amplitudes were predicted by the model to within 25% of experimental values. Differences in predicted and experimental wave speeds were between 2 and 4%, with the BEM model over-predicting the speed of the generated waves. Due to the boundary condition imposed at the shoreline of the BEM model, runup predictions could not be compared to experimental measurements.

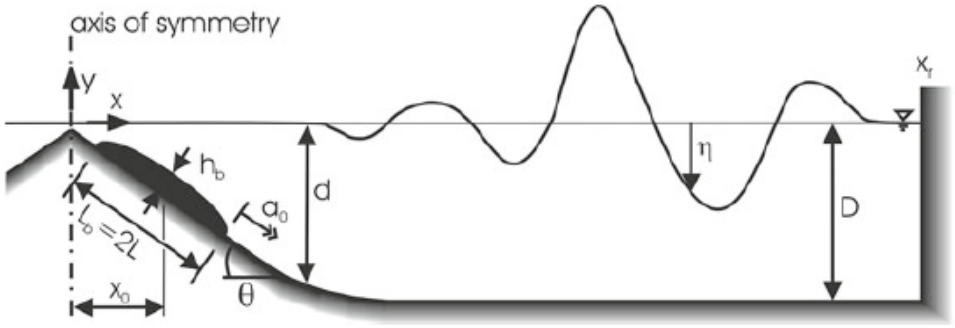

Figure 2.11: Problem domain used by Sue *et al.* (2011)

Nonlinear analytical and numerical models, one-dimensional wave propagation

Jiang & LeBlond (1992) conducted a numerical investigation of the coupling of a submarine landslide and the waves generated by its motion. Coupling was found to be important for landslide-generated tsunami, since the time of landslide motion was relatively long and the generated surface waves would also affect the landslide motion (contrary to the fundamental assumptions underlying the use of a solid block to model a submarine landslide). The 2D problem domain is shown in Figure 2.12. The governing equations used in this investigation were the nonlinear shallow-water equations.

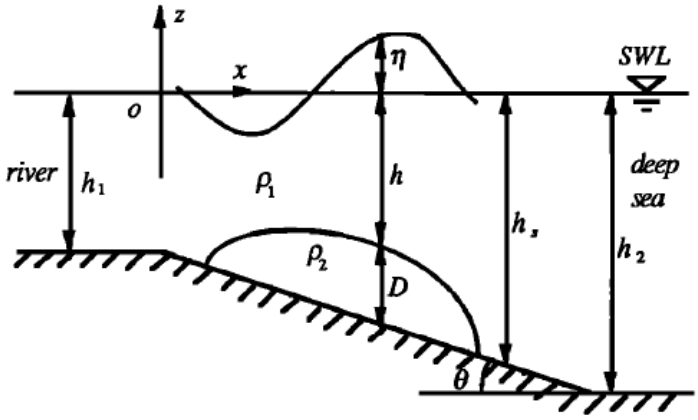

Figure 2.12: Numerical model for waves generated by underwater mudslide, from Jiang & LeBlond (1992)

The landslide was treated as the laminar flow of a viscous incompressible fluid. This approximation was justified by the calculation of the maximum Reynolds numbers for the flow (with the mud viscosity varying between $\mu = 20$ g/(cm s) and $\mu = 2000$ g/(cm s)). The maximum Reynolds numbers were smaller than the critical value at which the mudslide would become turbulent, and as such the viscous approximation of the landslide was valid. The long wave approximation was also used for the landslide, implying that the landslide's thickness was very small compared to a characteristic

length of the slide in the downslope direction. During motion, the mudslide exhibited amplitude dispersion, and the largest amplitudes (and velocities, due to the nonlinear behaviour of the slide) were located near the front of the mudslide.

The nonlinear shallow water equations were solved by a finite difference method. Model results compared the landslide motions and generated waves for three different cases: a submerged mudslide under a fixed surface; a model with one-way coupling (where the mudslide motion affected the free surface); and a model with full coupling (where the mudslide motion affected the free surface, and the surface pressure gradients acted on the mudflow in turn). In the coupled cases, three main waves were found to be generated by the mudslide; these were a seaward propagating crest, followed by a trough which propagated with the landslide front, and a small shoreward propagating trough. The density and initial submergence depth of the mudslide were found to be the two key parameters governing the free surface response. For deeper initial submergence depths, the interactions between the slide and the free surface were weaker, and the waves generated were small. The interactions were more significant for lower mud densities, although it should be noted that higher densities created larger waves. The possibility of resonance was very weak for field-scale flows, as the slide velocity would be subcritical (much slower than the generated waves), and the increasing water depth during motion would lead to increasingly weak interactions between the slide and the waves.

A similar study modelled the submerged landslide as an incompressible Bingham plastic flow (Jiang & LeBlond, 1993) instead of a viscous fluid. No deformation occurred in the Bingham fluid until a shear stress was applied which exceeded the yield stress of the material, after which it flowed as a viscous fluid. In addition to the landslide depth and submergence depth (from Jiang & LeBlond, 1992), the yield stress of the mud was found to be a critical parameter affecting the magnitude of the free surface response, and when the shear stress exerted on the bottom of the landslide became less than the yield stress, the slide stopped its motion down the slope. The Bingham behaviour significantly reduced the extent and speed of the mudslide, as well as reducing the magnitude of the waves generated. Runup was not investigated in these simulations.

Rzadkiewicz *et al.* (1997) carried out two-dimensional simulations to investigate the behaviour of waves generated by a deformable submarine landslide. The governing equations for this problem were the Navier-Stokes equations, based on a two-dimensional mixture model. In this case, both the dense flow close to the bottom boundary and the turbulent dispersion above were modelled (see section 2.2.4). The dense part of the slide was modelled as a viscoelastic fluid, and the turbulent dispersion was modelled as an ideal fluid. Both fluids were assumed to be incompressible.

The governing equations were solved by extending the 2D hydrodynamics program Nasa-Vof2D to a mixture (or diffusion) model. The model solved the Navier-Stokes

equations for a single fluid, and considered the sediments and ambient water as a mixture, rather than two separate fluids. The landslide material was modelled as a single-phase Bingham material (as in Jiang & LeBlond, 1993) for simplicity. The introduction of a diffusion flux into the model allowed the simulation of the development of a turbidity current above the dense landslide material, despite modelling the system as a fluid mixture. The rheological models were validated by comparison with analytical solutions for the motion of a Bingham fluid and a viscous fluid, with relative errors less than 1%. The governing equations were solved using an Eulerian finite difference technique.

Further validation was obtained by comparing the model results for a rigid triangular block sliding down a 45° slope to the experimental work of Heinrich (1992). The model predicted the amplitudes of the waves to within approximately ±1 cm, where the maximum crest amplitude was approximately 8 cm, and the maximum trough amplitude was approximately 25 cm. Some discrepancies between the model predictions and the experimental measurements occurred directly above the block, due to the highly turbulent motion at this location. As an extension to the rigid block simulations, further validation was undertaken in the laboratory, for the case of water waves generated by a sliding mass of sand underwater. Different rheological models were used for the landslide in the numerical model: a viscous fluid, a Bingham fluid without diffusion, and a Bingham fluid with diffusion. The Bingham model with diffusion was the most effective model at reproducing the amplitude (within approximately ±2 cm, relative to the maximum amplitudes of ±10 cm) of the experimentally-generated waves, although the waves were slightly more energetic than those observed in the experiments. The Bingham model is limited in its ability to simulate events at laboratory scales, where the slide is a granular flow composed of solid particles. Hence a model based on soil mechanics may be more appropriate at laboratory scales.

Grilli & Watts (1999) used a high-order two-dimensional boundary element method model to simulate tsunami generated by underwater landslides. The focus of the paper was the development of the model, and an associated sensitivity analysis on the input parameters, rather than a full parametric study. Simulations were carried out within a 'numerical wave tank' (NWT), which solved the fully nonlinear potential flow equations on a domain containing wave generation on the left extremity and an absorbing boundary on the right extremity. As such, the assumptions of incompressibility and inviscid-irrotational flow were employed, however no conditions were imposed on the amplitude or wavelength of the generated waves. The landslide was modelled as a rigid block of semi-elliptical shape (see Figure 2.13). A sensitivity analysis of the solution results on numerical parameters was performed, and the error due to free surface discretisation was one order of magnitude larger than the error due to mass conservation. These errors were still of order 0.1%. The BEM model solved for the solution on the

boundary of the problem domain only, making it attractive for landslide-generated tsunami applications, since this boundary incorporates the landslide motion and moving free surface.

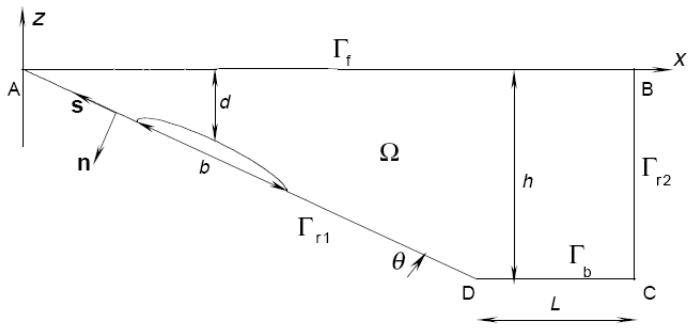

Figure 2.13: Problem domain specified for 2D landslide-generated tsunami simulation of Grilli & Watts (1999)

Tinti & Bortolucci (2000) investigated the energy of landslide-generated water waves within analytical and numerical models of 1D wave propagation. The model used the linearised shallow-water equations, and the bottom boundary of the domain was either specified as a constant-depth boundary or a constant-slope boundary. The landslide was modelled as a rigid block, with a shape of a $1 - \cos\alpha$ form. In the steady case of wave propagation in a flat channel due to a slide moving indefinitely with a constant velocity, the partition between potential and kinetic energy was

$$\frac{E_P}{E_K} = Fr^2, \quad Fr \neq 1 \tag{2.46}$$

where $E_P = \int_A \frac{1}{2}\rho g\zeta^2 dA$, $E_K = \int_A \frac{1}{2}\rho g u^2 dA$, ζ is the wave amplitude and u is the magnitude of the subsurface fluid velocity. In the more complicated case of a finite-duration slide, a solution was generated using the method of characteristics. The total energy was found to be time-dependent, and energy saturation within the system (where the total energy in the system, $E_P + E_K$, approaches a constant value) occurred when motion times were long enough that the generated wave packets completely separated. Energy saturation occurred for subcritical Fr only. Analytical predictions were compared to the results of numerical simulations using a finite-element model. Both 1D and 2D wave propagation were investigated numerically, a key difference being that 2D propagation did not exhibit the same energy-saturation characteristics as the 1D propagation case.

Fuhrman & Madsen (2009) extended a high-order Boussinesq-type model to include a moving seabed, for both coseismic and landslide-generated tsunami. First the extended model simulated waves generated by impulsive seafloor movements in both the positive and negative direction. The model then simulated landslide-generated tsunami

events in one and two horizontal dimensions, with results agreeing well to related physical experiments. Model geometry was selected to allow comparison with results from the models of Grilli *et al.* (2002); Lynett & Liu (2002). The Boussinesq-type model was able to reproduce all the different phases of wave development, from initial generation through the propagation phase to the final runup phase as the wave approaches a coastline, and included dispersive effects. The model maintained reasonable computational efficiency throughout the simulations.

Dotsenko (2005) investigated the runup of nonlinear solitary long waves, since this is the phase of motion of the most immediate concern to coastal communities at risk of inundation. One-dimensional propagation of long waves was considered in an idealised shelf zone, consisting of a basin of variable depth followed by a constant-sloping beach. The governing equations used were the shallow water wave equations, and the long wave was prescribed as a boundary condition on the domain, so that the wave generation was not explicitly modelled. Since many previous numerical models invoked the long wave assumption in the modelling of the generation of tsunami waves by submarine landslides, specifying the wave as a nonlinear long wave is reasonable. Dispersive effects were not considered in this study.

The governing equations were solved using a finite-difference scheme. A larger wave height led to a higher runup level, while a larger wavelength tended to decrease the runup. This effect was most pronounced at the shortest wavelengths, and may restrict the use of the shallow water equations to model tsunami runup. In some cases, wave heights increased by a factor of 2 to 4 during the shoaling and runup process. The results of the study were applied to provide preliminary estimates of runup due to tsunami waves in the coastal zone of Yalta.

Recently, the smoothed particle hydraulics (SPH) method has been used to simulate waves generated by submarine landslides (Qiu, 2008). SPH is a meshless Lagrangian method, and is advantageous in the simulation of flows with large amounts of free surface deformation, since particles implicitly define the location of the free surface without requiring a boundary condition. However, it should be noted that the treatment of solid boundaries within the flow can be more difficult in a SPH simulation, and often requires the use of 'ghost particles'. More details of the formulation of SPH models for free surface flows is provided in Gomez-Gesteira *et al.* (2010).

Qiu (2008) used SPH to simulate a triangular subaerial landslide sliding down a plane slope, and compared results to those of Heinrich (1992). The model solved the Euler equations for an inviscid incompressible fluid flow. SPH replaces the fluid in the governing equations with a series of points, and uses a kernel function to discretise the equations onto these points without the use of an underlying Eulerian mesh. Free surface elevations computed by the model and recorded during experiments agreed to within $\pm 5\%$, although the highly turbulent water motion near the impact location

caused some discrepancies between model predictions and experimental results. The far-field predicted wave record exhibited a slight phase shift compared to the experimental measurements, possibly due to numerical dissipation.

Nonlinear analytical and numerical models, two-dimensional wave propagation

In an extension to their two-dimensional simulations, Jiang & Leblond (1994) carried out a series of three-dimensional numerical simulations to determine the effect of an added lateral dimension on the waves generated by a viscous mudslide. The domain for this study is shown in figure 2.14. As in the two-dimensional study, the nonlinear shallow water equations were used as the governing equations (implying that the wavelengths of generated waves were much larger than the depth of the fluid). This assumption was found to be valid on shallow slopes between 1° and 10°. Dispersive effects were ignored during this investigation. The mudslide was again modelled as the viscous flow of an incompressible fluid, to simulate only the dense flow close to the slope, rather than the turbidity current generated above. The long wave assumption was also invoked for the mudslide, setting the length scale of the mudslide to be much greater than its thickness. Tangential stresses on the water-slide interface were neglected, and the mudslide was assumed to rapidly reach its terminal velocity, so that inertial forces on the slide during its acceleration could be neglected. The nonlinear shallow water equations were solved using an explicit finite-difference scheme.

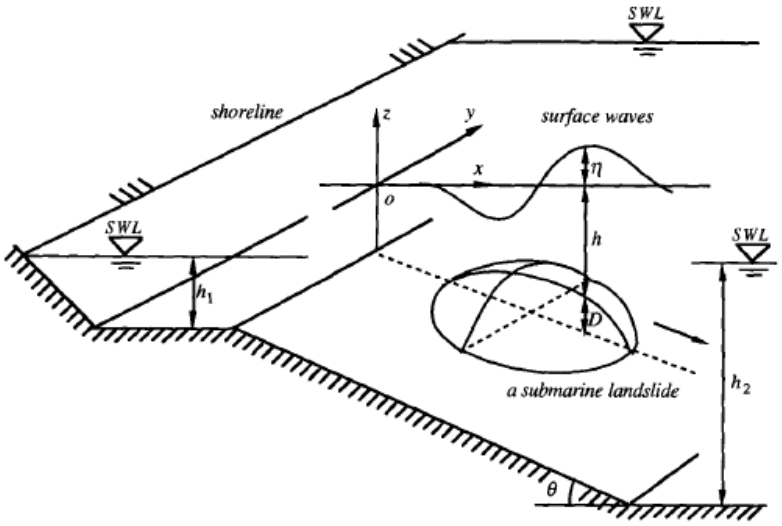

Figure 2.14: Problem domain specified for 3D mudslide-generated tsunami simulation of Jiang & Leblond (1994)

During motion, the mudslide quickly flattened and moved as a long, thin wave. As would be expected, the magnitude of the waves decreased significantly from the two-dimensional case, due to lateral spreading of the waves. The lateral spreading of the

mudslide was found to be less important than the lateral spreading of the generated waves in accounting for the decreased wave amplitude in the 3D simulations. Again, the runup caused by these waves impacting the shoreline was not considered in this study.

Liu *et al.* (2005) carried out an investigation on the runup and rundown generated by rigid masses sliding down a slope. This study was carried out using a large-eddy simulation, meaning that large eddy sizes were fully resolved, and small-scale turbulent fluctuations were modelled using the Smagorinsky subgrid scale model. The landslide was modelled as a solid triangular wedge, which translated down a planar slope under the influence of gravity. Both submarine and subaerial slides were tested during the simulations. Significantly larger runup was observed in simulations of subaerial slides compared to submarine slides, due to the different mechanisms of wave generation. In the submerged cases, the runup decreased as the initial submergence depth increased.

The simulation results were compared to a series of three-dimensional experiments (for details, see section 2.6). The lateral sidewalls of the wave tank were found to affect the runup and rundown, since the reflected waves from these walls created local maxima and mimima in the wave record. The numerical simulations successfully modelled the landslide motion and wave generation in both the submarine and subaerial cases, as well as the leading wave height and phase speed, and the maximum runup caused by the sliding mass.

Grilli *et al.* (2002) detail the development of a three-dimensional numerical wave tank (see also Grilli & Watts (1999)), able to model wave generation and absorption in a similar manner to a physical flume. The NWT solved fully nonlinear potential flow theory using a boundary element method (BEM), as in the 2D case, and had the capacity to model wave overturning. Again, this relied on the assumptions that fluid flow was inviscid and irrotational.

The landslide was modelled as a three-dimensional solid object moving in the negative x-direction down a slope, where the landslide shape was approximated by sech^2 curves. The use of these curves provided smoother bottom boundaries than the ellipses used in the 2D case, and eliminated the need for rounding of corners. Landslide motion followed the 2D wavemaker formulation of Grilli & Watts (1999). Comparisons were made with experimental results and 2D numerical results in a quasi-2D simulation (found to occur for landslides with a width:length aspect ratio larger than 2:1), with good agreement between the phase of the simulated and measured waves at four different wave gauges. The numerical model over-predicted the amplitude of the initial crest, and under-predicted the amplitude of the subsequent trough, with a maximum error of approximately 20%. Fully three-dimensional landslides were also simulated, along with a sensitivity analysis of the length and width of the domain on the waves generated. The characteristic tsunami amplitude was found to be independent of do-

main width for $w_0 \geq 2W$, where w_0 is the domain width, and W is the landslide width. In the same way, the characteristic tsunami amplitude was found to be independent of domain length for $L_0 \geq \lambda_0$, where L_0 is the domain length, and λ_0 is the characteristic wavelength of the generated waves.

Guyenne & Grilli (2006) simulated shoaling and breaking of solitary waves over a sloping ridge in the numerical wave tank of Grilli *et al.* (2002) (described above). The submerged sloping ridge was modelled as a constant 1:15 slope in the x-direction, with a lateral $\text{sech}^2(ky')$ shape for k values between 0.1 and 0.5. The same amplitude and speed of the incident solitary wave were used in all simulations. Both the free surface elevations and the internal velocity components of the waves were calculated. The transverse variation of the bottom boundary was an important factor for the wave properties and the type of breaking, as larger values of k led to more localised breaking processes on the ridge. Sensitivity to the domain size and the size of the incident wave was investigated. Although smaller incident wave heights took longer to break (an expected result), they also exhibited a larger ratio of breaker height to incident height. This may have been caused by a larger amount of refraction and focusing of wave energy during the increased shoaling time for these lower-amplitude waves.

Lynett & Liu (2005) examined the runup generated by 3D subaerial and submerged sliding masses.The goal of the study was to determine the dependence of the runup on the landslide shape, size and motion, as well as the slope of the beach. To eliminate the effects of changes in landslide velocity and slope angle on the height of the generated waves (and hence, on wave runup), both of these were held constant during the simulations. The model integrated the equations of motion through a number of constant-density layers of arbitrary thickness. In this study, a two-layer model was applied, shown to capture linear wave behaviour up to $kh \sim 8$, and nonlinear wave behaviour up to $kh \sim 6$, where k is the wavenumber and h is the water depth. The landslide had a Gaussian profile in the transverse direction, and used the profile of Lynett & Liu (2002) in the longitudinal direction. The model used a finite difference algorithm to solve the equations of motion. Some simulations were compared with available experimental data (Synolakis *et al.*, 2002), with a maximum error of 15%. Higher landslide specific gravity values were less well-predicted, possibly due to higher levels of turbulence arising from the faster slide motion.

Sammarco & Renzi (2008) analytically modelled the 3D propagation of landslide-generated waves along a plane beach. The beach was assumed to have a constant slope, and the governing equations were the shallow water wave equations. The landslide was modelled as a solid block of Gaussian profile. The solution consisted of a system of edge waves propagating along the shoreline at large times. The longest waves, which travelled fastest, did not possess the largest amplitudes in this case. Dispersive effects meant that the largest amplitudes occurred near the middle of a wave train. The

longshore propagation of landslide-generated waves is important, since the maximum wave amplitudes on the shoreline occur some distance away from the initial location of the landslide. Experimental studies of this problem were carried out by Di Risio *et al.* (2009a), and are described further in section 2.6.

2.6 Previous physical models of landslide-generated tsunami

Physical models used to investigate the waves generated by submarine landslides all have the common features of a domain of interest, a landslide model (or other appropriate wave forcing mechanism), and a means of measuring the properties of the generated waves. Previous experimental studies are discussed within this framework, with a particular focus on how the landslide was modelled, and how generated wave properties were measured. Findings and limitations of the different studies are discussed in this section as appropriate. For convenience, studies are classified as either simulating 1D wave propagation or 2D wave propagation.

2.6.1 Experimental studies: One-dimensional propagation

Heinrich (1992) validated a nonlinear model (Nasa-Vof2D, discussed in section 2.5) in a series of two-dimensional experiments on subaerial and submarine slides. Experiments were carried out in a 20 m long channel in the Hydraulic National Laboratory of Chatou in France. The landslide was modelled as a triangular box sliding down a 45° slope, and is shown in Figure 2.15. The triangular shape was selected to simplify the wave generation process, with the horizontally inclined face drawing down the water surface immediately above the block as a trough and the vertically inclined face pushing out water in a crest in front of the block. The box was released from rest using a hydraulic jack, and came to a stop at the base of the slope (so additional run-out of the landslide was not investigated). The mass of the box was varied by the insertion of lead weights, allowing different sliding velocities to be tested.

For data acquisition, Heinrich (1992) employed a video camera and several wave gauges located along the length of the flume to measure the generation, propagation and runup phases of wave motion. The error arising from the meniscus effect in the data recorded by the video camera was not discussed. Turbulent motions in the vicinity of the box caused some discrepancies between model predictions and experimental results, since Nasa-Vod2D did not contain any turbulence models.

Watts (2000) carried out two-dimensional physical experiments with an initially submerged landslide moving down a 45° inclined slope, with a similar solid landslide block to that of Heinrich (1992). The focus of the study was to distinguish between the

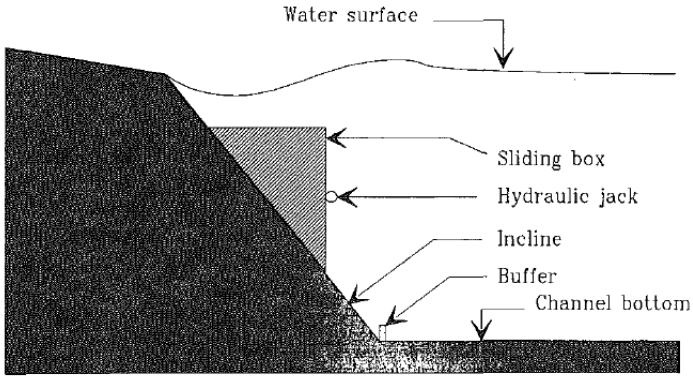

Figure 2.15: Experimental setup used by Heinrich (1992)

near-field and far-field features of the generated waves, and to generalise the motion of the landslide block, so that results could be applied to any block size or submergence. Subaerial landslides were not investigated during this study. Several different block sizes and densities were tested, and the experimental setup is shown in Figure 2.16. The dynamic coefficients associated with the landslide motion, and hence the landslide initial acceleration and terminal velocity, were determined experimentally. Wave gauges were used to measure water surface elevations in both the near field and the far field, giving the temporal variations in wave amplitude at two points within the wave tank.

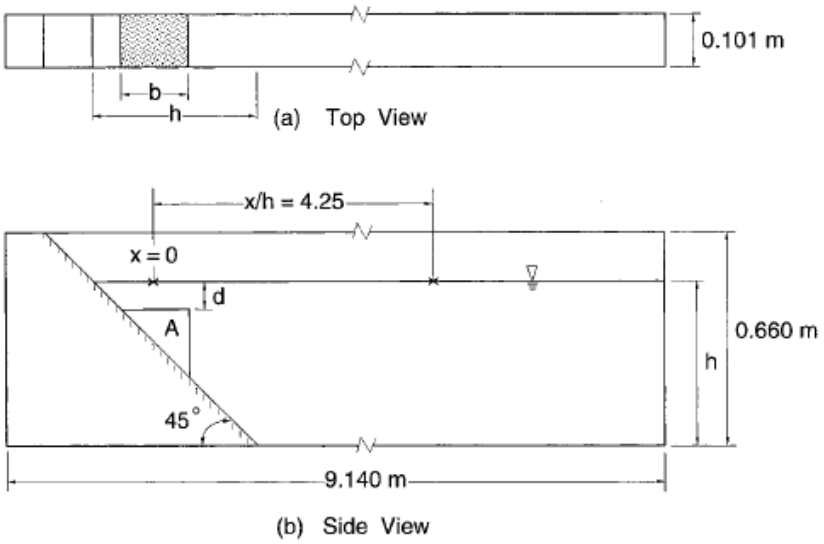

Figure 2.16: Schematic diagram of wave tank, incline, solid block and wave gauge positions used by Watts

In these experiments, Watts classified the physical domain into two regions, near-field and far-field, based on the measured characteristics of the waves. He also derived channel depth criteria to determine whether the waves generated by submarine landslides would propagate as deep water waves or shallow water waves,

$$h > t_0\sqrt{gd}, \tag{2.47}$$

where h is the channel depth, t_0 is the duration of landslide acceleration, g is the gravitational acceleration and d is the initial submergence depth. In a field situation where the landslide is long and the failure slope is mild, waves can be reasonably expected to behave as shallow water waves. The conversion from the maximum kinetic energy of the solid block to characteristic wave potential energy was found to be between 3% and 7% in these experiments. Only characteristic wave energy could be determined from experimental measurements, due to the discrete measurements of wave amplitude provided by the wave gauges. The ratio of nonlinear effects to dispersive effects was quantified using the Ursell parameter,

$$U \equiv \frac{a\lambda_d^2}{h^3} \tag{2.48}$$

where a is the wave amplitude. For $U \gg 1$, initially linear waves would later begin to exhibit nonlinear effects. Dispersive effects would always be observed in the far field, and if $U = O(1)$ then initially linear waves would never exhibit nonlinear effects (for propagation in a constant-depth channel).

Panizzo *et al.* (2002) carried out two-dimensional experiments for waves generated by dropping a weighted box into a wave flume (a reproduction of Scott Russell's wave generator, see figure 2.17). The aim of the experiments was to obtain a robust method for the analysis of free surface waves forced by a subaerial slide, although results could easily be applied to submarine slides. Wave amplitudes were measured at six locations throughout the flume using resistance wave gauges, calibrated to an accuracy of ±3%.

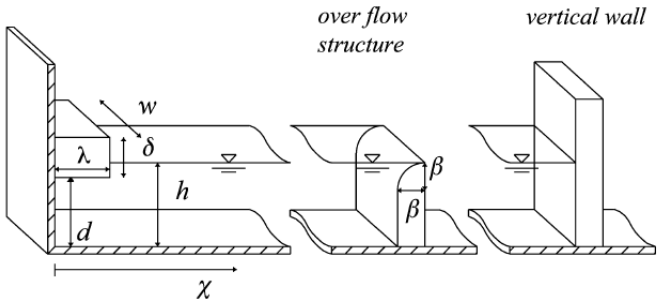

Figure 2.17: Schematic diagram of wave tank, solid block and overflow structure used by Panizzo *et al.* (2002)

The motion of the rectangular box was constrained to the vertical direction only by the use of guide rails. Wavelet transform analysis was used to investigate the celerity of the impact wave and the propagation of energy in the wavefield, as shown in figure 2.18. An overflow structure was employed at the end of the flume to minimimise the reflection of waves back into the domain of interest. The use of wavelet transform analysis also

allowed the estimation of the reflection coefficient of the overflow structure (found to be approximately 0.3), and the effect of reflected waves and seiche waves set up within the flume. The period of these seiche modes was estimated.

As the length and height of the falling box were increased, relative to the depth of water in the channel, the form of the leading wave changed gradually from an oscillatory wave to a solitary wave. At higher ratios of $\lambda : h$ and $\delta : h$ (see figure 2.17 for definitions), the leading wave became separated from the dispersive wave pattern, and began to form a complex bore.

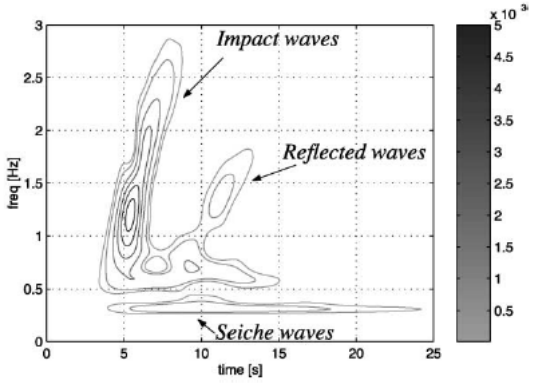

Figure 2.18: Typical wavelet spectra of generated waves, from Panizzo *et al.* (2002)

Fritz *et al.* (2003a) used particle image velocimetry (PIV) to visualise the surface and subsurface regions of the wavefield generated by a subaerial granular landslide, as shown in Figure 2.19. The landslide moved down a planar slope, which transitioned sharply to a horizontal boundary. A pneumatic landslide generator provided the slide's dynamic impact characteristics, so that realistic slide velocities could be achieved. The laser sheet (Nd-YAG) was introduced to the study area from downstream, since water splashing and landslide material did not allow the more traditional methods of illumination from either above or below. PIV particles had a diameter of 1.6 mm and a density of 1.006 g/cm^3. A progressive scan camera recorded images at a rate of 30 Hz.

The impact of the landslide caused mixing between the three phases of water, slide material and entrained air, and waves generated during experiments were unsteady and nonlinear. Flow separated from the slide shoulder for high impact velocities, and a secondary transient bore formed after the initial impact crater collapse and the first impact wave had propagated out of the impact area. The instantaneous velocity fields provided by analysis of PIV images allowed a detailed description of the kinematics of the tsunami formation.

The second part of this investigation (Fritz *et al.*, 2003b) focused on the hydrodynamic impact craters formed by the impact of the granular slide. Using velocity fields generated by the PIV system, the criteria for flow separation were developed based on

the thickness and Froude number of the slide. In the separated flow regime, impact craters were defined as either backward collapsing impact craters or outward collapsing impact craters, again depending on the slide thickness and Froude number. The water displaced by the slide was investigated, along with the time and rate of maximum volume displacement.

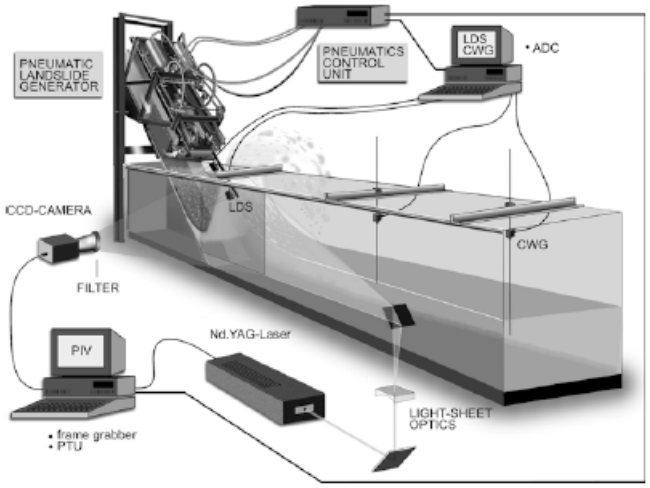

Figure 2.19: Experimental setup used by Fritz *et al.* (2003a)

Fritz *et al.* (2004) conducted a series of two-dimensional experiments to investigate the waves generated by a granular slide, using a similar setup to Fritz *et al.* (2003b). The granular slide mass, slide impact velocity, slide thickness and undisturbed water depth were varied during the experiments. The generated waves were recorded at seven discrete locations within the tank using capacitance wave gauges, and the velocity fields associated with the landslide impact into the water were captured using particle image velocimetry (PIV).

Four main classes of gravity wave were observed in the study: Weakly nonlinear oscillatory waves, nonlinear transition waves, solitary-like waves, and dissipative transient bores (prior to breaking). The occurrence of these wave types depended on the landslide Froude number and the landslide thickness relative to the undisturbed water depth. The applicability of classical nonlinear wave theories to these waves was investigated. Wave heights exceeded the breaking criterion for shallow water waves by up to 60% in some cases, as breaking and bore formation took time to occur. Between 4% and 50% of the kinematic slide impact energy was transfered to the impulse wave train (much higher than recorded for slides controlled by gravity alone). Predictive equations were developed for the generated wave amplitude and wavelength from the experimental results. These predictive equations were applied to the Lituya Bay landslide-generated tsunami of 1958, and compared to other model predictions of the runup and wave height for this event. The equations developed in this study predicted

the runup of the Lituya Bay tsunami to better than ±0.5%.

Grilli & Watts (2005) carried out two-dimensional experiments intended to validate a two-dimensional fully nonlinear potential flow (FNPF) numerical model (described in section 2.5). The landslide was approximated as a rigid block of semi-elliptical shape, constructed from plywood and mylar sheets. The initially submerged block slid down a 15° slope on small wheels, and contained an accelerometer to measure the motion of the block's centre of mass. Free surface variations generated by the sliding block were recorded by four capacitance wave gauges within the tank. Despite some issues with surface tension in the use of the wave gauges, the 2D-FNPF numerical model was successfully validated by the physical experiments.

To mark the 50th anniversary of the Lituya Bay landslide-generated tsunami, Fritz *et al.* (2009) carried out two-dimensional physical model tests to reproduce this event at a 1:675 scale. Results were compared with numerical model results in Weiss *et al.* (2009). The focus of the two-dimensional tests was the runup generated on the opposite side of the bay to the granular landslide impact location. The use of PIV provided vector plots of the landslide impact and wave generation, as described in Fritz *et al.* (2003b). The wave height and subsequent runup predicted by the two-dimensional model were compared to predictions from other numerical models and empirical equations. The runup measured by the experiments almost perfectly matched the highest elevation of forest destruction recorded in the actual event, 526 m compared to 524 m.

Sue (2007) (see also Sue *et al.*, 2011) used a two-dimensional benchmark setup to describe tsunami waves generated by submarine landslides. The benchmark setup involved a semi-elliptical rigid block landslide moving down a 15° slope under the influence of gravity, as shown in Figure 2.20. A laser-induced fluorescence technique provided spatial and temporal variations in free surface elevation throughout the tank. This technique was tested by comparison with traditional resistance wave gauges, with sub-millimetre agreement. Particle tracking velocimetry (PTV) was used to determine subsurface velocity fields to observe water motion around the landslide. The maximum efficiency of energy transfer from the slide to the wave field was approximately 6%. Results were compared to results from a BEM numerical model. The model predictions were within ±25% of the experimentally-measured maximum crest and trough amplitudes. However, the numerical model failed to reproduce the turbulent wake behind the landslide during its motion, and may not have adequately described the complex flow generated by the transition from the 15° slope to the horizontal bottom of the flume. Experimental measurements of runup could not be directly compared to numerical model results.

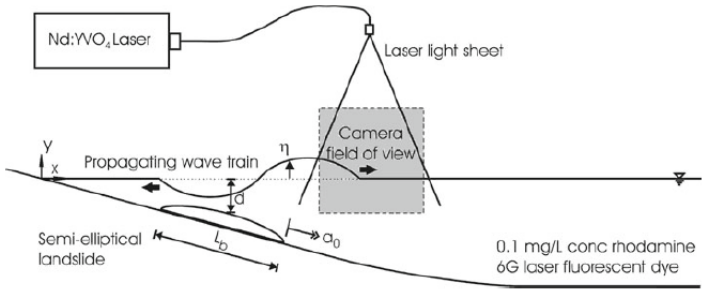

Figure 2.20: 2D experimental setup used by Sue *et al.* (2011)

2.6.2 Experimental studies: Two-dimensional propagation

In the modelling of the Lituya Bay landslide-generated tsunami of 1958, Fritz *et al.* (2009) also conducted three-dimensional experiments at a scale of 1:400. The three-dimensional wave generator used in these experiments is shown in figure 2.21. These tests highlighted the lateral spreading of the granular landslide, and the directional nature of the waves generated upon landslide impact. As with their two-dimensional experiments, PIV was used to visualise the velocities of the landslide and the waves in the impact region. Waves were extremely unsteady and nonlinear, and were located in the intermediate-depth regime. The height and runup of the generated waves were recorded using several wave gauges, however detailed three-dimensional bathymetry of the bay would be required for direct comparisons between the data measured in the lab and recorded in the field.

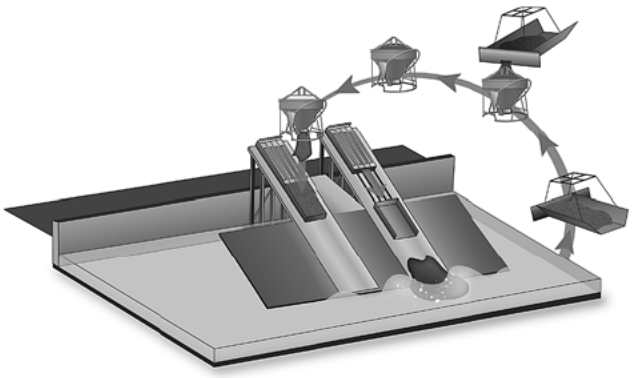

Figure 2.21: 3D wave generator used by Fritz *et al.* (2009)

Di Risio *et al.* (2009b) carried out three-dimensional physical experiments in a large wave tank to investigate the waves generated by a solid block landslide sliding along the flank of a conical island, as shown in Figure 2.22. Wave gauges measured water surface variations within the tank and shoreline movements on the slope. The subaerial landslide moved down the slope under the influence of gravity on a ramp to eliminate issues with changing slope curvature. The shoreline radius was varied

during experiments by changing the depth of water within the tank (greater depth caused a decrease in shoreline radius). The location of maximum inundation along the shoreline was determined, along with the properties of the generated three-dimensional wave field. These experimental results validated the 3D analytical model of Renzi & Sammarco (2010).

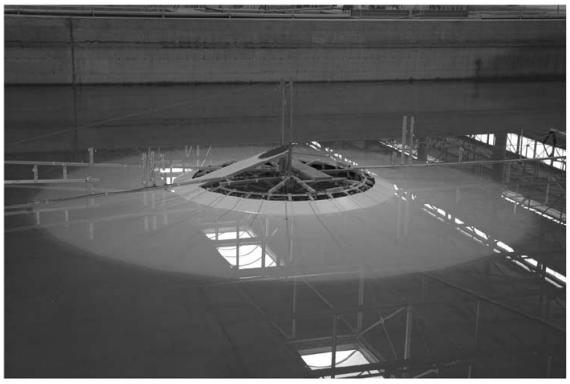

Figure 2.22: Conical island used in the 3D experiments of Di Risio *et al.* (2009b)

In a separate study, Di Risio *et al.* (2009a) investigated the edge waves generated by subaerial and partially submerged landslides on a straight sloping coast. Wave gauges provided water surface measurements, with a focus on the alongshore propagation of waves. The slope of 18.4° (1 vertical to 3 horizontal) was used, as it is similar to the slope in the wave generation region on the flank of Stromboli, Italy. Stromboli is a volcanic island, and as such is considered a likely location for the generation of tsunamigenic landslides. Far field analysis was difficult due to reflected waves from the sidewalls of the tank. Subaerial and partially submerged landslides were compared. The second wave almost always caused the maximum runup. This wave was double-peaked, and if the peaks separated then the third wave caused the maximum runup. These results were compared to the analytical solutions of Sammarco and Renzi Sammarco & Renzi (2008).

Liu *et al.* (2005) validated a three-dimensional large eddy simulation (LES) numerical model (described in section 2.5) using a series of three-dimensional experiments. The model investigated the waves generated by a sliding mass, and the interaction of these waves with the sloping beach. The landslide was modelled as a solid block sliding down a plane slope of 26.6°, and the initial positions ranged from subaerial to submerged. The shapes tested were triangular and hemispherical, with different masses. Wave gauges measured time histories of the water surface at different locations within the tank, and were combined with a video camera to determine runup on the inclined slope. Larger runup occurred for a subaerial slide than for a submerged slide.

Panizzo *et al.* (2005) used an experimental study to determine empirical parameters for the characteristics of tsunami waves generated by subaerial landslides, where

generated waves propagated in two dimensions. As with Panizzo *et al.* (2002), wavelet analysis was used to eliminate reflected signals in the wave record, and to define whether the wave propagated like a solitary wave or an oscillatory wave. This three-dimensional setup utilised the symmetry of the wave tank by placing the model landslide (approximated by a rectangular shaped trolley) next to one of the tank's sidewalls, as shown in figure 2.23.

The empirical formulae obtained from this work were correlated with experimental results with support from artificial neural networks (ANN). These formulae were subsequently compared to previous experimental work. The empirical equations were effective in both cases, although the first impulsive wave was characterised more successfully than the maximum wave in the generated wave group.

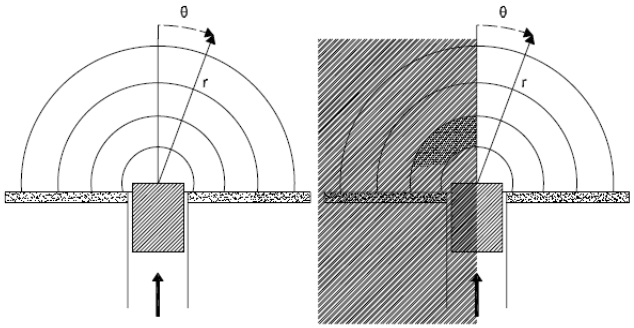

Figure 2.23: Use of wavefield symmetry in 3D experiments, from Panizzo *et al.* (2005)

Enet & Grilli (2007) carried out a series of three-dimensional tests using a submerged rigid block sliding down a plane 15° slope to generate tsunami waves, shown in figure 2.24. The landslide was constructed from aluminium sheets, and had a Gaussian shape in both directions. During the experiments, the landslide was released from an initially submerged position and slid under the influence of gravity until coming to a stop against a foam cushion at the bottom of the slope. An accelerometer recorded the motion of the landslide's centre of mass, capacitance wave gauges measured the free surface elevations within the tank and a video camera measured runup. The slide acceleration was found to be more important than its terminal velocity as a parameter associated with three-dimensional wave generation. Two runup regimes were observed, depending on the initial submergence depth of the slide compared to a reference depth d_{ref}, which followed simple power laws of d.

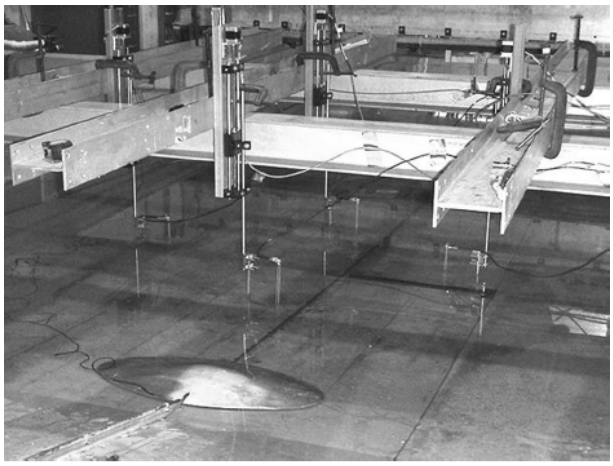

Figure 2.24: Three dimensional experimental setup used by Enet & Grilli (2007)

2.7 Tsunami risk mitigation: Education and community involvement

Education of local populations is an important step in the development of disaster-resilient communities (Morin *et al.*, 2008), and can be considered equally as important as the development of effective warning systems (Kurita *et al.*, 2007). Experiences from different countries affected by the Indian Ocean tsunami of 2004 highlight the fact that many of the lives lost were due to a lack of awareness about the signs of, or how to respond to, a natural disaster such as a tsunami. Communities must be involved in the preparation of disaster mitigation plans, as many disasters do not give enough time for a civic warning to reach residents. Preparing for disasters will also necessarily vary depending on the culture (Paton *et al.*, 2010), and the socio-economic status of the community at large. Poverty and lack of infrastructural development in many at-risk communities require a change in how communities are educated and prepared for a tsunami event.

Bird *et al.* (2011) discussed methodologies used in post-tsunami survivor surveys, and some of the challenges encountered in obtaining and interpreting timely and useful data from surveys. Communities could be classified as vulnerable to tsunami events due to their location and the lack of education about a disaster event. For example, many lives were unnecessarily lost during the Indian Ocean tsunami because of a mistaken belief that water levels at the beach would recede before the arrival of a crest from a tsunami wave. This did not occur in all the locations impacted by the tsunami, and many residents waited for the receding water level before evacuating (Bird *et al.*, 2011; Kurita *et al.*, 2007). Strong community ties could increase resilience to tsunami occurrence, as was observed in the South Pacific tsunami of 2009, since recovery efforts were cooperative and not completely dependent on civic or international intervention.

Said *et al.* (2011) report on the implementation of community-based tsunami preparedness and response plans in Malaysia based on experiences in the 2004 Indian Ocean tsunami. The case study focused on three villages affected by the Indian Ocean tsunami, and adopted a bottom-up approach, since the villages were too isolated to benefit from the actions of civic authorities during the event. Evacuation routes and safe zones were identified, and relevant information was made available for the education of the community by a variety of methods. A tsunami drill was implemented to assess community preparedness for a future tsunami event, and results indicated gains in understanding and preparedness based on the educational initiatives. A similar study was carried out in Sri Lanka (Kurita *et al.*, 2007), and also emphasised the need for high levels of community involvement (due to the lack of resources, compared to other at-risk countries). Two rounds of workshops were conducted, to enable the community education to be carried out by local authorities who understood the culture and context of the society. These workshops allowed the construction of tsunami hazard maps, as shown in the example in figure 2.25, and action plans based on these maps. Challenges to the effective participation of communities were the lack of participation by residents of areas identified as 'low-risk', and lack of participation by residents whose employment interfered with the timing of the workshops.

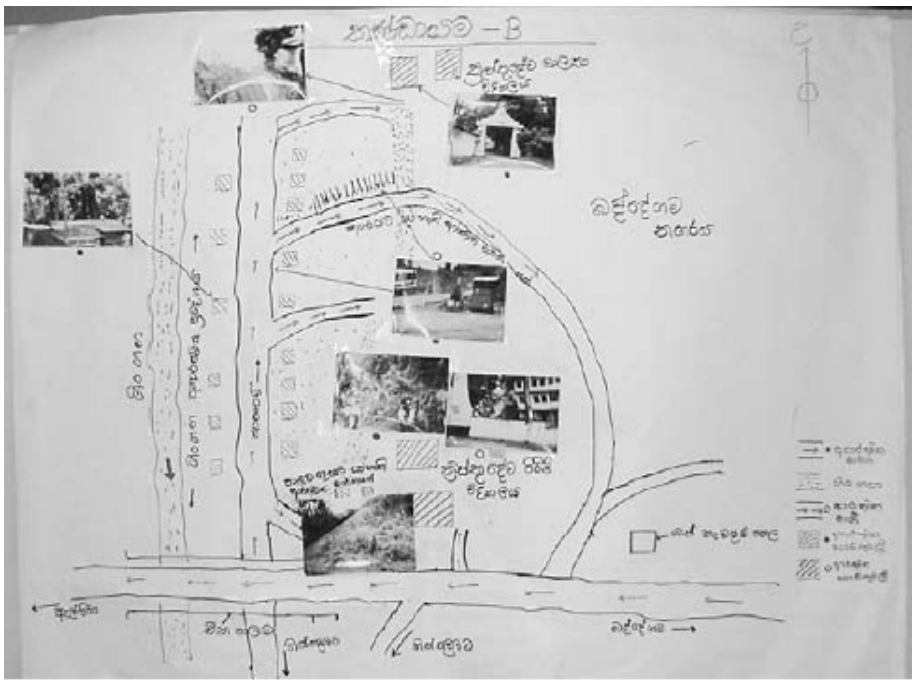

Figure 2.25: An example of a tsunami hazard map produced in the community workshops of Kurita *et al.* (2007)

Morin *et al.* (2008) identified knowledge and education gaps which contributed to the massive loss of life in Indonesia during the Indian Ocean tsunami. Educational initiatives to improve the resilience of communities need to be initiated in both a

top-down and a bottom-up approach to be fully effective. In many cases, even after increases in education about tsunami events, residents held to unfounded beliefs about the causes of tsunami. The findings of the study underscore the responsibility of the scientific community to share and adapt its knowledge to local contexts through the use of different communication tools (such as the brochures shown in figure 2.26). Lessons learned from the 2004 tsunami can contribute greatly to building more tsunami-resilient communities in the future.

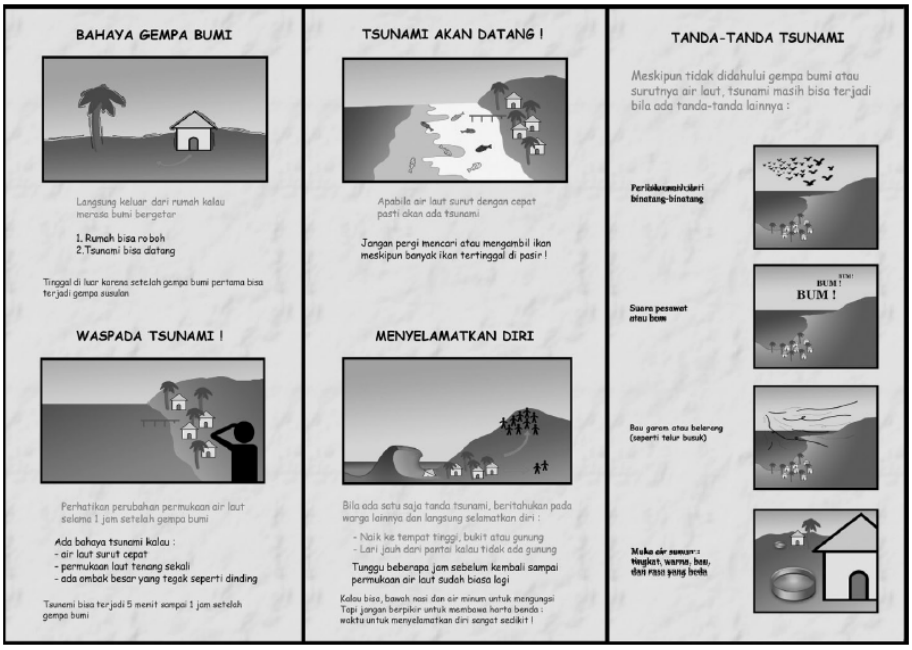

Figure 2.26: Educational brochures used by Morin *et al.* (2008)

Hawaii has experienced many tsunami events during its history (Gregg *et al.*, 2007), and has a siren system to warn residents of an impending tsunami. However, Gregg *et al.* (2007) found, through the use of questionnaires, that many residents were unable to identify the actual meaning of the siren, or the appropriate action to take as a response. Other information sources, such as television, radio, or social sources, were often relied upon before action was taken in an event. Public understanding of the natural warning signs of a tsunami was found to be relatively low, meaning that a future event could still claim lives unnecessarily.

Ronan *et al.* (2012) used a quasi-experimental methodology to determine the effectiveness of a tsunami education initiative within New Zealand schools. Students answered questionnaires before and after the education initiative, relating to their knowledge and awareness of natural hazards, fear of a tsunami, and their level of preparedness for an event. The education initiative improved all of these criteria, although many students did not note any change in their expected ability to psychologically cope with an event.

Tsunami are natural hazards with the ability to devastate large stretches of coast-

line, sometimes with little available warning time for local communities. Because of this, it is vital that communities learn from experiences gained in previous events, and actively participate in civil emergency plans, to increase their preparedness for future events. Education plays a crucial role in the dissemination of scientific knowledge to coastal communities, and can also help to reduce poor response choices.

2.8 Summary

In order to effectively model landslide-generated tsunami, it is important to understand where and how such landslides occur in the field. Tsunamigenic submarine landslides tend to mobilise larger volumes of sediment, and occur on shallower slopes, than subaerial landslides. Submarine landslides also tend to occur in sloping marine environments with high sediment accumulation rates. The failure of a submarine sediment mass depends on the driving gravitational force and the combination of seismic, wave and other actions to increase the destabilising stress or decrease the frictional strength of the sediment. The post-failure motion is governed by the nature of the failure, the sediment properties and environmental factors such as the angle of the failure slope and the presence of canyons or other bathymetric features.

Field observations following the historical occurrence of landslide-generated tsunami provide valuable data for the calibration of tsunami models. In some cases, a combined seismic and landslide tsunami source has been the only plausible explanation able to account for geographical differences in wave runup and the timing of wave impact on the shoreline. The experiences gained from historical tsunami events also help to inform current residents of high-risk areas in how best to prepare for, and react to, a tsunami event. Educational initiatives are an important means of ensuring life safety for future events, since many coastal communities do not have the infrastructure to defend against wave inundation, or the technology to warn residents of an impending tsunami threat. In the case of landslide-generated tsunami, warning times are very short, and so community preparedness through improved education is even more important as a hazard mitigation strategy.

Predictive mathematical models play an important role in tsunami warning systems, and in advancing understanding of the physical mechanisms of wave generation, propagation and inundation. Due to the complexity of tsunamigenic landslide composition, failure and subsequent motion, mathematical models must make a series of approximations to effectively simulate a landslide-generated tsunami. These approximations should be informed by a strong understanding of the underlying physics of the problem, so that robust models can be developed. Approximations include the geometry of the simulation domain, the treatment of boundary conditions and the nature of the landslide and the ambient fluid. The majority of mathematical models have assumed that the landslide can be modelled as a solid block moving down a linear slope under the influence of gravity. This leads to over-estimates of the amplitude of generated waves, and ignores the processes which act to deform the landslide during motion. Previous tsunami models have used viscous and inviscid approximations of the ambient fluid. Assumptions regarding the size and shape of the generated waves can further simplify mathematical models. Often previous models have used the long-wave

assumption to simplify the formulation of the model.

Laboratory models are used to validate mathematical models of landslide-generated tsunami for an idealised geometry. Since realistic grain size distributions are difficult to achieve at laboratory scales, most physical models of landslide-generated tsunami have also modelled the landslide as a solid block moving down a slope under the influence of gravity. Slopes were usually made steeper than typical continental slopes to achieve landslide motion capable of generating measurable free surface waves. Experimental studies often measured the amplitude of the generated waves using discrete wave gauges, although some more recent studies used non-intrusive measurement techniques to measure spatial and temporal variations in free surface elevation.

Previous models of landslide-generated tsunami, physical and mathematical, have either simulated an idealised problem or a historical event. The goal of this research is ultimately to effectively model realistic events, while gaining a fundamental understanding of the physics of the different phases of wave generation and evolution. Outputs from this research can be combined with lessons learned in historical events and used to prepare coastal communities for the occurrence of a landslide-generated tsunami, in order to save as many lives as possible. In a time where the costs of natural distasters to lives and infrastructure are ever increasing, such research is of vital importance.

Chapter 3

Project objectives

Previous two-dimensional experimental studies into tsunami generated by submarine landslides have generally modelled the landslide as a solid block sliding down a sloping boundary under the influence of gravity. Figure 3.1 shows a schematic of this setup, where the landslide is modelled as a semi-elliptical solid block, and the transition from the sloping boundary to the horizontal base of the flume is sharp. Although granular materials have been used in some experimental studies, the pneumatic piston used to provide motion to a granular slide in Fritz *et al.* (2003b) is only applicable for subaerial landslides, since the motion of a submerged piston would disrupt the wave field for a submarine slide. The landslide shape used in previous studies has either been triangular to separate out the wavemaking features of the block, or elliptical to approximate the shape of the dense landslide material during downslope motion.

In previous experiments, motion of the solid block down the sloping boundary generated waves throughout the flume. Free surface measurements were obtained at discrete locations using either resistance wave gauges (RWGs) or capacitance wave gauges (CWGs). More recently, optical methods have allowed the measurement of the

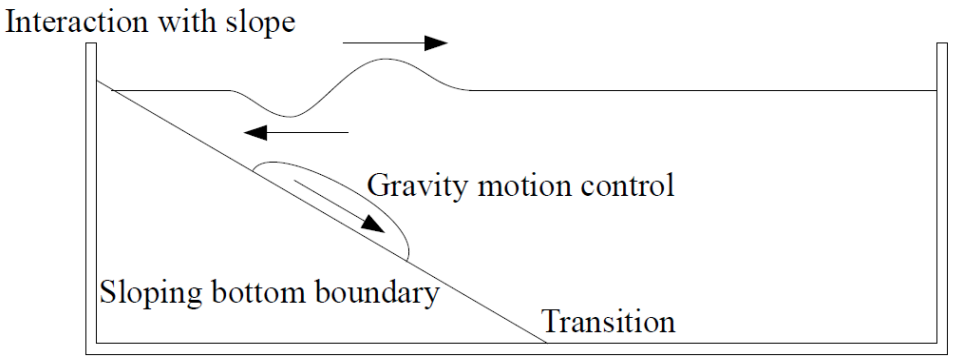

Figure 3.1: Main features of previous experimental setups used to investigate landslide-generated tsunami, including a sloping boundary, gravity-driven landslide motion and a transition to a horizontal bottom boundary.

full spatial and temporal variations in free surface elevation (such as Sue *et al.*, 2011), and the subsurface fluid velocities (such as the PIV technique used by Fritz *et al.* (2004) or the PTV technique used by Sue (2007)). Some studies simply used a video camera located outside the flume sidewall to track the location of the free surface, however the meniscus on the flume sidewall introduced errors in measurements obtained using this method.

The experimental setup used to investigate landslide-generated tsunami in previous studies has several limitations, including the limited range of motion able to be simulated. The use of a gravity control means that landslide motion may only be varied by changing either the landslide mass or slope angle. This limits the range of motion able to be investigated during experiments, since for shallow slopes the landslide often cannot reach its terminal velocity before decelerating at the base of the slope. The transition from the sloping boundary to the horizontal bottom of the flume also causes problems. A sharp transition at the base of the slope could result in an unrealistically sudden deceleration of the model landslide, while a gradual transition could result in aquaplaning issues when using a rigid block landslide. In either case, any additional waves generated when the landslide encountered the transition would contaminate the wave field.

However, the most problematic aspect of the sloping boundary used in previous experiments is the inability to measure the properties of onshore-propagating waves. Waves generated by the downslope motion of a landslide block propagate in both the onshore and offshore directions, where 'offshore' is defined as the direction of landslide motion (away from the sloping shoreline), and 'onshore' is defined as the opposite direction. Any waves propagating in the onshore direction would almost immediately interact with the slope, rendering their amplitude unable to be measured. Surface tension effects at laboratory scales also affect runup measurements (the only property of the onshore-propagating waves able to be measured using this setup).

The present study measures the properties of both offshore- and onshore-propagating waves generated by a submarine landslide, using a broader range of landslide motion than in previous studies. To achieve this, a series of two-dimensional experiments are carried out, with the landslide modelled as a solid block moving along a horizontal bottom boundary. Figure 3.2 shows the simpler geometry of the proposed experimental setup. Since the horizontal bottom boundary precludes the use of a shoreline within the problem domain, the offshore direction is again defined as the same direction as the landslide motion, and the onshore direction is the opposite direction.

Since the landslide moves along a horizontal boundary during the experiments, motion is no longer controlled by gravity. The proposed experiments use a mechanical system to control the landslide motion. It is anticipated that this will improve experimental repeatability, and allow a broader range of motion to be tested than has been

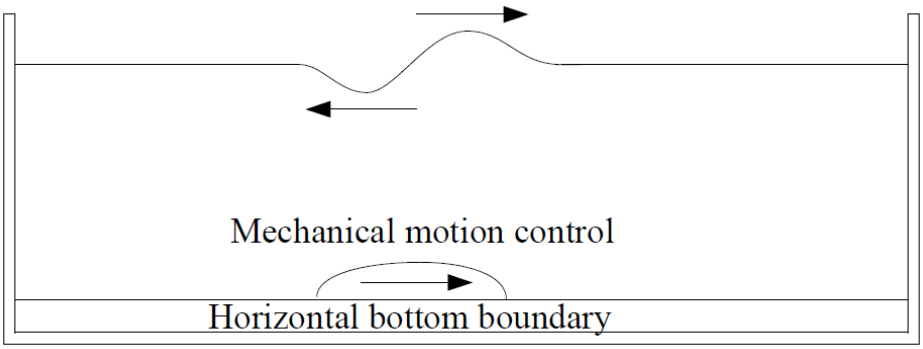

Figure 3.2: Main features of proposed experimental setup, including horizontal bottom boundary and mechanical control over landslide motion.

previously possible, since the motion is no longer dependent on the geometry of the experimental setup. This enables testing of different velocity profiles to determine the wave-making characteristics of different types of motion.

In reality, submarine landslides slide down a slope under the influence of gravity, so the proposed experimental setup is not representative of a field situation. However, such continental slopes typically range from 1° to 10°, which are too shallow to provide suitable landslide motion at laboratory scales. Most of the slope angles used in previous studies have ranged from 15° to 45°, which are extreme compared to typical continental slopes. Given the depth of water and distance of horizontal landslide motion compared to the distance of vertical landslide motion along a shallow slope, results obtained using a horizontal bottom boundary can be considered to be true in a local sense if applied to a field scenario.

The experimental results are directly compared to the predictions of three numerical models. The first two models are formulated using inviscid-irrotational flow theory, while the third assumes a viscous ambient fluid. One of the inviscid models invokes the linear assumption on the bottom boundary, while the second uses a nonlinear bottom boundary. Comparison between the different numerical models and the experimental measurements allows the effect of these different assumptions on the predictive capabilities of each model to be determined.

The predictions of the three numerical models are compared to the wave amplitudes and subsurface fluid velocities measured during the physical experiments. Wave amplitudes are measured using the laser-induced fluorescence (LIF) technique of Sue (2007), and the subsurface velocity field is measured using the particle tracking velocimetry technique described in the same studies. The experiments and spectral model simulations investigate the effect of landslide motion and fluid depth on the properties of the generated waves in a full parametric study.

In the application of numerical predictions to field situations, the two-dimensional

approximation of an infinite landslide width is usually not valid. To test the effect of an added lateral dimension on the properties of the generated waves, the linear inviscid model is extended to three dimensions. A series of preliminary simulations with this extended model determine the effect of the landslide aspect ratio on the properties of the generated waves, compared to the two-dimensional limiting case.

Chapter 4

Two-dimensional experimental method

4.1 Introduction

The purpose of the two-dimensional experiments described in this chapter was to measure the free surface waves generated by the motion of a landslide over a horizontal bottom boundary. The landslide was modelled as a solid block, following common practice in experimental studies of landslide-generated tsunami. A key objective of the experimental work was to measure the properties of waves propagating in both the onshore and offshore directions. The experiments required a high level of repeatability, and wave amplitudes needed to be measured to sub-millimetre accuracy.

Experiments were carried out in a long, narrow flume. The landslide block extended across the full width of the flume, so that generated waves propagated in one horizontal dimension only. Surface and subsurface measurements were obtained near the centre of the flume, to eliminate the effects of friction at the flume sidewalls. A false floor within the flume provided the horizontal boundary along which the landslide moved, and a mechanical system beneath the false floor provided motion to the landslide block. To enable measurement of both onshore- and offshore-propagating wave properties, the landslide motion was constrained to the central third of the flume length. This allowed the maximum time before wave reflections from the ends of the flume interacted with the generated waves.

An application of the laser-induced fluorescence (LIF) technique provided measurements of the landslide-generated waves during the experiments. This allowed full spatial and temporal resolution of the free surface elevation to be recorded during an experiment, over the full length of the flume.

The particle tracking velocimetry (PTV) technique provided measurements of subsurface fluid velocities generated by the motion of the submarine landslide. Particle

tracking velocimetry is a non-intrusive flow visualisation technique, which seeds a flow with small particles. A light sheet illuminates the particles, and a camera records the motion of the particles within the plane of the light sheet. Specialised software tracks particle motion between frames of the image record, allowing calculation of Lagrangian and Eulerian velocities within the flow.

Since landslide motion was provided by a mechanical system, a variety of landslide velocity profiles could be tested. For simplicity, and to provide a reasonable approximation of landslide motion in a field situation, the landslide motion consisted of an initial period of constant acceleration, followed by a period of constant velocity for a fixed length of time, followed by a final deceleration to rest. A parametric study investigated the dependence of the generated wave properties on the initial acceleration and the landslide velocity, as well as on the fluid depth.

Section 4.2 describes flow visualisation techniques in general, and specifically the LIF and PTV techniques. These descriptions include the general requirements for lighting, tracers (dye for LIF and particles for PTV) and image acquisition. The section also discusses the application of these two techniques to landslide-generated tsunami experiments.

Section 4.3 gives the details of the equipment used in the LIF and PTV experiments. This equipment includes the flume, baffles (used to remove residual free surface motions between experimental runs), laser, light box, dye, particles, and the camera used to record images. Section 4.3 also describes the mechanical system used to generate landslide motion during experiments, and a similar system used for the gantry supporting the image acquisition equipment.

Section 4.4 describes the motion control system used for the landslide block and gantry, and the checks to ensure that both systems achieved position and velocity targets to a high level of repeatability.

Section 4.5 gives details of the LIF experimental procedure and image processing used to calculate the amplitudes of the tsunami waves, and section 4.6 explains the details of the PTV experimental procedure and image processing used to calculate the subsurface velocity field generated by the landslide. Where appropriate, sections include a discussion of possible errors, and any strategies used to mitigate these errors.

4.2 Measurement techniques

4.2.1 Flow visualisation techniques

Flow visualisation techniques have been used for decades to gain an increased qualitative understanding of how fluids move. An excellent collection of flow visualisation images can be found in Van Dyke (1982). In the last twenty to thirty years, advances

in image capturing and computer processing technology have enabled flow visualisation to provide quantitative measurements of flow properties, such as the flow velocity field, the concentration and mixing of multi-fluid flows and variations in properties such as density, salinity and temperature.

Qualitative observations of flow behaviour can either use the addition of a tracer to a fluid, or a property of the fluid, to provide visualisation of the flow. The tracer is selected to be dynamically unimportant, so that the addition of the tracer to the flow will not alter the properties of the flow. Tracers in past experimental studies have included smoke, dye, small particles (such as magnesium flakes) and air bubbles.

Quantitative measurements allow the scalar or vector quantities of a particular flow feature to be measured. Often the calibration of these systems is more rigorous than for qualitative systems, to allow robust results to be reproduced. In a similar manner to qualitative observations, quantitative measurements can use the properties of the fluid as a means of visualisation (such as the different optical thicknesses arising from changes of density within a fluid), or rely on the addition of passive tracers into the flow. Flow properties which have been measured using flow visualisation include, but are not limited to, concentrations, velocities, temperature, salinity, and density.

The measurement of vector velocity fields within a fluid flow has been typically accomplished in the past using one of the forms of light velocimetry, such as laser speckle velocimetry, particle image velocimetry and particle tracking velocimetry. Previous studies of scalar quantities within a fluid flow obtained quantitative measurements using techniques such as laser-induced fluorescence, light attenuation or tomographic interferometry. More recent studies have combined scalar and vector measurements, allowing multiple flow properties to be measured within a single experiment, for example the measurement of velocity and temperature fields to determine the turbulent heat flux in Hishida & Sakakibara (2000) and mixing in Law & Wang (2000). Both studies used particle image velocimetry to measure the velocity field within the flow, and planar laser induced fluorescence to measure the scalar temperature field. Although these combined experiments are more difficult to set up, since they typically require the synchronisation of more than one image acquisition camera, they have the advantage that experiments do not need to be repeated to measure different flow properties. Such experiments are also able to provide information about the turbulent tracer flux during experiments.

4.2.2 Laser-induced fluorescence

Laser-induced fluorescence (LIF) is a flow visualisation technique used to determine the scalar concentration of a dye tracer within a fluid, and can be applied at a point, along a line, in a two-dimensional plane or over a three-dimensional volume (see Cri-

maldi, 2008). Currently planar laser-induced fluorescence (PLIF) is the most common application of LIF, and is used to determine concentrations within a two-dimensional flow structure (for example the centreline of a negatively buoyant jet, see Oliver, 2012). The technique uses a laser light to excite molecules of the tracer dye, which absorb some of the laser light and re-emit light at a different wavelength. The intensity of this emitted fluorescence can be used to deduce the concentration of the tracer dye within the flow. Since laser-induced fluorescence is a non-intrusive technique, it is an attractive option for the measurement of concentrations within a range of fluid flows. Lasers have the advantage over other light sources in that a laser beam can be collimated (i.e. all light rays within a laser beam are parallel), and a laser can emit light with a very narrow wavelength band, ensuring that the fluorescence generated only arises from the dye molecules excited by that wavelength band.

Recent improvements in light-emitting diode (LED) technology have led to the development of LED light boxes which are able to emit a narrow sheet of light in a narrow wavelength band. Such light boxes are able to excite fluorescent dye in a similar manner to a laser sheet, and have the advantage that they are significantly cheaper than lasers. Light boxes also do not require the same safety measures as lasers. However, light emitted from a LED is less bright than that emitted by a laser, and so higher dye concentrations are required for a LED light box to achieve the same fluorescence intensity as a laser sheet. This can cause problems with the attenuation of the light as it passes through highly dosed ambient fluid.

The key considerations in a laser-induced fluorescence experimental setup are the selection of a light source and dye which are compatible, and the use of an appropriate image capture system. Lasers used in LIF experiments can be continuous wave lasers, such as argon-ion lasers, or pulsed lasers, such as Nd-Yag lasers. Pulsed lasers have the advantage of a very high power output, and the ability to 'freeze' a flow due to the short duration of each pulse (Law & Wang, 2000). However, they have the disadvantage that they do not possess a Gaussian energy distribution, and there may be a slight difference in energy distribution between pulses (although this could be accounted for during image processing). The excitation species is either seeded into the flow, or (less often) produced in a chemical reaction within the flow itself. The main requirement for a tracer species is a high quantum efficiency, or high level of fluorescence intensity compared to excitation intensity, as well as an excitation wavelength corresponding to the wavelengths of available laser sources, and a sufficiently large gap between excitation frequency and fluorescence frequency so that the incident light can be excluded from image acquisition systems. Rhodamine dye has been used in experiments to investigate the mixing of turbulent jets (such as in Oliver, 2012; Law & Wang, 2000; Guillard *et al.*, 1998), while biacetyl was used as a tracer in gaseous turbulent jet mixing experiments (Cruyningen *et al.*, 1990). During experiments, the incident laser light is prevented

from being recorded by the camera using a physical filter, either a lowpass filter or a bandpass filter depending on the experimental setup. The choice of camera for a LIF experiment typically involves consideration of the camera's light sensitivity, bit depth, pixel resolution and frame rate. In general, high-performance monochrome cameras are used more often than colour cameras.

In the current experiments, LIF provided measurements of spatial and temporal variations in free surface elevation caused by the motion of a submarine landslide. A low concentration of fluorescent dye was mixed with the water in the flume (see section 4.3), and laser illuminated the free surface of the fluid in a 2D plane. The dyed water fluoresced in the plane of the laser sheet, and this allowed identification of the free surface as the intensity interface between the bright water and the dark air above. The use of LIF to measure free surface elevations in these experiments is described in more detail in section 4.5.

4.2.3 Particle tracking velocimetry

Overview of particle tracking velocimetry technique

Particle tracking velocimetry (PTV), and the similar particle image velocimetry (PIV), are techniques used to determine the velocity field within a flow. Although these techniques may be used to obtain measurements of a three-dimensional velocity field, the current discussion is limited to their use in the calculation of velocity fields within a two-dimensional plane. In both cases, the flow is seeded with dynamically unimportant tracer particles, which are illuminated by a light sheet from a suitable source. Images of an experiment are recorded by a camera located perpendicular to the light sheet. In general, the velocity fields are determined in each system by determining particle displacements between frames and multiplying this displacement by the frame rate, obtaining the local velocity from equation 4.1 (Adrian, 1991).

$$\mathbf{u}\left(\mathbf{x}, t\right) = \frac{\Delta \mathbf{x}\left(\mathbf{x}, t\right)}{\Delta t} \tag{4.1}$$

Particle image velocimetry uses a higher particle seeding density, and velocity fields within an image are determined by correlation of sub-windows of an image with sub-windows of a subsequent image. The advantage of this technique is that it allows relatively computationally inexpensive processing, however it has the disadvantage that velocity fields of flows with a high degree of spatial variability may not be well-resolved by the system. Particle tracking velocimetry uses a lower seeding density than particle image velocimetry, and the Lagrangian velocity of each particle between frames is determined from equation 4.1. The Lagrangian velocities of all particles are then interpolated onto a rectangular grid to provide the Eulerian velocity field for

the flow. The advantages of this technique are that it is able to resolve flows with a high degree of spatial variability, it can provide Lagrangian velocity data (which PIV does not naturally provide), and it is more flexible regarding the seeding density of tracer particles. The main disadvantages of the technique are that it does not directly provide the Eulerian velocity field for the flow (the interpolation process can also be problematic for very low seeding densities), and it tends to require more complex image processing than PIV. Although either technique would have served the purpose of calculating subsurface velocity fields within the current study, PTV was selected because the Fluid Mechanics Laboratory at the University of Cantebury had a state of the art PTV system available.

A particle tracking velocimetry system involves four main steps. These are image capture (and any required image preprocessing or filtering), particle identification, particle matching between frames, and velocity field interpolation. These steps are discussed in more detail in the following sections. Additional detail can be found in Adrian (1991) and Nokes (2009). The Streams software package is an image processing software package specifically designed for particle tracking velocimetry systems (Nokes, 2009), and some of the image processing steps are discussed based on the use of this software as a processing tool.

Particle and lighting selection

The basic consideration in a particle tracking velocimetry system is the requirement that particles can be clearly identified in images without altering the properties of the flow. As such, light sources used in two-dimensional PTV systems need to provide a light sheet of high intensity, with small thickness and divergence. The light intensity should also exhibit minimal spatial and temporal variations. This means that lasers are often the light source of choice for such experiments, since collimated beams are straight and narrow, and lasers can provide a high-intensity sheet of light within a narrow frequency band. The narrow light sheet limits the time that a particle is likely to be present within the sheet (possibly due to out-of-plane motions).

Particles used in PTV experiments must be small and near-neutrally buoyant. This is a requirement not only to ensure that the particles are dynamically unimportant while responding quickly to changes in the flow velocity, but also to limit the amount of particle settling during an experiment. Larger particles are more easily identified within images, however they settle more quickly, since the fall velocity of a particle is a function of its size. This may be a problem in experiments requiring multiple repetitions without replenishing the water and particle supply. If residual motions linger after an experiment (such as in Sue, 2007), the setup should be left undisturbed long enough for residual motions to dissipate, but not so long as to allow particles to settle. If particles settle too much between experimental repetitions, this can inhibit

measurements of the velocity at the top of the flow.

Image capture and preprocessing

Images within a PTV system need to be captured by a video camera, with requirements which depend on the properties of the flow under consideration. Flows which evolve quickly or which contain turbulent motions will require higher frame rates and higher pixel resolutions. The camera should be able to capture the macro-structure of the flow, while maintaining a high enough resolution to allow accurate identification of particles within each image. The frame rate should be high enough to enable particles to be easily matched between frames, that is the flow should evolve slowly compared to the frame rate selected. The shutter speed should be high enough so that rapidly-moving particles are not blurred or smeared, but low enough that sufficient light enters the CCD for particles to be identified within each image.

Once images are captured, they may need to be initially corrected for any optical errors within the experimental setup. Such errors include, but are not limited to: barrel/pincushion distortion (for wide angle images); background lighting (although ambient lighting should be removed during a PTV experiment); and any physical obstructions to the flow (such as supports or joins in the sidewall of a flume). These can be accounted for within image processing software, although some will require additional calibration images to be recorded. For example, to robustly account for barrel/pincushion distortion of images, the camera may record images of a rectangular grid (of lines or dots), and apply corrections to the recorded images to ensure that the grid is rectangular within the images (see Nokes, 2009).

Particle identification

When captured images have been pre-processed to remove any distortions, the particles within each image must be identified. Although PTV experiments have been carried out using dark particles on a light background (for example Biggs *et al.*, 2009), the majority of experiments have used a light sheet to illuminate particles against a dark background. In this case, particle identification is a matter of identifying the location of a particle (ideally to sub-pixel accuracy) using an intensity threshold.

The success of the particle tracking algorithms (described in the next section) depends on the success of the particle identification process. Particles could be incorrectly identified if, for example, a large particle was identified as two small particles, or if any false particle (such as a bubble or dust mote) was illuminated by the light sheet and identified as a particle. Some particles might not be identified at all if the threshold intensity is poorly selected, or if they pass through the light sheet. This is a reason why out-of-plane motions can be troublesome during PTV experiments.

Particle tracking between image frames

The critical step within a particle tracking velocimetry analysis is the tracking of particles between frames, since this allows calculation of their Lagrangian velocity. The process itself is challenging, regardless of the flow properties or the seeding density of the particles. Basically, a particle tracking process seeks to find the best possible match for a particle in frame A by checking its possible matches in frame B. This process is illustrated for particle 'x' in figure 4.1.

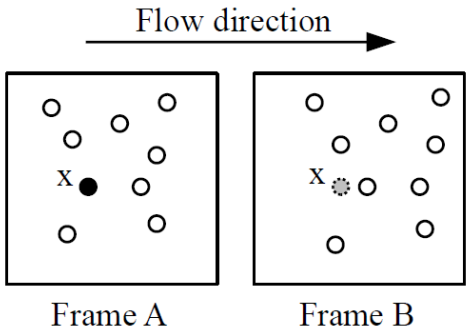

Figure 4.1: Illustration of particle tracking process between two frames.

Particle 'x' in frame A (also superimposed within frame B) has a total of nine possible matches within frame B. An optimisation algorithm determines which particle within frame B is the correct match for particle 'x' in frame A. This algorithm determines the cost of each match in frame B with particle 'x'. The process is then repeated for all particles within frame A, and the optimisation algorithm selects matches which have the lowest total cost. This may mean that some of the individual matches are not the lowest possible cost for that particular match, in order to ensure that the total cost is minimised.

A large number of costings exist, see Nokes (2009) for more details. These costings can be classified as either state-based costings (which determine the costs based on the particle properties in the two images only), or match-based costings (which use the results of previously-calculated matches to determine costings). The costings used in image processing within this study are described in a later section.

Velocity field interpolation

Once particles have been tracked between frames and their Lagrangian velocities calculated, the final step within a PTV analysis is to interpolate these velocities onto a regular grid, providing the Eulerian velocity field for the flow. This process is more accurate for more densely seeded flows, as more particle-centred velocities will be available for interpolation. Some care is therefore required in the selection of a grid, and

in the interpolation scheme used. Additionally, extrapolation may be acceptable, depending on the flow properties and the grid used.

4.3 Setup and equipment

4.3.1 Flume

All two-dimensional experiments were carried out in a flume of length 14.66 m, width 250 mm and working depth 505 mm, located within the Fluid Mechanics Laboratory of the Department of Civil and Natural Resources Engineering at the University of Canterbury. The flume was housed within an optically-isolated room, since the free surface measurement method required the use of laser equipment. Within this 18.9 m long and 3.7 m wide room, the flume was located approximately 1 m from the ground, and was supported by a frame constructed from steel hollow sections.

The flume sidewalls were constructed from 20 mm thick transparent acrylic sheets, and the base and ends of the flume were constructed from 17 mm thick transparent acrylic sheets. To ensure minimal visual obstructions for an observer viewing through the flume wall, no steel sections supported the sidewalls themselves. This meant that the sidewalls could deflect outwards due to hydrostatic pressures when the flume was filled with water. To minimise this sidewall deflection, a steel frame constrained the top of the sidewalls, and clamps were used to hold this frame in place. The flume is shown in figure 4.2.

The working depth of the flume was reduced by 80 mm due to the installation of a

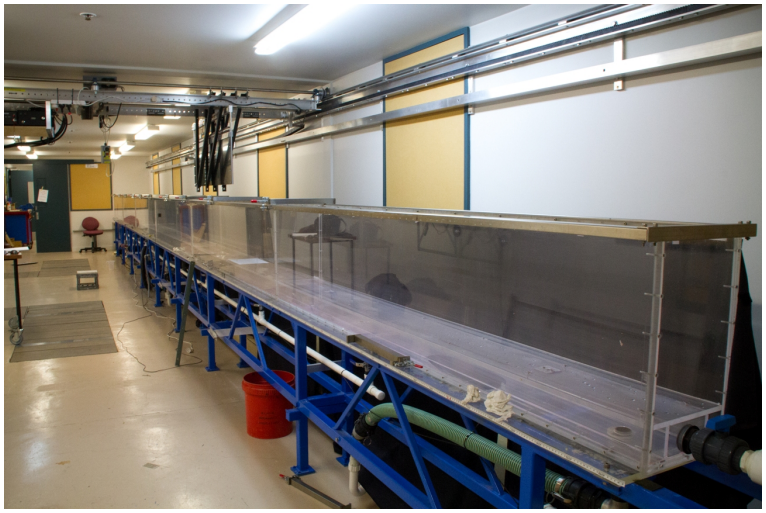

Figure 4.2: Flume used for two-dimensional experiments, with steel clamped frame around the top of the flume to minimise sidewall deflection. The white pipe beneath the flume, connected to a series of vertical pipes and valves, was used to fill the flume.

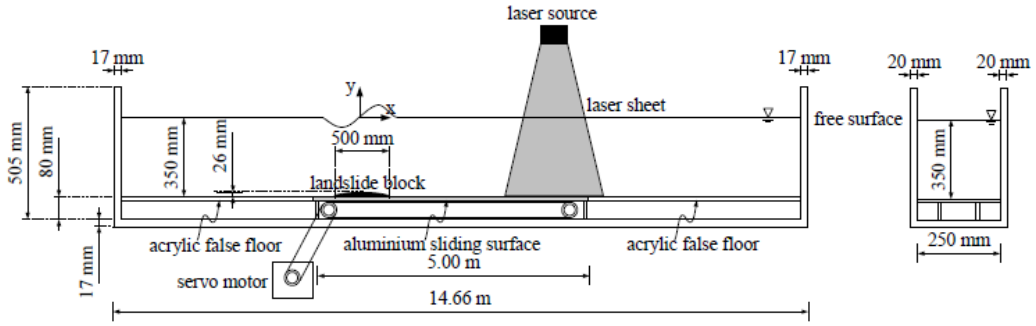

Figure 4.3: Flume used in two-dimensional experiments (not to scale).

false floor, as shown in figure 4.3. The maximum submergence depth (above the false floor) able to be tested in the flume was 350 mm, since greater depths meant that the crests of the generated waves could overtop the flume. Additionally, in the LIF experiments the camera viewed the free surface at a downwards angle (explained in section 4.3.9), and at greater submergence depths than 350 mm the steel frame at the top of the flume would obstruct the camera's view of the free surface.

The false floor in the flume provided the sliding surface upon which the landslide block moved, and was constructed from aluminium plate in the central 5 m of the flume and from 12 mm thick acrylic in the outer sections. The aluminium plate contained a slot, of 8 mm width, to allow connection of the landslide block to the mechanical system housed beneath the false floor. During experiments, the landslide block travelled only along the central (aluminium) section of the false floor, although some additional runout distance was provided in the acrylic sections to avoid damage to the mechanical system (explained in section 4.3.3). Due to the limited length of the flume, each experiment could run only for a short amount of time before reflected waves from the ends of the flume contaminated the wave field. The landslide motion was limited to the central 5 m of the flume to maximise the time between the initiation of motion and the appearance of reflected waves. Because the waves typically travelled faster than the landslide block, starting the landslide motion near one end of the flume would lead to a very short experiment and defeat the objective of measuring both onshore and offshore wave groups.

The flume was filled from two 2000 L tanks, connected in series, located on a mezzanine floor 5 m above the room containing the flume. The flume was filled by the gravity-driven flow from these tanks, by means of a riser pipe and a series of inlets in the base of the flume (see figure 4.2). This allowed controlled filling of the flume, and pre-mixing of the water in the tanks with either dye (for LIF experiments) or particles (for PTV experiments), as required. Pre-mixing in the tanks was preferable to mixing within the flume itself, as a more uniform concentration of dye or particles could be obtained without generating additional fluid motions from the mixing process.

4.3.2 Baffles

Experiments needed to be repeated multiple times to gain wave data over the length of the flume. However, each experiment needed to begin with an initially still free surface, and the free surface motions generated during an experiment did not dissipate for some time. Using the same flume as in this study, Sue (2007) found that a small amplitude seiche was set up within the flume after his wave generation experiments. This seiche persisted for over 15 minutes after the completion of an experiment. The generation of long-period (and long-duration) seiches was even more likely in these experiments, as the flume contained a uniform depth over its entire length, and did not contain the sloping surface of Sue (2007) to encourage wave shoaling and breaking.

To minimise the time between experiments, acrylic baffles of 2 mm thickness were used to limit the available wavelength of the seiche, and encourage dissipation (due to friction) to occur earlier than if these seiches were set up over the entire length of the flume. This follows the work of Sue (2007), who found that the baffles reduced the time between experiments to approximately 6 minutes.

The timing of baffle insertion and removal for the LIF experiments is stated in section 4.5, and the timing used for the PTV experiments is stated in section 4.6. Three baffles were staggered in position along the flume, and were located 3 m, 7 m, and 9.5 m from the onshore end of the flume.

4.3.3 Landslide mechanical system

The landslide was modelled as a semi-elliptical aluminium block, following the shape proposed in the benchmark configuration of Grilli *et al.* (2001), and subsequently used by Sue *et al.* (2011). The mechanical system which provided the landslide motion was housed beneath the false floor in the base of the flume. This system connected the landslide block to a servo motor, located outside of the flume, and consisted of two toothed timing belts, an aluminium I-section connector, and an acrylic base plate, as shown in figure 4.4.

The landslide block had dimensions 0.5 m long, 0.25 m wide and 0.026 m thick, and is shown in figure 4.5. A recess in the base of the landslide block, shown in figure 4.6, allowed the block to rest on the base plate with approximately 1 mm clearance from the sliding surface. The screws used to connect the landslide block to the base plate were positioned flush with the top of the landslide, so that these did not distort the smooth surface profile of the block. A magnet in the acrylic base plate (see figure 4.7) provided an emergency motion shut-off system. Each of the acrylic runout sections at either end of the aluminium sliding surface contained an embedded limit switch, which was connected to the drive system (described in section 4.4). If the magnet within the base plate passed over either of these limit switches, the motion would cease

immediately. This ensured that the mechanical system would not be damaged by the landslide impacting the non-slotted sections of the false floor, as the landslide motion would be shut off before this could occur.

The base plate was connected to the larger toothed belt, located beneath the slotted sliding surface, by an aluminium I-section. Two teflon guides, passing through the slot in the sliding surface, were also fitted to the front and back of the base plate. Although not connected to the belt, they ensured that the base plate and block did not lift off from the sliding surface at high velocities. The toothed timing belt, made from rubber reinforced by stainless steel mesh, ran between two stainless steel self-aligning bearings

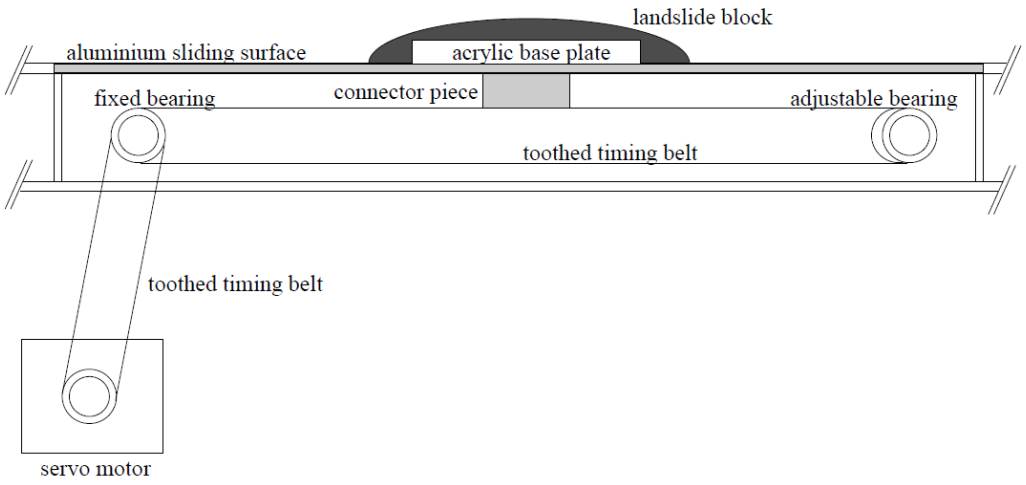

Figure 4.4: Components of the mechanical system used to provide motion to the landslide block.

Figure 4.5: Aluminium block used to simulate a submarine landslide during experiments.

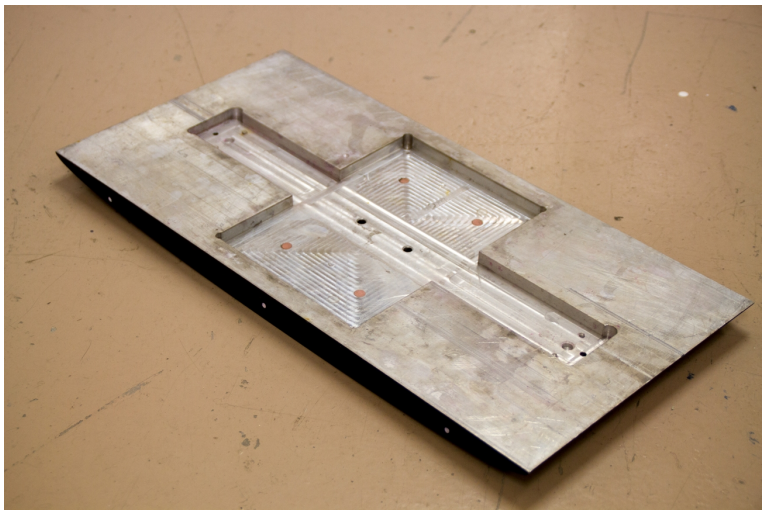

Figure 4.6: Recess milled into base of landslide block to allow connection to acrylic base plate.

(one fixed and one adjustable). The adjustable bearing was able to be moved and locked in place to ensure that the belt was operating at the correct tension and alignment. The fixed bearing penetrated the flume wall and a mechanical lip seal, running on a hardened and ground stainless steel sleeve and pressed onto the stainless steel drive shaft, ensured that the flume remained water-tight. A smaller toothed timing belt connected the fixed bearing to the motor, shown in figure 4.8. As a safety measure, the toothed timing belt and motor were housed within a protective acrylic casing. This casing also helped to protect the motor from any spilled or splashed water during the experiments.

The motor was a BL86-660 Watt brushless servo motor, of the kind used in computer

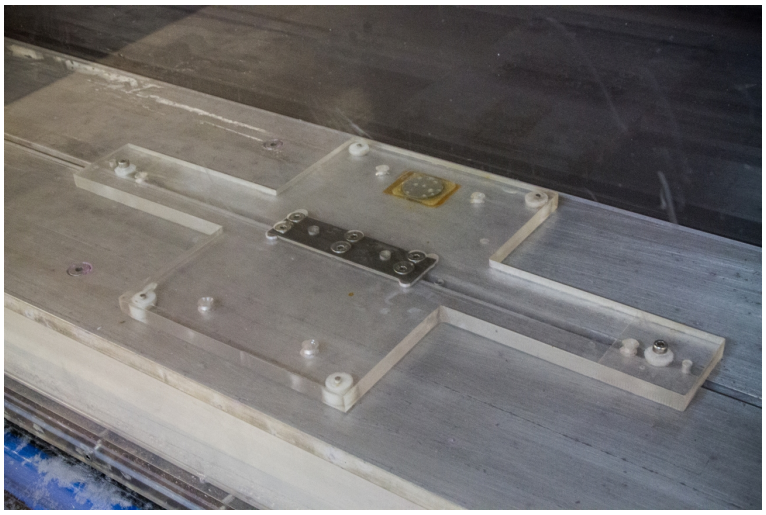

Figure 4.7: Acrylic base plate connecting the landslide block to the mechanical system.

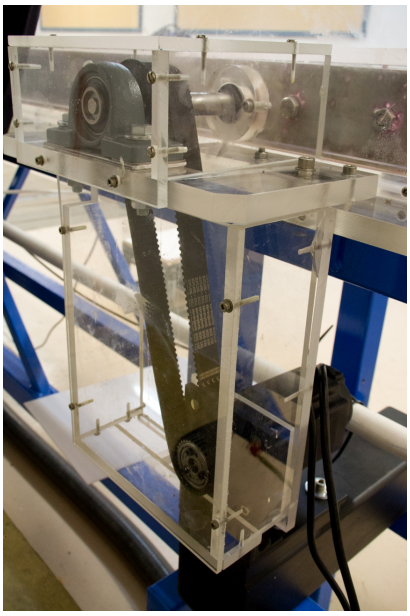

Figure 4.8: Toothed timing belt attached to servo motor, beneath protective casing.

numerical control (CNC) machines, driven by a Granite Devices VSD-E 160 drive system and controller. The drive system accepted input from a computer terminal, which specified motion as a csv file containing a series of displacement-time targets (explained in more detail in section 4.4). Displacements were relative to a 'home' switch at the left end of the sliding surface, which depressed slightly when the landslide block moved over it. After contacting the switch, the block moved a small distance off the switch (approximately 10 mm), with its resting position recorded as the 'home' position. Each motor step was 1/4000th of a motor revolution, with gearing equivalent to a linear displacement resolution of 3.2×10^{-5} m (or 31,250 steps/m).

To record the start time of the motion, a light-emitting diode (LED) flashed for approximately 0.1 s upon initiation of landslide motion via the control program. This LED was then placed within the camera field of view during image acquisition, so that images from different camera locations could be synchronised.

4.3.4 Gantry system

A gantry, mounted on a rack-and-pinion system on the walls of the flume room, supported the lighting and image acquisition equipment, allowing images to be recorded at any location along the length of the flume. The rack and pinion system extended for 13 m along the walls of the room, at a height of 2 m above the floor. A computer-controlled servo motor (of the same type as that used for the landslide mechanical system) provided the gantry motion, allowing accurate horizontal positioning of the system with acceptable repeatability. A description of the motion control system and

related checks are provided in section 4.4.

Confidence in the system to accurately achieve displacement targets was important in all experiments, since the camera's limited field of view necessitated the repetition of experiments, using multiple camera locations along the length of the flume. The lighting and image acquisition computer were both located on the gantry system itself, while an aluminium frame hanging down from the gantry supported the camera, as shown in figure 4.9. The image acquisition computer used a wireless keyboard and mouse, which were located on a small mobile desk. This allowed the image acquisition computer to be controlled without the operator touching the gantry or aluminium frame, ensuring the integrity of images recorded by the camera. The remainder of the gantry system is visible above the flume in figure 4.2.

Figure 4.9: Gantry system used to support free surface identification equipment.

4.3.5 Laser

The laser was a solid state 532 nm green laser, with a maximum output power of 800 mW. The laser produced a beam with 3 mm diameter, and 2 mr divergence. To transform the laser beam into a light sheet, the laser beam was first aligned into a multi-mode fibre-optic cable and then aligned from the end of the cable into a 45° splitter lens. The alignment used the OZ-Optics tilt alignment technique (Best & Sezerman, 1999). An input voltage box enabled control over the laser output power, since the laser control unit only contained an on/off switch. The voltage box supplied between 0 V and 5 V DC, where 5 V corresponded to full laser power.

In order to obtain robust measurements of free surface elevations, it was desirable

to quantify fluctuations in laser power during the experiments. A digital power meter recorded laser output power over a period of approximately 7 hours, to quantify short-term and long-term fluctuations. To determine power fluctuations during laser warmup, the power meter recorded output power during the laser warmup phase, which consisted of 1 hour at an input voltage of 1.5 V, followed by 1 hour at an input voltage of 2.5 V, followed by 1 hour at an input voltage of 3.5 V. The power meter also recorded the laser power for an additional 4 hours at 3.5 V to assess long-term stability at this power level. 5000 power measurements were taken in total, at a frequency of 0.2 Hz. Laser power was increased incrementally over a long time period because experience in the laboratory indicated that a shorter warm-up time tended to increase the short-term and long-term power fluctuations at peak power.

Figure 4.10 shows that an input voltage of 3.5 V corresponds to an output power of approximately 600 mW, after warming up the laser at 1.5 V and 2.5 V. All laser-induced fluorescence experiments used this warmup procedure to a power of 600 mW, and the laser power was kept at 600 mW during the experiments. Figure 4.11 shows a long-term trend in the laser output power, although the long-term variations in laser power were much smaller than the short-term fluctuations. Since the duration of an experiment was less than 10 seconds, the effect of these long term fluctuations is neglected.

The short-term power fluctuations during warmup were between 10 mW and 25 mW (for the different power levels), in terms of root mean squared (RMS) fluctuations from the mean value, while the short-term power fluctuations at maximum power were approximately 7.5 mW. The dominant frequency in the recorded fluctuations was 0.2 Hz, however since this is equal to the frequency of power measurement these fluctuations were conceivably at a much higher frequency than the recording frequency of 0.2 Hz. The effect of these fluctuations on LIF measurements is explained in section 4.5.

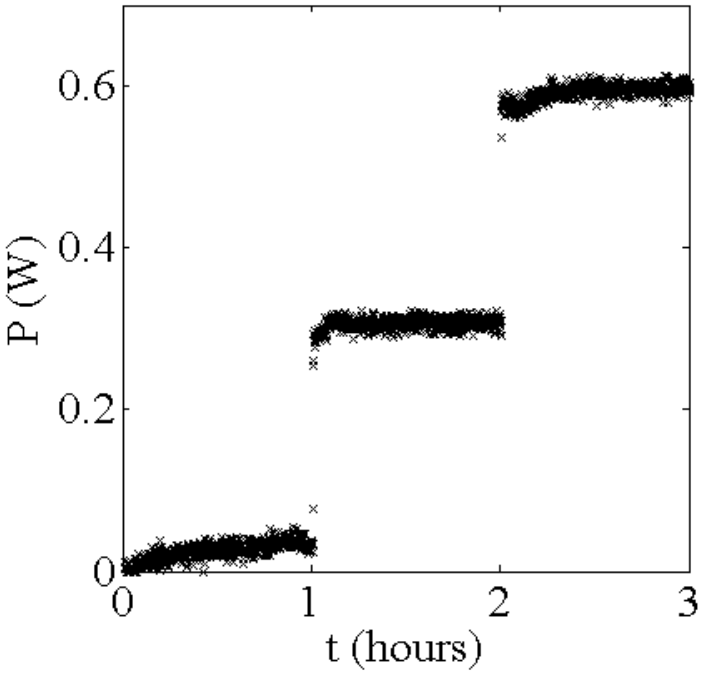

Figure 4.10: Laser warmup results

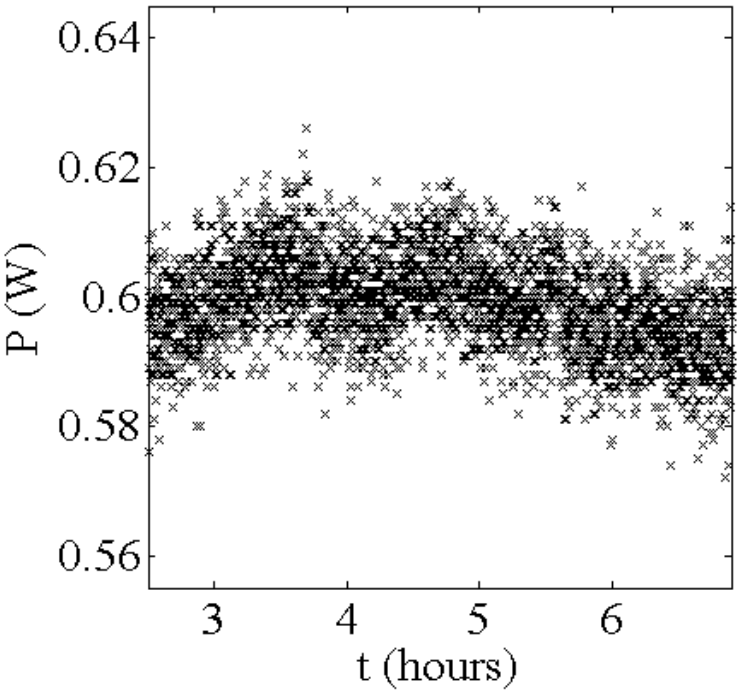

Figure 4.11: Laser long-term stability results

4.3.6 Dye

The laser-induced fluorescence experiments used Rhodamine B dye to illuminate the free surface of the water in the plane of the laser sheet. The 532 nm wavelength laser light excited the dye, which then emitted fluorescence at a wavelength of 555 nm. The LIF experiments used a dye concentration of 0.1 mg/L, since this concentration meant that the fluorescing light was of a sufficient intensity to give a sharp interface between the air and water without saturating the image. The dye was pre-mixed with the water in a separate tank before the dyed solution was added to the flume. A Heliopan orange-22 colour filter, mounted on the camera lens, prevented the laser light from entering the camera. This ensured that the camera only recorded the fluorescence emitted by the dye, and so the intensity interface between the dyed water and the air above was as sharp as possible.

4.3.7 White light box

A white light box, consisting of a number of modules of light-emitting diodes (LEDs) in series, provided illumination for the PTV experiments. Although the same laser sheet used in the LIF experiments could also provide illumination for the PTV experiments, the white light box was used for several reasons. First, the laser sheet was limited in its horizontal extent, since the sheet was formed by passing the laser beam through a 45° splitter lens. This also meant that the laser sheet was wider at the bottom of the flume than at the free surface (due to the 45° angle of spread). The light box was approximately 1.5 m in length, and this was limited only by the structural system which provided support for the box. This meant that the intensity of light was uniform over a much greater width than that of the laser sheet. The second, and most important, reason for the use of the light box was the short-term fluctuations in laser power (discussed in section 4.3.5). These short-term fluctuations did not significantly affect the free surface measurements obtained using LIF, since image processing accounted for spatial and temporal variations in laser power. However, they complicated the particle identification process during processing of images obtained from the PTV experiments, because the number of particles identified in an image (using a fixed intensity threshold) would increase as the intensity of the light source increased. Since the laser power fluctuated with a high frequency, this meant that the number of particles per image would alternate between low and high, making subsequent particle matching more difficult. The white light box exhibited much more stable output power than the laser, and so the light box was the preferred choice for lighting during the PTV experiments.

Figure 4.12 shows a schematic of the white light box used in the subsurface experiments. The light box contained a total of six LED modules over its length, connected in series, where each module contained eleven LEDs. Each module of LEDs was at-

tached to a heat sink, to avoid the need for a cooling fan. The LEDs were mounted between an aluminium bar and two angle plates, where the plate contained a slight ledge to ensure that all the LEDs were aligned correctly. The light from the LEDs passed between two black plastic plates, which contained an acrylic stiffener to ensure that they did not deform. Aluminium members supported the system at each end, and connected the entire assembly to the gantry.

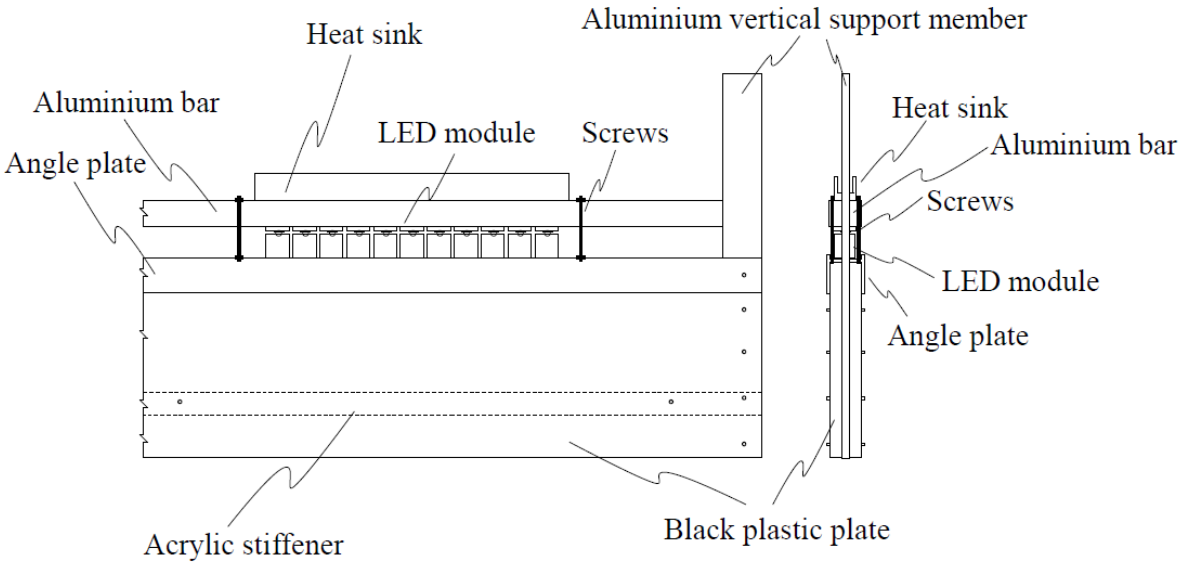

Figure 4.12: Side elevation and end elevation of the white light box used in PTV experiments.

4.3.8 Particles

The particles used in the PTV experiments were composed of Pliolite VTAC (vinyl toluene acrylate) resin. These were ground into very fine particles, and sorted into several different diameter ranges using fine sieves. The particles used in the PTV experiments had a size distribution of 125-180 μm. This size distribution meant that particles were small enough to be dynamically unimportant, and their presence did not affect the development of the subsurface velocity field during the experiments. The specific gravity of the particles was 1.03, and particles settled in the flume if left for long periods of time. However, the velocities generated by motion of the landslide during experiments and the water velocities beneath the generated waves were both significantly larger than the fall velocity, and as such the fall velocity could be ignored during processing of the experimental data. Therefore, for the purpose of the PTV experiments, the particles were assumed to be neutrally buoyant.

To ensure that particles were evenly distributed over the volume of the flume, they were premixed with water in two 2000 L tanks (see section 4.3.1 for details). To ensure

a sufficient particle density within each image, the particle concentration was 13 mg/L. To prevent the formation of undesirable bubbles in the flume, the water in these tanks was allowed to settle for several days before the particles were added. The particles were mixed with approximately 200 mL of water and a small amount of surfactant, to prevent particles from coagulating within the solution, before being added to the tanks.

Details of the PTV experiments, and the measures taken to limit particle settling between experimental runs, are provided in section 4.6.

4.3.9 Camera

The camera used in the experiments was a JAI M4$^+$ CL camera. The camera moved with the gantry, supported by an aluminium frame, allowing images to be recorded at any location along the flume. In its standard configuration, the camera captured images of size 1380 pixels (horizontal) by 1030 pixels (vertical), at a rate of 24 frames per second. The camera recorded images in bitmap format, and stored these directly to disk using custom image-capture software. Due to the different requirements of the LIF and PTV experiments, each type of experiment used different camera settings. Two of the settings adjusted depending on the type of experiment were the gain and the black level. The gain amplified the intensities of pixels within the image by a set amount, and the black level provided a threshold intensity value below which pixel intensities were recorded as zero. The camera location and inclination angle also depended on the type of experiment conducted (stated in the sections below). No measurable barrel/pincushion distortions were observed in images recorded by the camera during the LIF or PTV experiments.

LIF experiments

During the LIF experiments, partial scanning limited the vertical number of pixels to 256 (quarter-frame scanning), but allowed the camera to operate at an increased frame rate of 70 frames per second. The number of pixels in the horizontal direction remained unchanged when using partial scanning. The increased frame rate during partial scanning allowed better temporal resolution of the waves, while still capturing the full range of their amplitudes.

The camera captured images at a slight downwards angle (approximately 5°), so that the interface between the laser sheet and the free surface could be distinguished from the location where the free surface met the sidewall of the flume, as shown in figure 4.13. This technique, developed by Sue (2007), ensured that free surface measurements were unaffected by surface tension effects present at the sidewall of the tank. The laser was positioned off-centre so that it was not located directly above the slot in the false

floor (discussed in section 4.6). The LIF experiments used a gain level of 200, and a black level of 50. This ensured that the interface between the fluorescing water and the dark air above was as sharp as possible.

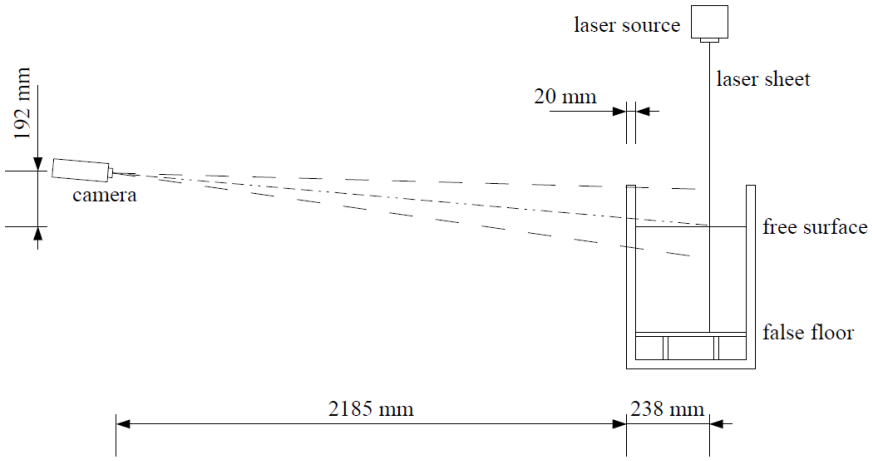

Figure 4.13: Downwards camera angle used in LIF experiments to eliminate meniscus effects at flume sidewall.

Images were captured using a 50 mm lens. Due to the camera's limited field of view (approximately 400 mm in the horizontal direction per frame), each experiment needed to be repeated 37 times to obtain a full data-set. This placed an added emphasis on the high repeatability required of the motion of the landslide block (discussed in section 4.4).

PTV experiments

The PTV experiments did not use partial scanning, since these experiments required images of particle motions over the entire depth of the flume. The gain level was set to 100, and the black level was reduced to 20, since these experiments aimed to identify as many particles as possible in each image. The camera was positioned so that its axis was perpendicular to the white light sheet, as shown in figure 4.14. The white light sheet was positioned off-centre to avoid measurement of the small exchange flow directly above the slot in the false floor (discussed in section 4.6).

Images were captured using a variable zoom lens. Recorded images had a larger width than the LIF images, approximately 500 mm. Experiments were repeated in the same manner as the LIF experiments to obtain subsurface velocity data over the length of the flume.

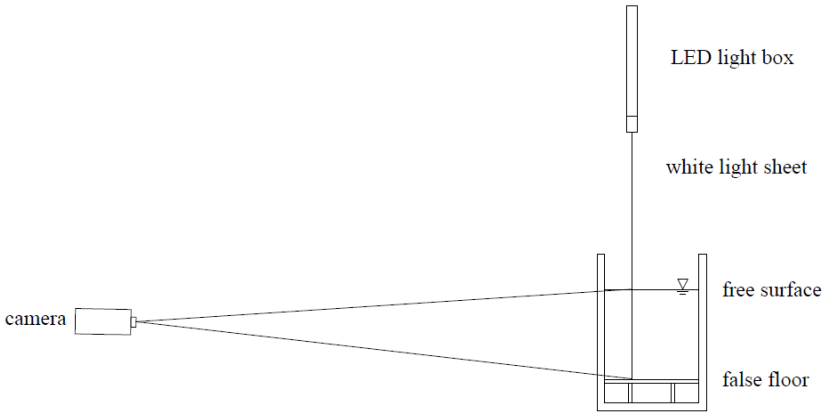

Figure 4.14: Camera orientation during PTV experiments.

4.4 Motion control

4.4.1 Requirements of motion control system

The same drive system controlled both the gantry motor and the landslide motor. The landslide motor provided motion to the mechanical system (see section 4.3.3), and generated the waves during the LIF and PTV experiments, while the gantry supported the lighting and image acquisition equipment. Both systems needed to achieve their motion targets with a high level of experimental repeatability.

Checks on the landslide system included the ability of the system to achieve displacement, velocity and acceleration targets. The acceleration and velocity performance of the system was assessed in profile mode (see section 4.4.2), while displacement checks simply used the position command in the motion control system. Since the gantry remained stationary during image acquisition in each experiment, no requirements existed for the gantry velocity and acceleration. However, the gantry needed to achieve displacement targets with high levels of repeatability, so that data from different locations could be effectively combined.

This section first discusses the motion control system used for the landslide and the gantry, in terms of the limits, tolerances and input options for the system. It then describes the checks carried out on the gantry positioning, and the landslide's ability to achieve a specified velocity profile. The velocity profiles tested included periods of constant acceleration, constant velocity and constant deceleration, and included a range of different accelerations and velocities. The landslide motion checks used PTV (described in section 4.2.3) to calculate the landslide velocity.

4.4.2 Motion control for landslide and gantry

The motors were controlled in steps, where 4000 steps equalled one motor revolution. The mechanical gearing of the two systems was different, hence the linear movement per step differed between the two systems. Each system measured this linear movement relative to a 'home' switch, and allowed the user the option of either moving to a specific location, moving at a constant velocity, or moving according to a predetermined motion profile. This profile consisted of a set of time-displacement targets, input using a text file.

The limitations of the system in terms of displacements were simply that the landslide block remained on the aluminium sliding surface (allowing a maximum displacement of approximately 4.5 m from the home position, due to the length of the landslide block), and that the gantry remained on the rack-and-pinion system (allowing a maximum displacement of approximately 12.6 m from the home position).

The overall velocity limits were governed by the rate at which the microcontroller could step the motor, provided in table 4.1.

Table 4.1: Overall limits on achievable velocity by landslide and gantry systems

System	**Step range** (steps/s)	**Gearing** (steps/m)	**Velocity range** (m/s)
Landslide	$187 \rightarrow 62500$	31250	$0.0060 \rightarrow 2.0000$
Gantry		113300	$0.0017 \rightarrow 0.5515$

4.4.3 Displacement checks on gantry system

To check the gantry system's ability to move small distances accurately, a 1 m ruler was placed on the inside wall of the flume. The camera, mounted on the gantry system, recorded images of the ruler, as shown in figures 4.15 and 4.16. The gantry then moved in increments of 100 mm, and at each new location the camera recorded a new image of the ruler. The pixel locations of the gradations (every 50 mm) on the ruler were checked, and the apparent displacement of the gantry was checked against the desired gantry displacement of 100 mm in each case. A total of 9 gantry locations were recorded, with 100 mm displacement between each gantry location.

On checking the pixel locations of the 50 mm gradations (giving 7 points in total) against the target displacement of 100 mm, the maximum positioning error was found to be ± 4 pixels, or ± 1.218 mm. The RMS error was found to be ± 2 pixels, or ± 0.573 mm. To check the sensitivity of these tests to the distance moved, an additional check was carried out where the gantry recorded an initial ruler image and then was moved by 500 mm, to record a second ruler image.

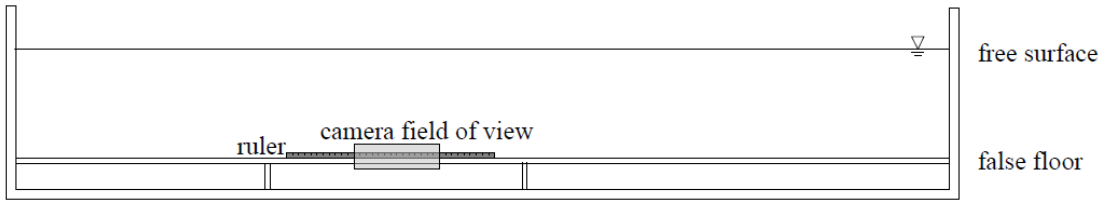

Figure 4.15: Side view of experimental setup used to check gantry displacement.

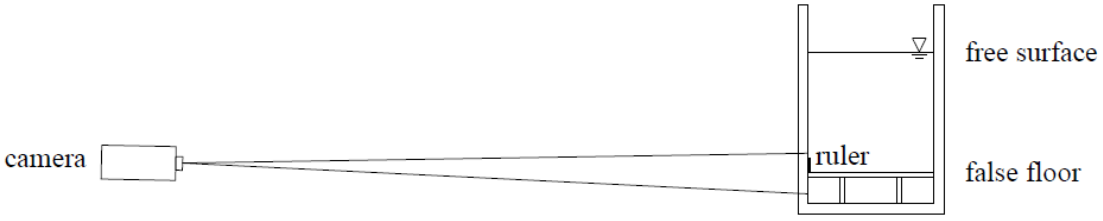

Figure 4.16: End view of experimental setup used to check gantry displacement.

In the case of the 500 mm displacement, the maximum horizontal error was found to be ±1 pixel, or ±0.281 mm, with a RMS error of ±0.79 pixels, or ±0.222 mm. These results are significantly better than those obtained for a smaller gantry displacement, and may be due to the built-in acceleration and deceleration functions in the motion control program performing poorly for very small gantry displacements. Additionally, due to the considerable mass carried by the gantry (attached eccentrically to the steel frame), the intertia of the gantry may have caused errors in gantry positioning during the acceleration and deceleration phases of motion. These effects appear to decrease in importance for larger gantry displacements. During the experiments, the gantry was moved in increments of 350 mm, and so the errors in gantry positioning are relatively unimportant (less than 0.2% using an error of ±2 pixels).

4.4.4 Displacement checks on landslide block

To carry out more robust checks on the landslide positioning when moving a fixed displacement (using the 'position' command), a series of particle tracking velocimetry (PTV) tests provided displacement data for the landslide block. Figures 4.17 and 4.18 show the setup used for the landslide PTV experiments. Three white dots (approximately 3 mm in diameter) were painted onto the side of the black landslide block. The camera, located beside the flume, recorded images of the landslide position. The landslide then moved a small distance (so that the dots remained within the camera

field of view), and the camera recorded a second series of images. The maximum landslide displacement tested was 300 mm, since the camera remained in one location for all landslide positions. This ensured that errors in landslide positioning were not contaminated by errors in the positioning of the gantry system (see section 4.4.3).

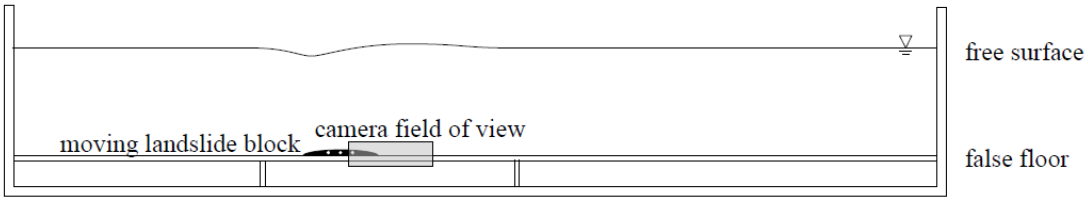

Figure 4.17: Side view of the experimental setup used to measure landslide displacement and velocity using particle tracking velocimetry.

Figure 4.18: End view of the experimental setup used to measure landslide displacement and velocity using particle tracking velocimetry.

The Streams software package (Nokes, 2009) determined the location of the dots within each image using a particle identification algorithm. The displacement of the dots between frames was then compared to the target displacement. This particle identification algorithm used a simple intensity threshold to locate the particles, however this was still more accurate than visually determining the pixel location of dots or ruler gradations within an image.

Three different tests were carried out for different displacements, while keeping the landslide within the camera's field of view. Table 4.2 lists the displacements tested, and the associated maximum and RMS errors between the target displacement and the actual displacement for each test. During the experiments, the landslide only ever moved using a full velocity profile (rather than a fixed displacement), however these results show that the gearing of the landslide system is correct to sub-millimetre accuracy.

Table 4.2: Errors in landslide positioning, measured using PTV

Displacement (mm)	**Maximum error** (mm)	**RMS error** (mm)
100	0.322	0.255
150	0.472	0.292
300	0.034	0.034

4.4.5 Profile checks on landslide block

The use of velocity profiles allowed testing of the landslide system's ability to achieve velocity and acceleration targets in a repeatable manner. The profiles tested in these experiments were the same profiles used in the laser-induced fluorescence experiments. Each profile contained three main phases of motion: an initial period of constant acceleration, a period of constant velocity, and a final period of constant deceleration to rest (at the same rate as the initial acceleration). The tests were carried out to quantify the errors in the system's ability to achieve its acceleration and velocity targets, and how these errors varied over the parameter space investigated.

Experimental procedure

The profile checks used PTV to determine the Lagrangian velocities of the three dots painted on the side of the landslide block, using the experimental setup described in section 4.4.4 (see figures 4.17 and 4.18). However, these experiments used multiple gantry locations to capture the full range of landslide displacements. This meant that the errors in the landslide motion also contained a contribution from the positioning error of the gantry. The flume was filled with water to a depth of 175 mm for these experiments, so that the landslide motion would be equivalent to that tested in the LIF experiments. Two halogen spotlights, located on either side of the camera, illuminated the dots on the side of the landslide block. This ensured that the intensity of the dots remained relatively uniform during the experiments, and improved the particle identification procedure.

The steps taken in each experiment were:

1. Fill the flume and leave for approximately one day to allow formation of entrained air bubbles.

2. Remove any bubbles from the flume sidewalls.

3. Turn on and 'home' the landslide and gantry systems, turn on the camera and associated image acquisition software.

4. Move the gantry to its initial location, ensuring that the LED is located within the camera's field of view.

5. Turn off the ambient lighting and turn on the two halogen spotlights.

6. Allow the water within the flume to settle, using the baffles to remove long-period free surface motions.

7. Begin recording images with the camera.

8. Initiate the landslide motion.

9. Wait for the image recording to finish, then return the landslide to its 'home' position.

10. Move the gantry to its next location, and move the LED and spotlights to the same location.

11. Repeat steps 6 - 10 until all of the gantry locations have been recorded.

Although the variations in free surface elevation were not of interest in these experiments, the water in the flume was allowed to settle between experiments. This eliminated the possibility of any residual pressure and velocity fields caused by the surface waves affecting the motion of the landslide block. Whenever the gantry was moved, the halogen spotlights were also re-positioned to achieve consistent lighting within the camera's field of view. A light-emitting diode (LED), placed in the camera's field of view at each gantry location, flashed once for approximately 0.1 s when landslide motion was initiated. This allowed synchronisation of image records at different gantry locations to within ± 0.007 s (or to within half of the capture rate).

Image processing

The Streams software package (Nokes, 2009) calculated the displacements and Lagrangian velocities of each of the dots, by carrying out a PTV analysis on the recorded images. Once the dots were identified as particles within Streams, they were tracked between frames.

Comparison to motion targets

Table 4.3 states the parameters for the 9 particle tracking velocimetry experiments. During each experiment, the landslide accelerated at a constant rate, a_0, to its terminal velocity, moved at its terminal velocity for 2 seconds and then decelerated to rest (at the same rate as the initial acceleration). A total of nine experiments were carried out, with three different accelerations and three terminal landslide velocities.

Table 4.3: Experimental parameters tested during PTV checks on achievement of motion profiles by landslide system

Run	$\mathbf{a_0}$ (m/s^2)	$\mathbf{u_t}$ (m/s)
1	0.5	0.164
2	0.5	0.328
3	0.5	0.655
4	1.0	0.164
5	1.0	0.328
6	1.0	0.655
7	1.5	0.164
8	1.5	0.328
9	1.5	0.655

Figure 4.19 contains an example of the landslide system's ability to achieve a velocity profile, and figure 4.20 shows the corresponding displacement profile for the experiment. In each case, the displacements and velocities of the individual particles were averaged, for clarity and to remove the effect of any errors in the particle identification process. The velocity and displacement plots for the remaining landslide PTV runs are provided in Appendix A, however the errors for all runs are summarised in this section.

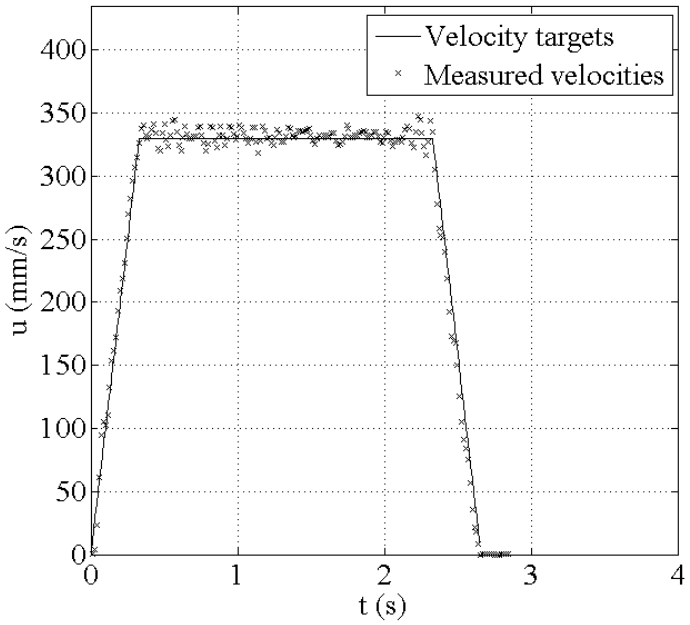

Figure 4.19: Landslide target and measured velocities for Run 5 ($a_0 = 1.0$ m/s^2, $u_t = 328mm/s$)

To quantify the errors in the landslide system's ability to achieve its motion targets,

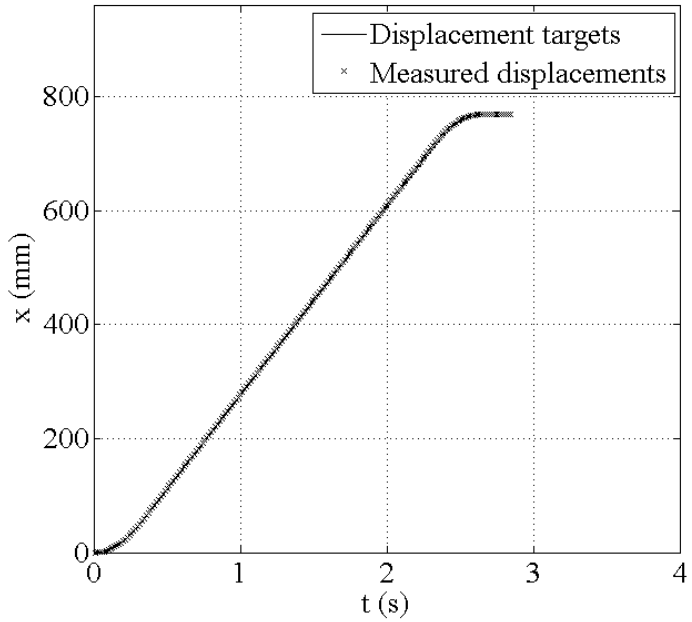

Figure 4.20: Landslide target and measured displacements for Run 5 ($a_0 = 1.0$ m/s^2, $u_t = 328mm/s$)

the landslide acceleration is compared to the target acceleration during the acceleration and deceleration phases of motion. The landslide velocity is compared to the target terminal velocity during the constant velocity phase of motion. Due to the rapid image capture rate, the calculation of the instantaneous landslide acceleration during the acceleration and deceleration phases was not practical, since small errors in velocity would be amplified by the short timestep. Instead, the landslide acceleration was calculated by fitting a straight line to each of the landslide dot velocities during the acceleration and deceleration phases of motion. The slope of this line was the average landslide acceleration during these phases of motion. RMS errors for the accelerations were calculated using the results of the three average accelerations (or decelerations) for the three dots. The RMS errors in velocity were calculated using the instantaneous particle velocities for the three dots throughout the constant velocity phase of motion. Tables 4.4 and 4.5 summarise these errors, where u_{RMS} is the RMS error in the landslide velocity, a_{RMS} is the RMS error in the landslide acceleration, and d_{RMS} is the RMS error in the landslide deceleration. Errors are presented both in an absolute sense and as a percentage of the target value.

As expected, the RMS velocity error increased as the landslide terminal velocity (or Froude number) increased, however the error actually decreased relative to the terminal velocity as the velocity increased. The RMS error in the acceleration was greatest for the low-Froude number experiments, since these experiments had a shorter duration of the constant-acceleration phase of motion. Because the acceleration was calculated

Table 4.4: RMS velocity errors arising from PTV checks on landslide motion

Run	$\mathbf{u_{RMS}}$ (mm/s)	$\mathbf{u_{RMS}}$ (% of u_t)
1	6.2	3.8
2	7.7	2.3
3	11.0	1.7
4	6.7	4.1
5	7.3	2.2
6	9.5	1.4
7	6.8	4.2
8	7.1	2.2
9	10.3	1.6

Table 4.5: RMS acceleration errors arising from PTV checks on landslide motion

Run	$\mathbf{a_{RMS}}$ (mm/s^2)	$\mathbf{a_{RMS}}$ (% of a_0)	$\mathbf{d_{RMS}}$ (mm/s^2)	$\mathbf{d_{RMS}}$ (% of -a_0)
1	29.8	6.0	5.8	1.2
2	10.1	2.0	3.2	0.6
3	7.2	1.4	7.4	1.5
4	121.7	12.2	32.4	3.2
5	40.5	4.1	12.9	1.3
6	21.9	2.2	17.8	1.8
7	369.1	24.6	74.6	5.0
8	94.5	6.3	19.1	1.3
9	40.1	2.7	15.7	1.0

using a straight line fit to the velocity profile, a shorter duration of the acceleration phase of motion meant that errors in the landslide velocity had a greater effect on the calculated value. The errors in the deceleration were significantly less than the errors in the acceleration, although these errors were also greatest for the low Froude numbers and high accelerations.

Experimental uncertainties in the PTV measurements arose from the uncertainties in the identification of the location of each dot and the frame rate of the camera. The camera captured images at a rate of 70 frames/s, with a pixel scale of 0.305 mm/pixel. Assuming that the location of each dot could be identified to an accuracy of ± 0.5 pixels (a worst-case figure), this gives a potential displacement error of ± 0.1525 mm. At a capture rate of 70 frames/s, this leads to a velocity error of ± 10.68 mm/s. The RMS errors in the velocity achieved by the system in table 4.4 are less than this value, except for Run 3, which had the highest Froude number and the lowest landslide acceleration.

4.4.6 Repeatability of landslide motion

To assess the repeatability of the landslide PTV experiments, Run 5 was repeated an additional two times. Figure 4.21 shows the velocities obtained for one of the dots over three different runs, and figure 4.22 shows the equivalent displacement plot for the three runs.

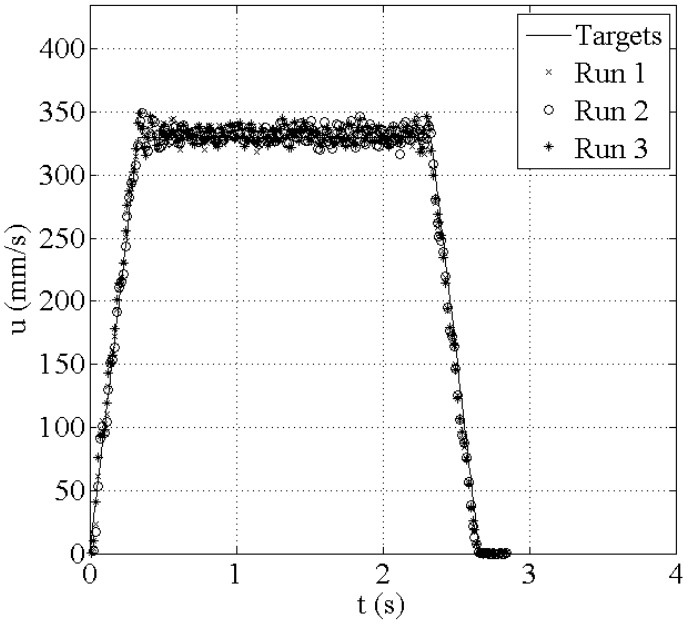

Figure 4.21: Velocity repeatability check for Run 5 ($a0 = 1.0$ m/s^2, $u_t = 0.328$ m/s)

Table 4.6 shows the RMS errors in velocity, acceleration and deceleration for the three repetitions of Run 5, to check whether these errors are consistent over the three repetitions. The RMS errors in acceleration and velocity are all very consistent over the three repetitions, however the error in the deceleration is more variable between the three runs. During the experiments, wave reflections had often occurred by the time the landslide began to decelerate, and so these variations are relatively less important than those in the acceleration phase of motion.

Table 4.6: RMS acceleration, velocity and deceleration errors in repetitions of Run 5

Run	$\mathbf{a_{RMS}}$ (mm/s^2)	$\mathbf{u_{RMS}}$ (mm/s)	$\mathbf{d_{RMS}}$ (mm/s^2)
5a	40.5	7.3	12.9
5b	41.1	7.8	17.4
5c	40.8	7.6	6.8

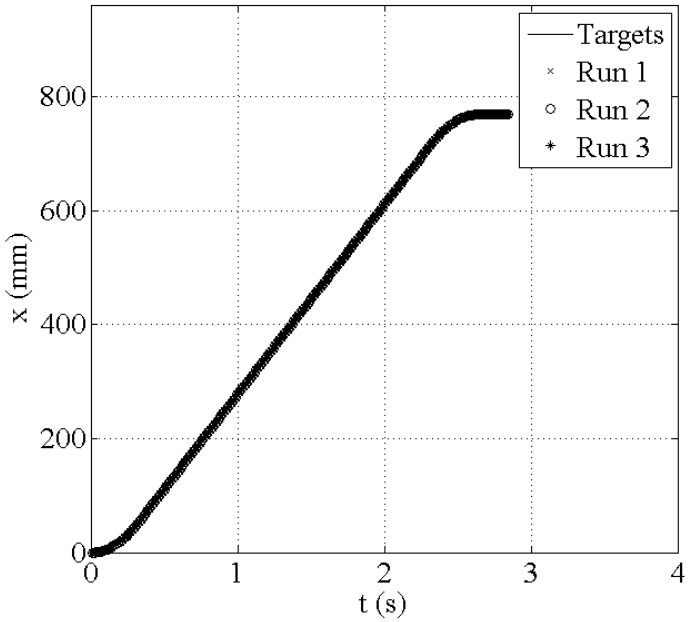

Figure 4.22: Displacement repeatability check for Run 5 ($a0$ = 1.0 m/s^2, u_t = 0.328 m/s)

4.5 Free surface identification

4.5.1 Experimental procedure

The purpose of the laser-induced fluorescence (LIF) experiments was to measure the amplitudes of the free surface waves generated by the motion of the submarine landslide. Within these experiments, the accurate identification of the spatial and temporal variations in free surface elevation was equally as important as a high level of repeatability of landslide motion. These experiments used the application of laser-induced fluorescence (LIF) of Sue *et al.* (2011) to achieve this.

During an experiment, the laser illuminated a 2D section of the flume from above (see figure 4.23), with a power level of approximately 600 mW. The Rhodamine dye fluoresced under the laser light, creating a sharp intensity interface between the bright water and the dark air above where the laser sheet intersected with the water in the flume. A camera, located 2.1 m from the flume sidewall, captured images of this intensity interface at a rate of 70 frames/second. The camera captured images at an angle of 5° downwards from the horizontal, as shown in figure 4.13.

The flume was filled with water pre-mixed with 0.1 mg/L of Rhodamine B fluorescent dye, and allowed to settle for one day, to encourage formation of bubbles on the flume sidewalls (which were then removed). The LIF experiments were most affected by the prescence of bubbles on the free surface, either in the plane of the laser sheet

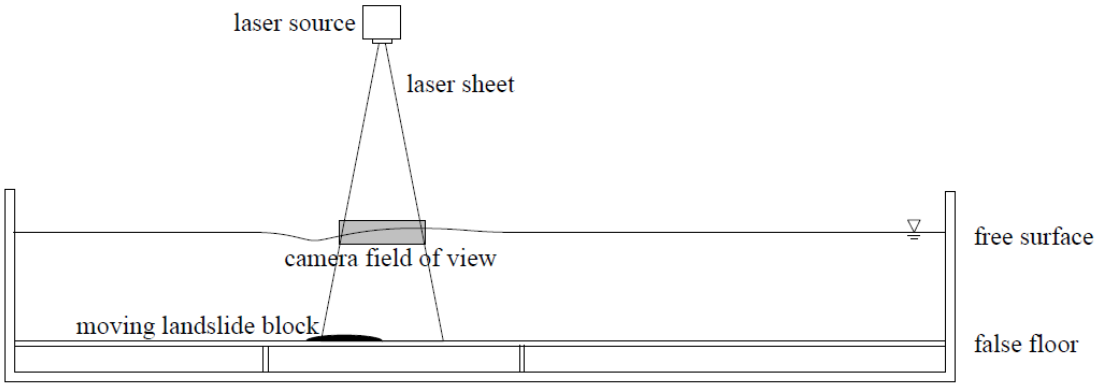

Figure 4.23: Side view of experimental setup used to measure free surface elevations using LIF.

or along the flume sidewalls. Bubbles within the plane of the laser sheet distorted the free surface, and created bright spots within the image recorded by the camera. This created small spikes in the free surface record obtained from the image processing (explained in more detail in section 4.5.2). Bubbles on the flume sidewalls also created spots of high pixel intensity. If located on the near flume sidewall, these bubbles appeared beneath the free surface interface in the recorded images, and did not cause any problems during image processing. If located on the far flume sidewall, these bubbles appeared above the free surface interface in the recorded images, and could create large spikes in the processed free surface record. Some correction for these bubbles could be made during image processing, however it was simpler to remove the majority of the bubbles from the flume before commencing an experiment.

Each experiment was repeated 37 times to measure the spatial and temporal variations in free surface elevation over the length of the flume. The gantry system moved 350 mm between each experiment, providing some overlap between recorded images (with an approximate image width of 400 mm, see section 4.3.9). A light-emitting diode (LED) synchronised the image records in time (see section 4.4). The overlap between images allowed the removal of the LED from each image without creating gaps in the processed free surface record.

To decrease the time between experiments, while ensuring that all experiments started with an initially undisturbed free surface, three baffles were inserted into the water for a short time after the completion of a run. The baffles (see section 4.3.2) limited the available length over which a seiche could develop, and encouraged earlier dissipation of wave energy due to friction. Care needed to be taken when inserting or removing the baffles, to avoid the generation of additional free surface waves within the flume.

The experimental procedure used to capture images during each LIF experiments is stated below.

1. Fill the flume with water containing a concentration of 0.1 mg/L Rhodamine. Leave the flume for at least 12 hours, then remove any air bubbles from the flume sidewalls.

2. Warm up the laser to its correct power level (600 mW).

3. Turn on the landslide and gantry motion control systems.

4. Home the landslide block and gantry. Move the gantry to its initial location.

5. Use baffles to remove any long-period waves generated by the homing motion of the landslide. Allow the water in the flume to settle.

6. Turn on the camera and image acquisition systems, ensuring that the filter is mounted correctly on the camera lens. Turn off all ambient lighting within the room.

7. Place the LED within the camera's field of view.

8. Begin recording images of the experiment. Initiate the landslide motion, and continue recording images for a further 10 s.

9. Return the landslide block to its home position after the camera has finished recording images.

10. Insert the baffles into the flume at the appropriate locations. Leave the baffles in place for 2 minutes.

11. Carefully remove the baffles, ensuring that no additional waves are created by their removal. Allow the free surface to settle for at least 5 minutes after removal of the baffles.

12. Move the gantry to its next location.

13. Repeat steps 7-12 until free surface elevations have been recorded at all of the gantry locations.

4.5.2 Image processing

This section describes the image processing to obtain the free surface record generated by the landslide motion during a LIF experiment. The Streams software package (Nokes, 2009) provided the scalar intensity fields for each image record. Matlab was

used to identify the location of the free surface within each intensity field, and combine the records from each gantry location into a free surface record for the entire flume. These different steps are explained in detail below.

Figure 4.24 shows a raw image recorded during a typical LIF experiment. The dark box at the right edge of the image is the LED, which flashed briefly at the start of the landslide motion, synchronising all camera locations in time. The fluorescing water in the plane of the laser sheet was much brighter than the dark air above. The intensity of the fluorescing water decreased slightly at the edges of the image, due to the limited horizontal extent of the laser sheet. The higher intensity near the bottom of the image is located beneath the intersection of the free surface and the near flume sidewall.

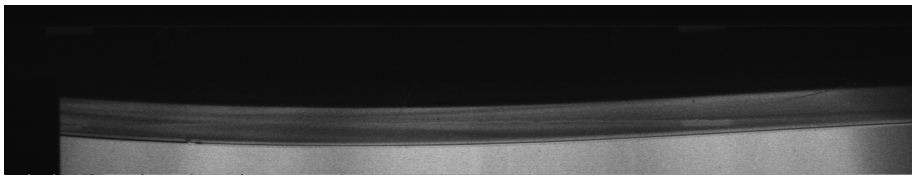

Figure 4.24: Raw image recorded by camera during LIF experiments.

The Streams software package (Nokes, 2009) created a text file of the pixel intensities within each image, used in the subsequent Matlab processing. This is referred to as the intensity field of the image in the remainder of this section. The steps within the free surface identification process in Matlab are summarised below. Each step is explained in detail following this summary.

1. Import the intensity field from the output of the Streams software package.
2. Create the locally averaged intensity field (averaged over every 20 pixels in the x-direction).
3. Identify and remove joints in the flume sidewalls from the intensity field, as required.
4. Calculate the free surface elevation at each horizontal x-location, at each time t.
   (a) Calculate the average background (air) intensity, I_0.
   (b) Search for the maximum vertical y-pixel with $I > 3I_0$, as the first vertical location (from the top of the image) where the free surface interface begins, y_0.
   (c) Find the maximum intensity gradient in the vicinity of y_0.
   (d) Fit a straight line to the intensity profile at the location of maximum intensity gradient, p_I.

(e) Fit a straight line to the intensity profile of the water below the interface, p_W.

(f) Determine the intersection point of p_I and p_W. This is the location of the end of the free surface interface, with vertical location y_1 and intensity I_1.

(g) Calculate the threshold intensity as $I_t = 0.6(I_1 - I_0) + I_0$.

(h) Interpolate between the adjacent pixels to determine the location where I_t is first exceeded (in the negative vertical y-direction). This is the free surface elevation, η.

5. Interpolate over the sidewall joint locations, if present.

6. Trim the free surface record to a length of 350 mm.

7. Check for any spikes in the free surface record (caused by bubbles or sidewall scratches), and remove these if found.

8. Save the free surface record at this gantry location to the total free surface record for this experiment.

9. Repeat the above steps for all recorded gantry locations.

To decrease the computational cost of the Matlab processing, the surface identification program first averaged the pixel intensities over every 20 pixels in the x-direction onto a coarser grid. This meant that intensities were recorded at a spatial resolution of approximately 3 mm, instead of 0.3 mm, in the horizontal direction. Figures 4.25 and 4.26 show examples of the imported intensity field and the averaged intensity field.

The free surface records obtained with and without this averaging process are overlaid on the two intensity fields in figures 4.25 and 4.26. There is no appreciable difference in the phase and amplitude of the free surface records obtained using the two methods, but the averaging process removes some of the noise in the free surface record (arising from noise in the intensity field). The program did not average the pixel intensities in the vertical direction, since this would defeat the objective of identifying the free surface location to sub-pixel accuracy. The advantages of the averaging process were a significant decrease in computational cost of the free surface identification procedure, and a slight decrease in the noise in the free surface record. This noise was due to small spatial variations in laser light intensity, however all noise was less than 0.1 mm in magnitude.

The joins between the acrylic sections of the flume sidewalls were transparent, however the free surface could not be identified within the joins by the identification algorithm. Therefore, the surface identification program deleted all pixels within the join region in the intensity field before identifying the free surface. After identifying

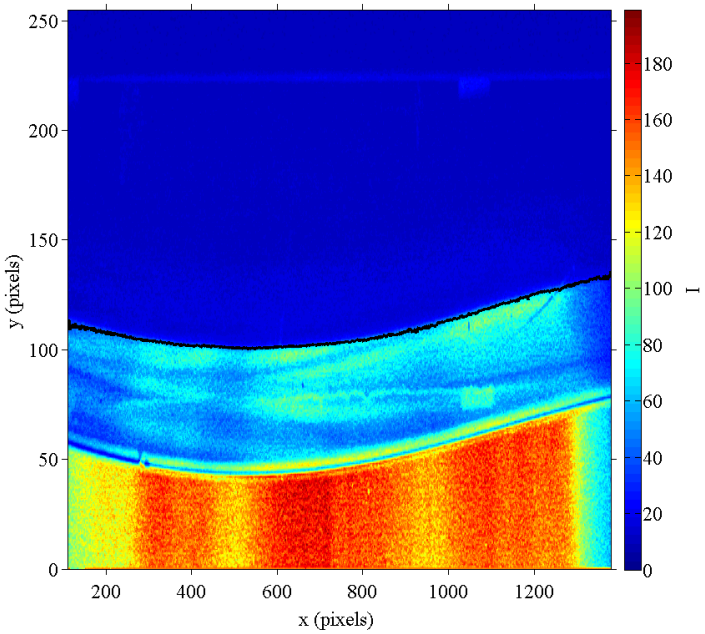

Figure 4.25: Intensity field from processing of image shown in figure 4.24. The free surface is overlaid as a black line.

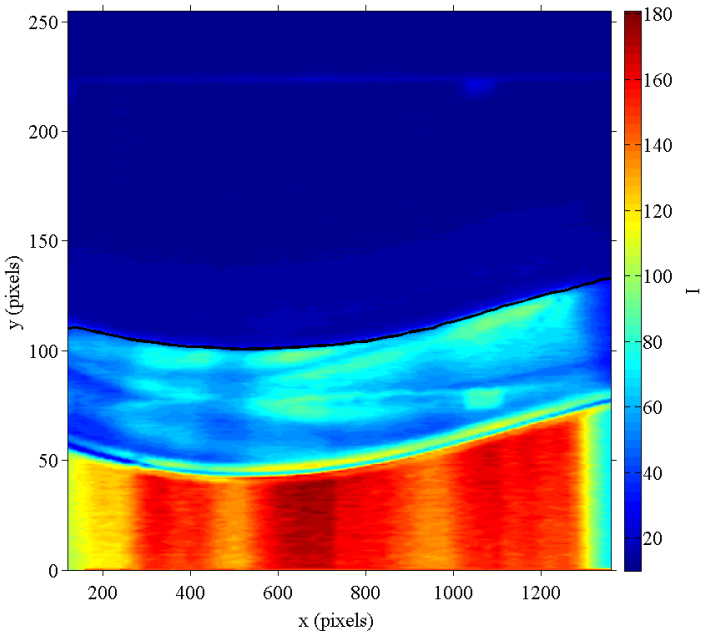

Figure 4.26: Intensity field from processing of image shown in figure 4.24, taking the average over every 20 pixels in the x-direction. The free surface is overlaid as a black line.

the free surface, the program linearly interpolated the free surface record over the gap left by the join, to obtain a continuous free surface record over the length of the flume.

The free surface identification algorithm determined the free surface elevation at each x-t location within the intensity field. Figure 4.27 shows a typical intensity profile in the vertical direction at a particular horizontal location x and time t. Due to spatial variations in laser power over the width of the laser sheet, this algorithm could not simply use one threshold intensity to determine the location of the free surface (as used by Sue, 2007).

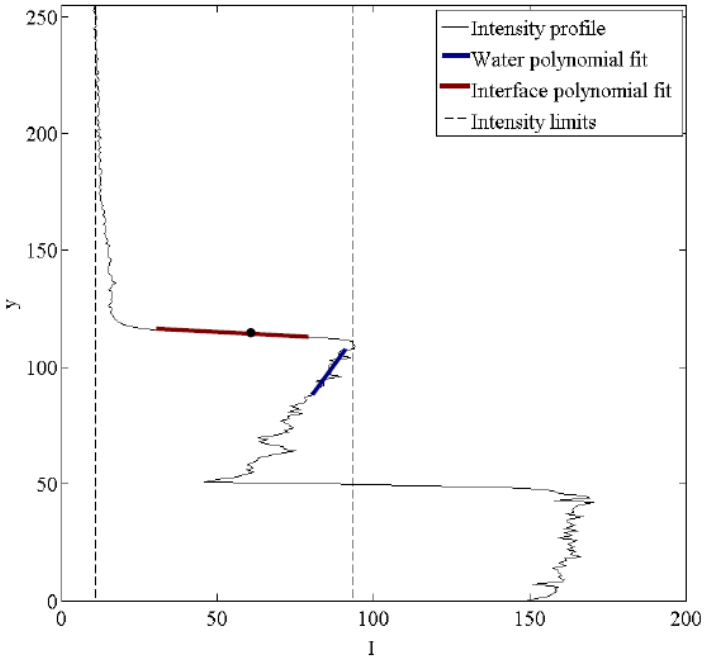

Figure 4.27: Typical vertical intensity profile at a given x, t location.

The algorithm required an intensity threshold, corresponding to the free surface location, which varied depending on the intensity of the fluorescing dye beneath the free surface. To calculate this intensity threshold, the algorithm first determined the approximate location of the free surface. The algorithm searched through the pixel intensities in the negative y-direction (starting from the top of the intensity field) until it found a pixel with $I > 3I_0$, where I_0 is the average intensity of the top 20 pixels (shown as a dashed line in figure 4.27). It then searched in the neighbourhood of this pixel location to find the location of the steepest intensity gradient. This intensity gradient was due to the sharp increase in intensity between the air above and the water below, and the vertical pixel location assigned to the free surface was found in this region. The algorithm fitted a straight line to this intensity gradient, and fitted a second straight line to the water beneath the free surface. The linear fit to the intensity gradient is illustrated by the red line in figure 4.27, and the blue line represents the linear fit to the intensity of pixels beneath the free surface. The intersection of these two polynomials was the lower boundary of the intensity interface defining the free surface,

with intensity I_1 and location y_1 (shown as a dashed line in figure 4.27). Equation 4.2 was then used to calculate the intensity threshold, I_t, based on I_0 and I_1. This ensured that the free surface would be identified in the same location, even for varying laser intensities (corresponding to different I_1 values). The free surface location is shown as a black circle in figure 4.27.

$$I_t = 0.6(I_1 - I_0) + I_0 \tag{4.2}$$

After calculating I_t, the algorithm determined the location of the free surface ($\eta(x,t)$) by linearly interpolating between the adjacent vertical pixels y_a and y_b, where $I(y_a) < I_t$ and $I(y_b) > I_t$.

The free surface identification program applied this algorithm at every x-t location within the intensity record. Once identified in pixel space, the free surface location was converted to physical units using the pixel scale of the camera. The pixel scale was 0.305 mm/pixel during the LIF experiments, and was determined by recording images of a ruler before commencing the experiments. Since the free surface record was wider than 350 mm, the program trimmed the pixels at each end of the record until the width of the free surface record at each gantry location was 350 mm. The program then checked the free surface record for any spikes caused by bubbles or dust particles on the free surface, or by marks on the flume sidewalls. Spikes were removed by linear interpolation of the free surface elevation between adjacent pixels. All free surface records for the different gantry positions were then combined to form the free surface record for the length of the flume.

Due to the pitch of the rack and pinion system, sometimes the camera was at a slightly different vertical elevation or angle to the horizontal when recording images at different gantry locations. To eliminate the effect of a change in gantry elevation or inclination on the free surface records, a polynomial was fitted to the initial (undisturbed at $t = 0$) free surface profile at each gantry location. This polynomial corrected all subsequent free surface profiles so that each free surface record began with the initial condition $\eta(x, 0) = 0$

4.5.3 Wave gauge validation

To ensure that the free surface identification technique provided robust data, measurements taken using LIF were compared to measurements taken using a resistance wave gauge. Resistance wave gauges (RWGs) and capacitance wave gauges (CWGs) have been used in many experimental studies of tsunami generation, propagation and runup (Watts, 2000; Grilli & Watts, 2005; Heinrich, 1992). These wave gauges are only able to capture temporal variations in free surface elevation at discrete locations, however they can measure these temporal variations to high levels of accuracy. Sue (2007) found

that LIF was capable of capturing free surface elevation data to comparable levels of accuracy to a capacitance wave gauge for both large-amplitude (O(10 mm)) waves and small-amplitude (O(1 mm)) waves.

The gauge itself was manufactured by Churchill Controls, and consisted of two parallel stainless steel wires connected to a wave monitor module. The wires were 1.5 mm in diameter, and were spaced 12.5 mm apart. The unit operated by measuring the current flowing between the two wires, where the current between the two wires was proportional to the depth of immersion. The current was sensed by an electronic circuit, which provided an output voltage (proportional to the depth of immersion) to a data logger. The data logger operated at a rate of 100 Hz, and provided output in the form of csv files containing a series of time-voltage measurements over the duration of the experiment.

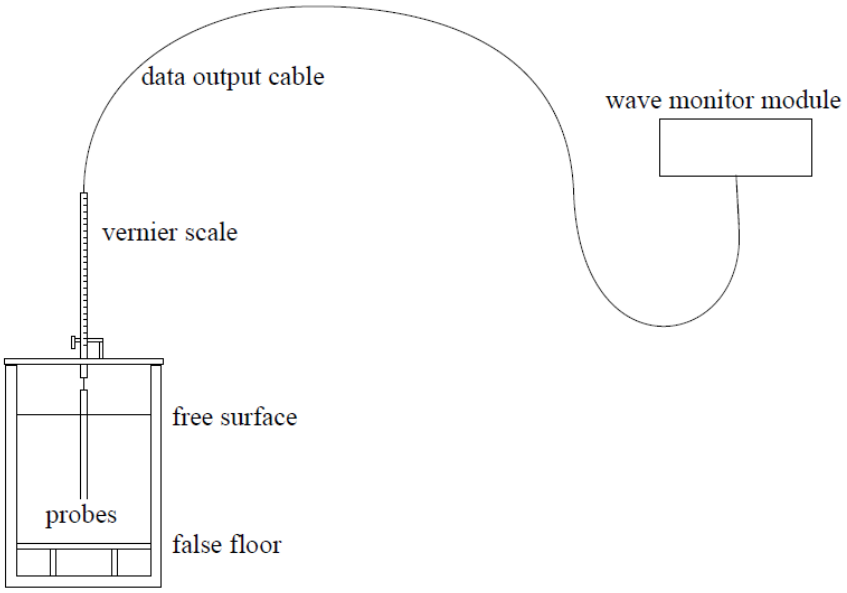

Figure 4.28: Experimental setup for wave gauge validation tests

The unit was calibrated by immersing the wires in a known depth of water (free of any surface motions) and recording the voltage output. This was then repeated at increments of 0.2 mm to determine the relationship between the output voltage from the unit and the immersion depth of the wires. A vernier gauge determined the incremental change in immersion during calibration. The relationship between immersion depth and output voltage was linear over the range of depths tested, as was found in Sue (2007). Experiments were carried out immediately after calibration of the unit, to avoid any possible temperature effects on the probes.

To enable comparison between the wave gauge data and the equivalent LIF data, the gantry was moved to the same position along the flume as the wave gauge. The

camera recorded the location of the wave gauge, so that data could be compared at the same horizontal location within the flume. The experiment used to validate the LIF measurement technique had an acceleration of 1.0 m/s^2, a Froude number (defined in section 4.4) of 0.25 and a depth of 175 mm. After performing two experiments using the wave gauge (allowing the water in the flume to settle between experiments), a small amount of Rhodamine dye was added to the flume, and the experiment was repeated twice using LIF (as described previously in this section). The wave gauge and LIF experiments were each carried out twice to check the repeatability of each measurement technique. Figure 4.29 shows the time series of the free surface elevation for these four runs (two using the wave gauge and two using LIF).

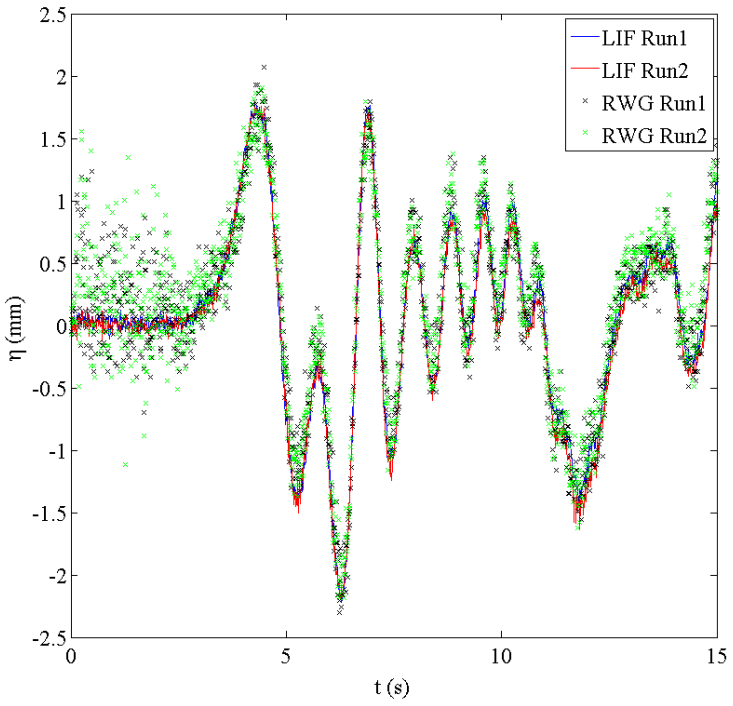

Figure 4.29: Time series of wave gauge and LIF measurements of free surface elevation

The high noise levels present in the initial 3 s of the wave gauge records occurred because the same computer controlled the landslide motion and recorded the wave gauge data. When the landslide motion was initiated, this created noise in the wave gauge record for several seconds. However, since the wave gauge was located approximately 5 m from the initial location of the landslide, this noise had mostly disappeared from the record by the time the first wave crest reached the wave gauge. The LIF system appears to slightly underestimate some of the crests in the high-frequency trailing waves at approximately $t = 8$ s. However, the LIF system reproduced the amplitude and phase of the waves, as measured by the wave gauges, to better than ± 1 pixel (or ± 0.3 mm).

4.5.4 Repeatability of free surface measurements

To ensure that the free surface data recorded during the LIF experiments were repeatable, an experiment was repeated four times at three different gantry locations. The experiments were conducted using a depth of 175 mm, an acceleration of 1.5 m/s^2, and a Froude number of 0.25, and the three gantry locations selected were at 350 mm, 7000 mm and 12250 mm from the onshore end of the flume. Figures 4.30 to 4.32 show time series plots of the wave elevation at a discrete point within the camera field of view at each gantry location. This provides essentially the same data as a wave gauge placed at this point within the flume.

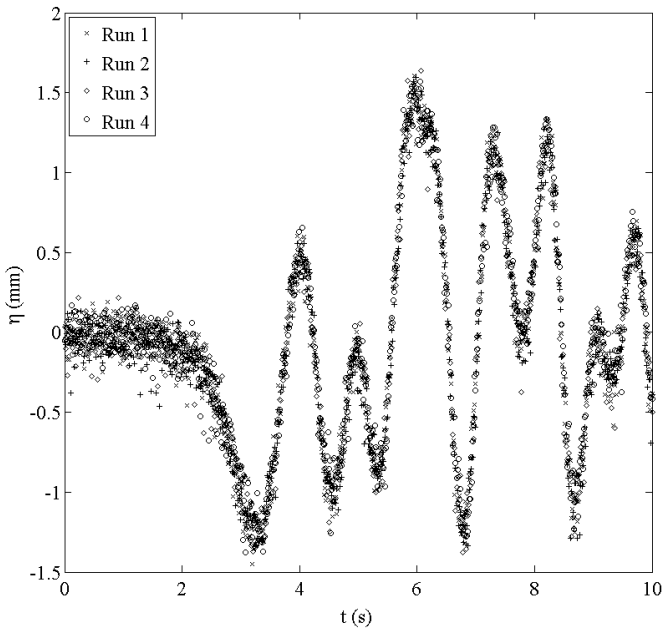

Figure 4.30: Time series of repeated LIF measurements of free surface elevation at a gantry location of 350 mm.

Figures 4.30 to 4.32 show that the time series of the free surface elevation are highly repeatable in each of the three locations. To quantify the scatter in each plot, the standard deviation between the four repetitions was calculated as a function of time. The maximum values of the standard deviations at the three locations were 0.29 mm, 0.34 mm and 0.29 mm respectively. However, the majority of standard deviation values were less than 0.1 mm, demonstrating that the LIF experiments were able to provide repeatable measurements of free surface elevation to sub-pixel accuracy (at a pixel scale of 0.3 mm). Although the noise in the record is most apparent prior to the wave reaching the given location, this noise is still less than ± 0.5 pixels in magnitude.

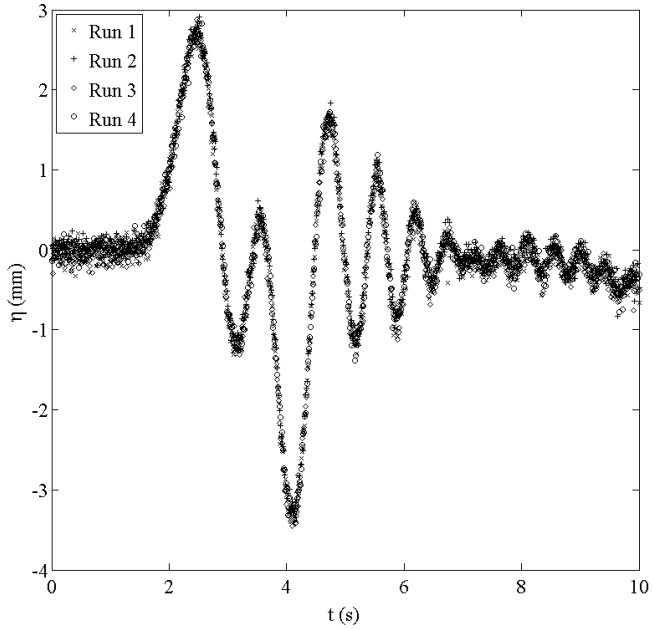

Figure 4.31: Time series of repeated LIF measurements of free surface elevation at a gantry location of 7000 mm.

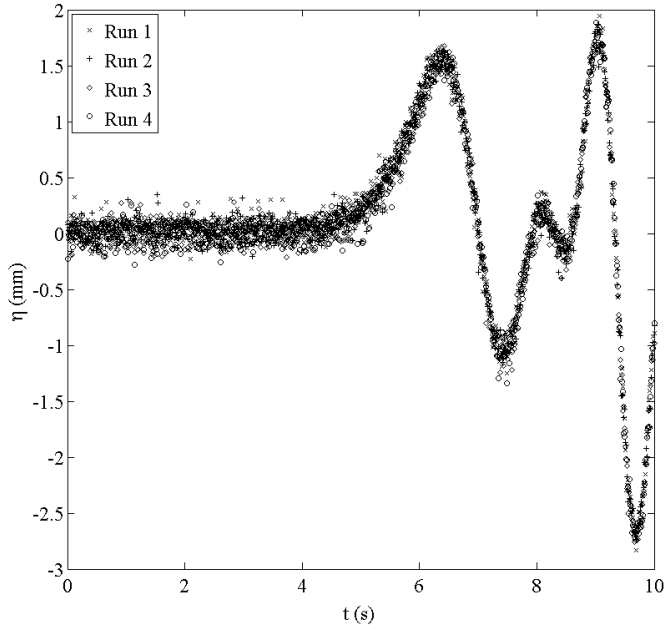

Figure 4.32: Time series of repeated LIF measurements of free surface elevation at a gantry location of 12250 mm.

4.6 Subsurface velocity measurement

4.6.1 Experimental procedure

The subsurface experiment used the particle tracking velocimetry (PTV) technique to calculate the Eulerian velocity field generated by the motion of the landslide block. The free surface waves resulting from the motion of the landslide block also affected the subsurface velocity field within the fluid, since fluid particles tend to move in orbital motions beneath free surface waves. Section 4.3 describes the equipment used in the PTV experiment, and figure 4.33 shows the experimental setup.

A white light box provided lighting for this experiment in the form of a white light sheet, which illuminated small particles within a 2D section of the flume. A camera located outside of the flume recorded images of the particle motion during an experiment. Unlike the laser-induced fluorescence (LIF) experiments, where the camera viewed the free surface at a slight downwards angle, the camera was positioned horizontally during the PTV experiments (see figure 4.14). The light sheet was located between the flume centreline and the near sidewall (as shown in figure 4.14). Initially, the light sheet was located along the flume centreline, directly above the slot in the false floor. However, this led to some experimental issues, due to a small exchange flow through the slot during the experiments. This exchange flow was predominantly in the vertical direction, and had a negligible impact on the PTV measurements after moving the light box away from the slot (by approximately 60 mm).

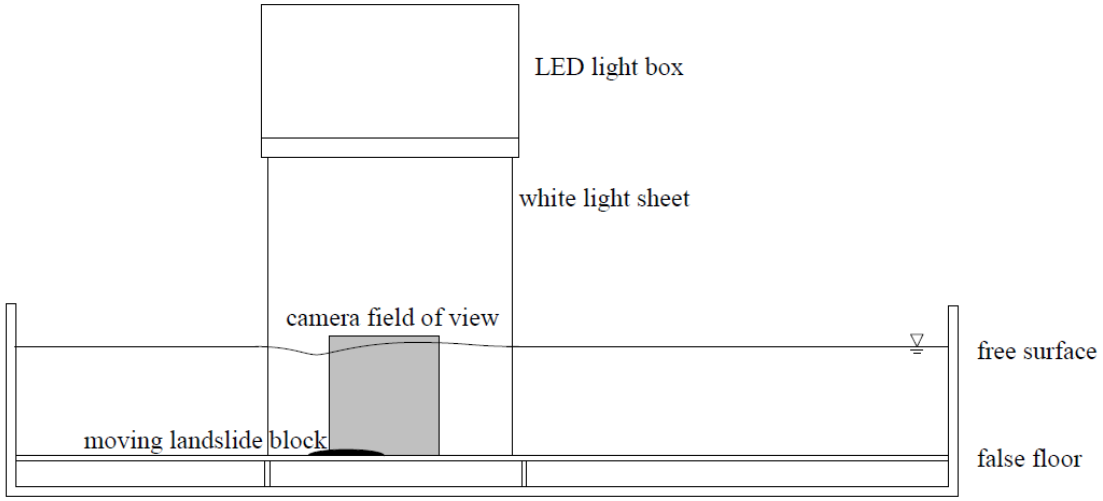

Figure 4.33: Side view of experimental setup used to measure subsurface fluid velocities using PTV.

The flume was filled with water containing Pliolite VTAC (vinyl toluene acrylate) particles, with a size range of 125-180 μm. To achieve the desired particle density, the

particle concentration was 13 mg/L. Some small bubbles also formed underneath the aluminium sliding surface, and if not removed these could rise through the slot during an experiment as the landslide block passed above them. These rising bubbles could be identified as particles during image processing, due to their small size, and hence they could introduce incorrect vertical velocities into the subsurface velocity field. Since the slot in the sliding surface was too narrow to allow mechanical bubble removal, these were removed by running the landslide block along the length of the sliding surface at high velocity several times after removal of the bubbles from the flume sidewalls. The rapid motion of the landslide along the sliding surface caused some of the bubbles to rise through the slot, ensuring that this same behaviour would not occur during an actual experimental run.

Due to the limited horizontal extent of the camera's field of view, each experiment was repeated a total of 37 times to obtain subsurface velocity data over the length of the flume. The gantry system was moved by 350 mm between each experiment, allowing some overlap between images. Section 4.6.2 gives details of the processing of velocity fields for the entire flume and the treatment of the overlap between images. In a similar manner to the LIF experiments, a single light-emitting diode (LED) enabled synchronisation of the landslide motion and the recorded images. Due to the slower frame rate at full frame scanning (see section 4.3.9), the LED synchronised images to within approximately 0.021 seconds (since the camera recorded images every 0.042 seconds, at a rate of 24 frames/second).

Subsurface motions remained for a significant length of time after an experiment had finished, in the same manner that free surface motions within the flume persisted for over 15 minutes after the end of an experiment. However, since the specific density of the particles was 1.03, allowing a long time period between experiments would cause fewer particles to remain in the upper section of the water column. The two-step approach used to resolve this conflict was to first stir up all particles within the flume after the end of an experiment, to ensure that particles were evenly distributed throughout the fluid depth. Second, the insertion of baffles (after particles were stirred) encouraged the dissipation of free surface and subsurface fluid motions (see section 4.3.2), so that these motions would cease before particles had settled any significant distance. Therefore, each experiment could begin with the fluid particles at rest, while still containing particles distributed over the entire fluid depth.

The procedure for a single PTV experiment is stated below.

1. Fill the flume with the water-particle mixture, allowing one day for bubble formation.

2. Turn on the landslide motion control system.

3. Remove any bubbles from sidewalls and the underside of sliding surface, as required.

4. Record a calibration image of a ruler located in the plane of the white light sheet.

5. Turn on the camera, the LED light box and the gantry system.

6. Stir up the particles located on the false floor of the flume to ensure an even distribution of particles throughout the water column.

7. Insert the baffles into the flume at appropriate locations. Leave the baffles in place for three minutes.

8. Carefully remove the baffles, and allow any remaining water motions to dissipate over a further five minutes.

9. Move the gantry to its correct position using the motion control system, and place the LED within the field of view of the camera.

10. Begin recording images of the experiment.

11. Initiate the landslide motion (using the appropriate velocity profile).

12. Cease recording images approximately 10 s after the start of the landslide motion.

13. Return the landslide block to its 'home' position.

14. Repeat steps 7-13 until the entire velocity field has been recorded.

The camera recorded a total of 500 images at each gantry location, in bitmap format. The Streams software package processed these images to calculate the time-dependent subsurface velocity field at each gantry location, and for the entire flume. The image processing procedure is described in section 4.6.2.

4.6.2 Image processing

This section describes the steps followed in the processing of the recorded images to obtain the subsurface velocity field generated by the landslide and wave motion in a PTV experiment. All image processing in the PTV experiments used the Streams software package (Nokes, 2009). This image processing involved several steps, listed below.

1. Filter the raw images to remove any unwanted lines and objects.

2. Identify the particles within each image.

3. Match the identified particles between frames of the image record.

4. Calculate the Lagrangian velocities of the particles, and interpolate these velocities onto an Eulerian grid.

5. Combine the Eulerian velocity fields at all gantry locations, to obtain the total velocity field over the length of the flume.

Figure 4.34 shows a typical image recorded during a PTV experiment. The particles located in the plane of the white light sheet are only faintly visible within the image as white dots. The particles are shown more clearly in subsequent images, however figure 4.34 illustrates several objects that needed to be removed before subsequent image processing could take place.

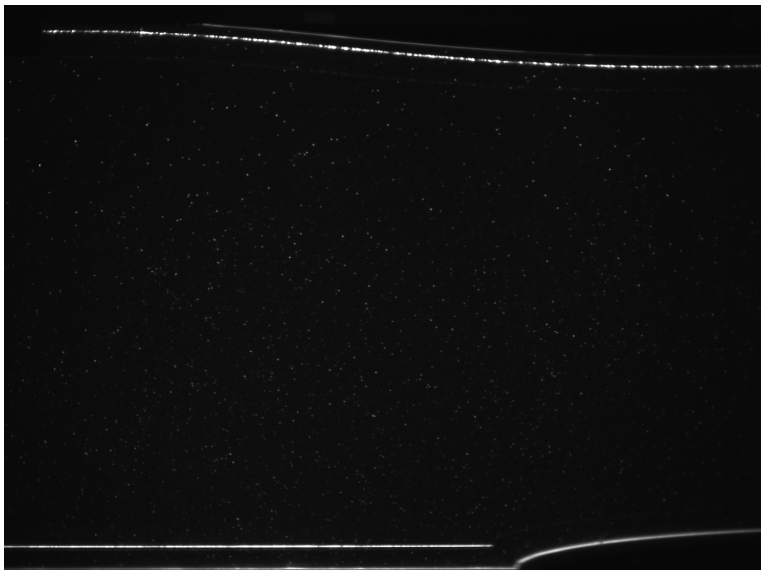

Figure 4.34: Example image recorded during a PTV experiment.

In figure 4.34, the free surface is visible as a bright line in the plane of the light sheet, due to particles which lie upon the free surface. The more faint line above the free surface is the interface between the free surface and the near flume sidewall, and the intersection between the false floor and the flume sidewall is also visible as a bright line near the bottom of the image. If allowed to remain, some locations along these lines could be incorrectly identified as particles. In the same manner, joins between acrylic sections of the flume sidewalls could be incorrectly identified as particles. Any matches between these false particles would contaminate the velocity field, and as such the image processing software removed these bright lines prior to the particle identification process. The lines were removed using a similar operation to the particle identification algorithm, which identified objects based on their size and intensity, then removed these objects. Figure 4.35 shows the same image as figure 4.34, after removal

of the lines. The blue region within this image is used to illustrate the identified and matched particles in subsequent images.

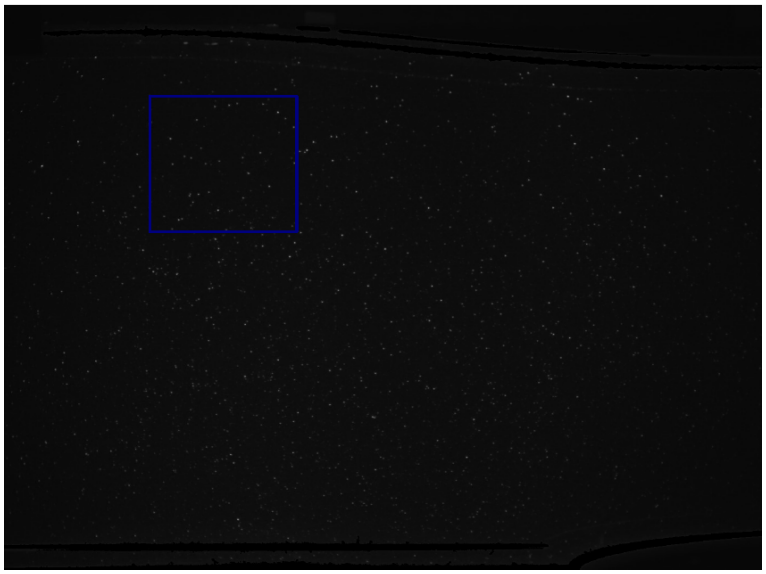

Figure 4.35: Image from figure 4.34, after applying 'remove objects' filter to eliminate free surface and sliding surface lines.

After removal of the lines within the image, a 'particle identification' algorithm located the size and position of particles within the image. The algorithm identified potential particle locations as any pixels whose intensity exceeded a threshold intensity. All pixels adjacent to the high-intensity pixel were assumed to belong to the same particle if their intensity was greater than an edge threshold intensity (set lower than the main threshold intensity). The algorithm assumed a Gaussian intensity distribution for each particle (in both the x and y directions), allowing location of the particle centre to sub-pixel accuracy.

Figure 4.36 shows the particles identified within the blue box in figure 4.34. After correct identification of the particles for the entire image sequence, Streams carried out a PTV analysis to match the particles between frames. This step was the most complicated part of the entire PTV image processing, and used an optimisation algorithm to select the matches based on the criteria of lowest 'cost'. The cost of a particular match depended on the costing criteria used within the analysis. Several sources generated the complex particle motion during experiments. The first source was the motion of the landslide itself, as fluid particles moved rapidly over the landslide during its motion. The second source was the waves generated on the free surface by the motion of the landslide. Fluid particles beneath these waves moved in circular or elliptical orbits (depending on the wavelength of the wave relative to the fluid depth). The third source was the turbulent wake generated by the landslide motion. This was the most difficult part of the flow to match, since the particle motion was chaotic, and hence it was more

difficult to determine particle displacements within the wake.

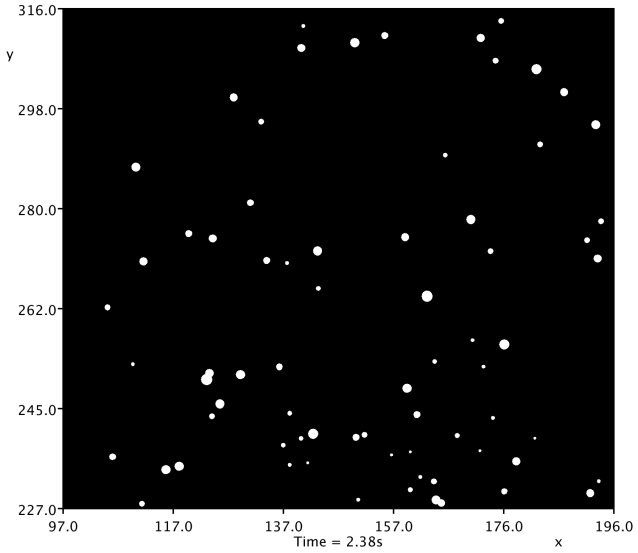

Figure 4.36: Particle record obtained from applying particle identification algorithm to the blue box of the filtered image in figure 4.35, where x and y are the horizontal and vertical distances in mm.

To track particle motions arising from these three sources (landslide, waves and wake) required a combination of several state-based and match-based costings (defined in section 4.2.3). The costs of each potential match with a particle in the next frame were calculated, and the potential matches were optimised by selecting the combination of matches with the lowest total cost.

Figure 4.37 shows the particle record of figure 4.36, with 10 frames overlaid. The orbital nature of the particle motion beneath the free surface waves is clearly visible from the particle tracks. The particle orbits are approximately circular in this area of the image. The matches between particles in this record are illustrated as blue lines. The PTV processing algorithm clearly performs well at making robust matches between particles in the record, although matches were more difficult to make within the turbulent wake (not present in figure 4.37).

The particle matches between frames provided the Lagrangian velocities for all particles, based on a central difference approximation (where matches in the previous and following frames were available). Figure 4.38 shows the vector velocity field calculated from the Lagrangian matches within the particle record of figure 4.36. The particle velocities were interpolated onto a rectangular grid to obtain the Eulerian velocity field for the flow. The spacing between grid points was 5 mm in the x-direction, and 4.7 mm in the y-direction, forming a grid containing 101 x points and 81 y points.

Velocities were interpolated onto the grid using a Thiessen trianglulation (see Nokes, 2009), which effectively ensured that triangles were as close to equilateral as possible.

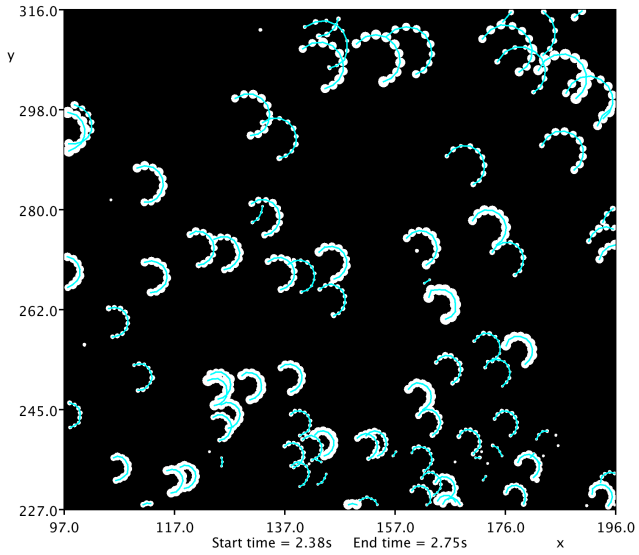

Figure 4.37: 10 frames overlaid from the particle record of figure 4.36, including PTV matches (blue lines), where x and y are the horizontal and vertical distances in mm.

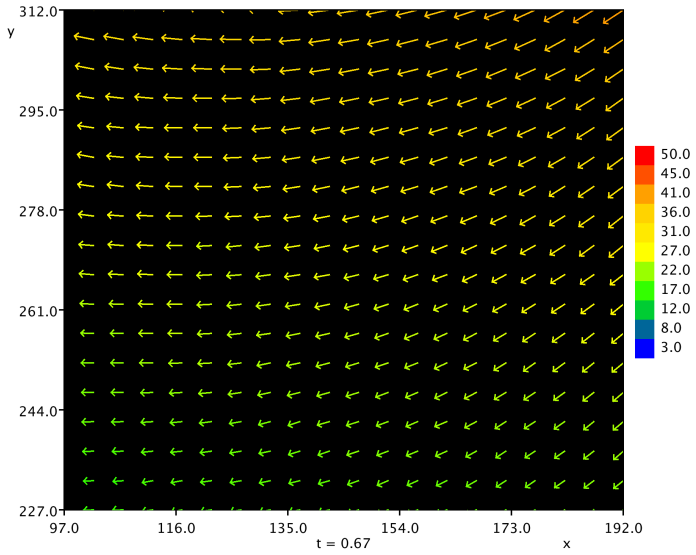

Figure 4.38: Vector velocity field calculated from the final frame of the particle record shown in figure 4.37, where x and y are the horizontal and vertical distances in mm, and the colour scale represents the fluid velocity in mm/s.

This meant that interpolations within a triangle would not be based on velocities of particles that were relatively distant from each other. The velocity was linearly interpolated onto a grid point within each triangle using the interpolation scheme of a triangular element in the finite element method (FEM). Extrapolation of velocities, by projecting velocities into regions of the grid containing no particles, was not permitted. The reason for not allowing extrapolation was that the velocity field did not

extend above the free surface, and the overlap between images (from the small gantry displacement compared to the image width) filled in any gaps at the horizontal edges of each velocity field.

After calculation of the velocity fields at all gantry locations, the velocity fields over the length of the flume were combined into one record. Where velocity fields overlapped, the velocities in the overlapping regions were averaged.

4.6.3 Repeatability of subsurface velocity measurements

To check the validity of this averaging process, and to check the repeatability of the PTV experiments in general, the horizontal and vertical velocities within the overlapping regions were compared between two gantry locations. The gantry locations selected in this case were 9100 mm and 9450 mm from the onshore end of the flume. Figures 4.39 and 4.40 show the time series of the vertical and horizontal velocities calculated at a common horizontal location in the two image records, at $y = 75$ mm above the false floor of the flume.

From figures 4.39 and 4.40, the velocities measured during the PTV experiments are seen to be highly repeatable. The errors in the vertical velocities measured by the PTV system appear to be slightly larger than those in the horizontal velocities. Discrepancies between the two runs appear to be caused by a slight temporal offset between the runs, since the full-frame scanning requires that the camera captures images at 24 frames per second. Thus, the start time of the record could only be known to within ± 0.2 s. However, these results show that the fluid velocities measured using PTV were highly repeatable.

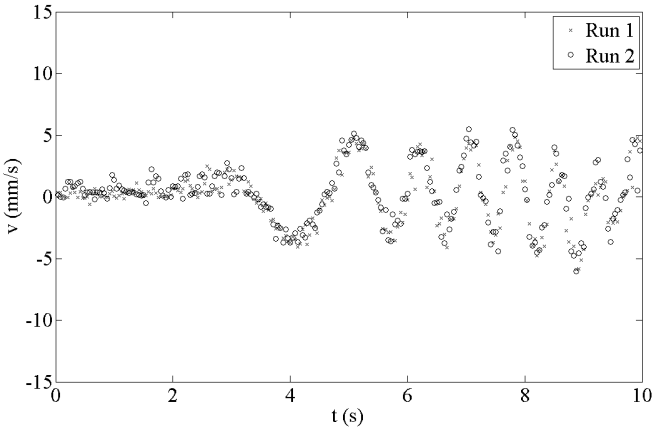

Figure 4.39: Time series of vertical velocity measurements within overlapping zone between two gantry locations

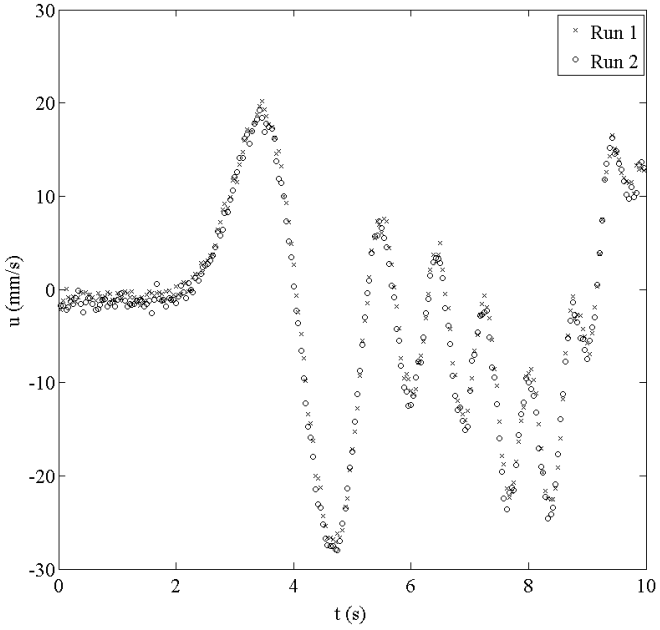

Figure 4.40: Time series of horizontal velocity measurements within overlapping zone between two gantry locations

4.7 Summary

The purpose of the two-dimensional experiments was to measure the surface waves and subsurface velocity fields generated by a submarine landslide. A solid block approximated the landslide, and a mechanical system provided landslide motion over a horizontal boundary. Use of a horizontal bottom boundary ensured that properties of waves propagating in both offshore and onshore directions could be measured, and eliminated experimental issues associated with a transition from a sloping boundary to a horizontal boundary. The use of a mechanical system allowed a broader range of motion to be investigated than possible with gravity-controlled landslide motion, without requiring changes to the landslide block or slope geometry. Experiments aimed to achieve full spatial and temporal resolution of the free surface waves and subsurface velocity fields (in two dimensions).

To ensure a high level of experimental repeatability, a series of preliminary tests was undertaken to check the positioning accuracy of the gantry system and the ability of the landslide system to achieve a given velocity profile. Additional tests assessed the ability of the mechanical system to achieve the velocity and acceleration targets within a trapezoidal velocity profile. Several repetitions of one of the landslide PTV experiments showed that the motion of the landslide was highly repeatable.

During the experiments, the laser-induced fluorescence (LIF) technique provided measurements of the spatial and temporal variations in free surface elevation. Discrete

measurements of free surface elevation using a resistive wave gauge (RWG) provided validation of the LIF system's ability to resolve free surface elevations to sub-millimetre accuracy. The particle tracking velocimetry (PTV) technique provided the subsurface velocity fields generated by the landslide.

Chapter 5

Numerical model formulation

5.1 Numerical modelling overview

The objective of the numerical modelling undertaken within this project was to predict the waves generated by the motion of a submarine landslide. A series of physical laboratory experiments were used to validate these predictions. Other properties of interest include the fluid velocity and pressure fields beneath the free surface (referred to hereafter as subsurface properties), since these can provide insights into the generation mechanism of the waves, and the transfer of energy between the submarine landslide and the wave field.

Chapter 2 discussed the mathematical framework within which tsunami models are formulated. This discussion included the possible treatments of the problem domain, the boundary conditions, the landslide, the ambient fluid and the generated waves. The models formulated in the current chapter all aim to simulate the geometry of the physical experiments, and therefore the problem domain of each model will contain a horizontal bottom boundary only. The lateral boundary conditions can either be solid boundaries (to simulate the ends of the flume), or effectively infinite boundaries which allow the generated waves to propagate out of the domain. These are discussed separately for each model within this chapter. All of the models represent the landslide as a solid block, of the same approximate size and shape as the aluminium block used in the physical experiments.

In mathematically simulating the solid block landslide experiments, the treatment of the ambient fluid and the generated waves will determine the complexity of the model. If the ambient fluid is treated as viscous, then the model is more mathematically complex, but will be able to simulate boundary layer effects. Conversely, a model assuming an inviscid ambient fluid will be simpler to formulate and solve, but will not include boundary layer development and possible separation. The use of simplifying assumptions regarding the amplitude or wavelength of the generated waves will also

greatly simplify the mathematical formulation of the model, while limiting the range of amplitudes and wavelengths that the model can realistically simulate. To gain an understanding of the effects of these simplifying assumptions on the model predictions, several different models are formulated.

The first model described is a two-dimensional inviscid-irrotational model. The inviscid-irrotational assumption allows the problem to be formulated in terms of the (scalar) velocity potential. The linear assumption is invoked for perturbations to the free surface (by the generated waves) and the bottom boundary (by the moving landslide), allowing the solution for the wave amplitude to be determined as a Fourier decomposition of free wave modes. This model is solved in a semi-analytical manner, as the governing partial differential equation (Laplace's equation for the velocity potential) can be reduced to a system of ordinary differential equations. These ordinary differential equations are solved for the spectral wave coefficients, which are then integrated over a range of wavenumbers to calculate the wave amplitude. The subsurface velocity and pressure fields may also be calculated by numerically integrating the spectral coefficients for the velocity potential.

The linear inviscid model is computationally efficient and simple to formulate, but it is limited in its ability to represent the physics of the laboratory experiments. This model was published in Sue (2007), however the solution process is different in this formulation of the model (due to the different goals of the model in this study). Therefore, the full mathematical formulation of the model used in the current study is presented in section 5.2 for completeness.

The second model is an extension of the linear inviscid model to include propagation in two horizontal dimensions, so that the model itself is a three-dimensional model. Two-dimensional models of tsunami propagation reflect a field situation where the submarine landslide is much wider than it is long, and so waves effectively propagate in one dimension only. As the aspect ratio (defined as $width : length$) of the landslide decreases, this approximation becomes less valid. Previous studies have found that the effect of an added lateral dimension is to decrease the amplitude of generated waves (since these waves can now propagate in both horizontal directions), and to change the resonant behaviour of the waves, since energy no longer propagates in one horizontal dimension only. The extension of the linear inviscid model to three dimensions, presented in section 5.3, allows these effects to be quantified through a preliminary set of simulations. This extension also provides a better understanding of the possible application of two-dimensional experimental and numerical modelling to field events.

The final two models described in this chapter are intended to test the applicability of some of the assumptions used to formulate the two-dimensional spectral model. The first of these is a nonlinear inviscid-irrotational model. This model solves Laplace's

equation on the boundaries of the domain using a boundary element method (BEM). The solution on the free surface provides the wave field generated by the moving landslide. This model does not use the linear assumption on the bottom boundary, and therefore can assess the limitations of this assumption in predicting the amplitude and energy of the generated waves. The model does assume linearity of the free surface waves themselves. This model was published by Sue *et al.* (2011) for a landslide moving along a sloping boundary under the influence of gravity. Section 5.4 describes the application of this model to a domain containing a horizontal bottom boundary.

The fourth model described in this chapter models the ambient fluid as a viscous fluid and removes the linear assumptions on the free surface and the bottom boundary. Modelling the ambient fluid as an incompressible viscous fluid allows assessment of boundary layer effects on the generated waves (if any), as well as the energy dissipation within the system due to the fluid viscosity. The removal of the linear assumption on the domain boundaries eliminates the restrictions on the amplitude and wavelength of the generated waves, and allows simulation of a more realistic bottom boundary. This model is formulated using the direct numerical simulation (DNS) solver Gerris (Popinet, 2003). The viscous model better reflects the physics of the experiments, but is significantly more computationally expensive than either of the inviscid-irrotational models. The differences in the properties of the generated waves due to the different levels of model approximation may be assessed by comparing predictions of the different numerical models with the results of the physical experiments. The formulation of the Gerris model is presented in section 5.5.4.

In the formulation of the mathematical models, each section of this chapter presents the model domain and treatment of the boundaries within the model. Next, each section describes the approximations used to formulate each model, and the governing equations and boundary conditions resulting from this level of simplification. In the case of the spectral model, the sections give the analytical working needed to reduce the governing equations into a solveable form, including the assumed solution form to the governing equations. In the case of the viscous model, a dimensional analysis is provided to formulate the model in the correct dimensionless variables.

5.2 Two-dimensional linear inviscid model

5.2.1 Model domain

Figure 5.1 shows the problem domain of the two-dimensional linear inviscid model. The landslide was modelled as a solid block, and its motion along the horizontal bottom boundary generated waves on the free surface of the fluid. The domain was assumed to be infinite in horizontal extent, so that any waves reaching the boundaries of the domain would continue propagating out of the domain without reflection (these are the onshore and offshore conditions shown in figure 5.1). The landslide was incorporated into the mathematical expression for the impermeable bottom boundary, $y_b(x,t)$. Thus,

$$y_b(x,t) = -D + h_b f(\theta(x,t)), \tag{5.1}$$

where $\theta(x,t) = x - x_0(t)$ is the horizontal coordinate relative to the position of the landslide centre of mass at time t.

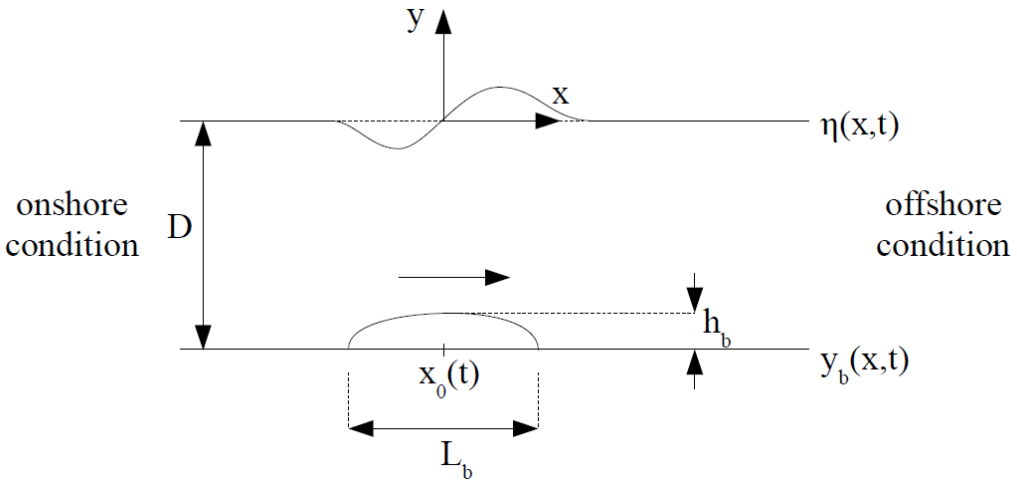

Figure 5.1: Domain for two-dimensional linear inviscid model formulation

The origin of the coordinate system was located on the undisturbed free surface above the initial position of the landslide centre of mass. The fluid had a constant depth, D, above the horizontal bottom boundary. The landslide had length L_b and thickness h_b, and moved in the positive x-direction only. In this case, the landslide motion could be described by the position of its centre of mass, x_0, and its corresponding velocity, $\frac{dx_0}{dt}$ and acceleration, $\frac{d^2x_0}{dt^2}$. The motion of the landslide along the bottom boundary was an idealisation of the motion of a landslide down a constant-sloping boundary, as discussed in section 5.2.8.

The variable η represents the free surface elevation within the model domain. Subsurface horizontal and vertical fluid velocities are represented by the variables $u\,(x,y,t)$ and $v\,(x,y,t)$ respectively. These fluid velocities beneath the free surface were gene-

rated by both the landslide forcing and by the oscillatory fluid motion beneath the waves.

5.2.2 Model approximations

The inviscid assumption neglects the fluid viscosity. Provided that boundary layers are small and play no role in the flow dynamics, this assumption is valid for a sufficiently high Reynolds number within the flow. The Reynolds number is defined as

$$Re = \frac{uD}{\nu}, \tag{5.2}$$

where u is the flow velocity, D is the fluid depth and ν is the fluid viscosity.

Under the inviscid assumption, the no-slip condition could no longer be applied on a solid boundary. Instead, the condition on these solid boundaries was the flow tangency condition, which required that fluid particles on the boundary had zero velocity in the direction normal to the boundary. Due to this change in boundary conditions, boundary layers could no longer form on these solid surfaces.

The model also invoked the linear assumption on both the free surface and the bottom boundary. Applied to the free surface, the linear assumption required that, within a spectrum of generated waves, the characteristic wave amplitude, η_0, was much less than both the fluid depth, D and the characteristic wavelength, λ_0. The first consequence of this assumption was that all nonlinear terms were removed from the governing equations and free surface boundary conditions. The second consequence of this assumption was that the free surface boundary conditions (discussed in section 5.2.3) could now be applied to the undisturbed free surface, $y = 0$, rather than the actual free surface, $y = \eta(x,t)$. The use of the linear assumption on the bottom boundary required that the thickness of the landslide, h_b, was very small compared to both the water depth, D, and the landslide length, L_b. The application of the linear assumption to the bottom boundary allowed all nonlinear terms to be neglected from the bottom boundary condition, and this condition could now be applied on the undisturbed bottom boundary, $y = -D$, rather than the actual bottom boundary, $y = y_b(x,t)$.

In reality, the bottom boundary condition had the form:

$$\frac{\partial \phi}{\partial y} = \frac{\partial y_b}{\partial t} + \frac{\partial \phi}{\partial x}\frac{\partial y_b}{\partial x} \qquad \text{on } y = y_b(x,t), \tag{5.3}$$

where the second term is the nonlinear term neglected in the spectral model formulation. Upon substitution of the expression for y_b in equation 5.1, the nonlinear boundary condition may be written as:

$$\frac{\partial \phi}{\partial y} = -h_b \frac{\partial f}{\partial \theta} \frac{dx_0}{dt} + h_b \frac{\partial f}{\partial \theta} \frac{\partial \phi}{\partial x}. \tag{5.4}$$

Therefore, by neglecting the nonlinear term from this boundary condition, it was implicitly assumed that the magnitude of the landslide velocity was much larger than the magnitude of the horizontal fluid velocity along the boundary. This is mathematically stated as:

$$\frac{dx_0}{dt} \gg \frac{\partial \phi}{\partial x} \qquad \text{on } y = y_b(x,t). \tag{5.5}$$

In the case of a viscous fluid, the horizontal velocity of the boundary fluid would be equal to the horizontal landslide velocity (by the no-slip condition). In an inviscid fluid, there is no condition on the tangential fluid velocity on the boundary. However, it is likely that significant horizontal fluid velocities would be generated by the landslide motion near the corners of the landslide. Therefore, the linearisation of the bottom boundary condition may lead to errors in the prediction of the flow in the vicinity of the landslide.

5.2.3 Governing equations and boundary conditions

Since the model was formulated using inviscid-irrotational flow theory, the governing equation for the problem is Laplace's equation, expressed in terms of the velocity potential $\phi(x, y, t)$ as

$$\nabla^2 \phi = 0. \tag{5.6}$$

Laplace's equation is expressed in two-dimensional Cartesian coordinates as

$$\frac{\partial^2 \phi}{\partial x^2} + \frac{\partial^2 \phi}{\partial y^2} = 0. \tag{5.7}$$

Due to the assumption of an inviscid fluid, the condition on the bottom boundary was the condition of flow tangency, so that the normal velocity of the fluid on the boundary (relative to the velocity of the boundary) was zero. Under the linear assumption, the landslide motion imparted a moving vertical velocity to the fluid from the horizontal bottom boundary. Thus,

$$\frac{\partial \phi}{\partial y} = \frac{\partial y_b}{\partial t} \qquad \text{on } y = -D. \tag{5.8}$$

Although the condition was applied on the undisturbed bottom boundary ($y = -D$), the thickness and shape of the landslide would determine the magnitude and spatial distribution of these velocities.

The two conditions applied on the free surface were the kinematic and dynamic

conditions. Under the linear assumption, both of these boundary conditions were applied to the undisturbed free surface, $y = 0$, since it was assumed that the amplitude of the generated waves was negligible compared to the water depth. The linearised kinematic condition on the free surface was

$$\frac{\partial \phi}{\partial y} = \frac{\partial \eta}{\partial t} \qquad \text{on } y = 0, \tag{5.9}$$

and the linearised dynamic free surface boundary condition was

$$\frac{\partial \phi}{\partial t} + g\eta = 0 \qquad \text{on } y = 0. \tag{5.10}$$

The initial conditions for this problem were that the free surface (and the ambient fluid beneath the free surface) are stationary. Thus,

$$\phi\left(x, y, 0\right) = 0, \tag{5.11}$$

and

$$\eta\left(x, 0\right) = 0. \tag{5.12}$$

5.2.4 Nondimensionalisation and scaling

Mathematical models of physical phenomena are most conveniently formulated in non-dimensional variables, so that the model can be applied to any scale without requiring reformulation. Additionally, formulation of a model in nondimensional variables allows the key nondimensional parameters affecting model behaviour to be determined.

The horizontal and vertical distances in the model, x and y, were nondimensionalised by the same length scale. The length scale used for this nondimensionalisation could be either the fluid depth, D, or the landslide length, L_b. Since valid arguments could be made for either scale, the length scale used for nondimensionalisation in the model was initially set to an arbitrary length scale, L, which could be either D or L_b. The length scale used for perturbations to the system was the landslide thickness, h_b. These perturbations are the time-dependent bottom boundary, $y_b(x, t)$, since this included the shape of the landslide, and the free surface elevation, $\eta(x, t)$. The gravitational acceleration, g, was used in conjunction with the length scale, L, to nondimensionalise variables involving time. This resulted in the set of nondimensional variables

$$x' = \frac{x}{L}, \tag{5.13a}$$

$$y' = \frac{y}{L}, \tag{5.13b}$$

$$y'_b = \frac{y_b}{h_b}, \tag{5.13c}$$

$$t' = t\sqrt{\frac{g}{L}}, \tag{5.13d}$$

$$\eta' = \frac{\eta}{h_b}, \tag{5.13e}$$

$$\phi' = \frac{\phi}{h_b\sqrt{gL}}, \tag{5.13f}$$

$$u' = \frac{u}{h_b}\sqrt{\frac{L}{g}}, \tag{5.13g}$$

$$v' = \frac{v}{h_b}\sqrt{\frac{L}{g}}, \tag{5.13h}$$

$$k' = kL, \tag{5.13i}$$

$$\omega' = \omega\sqrt{\frac{L}{g}}, \tag{5.13j}$$

where k is the wavenumber of the generated waves, and ω is the corresponding angular frequency of the generated waves. This angular frequency is related to the wavenumber by the nondimensional dispersion equation (with primes dropped),

$$D(k) = -\omega^2 + k\tanh(k\tau) = 0, \tag{5.14}$$

where τ is the nondimensional fluid depth. This parameter is defined as

$$\tau = \frac{D}{L}. \tag{5.15}$$

The nondimensional depth was important since it related the fluid depth to the landslide length, and its size affected the range of wavelengths generated by the landslide motion.

Regarding the motion of the landslide, let $x_0(t)$ be the position of the landslide centre of mass, and let its derivatives be $\frac{dx_0}{dt}$ and $\frac{d^2x_0}{dt^2}$. These were nondimensionalised

in a similar manner to the variables above, such that

$$x_0' = \frac{x_0}{L}, \tag{5.16a}$$

$$\left(\frac{dx_0}{dt}\right)' = \frac{dx_0}{dt}\frac{1}{\sqrt{gL}}, \tag{5.16b}$$

$$\left(\frac{d^2x_0}{dt^2}\right)' = \frac{d^2x_0}{dt^2}\frac{1}{g} = \lambda. \tag{5.16c}$$

The second parameter of interest arising from this nondimensionalisation was the nondimensional landslide acceleration parameter, λ. Since the landslide forcing in this project used a constant acceleration and deceleration, this parameter was constant. The parameter λ is defined to be

$$\lambda = \frac{a_0}{g}, \tag{5.17}$$

where $a_0 = \frac{d^2x_0}{dt^2}$ is the landslide acceleration, and g is the acceleration due to gravity.

Under the nondimensionalisation of equations 5.13, Laplace's equation remained unchanged. Therefore, equation 5.7 is the governing equation in the nondimensional formulation of the linear inviscid model. The initial conditions also remained unchanged in nondimensional form. However, two of the boundary conditions for the problem did change when nondimensionalised according to equations 5.13. The conditions stated in equations 5.8 and 5.10, in nondimensional form, become

$$\frac{\partial\phi'}{\partial y'} = \frac{\partial y_b'}{\partial t'} \qquad \text{on } y' = -\tau, \tag{5.18}$$

and

$$\frac{\partial\phi'}{\partial t'} + \eta' = 0 \qquad \text{on } y' = 0. \tag{5.19}$$

For the remainder of this section, all variables will be presented in nondimensional form, unless explicitly stated otherwise, with primes dropped for convenience. During the numerical simulations, L_b was selected as the representative length scale, as opposed to the fluid depth. The experimental results were nondimensionalised in a similar manner, as discussed in chapter 6.

5.2.5 Solution process for wave amplitude, $\eta(x,t)$

Assumed solution form

The solution of the governing equation followed the formulation of Sue (2007), and was based on the solution of Lighthill (1978) for the waves generated by objects in a steady stream. The assumed solution for the velocity potential is therefore

$$\phi\left(x,y,t\right)=\int_{-\infty}^{\infty}e^{i(kx-\omega t)}\left[a\cosh k\left(y+\tau\right)+b\sinh k\left(y+\tau\right)\right]dk, \tag{5.20}$$

and the assumed solution for the free surface displacement is

$$\eta(x,t)=\int_{-\infty}^{\infty}e^{i(kx-\omega t)}c\left(k,t\right)dk, \tag{5.21}$$

where only the real parts of these solutions were required. In equations 5.20 and 5.21, $a(k,t)$ and $b(k,t)$ are the spectral coefficients associated with the velocity potential, and $c(k,t)$ is the spectral coefficient associated with the wave amplitude.

The assumed solution was substituted into the three nondimensional boundary conditions to determine the spectral coefficients, $a(k,t)$, $b(k,t)$ and $c(k,t)$. To determine the wave amplitude, $\eta(x,t)$, the spectral coefficients $c(k,t)$ were integrated over all wavenumbers according to equation 5.21. The $a(k,t)$ and $b(k,t)$ were integrated to determine the velocity potential of the fluid using equation 5.20, which was then used to calculate the subsurface velocity and pressure fields.

Application of boundary conditions

This solution procedure first applied the assumed solution form to the bottom boundary condition. The nondimensional form of the impermeable bottom boundary is

$$y_b(x,t)=-\xi+f(\theta(x,t)), \tag{5.22}$$

where $f(\theta(x,t))$ is the shape of the landslide, $\theta(t)=x-x_0(t)$ is the x-position relative to the position of the landslide block at a particular time t, and $\xi=\frac{D}{h_b}$. Upon substitution of this expression, the bottom boundary condition becomes

$$\frac{\partial y_b}{\partial t}=-\frac{\partial f}{\partial\theta}\frac{dx_0}{dt}. \tag{5.23}$$

Since the assumed solutions for ϕ and η were in the form of a Fourier decomposition of wave modes, the bottom boundary must also be expressed in the same form. Thus,

$$\frac{\partial f}{\partial\theta}=\int_{-\infty}^{\infty}e^{i(k\theta)}p(k)dk. \tag{5.24}$$

Upon substitution of the assumed solution, the bottom boundary condition becomes

$$\int_{-\infty}^{\infty} ke^{i(kx-\omega t)} \left[a \sinh k\left(y+\tau\right) + b \cosh k\left(y+\tau\right)\right] dk = -\frac{dx_0}{dt} \int_{-\infty}^{\infty} e^{i(k\theta)} p(k) dk$$

$$\text{on } y = -\tau. \quad (5.25)$$

$$\therefore -\frac{dx_0}{dt} \int_{-\infty}^{\infty} e^{i(k\theta)} p(k) dk = \int_{-\infty}^{\infty} ke^{i(kx-\omega t)} b dk. \quad (5.26)$$

Under the linear assumption, the wave solution was expressed as the integral of an infinite number of linearly independent Fourier modes. Therefore, the spectral coefficients b in equation 5.26 were also linearly independent. This equation was solved at each wavenumber k for the spectral coefficients associated with that wavenumber. Thus,

$$-\frac{dx_0}{dt} e^{i(k\theta)} p(k) = ke^{i(kx-\omega t)} b. \quad (5.27)$$

$$\therefore b(k,t) = -\frac{dx_0}{dt} \frac{p(k)}{k} e^{i(\omega t - kx_0)}. \quad (5.28)$$

For simplicity in the remainder of this chapter, the variables $\varphi(k,x,t)$, $\epsilon(k,t)$ and $F(k,t)$ are defined as

$$\varphi = kx - \omega t. \quad (5.29)$$

$$\epsilon = \omega t - kx_0, \quad (5.30)$$

$$F = \frac{dx_0}{dt} \frac{p(k)}{k}. \quad (5.31)$$

Thus the spectral coefficients $b(k,t)$ can be re-written as

$$b(k,t) = -Fe^{i\epsilon}. \quad (5.32)$$

Next, the assumed solution was applied to the free surface boundary condition. Thus,

$$\int_{-\infty}^{\infty} ke^{i\varphi} \left[a \sinh k\left(y+\tau\right) + b \cosh k\left(y+\tau\right)\right] dk = \int_{-\infty}^{\infty} e^{i\varphi} \left[\frac{\partial c}{\partial t} - i\omega c\right] dk$$

$$\text{on } y = 0. \quad (5.33)$$

$$\therefore \int_{-\infty}^{\infty} ke^{i\varphi} \left[a \sinh(k\tau) + b \cosh(k\tau)\right] dk = \int_{-\infty}^{\infty} e^{i\varphi} \left[\frac{\partial c}{\partial t} - i\omega c\right] dk. \tag{5.34}$$

Equating coefficients as before,

$$a(k,t) = \frac{1}{k \sinh(k\tau)} \left[\frac{\partial c}{\partial t} - i\omega c + k \cosh(k\tau) F e^{i\epsilon}\right]. \tag{5.35}$$

The time derivatives of the spectral coefficients a and b, required in the dynamic boundary condition, are

$$\frac{\partial b}{\partial t} = -e^{i\epsilon} \left(\frac{\partial F}{\partial t} + iF\frac{\partial \epsilon}{\partial t}\right), \tag{5.36}$$

and

$$\frac{\partial a}{\partial t} = \frac{1}{k \sinh(k\tau)} \left[\frac{\partial^2 c}{\partial t^2} - i\omega \frac{\partial c}{\partial t} + k \cosh(k\tau) e^{i\epsilon} \left(\frac{\partial F}{\partial t} + iF\frac{\partial \epsilon}{\partial t}\right)\right]. \tag{5.37}$$

Upon substitution into the dynamic free surface condition,

$$\int_{-\infty}^{\infty} e^{i\varphi} \left[\cosh(k\tau) \left(\frac{\partial a}{\partial t} - i\omega a\right) + \sinh(k\tau) \left(\frac{\partial b}{\partial t} - i\omega b\right)\right] dk + \int_{-\infty}^{\infty} e^{i\varphi} \left[c\right] dk = 0. \tag{5.38}$$

Equating coefficients as before,

$$\cosh(k\tau) \left(\frac{\partial a}{\partial t} - i\omega a\right) + \sinh(k\tau) \left(\frac{\partial b}{\partial t} - i\omega b\right) + c = 0. \tag{5.39}$$

Upon substitution of the spectral coefficients $a(k,t)$ and $b(k,t)$ (equations 5.32 and 5.35), and the time derivatives of these coefficients (equations 5.36 and 5.37), equation 5.39 is reduced to

$$c\left(k \tanh(k\tau) - \omega^2\right) + \frac{\partial^2 c}{\partial t^2} - 2i\omega \frac{\partial c}{\partial t} + k \cosh(k\tau) e^{i\epsilon} \left(\frac{\partial F}{\partial t} + iF\frac{\partial \epsilon}{\partial t} - i\omega F\right) - k \tanh(k\tau) \sinh(k\tau) e^{i\epsilon} \left(\frac{\partial F}{\partial t} + iF\frac{\partial \epsilon}{\partial t} - i\omega F\right) = 0, \tag{5.40}$$

where the first term in equation 5.40 is identically zero due to the dispersion relation in equation 5.14. This yields the equation

$$\frac{\partial^2 c}{\partial t^2} - 2i\omega\frac{\partial c}{\partial t} + \frac{e^{i\epsilon}p(k)}{\cosh(k\tau)}\left(\frac{d^2x_0}{dt^2} - ik\left(\frac{dx_0}{dt}\right)^2\right) = 0. \tag{5.41}$$

Equation 5.41 held for each wavenumber, k, based on the linear independence of the Fourier modes in the solutions for ϕ and η. Thus k could be treated as a parameter in the equation, such that

$$\frac{d^2 c}{dt^2} - 2i\omega\frac{dc}{dt} + \frac{e^{i\epsilon}p(k)}{\cosh(k\tau)}\left(\frac{d^2x_0}{dt^2} - ik\left(\frac{dx_0}{dt}\right)^2\right) = 0. \tag{5.42}$$

Let the wave forcing due to the landslide motion be represented by the function $G(k,t)$. This forcing function is defined as

$$G(k,t) = \frac{e^{i\epsilon}p(k)}{\cosh(k\tau)}\left(\frac{d^2x_0}{dt^2} - ik\left(\frac{dx_0}{dt}\right)^2\right), \tag{5.43}$$

such that equation 5.42 is finally expressed as

$$\frac{d^2 c}{dt^2} - 2i\omega\frac{dc}{dt} + G(k,t) = 0. \tag{5.44}$$

The spectral coefficients calculated using equation 5.44 were integrated over all wavenumbers to obtain the wave amplitude, $\eta(x,t)$, for the entire domain.

Numerical solution procedure

The numerical solution of this problem involved two steps. The first step was to solve equation 5.44 for the spectral coefficients $c(k,t)$. The second step was to integrate these coefficients over all wavenumbers, obtaining the wave amplitude η. To simplify the solution process, equation 5.44 can be expressed as a system of first-order ODEs. Using the change of variables

$$C_1 = c, \tag{5.45a}$$

$$C_2 = \frac{dc}{dt}, \tag{5.45b}$$

equation 5.44 becomes

$$\frac{dC_1}{dt} = C_2, \tag{5.46a}$$

$$\frac{dC_2}{dt} = 2i\omega C_2 - G(k,t). \tag{5.46b}$$

The ODE solver, 'ode45', within the computer program Matlab, solved the system of equations 5.46 for the spectral coefficients $c(k,t)$ over a range of wavenumbers. The range and resolution of the wavenumber domain determined the smallest and largest wavelengths able to be resolved by the model (discussed in Sue, 2007). These coefficients were then numerically integrated over the wavenumber domain according to

$$\eta(x,t) = \int_{k_{min}}^{k_{max}} c_r \cos(kx - \omega t) - c_i \sin(kx - \omega t)\, dk, \tag{5.47}$$

where the r subscript refers to the real component of the spectral coefficients, and the i subscript refers to the imaginary components of the spectral coefficients.

5.2.6 Solution process for subsurface velocity and pressure field

The subsurface velocity field, composed of the horizontal velocity $u(x,y,t)$ and the vertical velocity $v(x,y,t)$, depended on the velocity potential, ϕ, according to

$$u = \frac{\partial \phi}{\partial x}, \tag{5.48a}$$

$$v = \frac{\partial \phi}{\partial y}. \tag{5.48b}$$

The pressure field could also be calculated from the velocity potential, using the linearised Bernoulli equation for an inviscid-irrotational flow (where the pressure, $P(x,y,t)$, is relative to the hydrostatic pressure). In this case, the pressure is related to the velocity potential according to

$$P = -\frac{\partial \phi}{\partial t}. \tag{5.49}$$

Upon substitution of the assumed solution for ϕ from equation 5.20, equations 5.48a and 5.48b can be stated in the form

$$u = \int_{-\infty}^{\infty} ike^{i(kx-\omega t)} \left[a \cosh k(y+\tau) + b \sinh k(y+\tau)\right] dk, \tag{5.50}$$

$$v = \int_{-\infty}^{\infty} ke^{i(kx-\omega t)} \left[a \sinh k(y+\tau) + b \cosh k(y+\tau)\right] dk. \tag{5.51}$$

Likewise, the assumed solution form of equation 5.20 can be applied to equation 5.49 to provide

$$P = -\int_{-\infty}^{\infty} e^{i(kx-\omega t)} \left[\cosh k\,(y+\tau)\left(\frac{\partial a}{\partial t} - i\omega a\right) + \sinh k\,(y+\tau)\left(\frac{\partial b}{\partial t} - i\omega b\right)\right] dk. \tag{5.52}$$

Equations 5.50 and 5.51 all required the calculation of the spectral coefficients $a(k,t)$ and $b(k,t)$. However, after calculation of the spectral coefficients $c(k,t)$ (and the time derivative $\frac{dc}{dt}$), these were calculated using equations 5.32 and 5.35. Since the numerical solution process for the wave amplitude, η, already involved the calculation of c and $\frac{dc}{dt}$ (both are calculated by the ODE solver), the extension of the solution to calculate the subsurface velocity field was straightforward.

The solution for the subsurface pressure field required the time derivatives of the coefficients $a(k,t)$ and $b(k,t)$, which in turn depended on the second derivative of the $c(k,t)$ coefficients. The second derivative, $\frac{d^2c}{dt^2}$ was not calculated during the solution of the ODE system (from equation 5.46). However, since the ODE solution process provided all of the variables required to calculate the subsurface velocity potential, $\phi(x,y,t)$, the subsurface pressure field could be calculated using a finite difference approximation for $\frac{\partial \phi}{\partial t}$ at each (x,y) location.

5.2.7 Landslide shape

Sue (2007) found that the wave field did not exhibit strong dependence on the landslide shape, provided that the landslide volume remained constant for all shapes tested. The shapes tested in this project were a quartic profile, defined as

$$f(\theta) = 1 - \left(\frac{2}{\alpha}\theta^4\right) \qquad -0.5\alpha < \theta < 0.5\alpha, \tag{5.53}$$

and a sawtooth profile, defined as

$$f(\theta) = 1 + \frac{2}{\alpha}\theta \qquad -0.5\alpha \leq \theta < 0, \tag{5.54a}$$

$$1 - \frac{2}{\alpha}\theta \qquad 0 \leq \theta \leq 0.5\alpha, \tag{5.54b}$$

where α is the nondimensional landslide length. This length is defined as

$$\alpha = \frac{L_b}{L}. \tag{5.55}$$

Depending on the length scale, α could take a value of unity (in the case where $L = L_b$), or a value of $\frac{L_b}{D}$ (in the case where $L = D$). The quartic profile most closely represented the semi-elliptical landslide profile used during the physical experiments.

Figure 5.2 shows the quartic and sawtooth landslide profiles used during the two-dimensional linear inviscid model simulations, with a maximum nondimensional landslide thickness of 1.0 for both shapes. A mathematical amplification factor (defined as A in equation 5.59) ensured that the nondimensional volume of the landslide block was equal to that of the elliptical landslide block used in experiments. This amplification factor, A, was equal to $\frac{5\pi}{16}$ for the quartic shape, and $\frac{\pi}{2}$ for the sawtooth shape.

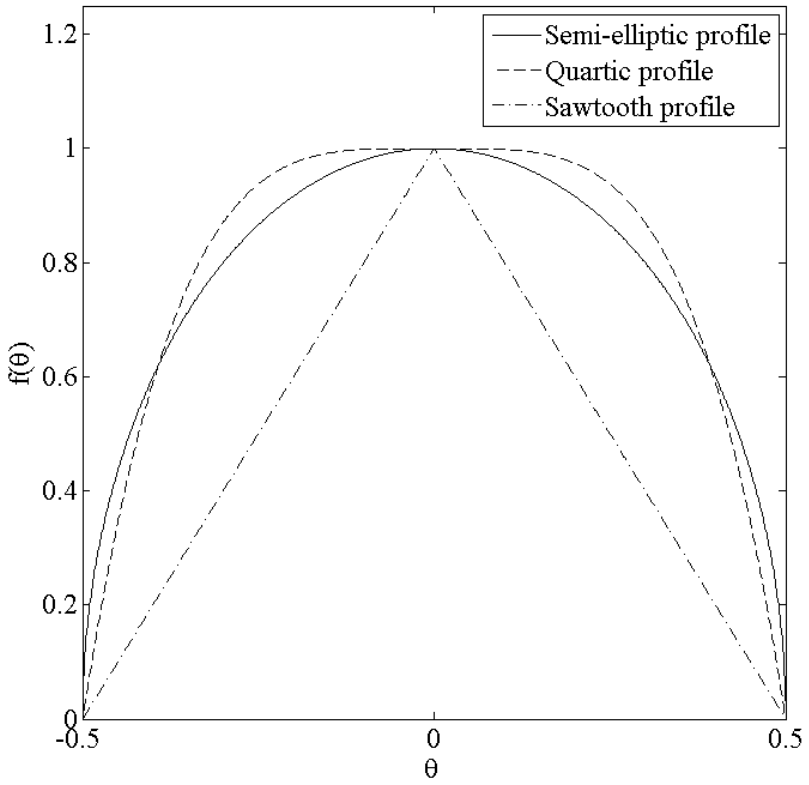

Figure 5.2: Quartic and sawtooth shapes used to approximate the elliptical landslide block within the 2D linear inviscid model.

In equation 5.53, θ is non-zero only between -0.5α and 0.5α. Assuming a quartic shape, the landslide slope is

$$\frac{\partial f}{\partial \theta} = -\frac{64}{\alpha^4}\theta^3, \tag{5.56}$$

while the equivalent expressions for a sawtooth shape are

$$\frac{\partial f}{\partial \theta} = \frac{2}{\alpha} \qquad -0.5\alpha \leq \theta < 0, \tag{5.57a}$$

$$\frac{2}{\alpha} \qquad 0 \leq \theta \leq 0.5\alpha. \tag{5.57b}$$

Using the Fourier decomposition of equation 5.24, the shape coefficients $p(k)$ for each landslide shape can be determined using

$$p(k) = \int_{-0.5}^{0.5} e^{-2\pi i\theta} \frac{\partial f}{\partial \theta} d\theta. \tag{5.58}$$

Solution of equation 5.58 yields the shape coefficients $p(k)$ for a quartic shape,

$$p(k) = -A\frac{32i}{\pi\alpha^4 k}\left[\left(\frac{\alpha^3}{4} - \frac{6\alpha}{k^2}\right)\cos\left(\frac{\alpha k}{2}\right) + \left(\frac{12}{k^3} - \frac{3\alpha^2}{2k}\right)\sin\left(\frac{\alpha k}{2}\right)\right], \tag{5.59}$$

where the equivalent shape factors for a sawtooth shape are

$$p(k) = A\frac{2i}{\pi\alpha k}\left[1 - \cos\left(\frac{\alpha k}{2}\right)\right]. \tag{5.60}$$

5.2.8 Landslide motion

To enable comparison of the linear inviscid model predictions with the experimental measurements, the landslide motion within the model simulations was identical to that provided during experiments by the mechanical system. This motion consisted of three different phases. The landslide accelerated at a constant rate up to its terminal velocity, moved at its terminal velocity for a short time and then decelerated to rest, at the same rate as the initial acceleration. Figure 5.3 shows the velocity profile of the landslide motion.

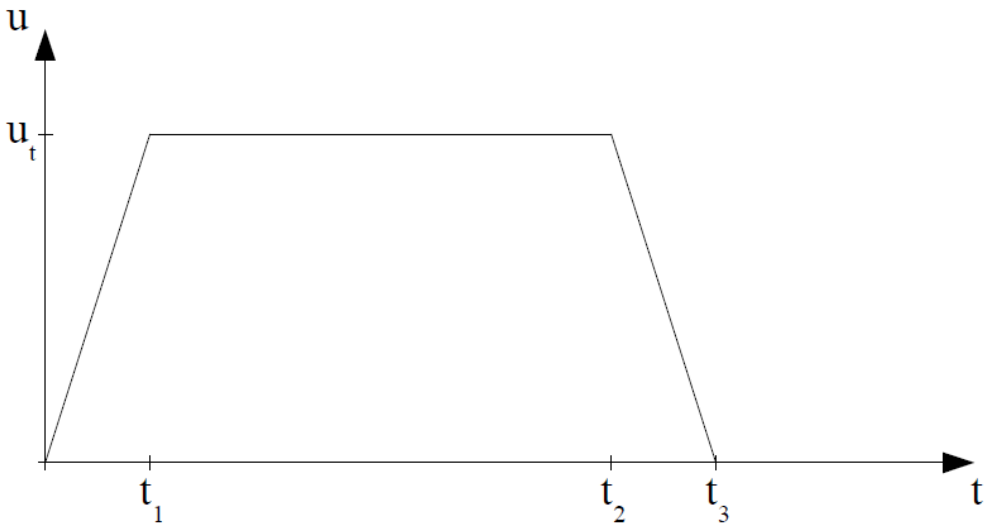

Figure 5.3: Typical landslide velocity profile used in model simulations.

From figure 5.3, if u_t, t_1, t_2 and t_3 are all dimensionless, then it follows that the non-dimensional landslide displacement, velocity and acceleration are defined respectively

as

$$x_0 = \frac{1}{2}\lambda t^2 \qquad 0 < t < t_1, \tag{5.61a}$$

$$= \frac{1}{2}\lambda t_1^2 + \lambda t_1(t - t_1) \qquad t_1 < t < t_2, \tag{5.61b}$$

$$= \frac{1}{2}\lambda t_1^2 + \lambda t_1(t_2 - t_1) + \frac{1}{2}\lambda t_1(t_1 - (t - t_2)) \qquad t_2 < t < t_3, \tag{5.61c}$$

$$= 0 \qquad t > t_3, \tag{5.61d}$$

$$\frac{dx_0}{dt} = \lambda t \qquad 0 < t < t_1, \tag{5.62a}$$

$$= \lambda t_1 \qquad t_1 < t < t_2, \tag{5.62b}$$

$$= \lambda(t_1 - (t - t_2)) \qquad t_2 < t < t_3, \tag{5.62c}$$

$$= 0 \qquad t > t_3, \tag{5.62d}$$

$$\frac{d^2x_0}{dt^2} = \lambda \qquad 0 < t < t_1, \tag{5.63a}$$

$$= 0 \qquad t_1 < t < t_2, \tag{5.63b}$$

$$= -\lambda \qquad t_2 < t < t_3, \tag{5.63c}$$

$$= 0 \qquad t > t_3. \tag{5.63d}$$

The landslide Froude number can be used to express the terminal velocity of the landslide, relative to the velocity of a shallow water wave propagating in a constant-depth channel. This nondimensional parameter is a useful predictor of the behaviour of the wave field, and is discussed more thoroughly in chapter 7. The landslide Froude number is defined as

$$Fr = \frac{dx_0}{dt}\frac{1}{\sqrt{gL}}, \tag{5.64}$$

where $\frac{dx_0}{dt}$ is the dimensional landslide velocity.

5.2.9 Wavenumber resolution of model

In theory, the spectral coefficients are integrated over an infinite wavenumber space, however in practice a suitable (finite) wavenumber range must be selected for the numerical solution for η, ϕ, u, v and p. This section describes the effect of the wavenumber range used by the model on the wave field, following the work of Sue (2007) (included in this chapter for completeness). The smallest non-zero wavenumber governed the largest wavelengths able to be resolved by the model, which was equal to the wavenumber spacing, dk, in these simulations. The largest magnitude wavenumber determined the smallest wavelengths able to be resolved. If an insufficient number of wavenumbers were included in the integration, the integrated surface and subsurface results would be incomplete.

An additional consideration regarding the wavenumber resolution of the model was the periodic nature of the assumed solutions. Because of this periodic solution form, the solutions repeated in the x domain, with a spacing between the solutions controlled by dk. If the value of dk was too small, then waves generated by the repeated solutions would propagate into the actual wave field for large spatial domains and long simulation times.

This section shows the effect of the wavenumber resolution on the calculated spectral coefficients and wave amplitudes for a simulation carried out with the parameters $\lambda = 0.102$, $Fr = 0.25$ and $\tau = 0.35$. Figure 5.4 shows the wave field generated using different wavenumber domains, and figure 5.5 provides the corresponding real spectral coefficients $c(k,t)$. The imaginary parts of the spectral coefficients showed similar agreement, so only the real parts are shown for clarity.

Figure 5.5 shows that most of the energy of the spectral coefficients was concentrated between $k = -10$ and $k = 10$, and the range of k values does not affect the calculation of the coefficients themselves. However, the wave field generated by the wavenumber range $k = -5 : 0.01 : 5$ (referring to the minimum value, the spacing, and the maximum value) was unable to resolve the smallest wavelength waves generated by the landslide motion, since this excluded the non-negligible contributions from wavenumbers between 5 and 10.

Figures 5.6 and 5.7 show the effect of the wavenumber resolutions on the wave field and the spectral coefficients, also by showing the solutions at $t = 6$. At this time, the wavelengths were not sufficiently large to show discrepancies caused by the different wavenumber resolutions in the wave field plot. However, figure 5.7 shows that the coarser resolutions were not able to capture the variation in the spectral coefficients well, even at this relatively early time in the simulation. As time passed in the simulation, the energy in the spectral coefficients tended to concentrate in the lower wavenumber values, and oscillated more over the wavenumber space. Therefore, the

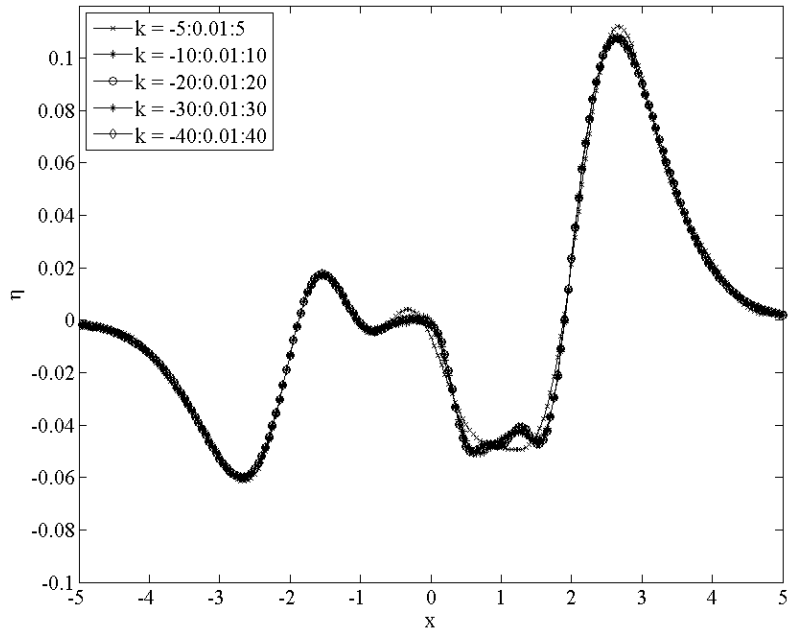

Figure 5.4: Wave field at $t = 6$, for different ranges of k values, at a fixed wavenumber resolution of $dk = 0.01$, where the legend entries are shown as $k_{min} : dk : k_{max}$.

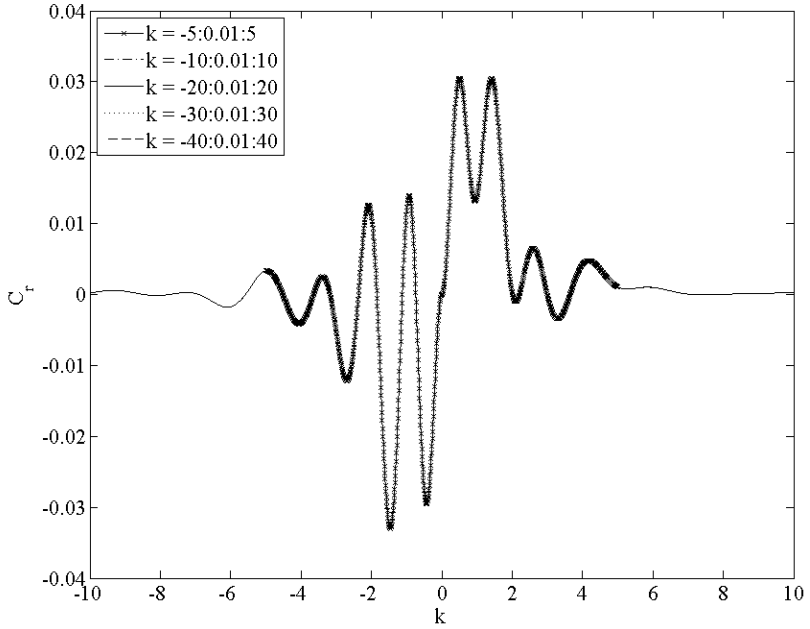

Figure 5.5: Real spectral coefficients at $t = 6$, for different ranges of k values, at a fixed wavenumber resolution of $dk = 0.01$.

effect of the wavenumber resolution would become more severe for longer simulations.

Figure 5.8 shows the variation in pressure in the x-direction along the bottom boundary ($y = -\tau$), calculated using different ranges of k (wavenumber). The interval

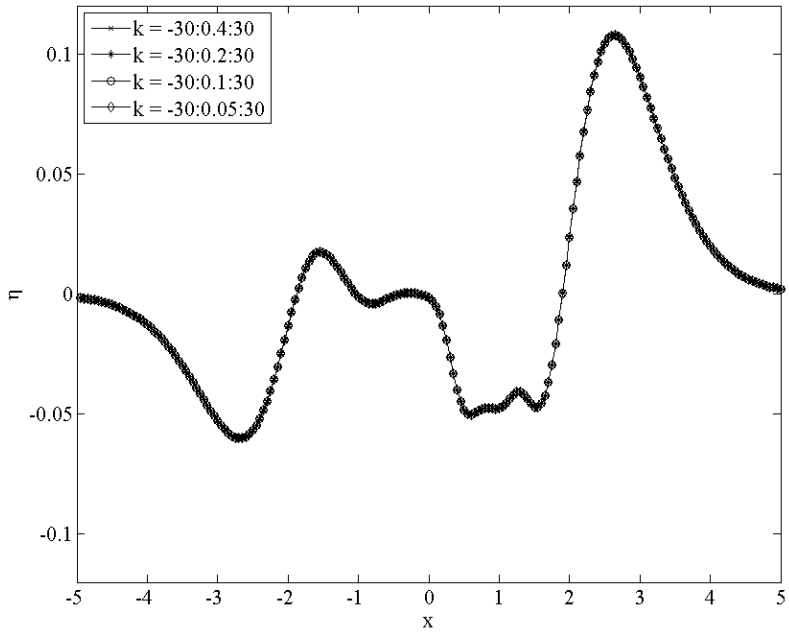

Figure 5.6: Wave field at $t = 6$, for different wavenumber resolutions, at a fixed wavenumber range of $|k_{max}| = 30$.

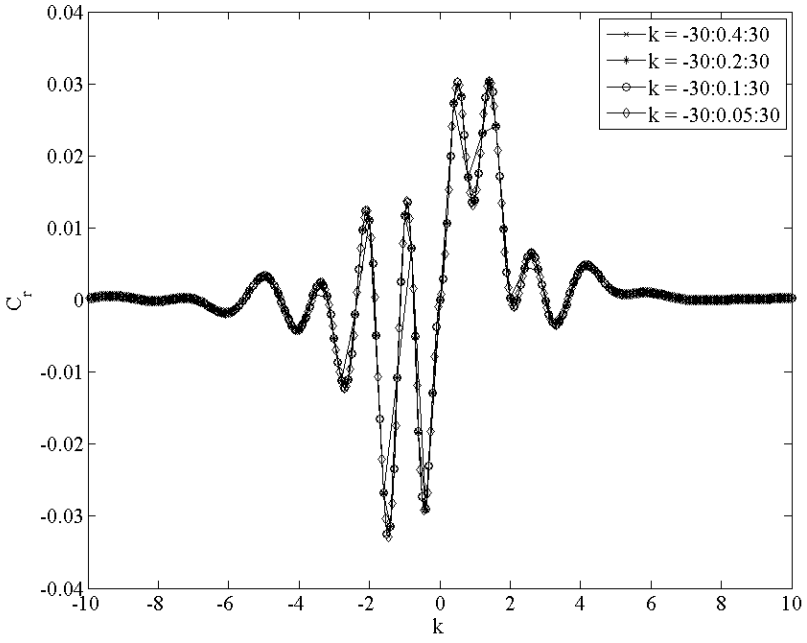

Figure 5.7: Real spectral coefficients at $t = 6$, for different ranges of k values, at a fixed wavenumber resolution of $dk = 0.01$.

between k values was kept constant during the simulations. Although the pressure variation is approximately the same for all k ranges, there was significant noise in the pressure signals calculated using $k = -10 : 0.05 : 10$ and $k = -20 : 0.05 : 20$.

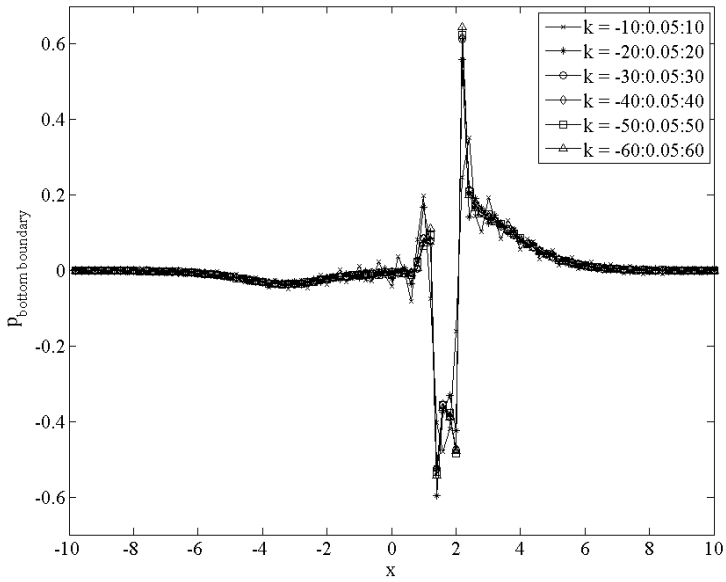

Figure 5.8: Noise in pressure along bottom boundary, for different ranges of k values.

Interestingly, the noise in the pressure signal at extreme x-values (not shown in figure 5.8) actually increased for the broadest range of k values ($k = -50 : 0.05 : 50$), compared to $k = -40 : 0.05 : 40$. This increase in noise with the larger k range was caused by the two conflicting sources of error in the integration routine for ϕ (these sources of error are also present for η, u and v, however ϕ is used directly to calculate of the pressure and so is the focus of this discussion). The first error source was the periodic nature of the integrand in equation 5.20. Although this function approached zero as $|k| \to \infty$, a limited wavenumber range would not capture a sufficient number of periods of the integrand within the limits of integration, and so an error would be introduced in the calculated value of ϕ, which varies with x and t. This error is evident in the wave field plot of figure 5.4.

The second source of error was a numerical error. Within equation 5.20, the hyperbolic sine and cosine terms would approach infinity as $|k| \to \infty$. Since the spectral coefficients a and b approached zero as $|k| \to \infty$, the entire integrand should have still approached zero. However, at large $|k|$ values, numerical rounding errors caused additional noise to be generated in the integrand due to the hyperbolic sine and cosine terms. Although this noise could be removed by eliminating the rounding errors at large $|k|$ values, figure 5.8 shows that the first source of error was negligible for a k range between -40 and 40. Because of this, a k range of -40 to 40 was used in all model simulations (for this depth).

5.2.10 Computational efficiency

The linear inviscid model domain was larger than the nondimensional length of the physical flume, so that the domain contained the entire wave field for as long as possible (since waves were not reflected from the lateral boundaries of the problem domain in the model). However, at early times within the simulation, the generated waves were only present in a limited region at the center of the domain. Because of this, it was computationally inefficient to calculate the wave amplitude, η, over the entire domain at these early times. These inefficiencies were even more pronounced considering the subsurface velocity potential, ϕ, and the horizontal and vertical components of the subsurface velocity, u and v, due to the additional vertical dimension.

To ensure that the model was computationally efficient, an algorithm limited the domain used by the integration routines to calculate η, ϕ, u and v. This algorithm searched for the first value in the positive and negative x directions satisfying $\eta < tol$ at some time t, where tol is a suitably small tolerance. The algorithm recorded these locations as the positive and negative limits of the integration domain at time t. Figure 5.9 illustrates the limiting values at an early time and late within the simulation. These limiting values could only move outwards within the spatial domain, avoiding issues with the zero-crossing points between waves or the zone of quiet between the onshore and offshore-propagating wave packets long after the cessation of landslide motion.

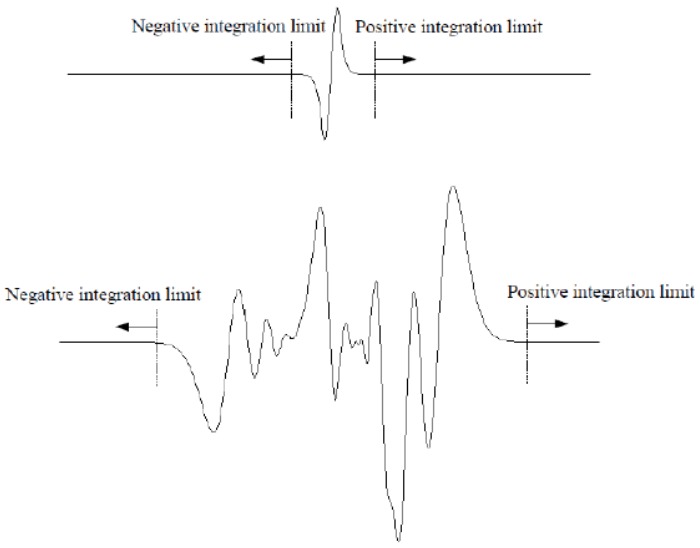

Figure 5.9: Limiting values on integration for η at early and late times within an example simulation

5.3 Three-dimensional linear inviscid model

5.3.1 Problem domain

As explained in section 5.1, the two-dimensional approximation represented the limiting case of a landslide with a very large width relative to its length. Therefore, propagation in the lateral direction was neglected, and waves propagated in one horizontal dimension only. This approximation tends to over-estimate the amplitudes of the generated waves. To assess the effect of an added lateral dimension, and the dependence of solutions on the landslide width, in this section the linear inviscid model described in section 5.2 was extended to three dimensions. Figure 5.10 shows cross-sections of the problem domain at $z = 0$ and $x = 0$ where both the landslide thickness and the amplitude of the generated waves have been exaggerated.

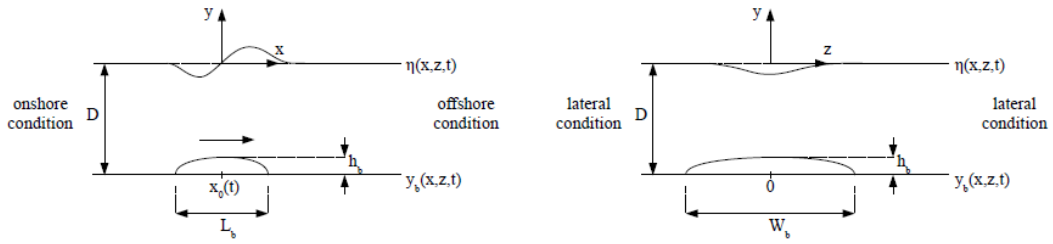

Figure 5.10: Model domain, showing sections at $z = 0$ and $x = 0$ respectively

All parameters in figure 5.10 are in dimensional form. D is the undisturbed water depth above the horizontal bottom boundary, L_b is the length of the landslide, h_b is the thickness of the landslide, W_b is the width of the landslide, and $\eta\,(x, z, t)$ is the free surface displacement. The origin of the Cartesian coordinate system was located on the undisturbed free surface, above the initial position of the landslide's centre of mass. The landslide moved in the positive x-direction only. Landslide motion followed the same three phases of constant acceleration, constant velocity and constant deceleration used for the 2D model. Details of the displacement, velocity and acceleration of the landslide for this trapezoidal velocity profile are discussed in section 5.2.8. Since wave propagation could now occur in two lateral directions, the wavenumber was represented as a vector $\mathbf{k}$, with components k_x and k_z associated with propagation in the x and z directions respectively.

The assumptions used in the formulation of this model were the same as those used for the 2D model (these are stated in section 5.2.2). The landslide was a solid block, now with shape profiles in the x and z directions. The landslide shape could be the same in both directions, as shown in figure 5.10, or different profiles could be used in the two directions. For example, the landslide could have a quartic profile in the x-direction and a square wave profile in the z-direction. The shape profiles, and

calculation of the resulting shape coefficients for the different shapes, are discussed in section 5.3.5

5.3.2 Equations

Governing equation

Upon invoking the inviscid/irrotational assumption, the governing equation was Laplace's equation. Laplace's equation, in 3D Cartesian coordinates, is

$$\frac{\partial^2 \phi}{\partial x^2} + \frac{\partial^2 \phi}{\partial y^2} + \frac{\partial^2 \phi}{\partial z^2} = 0. \tag{5.65}$$

Boundary and initial conditions

The problem had two free surface boundary conditions and one bottom boundary condition. The bottom boundary shown in figure 5.10 may be mathematically expressed as

$$y_b\left(x, y, z\right) = -D + h_b f\left(\theta, z\right). \tag{5.66}$$

The spatial domain was considered infinite in the x and z directions, so no boundary conditions were imposed on the edges of the simulation domain. Any waves reaching the edges of the domain would continue propagating out of the domain (without reflection). The boundary conditions on the free surface and the bottom boundary were the same as for the two-dimensional model. These include the kinematic condition on the bottom boundary (stated in equation 5.8), the kinematic condition on the free surface (stated in equation 5.9), and the dynamic condition on the free surface (stated in equation 5.10). The initial conditions for the three-dimensional problem are

$$\phi\left(x, y, z, 0\right) = 0, \tag{5.67}$$

$$\eta\left(x, z, 0\right) = 0. \tag{5.68}$$

5.3.3 Nondimensionalisation and scaling

It is convenient to express the 3D problem in a dimensionless framework, following the nondimensionalisations in the 2D model (see section 5.2.4). Thus the additional nondimensional variables are

$$z' = \frac{z}{L}, \tag{5.69a}$$

$$k'_x = k_x L, \tag{5.69b}$$

$$k'_z = k_z L, \tag{5.69c}$$

$$w' = \frac{w}{h_b}\sqrt{\frac{L}{g}}, \tag{5.69d}$$

where h_b is the length scale used for ϕ, η, u and v. An arbitrary length scale L was used for x, z, k_x, and k_z, following the reasoning used in the 2D model formulation. Ultimately L_b, W_b or D would be substituted for L.

The nondimensionalisation of the 3D model also provided the nondimensional parameters τ, λ and α (defined in section 5.2). An additional nondimensional parameter, σ, relates the landslide width to the general length scale, according to

$$\sigma = \frac{W_b}{L}. \tag{5.70}$$

This parameter could therefore take the value $\frac{W_b}{L_b}$ for $L = L_b$, $\frac{W_b}{D}$ for $L = D$, or unity for $L = W_b$. As with the 2D model, valid arguments could be made for either length scale, since the wavelengths of the generated waves in the x direction depended on both L_b and D, while the wavelengths of the generated waves in the z direction depended on both W_b and D. For consistency with the 2D model, and with the physical experiments (see chapter 6), L_b was used as the general length scale.

The governing equation (Laplace's equation) was unchanged from equation 5.65 in nondimensional form. The nondimensional form of the boundary conditions was the same as for the 2D model. Equation 5.18 states the nondimensional kinematic condition on the bottom boundary, the free surface kinematic condition (see equation 5.9) was unchanged in nondimensional form, and equation 5.19 states the nondimensional dynamic boundary condition. The nondimensional form of the bottom boundary, $y_b(x, z, t)$, is

$$y'_b = -\frac{D}{h_b} + f\left(\theta\left(t\right), z\right). \tag{5.71}$$

Primes will be dropped for the remainder of this section for convenience. The nondimensional time derivative of the bottom boundary (required for the kinematic condition on the bottom boundary) is

$$\frac{\partial y_b}{\partial t} = -\frac{\partial f}{\partial \theta}\frac{dx_0}{dt}, \tag{5.72}$$

where $f(\theta(t), z)$ was only non-zero within the limits $-\frac{\alpha}{2} \leq \theta \leq \frac{\alpha}{2}$ in the x-direction, and $-\frac{\sigma}{2} \leq z \leq \frac{\sigma}{2}$ in the z-direction.

It was assumed that the landslide slope can be represented by the Fourier decomposition

$$\frac{\partial f}{\partial \theta} = \int_{-\infty}^{\infty}\int_{-\infty}^{\infty} e^{i(k_x\theta + k_z z)} p(k_x)\, q(k_z)\, dk_x dk_z, \tag{5.73}$$

where $p(k_x)$ and $q(k_z)$ are the (complex) shape functions associated with the x- and z-directions respectively. It was assumed that the integral in equation 5.73 could be separated into its k_x and k_z components. The calculation of these shape functions in their separated form is described in section 5.3.5.

The nondimensional dispersion relation for free wave modes propagating in two horizontal dimensions is

$$D(\omega, k_x, k_z) = -\omega^2 + \sqrt{k_x^2 + k_z^2}\tanh\left(\tau\sqrt{k_x^2 + k_z^2}\right) = 0. \tag{5.74}$$

5.3.4 Solution method

Assumed solution form

The 3D form of the assumed solution for the velocity potential is

$$\phi(x, y, z, t) = \int_{-\infty}^{\infty}\int_{-\infty}^{\infty} e^{i\varphi} a(k_x, k_z, t)\cosh\left((y+\tau)\sqrt{k_x^2 + k_z^2}\right) + e^{i\varphi} b(k_x, k_z, t)\sinh\left((y+\tau)\sqrt{k_x^2 + k_z^2}\right) dk_x dk_z, \tag{5.75}$$

where $\varphi = k_x x + k_z z - \omega t$. The 3D form of the assumed solution for the wave amplitude is

$$\eta(x, z, t) = \int_{-\infty}^{\infty}\int_{-\infty}^{\infty} c(k_x, k_z, t)\, e^{i\varphi} dk_x dk_z. \tag{5.76}$$

Equations 5.75 and 5.76 extended the assumed solution in the 2D model to include propagation in the z-direction, shown by the inclusion of $k_z z$ in the exponential term, and the replacement of k with $\sqrt{k_x^2 + k_z^2}$ in the cosh and sinh terms. This reflects the

fact that the wavenumber was a vector within the three-dimensional model, with both x and z components.

Only the real part of these solutions were sought and $a(k_x, k_z, t)$, $b(k_x, k_z, t)$, and $c(k_x, k_z, t)$ are all complex spectral coefficients. These will be referred to as a, b, and c in the remainder of this section for clarity. The assumed solutions fully satisfy Laplace's equation.

Application of boundary conditions

Upon inclusion of the landslide shape function, the unsteady bottom boundary due to the landslide forcing is expressed as

$$\frac{\partial y_b}{\partial t} = \int_{-\infty}^{\infty}\int_{-\infty}^{\infty} e^{i(k_x\theta + k_z z)} F\left(k_x, k_z, t\right) dk_x dk_z, \tag{5.77}$$

where $F\left(k_x, k_z, t\right) = -\frac{dx_0}{dt} p\left(k_x\right) q\left(k_z\right)$ is the forcing function due to landslide motion in wavenumber space. Upon substitution into the kinematic bottom boundary condition,

$$\begin{aligned}
&\int_{-\infty}^{\infty}\int_{-\infty}^{\infty} e^{i\varphi}\sqrt{k_x^2+k_z^2}\; a\left(k_x, k_z, t\right)\sinh\left(\left(y+\tau\right)\sqrt{k_x^2+k_z^2}\right) \\
&\qquad + e^{i\varphi}\sqrt{k_x^2+k_z^2}\; b\left(k_x, k_z, t\right)\cosh\left(\left(y+\tau\right)\sqrt{k_x^2+k_z^2}\right) dk_x dk_z \\
&\qquad\qquad = \int_{-\infty}^{\infty}\int_{-\infty}^{\infty} e^{i(k_x\theta + k_z z)} F\left(k_x, k_z, t\right) dk_x dk_z \text{ on } y = -\tau.
\end{aligned} \tag{5.78}$$

Defining $k = \sqrt{k_x^2 + k_z^2}$ as the magnitude of the wavenumber vector, equation 5.78 is simplified to the form

$$\int_{-\infty}^{\infty}\int_{-\infty}^{\infty} k e^{i\varphi} b dk_x dk_z = \int_{-\infty}^{\infty}\int_{-\infty}^{\infty} F\left(k_x, k_z, t\right) e^{i(k_x\theta + k_z z)} dk_x dk_z. \tag{5.79}$$

Under the assumption that the Fourier modes are linearly independent, equation 5.79 may be solved for b at each wavenumber. Equation 5.80 provides the resulting expression for the spectral coefficient b, where $\epsilon = \omega t - k_x x_0$.

$$b = \frac{F\left(k_x, k_z, t\right)}{k} e^{i\epsilon}. \tag{5.80}$$

Following the working used to formulate the two-dimensional model, the result of

equation 5.80 allows calculation of the spectral coefficient a. The assumed solutions were substituted into the kinematic free surface condition,

$$\int_{-\infty}^{\infty}\int_{-\infty}^{\infty} e^{i\varphi}\left[\frac{\partial c}{\partial t} - i\omega c\right] dk_x dk_z =$$

$$\int_{-\infty}^{\infty}\int_{-\infty}^{\infty} e^{i\varphi}\left[ka\sinh(k\tau) + F(k_x, k_z, t)\, e^{i\epsilon}\cosh(k\tau)\right] dk_x dk_z. \quad (5.81)$$

$$\therefore a = \frac{1}{k\sinh(k\tau)}\left[\frac{\partial c}{\partial t} - i\omega c - F(k_x, k_z, t)\, e^{i\epsilon}\cosh(k\tau)\right]. \quad (5.82)$$

Upon substitution of the assumed solution, and the expressions for a and b, the dynamic free surface condition may be written as

$$\int_{-\infty}^{\infty}\int_{-\infty}^{\infty} -i\omega e^{i\varphi}\left[a\cosh(k\tau) + \frac{F}{k}e^{i\epsilon}\sinh(k\tau)\right]$$

$$+ e^{i\varphi}\left[\frac{\partial a}{\partial t}\cosh(k\tau) + \frac{\sinh(k\tau)}{k}e^{i\epsilon}\left(\frac{\partial F}{\partial t} + iF\frac{\partial \epsilon}{\partial t}\right)\right] dk_x dk_z$$

$$+ \int_{-\infty}^{\infty}\int_{-\infty}^{\infty} c e^{i\varphi} dk_x dk_z = 0. \quad (5.83)$$

Following the same solution procedure as the 2D model (including application of the nondimensional dispersion relation), the spectral coefficients c were calculated using the ordinary differential equation

$$\frac{d^2 c}{dt^2} - 2i\omega\frac{dc}{dt} = G(k_x, k_z, t), \quad (5.84)$$

where $G(k_x, k_z, t)$ is the forcing function for the wavefield given by:

$$G\left(k_x, k_z, t\right) = \frac{e^{i\epsilon}}{\cosh\left(k\tau\right)}\left(\frac{\partial F}{\partial t} - ik_x F\frac{dx_0}{dt}\right)$$

$$= \frac{e^{i(\omega t - k_x x_0)}}{\cosh\left(k\tau\right)} p\left(k_x\right) q\left(k_z\right)\left[-\frac{d^2 x_0}{dt^2} + ik_x\left(\frac{dx_0}{dt}\right)^2\right]. \quad (5.85)$$

Again, the free surface was obtained by numerically integrating these spectral coefficients over the wavenumber domain. Thus,

$$\eta\left(x, z, t\right) = \int_{-\infty}^{\infty}\int_{-\infty}^{\infty} c_r\left(k_x, k_z, t\right)\cos\left(k_x x + k_z z - \omega t\right)$$

$$- c_i\left(k_x, k_z, t\right)\sin\left(k_x x + k_z z - \omega t\right)dk_x dk_z. \quad (5.86)$$

5.3.5 Landslide shape coefficients in two lateral dimensions

The landslide shape in the three-dimensional model was given by the function $f(\theta, z)$ (this modified the bottom boundary in equation 5.66), which may be separated into separate functions in the x and z directions, $f_1(x)$ and $f_2(z)$,

$$f(\theta, z) = f_1(x) + f_2(z). \quad (5.87)$$

As in the two-dimensional model, this shape was expressed as a Fourier integral of shape functions. Thus, these functions were associated with shape coefficients $p(k_x)$ and $q(k_z)$, respectively. This Fourier integral (equation 5.73) may be separated into its x and z components,

$$\frac{\partial f}{\partial \theta} = \int_{-\infty}^{\infty} e^{ik_x\theta} p\left(k_x\right) dk_x \int_{-\infty}^{\infty} e^{ik_z z} q\left(k_z\right) dk_z. \quad (5.88)$$

This allowed the different shape coefficients associated with the landslide profiles in the x and z directions to be solved separately, and the shape functions $p(k_x)$ and $q(k_z)$ to be combined at a given point in wavenumber space. The solution for the different shape coeffients followed the working shown in section 5.2.7. The shapes used in the x-direction were identical to those used in the two-dimensional model, and are not repeated here. In the z-direction, the two shapes used were a quartic profile (which closely resembled the semi-elliptical geometry used in the physical experiments) and a square wave profile. These are shown in figure 5.11, for a nondimensional landslide width of 1.0.

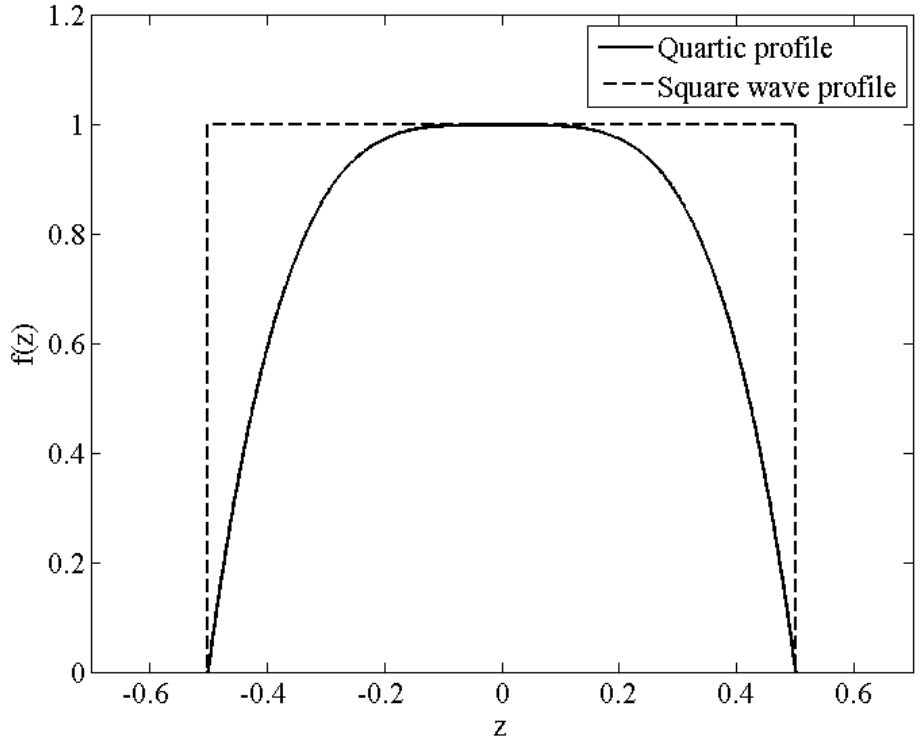

Figure 5.11: Shape functions used in z-direction, assuming the landslide width σ is equal to 1.0.

Since the landslide motion was in the x-direction only, the shape coefficients associated with the z-direction, $q\left(k_z\right)$, depended on $f_2(z)$, rather than its derivative. The equation for the quartic shape is

$$f(z) = 1 - (2z)^4 \qquad -0.5\sigma \leq z \leq 0.5\sigma, \tag{5.89}$$

where σ is the nondimensional landslide width. The square landslide block is defined as

$$f(z) = 1 \qquad -0.5\sigma \leq z \leq 0.5\sigma. \tag{5.90}$$

The resulting shape coefficients, $q\left(k_z\right)$, associated with the quartic and square wave profiles respectively, are

$$q\left(k_z\right) = -\frac{32i}{\pi\sigma^4 k_z}\left[\left(\frac{\sigma^3}{4} - \frac{6\sigma}{k_z^2}\right)\cos\left(\frac{\sigma k_z}{2}\right)\left(\frac{12}{k_z^3} - \frac{3\sigma^2}{2k_z}\right)\sin\left(\frac{\sigma k_z}{2}\right)\right], \tag{5.91}$$

and

$$q\left(k_z\right) = \frac{1}{\pi k_z}\sin\left(\frac{\sigma k_z}{2}\right). \tag{5.92}$$

Since the experimental landslide is only two-dimensional, the amplification factors, A, applied to the shape coefficients (explained in section 5.2.7) did not need to provide the same volume as a semi-ellipse. However, if different shapes were used during simulations then these factors would be required to ensure that the landslide volume is consistent between the simulations.

5.4 Two-dimensional nonlinear inviscid model

As explained in section 5.2.2, one of the simplifying assumptions made in the formulation of the linear inviscid model is that the thickness of the landslide is negligible compared to both the water depth and the landslide length. This allows the linearisation of the bottom boundary condition, such that all nonlinear terms are neglected and the condition is applied on the undisturbed bottom boundary. However, as discussed in section 5.2, this assumption is likely to compromise the model's ability to model the actual flow generated by the landslide motion on the bottom boundary. The landslide thickness will also affect the generation and propagation of the waves generated by the landslide motion.

The effect of the linearised bottom boundary condition on the solutions can be assessed in part by comparing the predictions of the two-dimensional linear inviscid model with the free surface measurements obtained during the physical experiments of this project. However, this effect will be difficult to isolate during this comparison, since this model also uses the inviscid-irrotational assumption for the fluid flow, as well as linear conditions on the free surface. The physical experiments may be considered as a perfect Navier-Stokes solver, and therefore none of the simplifying assumptions apply. To assess the effect of the linear assumption on the bottom boundary on the model predictions, the two-dimensional nonlinear inviscid model of Sue (2007) and Sue *et al.* (2011) was adapted to the case of a landslide moving along a horizontal bottom boundary beneath a constant-depth fluid.

Figure 5.12 shows the simulation domain for the 2D nonlinear inviscid model, where the offshore and onshore conditions are now reflective boundaries, such that any waves reaching these boundaries will be reflected into the generated wave field. Thus the simulation domain needs to be large enough to contain all of the generated waves for the duration of the simulation. It should be noted that Sue's formulation defined the landslide length as $2L$. For consistency with the other models of this project, the landslide length is defined as L_b within this formulation of the model.

The model was formulated using inviscid-irrotational flow theory, and solved Laplace's equation for the velocity potential, ϕ, on the boundary of the domain only, using a boundary element method (BEM) formulation. This solution method is useful in wave propagation problems, since the wave amplitudes occurring on the free surface

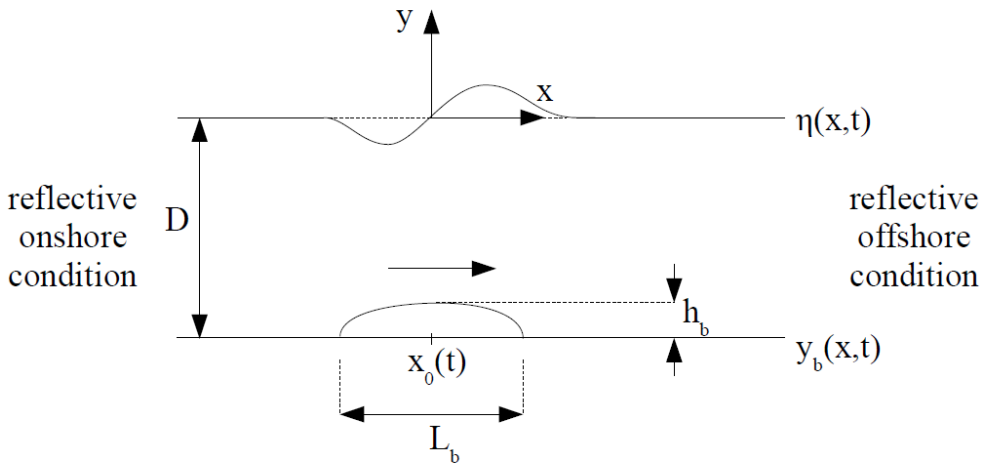

Figure 5.12: Simulation domain used for the 2D nonlinear inviscid model.

(the upper boundary of the simulation domain) are of the most immediate interest. The initial conditions and the boundary conditions on the free surface, are the same as for the linear inviscid model (see section 5.2.3). The bottom boundary condition in this model is

$$\frac{\partial \phi}{\partial y} = -h_b \frac{\partial f}{\partial \theta} \frac{dx_0}{dt} + h_b \frac{\partial f}{\partial \theta} \frac{\partial \phi}{\partial x}. \tag{5.93}$$

The landslide motion in the nonlinear inviscid model followed the trapezoidal profile of the linear inviscid model. Therefore the landslide initially accelerated at a constant rate, then moved at a constant velocity, then decelerated to rest at the same rate as its initial acceleration. The landslide was assumed to have a quartic shape (details in section 5.2.7).

For further details on the solution process, and the application of this model to a sloping boundary, refer to Sue *et al.* (2011).

5.5 Two-dimensional viscous model

5.5.1 Introduction

As a check on the applicability of the inviscid-irrotaional assumption to the prediction of the experimental wave amplitudes, the 2D problem was formulated in the direct numerical simulation (DNS) solver Gerris. Gerris is an open-source program which solves the time-dependent Navier-Stokes equations for an incompressible fluid. A detailed explanation of the mathematical formulation of the solver, along with convergence tests, are given in Popinet (2003).

Gerris employs a multi-level Poisson solver, allowing second-order convergence in

space and time. A key feature of the program is that the domain is discretised into quadtrees, and the mesh is able to be dynamically refined at every step of a simulation with small overhead. The refinement allows complex geometries to be handled effectively, and the mesh can be refined to track certain flow features, such as vorticity. This adaptive refinement means that Gerris is able to solve complex flow problems in a computationally efficient manner. A volume of fluid approach tracks the interface between different fluids.

5.5.2 Problem domain

Figure 5.13 shows the two-dimensional problem domain used in the formulation of the viscous model. The discretisation of the simulation domain within Gerris is discussed in section 5.5.4.

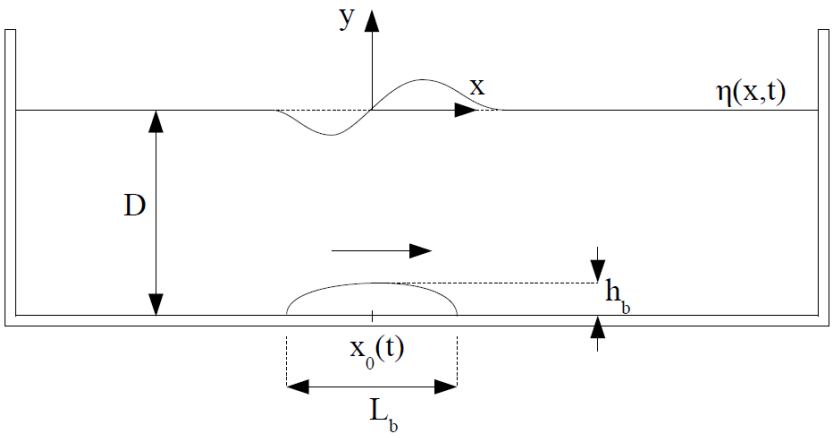

Figure 5.13: Simulation domain used in the viscous model. The lateral boundaries of the domain approximate the end conditions in the experimental flume.

5.5.3 Nondimensionalisation

Gerris solves the Navier-Stokes equations in nondimensional form within the domain described in section 5.5.2. In the inviscid-irrotational models, different variables were nondimensionalised using different length scales. This allowed the spatial variables (x and y within the 2D model) to be nondimensionalised by the general length scale, L, while nondimensionalising the wave amplitude, η, by the landslide thickness, h_b. However, Gerris nondimensionalises all length scales by the length of one box within the simulation domain, set equal to the landslide length, L_b. Therefore, the nondimensionalisation applied to the variables in the viscous model is different to that used in the spectral model formulation.

Table 5.1 lists the physical variables and parameters within the viscous model, classified as either geometric variables, landslide motion variables, fluid properties, physical constants or outputs.

Table 5.1: Variables and parameters within viscous model formulation

Quantity	**Description**	**Units**
Geometric variables and parameters		
x	Horizontal coordinate direction	L
y	Vertical coordinate direction	L
D	Depth of the fluid	L
L_b	Length of landslide block	L
h_b	Thickness of landslide block	L
Landslide motion variables		
a_0	Initial (constant) landslide acceleration	L/T^2
u_t	Landslide terminal velocity	L/T
x_0	Landslide position	L
t	Time since start of motion	T
Fluid properties		
ν_w	Viscosity of water	L^2/T
ν_a	Viscosity of air	L^2/T
ρ_w	Density of water	M/L^3
ρ_a	Density of air	M/L^3
ST	Surface tension of interface	M/T^2
Physical constants		
g	Gravitational acceleration	L/T^2
Outputs		
η	Wave amplitude	L
u	Subsurface horizontal velocity	L/T
v	Subsurface vertical velocity	L/T
P	Fluid pressure field	M/LT^2

The variables listed in table 5.1 are all in dimensional form. The landslide length, L_b, nondimensionalised all length scales within the model, and so this was used as the length of each simulation box. The gravitational acceleration, g, nondimensionalised all time scales (in conjunction with the landslide length). The density of water, ρ_w, nondimensionalised all mass terms. Equations 5.94 to 5.107 state the nondimensional form of all the variables of interest.

$$x' = \frac{x}{L_b}, \tag{5.94}$$

$$y' = \frac{y}{L_b}, \tag{5.95}$$

$$a_0' = \frac{a_0}{g}, \tag{5.96}$$

$$u_t' = \frac{u_t}{\sqrt{gL_b}}, \tag{5.97}$$

$$x_0' = \frac{x_0}{L_b}, \tag{5.98}$$

$$t' = t\sqrt{\frac{g}{L_b}}, \tag{5.99}$$

$$\nu_w' = \frac{\nu_w}{\sqrt{L_b^3 g}}, \tag{5.100}$$

$$\nu_a' = \frac{\nu_a}{\sqrt{L_b^3 g}}, \tag{5.101}$$

$$\rho_a' = \frac{\rho_a}{\rho_w}, \tag{5.102}$$

$$ST' = \frac{ST}{\rho_w g L_b^2}, \tag{5.103}$$

$$\eta' = \frac{\eta}{L_b}, \tag{5.104}$$

$$u' = \frac{u}{\sqrt{gL_b}}, \tag{5.105}$$

$$v' = \frac{v}{\sqrt{gL_b}}, \tag{5.106}$$

$$P' = \frac{PL_b^2}{\rho_w g}, \tag{5.107}$$

$$c_p' = \frac{c_p}{\sqrt{gL_b}}. \tag{5.108}$$

5.5.4 Formulation of viscous problem within Gerris

Simulation domain discretisation

Within Gerris, a simulation is carried out within a square domain of unit width and height, in nondimensional units. The use of a square domain in the current formulation would be acceptable, however the results would only be required in a small area of this domain. Therefore, a rectangular domain was selected.

Two options existed to change the domain from a square to a rectangle. The first option was to scale the x and y coordinates, so that the domain would become a rectangle of similar size to the experimental flume. However, the problem with this approach is that all dimensions in the model would be scaled accordingly. Since the generated waves vary rapidly in the x-direction, elongating this coordinate may compromise the model's horizontal resolution. The second option was to compose the simulation domain of multiple boxes, until the entire length of the flume could be simulated effectively. The conditions between internal boxes would need to ensure that the landslide, and the generated waves, could move between boxes without any distortions. This approach was selected since it ensured that the x and y scales within the model were consistent. Figure 5.14 illustrates these two options, for the simple example where the length of the simulation domain is three times greater than its height. In the physical experiments, the flume was approximately 15 m long, and the maximum submergence depth tested was 350 mm, so the *length* : *height* ratio would be significantly greater than the situation illustrated in figure 5.14. These methods could also be combined if required, using a series of rectangular boxes.

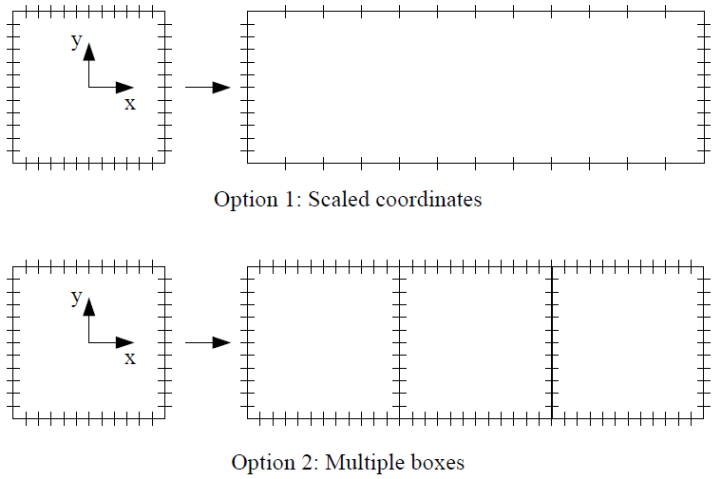

Figure 5.14: Possible changes to simulation boxes within Gerris, shown for the example of a domain with a *length* : *height* ratio of 3.

As discussed in section 5.5.3, the length scale selected for nondimensionalisation of

the viscous model was the length of the landslide block, $L_b = 500$ mm. This means that the fluid occupied approximately 70% of the domain height, allowing all free surface perturbations to be contained within the simulation domain. Free inflow/outflow conditions on the top boundary of the box ensured that air could move freely above the water surface, and effectively provided an infinite column of air in the vertical direction.

Unlike the linear inviscid model, which contained infinite boundaries in the horizontal direction, the viscous model used solid (reflective) boundaries in the lateral direction. These boundaries were set up in the same manner as the bottom boundary, as impermeable surfaces with the no-slip condition.

A total of 25 boxes were used to simulate the flume length. This is slightly less than the total experimental flume length, however the numerical flume length is consistent with the length of the experimental flume over which measurements of free surface elevation were recorded. Thus, reflections would occur slightly earlier in the viscous model than in the experiments, since the experiments would contain a slight time delay between waves leaving the domain and being reflected back into the generated wave field. However, the reflection of waves and the propagation of waves out of the domain both effectively end an experiment or simulation, so the use of the reflective boundaries in the viscous model is justified. Gerris allows simulation boxes to be linked together in a model. Linking together the 25 boxes (on the internal edges only) ensured that the landslide and fluid could move between the boxes during the simulations without any distortions or changes.

Volume of fluid tracer

The two fluids in the simulation (air and water) were tracked using a volume of fluid (VOF) tracer, which had a value of 1 for water and 0 for air. The free surface location was initially defined within the simulation file as the initial fraction of this VOF tracer within the domain. Use of this tracer allowed the properties of the two fluids, resulting from the nondimensionalisation process completed above, to be defined mathematically in the simulation input file.

The VOF tracer also enabled tracking of the free surface location during the simulations, by assigning a special variable to track the y-position of the surface defined by the VOF tracer. The use of adaptive refinement within Gerris (discussed below) also allowed the free surface to be well refined without greatly increasing the computational cost of the model.

Moving landslide

Although simple shapes can be defined within the Gerris input file itself, most solid objects used in Gerris files needed to be input in the form of an externally-generated shape file, called a 'gts' file. The landslide followed the quartic shape used in the spectral model and BEM model simulations. The shape was generated in three dimensions, such that a two-dimensional section of the shape was located within the simulation domain.

The motion of the landslide followed the trapezoidal profile adopted during the physical experiments and inviscid-irrotational models. This consisted of an initial period of constant acceleration, followed by a period of constant velocity, followed by a final deceleration to rest (at the same rate as the initial acceleration).

Adaptive refinement

One advantage of Gerris as a flow solver is its feature of adaptive grid refinement. This means that the grid could be adapted to be refined around certain flow features during a simulation, while remaining coarse in areas of less interest. In these simuations, the maximum level of refinement used was 9, while the minimum level of refinement used was 4. The maximum refinement was used on the free surface and on the surface of the landslide block. This ensured that the wave forcing, and the waves themselves, were always well resolved by the model. The grid refinement throughout the rest of the model domain followed the vorticity of the fluid flow. This ensured that any turbulent flow structures, as well as the rotational flow beneath the free surface waves, were well resolved by the model.

Several simulations using different maximum refinement levels allowed assessment of the effect of the maximum grid resolution on the viscous model predictions. Chapter 8 provides discussion on the effects of the grid resolution on the solutions for the free surface amplitude and subsurface velocity field.

Data output

Gerris provides the capability to output solution variables at given spatial and temporal locations during a simulation. Therefore, data on the free surface and the subsurface flow properties were recorded at timesteps of $dt = 0.1$ (in nondimensional terms). Data was output onto a rectangular grid, which covered the entire flow domain. The grid resolution was more refined in the y-direction than in the x-direction, to limit the size of the output data, and because of the relatively small amplitudes of the generated waves (compared to their wavelengths). The grid spacing was 0.05 in the x-direction, and 0.01 in the y-direction.

One of the output variables used by Gerris was the location of the VOF interface, as defined by a tracer variable. As long as this interface was located within one of the vertical cells at each horizontal location, the location of the interface would be captured by this output grid. The free surface elevation could also be checked by using the grid as a series of virtual wave gauges. The tracer value could be integrated over the vertical extent of the grid at each horizontal location to calculate the value of the free surface elevation. These values were found to be identical during initial simulations, and the VOF interface value output by Gerris was used during subsequent simulations.

Although still finely resolved during physical experiments, the subsurface velocity measurements were not the primary focus of this project. Therefore, the output grid used for the subsurface velocity and pressure values was less refined than the grid used to obtain the free surface elevations.

5.6 Summary

Several numerical models were formulated to predict the waves generated during the physical experiments of this project. The horizontal bottom boundary and mechanical landslide forcing used in the physical experiments allowed simplification of both the model domain geometry and the landslide motion. Details of the model domain, assumptions, and numerical solution procedure were stated for each model.

The linear inviscid model used to carry out the parametric study followed the formulation of Sue (2007), and was formulated using inviscid-irrotational flow theory. Linearisation of the boundary conditions allowed the solution to be expressed as a spectral decomposition of wave modes, and solved semi-analytically. This model was formulated in both two and three dimensions.

A nonlinear inviscid model, solved using the boundary element method (BEM) was formulated to assess the effects of the linearisation of the bottom boundary condition (see Sue *et al.* (2011)) . This model also used inviscid-irrotational flow theory. A viscous model simulation within the direct numerical simulation (DNS) solver Gerris (Popinet, 2003) was formulated to assess the effect of fluid viscosity on the solution, including the formation and separation of boundary layers on the moving landslide.

Chapter 6

Results - parameter space and nondimensionalisation

6.1 Nondimensionalisation

To facilitate effective comparison of the mathematical predictions with the measurements, it is convenient to present the numerical predictions and experimental measurements within a common nondimensional framework. This chapter details the nondimensionalisation of the problem variables, and the parameter space investigated during the experiments.

To enable direct comparison between the experimental results and the predictions of the spectral model, the experimental results are nondimensionalised in the same manner as the variables within the spectral model formulation. Figure 6.1 illustrates the domain of the physical experiments. Table 6.1 lists the variables of interest for this problem, some of which are shown in figure 6.1.

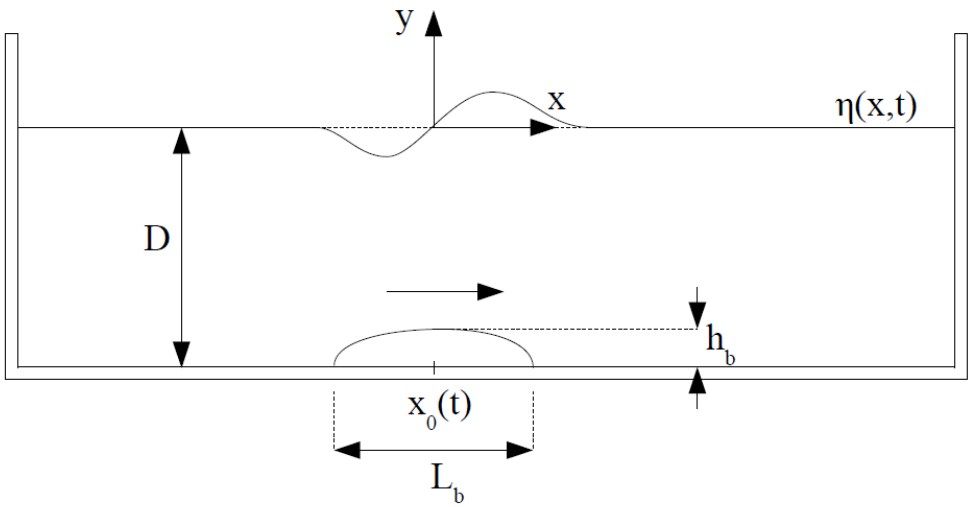

Figure 6.1: Diagram of experimental problem domain, including variables of interest.

Table 6.1: Variables of interest in experiments.

Variable	**Description**	**Units**
x	Horizontal coordinate direction	mm
y	Vertical coordinate direction	mm
t	Time since experiment start	s
η	Wave amplitude	mm
λ	Wavelength	mm
ω	Angular frequency of waves	1/s
u	Subsurface fluid velocity in x-direction	mm/s
v	Subsurface fluid velocity in y-direction	mm/s
x_0	Landslide displacement	mm
$\frac{dx_0}{dt}$	Landslide velocity	mm/s
$\frac{d^2x_0}{dt^2}$	Landslide acceleration	mm/s^2

Table 6.2 lists the scaling quantities used to nondimensionalise the variables in the physical experiments, and their values within this experimental setup. The general length scale was the length of the landslide block, L_b, although perturbations to the system (the waves and subsurface velocities generated by the landslide motion) were nondimensionalised by the thickness of the landslide block, h_b. The gravitational acceleration, g, and the length scale, L_b, were used to nondimensionalise time scales. Equations 6.1 to 6.11 provide the list of nondimensional experimental variables. These nondimensionalisations are similar to those used in the formulation of the spectral model (see chapter 5), and are presented here for convenience.

Table 6.2: Scales used to nondimensionalise experimental results.

Scaling quantity	**Description**	**Value**
L_b	Length of landslide block	500 mm
g	Gravitational acceleration	$9.81 m/s^2$
h_b	Landslide thickness	26 mm

$$x' = \frac{x}{L_b} \tag{6.1}$$

$$y' = \frac{y}{L_b} \tag{6.2}$$

$$t' = t\sqrt{\frac{g}{L_b}} \tag{6.3}$$

$$\eta' = \frac{\eta}{h_b} \tag{6.4}$$

$$\lambda' = \frac{\lambda}{L_b} \tag{6.5}$$

$$\omega' = \omega\sqrt{\frac{L_b}{g}} \tag{6.6}$$

$$u' = \frac{u}{h_b}\sqrt{\frac{L_b}{g}} \tag{6.7}$$

$$v' = \frac{v}{h_b}\sqrt{\frac{L_b}{g}} \tag{6.8}$$

$$x_0' = \frac{x_0}{L_b} \tag{6.9}$$

$$\left(\frac{dx_0}{dt}\right)' = \left(\frac{dx_0}{dt}\right)\frac{1}{\sqrt{gL_b}} \tag{6.10}$$

$$\left(\frac{d^2x_0}{dt^2}\right)' = \left(\frac{d^2x_0}{dt^2}\right)\frac{1}{g} \tag{6.11}$$

where a_0 is the (constant) landslide acceleration, in mm/s^2.

6.2 Parameter space investigated during experiments

In this study, it is desirable to understand the dependence of both experimentally modelled and numerically simulated waves on the motion of the landslide, and on the geometry of the problem (such as the length of the landslide relative to the fluid depth). To achieve this aim, the fluid depth and landslide motion were varied during

the experiments.

A mechanical system provided the landslide motion, and so the range and form of the velocity profiles able to be modelled was virtually unlimited, within the constraints of the system itself. The landslide motion modelled in this project followed an idealisation of the motion of a solid block moving down a sloping boundary, since this has been the method used to model tsunamigenic landslides in most previous experimental studies.

The motion of a solid block down a slope would typically consist of an initial period of acceleration, followed by a period of constant (or near-constant) velocity, followed by a deceleration to rest. In some previous studies, the landslide did not reach its terminal velocity, and so the motion consisted of an initial period of acceleration followed by a deceleration to rest. In reality, the dynamic forces acting on the block during its downslope motion would complicate the kinematics of the landslide block. However, it is convenient to model the landslide motion in the experiments and numerical simulations in an idealised form.

The landslide motion in this project consisted of three different phases. As discussed in chapter 5, these phases were an initial period of constant acceleration to a constant velocity, a period of motion at this constant velocity and a constant deceleration to rest. To limit the required number of experiments within the parametric study, the magnitude of the deceleration was set to be equal to the magnitude of the inital acceleration. Therefore, the independent landslide motion parameters investigated in this study were the magnitude of the initial acceleration and the magnitude of the constant velocity.

Equation 6.11 provides the nondimensional form of the landslide acceleration, and equation 6.10 states the nondimensional form of the landslide velocity. However, a more familiar (and more useful) nondimensional form of the landslide velocity is the landslide Froude number. This parameter is defined in chapter 5, and repeated here for convenience as

$$Fr = \frac{u_t}{\sqrt{gD}}. \tag{6.12}$$

The Froude number provides a measure of the relative sizes of the landslide terminal velocity (u_t) and the phase speed of a shallow water wave propagating in a channel of depth D.

Table 6.3 lists the three nondimensional parameters varied during the physical experiments and numerical simulations. Two nondimensional depths were selected, $\tau = 0.35$ and $\tau = 0.7$, corresponding to dimensional depths of 175 mm and 350 mm. Three different nondimensional landslide accelerations were tested within the range of accelerations able to be achieved by the mechanical system; these were $\lambda = 0.051$, $\lambda =$

0.102, and $\lambda = 0.153$, corresponding to dimensional accelerations of 0.5 m/s^2, 1.0 m/s^2 and 1.5m/s^2. A total of four landslide Froude numbers were investigated. These were $Fr = 0.125$, $Fr = 0.250$, $Fr = 0.375$, and $Fr = 0.500$.

Table 6.3: Nondimensional parameters investigated during experiments.

Nondimensional parameter	**Description**	**Equation**
τ	Nondimensional water depth	$\tau = \frac{D}{L_b}$
λ	Nondimensional landslide acceleration	$\lambda = \frac{a_0}{g}$
Fr	Landslide Froude number	$Fr = \frac{u_t}{\sqrt{gD}}$

This selection of experimental parameters led to a total of 24 experiments within the main parametric study of this project. Table 6.4 lists the nondimensional parameters tested in each experimental run, and table 6.5 provides the equivalent dimensional values. Note that t_1, t_2 and t_3 are the times of landslide motion change, illustrated in figure 5.3. The time during which the landslide moved at a constant velocity was set equal to 2 s in all experiments. In nondimensional form, this is expressed as $t_2 - t_1 = 8.859$. The time at constant velocity was selected so that the landslide completed as much of its motion as possible before the wave reflections interfered with the wave field.

In addition to these LIF experiments, one particle tracking velocimetry (PTV) experiment was undertaken to provide subsurface velocity field measurements in run 12. Measurement of the subsurface velocity field allowed comparison between the subsurface fluid motions and the waves generated on the free surface.

Table 6.4: Nondimensional parameters for the two-dimensional experiments contained within main parametric study.

Run	λ	Fr	τ	t_1	t_2	t_3
1	0.051	0.125	0.70	2.052	10.911	12.963
2	0.051	0.250	0.70	4.104	12.963	17.067
3	0.051	0.375	0.70	6.156	15.015	21.170
4	0.051	0.500	0.70	8.208	17.067	25.274
5	0.051	0.125	0.35	1.451	10.310	11.761
6	0.051	0.250	0.35	2.902	11.761	14.663
7	0.051	0.375	0.35	4.353	13.212	17.564
8	0.051	0.500	0.35	5.804	14.663	20.466
9	0.102	0.125	0.70	1.026	9.885	10.911
10	0.102	0.250	0.70	2.052	10.911	12.963
11	0.102	0.375	0.70	3.078	11.937	15.015
12	0.102	0.500	0.70	4.104	12.963	17.067
13	0.102	0.125	0.35	0.725	9.584	10.310
14	0.102	0.250	0.35	1.451	10.310	11.595
15	0.102	0.375	0.35	2.176	11.035	13.212
16	0.102	0.500	0.35	2.902	11.761	14.663
17	0.153	0.125	0.70	0.684	9.543	10.227
18	0.153	0.250	0.70	1.368	10.227	11.595
19	0.153	0.375	0.70	2.052	10.911	12.963
20	0.153	0.500	0.70	2.736	11.595	14.331
21	0.153	0.125	0.35	0.484	9.343	9.826
22	0.153	0.250	0.35	0.967	9.826	10.793
23	0.153	0.375	0.35	1.451	10.310	11.761
24	0.153	0.500	0.35	1.935	10.793	12.728

Table 6.5: Dimensional parameters for all two-dimensional experiments.

Run	a_0 (mm/s^2)	u_t (mm/s)	D (mm)	t_1 (s)	t_2 (s)	t_3 (s)
1	500	232	350	0.463	2.463	2.926
2	500	463	350	0.926	2.926	3.853
3	500	695	350	1.390	3.390	4.779
4	500	926	350	1.853	3.853	5.706
5	500	164	175	0.328	2.328	2.655
6	500	328	175	0.655	2.655	3.310
7	500	491	175	0.983	2.983	3.965
8	500	655	175	1.310	3.310	4.620
9	1000	232	350	0.232	2.232	2.463
10	1000	463	350	0.463	2.463	2.926
11	1000	695	350	0.695	2.695	3.390
12	1000	926	350	0.926	2.926	3.853
13	1000	164	175	0.164	2.164	2.328
14	1000	328	175	0.328	2.328	2.655
15	1000	491	175	0.491	2.491	2.983
16	1000	655	175	0.655	2.655	3.310
17	1500	232	350	0.154	2.154	2.309
18	1500	463	350	0.309	2.309	2.618
19	1500	695	350	0.463	2.463	2.926
20	1500	926	350	0.618	2.618	3.235
21	1500	164	175	0.109	2.109	2.218
22	1500	328	175	0.218	2.218	2.437
23	1500	491	175	0.328	2.328	2.655
24	1500	655	175	0.437	2.437	2.873

6.3 Additional experiments to investigate constant-velocity phase of motion

Significant interactions between the landslide and the generated wave field occurred during the constant velocity phase of motion. These interactions exhibited strong dependence on the landslide Froude number, as discussed in chapter 7. Six additional experiments allowed further investigation of these interactions. The first two experiments investigated the behaviour of the wave field at higher Froude number values of 0.625 and 0.75, for a fixed depth and landslide acceleration. This allowed an understanding of the behaviour of the generated waves as the landslide approached a critical (or resonant) terminal velocity. The last four experiments allowed the constant velocity phase of motion to last longer than 2 seconds, so that the interaction between the landslide and the generated waves could be observed for a longer period of time. The four experiments each tested one of the landslide Froude numbers investigated in the main parametric study (again, for a fixed depth and landslide acceleration).

Table 6.6 provides the nondimensional parameters for these additional six runs, and table 6.7 provides the equivalent dimensional values. For runs 27 to 30, the time of the constant velocity phase of motion varied between experiments. This variation occurred because the landslide had a higher velocity in the case of a higher Fr, and the available length of the sliding surface (approximately 5 m) therefore limited the time that the landslide could move at its terminal velocity. For a low Fr, the landslide moved so slowly that the reflected waves moved through the entire wavefield before the landslide reached the end of the sliding surface. Therefore, the time of the constant velocity phase of motion varied between 6 s and 12 s in these experimental runs.

Table 6.6: Nondimensional parameters for additional two-dimensional runs used to investigate constant-velocity phase of motion.

Run	λ	Fr	τ	t_1	t_2	t_3
25	0.153	0.625	0.35	2.418	11.277	13.695
26	0.153	0.750	0.35	2.902	11.761	14.663
27	0.153	0.125	0.35	0.484	40.349	40.832
28	0.153	0.250	0.35	0.967	54.121	55.088
29	0.153	0.375	0.35	1.451	36.886	38.337
30	0.153	0.500	0.35	1.935	28.511	30.446

Table 6.7: Dimensional parameters for additional two-dimensional runs used to investigate constant-velocity phase of motion.

Run	a_0 (mm/s^2)	u_t (mm/s)	D (mm)	t_1 (s)	t_2 (s)	t_3 (s)
25	1500	819	175	0.546	2.546	3.092
26	1500	983	175	0.655	2.655	3.310
27	1500	164	175	0.109	9.109	9.218
28	1500	328	175	0.218	12.218	12.437
29	1500	491	175	0.328	8.328	8.655
30	1500	655	175	0.437	6.437	6.873

6.4 Summary

This chapter presents the nondimensional framework used to compare the experimental results to the predictions of the two numerical models. Subsequent chapters will use this framework when presenting the experimental and numerical results. This chapter also describes the parameters varied during the experiments and simulations, and the range of values tested during the parametric study. It should be noted that only the laser-induced fluorescence (LIF) experiments and the two-dimensional linear models explored the entire parameter space described in this chapter.

The viscous model (using the DNS solver, Gerris) explored a limited range of parameters, however the computational expense of the model precluded coverage of the full parameter space. A particle tracking velocimetry (PTV) experiment provided subsurface velocity field data for run 12 only.

Chapter 7

Experimental results

7.1 Introduction

This chapter describes the results of the physical experiments investigating the waves generated by the motion of a submarine landslide along a horizontal bottom boundary. The purpose of these physical experiments was to provide a high quality dataset of wave amplitude measurements for direct comparison with the numerical model predictions (described in chapter 8). The use of a horizontal boundary allowed measurement of waves propagating in the onshore and offshore directions, and the mechanical system enabled a more complete investigation into the wave generation characteristics of the separate phases of landslide motion.

The first section of this chapter qualitatively describes the properties of the generated waves. This section focuses on the results of one experiment, for the sake of convenience. The description includes the types of waves generated during the different phases of landslide motion, the interaction between the waves and the moving landslide, and the effects of dispersion on the evolution of the wave field. This section concludes with a discussion on the timing and effect of wave reflections from the ends of the flume.

The second section of this chapter describes the wave field behaviour over the parameter space. Since the landslide Froude number was the parameter with the greatest effect on the behaviour of the wave field, this behaviour is discussed separately for each of the Fr values. The discussion in this section focuses on the energy exchange between the landslide and the generated waves during the different phases of motion, the differences between the onshore- and offshore-propagating wave groups (including the mass and energy contained within each group), and the effects of interaction between the offshore-propagating waves and the moving landslide.

The third section of this chapter investigates the interaction between the offshore-propagating waves and the landslide during the constant-velocity phase of motion in

greater detail. The longer period of constant velocity used in Runs 27-30 are the focus of this section.

The fourth section of this chapter discusses the subsurface velocity field generated by the motion of the landslide, using the results of a particle tracking velocimetry experiment. The effect of the turbulent wake on the flow around the landslide, and the phasing of this flow relative to the free surface waves, are discussed in this section.

7.2 Description of wave properties

7.2.1 Waves generated during different phases of motion

This section provides a general description of the waves generated during the physical experiments, using measurements recorded during one representative experimental run. The experiment selected was Run 14, with nondimensional parameters $\lambda = 0.102$, $Fr = 0.25$ and $\tau = 0.35$. This experiment was chosen because it used the mid-range values of λ and Fr. Since only two depths were used in the parametric study, the choice of a representative depth was somewhat arbitrary, and the shallower depth was selected. In this experiment, the wave amplitude ranged from approximately $\eta = -0.18$ to $\eta = 0.18$, corresponding to a dimensional amplitude range of approximately ± 4.5 mm.

Figure 7.1 shows a two dimensional wave amplitude plot of the waves (equivalent wave field plots for all other experiments are provided in appendix B). The horizontal axis represents the distance along the flume, x (where the origin is the initial location of the landslide centre of mass), the vertical axis represents time, t, and the colour scale represents the wave amplitude, η. Red indicates a positive value of η, corresponding to a wave crest, and blue indicates a negative value of η, corresponding to a wave trough. The diagonal bands of colour thus correspond to the characteristic curves of each generated wave in the $x - t$ plane. Note that the positive x-direction is defined as the offshore direction (as this was the direction of landslide motion), and the negative x-direction is defined as the onshore direction.

The solid black line shows the position of the landslide centre of mass during its motion, and the dashed black lines show the times of change between the different phases of landslide motion. Since the landslide displacement was not measured during the LIF experiments, the landslide location used in this chapter was obtained from the motion input files. Figure 7.2 shows five wave field snapshots from the same experiment, taken at $t = 2.85$, 5.69, 8.54, 11.39 and 14.24, to assist in the interpretation of the contour plot shown in figure 7.1.

The landslide initially accelerated at a constant rate until $t = 1.45$, after which it moved at a constant velocity until $t = 10.31$. Between $t = 10.31$ and $t = 11.60$, the

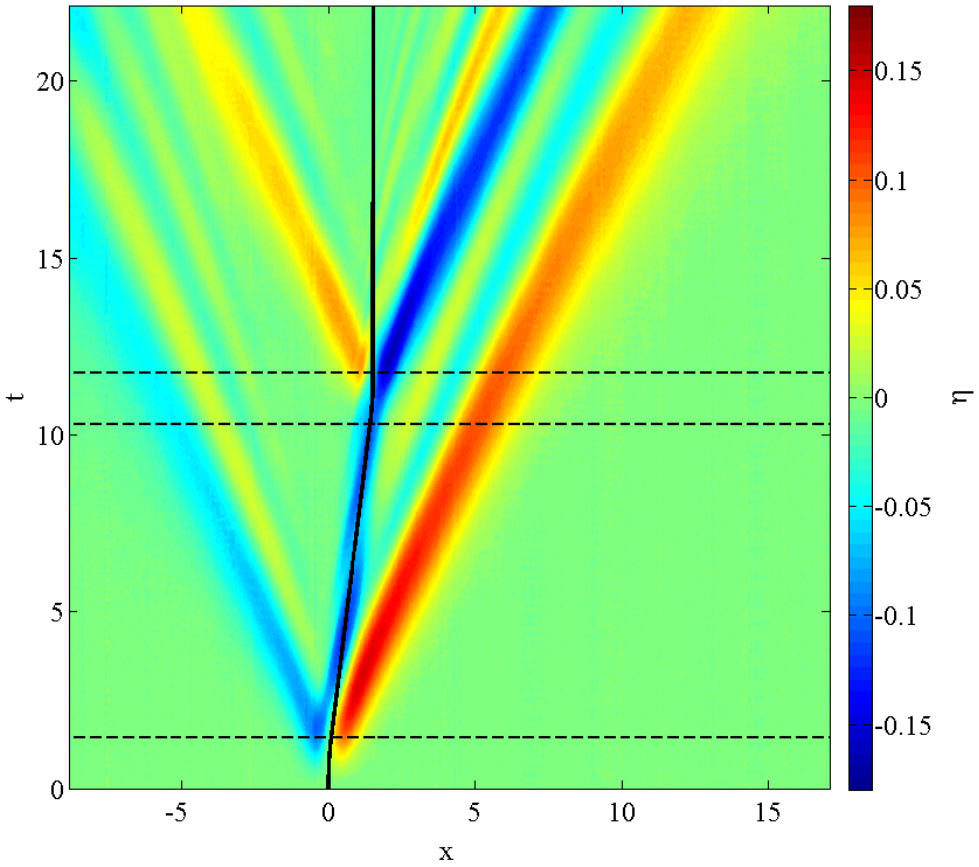

Figure 7.1: Nondimensional contour plot of the wave field measured using LIF, from Run 14 ($\lambda = 0.1$, $Fr = 0.25$, $\tau = 0.35$). The position of the landslide centre of mass is shown by a solid black line, and the times of motion change are shown by dashed black lines.

landslide decelerated to rest at the same rate as its initial acceleration. The acceleration and deceleration of the landslide each generated two dispersive packets of waves, which propagated in the onshore and offshore directions respectively. The wave packets evolved as dispersive packets, mostly within the intermediate depth regime, and this evolution continued after the landslide motion ceased.

The initial acceleration of the landslide generated a leading crest in the offshore direction and a leading trough in the onshore direction. Each of these leading waves was followed by a series of crests and troughs, with successively smaller amplitudes and wavelengths than the leading waves. The two groups of waves each travelled in a dispersive wave group, or packet. These packets were responsible for positive mass transport in the offshore direction, and negative mass transport in the onshore direction (discussed in section 7.3). The landslide interacted with the offshore-propagating waves throughout its motion, but only interacted with the onshore-propagating waves for a

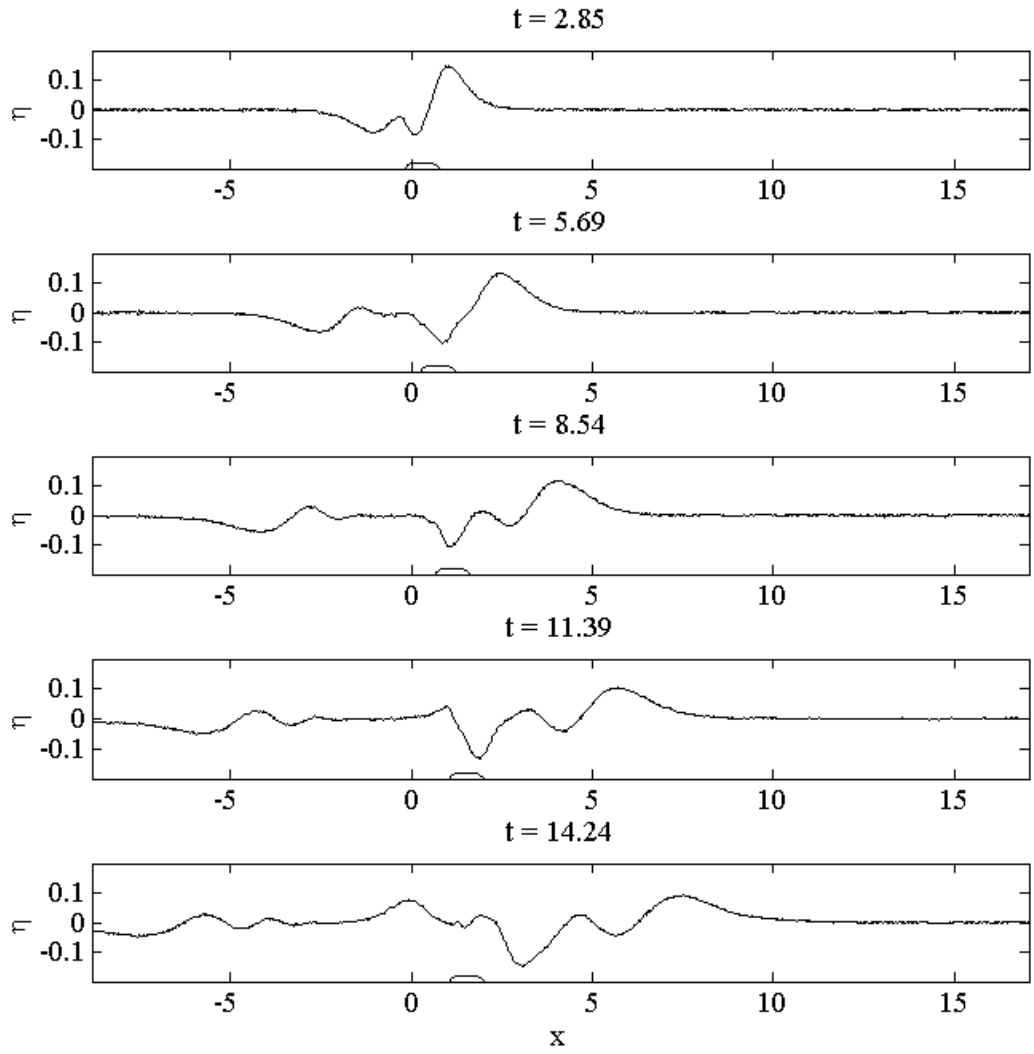

Figure 7.2: Snapshots of the wave field from Run 14, where the first three images occurred during the constant-velocity phase of motion, and the last two images occurred after the landslide had ceased its motion.

short time period. The landslide Froude number was less than unity over the entire parameter space. Since the leading offshore-propagating crest moved at a velocity approximately equal to the shallow water wave speed, the landslide always moved at a slower speed than this crest.

The high velocity of the fluid passing over the landslide during its constant-velocity motion created a region of low pressure above the landslide. The free surface became slightly depressed above this low-pressure region, and this free surface depression remained above the landslide during this phase of motion. This is evident in figure 7.1, in the dark blue colour band above the moving landslide between t_1 and t_2. The free

surface depression increased the amplitude of the offshore-propagating troughs that passed through it, and decreased the amplitude of the offshore-propagating crests that passed through it.

The deceleration of the landslide block generated two additional wave packets, similar to those generated by the landslide acceleration. The offshore-propagating wave packet contained a leading trough and a dispersive train, and the onshore-propagating wave packet contained a leading crest and a dispersive train. Again, because the duration of the deceleration was short, only the leading waves in these packets were visible when the landslide came to rest.

During the landslide deceleration, the trough which had previously been trapped above the landslide began to propagate in the offshore direction as a free wave. Since an offshore-propagating trough was also passing above the landslide at the start of the landslide deceleration (in addition to this free surface depression), this had the effect of temporarily increasing the amplitude of the leading trough in the offshore direction. The leading waves generated during the landslide deceleration immediately interacted with the offshore-propagating wave packet. The onshore-propagating crest generated by the landslide deceleration also quickly caught up with the rear of the onshore-propagating wave packet generated by the landslide acceleration, since the phase velocity of this wave was larger than the group velocity of the smallest waves in the offshore-propagating packet.

7.2.2 Dispersive effects on wave propagation

The leading crest and trough generated by the landslide acceleration possessed wavelengths greater than the water depth, and these waves approached the behaviour of shallow water waves (such that their phase velocity approached the value $\sqrt{gD}$). However, the wavelengths of the trailing waves were significantly lower, and these waves generally propagated as deep-water waves with lower phase velocities. The characteristic curves of the trailing waves within each packet were initially slightly curved, and became straighter during their propagation. The characteristic curves of the leading waves were straight throughout their propagation. Additionally, the slopes of the characteristic curves of the leading offshore- and onshore-propagating waves were approximately equal.

Because of the dispersive nature of the generated wave packets, waves with short wavelengths were created at the back of each packet. The velocities of the front and back of the wave packets are best illustrated using the onshore-propagating wave packet, since this wave packet exhibited less ongoing interaction with the moving landslide. The wavelength of the smallest wave present in the group was approximately 1.0 in nondimensional terms, leading to a group velocity of approximately 0.2 while the

nondimensional shallow water phase speed was approximately 0.59.

It should be noted that the reason for $c_{shallow} \neq 1$ is the choice of L_b in nondimensionalising the horizontal length scales (and times, when combined with the gravitational acceleration, g). This gives a nondimensional wave celerity of

$$c' = \frac{c}{\sqrt{gL_b}}, \tag{7.1}$$

as opposed to the more standard definition of

$$c' = \frac{c}{\sqrt{gD}}. \tag{7.2}$$

Clearly, the phase velocity of a shallow water wave would only take a value of unity if nondimensionalised according to equation 7.2.

The location of the back of the wave packet moved with the group velocity of the smallest wavelengths generated by the landslide motion, while the location of the front of the wave packet moved with the phase velocity of the leading wave (this was close to the shallow-water phase speed associated with this submergence depth). Therefore, waves continued to be generated within these wave packets even after the acceleration itself had ceased, and both wave packets grew in horizontal extent as they propagated along the length of the flume.

Figure 7.3 shows a contour plot of the onshore-propagating waves generated during this experiment, with lines corresponding to the phase velocity of the leading trough and the group velocity of the rearmost trough overlaid. The onshore-propagating wave packet is effectively contained within these two lines. The onshore-propagating crest generated by the landslide deceleration caught up to the onshore-propagating wave packet at approximately $t = 18.0$.

At the higher landslide Froude numbers tested, nonlinear steepening of the waves propagating at the landslide velocity reduced the effects of dispersion on these waves. The effect of this wave nonlinearity is discussed in sections 7.3 and 7.4.

7.2.3 Free surface depression during constant-velocity motion

As discussed in the previous section, the constant-velocity landslide motion generated a free surface depression which propagated above the landslide until it began to decelerate. This depression interacted with the offshore-propagating waves, since these waves moved more rapidly than the landslide. The amplitude of the depression itself can be predicted using standard hydraulic theory. The relatively short flume length, and finite duration of the constant-velocity landslide motion, limit the applicability of these predictions. However, they can still be used to gain a simple estimate of the amplitude of the depression above the landslide, and the effect of changing τ or Fr on this

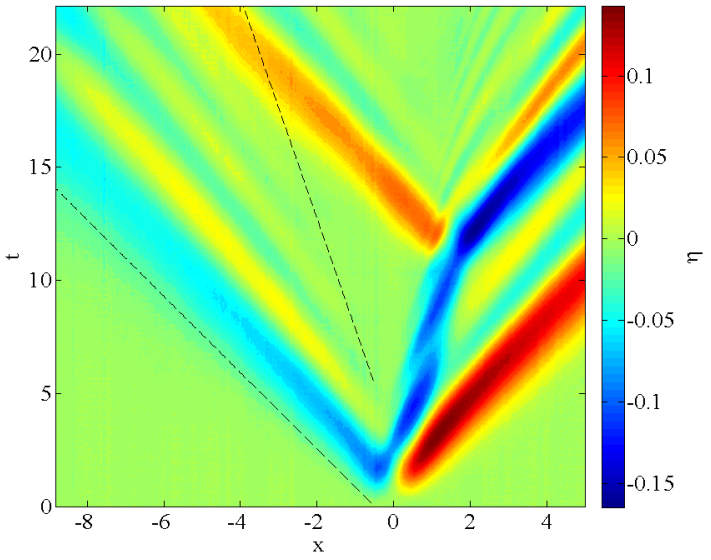

Figure 7.3: Nondimensional contour plot of wave field measured using LIF, from Run 14 ($\lambda = 0.1$, $Fr = 0.25$, $\tau = 0.35$), with the shallow water wave phase speed and the group velocity corresponding to a wavelength of 1.0 overlaid.

amplitude. Section 7.4 compares the predictions of this section with experimental measurements of the depression amplitude for experiments with a long constant-velocity phase of motion.

Considering a frame of reference moving with the landslide, the steady-state problem is illustrated in figure 7.4, where q is the flow per unit width (and the negative flow direction ensures landslide motion in the positive x-direction). This steady-state problem assumes an infinite period of constant velocity, and that any transient free surface disturbances have propagated away from the area of interest. Thus, the landslide acceleration is irrelevant in this problem. The flow is assumed to be subcritical throughout the region of interest, consistent with the range of landslide Froude numbers tested in this project.

The free surface depression above the landslide, η, can be predicted using the conservation of energy along the length of the channel. For example, in an experiment with $y_1 = 0.175$ m, $u_t = 0.328$ m/s (corresponding to a Froude number of 0.25), the flow per unit width is $q = 0.057$ m^2/s. The specific energy in the channel at section 1 is

$$E_1 = y_1 + \frac{q^2}{2gy_1^2} = 0.180 \text{ m}. \tag{7.3}$$

The specific energy in the flow (and hence the flow depth) are reduced at section 2 due to the presence of the submerged block. Changes in flow depth are assumed to occur gradually, so the applicability of this theory is limited by the relatively short length of the landslide. The landslide thickness is 0.026 m, thus the specific energy at

section 2 is

$$E_2 = E_1 - h_b = 0.154 \text{ m}. \tag{7.4}$$

The corresponding change in flow depth over the landslide is 0.0023 m, or η = -0.089 in nondimensional units.

The amplitude of this free surface depression increases with increasing flow velocity (achieved by increasing the landslide Froude number in the current experiments), or by increasing the landslide thickness relative to the fluid depth (achieved by decreasing τ in the current experiments). Table 7.1 states the predictions and measured values of free surface depression amplitude for Runs 5 to 8. The η values are reported in nondimensional form, according to the nondimensionalisation described in chapter 6). The experimental measurements of the free surface depression amplitude were obtained from Runs 27 to 30, since these experiments contained a long enough period of constant velocity for the depression amplitude to be correctly determined. In the other experiments, the landslide deceleration occurred before the depression amplitude had reached its steady value. The hydraulic theory prediction of the depression amplitude was equal to the measured value at the lowest Froude number, however the amplitude was under-predicted at all of the other Froude numbers. Results from these experiments are discussed further in section 7.4.

7.2.4 Wave reflections

Upon reaching the ends of the flume, the leading waves were reflected back into the generated wave field. Due to the starting location of the landslide (see chapter 4 for details), the leading onshore-propagating trough was the first of the leading waves to reach the end of the flume. The gantry system did not extend to the extreme ends

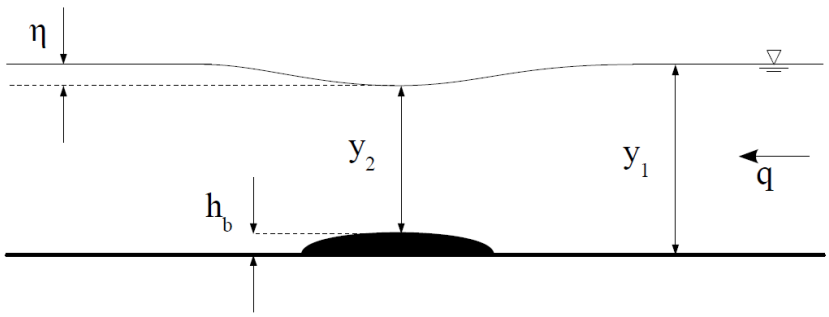

Figure 7.4: Open channel flow approximation of constant-velocity landslide motion, showing free surface depression above landslide.

Table 7.1: Free surface depressions above the moving landslide, as predicted by hydraulic theory. Predicted free surface elevations are indicated by a p subscript, while measured values are indicated by a m subscript.

Run	Fr	τ	η_p	η_m
5	0.125	0.35	-0.020	-0.020
6	0.250	0.35	-0.089	-0.113
7	0.375	0.35	-0.237	-0.268
8	0.500	0.35	-0.607	-0.802

of the flume, so there was a short delay between a leading wave reaching the edge of the camera's field of view and the reflection of the wave. Figure 7.5 shows the wave amplitude time series for pixels located on the extreme onshore and offshore boundaries of the spatial domain.

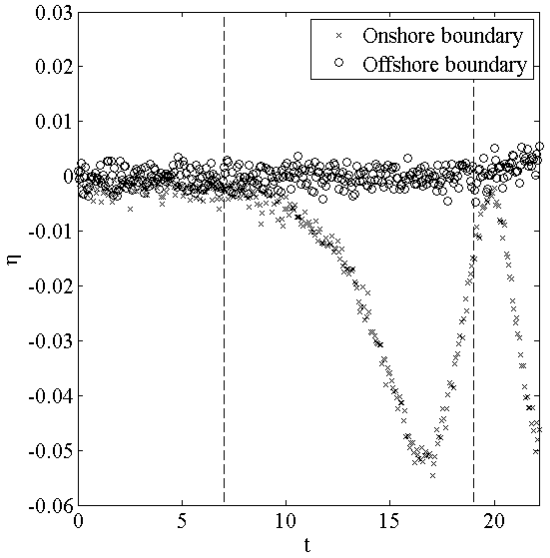

Figure 7.5: Time series of wave amplitudes at offshore and onshore edges of domain, showing approximate reflection times of the leading waves.

The noise in the wave amplitude time series was approximately ± 0.004 in nondimensional units, corresponding to a dimensional range of ± 0.1 mm (the pixel scale in these experiments was approximately 0.3 mm/pixel). The leading onshore-propagating trough began to leave the domain at approximately $t = 7.0$, and was reflected soon after this time. The leading offshore-propagating crest began to leave the domain at approximately $t = 18.0$, and reflections were not as pronounced in the wave field plot of figure 7.1. The reflection of these waves affected the calculation of the potential energy and mass within the wave field, as discussed in section 7.3.

7.3 Wave field behaviour over entire parameter space

7.3.1 Wave field behaviour at $Fr = 0.125$

At the lowest landslide Froude number of 0.125, the periods of acceleration and deceleration were very brief compared to the period of constant velocity. However, the acceleration and deceleration of the landslide were responsible for almost all of the energy transfer between the landslide and the wave field. Figure 7.6 shows the wave field plot for Run 21, with parameters $\lambda = 0.153$, $\tau = 0.35$ and $Fr = 0.125$.

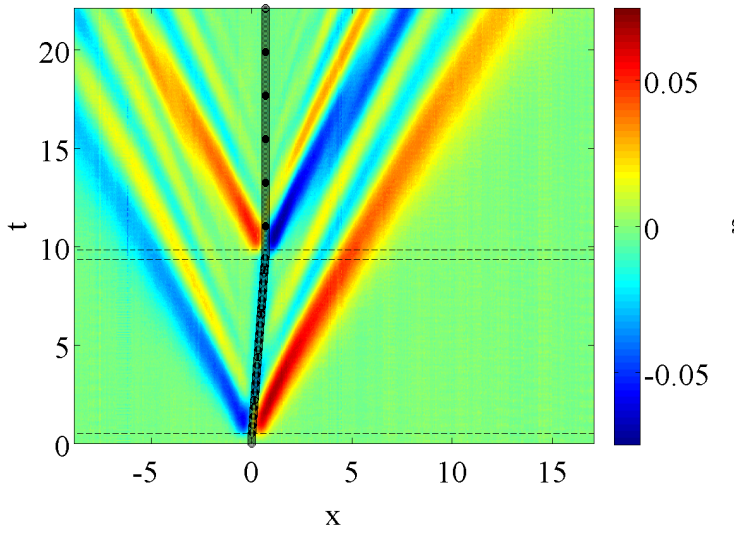

Figure 7.6: Wave field generated during an experiment with $\lambda = 0.153$, $\tau = 0.35$ and $Fr = 0.125$.

All of the waves generated during this experiment possessed low amplitudes, with the maximum amplitude of $\eta = 0.08$ corresponding to a dimensional value of approximately 2 mm. The leading waves generated by the landslide acceleration (and later by the landslide deceleration) were the largest-amplitude waves present in the wave field. By comparison, the free surface depression above the landslide during its constant-velocity motion had a maximum amplitude of approximately η = -0.04. The amplitudes of the onshore-propagating waves were approximately equal to the amplitudes of the offshore-propagating waves in this experiment.

Based on the relative sizes of the leading waves and the free surface depression in figure 7.6, it follows that most of the energy exchange between the landslide and the wave field occurred during the acceleration and deceleration phases of motion. Figure 7.7 shows that this behaviour was consistent over all experiments conducted at this Froude number. This figure compares the maximum recorded amplitudes of the

leading waves and the free surface depression for all combinations of λ and τ. The contribution of the leading waves to the energy within the wave field was larger than the contribution of the free surface depression, due to the much longer wavelengths (and larger amplitudes) of the leading waves.

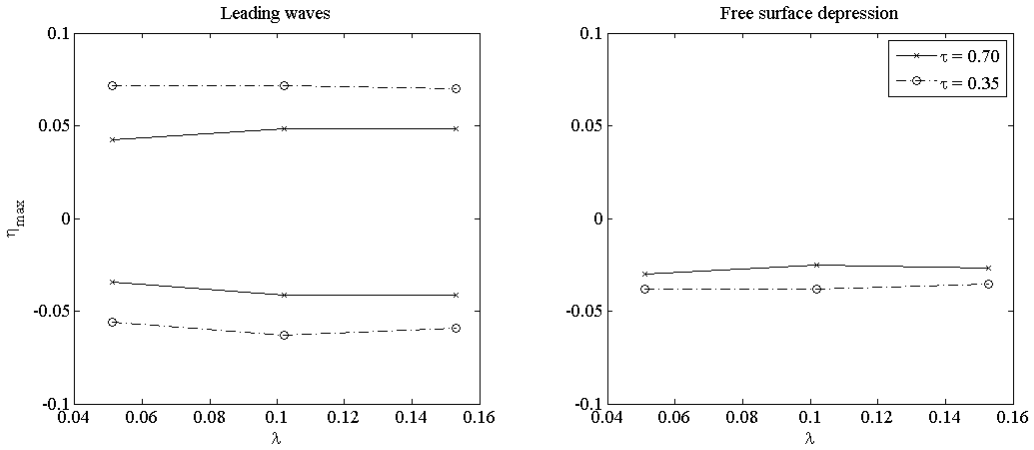

Figure 7.7: Variation in peak wave amplitudes for all experiments with $Fr = 0.125$.

Figure 7.7 also illustrates the dependence of the different wave amplitudes within the wave field on the landslide acceleration and submergence depth at this Froude number. As expected, the waves generated over the shallower submergence depth ($\tau = 0.35$) possessed larger amplitudes than those generated over the deeper submergence depth ($\tau = 0.70$), although their wavelengths were shorter. The peak amplitudes showed minimal dependence on the landslide acceleration at this Froude number. This weak λ dependence may be caused by the short duration of the landslide acceleration compared to the timescale of wave propagation at this Froude number, regardless of the magnitude of the acceleration itself.

The relative sizes of the waves generated during the different phases of motion gives some insight into the importance of each phase in the exchange of energy between the landslide and the generated waves. However, since the measurements of wave amplitude cover the entire spatial domain, these amplitudes may be integrated to calculate the nondimensional potential energy within the wave field at a particular time, according to

$$E_P(t) = \frac{1}{2}\int_{-\infty}^{\infty} (\eta(t))^2 dx. \tag{7.5}$$

Figure 7.8 shows the time variation in potential energy for all experiments carried out at this Froude number. The initial peak in the time series was caused by the waves generated by the landslide acceleration (although there was a slight lag between t_1 and the occurrence of this peak value), while the second peak was caused by the additional waves generated during the deceleration phase of motion. Most of the energy

exchange between the landslide and the wave field occurred during the acceleration and deceleration phases of motion. Variations during the constant-velocity phase of motion are discussed below, in terms of the energy contained within the onshore and offshore regions.

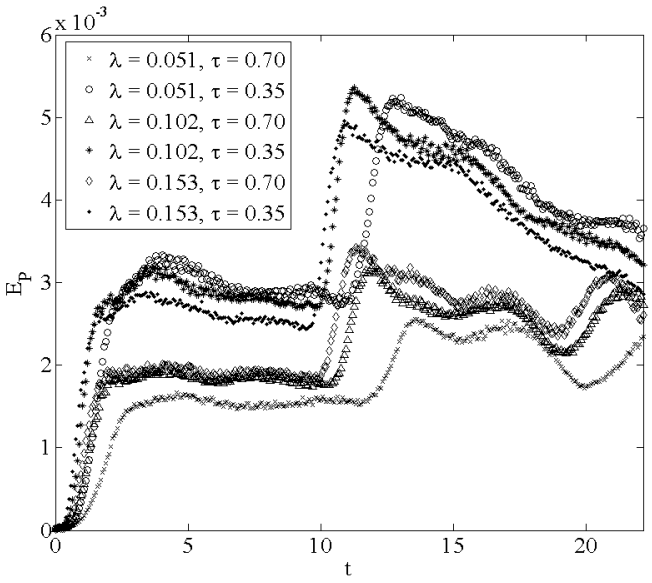

Figure 7.8: Time variation in wave field potential energy for all experiments with Fr = 0.125.

Previous sloping-boundary experimental setups were unable to measure the amplitudes of the onshore-propagating waves, and the current series of experiments enabled comparison between the properties of the onshore-propagating wave group and the properties of the offshore-propagating wave group. Although the wave field plots in figure 7.6 provide the range of amplitudes present within these two wave groups, the potential energy contained within each wave group may also be estimated by applying equation 7.5 to the onshore (negative x) and offshore (positive x) domains separately. It should be noted that this is only an estimate of the energy contained within each wave group, since the waves would not have fully separated into their onshore-propagating and offshore-propagating components at early times. Additionally, the waves generated by the landslide deceleration were all initially located in the offshore region. Thus, even the onshore-propagating waves generated by the deceleration would initially contribute to the estimate of the energy in the offshore region.

Figure 7.9 shows the time variation in the potential energy within the onshore and offshore regions of the experimental domain, for those experiments carried out at Fr = 0.125 with a submergence depth of $\tau = 0.35$. The behaviour was the same at the two submergence depths, however only the shallower depth is shown in this section since the reflection of waves occurred at a later time, due to the lower wave celerities

in the shallower experiments. In the deeper experiments, carried out at $\tau = 0.70$, the leading onshore-propagating trough reached the edge of the domain at approximately $t = 5.0$, while the leading offshore-propagating crest reached the edge of the domain at approximately $t = 15.0$. The equivalent times for the shallower experiments were approximately $t = 7.0$, and $t = 18.0$.

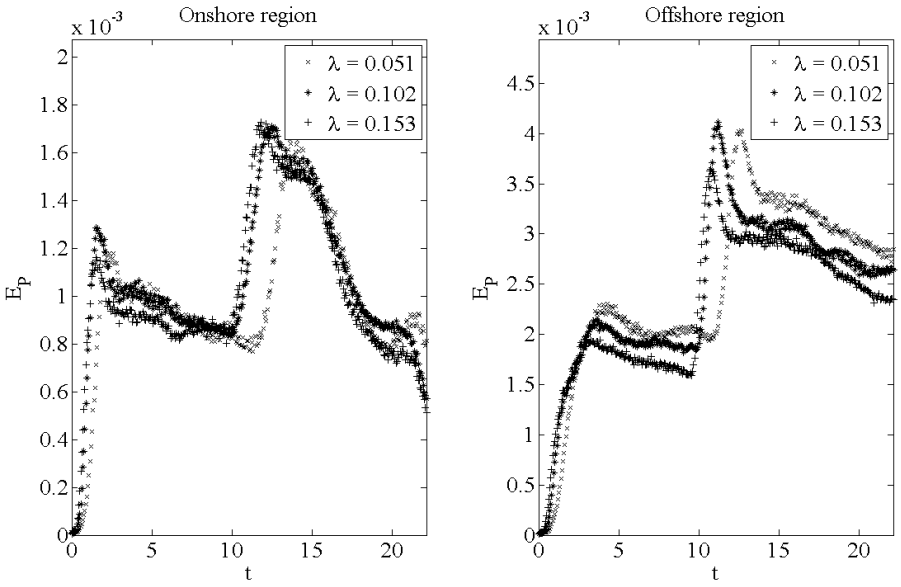

Figure 7.9: Time variation in onshore and offshore potential energy for all experiments with $Fr = 0.125$ and $\tau = 0.35$.

At early times, the leading waves generated by the landslide acceleration had not separated into their onshore- and offshore-propagating components. This caused the initial energy peak within the onshore region, since the initial trough had not separated into the leading onshore-propagating trough and the free surface depression above the moving landslide. During the constant-velocity phase of motion, approximately twice as much potential energy was contained within the offshore region as in the onshore region.

The energy within the onshore domain decreased during this phase of motion. Part of this decrease at early times may also be explained by the selection of $x = 0$ as the boundary between the onshore and offshore domains. After the peak but before $t = 5.0$, part of the free surface depression was located within the onshore region. As the landslide moved in the positive x-direction, the free surface depression left the onshore domain, causing the energy within this region to decrease. After $t = 7.0$, the leading trough began to leave the onshore region, which caused additional decreases in the energy within this region. Shortly after this time, the trough was reflected into the domain and contaminated the wave field. However, the observed attenuation of energy also occurred between these two times, and may be caused by

viscous dissipation at the flume sidewalls. Section 7.6 discusses this possible mechanism of energy attenuation in more detail, including some order-of-magnitude calculations. As shown in subsequent sections, the attenuation of energy during the constant-velocity phase of motion (particularly in the onshore region) was reasonably consistent over all the Froude numbers tested. Some energy attenuation can also be observed within the offshore region during the constant-velocity phase of motion, particularly in Run 21 (with $\lambda = 0.153$).

The ability to measure both onshore- and offshore-propagating wave properties also enables the experimental validation of the directional mass transport observed in the numerical simulations of Sue (2007). The nondimensional mass within the wave field is defined as

$$m'(t) = \int_{-\infty}^{\infty} \eta(t) dx, \tag{7.6}$$

where all variables are in their nondimensional form. The mass within the onshore or offshore domains may be calculated separately by considering either the positive or negative x-domain in isolation. It should be noted that the dimensional form of the mass within the wave field is

$$m(t) = \rho w \int_{-\infty}^{\infty} \eta(t) dx, \tag{7.7}$$

where ρ is the fluid density and w is the flume width. The fluid is assumed to be incompressible, and as such the nondimensional mass term does not include the fluid density (and is equivalent to a fluid volume).

Figure 7.10 shows the mass within the onshore and offshore regions calculated from the wave amplitudes measured in experiments with $Fr = 0.125$ and $\tau = 0.35$. This figure confirms the findings of Sue (2007), where the offshore-propagating waves transported positive mass and the onshore-propagating waves transported negative mass. The waves generated by the landslide deceleration balanced this initial mass transport, such that the residual transport after the landslide returned to rest was zero. The reflection of the onshore-propagating waves into the domain effectively ended the balance between the mass contained within the onshore and offshore waves.

Minimal interaction occurred between the landslide and the offshore-propagating waves at this Froude number, as indicated by the amplitudes shown in figure 7.6 and the potential energy time series shown in figure 7.8. To more closely investigate this behaviour, figure 7.11 shows a series of wave field plots captured during the constant-velocity phase of motion, from Run 21. The depression above the moving landslide is clearly visible throughout this phase of motion, however its amplitude was small compared to the leading wave amplitudes. Additionally, the free surface depression amplitude did not vary greatly over time, since the only offshore-propagating waves

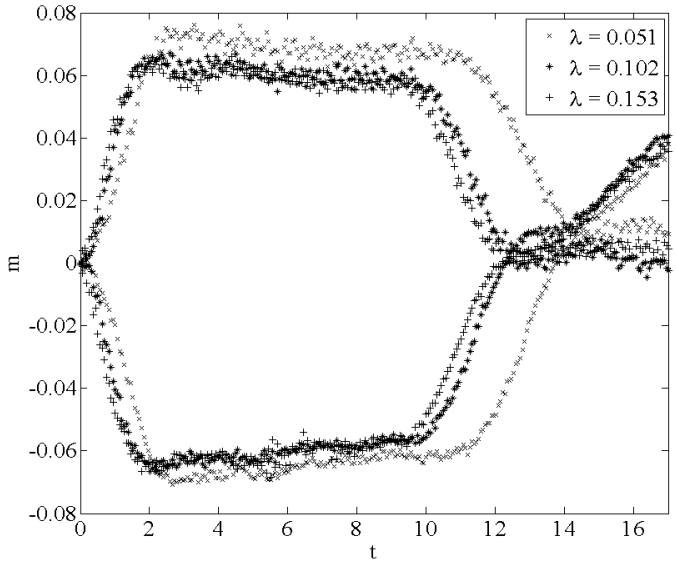

Figure 7.10: Time variation in onshore and offshore mass for all experiments with $Fr = 0.125$ and $\tau = 0.35$.

propagating through the depression were at the back of the group, and thus had very low amplitudes.

7.3.2 Wave field behaviour at $Fr = 0.250$

In the experiments conducted with $Fr = 0.250$, the majority of the energy transfer between the landslide and the wave field still occurred within the acceleration and deceleration phases of motion. However, the constant-velocity phase of motion caused fluctuations in the energy within the wave field, due to increased interactions between the free surface depression and the offshore-propagating waves. Figure 7.12 shows the wave field plot for Run 22, with parameters $\lambda = 0.153$, $\tau = 0.35$, and $Fr = 0.250$. In this experiment, the amplitudes of all of the generated waves were larger than those in Run 21, as shown by the colour scale. The size of the free surface depression increased relative to the size of the leading waves, and the amplitude of this trough was modulated as successive offshore-propagating crests and troughs passed through it. The offshore-propagating waves generated by the landslide acceleration and deceleration were larger in amplitude than the corresponding onshore-propagating waves.

As indicated by the wave field plot shown in figure 7.12, the landslide acceleration and deceleration were still the dominant periods of energy exchange between the landslide and the wave field. However, at this Froude number the amplitude of the free surface depression above the landslide was approximately 10% larger than the amplitude of the leading onshore-propagating trough generated by the landslide acceleration. Figure 7.13 compares the peak amplitudes of the leading waves and the free surface

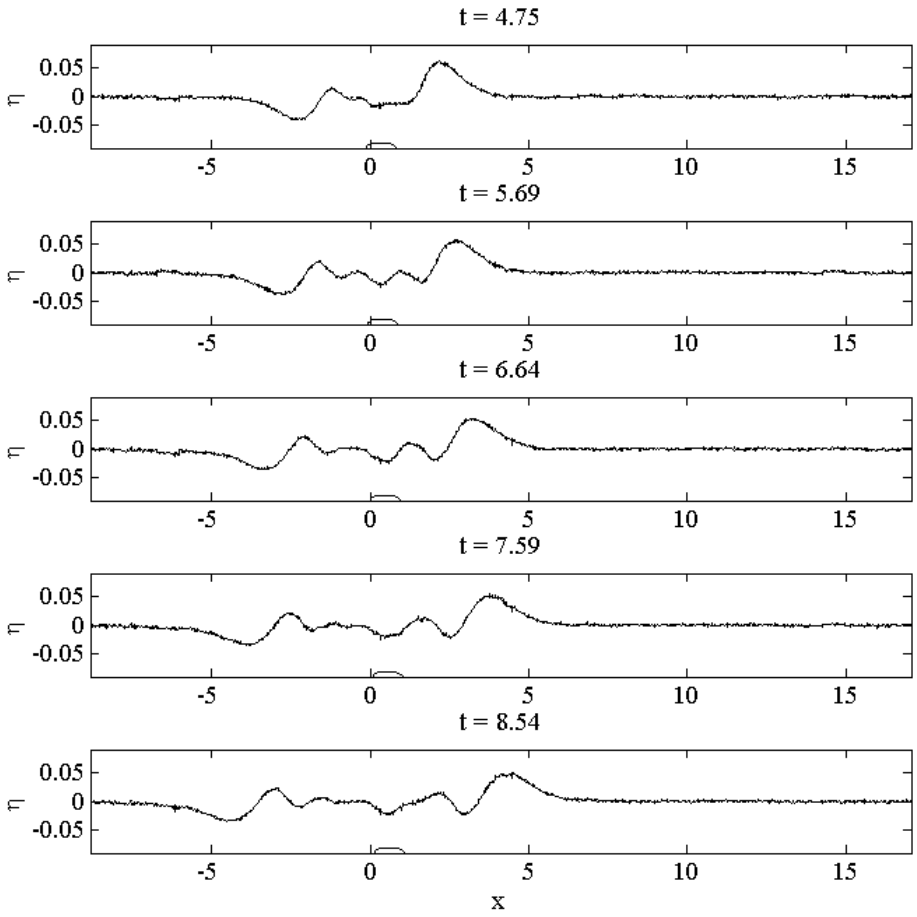

Figure 7.11: Interaction between moving landslide and offshore-propagating waves for Run 21, with parameters $\lambda = 0.153$, $Fr = 0.125$, and $\tau = 0.35$.

depression for all experiments undertaken at this Froude number. In this case, the leading offshore-propagating crest had an amplitude approximately 40% larger than the leading onshore-propagating trough. This indicates that more energy was contained within the offshore-propagating waves at this landslide Froude number. The dependence of the peak wave amplitudes on τ was similar to that observed at $Fr = 0.125$, however the waves generated by the landslide acceleration and deceleration exhibited a greater dependence on λ.

The potential energy time series, shown in figure 7.14, also showed a greater dependence on λ than observed at $Fr = 0.125$. In this case, the higher values of λ led to the higher E_P values during the constant-velocity phase of motion, as well as causing a more rapid increase in potential energy during the landslide acceleration and deceleration. Additionally, the interaction between the landslide and the offshore-propagating waves (discussed in more detail below) led to greater fluctuations in potential energy

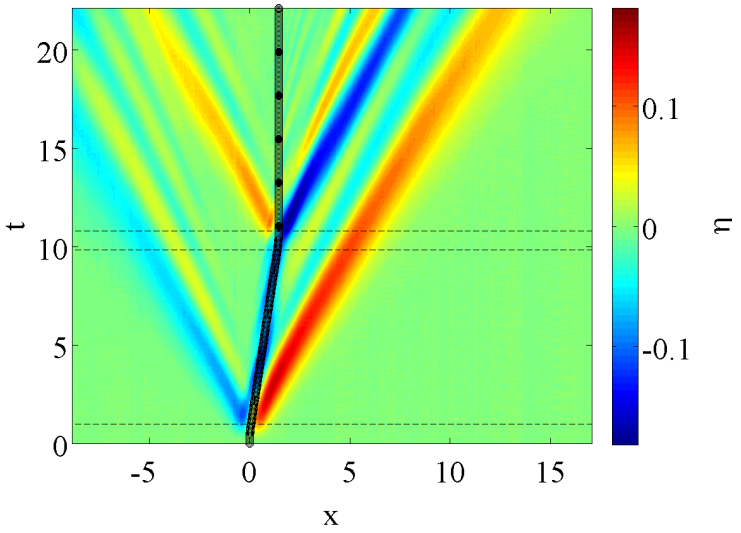

Figure 7.12: Wave field generated during an experiment with $\lambda = 0.153$, $\tau = 0.35$ and $Fr = 0.250$.

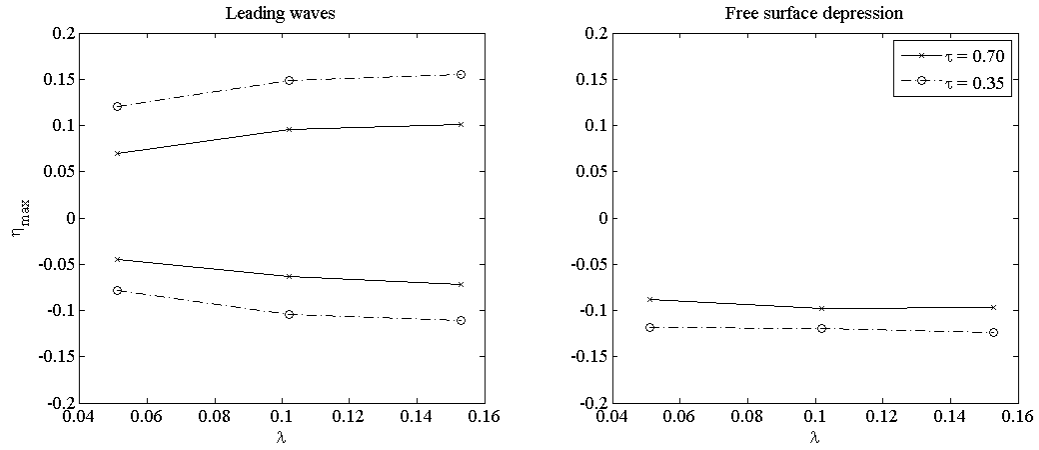

Figure 7.13: Variation in peak wave amplitudes for all experiments with $Fr = 0.250$.

during the constant-velocity phase of motion. The landslide acceleration and deceleration were still responsible for most of the energy input into the wave field.

The longer duration of the landslide acceleration and deceleration periods, as well as the increased interactions between the landslide and the offshore-propagating waves during the constant-velocity period, led to a larger increase in the 'offshore' energy compared to the 'onshore' energy at this Froude number. Figure 7.15 shows the time variation in potential energy in the offshore and onshore regions of the wave field for all experiments with $Fr = 0.250$ and $\tau = 0.35$. In this case, the energy within the offshore region was approximately three times larger than the energy within the onshore region, and the energy within both regions showed similar dependence on the nondimensional landslide acceleration, λ. The initial peak in the energy contained within both regions

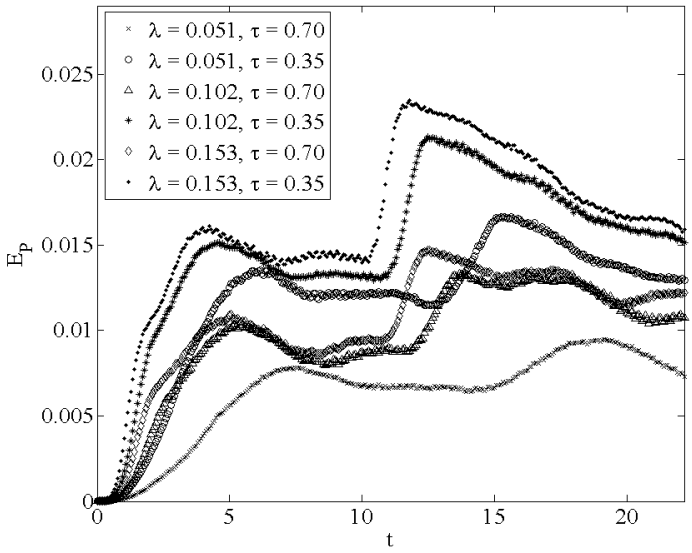

Figure 7.14: Time variation in wave field potential energy for all experiments with Fr = 0.250.

occurred before the two wave packets had fully separated, such that the onshore and offshore regions contained waves propagating in both directions. In a similar manner, the second energy peak in the offshore region would contain contributions from both onshore- and offshore-propagating waves. The attenuation of energy within the onshore region observed at $Fr = 0.125$ was also observed at this Froude number, even before the leading wave began to leave the domain.

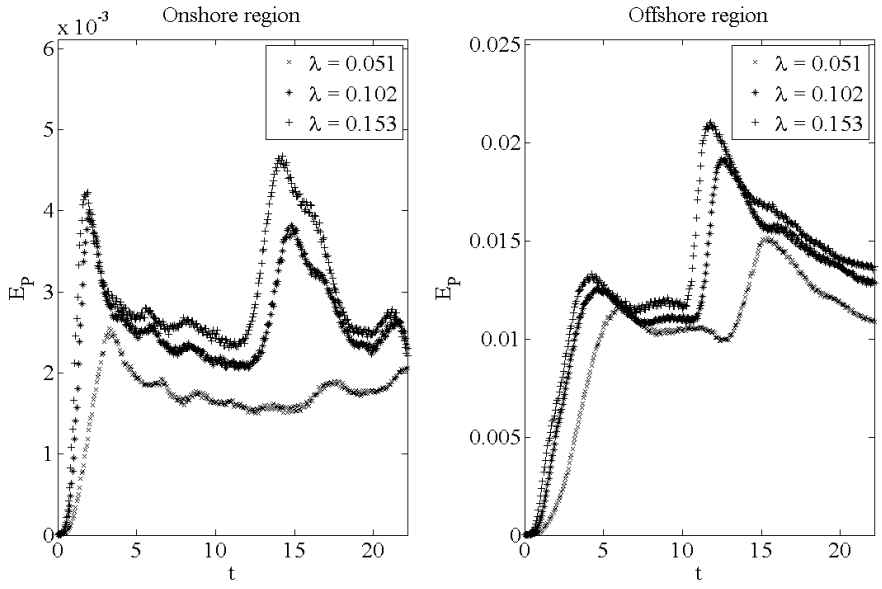

Figure 7.15: Time variation in onshore and offshore potential energy for all experiments with $Fr = 0.250$ and $\tau = 0.35$.

Figure 7.16 shows the directional mass transport by the onshore- and offshore-propagating wave packets for the experiments with $Fr = 0.250$ and $\tau = 0.35$. This mass transport was larger at this Froude number than at $Fr = 0.125$, however the 'steady' peak value of this mass transport during the constant-velocity phase of motion was approximately equal for all λ values tested. As with the potential energy in the wave field, the directional mass transport increased more rapidly for the higher nondimensional landslide accelerations, and the peak values observed at these accelerations occurred before the two wave groups had completely separated. The mass did not exhibit this initial peak at the lowest λ value, since the wave groups had separated before the landslide began its constant-velocity motion.

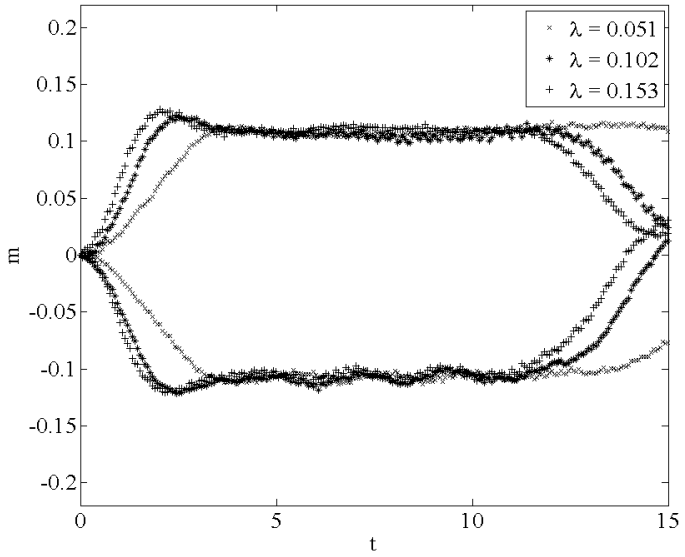

Figure 7.16: Time variation in onshore and offshore mass for all experiments with $Fr = 0.250$ and $\tau = 0.35$.

The interaction between the landslide and the offshore-propagating wave group at this Froude number is illustrated in the wave field plots of figure 7.17, from Run 22. The free surface depression amplitude was comparable to the amplitude of the leading onshore-propagating trough during the constant-velocity phase of motion. However, although dispersion acted to increase the wavelength and decrease the amplitude of the leading onshore-propagating trough, the free surface depression amplitude fluctuated as successive offshore-propagating crests and troughs passed through it. As discussed in section 7.2, the back of each wave packet propagated at approximately the group velocity of the shortest-wavelength wave within the packet. Thus, the larger terminal velocity associated with this Froude number caused the landslide to be closer to the front of the offshore-propagating wave packet, and hence the free surface depression interacted with larger-amplitude (and longer-wavelength) waves. The combination of the

larger free surface depression amplitude and the trough location within the offshore-propagating wave packet were responsible for the increased interactions during the constant-velocity phase of motion at this landslide Froude number. Additionally, the input of energy from the landslide into waves propagating with a phase velocity approximately equal to the terminal landslide velocity led to slightly nonlinear behaviour in the waves directly behind the free surface depression. This behaviour is discussed in section 7.4, where experiments were carried out with a longer period of constant velocity.

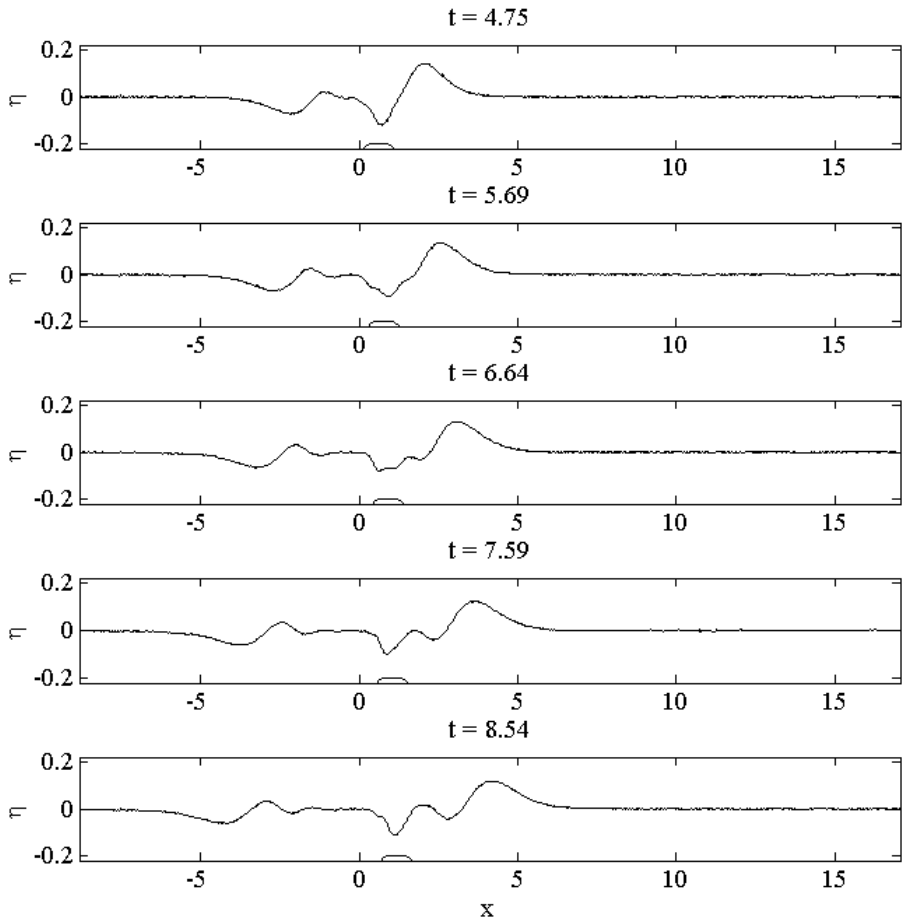

Figure 7.17: Interaction between moving landslide and offshore-propagating waves for Run 22, with parameters $\lambda = 0.153$, $Fr = 0.250$, and $\tau = 0.35$.

7.3.3 Wave field behaviour at $Fr = 0.375$

As the landslide Froude number increased to 0.375, the behaviour of the wave field changed slightly compared to the previous two Froude numbers. Figure 7.18 shows the wave field plot for Run 23, with parameters $\lambda = 0.153$, $\tau = 0.35$, and $Fr =$

0.375. In this experiment, the wave amplitudes were larger than observed at the previous Froude number; this trend was observed over all Froude numbers tested. The amplitudes of the offshore-propagating waves were considerably larger than those of the onshore-propagating waves, demonstrating that the size of the offshore-propagating waves relative to the onshore-propagating waves increased as the landslide Froude number increased. The size of the free surface depression during the constant-velocity phase of motion again increased relative to the sizes of the leading waves, as predicted by the hydraulic theory discussed in section 7.2, and this depression was larger than the leading onshore-propagating trough generated by the landslide acceleration.

An interesting feature of the experiments carried out at $Fr = 0.375$ was the formation of an additional group of waves behind the landslide during its constant-velocity motion. These waves had a relatively short wavelength, however their amplitude was considerably larger than would be expected given their position within the offshore-propagating wave packet. This relatively large amplitude, combined with the short wavelength of the waves, meant that these waves may be classified as weakly nonlinear. The effect of this nonlinearity is discussed in greater detail in section 7.4. The waves themselves propagated in a dispersive packet. The phase velocity of these waves was greater than the landslide terminal velocity, so that waves at the front of the packet propagated over the landslide and were destroyed and new waves were created at the rear of the packet. However, the landslide velocity was greater than the group velocity of these waves, so that the landslide remained within the packet for the duration of the constant-velocity phase of motion.

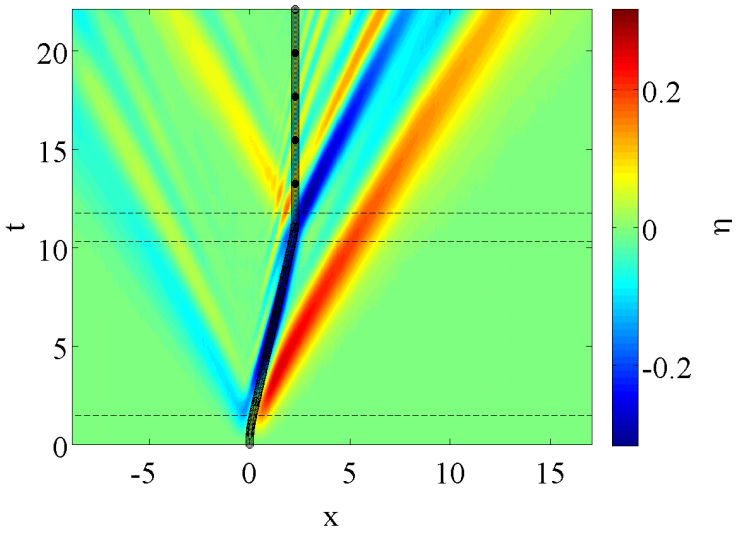

Figure 7.18: Wave field generated during an experiment with $\lambda = 0.153$, $\tau = 0.35$ and $Fr = 0.375$.

As shown by the wave field plot of figure 7.18, the amplitude of the free surface de-

pression was significantly larger than the amplitude of the leading onshore-propagating trough. Thus, the constant-velocity landslide motion played a larger role in the exchange of energy between the landslide and the generated waves than at the lower Froude numbers. Figure 7.19 shows that this behaviour was consistent for all experiments at this Froude number. The peak amplitude of the onshore-propagating crest is not shown in this figure, due to the superposition of this wave with the group of trapped waves generated during the constant-velocity landslide motion. The dependence of the peak leading wave amplitudes on λ and τ was similar to $Fr = 0.250$.

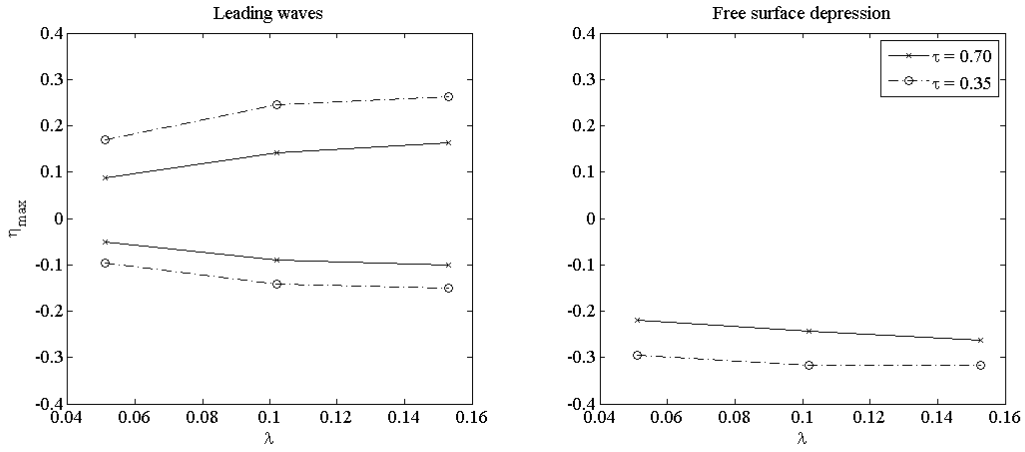

Figure 7.19: Variation in peak wave amplitudes for all experiments with $Fr = 0.375$.

Figure 7.20 shows the time variation of the potential energy within the entire wave field for all experiments conducted with $Fr = 0.375$. The longer duration of the landslide acceleration led to a more gradual increase to the peak E_P value, however the fluctuations in energy observed during the constant-velocity phase of motion had longer periods than those observed at $Fr = 0.250$. This is partly due to the landslide's position within the wave packet. Since the terminal velocity of the landslide was higher, waves within the offshore-propagating wave packet had longer wavelengths when they passed over the landslide. The longer wavelengths hence increased the period of interaction between a given wave and the free surface depression above the landslide, so that the fluctuations in potential energy due to this interaction also had longer periods than observed at $Fr = 0.250$.

The potential energy within the wave field increased more rapidly to its peak value at the higher λ values, where the peak value increased with λ. However, the potential energy within the wave field during the constant-velocity phase of motion was almost identical for the experiments with $\lambda = 0.102$ and $\lambda = 0.153$. The occurrence of wave reflections before the start of the landslide deceleration caused the second peak to be less pronounced than at previous Froude numbers.

The increased interaction between the offshore-propagating waves and the moving

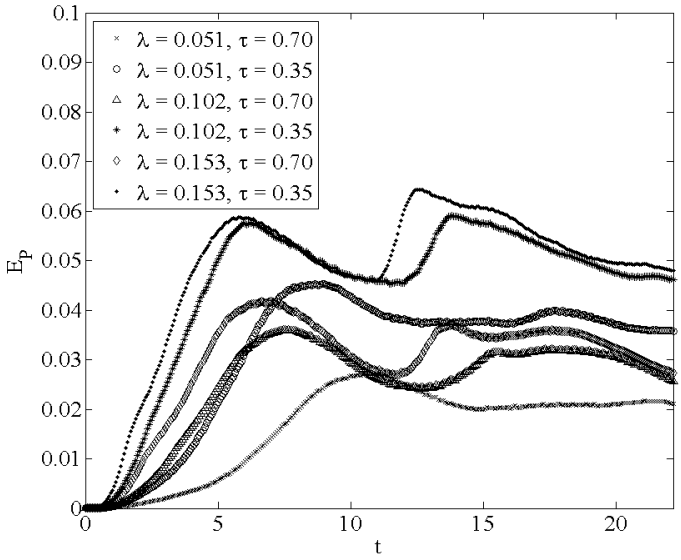

Figure 7.20: Time variation in wave field potential energy for all experiments with Fr = 0.375.

landslide resulted in significantly greater amounts of energy contained in the offshore region than in the onshore region at this landslide Froude number. Figure 7.21 compares the energy within the onshore and offshore regions for all experiments with Fr = 0.375 and τ = 0.35. At this Froude number, the energy contained within the offshore region was approximately one order of magnitude larger than the energy contained within the onshore region. The initial peak in the onshore energy was very pronounced at the two larger λ values, as was the effect of the wave reflections on the energy within this region. The attenuation of onshore energy during the constant-velocity phase of motion was also observed at this Froude number.

The general behaviour of the directional mass transport by the two wave packets (shown in figure 7.22 for τ = 0.35) was similar to that observed at the previous two landslide Froude numbers, although the magnitude of this mass transport was larger at this Froude number. The higher landslide accelerations caused an initial peak in the directional mass transport, and the 'steady' values of mass within the onshore and offshore regions effectively balanced.

As shown in figure 7.23, the interaction between the landslide and the offshore-propagating waves was different at this Froude number to the lower landslide Froude numbers. The amplitude of the free surface depression did not oscillate as rapidly as at the lower Froude numbers (discussed above), and the steepening of the short-period waves directly behind the landslide decreased the dispersion of energy into the longer-wavelength waves in front of the landslide.

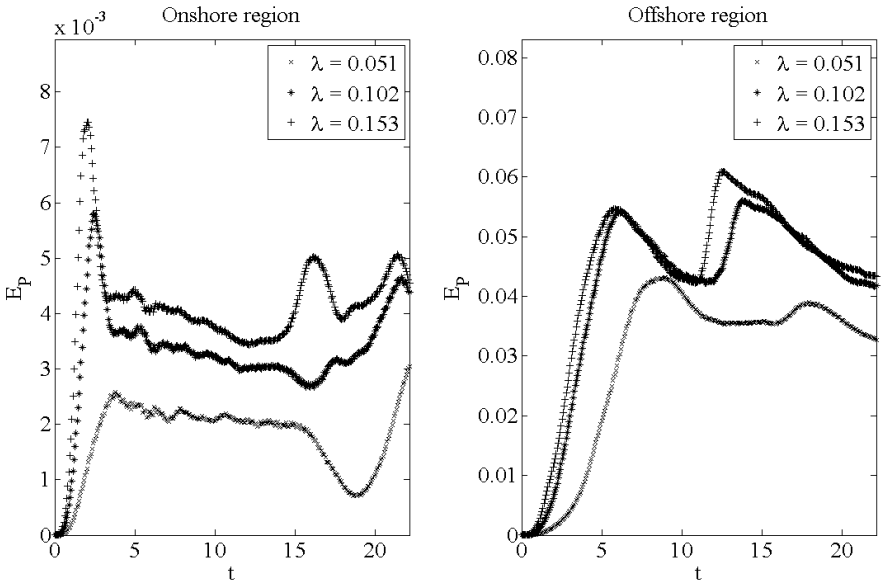

Figure 7.21: Time variation in onshore and offshore potential energy for all experiments with $Fr = 0.375$ and $\tau = 0.35$.

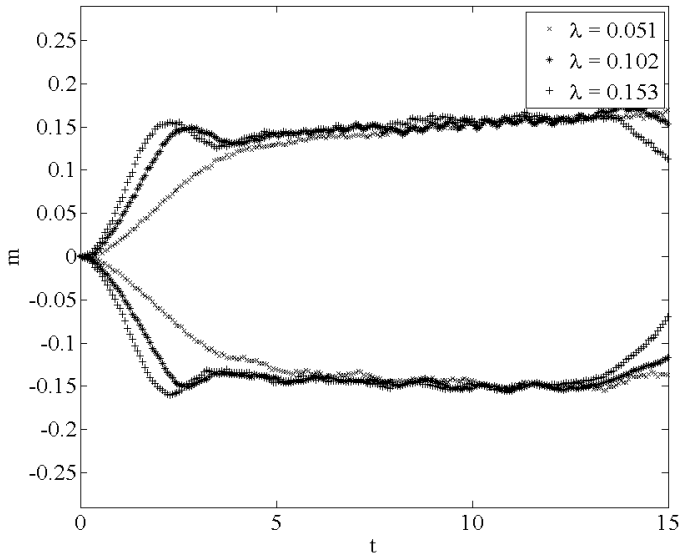

Figure 7.22: Time variation in onshore and offshore mass for all experiments with $Fr = 0.375$ and $\tau = 0.35$.

7.3.4 Wave field behaviour at $Fr = 0.500$

The highest landslide Froude number tested during the main parametric study was 0.500, and the trends in wave field behaviour observed at the previous Froude numbers were also observed during experiments at this Froude number. Figure 7.24 shows the wave field generated during Run 24, with the parameters $\lambda = 0.153$, $\tau = 0.35$ and Fr

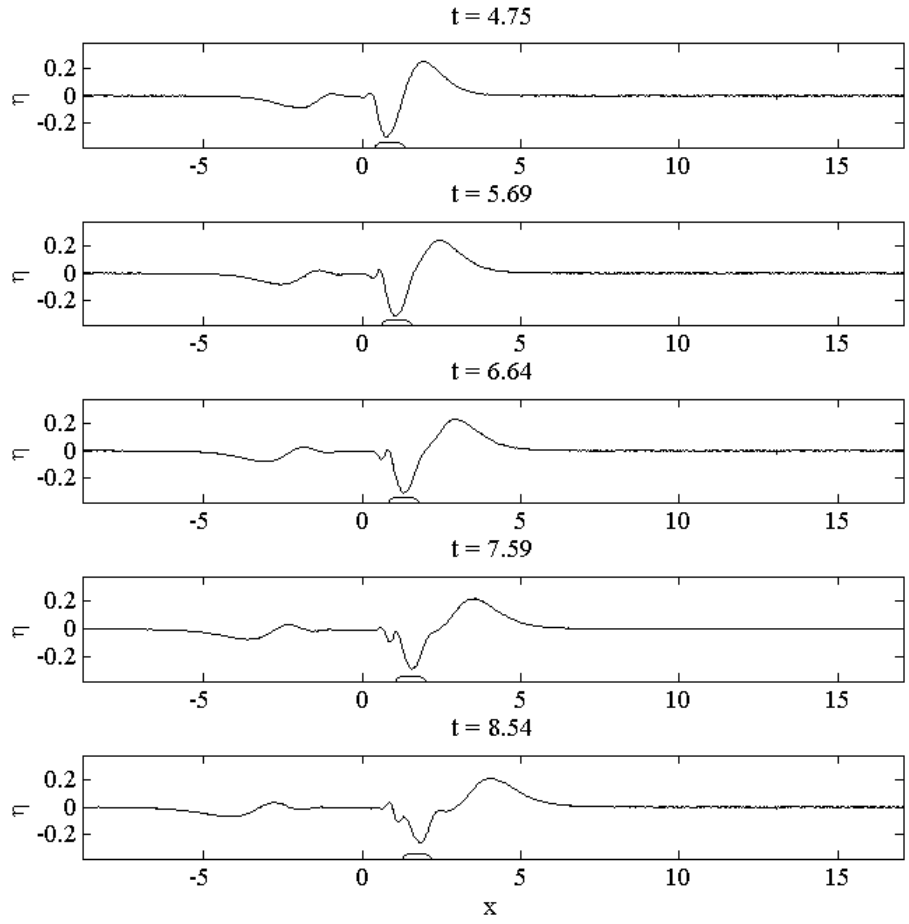

Figure 7.23: Interaction between moving landslide and offshore-propagating waves for Run 23, with parameters $\lambda = 0.153$, $Fr = 0.375$, and $\tau = 0.35$.

$= 0.500$. The offshore-propagating waves in this experiment were much larger than the onshore-propagating waves, as shown by the relatively faint colour bands associated with the onshore-propagating waves. The majority of the energy exchange between the landslide and the wave field occurred during the constant-velocity phase of motion.

The free surface depression above the landslide was now approximately double the amplitude of the leading offshore-propagating crest, and the group of trapped waves identified in Run 23 exhibited much stronger nonlinear behaviour. These trapped waves propagated behind the landslide during its constant-velocity motion, and quickly grew in amplitude until they were also larger than the leading offshore-propagating crest. The trapped waves were almost uniform in wavelength during the constant-velocity phase of motion, with a nondimensional wavelength of 0.508. The effects of the nonlinearity of these waves on the wave field behaviour in the vicinity of the landslide are discussed later in this section.

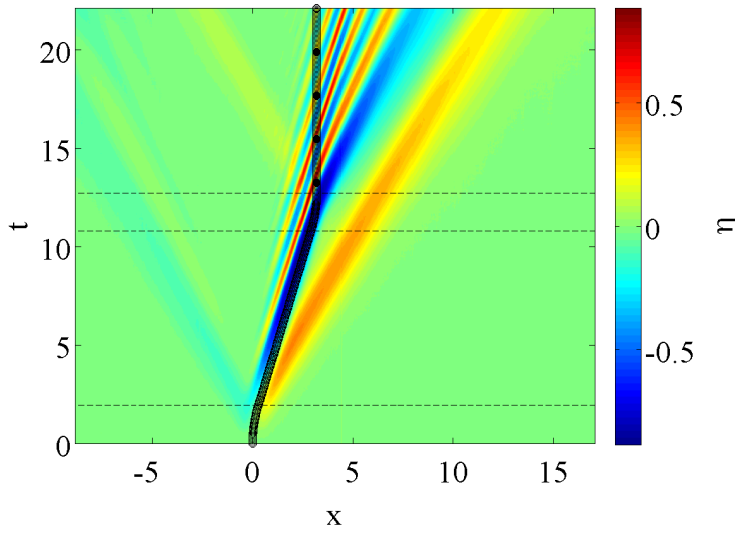

Figure 7.24: Wave field generated during an experiment with $\lambda = 0.153$, $\tau = 0.35$ and $Fr = 0.500$.

Figure 7.25 shows the variation in the peak leading wave and free surface depression amplitudes for all experiments conducted at $Fr = 0.500$. The onshore-propagating crest amplitudes are not shown due to the presence of the trapped waves behind the landslide (similar to the behaviour at $Fr = 0.375$). The peak amplitudes of the free surface depression were approximately twice as large as the leading crest amplitudes, and approximately four times as large as the leading trough amplitudes. Although the leading wave amplitudes showed similar λ and τ dependence to those measured at previous Froude numbers, the free surface depression exhibited virtually no dependence on λ. This is an expected result, since the hydraulic theory predictions consider this free surface depression a steady-state phenomenon.

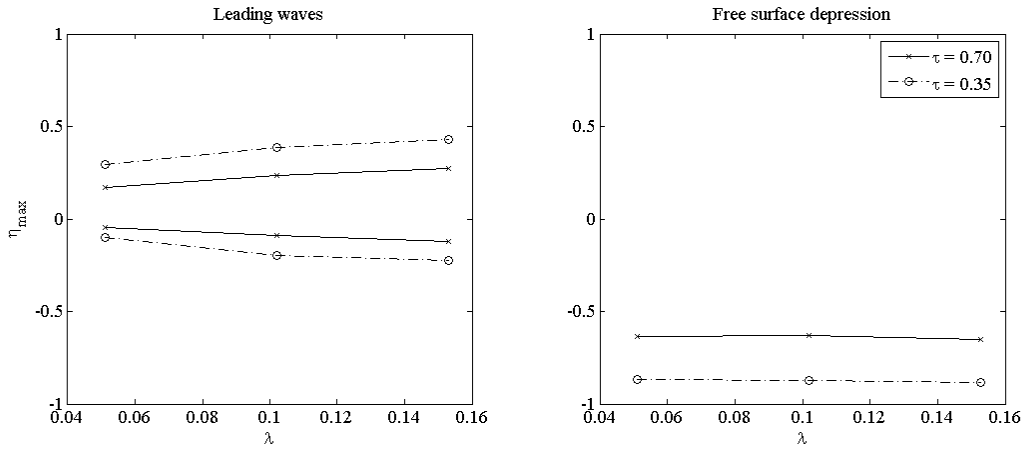

Figure 7.25: Variation in peak wave amplitudes for all experiments with $Fr = 0.500$.

The large amplitudes of the trapped waves behind the landslide meant that the constant-velocity phase of motion was more important than the acceleration or deceleration periods in the exchange of energy between the landslide and the generated wave field. However, the rate at which the potential energy within the wave field initially increased still depended on the magnitude of the landslide acceleration. Figure 7.26 shows the time variation in potential energy within the wave field for all experiments carried out at this Froude number. In this case, the energy within the wave field continued to increase after the landslide acceleration had finished, and reached its peak value much later than at the lower Froude numbers.

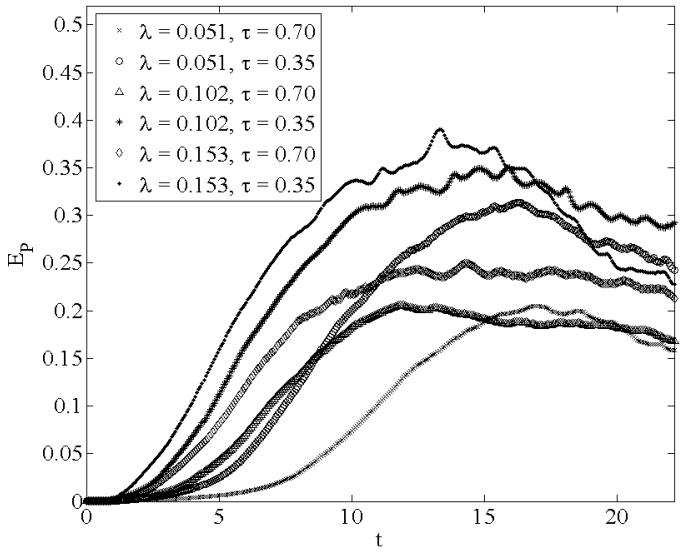

Figure 7.26: Time variation in wave field potential energy for all experiments with $Fr = 0.500$.

Figure 7.27 shows the potential energy contained within the onshore and offshore domains for experiments conducted at $Fr = 0.500$ and $\tau = 0.35$. The results at this Froude number continued the trend in energy distribution between the onshore and offshore wave groups observed at previous Froude numbers, and the energy within the offshore region was at least 30 times larger than the energy within the onshore region. Thus, the majority of the potential energy within the wave field was contained in the offshore region, and most of this energy was input into the wave field by the constant-velocity landslide motion. The energy within the onshore region generally exhibited similar attenuation to previous Froude numbers, with attenuation between 5% and 10% of the peak onshore energy. However, at the lowest nondimensional landslide acceleration the potential energy within the onshore region slightly increased during the constant-velocity phase of motion. The energy within the offshore region also exhibited some fluctuations during the constant-velocity phase of motion. These

fluctuations were even more evident in the plots of the mass within the offshore region, and are discussed below.

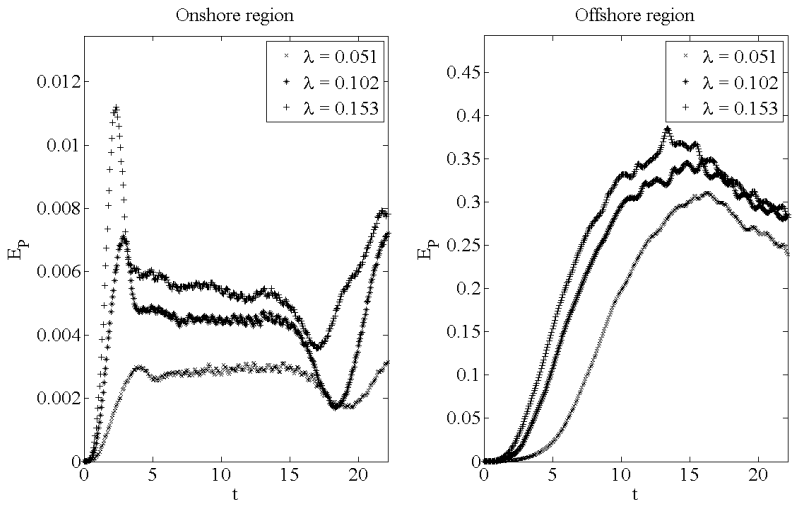

Figure 7.27: Time variation in onshore and offshore potential energy for all experiments with $Fr = 0.500$ and $\tau = 0.35$.

Despite the significantly higher potential energy contained within the offshore region, the mass contained within the onshore and offshore regions was approximately equal during this experiment. However, at this landslide Froude number the mass in the offshore region exhibited some relatively low-frequency fluctuations during the constant-velocity phase of motion. These fluctuations had an amplitude of approximately 20% of the peak mass within the offshore region, and a period of approximately 2 nondimensional time units. Interestingly, although these fluctuations may also be observed in the offshore energy at this Froude number, they were much more prominent in the offshore mass. Since the energy depends on η^2, this is a somewhat surprising result, however it may be due to the large amount of energy within the leading offshore-propagating crest compared to the trapped waves.

As an example of these fluctuations in energy and mass, figure 7.28 compares the time-dependent behaviour of potential energy and mass calculated from the wave field of Run 16, with the parameters $\lambda = 0.102$, $\tau = 0.35$, and $Fr = 0.500$. The fluctuations in the mass record were relatively much larger than the fluctuations in the potential energy, and the mass appeared to fluctuate at a slightly lower frequency than the energy.

Sue (2007) observed very similar fluctuations in mass during his experiments, and found that these were caused by the errors associated with joining together the water surface profiles from his different camera positions. Since his camera captured images at a rate of 15 Hz, the frame rate of 70 Hz used in the LIF experiments within the current study greatly reduced these positioning inaccuracies. However, the waves pro-

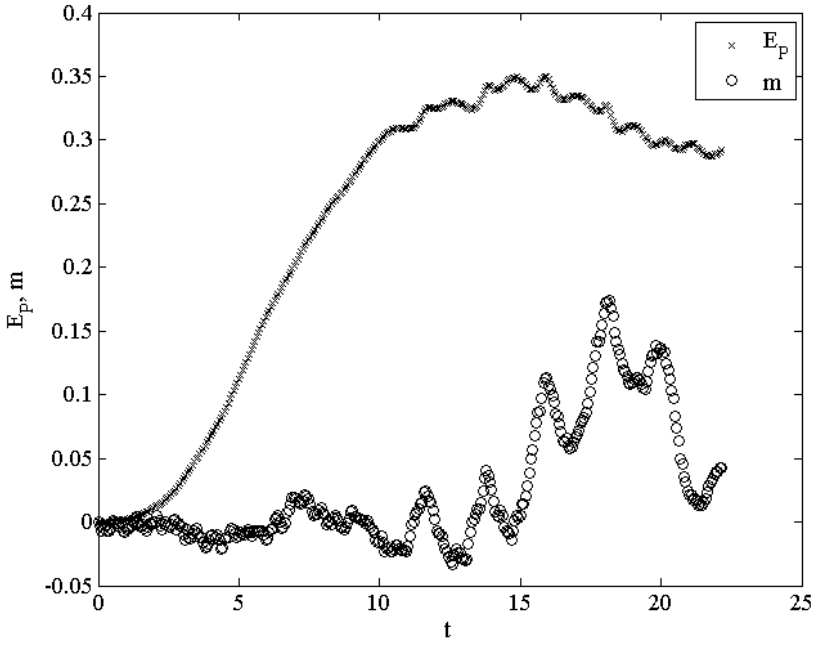

Figure 7.28: Time variation in total potential energy and mass for all experiments with $Fr = 0.500$ and $\tau = 0.35$.

pagating at the landslide velocity at this Froude number were very steep, so that a small positioning inaccuracy could lead to relatively large errors in free surface displacement. Additionally, the joins in the acrylic sidewalls were approximately 30 mm wide (or 0.06 in nondimensional terms), and LIF measurements were not available over the joins. Although interpolation of the free surface record led to negligible errors for the longer-wavelength waves, the relatively short wavelengths and high amplitudes of the trapped waves could have caused slight under-estimation of the peak crest and trough amplitudes. This would lead to alternating under-estimation and over-estimation of the mass within the system, as observed in figure 7.28

The interaction between the landslide and the offshore-propagating waves at this Froude number led to the high amplitudes of the short-wavelength waves directly behind the landslide. These waves propagated with a phase speed approximately equal to the terminal velocity of the landslide, such that they received energy input from the landslide. This is similar to the Proudman resonance, where an atmospheric disturbance travelling at the same speed as the waves it generated is able to continuously input energy into the waves. Due to their short wavelengths, the steepness of these waves quickly increased to the point where nonlinear effects became pronounced. These waves are illustrated in figure 7.30, which shows wave field plots captured during the constant-velocity phase of motion during Run 12 ($\lambda = 0.153$, $Fr = 0.500$, and $\tau = 0.35$).

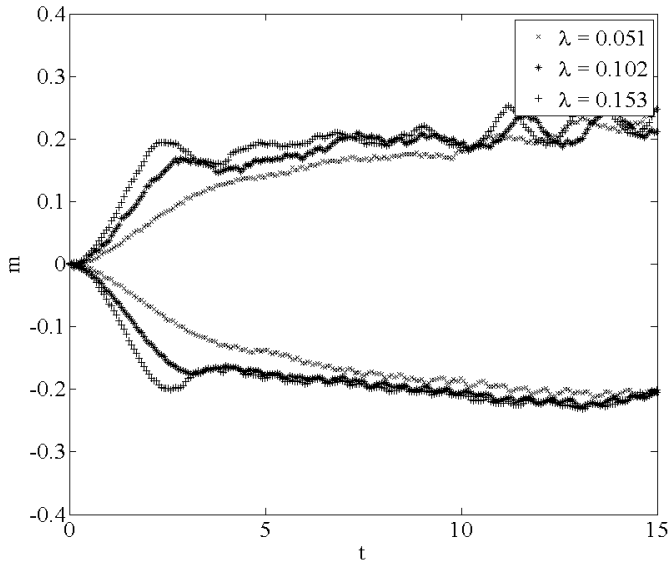

Figure 7.29: Time variation in onshore and offshore mass for all experiments with Fr = 0.500 and τ = 0.35.

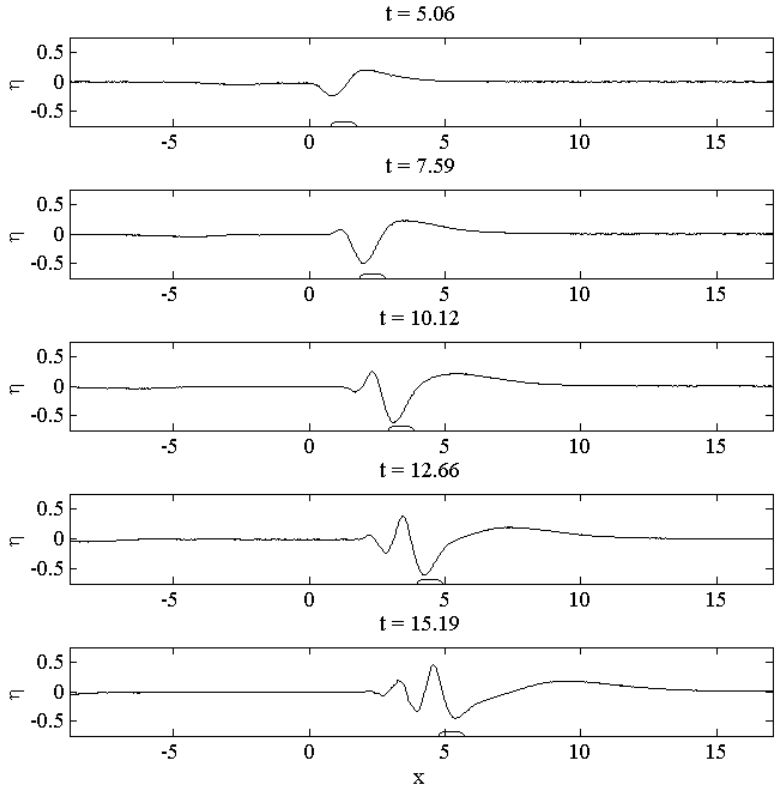

Figure 7.30: Interaction between moving landslide and offshore-propagating waves during the constant velocity phase for Run 12, with parameters λ = 0.102, Fr = 0.500, and τ = 0.70.

7.4 Interaction between landslide and offshore-propagating waves

This section examines the interaction between the landslide and the offshore-propagating wave packet in more detail, using the results of Runs 27-30. These experiments had the same parameters as Runs 21-24, however the constant-velocity phase of motion lasted much longer, so that the landslide did not decelerate until after the cessation of image capture. This longer period of constant velocity led to a longer period of preferential energy exchange between the landslide and a narrow band of wavelengths, which approximately satisfied $c_p = u_t$.

Due to the longer duration of the constant-velocity phase of motion, the free surface depression remained above the landslide for the majority of each experiment. This allowed the behaviour of this free surface depression to approach the steady state assumed by the predictions of hydraulic theory discussed in section 7.2. Figure 7.31 shows the time variation of the free surface depression amplitude recorded during Runs 27-30. The dotted lines show the amplitude predicted by hydraulic theory for each experiment, from table 7.1.

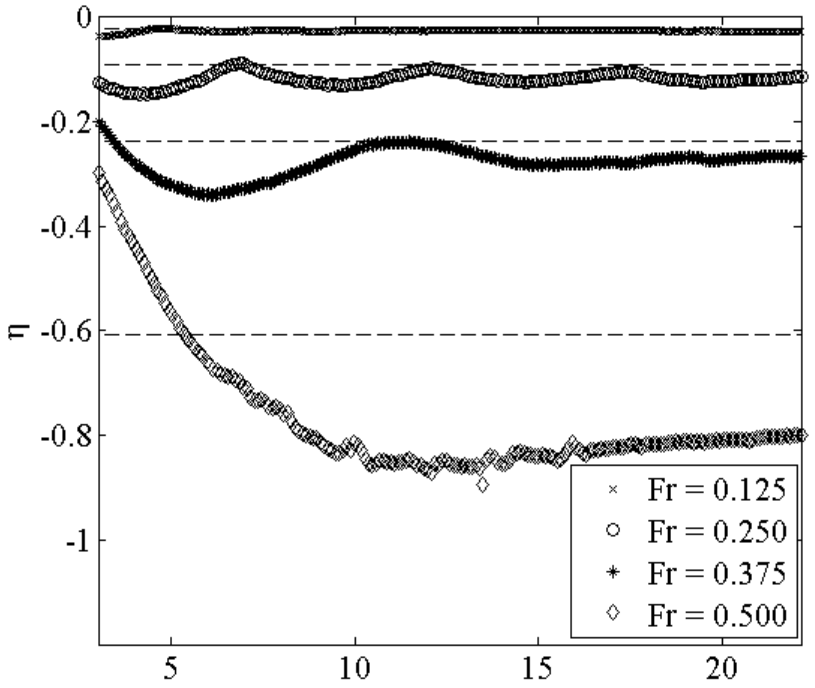

Figure 7.31: Time series of free surface depression amplitude for all landslide Froude numbers.

Figure 7.31 shows that hydraulic theory correctly predicted the increase in free surface depression amplitude observed throughout the parameter space in the physical

experiments. However, at each of the Froude numbers the actual depression amplitude was larger than the predicted value. Additionally, figure 7.31 also shows that the depression amplitude fluctuated around its steady value over time, due to interactions with the offshore-propagating waves. The time period of these fluctuations increased with Fr, due to the larger wavelengths of the waves passing over the landslide. These fluctuations made the level of under-prediction difficult to quantify (particularly at the higher Froude numbers). However, the under-predictions may be estimated to be between 16% and 20% for the lower Froude numbers, increasing to approximately 25% at $Fr = 0.500$.

As discussed in section 7.3, the interaction between the landslide and the offshore-propagating waves also generated a group of trapped waves behind the landslide. These waves, which propagated at approximately the terminal velocity of the landslide, increased in amplitude due to the energy input from the moving landslide, with a greater energy input occurring at higher landslide Froude numbers. This increase in amplitude also had the effect of increasing the steepness of the waves. At the experiments conducted at Froude numbers of 0.375 and 0.500, this increase in steepness increased the nonlinearity of these waves. The applicability of linear wave theory may be estimated by the size of the parameter ϵ, defined as

$$\epsilon = \frac{a}{\lambda}, \tag{7.8}$$

where a is the wave amplitude and λ is the wavelength (rather than the landslide acceleration, as used elsewhere in this report). According to Le Mehaute (1976), waves exceeding $\epsilon = 0.0031$ are defined as nonlinear waves, although linear wave theory may be used for waves beyond this range. The breaking limit for waves is $\epsilon = 0.07$. At the lowest Froude number of 0.125, this group of trapped waves was not evident even with the longer period of constant velocity. However, they could be observed for the other Froude numbers. Table 7.2 shows the values of ϵ recorded for the experiments conducted with $Fr = 0.250$, 0.375 and 0.500. The waves propagating with the landslide were very weakly nonlinear at $Fr = 0.250$, however they were mildly and strongly nonlinear at $Fr = 0.375$ and 0.500 respectively. The waves can also be classified as deep-water waves, according to the equation

$$\mu = \frac{D}{\lambda}, \tag{7.9}$$

where D is the fluid depth and λ is the wavelength. A value of μ greater than 0.5 implies fully dispersive deep-water waves. The lowest value of μ within these trapped wave groups was 0.69, demonstrating that the waves may be classified as dispersive deep-water waves over the range of Froude numbers investigated in the experiments.

The wave field generated during Run 30 allows a closer investigation of the effects

Table 7.2: Nonlinearity of the waves propagating with the landslide during its constant-velocity motion

Fr	ϵ
0.250	0.0033
0.375	0.0159
0.500	0.047

of nonlinearity on this group of generated waves. Figure 7.32 shows the wave field plot for this experiment, Run 30. The group of trapped waves had almost uniform wavelengths during the constant-velocity motion, and propagated at approximately the phase velocity of the landslide.

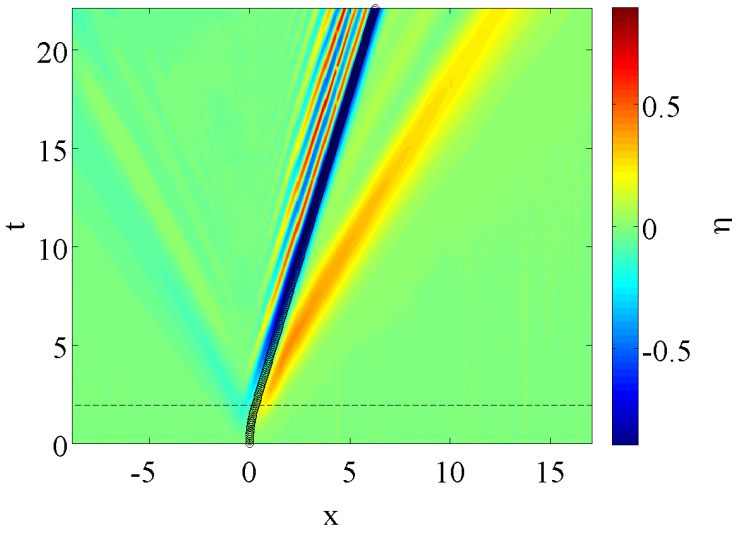

Figure 7.32: Wave field plot, showing trapped waves behind landslide, for Run 30 (with $\lambda = 0.153$, $\tau = 0.35$, $Fr = 0.500$ and no landslide deceleration).

The effects of nonlinearity on waves are generally to increase their phase velocity, and to steepen their crests. This steepening conflicts with the effects of wave dispersion, which broadens wave fronts. The effect of nonlinearity on the phase velocity may be deduced by calculating the phase velocity of the waves according to linear theory, and comparing this with the phase velocity calculated using Stokes' expansion for weakly nonlinear waves. For deep-water waves, the phase velocity of a linear wave may be calculated as

$$c_p = \sqrt{\frac{g\lambda}{2\pi}}, \tag{7.10}$$

while the phase velocity of a weakly nonlinear wave may be calculated as

$$c_p = \sqrt{\frac{g\lambda}{2\pi}\left(1 + \frac{H^2\pi^2}{\lambda^2}\right)}, \tag{7.11}$$

where λ again represents the wavelength of the wave, and H is the wave height. The trapped waves in Run 30 had a wavelength of approximately 0.508 (in nondimensional terms). Assuming linearity of the waves, this corresponds to a nondimensional phase velocity of 0.284, while the nondimensional phase velocity calculated according to equation 7.11 is 0.297. The actual terminal velocity of the landslide was 0.296 in nondimensional terms. Thus, the effect of wave nonlinearity was to increase the phase velocity of the trapped waves in Run 30 by approximately 4%.

The deep-water classification of these waves meant that dispersion acted to broaden the wave fronts, spreading their energy over longer wavelengths. However, nonlinearity acted to steepen the waves, so that the amount of energy passed to longer wavelengths (or lower wavenumbers) due to dispersion was reduced. Figure 7.33 shows the shape of the waves propagating with the landslide during Run 30. The trapped waves had narrow crests and broad troughs, demonstrating that nonlinearity had a significant effect on their shape.

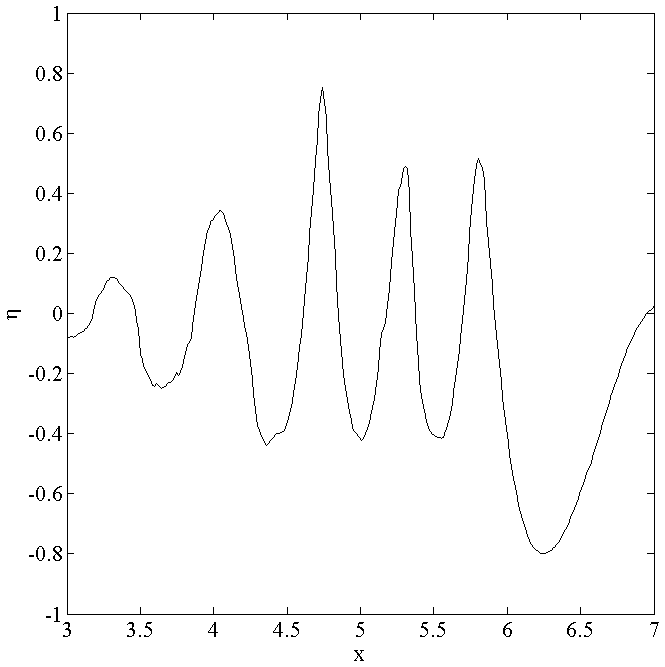

Figure 7.33: Snapshot of trapped waves, showing narrow crests and broader troughs, for Run 30 (with $\lambda = 0.153$, $\tau = 0.35$, $Fr = 0.500$ and no landslide deceleration).

In the extreme case where nonlinear effects fully balance dispersive effects, wave propagation is governed by the KdV equation, and waves propagate without any change

in form. However, the effects of dispersion were stronger than the effects of nonlinearity on these waves for several reasons. First, the KdV equation assumes that $\alpha = a/D \ll 1$ and $\beta = D/\lambda \ll 1$, where α represents nonlinear effects and β represents dispersive effects. In these experiments, the maximum value of α was approximately 0.069, and so this condition was satisfied. However, the minimum value of β was approximately 0.69, such that this condition clearly was not satisfied (and dispersive effects can be assumed to be more prominent than nonlinear effects). Additionally, the KdV equation assumes that the waves propagate at a velocity that is asymptotically close to the shallow water wave speed, while the maximum phase velocity of these trapped waves during the experiments was half of this speed (for $Fr = 0.5$). Thus, the effects of nonlinearity and dispersion were not in balance within this wave group, although the energy input from the landslide into the trapped waves acted to increase their amplitude (and hence, steepness), so that nonlinear effects lasted longer than would otherwise be possible. The effect of nonlinearity on the waves propagating past the moving landslide is examined in more detail in chapter 8.

Since the waves propagated as deep-water waves, the group velocity of the waves was approximately half of their phase velocity. For this reason, new waves were created at the back of the group of the trapped waves. However, since the landslide travelled at approximately the phase velocity of the leading wave within the group during Run 30, the landslide could constantly input energy into this wave. Therefore, waves were not destroyed at the front of the wave packet (due to the input of energy from the landslide), and so the group grew in spatial extent throughout the constant-velocity phase of landslide motion.

To investigate the nonlinear behaviour of the trapped waves observed at the higher Froude numbers, two additional experiments (Run 25 and Run 26) were carried out at the higher Froude number values of 0.625 and 0.750. Figures 7.34 and 7.35 show the wave field plots for these two experiments. These wave field plots are very similar, in terms of the wave field behaviour and the amplitudes of the generated waves. The first crest behind the landslide broke in both experiments. This breaking is unsurprising, given the trends in wave nonlinearity observed in Runs 28 to 30, as stated in table 7.2. Since the trapped waves approached the breaking limit for $Fr = 0.500$, the further increase in wave steepness at $Fr = 0.625$ and 0.750 was sufficient to cause breaking of this wave.

Figures 7.36 to 7.38 show the raw images of the breaking wave crest recorded during Run 25. Each image was recorded at a different gantry location, since the rapid landslide motion meant that the wave breaking occurred over several gantry locations.

The wave breaking complicated the free surface identification process, since the free surface became multi-valued near the location of the wave breaking. The surface identification algorithm simply located the first vertical location (starting from above)

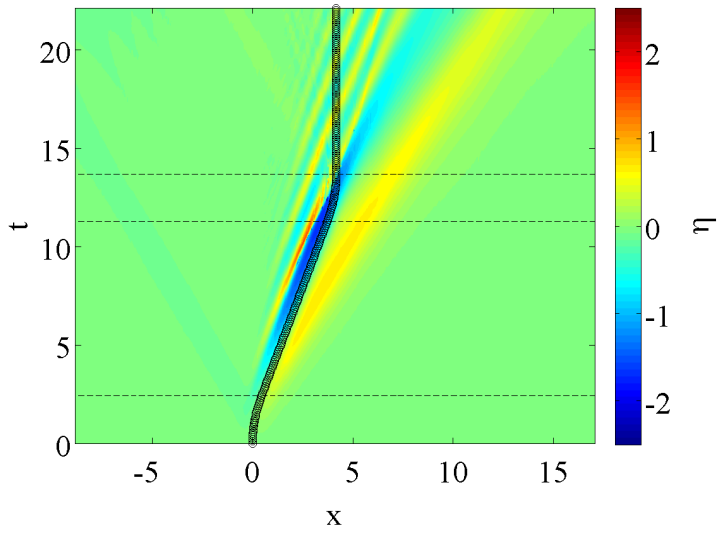

Figure 7.34: Wave field generated during an experiment with $\lambda = 0.153$, $\tau = 0.35$ and $Fr = 0.625$.

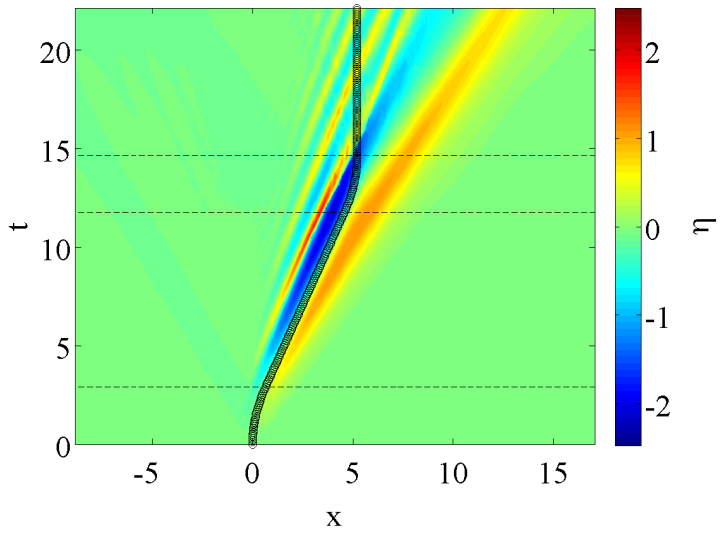

Figure 7.35: Wave field generated during an experiment with $\lambda = 0.153$, $\tau = 0.35$ and $Fr = 0.750$.

where an air-water interface was present. This meant that droplets could be incorrectly identified as the free surface, and the presence of entrained air within the breaking wave could not be determined. Because of this, the results of these experiments may only be used in a qualitative manner. However, it is evident that resonant behaviour occurred at landslide Froude numbers greater than 0.500, due to the waves trapped behind the landslide.

The open channel flow analogy used to predict the approximate amplitude of the free surface depression during the constant-velocity phase of motion was unable to

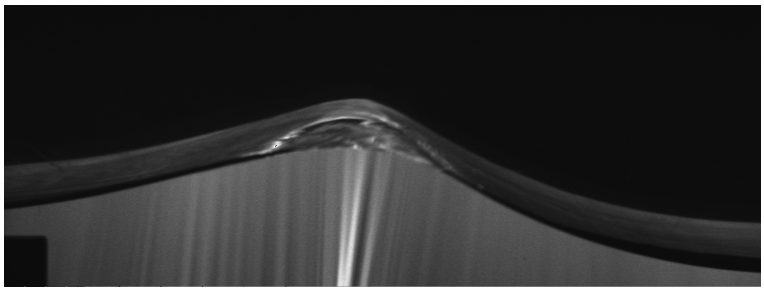

Figure 7.36: Raw image from Run 25, showing wave steepening prior to breaking, for the gantry located at $x = 1.66$.

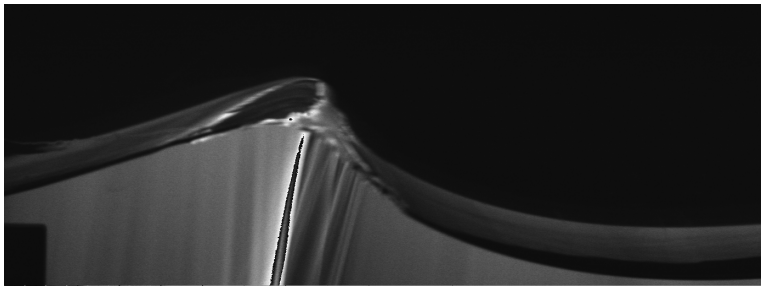

Figure 7.37: Raw image from Run 25, showing initial wave breaking, for the gantry located at $x = 2.36$.

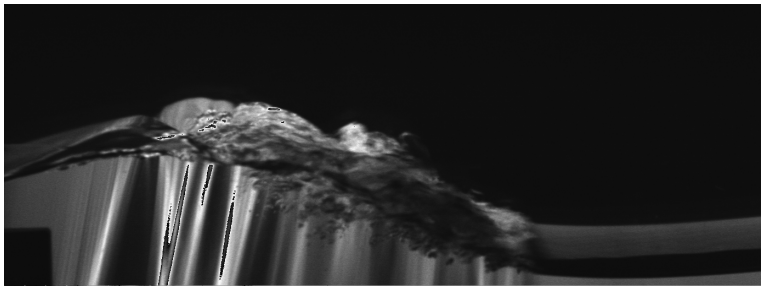

Figure 7.38: Raw image from Run 25, showing free surface after breaking of the trapped wave crest, for the gantry located at $x = 3.06$.

provide stable predictions for either Run 25 or Run 26. At these combinations of τ and Fr, the change in bed elevation (due to the landslide thickness) decreased the specific energy to a point below its critical value. Since the open channel flow analogy assumes steady flow, and the breaking of the highly nonlinear waves occurred relatively early in the physical experiments at these Froude numbers, the open channel flow analogy is limited in its applicability.

7.5 Subsurface velocity measurements

7.5.1 Eulerian velocity field

The particle tracking velocimetry experiment was conducted to allow further investigation into the wave trapping mechanism observed in the higher-Fr experiments (using Run 12, with $\lambda = 0.102$, $\tau = 0.70$ and $Fr = 0.500$), and to provide experimental data to validate the subsurface predictions of the numerical models. Chapter 8 discusses the key differences between the predicted and measured velocity fields, and their effects on the predictive capabilities of the inviscid and viscous numerical models. This section describes observations of the subsurface velocity field, and the interaction between flow around the moving landslide and the generated waves.

The initial acceleration of the landslide generated strong positive vertical velocities at the front of the landslide, and negative vertical velocities at its rear. The horizontal velocities were positive at both ends of the landslide, and negative above the landslide, as fluid flowed over it. Thus, the magnitudes of the velocity field were almost symmetrical about the landslide (with slightly higher velocities near the rear of the landslide). Figure 7.39 shows the magnitude of the velocity field generated by the landslide motion at $t = 2.95$, near the end of the acceleration period. The free surface measured during the LIF experiments is overlaid (nondimensionalised by the landslide thickness, and scaled by 1:2 to assist visualisation), as is the location of the landslide. It should be noted that the vertical coordinate direction, y, was scaled by L_b in these images, hence the wave amplitudes are exaggerated. The landslide location itself was not recorded during the PTV experiments.

During the landslide acceleration, the highest fluid velocities were in the flow around the moving landslide. However, fluid particles also moved in orbital motions beneath the waves on the free surface. At $t = 2.95$, the highest velocities near the free surface were located beneath the depression, rather than beneath the leading waves. No wake could be observed during the acceleration of the landslide.

During the constant-velocity phase of motion, a turbulent wake was generated behind the landslide, and this affected the flow field around the landslide. Figure 7.40 shows the horizontal velocity field recorded at $t = 9.95$, and figure 7.41 shows the equivalent vertical velocity field. The vertical velocities beneath the free surface waves decayed rapidly with depth, in a similar manner to the vertical velocities generated at the front and rear of the landslide. The horizontal velocities beneath the free surface depression and above the moving landslide were larger in magnitude, and exhibited less decay over the fluid depth, since the free surface depression is more a contraction in flow depth due to energy considerations than a wave. Figures 7.40 and 7.41 also clearly show the presence of the turbulent wake behind the landslide. The wake moved in the positive horizontal direction, and the mean horizontal velocities within the wake

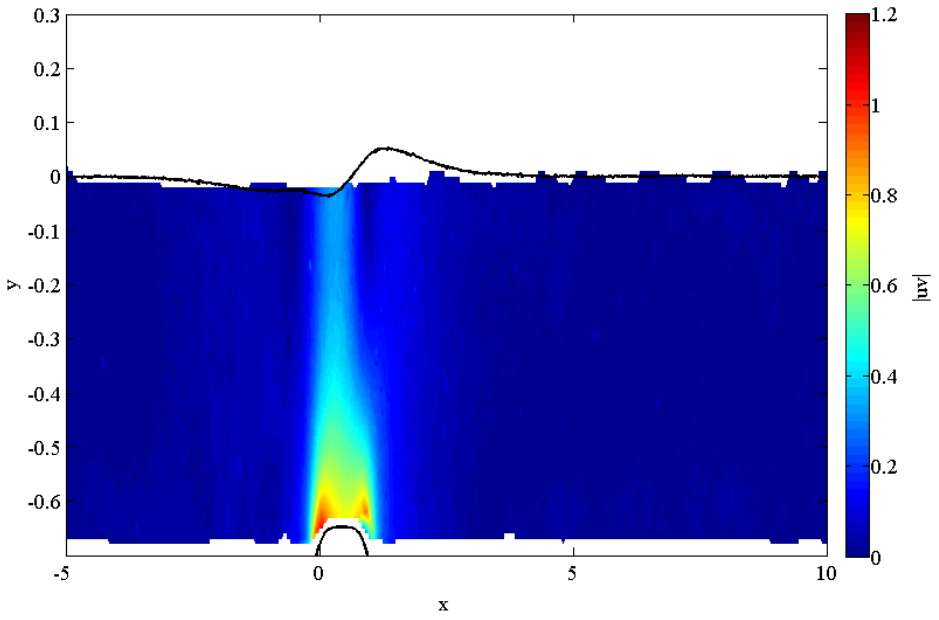

Figure 7.39: Magnitude of the velocity field generated by the landslide acceleration.

were higher than the alternating vertical velocities.

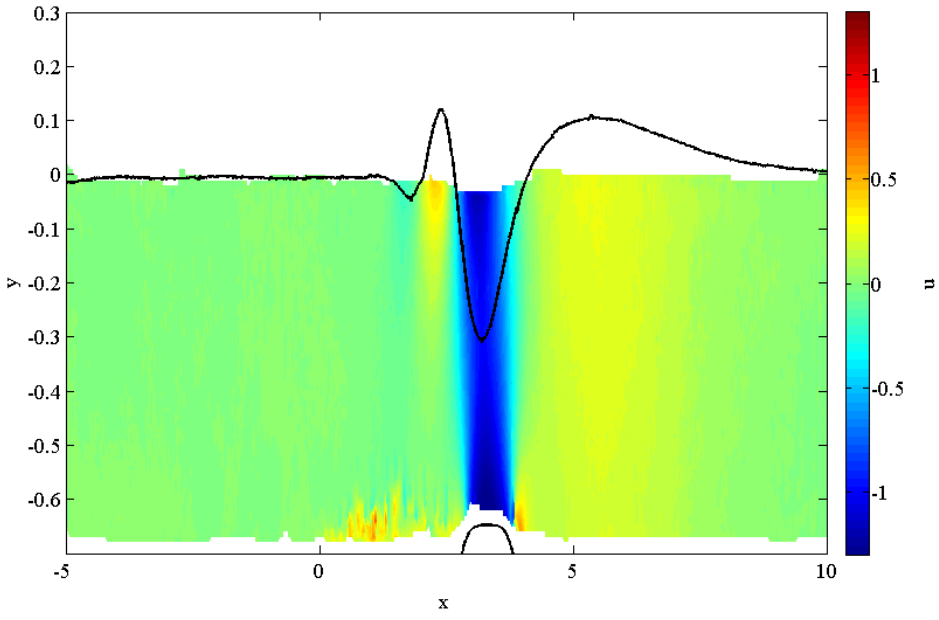

Figure 7.40: Horizontal velocity field generated by the constant-velocity landslide motion.

The fluid velocities around the moving landslide were still similar to those during the acceleration period, however the velocities near the rear of the landslide were modified by the presence of the turbulent wake. As observed in the previous sections, the free

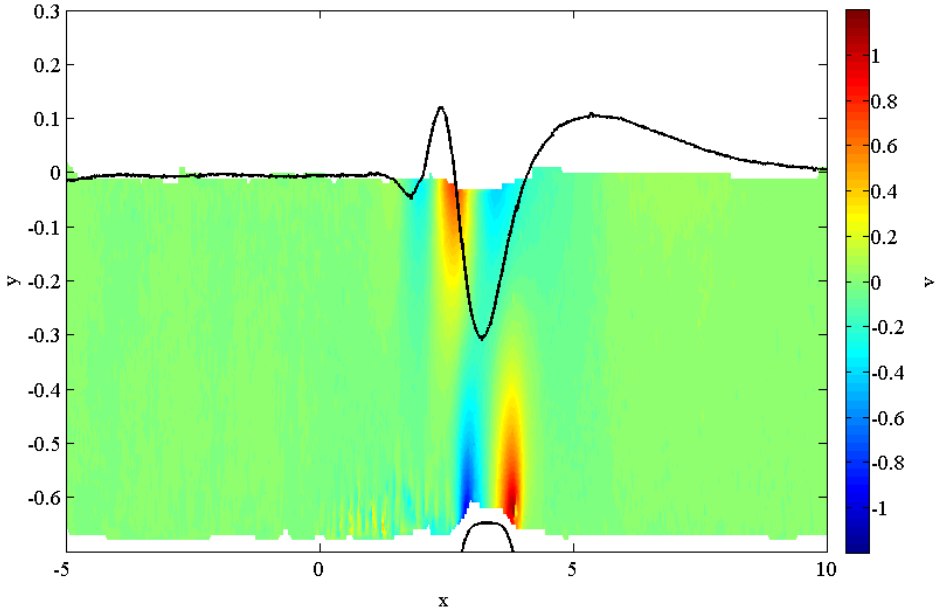

Figure 7.41: Vertical velocity field generated by the constant-velocity landslide motion.

surface depression was located slightly behind the landslide centre of mass, and figure 7.42 shows the location of this free surface depression relative to the magnitude of the subsurface fluid velocities. Due to the longer wavelength of the leading offshore-propagating crest, the velocities beneath this wave were almost independent of the fluid depth, although these velocities were approximately 25% of the magnitude of the velocities beneath the free surface depression.

After the landslide came to rest, the highest velocities within the fluid were beneath the free surface waves. The turbulent wake continued to propagate in the positive x-direction, and eventually rolled over the landslide.

7.5.2 Particle velocities beneath free surface waves

Although the Eulerian velocity fields are useful in considering the subsurface fluid velocities throughout the length of the flume, the Lagrangian velocities of individual particles also offer insights into the subsurface fluid motion. As shown in the previous sections of this chapter, the offshore- and onshore-propagating wave packets transported positive and negative mass (respectively). The Lagrangian particle velocities allow determination of the effect of this mass transport on the particle trajectories. The velocities and trajectories of particles discussed in this section use particles located at approximately $x = 9.7$, and hence consider the offshore-propagating waves only.

Figure 7.43 compares the time series of the wave amplitudes at $x = 9.7$ with the horizontal and vertical velocities of a single particle at the same horizontal location.

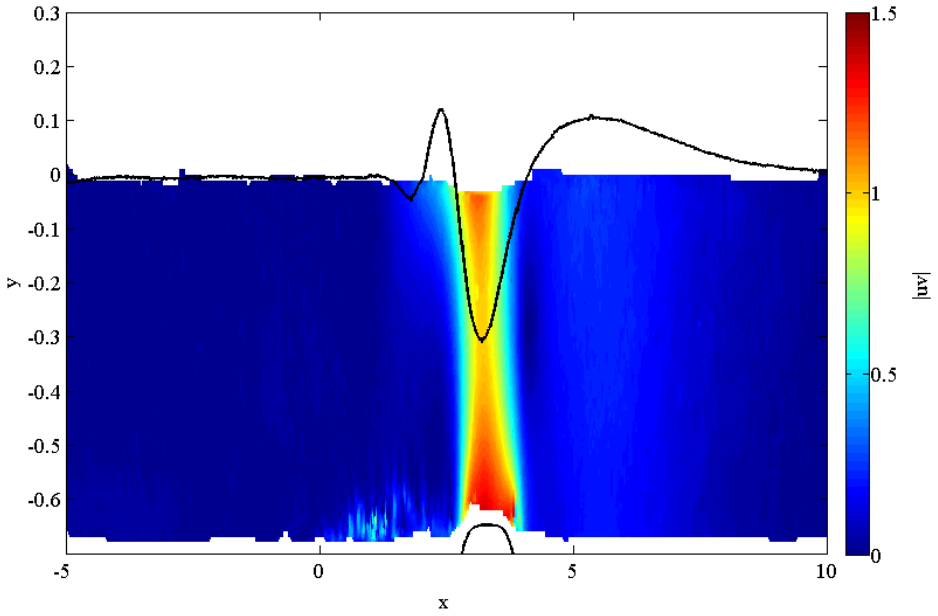

Figure 7.42: Magnitude of the velocity field generated by the constant-velocity landslide motion.

The particle was located at y = -0.05, relatively near the free surface. This figure exhibits the phasing of the free surface elevation and subsurface velocity components predicted by linear wave theory.

Beneath a shallow-water wave, particle trajectories are expected to be predominantly horizontal, with relatively little depth dependence. Beneath deep-water waves, the particle trajectories are expected to be approximately circular. In this case, the size of the particle orbits will decrease with increasing fluid depth. Figure 7.44 shows the trajectories of several particles located at x = 9.7. For simplicity, the horizontal displacement of each particle is translated by its initial x-location, so that all particles begin the record at $x - x_0 = 0$. Thus, under the leading offshore-propagating crest the particles moved in an elliptical orbit. After the passing of this wave, the particles in the upper portion of the flume had a positive residual displacement. This supports the finding that the offshore-propagating wave packet contained positive mass. The magnitude of this positive displacement decreased as the fluid depth increased, and the particle at y = -0.52 had a slightly negative residual displacement. This may be partly explained using the horizontal velocity plot of figure 7.45. The positive and negative horizontal particle velocities were approximately equal beneath the leading crest throughout the fluid depth, due to the long wavelength of this leading wave. However, the positive velocities at approximately t = 23 decayed with depth, since the second offshore-propagating wave had a smaller wavelength than the leading wave. Thus, the particles located nearer to the bottom of the fluid depth would travel further in the

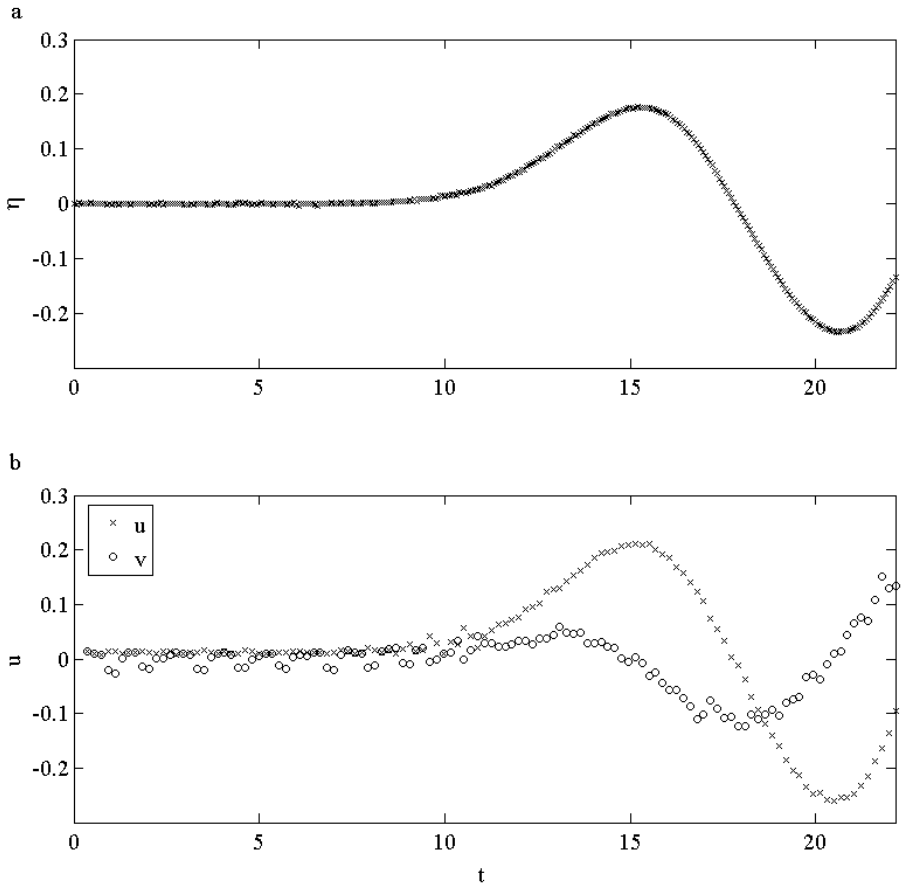

Figure 7.43: Phasing of (a) free surface waves with (b) subsurface particle velocities at $x = 9.7$.

negative x-direction than those near the free surface.

After the passing of the leading crest, the particles moved in approximately circular orbits as the subsequent offshore-propagating waves passed. These circular orbits decreased in size with the fluid depth as expected. The shape of the particle orbits are best illustrated in figure 7.46, which shows the trajectory of the particle located at $y = -0.05$ only (so that the x-scale is not exaggerated).

7.5.3 Kinetic energy in subsurface velocity field

The full spatial and temporal resolution of the subsurface velocity field enables the calculation of the total energy within the system, consisting of the potential energy in the generated wave field and the kinetic energy within the subsurface velocity field. The nondimensional potential energy is calculated according to equation 7.5, while the nondimensional kinetic energy in the velocity field is calculated as

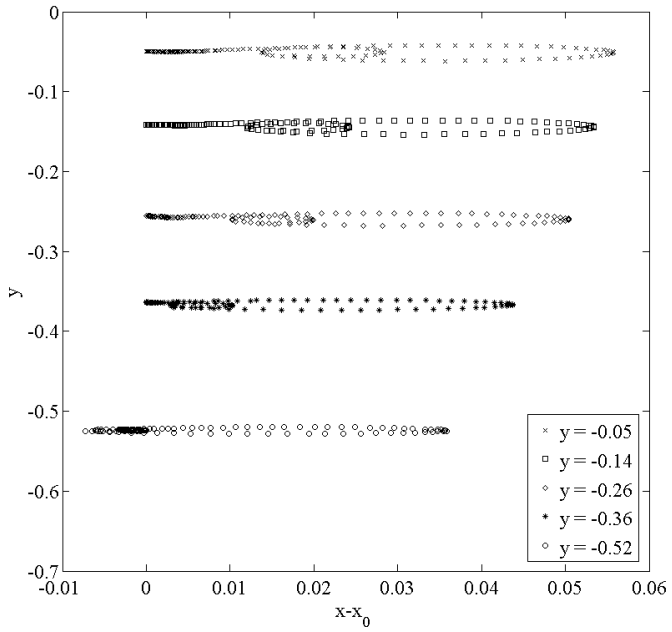

Figure 7.44: Particle trajectories at $x = 9.7$.

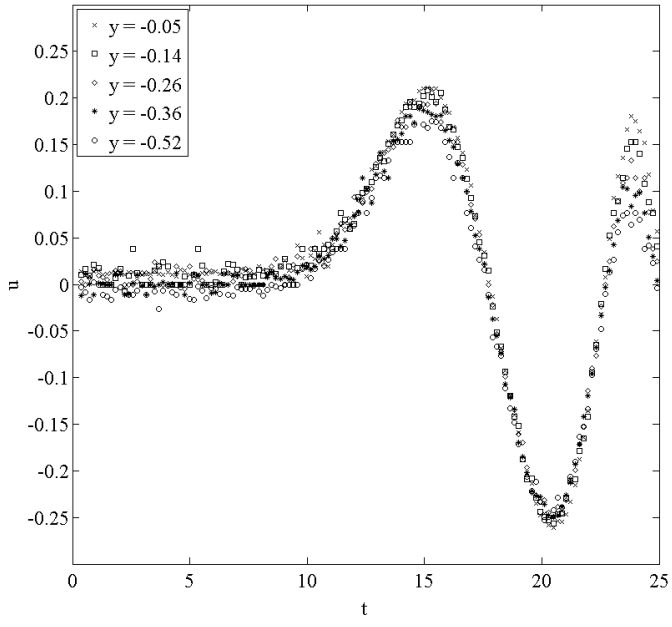

Figure 7.45: Horizontal particle velocities at $x = 9.7$.

$$E_K(t) = \frac{1}{2} \int \int (u(t)^2 + v(t)^2) dx dy, \tag{7.12}$$

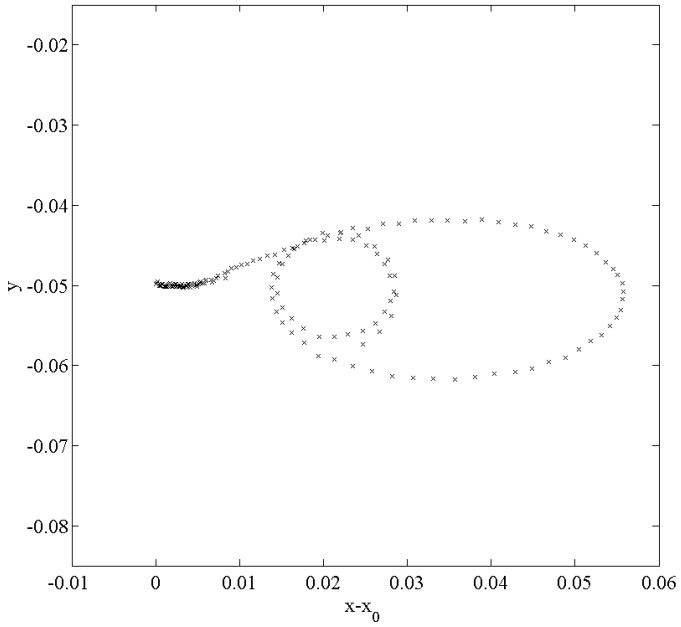

Figure 7.46: Particle trajectory at x = 9.7 and y = -0.05.

where all variables are in their nondimensional form. Figure 7.47 compares the time-dependent behaviour of the potential energy in the wave field to the kinetic energy in the velocity field for Run 12. The landslide ceased its acceleration at $t = 4.1$, began its deceleration at $t = 13.0$, and returned to rest at $t = 17.1$. During the period of landslide motion, the kinetic energy in the subsurface velocity field was significantly higher than the potential energy within the wave field. However, this energy began to decrease rapidly during the landslide deceleration. As discussed in previous sections, the second peak in the potential energy due to the landslide deceleration was relatively weak at this landslide Froude number. By the time that the landslide motion ceased, the kinetic energy within the subsurface velocity field was approximately 90% of the potential energy within the wave field. After the motion of the landslide ceased, it is expected that the total energy in the system would be approximately equipartitioned between potential and kinetic energy. However, the reflections of the onshore-propagating waves from the end of the flume occurred before the landslide motion ceased. Thus, the two components of energy were not equal even after the landslide motion ceased. The nonlinearity of some of the offshore-propagating waves may have also affected the partitioning of energy in this experiment, since equipartitioning of energy is predicted by linear wave theory.

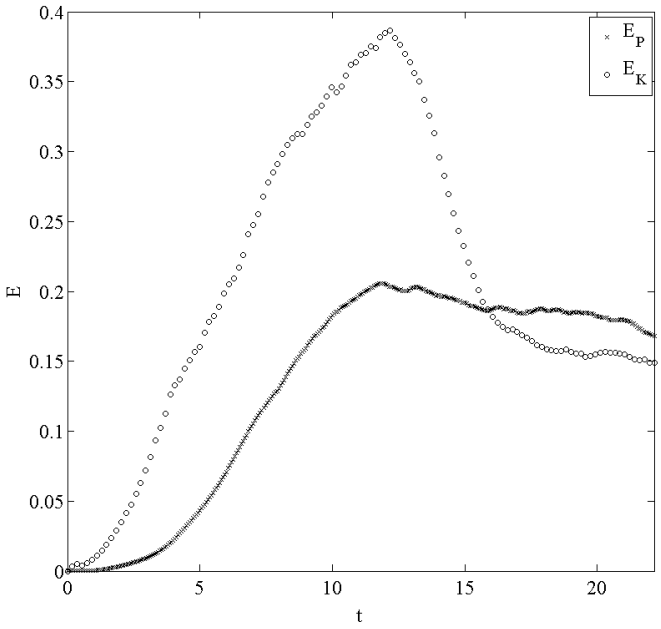

Figure 7.47: Comparison between potential and kinetic energy generated during Run 12.

7.6 Dissipation of energy

A slight attenuation of potential energy is evident within the wave fields generated over the entire parameter space. This attenuation is most easily observed in the potential energy within the onshore region. Due to the lack of ongoing interaction between the onshore-propagating waves and the landslide, it is reasonable to expect that the potential energy within this region would not vary during the constant-velocity motion of the landslide. However, the energy in this region decreased over time. This decrease occurred even before waves began to leave the domain. One possible reason for the decrease in potential energy during this time period is the dissipation of energy due to friction at the flume sidewalls. Although detailed calculations of the energy dissipation are difficult and would require the free surface elevation and subsurface velocity records for the entire flume width, this section provides an order-of-magnitude calculation to determine whether energy dissipation due to sidewall friction may have contributed to the attenuation of energy observed in the physical experiments. For simplicity, all calculations are presented in dimensional form.

The calculation of the energy dissipation due to sidewall friction uses the surface and subsurface measurements of Run 12 ($\lambda = 0.102$, $\tau = 0.70$, $Fr = 0.500$) to determine the energy contained within one wavelength of the leading onshore-propagating trough, and the approximate rate of dissipation due to friction at the flume sidewalls. For the purposes of these calculations, the wave is approximated as a sinusoidal wave with a

wavelength of 2.0 m and a maximum amplitude of 1 mm. As discussed in previous sections, the behaviour of the leading waves approached the shallow water limit, so that the motion of fluid particles beneath the wave may be approximated as oscillatory motion in the x-direction only. The horizontal velocity of the fluid far from the sidewalls is therefore defined as

$$u_\infty = U_0 \cos(\omega t), \tag{7.13}$$

where $U_0 = 4.0$ mm/s, and $\omega = 4.9$ rad/s. The fluid depth in this experiment was 350 mm, while the flume width was 250 mm. The fluid velocity is zero on the sidewall itself, due to the no-slip condition. The velocity distribution of the fluid in the z-direction (normal to the flume sidewall) may be approximated using the analytical solution for the velocity profile in a Stokes boundary layer,

$$u(z,t) = U_0 \left[\cos(\omega t) - e^{-\kappa z}\cos(\omega t - \kappa z)\right], \tag{7.14}$$

where the boundary layer associated with the flume sidewall propagates as a damped wave in the z-direction with a wavenumber κ. This wavenumber is defined as

$$\kappa = \sqrt{\frac{\omega}{2\nu}}, \tag{7.15}$$

where ν is the viscosity of the fluid. Thus $\kappa = 1565$ m^{-1} for this problem. The boundary layer thickness is typically defined as the distance over which the amplitude of the damped wave reduces to $e^{-2\pi}$, or

$$\delta = \frac{2\pi}{\kappa}. \tag{7.16}$$

In this case, the boundary layer thickness is approximately 4 mm. The rate of energy dissipation per unit area of sidewall per unit time is

$$D = \int_0^\infty \mu \left(\frac{\partial u}{\partial z}\right)^2 dz, \tag{7.17}$$

$$= \mu\kappa U_0^2 \left[\frac{1}{2\kappa} + \frac{1}{4}\left(\cos 2\omega t - \sin 2\omega t\right)\right]. \tag{7.18}$$

Using the representative values for this problem, and considering the dissipation over the entire fluid depth and one wavelength, the mean dissipation rate is approximately 9×10^{-6} J/s. To determine the effect of this dissipation rate on the energy within one wavelength of the leading wave requires calculation of the potential energy of the wave, and the kinetic energy of the fluid beneath the wave. The dimensional

potential energy is defined as

$$E_P = 0.5\rho w \int \eta^2 \, dx, \tag{7.19}$$

where ρ is the fluid density, w is the flume width and the amplitudes are integrated over the 2 m wavelength of the wave. The kinetic energy of the fluid beneath the wave is defined as

$$E_K = 0.5\rho w A u^2, \tag{7.20}$$

where A is the area of fluid beneath the wave, and u is the area-averaged horizontal fluid velocity.

Using the representative values for this problem, the potential energy of the wave is approximately 9×10^{-4} J, while the kinetic energy beneath the waves is approximately 1.4×10^{-3} J. Thus, the total energy of the wave is approximately 2.3×10^{-3} J. If the dissipation rate remained constant, the energy within the wave would be dissipated in approximately 130 s, considering the contributions of both sidewalls. However, in reality as the kinetic energy beneath the wave decreased, the subsurface fluid velocity would also decrease. Thus, the dissipation rate would decrease over time, and the wave energy would take significantly longer to fully dissipate. Interestingly, the energy dissipation rate showed a dependence on η^2, in a similar manner to the potential energy within the surface waves and the kinetic energy beneath the free surface (since the subsurface velocity approximately scaled as $\eta\omega$. Thus, the dissipation rate is effectively independent of Fr, and even high-Fr experiments showed this decrease in energy over time.

The potential energy within the onshore region exhibited an attenuation of approximately 5% of its peak value during the constant-velocity phase of motion. Considering a constant dissipation rate of 9×10^{-6} J/s for each flume sidewall (over one wavelength of the leading wave), the equivalent total dissipation during this 2 s period is approximately 3.6×10^{-5} J. Given that the total energy within one wavelength of the wave is approximately 2.3×10^{-3} J, the total dissipation is of the same order as the observed attenuation during the experiment itself. Note that the values and calculations presented in this section are simplistic in nature, and so only the order of the different terms is considered. However, these brief calculations show that at least some of the energy attenuation observed during the physical experiments may have been caused by dissipation at the flume sidewall. Since the effective boundary layer thickness was quite small (approximately 4 mm), these effects may not have immediately exhibited themselves in the wave amplitudes in the plane of the laser sheet. The dissipation of energy by the turbulent wake behind the landslide may have also contributed to the attenuation, although this may have been more limited in its spatial extent.

7.7 Summary

The experiments described in this chapter investigated the dependence of waves generated by a submarine landslide on the landslide's initial acceleration, terminal velocity (defined by the landslide Froude number), and submergence depth. The initial acceleration of the submarine landslide generated a leading offshore-propagating crest and a leading onshore-propagating trough, followed by dispersive wave packets in both directions. The leading waves approached the behaviour of shallow-water waves, while the trailing waves propagated as dispersive deep-water waves. A free surface depression propagated above the low-pressure region created by the moving landslide during the constant-velocity phase of motion, which then propagated as a free wave after the landslide decelerated. The landslide deceleration generated additional dispersive wave packets in the offshore and onshore directions, with the opposite polarity to the waves generated by the landslide acceleration.

The waves generated by the landslide acceleration transported negative mass in the onshore direction, and positive mass in the offshore direction. This mass transport was balanced by the groups of waves generated during the landslide deceleration. The magnitude of the mass transported by the groups of waves increased with the landslide Froude number, but showed negligible dependence on the landslide acceleration and submergence depth.

The landslide Froude number was the dominant parameter in its effect on both wave amplitudes and the behaviour of the generated waves. At lower Froude numbers, the landslide acceleration and deceleration generated the highest-amplitude waves, and were responsible for most of the energy exchange between the landslide and the wave field. As the Froude number increased, the free surface depression above the landslide became responsible for a greater proportion of the energy within the wave field. The amplitude of this free surface depression was predicted using a simple application of hydraulic theory, using the analogy of a subcritical uniform flow over a stationary object. The predictions of hydraulic theory were less than the measured values of the depression amplitude over the entire parameter space. At higher Froude numbers, an additional group of short-wavelength waves also propagated with the landslide; these waves showed increasingly nonlinear behaviour as the Froude number increased. The first crest behind the landslide broke for $Fr \geq 0.500$.

The waves generated at the shallower submergence depth ($\tau = 0.35$) had larger amplitudes, but shorter wavelengths, than those generated at the deeper submergence depth ($\tau = 0.70$). The leading waves (arising from either the landslide acceleration or deceleration) generated by larger landslide accelerations had higher amplitudes than those generated at lower landslide accelerations, although this dependence was weaker than the depth dependence.

The potential energy within the wave field increased more rapidly as the landslide acceleration increased, however this quantity also showed strongest dependence on the landslide Froude number and submergence depth. The energy within the onshore- and offshore-propagating wave groups could be estimated by evaluating the potential energy within the onshore (negative x) and offshore (positive x) regions. The energy within the onshore region was always less than the energy within the offshore region, due to the ongoing interaction between the landslide and the offshore-propagating waves, and this difference became greater as the Froude number increased. Some attenuation of energy was observed during the constant-velocity phase of motion, particularly within the onshore region. Although waves leaving the domain, and the boundary between the onshore and offshore regions, could account for some of this attenuation, the amount of attenuation (and its timing throughout the constant-velocity phase of motion) suggests that sidewall friction may have also caused a decrease in the energy within the wave field over time.

The interactions between the flow generated by the moving landslide and the free surface waves were further investigated in a particle tracking velocimetry (PTV) experiment. The turbulent wake behind the landslide affected the fluid velocity near the rear of the landslide, which in turn affected the phasing of the waves relative to the subsurface fluid velocity field.

Chapter 8

Results - Predictive capabilities of numerical models

8.1 Objectives of numerical simulations

The objectives of the numerical simulations were to predict the properties of free surface waves generated by the motion of a submerged landslide along a horizontal boundary. In this chapter, the predictions of the two-dimensional numerical models are compared to the experimental results described in chapter 7. Two of the models invoked the inviscid irrotational assumption for fluid flow, and the third model assumed a viscous incompressible ambient fluid (referred to as the viscous model). One of the inviscid models assumed a linear bottom boundary condition (referred to as the linear model), and was solved using a spectral decomposition of wave modes. The second inviscid model did not assume a linear bottom boundary condition (referred to as the nonlinear model), and was solved using a boundary element method. Both inviscid models assumed linearity of the generated waves. Details of the formulations of the different numerical models are provided in chapter 5.

The behaviour of the generated wave fields varied greatly over the parameter space during the physical experiments (most notably with variations in the landslide Froude number). These changes concerned the importance of the different phases of the landslide motion in the exchange of energy between the moving landslide and the wave field, the relative size of the onshore- and offshore-propagating wave groups, and especially the interaction between the moving landslide and the offshore-propagating waves. This interaction led to the formation of a group of trapped waves behind the landslide, which exhibited nonlinear behaviour leading to breaking at high Froude numbers. The applicability of the numerical models to the modelling of landslide-generated tsunami will be assessed based on their performance in predicting these three behavioural features of the experimentally-generated waves.

The two inviscid-irrotational models provided predictions of the generated wave amplitudes over the entire parameter space described in chapter 6. Due to the differences in wave field behaviour over the parameter space, the comparisons between the numerical predictions and experimental measurements of $\eta(x,t)$ (and associated quantities such as potential energy and mass transport) will be assessed separately at each Froude number. Comparisons are made over the entire parameter space wherever possible. For the sake of clarity, in some cases detailed comparisons between the predicted and measured wave fields are made considering the results of one experiment only. The trapped waves behind the landslide broke at Froude numbers greater than 0.5, and as such these high-Fr experiments are not considered in this chapter. Comparison between the linear and nonlinear models allows the effect of the linear assumption on the bottom boundary on the model predictions to be determined. Where the predicted amplitudes are compared to the measured amplitudes, the amount of under-prediction is defined as:

$$\Delta = 1 - \frac{\eta_M}{\eta_E} \tag{8.1}$$

where η_E is the experimentally-measured wave amplitude, η_M is the amplitude predicted by the model, and Δ is expressed as a percentage.

Due to its computational expense, the viscous model was only used to predict the properties of the waves generated during Run 12. This experiment had the parameters $\lambda = 0.102$, $Fr = 0.500$, and $\tau = 0.70$. This parametric combination is of particular interest due to the nonlinear behaviour of the waves trapped behind the landslide. The use of this model allowed assessment of the effects of the inviscid-irrotational assumption and the linear free surface assumption on the prediction of the generated waves.

As discussed in chapter 7, Run 12 was repeated using particle tracking velocimetry to measure the subsurface velocity field generated by the landslide motion. The two-dimensional linear inviscid model was also extended to the subsurface domain, so that the predictions of this model included the velocity and pressure fields. The predictions of the landslide interaction with the generated waves, and the mechanism of wave trapping, are assessed in this chapter by comparing the measured velocity fields with those predicted by the model. The subsurface pressure field was not measured during the PTV experiment, however the pressure field predicted by the inviscid model provides additional insight into the interactions between the landslide and the generated waves.

This chapter concludes with a discussion on the mechanism by which waves were trapped behind the moving landslide. This discussion focuses on the effect of the different model assumptions on their ability to correctly predict the wave trapping observed during the physical experiments. The effect of the experimental parameters

on the trapping of waves is also discussed in this section.

8.2 Predictions at $Fr = 0.125$

The wave fields generated during the physical experiments at this Froude number had very low amplitudes (less than 0.1 in nondimensional terms), and most of the energy exchange between the landslide and the wave field occurred during the acceleration and deceleration periods. The amplitudes of the offshore- and onshore-propagating waves were similar at this Froude number, where the peak amplitude of the leading onshore-propagating trough was approximately 86% of the peak amplitude of the leading offshore-propagating crest in run 21 (see chapter 7). The free surface depression above the landslide during the constant-velocity phase of motion was approximately half the amplitude of the leading waves.

Figures 8.1 to 8.3 compare the predicted and measured wave amplitudes in a series of wave field plots from Run 21, with $\lambda = 0.153$, $\tau = 0.35$ and $Fr = 0.125$. This run was selected as a representative of the predicted and measured behaviour in the wave field at this Froude number. Comparisons between model predictions and experimental measurements over the entire parameter space are discussed later in this section. It should be noted that the (nondimensional) duration of the initial acceleration period was 0.48, and the duration of the constant-velocity was 8.86, so that all the wave field plots in figures 8.1 and 8.2 were recorded during the constant-velocity period, and the wave field plots in figure 8.3 were recorded after the landslide motion had ceased.

Figure 8.1 shows that both inviscid models under-predicted the amplitudes of the leading offshore crest and onshore trough, although the level of under-prediction by the nonlinear model was considerably less than that of the linear model. At $t = 2.72$, the linear model under-predicted the amplitudes of the leading crest and trough by 18% and 17% respectively, while the nonlinear model under-predicted the respective amplitudes by 4% and 1%. The models captured the phasing of the leading waves very well, with nondimensional (spatial) phase offsets of approximately 0.02 for both models (evaluated at $t = 1.14$). At later times, the leading wave amplitudes predicted by the nonlinear model were actually slightly larger than the experimentally-measured values. For example, at $t = 13.8$ the linear model under-predicted the amplitude of the leading offshore-propagating crest by 8%, while the nonlinear model over-predicted its amplitude by 11%. This may be indicative of differences in the dispersion of waves predicted by the models and observed in the physical experiments. Some attenuation of potential energy during the physical experiments, as discussed in chapter 7, may have also contributed to these differences.

The models both under-predicted the amplitude of the free surface depression, which propagated above the landslide during its constant-velocity motion, although

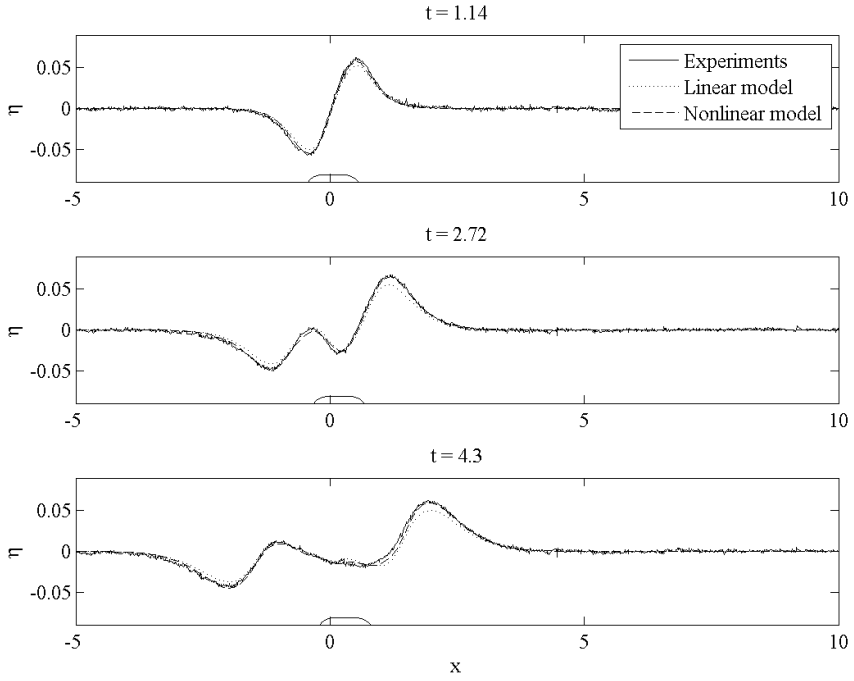

Figure 8.1: Comparisons between measured and predicted wave amplitudes in Run 21, between $t = 1.1$ and $t = 4.3$.

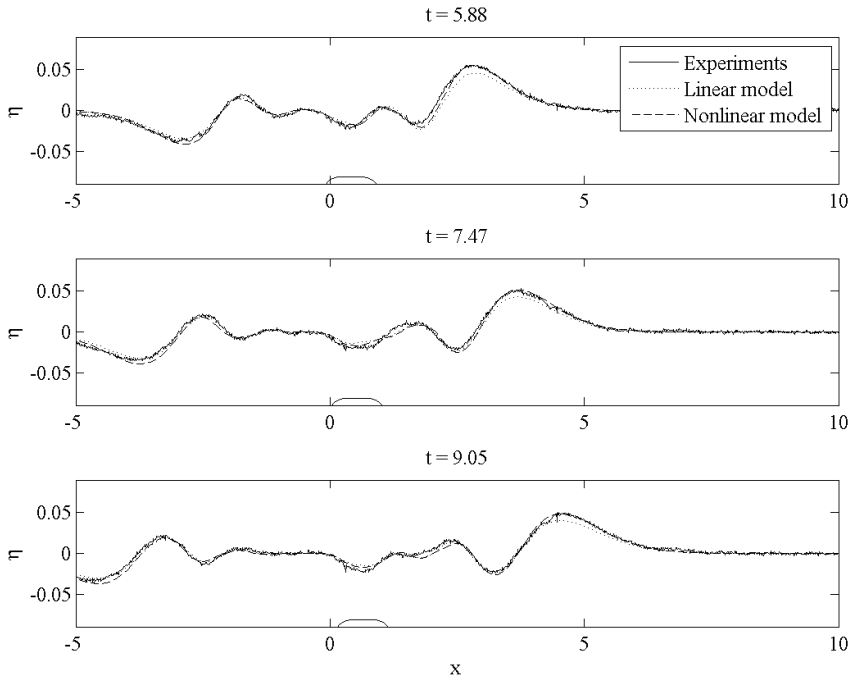

Figure 8.2: Comparisons between measured and predicted wave amplitudes in Run 21, between $t = 5.9$ and $t = 9.1$.

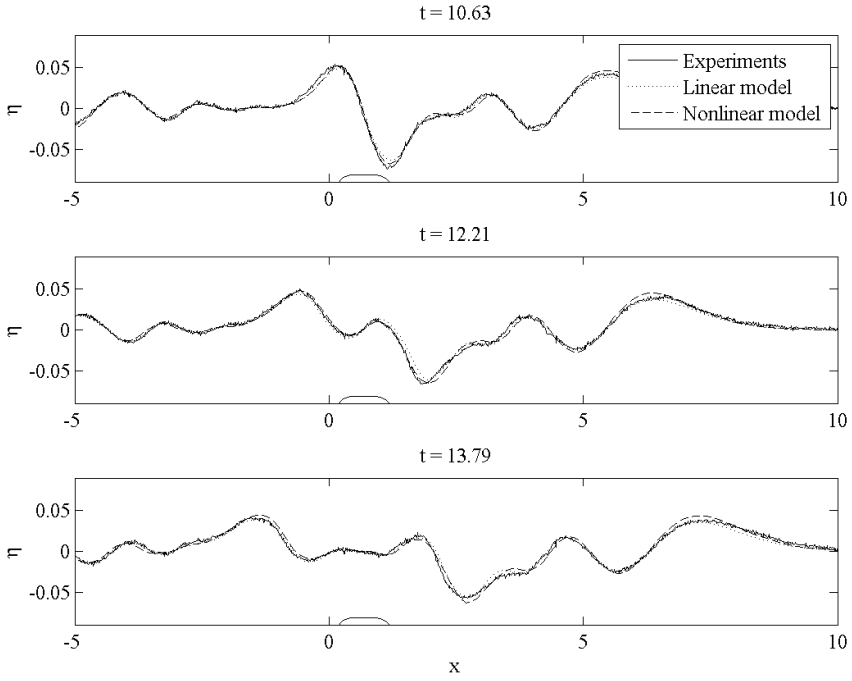

Figure 8.3: Comparisons between measured and predicted wave amplitudes in Run 21, between $t = 10.6$ and $t = 13.8$.

both models predicted the location of this depression to within ± 0.1 (in nondimensional units) In this experiment, the depression was located almost directly above the landslide centre of mass, in agreement with the predictions of hydraulic theory discussed in chapter 7. Again, the nonlinear model predictions of the amplitude of this depression were closer to the experimental measurements than the linear model predictions, with under-predictions of 26% and 36% respectively at $t = 9.1$.

Despite correctly predicting the location of the free surface depression, the models did not correctly predict the phasing of the offshore-propagating waves in the vicinity of the landslide. This is particularly evident in the wave field plots captured at $t = 4.3$ and 5.9. At $t = 4.3$, an offshore-propagating trough passed over the landslide, interacting with the free surface depression. However, the trough appeared to pass over the landslide more rapidly in the numerical simulations, and at $t = 5.9$ the predicted amplitude of this offshore-propagating trough was 24% larger than the experimentally-measured amplitude in the linear model, and 32% larger in the nonlinear model. These phasing differences, and hence differences in wave amplitude, were evident in the subsequent offshore-propagating waves as they propagated past the landslide.

The linear and nonlinear models initially under-predicted the amplitudes of the onshore-propagating crest and offshore-propagating trough generated by the landslide deceleration (illustrated in figure 8.3), by 10% and 6% respectively at $t = 10.6$.

However, as these waves propagated away from the (now stationary) landslide, the experimentally-measured wave amplitudes decayed more rapidly than the predicted wave amplitudes, so that at $t = 13.8$ the nonlinear model over-predicted the crest amplitude by 6%, and the under-prediction by the linear model had reduced to 4%. The nondimensional differences in predicted and measured phase in the onshore- and offshore-propagating wave packets were 0.05 in the nonlinear model, and 0.08 in the linear model, at $t = 13.8$.

Despite the phasing discrepancies in the vicinity of the moving landslide, and the general under-prediction of wave amplitudes, the inviscid-irrotational models were able to correctly predict the relative importance of the different phases of motion in the exchange of energy between the landslide and the wave field. In the experiments and simulations undertaken at $Fr = 0.125$, the majority of this exchange occurred during the periods of landslide acceleration and deceleration.

The wave field plots in figures 8.1 to 8.3 compare the measured and predicted wave fields within one experiment only. However, the behaviour observed in these figures was consistent over the range of τ and λ values tested at this landslide Froude number. Figure 8.4 compares the peak amplitudes of the leading waves and the free surface depression predicted by the two numerical models with those measured during the physical experiments with $Fr = 0.125$ and $\tau = 0.70$, and figure 8.5 shows the same information for $\tau = 0.35$.

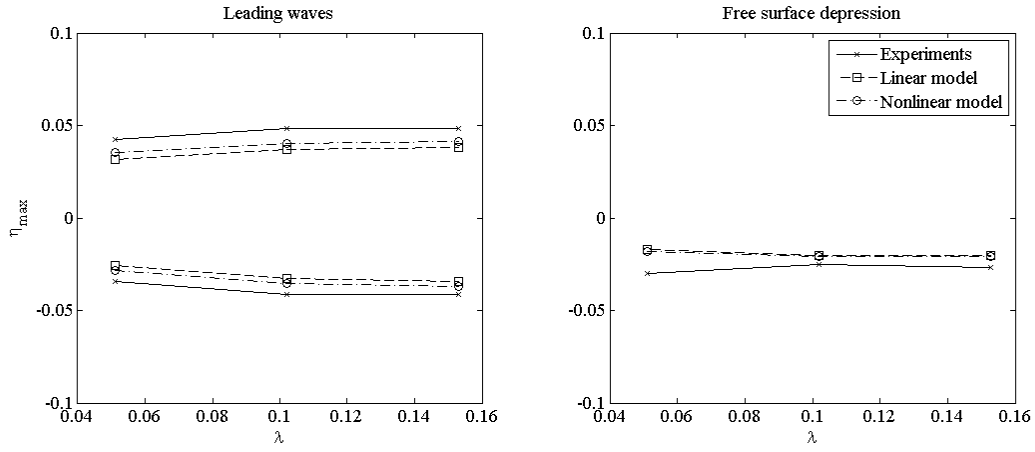

Figure 8.4: Comparisons between measured and predicted peak wave amplitudes for all experiments with $Fr = 0.125$ and $\tau = 0.70$.

Figures 8.4 and 8.5 show that the under-prediction of the peak wave amplitudes by the two inviscid models were similar for all experiments undertaken at this landslide Froude number. The level of under-prediction decreased slightly as the landslide acceleration increased. The linear model under-predicted the leading wave amplitudes by between 22% and 27% at $\lambda = 0.051$, with the under-predictions decreasing to between

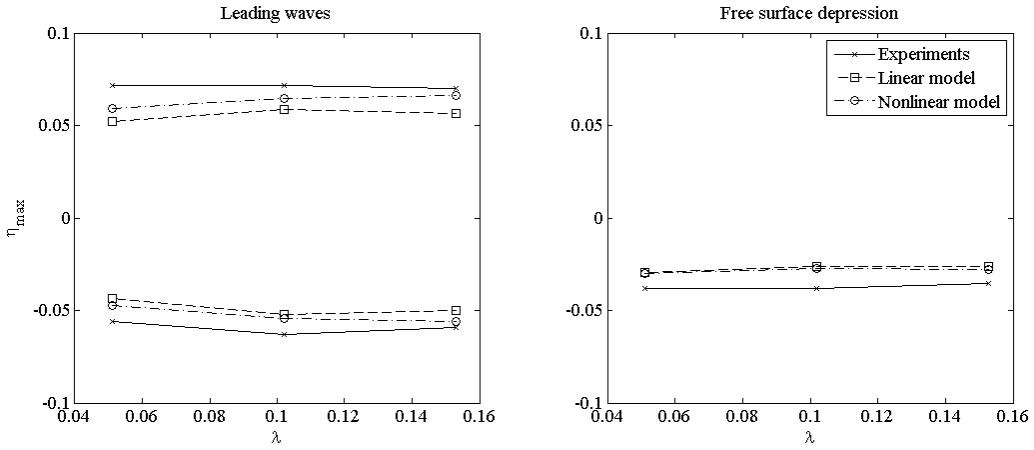

Figure 8.5: Comparisons between measured and predicted peak wave amplitudes for all experiments with $Fr = 0.125$ and $\tau = 0.35$.

15% and 22% at $\lambda = 0.153$. The nonlinear model under-predictions varied between 13% and 18% at $\lambda = 0.051$, decreasing to between 5% and 15% at $\lambda = 0.153$. The dependence of the peak amplitudes on τ and λ was well predicted by the models.

As discussed in chapter 7, the potential energy within the wave field is a more useful global measure than the wave amplitude of the relative importance of the different phases of motion. Figure 8.6 compares the potential energy within the wave field as predicted by the inviscid models and calculated from the experimental wave amplitudes. For clarity, only the results from Run 21 are shown, however the potential energy comparisons over the entire parameter space are provided in appendix C. The time-dependent potential energy behaviour was consistent over all the experiments undertaken at $Fr = 0.125$.

Given the under-prediction of the leading wave amplitudes by the models, it is unsurprising that the models also under-predicted the total potential energy within the wave field at this Froude number. The linear model under-predicted the peak energy by 35%, while the nonlinear model under-predicted the peak energy by 11%. However, the models captured the variation of the potential energy with time very well. In particular, the shape and timing of the initial energy peak was almost perfectly predicted by both models (aside from the under-prediction of the magnitude). During the constant-velocity phase of motion, the energy within the predicted wave fields remained almost constant, apart from some small fluctuations. However, the energy within the measured wave field decreased throughout the constant-velocity phase of motion. Because of this decrease, the energy within the measured wave field was slightly less than the energy in the wave field predicted by the nonlinear model at the start of the landslide deceleration. Thus, the magnitude of the second energy peak (caused by the additional waves generated during the landslide deceleration) predicted

by the nonlinear model was approximately equal to the experimental value, while the under-prediction by the linear model was reduced to 22%. The onshore-propagating waves were reflected from the end of the experimental flume before this second peak, so the remainder of the energy record cannot be used.

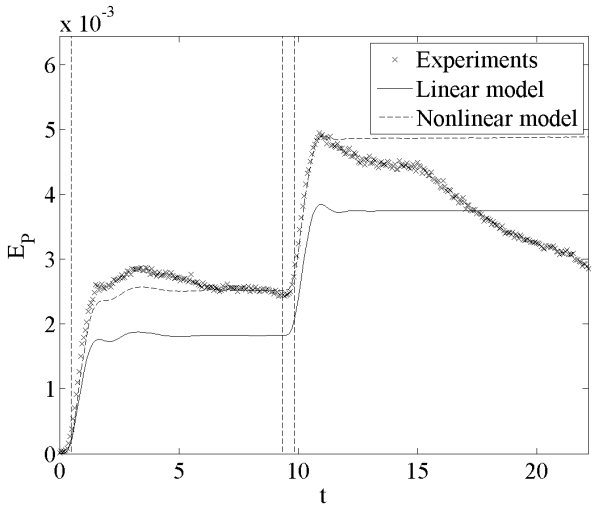

Figure 8.6: Comparisons between measured and predicted wave field potential energy for Run 21.

Figure 8.7 compares the model predictions of the energy contained in the offshore and onshore regions with the measured values, where Run 21 is again used as a representative experiment for this Froude number. The equivalent plots over the full parameter space are provided in appendix D. However, the behaviour in Run 21 was also observed for all λ and τ values tested at $Fr = 0.125$.

The under-prediction of potential energy by the linear model were approximately the same in the offshore and onshore regions. The nonlinear model predictions of the energy within the onshore region were very close to the experimental values. In fact, the slight decrease in experimental energy during the constant-velocity phase of motion led to a slight over-prediction of energy within this region by the nonlinear model after approximately $t = 7$. Both models correctly predicted the time variation of energy within the onshore and offshore regions.

Chapter 7 discusses the positive mass transported by the offshore-propagating wave packet, and the balancing negative mass transported by the onshore-propagating wave packet. Figure 8.8 compares the model predictions of this mass transport with the values calculated from the experimental measurements of Run 21. Again, the mass transport plots for all remaining experiments are provided in appendix E. The under-prediction of the wave amplitudes by the models is also observed in their predictions of the directional mass transport (23% by the linear model and 11% by the nonlinear model). The time variation of the mass transport was well predicted by both models.

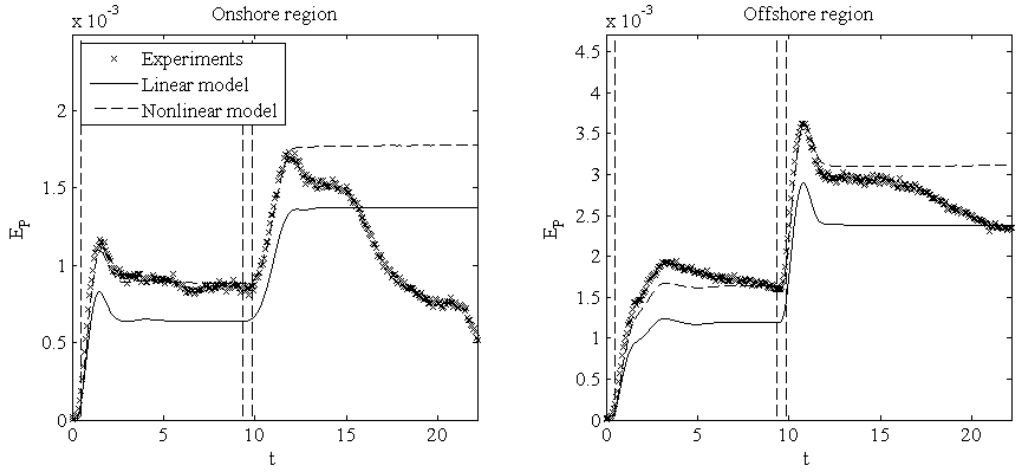

Figure 8.7: Potential energy contained in the onshore and offshore regions of the wave field for Run 21.

The reason for the non-zero residual mass values in the linear model is that waves began to leave the simulation domain at later times. Although these waves were not reflected (as in the physical experiments), the timing of these waves leaving the domain prevented the mass within the two regions from returning to a zero value.

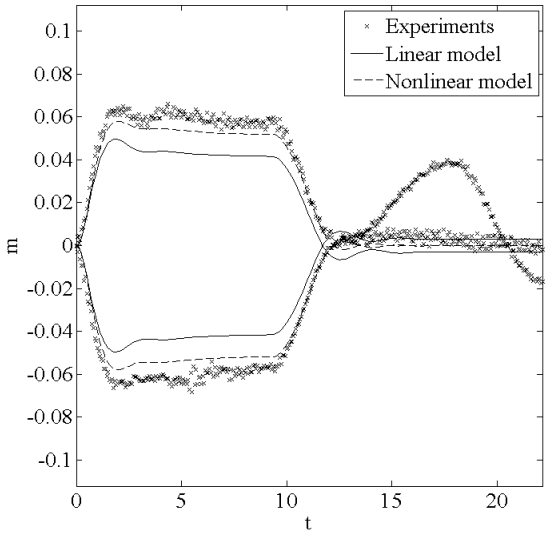

Figure 8.8: Mass transported by the onshore and offshore wave packets in Run 21.

8.3 Predictions at $Fr = 0.250$

At this landslide Froude number, the longer landslide acceleration period increased the amplitudes of all the waves within the wave field (particularly the offshore-propagating

waves). The higher landslide terminal velocity increased the amplitude of the free surface depression above the landslide, and also increased the amount of interaction between the landslide and the offshore-propagating waves. Thus, the ability of the inviscid models to correctly predict the bulk properties of the wave field became more dependent on their ability to model these interactions during the constant-velocity phase of motion.

Figures 8.9 to 8.11 show a series of wave field plots comparing the numerical predictions and experimental measurements of the wave field generated during Run 22, with the parameters $Fr = 0.250$, $\tau = 0.35$ and $\lambda = 0.153$. This is used as a representative experiment for this landslide Froude number in this initial discussion, since the behaviour observed in this experiment was consistently observed over all experiments with $Fr = 0.250$. The nondimensional duration of the initial acceleration period was 0.97, and the duration of the constant-velocity was again 8.86.

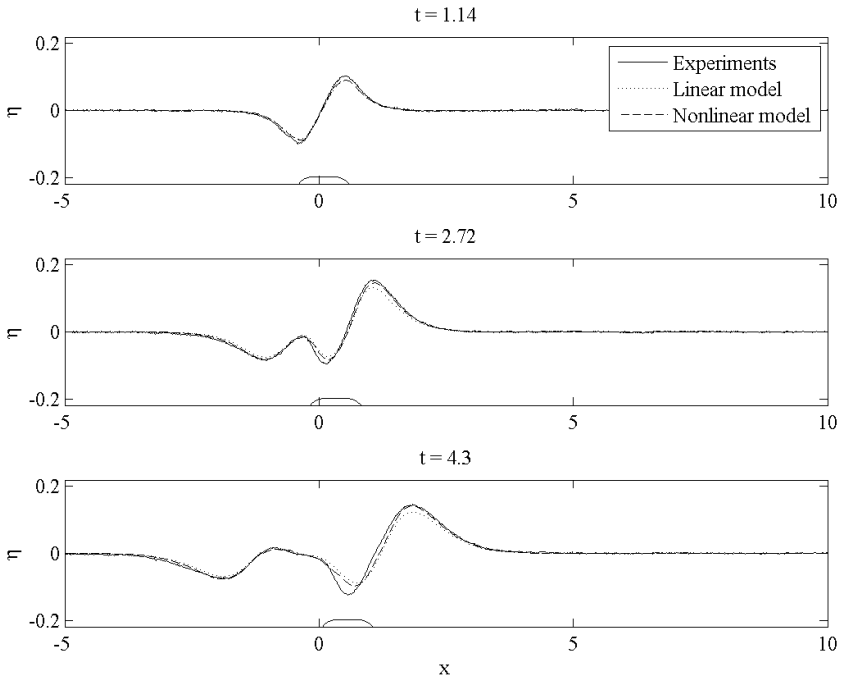

Figure 8.9: Comparisons between measured and predicted wave amplitudes in Run 22, between $t = 1.1$ and $t = 4.3$.

Generally speaking, the predictions of the inviscid models worsened slightly at this Froude number, due to the increased interactions between the landslide and the offshore-propagating waves. As discussed in chapter 7, the nonlinearity of the waves proapgating with the landslide during its constant-velocity motion also increased with the landslide Froude number. Thus, since both models assumed linearity of the free surface waves, their predictions of these waves are expected to worsen as the Froude

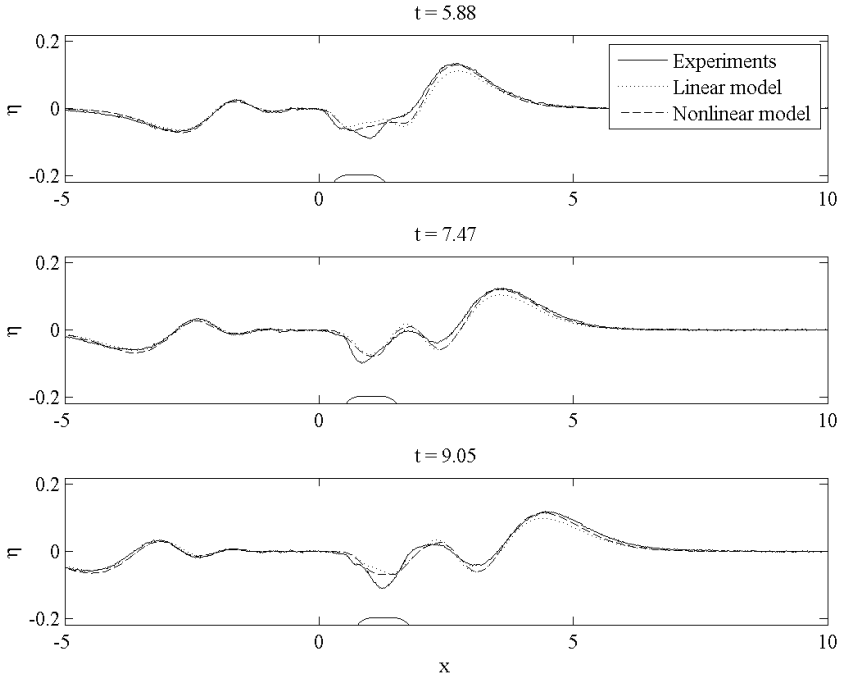

Figure 8.10: Comparisons between measured and predicted wave amplitudes in Run 22, between $t = 5.9$ and $t = 9.1$.

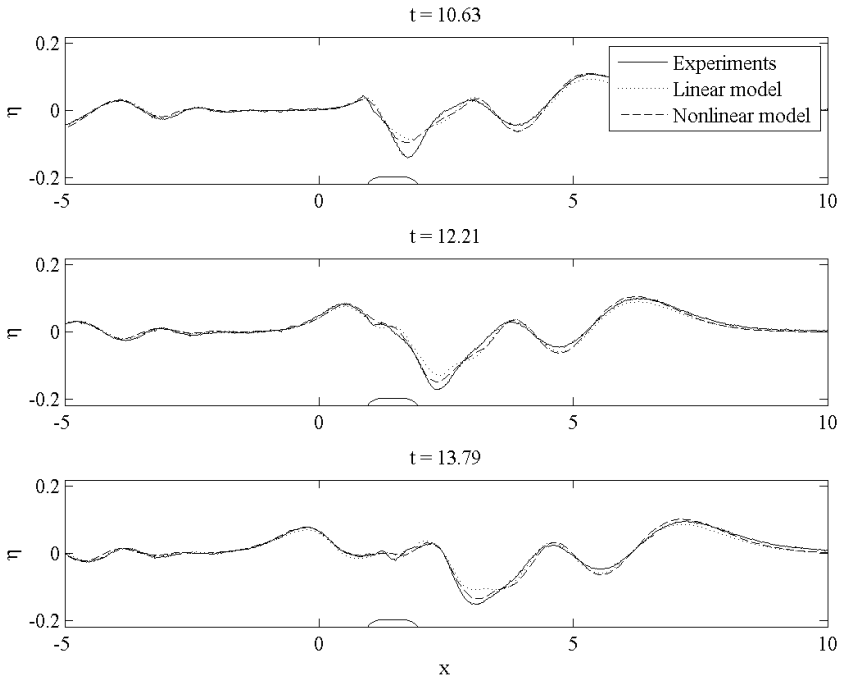

Figure 8.11: Comparisons between measured and predicted wave amplitudes in Run 22, between $t = 10.6$ and $t = 13.8$.

number increases.

The wavelength and velocity of the leading crest and trough generated by the landslide acceleration were well predicted by the models, although the amplitudes of these leading waves were under-predicted. At $t = 1.1$, the nonlinear model under-predicted the amplitudes of the leading waves by 12%, while the linear model under-predicted the leading crest amplitude and leading trough amplitude by 14% and 13% respectively. By $t = 2.7$, the nonlinear under-prediction of the offshore-propagating crest had improved to 5%, while the linear model under-prediction was 15%.

The onshore-propagating wave packet did not exhibit any ongoing interaction with the landslide, and the model predictions of the phasing within this wave packet were very robust, predicting the locations of the wave maxima to within ± 0.05. The experimentally-measured waves again appeared to exhibit stronger amplitude attenuation during their propagation, so that the leading trough amplitude was over-predicted by 13% by the nonlinear model at $t = 7.5$.

The free surface depression above the landslide was initially located just behind the leading offshore-propagating crest, and thus was superposed with the first offshore-propagating trough during the initial stages of the constant-velocity phase of motion. As with the previous Froude number, the inviscid models did not correctly predict the interaction between these two waves, as shown in the wave field plots between $t = 2.7$ and 5.9. At $t = 2.7$, the nonlinear and linear models under-predicted the amplitude of the combined wave by 3% and 12% respectively, with a phase shift of approximately 0.05 (in nondimensional spatial units). However, at $t = 4.3$, the trough predicted by the model was out of phase with the measured trough by over 0.15. The models thus predicted the offshore-propagating trough moved over the landslide more rapidly than occurred in the experiments.

The models also predicted a different energy distribution between the free surface depression and offshore-propagating trough, once they had separated, than was observed in the experiments. These differences are illustrated at $t = 5.9$ in figure 8.10. In the model predictions, the offshore-propagating trough retained most of its energy, while the experimental measurements showed that more energy was input into the free surface depression above the landslide. As a result, the amplitude of the offshore-propagating trough (after separation of the two waves) was larger in the linear and nonlinear model predictions than in the experimental measurements. These amplitude differences are reported in absolute terms, to prevent the very low amplitude of the measured trough (η = -0.02) amplifying any percentage differences. The linear model over-predicted the amplitude by 0.03, and the nonlinear model over-predicted the amplitude by 0.02. The amplitude of the free surface depression at $t = 5.9$ was under-predicted by 40% and 26% by the linear and nonlinear models, respectively.

The amplitude of the second offshore-propagating crest decreased as it passed over

the landslide (at $t = 5.9$), due to the low pressure of the fluid moving over the landslide. After passing the landslide (at $t = 7.5$), its amplitude increased again, as shown in figure 8.10. However, the predicted amplitudes of this crest during the remainder of its propagation were again larger than the measured amplitudes, with the linear model over-predicting the crest amplitude by 0.02, and the nonlinear model over-predicting the amplitude by 0.01 (the experimental value was again approximately zero, hence percentage over-predictions were not calculated). Interestingly, the over-prediction of the offshore-propagating waves in front of the landslide was more severe by the linear model than the nonlinear model. This implies that the inclusion of the bottom boundary nonlinearity improved the inviscid-irrotational model's ability to correctly predict the interaction between the landslide and the offshore-propagating waves.

The second offshore-propagating trough was superposed with the leading offshore-propagating trough generated by the landslide deceleration. The amplitude of these leading deceleration-generated waves were under-predicted by the inviscid models, in a similar manner to the leading waves generated by the landslide acceleration. At $t = 12.2$, the linear and nonlinear models under-predicted this trough amplitude by 25% and 14% respectively. The smaller trailing waves within these packets also appeared to be under-predicted by the models, as shown by the small-wavelength waves above the landslide at $t = 13.8$.

During Run 22, the inviscid models under-predicted the peak amplitudes of the leading waves. The level of under-prediction was more severe in the linear model predictions, and the under-predictions became less as λ increased, with average under-predictions of 25% and 15% (for the linear and nonlinear models respectively) at $\lambda = 0.051$ reducing to 17% and 8% at $\lambda = 0.153$. The reduction in under-prediction was approximately linear over the λ values tested during these experiments, and the under-predictions were approximately 5% lower at the shallower submergence depth.

The models predicted different interactions between the moving landslide and the offshore-propagating wave packet than were observed in the experiments, leading to over-prediction of the trailing offshore-propagating wave amplitudes and under-prediction of the free surface depression amplitude. The under-prediction of the peak trough amplitude also decreased with increasing λ, with average under-prediction by the linear model decreasing from 34% at $\lambda = 0.051$ to 21% at $\lambda = 0.153$. The average under-prediction by the nonlinear model decreased from 25% to 13% over the same range.

When considering the wave field behaviour over the entire parameter space, figure 8.12 illustrates the predicted and measured peak amplitudes of the leading waves and the free surface depression for all experiments with $Fr = 0.250$ and $\tau = 0.70$. Figure 8.13 provides the same comparisons for the shallower experiments, with $\tau = 0.35$.

In the physical experiments, the majority of the energy exchange between the landslide and the wave field was caused by the wave packets generated by the landslide

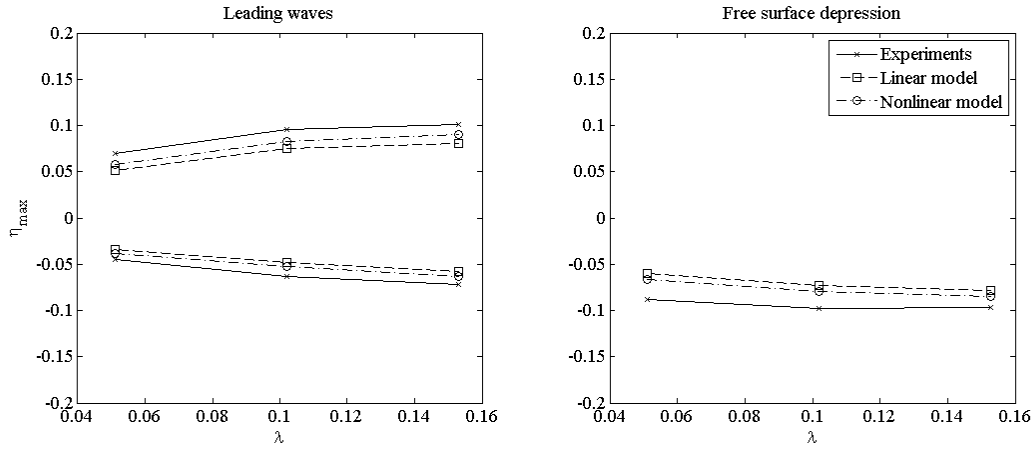

Figure 8.12: Comparisons between measured and predicted peak wave amplitudes for all experiments with $Fr = 0.250$ and $\tau = 0.70$.

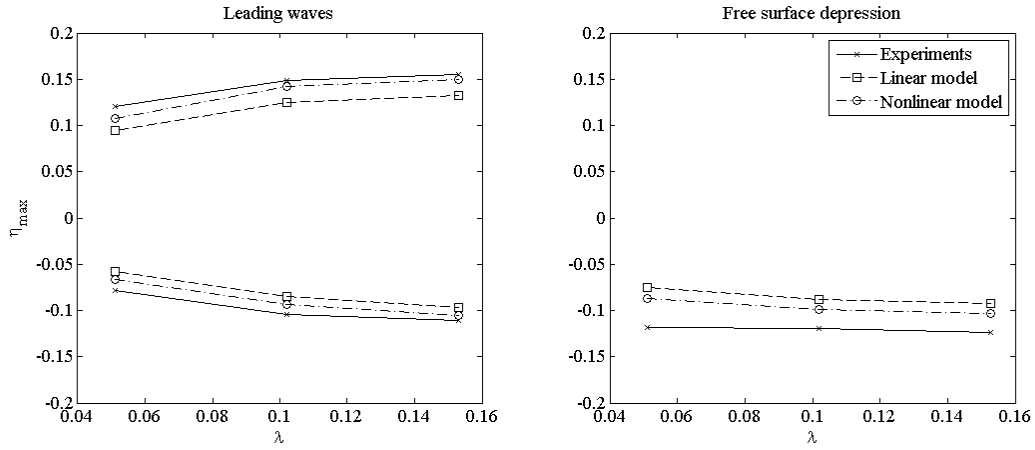

Figure 8.13: Comparisons between measured and predicted peak wave amplitudes for all experiments with $Fr = 0.250$ and $\tau = 0.35$.

acceleration and deceleration, although some energy was input during the constant velocity phase of motion. Thus, there was a delay between the end of the acceleration period and the time at which the potential energy within the wave field reached its maximum value. The interaction between the landslide and the offshore-propagating waves caused some fluctuations of the energy within the wave field.

Figure 8.14 compares the numerical predictions of the total potential energy within the wave field with the experimental values, using Run 22 as a representative experiment at this Froude number (plots at all other τ and λ values are provided in appendix C). Both models under-predicted the potential energy within the wave field throughout the duration of the experiment, which follows from the under-prediction of the leading wave amplitudes shown in figures 8.12 and 8.13. In this experiment, the nonlinear model under-predicted the first energy peak by 17%, while the linear model

under-predicted the same peak by 34%. Due to the attenuation of energy during the constant-velocity landslide motion (see chapter 7), the under-prediction of the second peak in the energy record was less by both models, with under-predictions of 5% and 25% respectively. The models did capture the timing of the energy peaks caused by the landslide acceleration and deceleration to within ± 0.2.

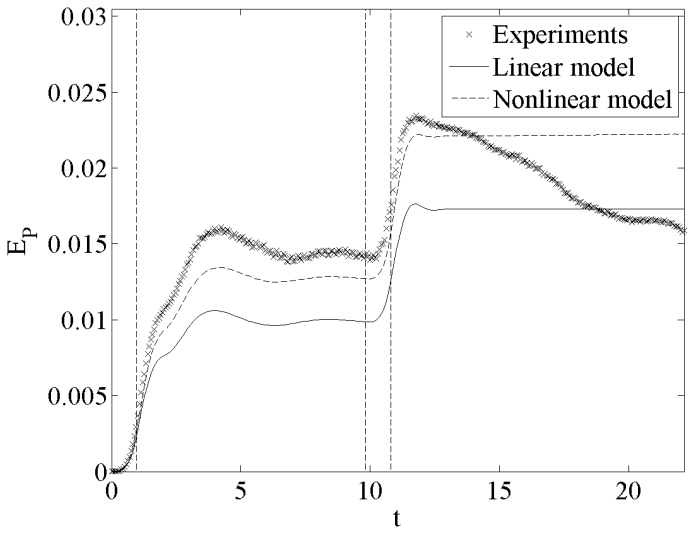

Figure 8.14: Comparisons between measured and predicted wave field potential energy for Run 22, with $\lambda = 0.153$, $Fr = 0.250$ and $\tau = 0.35$.

The predictions of the energy during the constant-velocity phase of motion were similar to the experimental values, a slightly surprising result considering the different interactions between the landslide and the offshore-propagating waves observed in figures 8.9 to 8.11. However, this may simply mean that the interaction between the landslide and the generated waves affected the spatial distribution of energy within the wave field, while conserving the total integrated quantity over the entire spatial domain. Another possibility is that the increased interactions during the physical experiments were balanced by attenuation of the energy within the wave field.

Figure 8.15 compares the numerical and experimental potential energy within the onshore and offshore regions of the wave field from Run 22. The amount of energy within the offshore region was approximately 3 times the amount of energy within the onshore region. Both models correctly predicted the distribution of energy between the two regions. In the onshore region, the energy remained relatively constant after the initial peak (although the energy calculated from the experimental wave amplitudes exhibited some attenuation, as observed at $Fr = 0.125$). The time-varying behaviour of the energy within the offshore region was very similar to that of the total energy within the wave field, since most of the potential energy in the wave field was contained within this region. The under-prediction of the potential energy by the inviscid models was

slightly more severe in the offshore region than in the onshore region. The nonlinear model under-predicted the initial energy peak by 11% in the onshore region, and by 19% in the offshore region, compared to under-predictions of 25% and 36% by the linear model. This behaviour was consistent over all experiments conducted at $Fr = 0.250$, and the plots of the energy contained within the onshore and offshore regions for the remaining experiments are provided in appendix D.

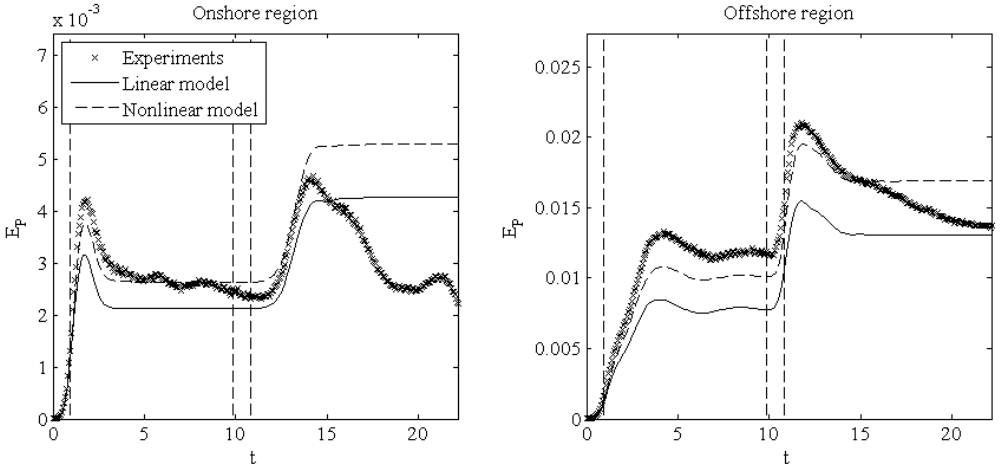

Figure 8.15: Potential energy contained in the onshore and offshore regions of the wave field for Run 22.

Figure 8.16 shows the mass within the offshore and onshore regions, as predicted by the two inviscid models and calculated from the measured wave amplitudes within Run 22. All other plots from this Froude number are provided in appendix E. The time-dependent behaviour of the mass in the two regions is very similar to the previous Froude number. The linear model under-predicted the peak positive mass in the offshore region by 23%, while the nonlinear model under-prediction was 15%.

8.4 Predictions at $Fr = 0.375$

In the experiments conducted at this Froude number, the interaction between the landslide and the offshore-propagating waves became more prominent, evidenced by the large amplitude of the free surface depression and the apparent trapping of a group of short-wavelength waves behind this trough (although these did not show the resonant behaviour observed at higher Froude numbers). The prediction of these interactions therefore became more important in determining the inviscid models' abilities to predict the evolution of the entire wave field.

As with the previous two Froude numbers, the initial comparisons between the model predictions and experimental measurements consider the wave field plots from one experiment. In this case, the experiment selected was Run 23, with the parameters

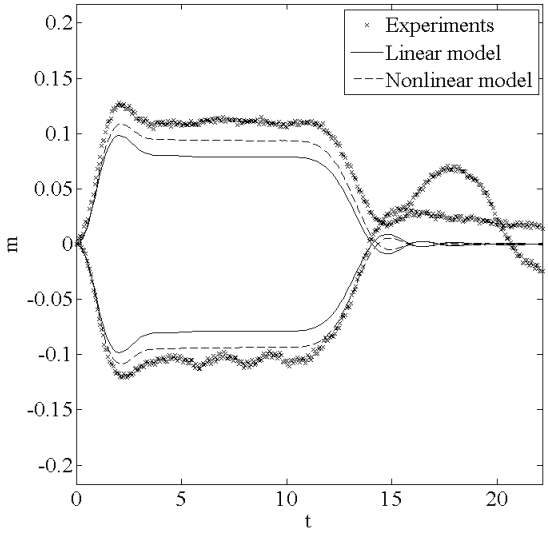

Figure 8.16: Mass transported by the onshore and offshore wave packets in Run 22.

$\lambda = 0.153$, $\tau = 0.35$, and $Fr = 0.375$, and figures 8.17 to 8.19 compare the predicted and measured wave fields within this experiment. The nondimensional duration of the landslide acceleration in this experiment was 1.45. This longer duration of the acceleration period meant that the effect of the landslide acceleration and submergence depth on the wave field evolution were greater than at the lower Froude numbers.

The landslide acceleration again generated offshore- and onshore-propagating wave packets, with a leading offshore-propagating crest and onshore-propagating trough. The amplitudes of both leading waves were initially under-predicted by 11% by the nonlinear model, and by 12% by the linear model (at $t = 1.1$). The under-prediction of the leading offshore-propagating crest by the nonlinear model had decreased to 4% by $t = 2.7$, compared to 12% by the linear model. At this time, the onshore-propagating trough was under-predicted by 7% by the linear model, and over-predicted by 2% by the nonlinear model. The over-prediction of the onshore-propagating trough by the nonlinear model (and after $t = 7.5$ by the linear model) increased until the reflection of this wave, at approximately $t = 12$.

The offshore region contained the greatest discrepancies between the predicted and measured wave fields. At $t = 2.7$, the free surface depression was superposed with the first offshore-propagating trough. At this time, the linear and nonlinear models under-predicted the amplitude of this combined trough by 19% and 10%, respectively. The predicted location of the free surface depression was also 0.06 in front of the measured location.

The free surface depression and the offshore-propagating trough separated by $t = 7.5$, however the actual amplitude of the trough after separation was much lower than

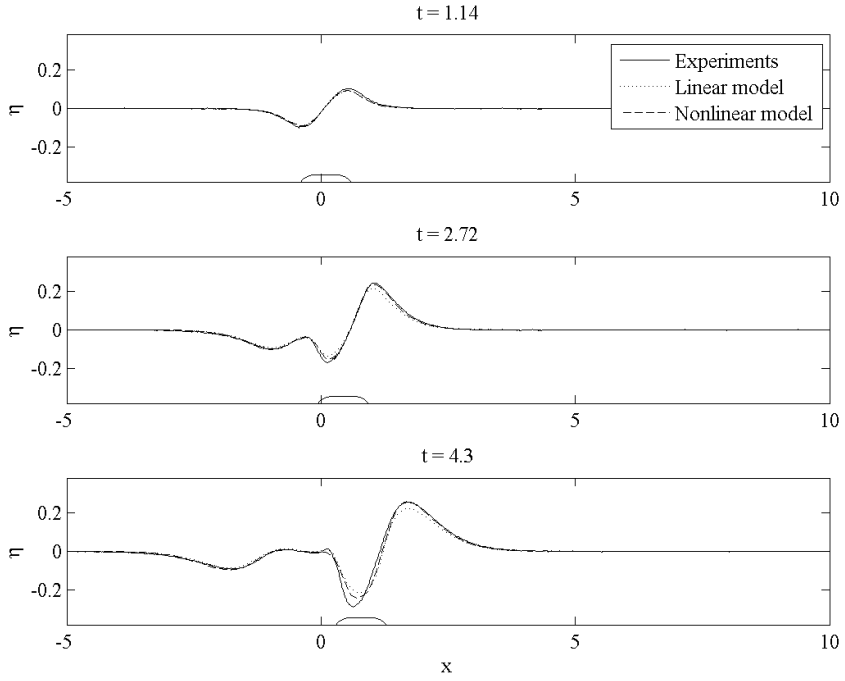

Figure 8.17: Comparisons between measured and predicted wave amplitudes in Run 23, between $t = 1.1$ and $t = 4.3$.

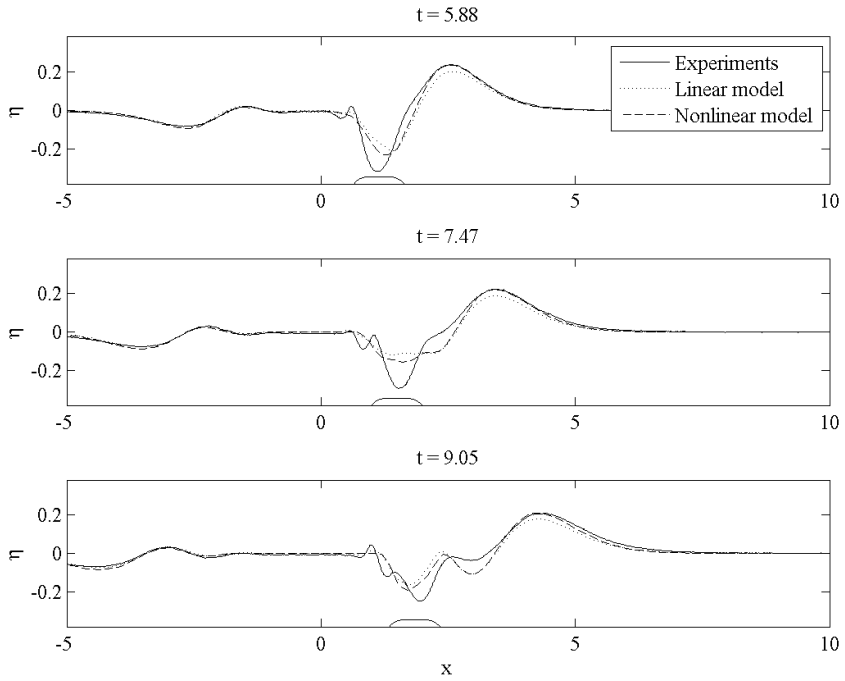

Figure 8.18: Comparisons between measured and predicted wave amplitudes in Run 23, between $t = 5.9$ and $t = 9.1$.

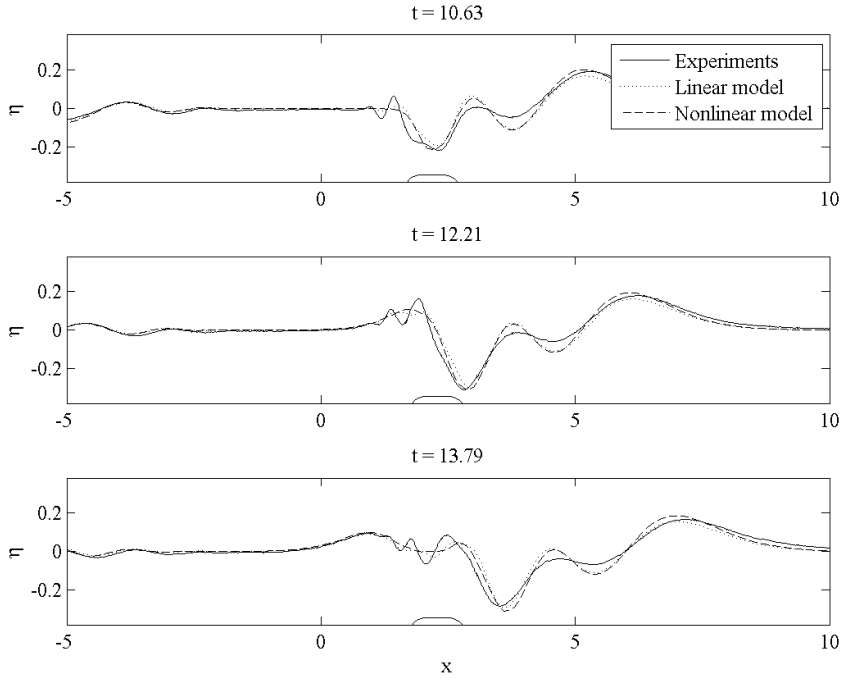

Figure 8.19: Comparisons between measured and predicted wave amplitudes in Run 23, between $t = 10.6$ and $t = 13.8$.

predicted by the two models. Figure 8.18 shows that the amplitudes predicted by the two models were almost identical for this offshore-propagating trough, but were approximately three times larger than the measured value (where these amplitude comparisons were made at $t = 9$). The models were not able to correctly predict the amplitudes of the experimentally-measured waves directly behind the free surface depression. These waves were weakly nonlinear, and the nonlinear steepening of these waves appeared to slightly reduce the effects of dispersion. Thus, dispersive effects appeared to be more significant in the model predictions of the offshore-propagating wave packet than in the experimental measurements.

The first crest in the group of small-wavelength waves was observed at $t = 4.3$, and by $t = 9.1$ two crests and troughs were present in this group. The waves propagated as a dispersive group containing several waves of relatively uniform wavelength. The waves within this group satisfied the condition

$$c_g \leq u_t \leq c_p, \tag{8.2}$$

where c_g is the wave group velocity, u_t is the landslide terminal velocity and c_p is the wave phase velocity. In this experiment, the nondimensional wavelength was 0.5, leading to a nondimensional phase velocity of 0.282 and a nondimensional group velocity of 0.141. The nondimensional landslide terminal velocity was 0.222. Thus, waves were

created at the back of the wave group, and were destroyed at the front of the group (as they propagated past the moving landslide). After the landslide motion ceased, these waves propagated in the offshore direction, and were superposed with the additional waves generated by the landslide deceleration.

The models were able to predict the waves generated by the landslide deceleration, as shown by the onshore-propagating crest at $t = 13.8$. At this time, the nonlinear model over-predicted the crest amplitude by 2%, while the linear model under-predicted its amplitude by 9%. Superposition with the steep waves behind the landslide made the accuracy of the predictions of the trailing waves generated by the landslide deceleration more difficult to quantify.

Figures 8.20 and 8.21 compare the predicted and measured peak wave amplitudes for all experiments at this Froude number, considering the deeper and shallower submergence depths respectively. The nonlinear model under-predictions of the peak wave amplitudes were on average 7% less than the linear model under-predictions. Again, the under-prediction of both models improved with increasing λ, and the average under-prediction decreased by 5% between $\lambda = 0.051$ and $\lambda = 0.153$. The leading trough predictions in the experiments with $\tau = 0.35$ were approximately 9% larger than the other leading wave under-predictions, at all landslide accelerations. This may be due to an amplitude increase in this trough before it had separated fully from the free surface depression above the landslide.

The τ dependence of the leading trough under-prediction was also observed in the predictions of the free surface depression amplitude. The linear model under-predictions of this trough amplitude were approximately 13% larger at $\tau = 0.35$ than at $\tau = 0.70$, while the nonlinear model predictions were approximately 10% larger at $\tau = 0.35$. Thus, it appears that the wave trapping behind the moving landslide (which the inviscid models did not correctly resolve) was more pronounced at the shallower submergence depth. Since the waves generated above the shallower submergence depth had smaller wavelengths, the steepness of these waves may have been greater than those generated over the deeper submergence depth.

The potential energy time series shown in figure 8.22 again highlights the differences between the predicted and measured wave fields during the constant-velocity phase of motion, where Run 23 is used as a representative experiment at this Froude number. Both models predicted the initial increase in potential energy during the acceleration period, and the subsequent increase to the peak value during the constant-velocity period. The peak energy occurred slightly earlier in the numerical simulations than in the experiment, with the linear model predicting the peak at $t = 5.06$, the nonlinear model predicting the peak at $t = 5.30$, and the actual peak occurring at $t = 5.82$. The nonlinear model under-predicted the magnitude of the energy peak by 19%, while the under-prediction of the linear model was 38%. The models predicted more

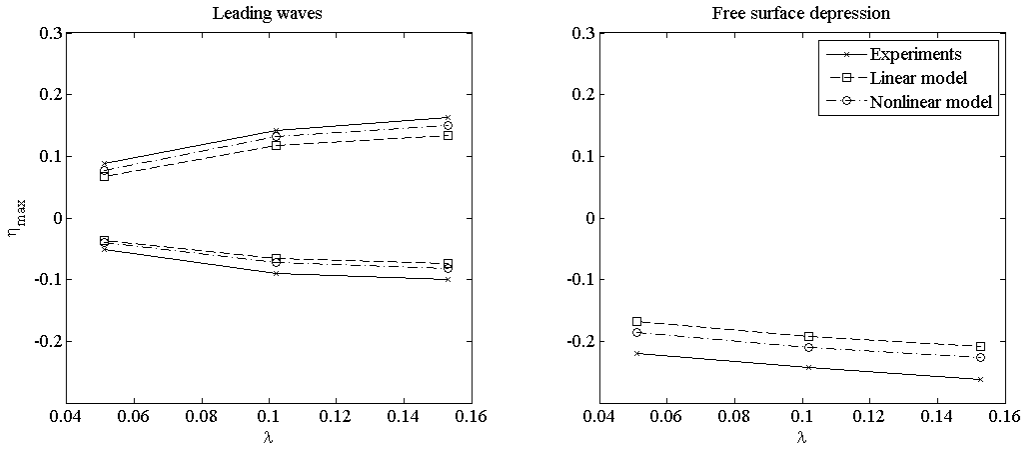

Figure 8.20: Comparisons between measured and predicted peak wave amplitudes for all experiments with $Fr = 0.375$ and $\tau = 0.70$.

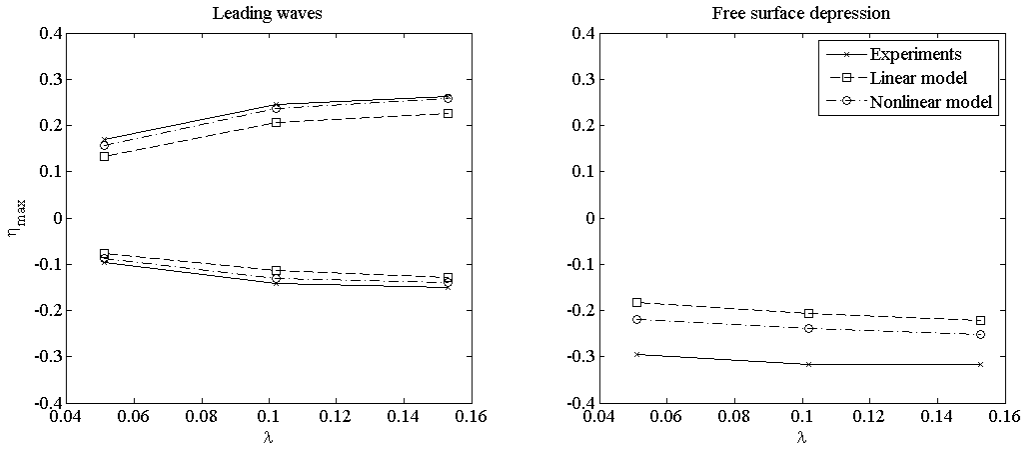

Figure 8.21: Comparisons between measured and predicted peak wave amplitudes for all experiments with $Fr = 0.375$ and $\tau = 0.35$.

frequent energy fluctuations following the initial energy peak than were observed in the experimental record.

Figure 8.23 shows the distribution of energy in the offshore and onshore regions, again calculated using Run 23 as a representative experiment. Approximately 85% of the energy within the wave field was located within the offshore region, and thus the time-dependent behaviour of the energy within this region was almost identical to that of the entire wave field, discussed above. In the onshore region, the initial peak due to the superposition of the two troughs was followed by a period of constant energy in the model predictions, and a period of attenuation in the experimental measurements. As with the previous Froude numbers, the under-predictions of energy by the linear and nonlinear models were lower in the onshore region (23% and 8%, respectively) than in the offshore region (39% and 21%, respectively).

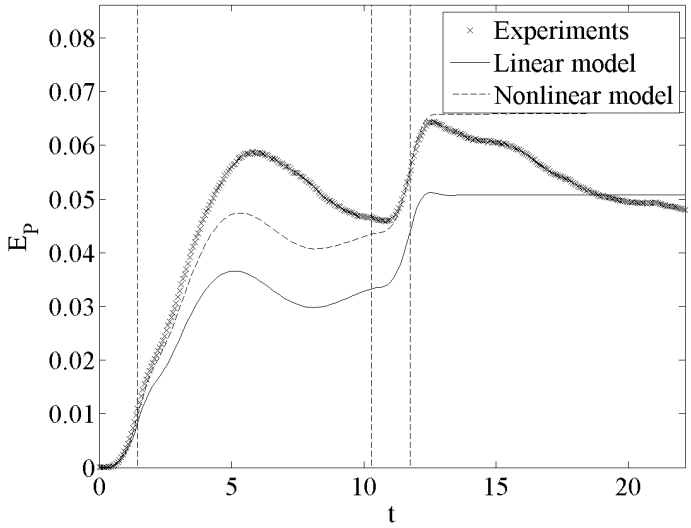

Figure 8.22: Comparisons between measured and predicted wave field potential energy for Run 23, with $\lambda = 0.153$, $Fr = 0.375$ and $\tau = 0.35$.

The under-prediction of the directional mass transport at this Froude number was 15% for the linear model, and 8% for the nonlinear model. The time variation of mass within the onshore and offshore regions for all experiments undertaken at this Froude number are provided in appendix E (potential energy comparisons are provided in appendices C and D).

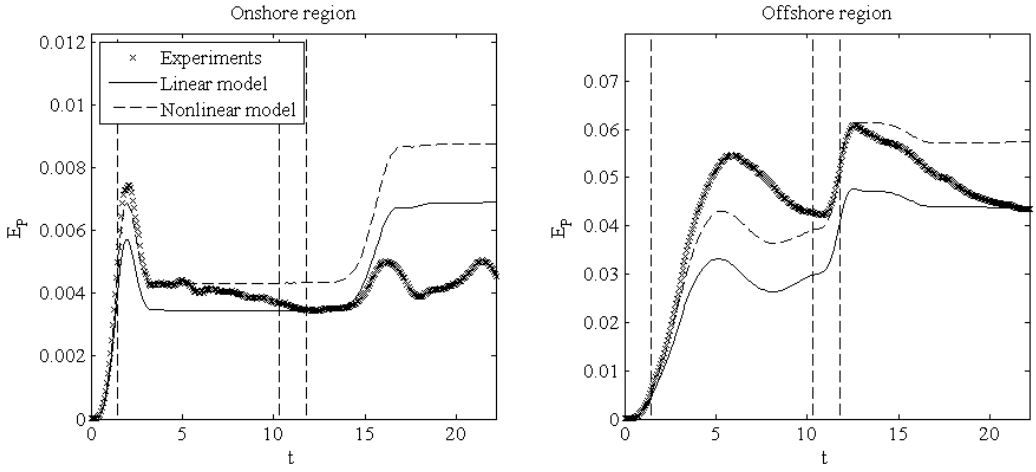

Figure 8.23: Potential energy contained in the onshore and offshore regions of the wave field for Run 23.

8.5 Predictions at $Fr = 0.500$

In the physical experiments carried out at $Fr = 0.500$, the constant-velocity phase of motion had the greatest influence on the evolution of the wave field. The trapped waves propagating with the landslide began to exhibit highly nonlinear behaviour, and their amplitudes were larger than the amplitude of the leading offshore-propagating crest. The nondimensional duration of the acceleration phase of motion was 1.94.

Figures 8.24 to 8.26 show a series of wave field plots captured during Run 24, with parameters $\lambda = 0.153$, $\tau = 0.35$ and $Fr = 0.500$. This experiment is used as a representative experiment in this initial discussion of the wave field behaviour. Figure 8.24 shows that the inviscid models correctly predicted the phase of the leading waves. The linear model under-predicted the leading crest and trough amplitudes at $t = 1.1$ by 11% and 9% respectively, while the nonlinear model under-predicted the same amplitudes by 10% and 8%. By $t = 4.3$, however, there was a phase difference of approximately 0.2 between the model predictions and the experimental measurements of the free surface depression above the moving landslide. The experimentally-measured depression had a larger amplitude, and was located slightly further behind the landslide, than the models predicted. The under-prediction of the free surface depression amplitude at $t = 4.3$ was 14% by the nonlinear model, and 24% by the linear model.

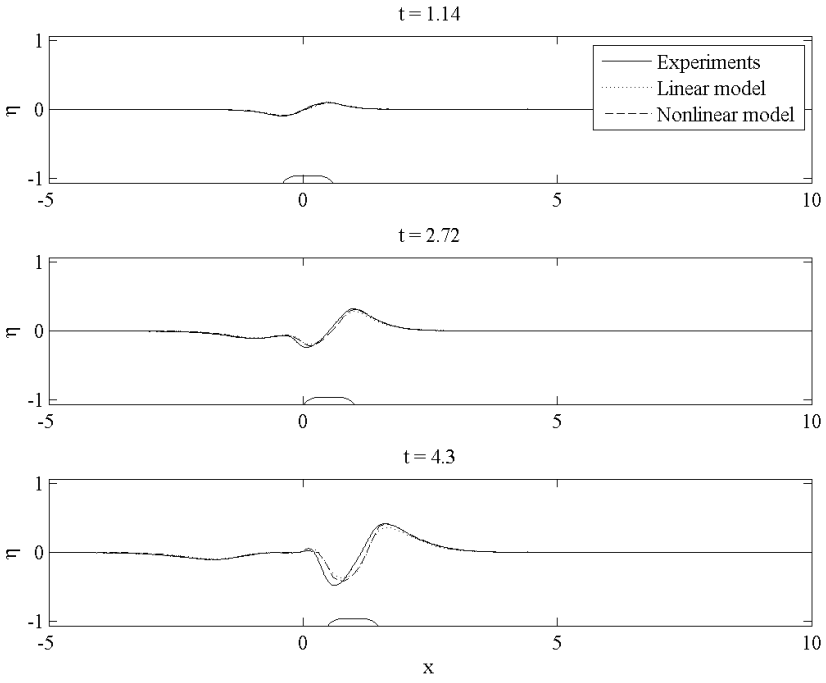

Figure 8.24: Comparisons between measured and predicted wave amplitudes in Run 24, between $t = 1.1$ and $t = 4.3$.

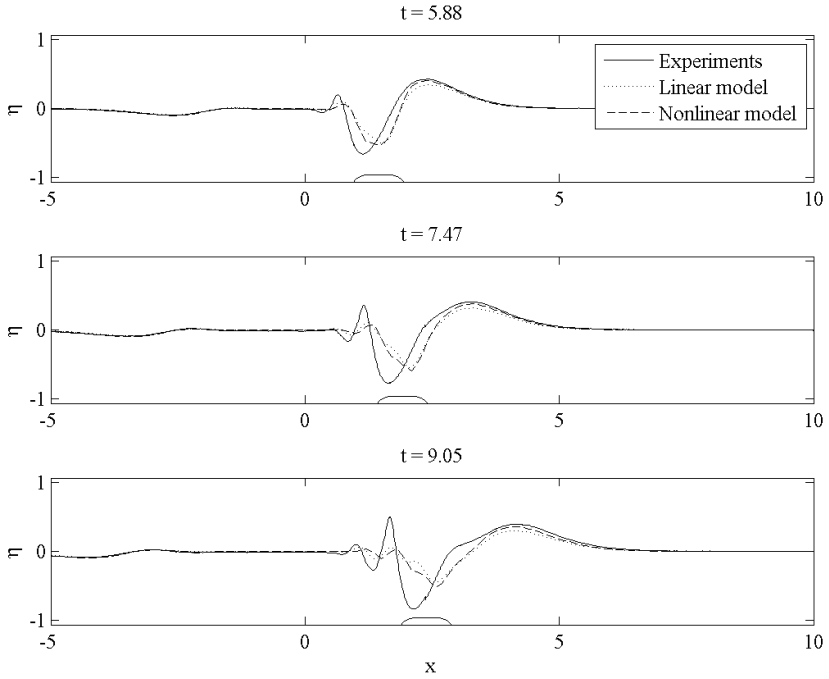

Figure 8.25: Comparisons between measured and predicted wave amplitudes in Run 24, between $t = 5.9$ and $t = 9.1$.

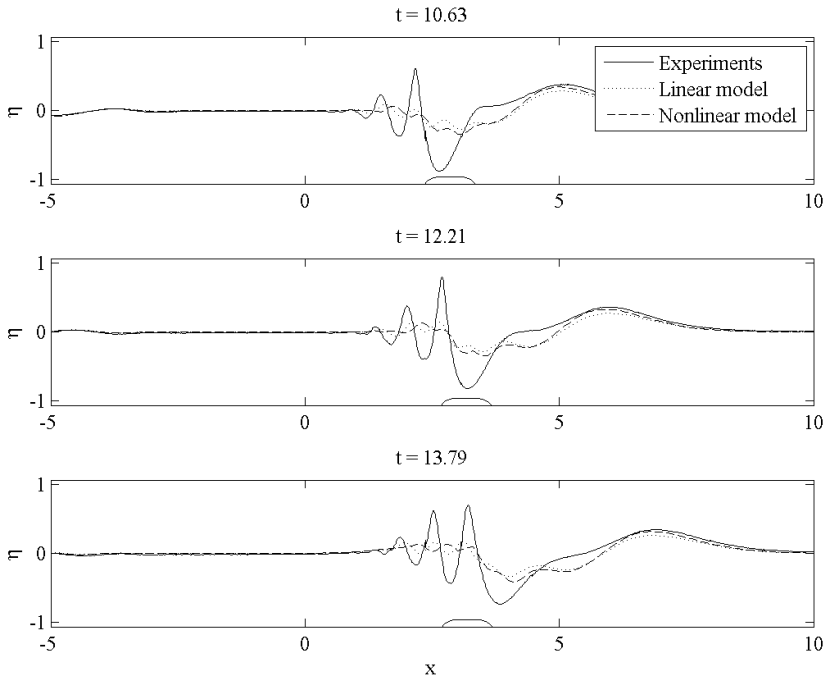

Figure 8.26: Comparisons between measured and predicted wave amplitudes in Run 24, between $t = 10.6$ and $t = 13.8$.

As shown in figure 8.25, the discrepancies between the predicted and measured wave field became more pronounced during the constant-velocity motion of the landslide. The free surface depression measured during the experiments was located closer to the rear of the landslide, while the models predicted that the depression was located above the landslide centre of mass. The location of maximum depression amplitude exhibited greater variation in the model predictions, as this was modified when successive offshore-propagating waves passed above the landslide. In the physical experiments, nonlinear effects reduced the dispersive spreading of the offshore-propagating waves, so that these waves propagated with the landslide for a longer time period. This allowed a longer period of energy exchange between the landslide and these waves. Thus, at $t = 7.5$, the nonlinear model under-predicted the depression amplitude by 23%, and the linear model under-predicted the depression amplitude by 29%.

As a result of their under-prediction of the trapped wave amplitudes, the models over-predicted the amplitudes of the offshore-propagating waves in front of the landslide, with nondimensional differences in amplitude of approximately 0.2 (percentage over-predictions are not considered since the trough in the experiments had a positive η value in front of the landslide). Again, this is indicative of the effect of the linearised free surface assumption on the model predictions, since these models could only include dispersive effects (as opposed to the increasingly nonlinear effects observed during the experiments).

The trapped waves were much more prominent in the experimental wave field at this Froude number than at $Fr = 0.375$. Although a limited number of these waves formed, due to the limited duration of the constant-velocity landslide motion, they still possessed a uniform wavelength of approximately 0.508 and propagated as a dispersive group. Since the landslide velocity was equal to the phase velocity of the leading wave within this group, the initial crest did not propagate past the landslide. Thus, the landslide was able to continually input energy into this leading wave, which increased the nonlinearity of these waves and further reduced the effects of dispersion, so that the wave propagated with a relatively unchanging amplitude and shape. Since new waves were still created at the rear of the wave group (since the group velocity was approximately half of the phase velocity), the spatial extent of this wave group grew during the constant-velocity phase of motion.

Although some short-wavelength waves were predicted to propagate behind the landslide by the inviscid models, the apparent trapping of energy within these waves was not evident in the model predictions, and so the amplitudes of these waves were significantly smaller than those measured during the experiment. Although the landslide would still input energy into the leading wave within this group, dispersion would act to almost immediately broaden the wave itself. Thus, the wave celerity would increase, and it would pass over the landslide. Since the models could not account for wave non-

linearity, they could not predict the steepening of these waves (and hence, lessening of dispersive effects). At $t = 7.5$, the linear model under-predicted the amplitude of the first crest behind the landslide by 70%, while the nonlinear model under-predicted the amplitude by 80%. Both models predicted the location of this crest in front of the measured location (by 0.07 and 0.14 respectively), showing the lack of trapping in the model predictions.

At this landslide Froude number, the free surface depression was much larger than the leading offshore-propagating trough. The difference between the two wave amplitudes was more pronounced at the shallower submergence depth. Figure 8.27 compares the predicted and measured peak amplitudes for all experiments with $Fr = 0.500$ and $\tau = 0.70$, and figure 8.28 shows the same comparisons for $\tau = 0.35$.

The amplitude of the free surface depression relative to the leading trough amplitude was larger at $\tau = 0.35$, and the level of under-prediction by the two numerical models was also much larger at this submergence depth. The under-predictions at $\tau = 0.35$ were approximately 14% larger in the linear model, and 17% larger in the nonlinear model. The nonlinear model under-predictions were 6% lower than the under-predictions by the linear model at $\tau = 0.35$, and 9% lower at $\tau = 0.70$.

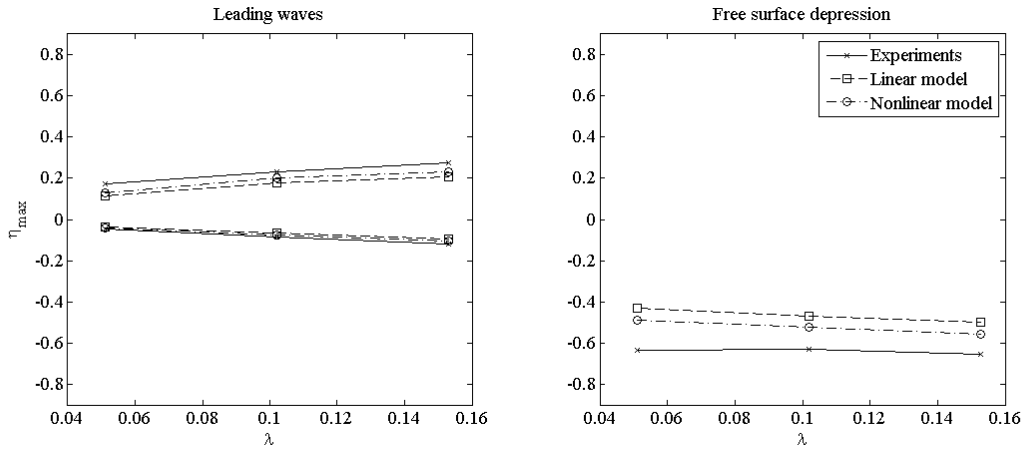

Figure 8.27: Comparisons between measured and predicted peak wave amplitudes for all experiments with $Fr = 0.500$ and $\tau = 0.70$.

Figure 8.29 compares the time variation of the potential energy within the wave field calculated from the experimental wave amplitudes and predicted by the inviscid models. The time-varying behaviour of the predicted potential energy was very similar to that of previous Froude numbers, with an initial increase to a peak value, followed by fluctuations during the constant-velocity phase of motion and a second peak caused by the deceleration-generated waves. However, the potential energy within the experimental wave field continued to increase over the entire landslide motion period, and did not exhibit a clearly-defined peak. This steady increase in potential energy within

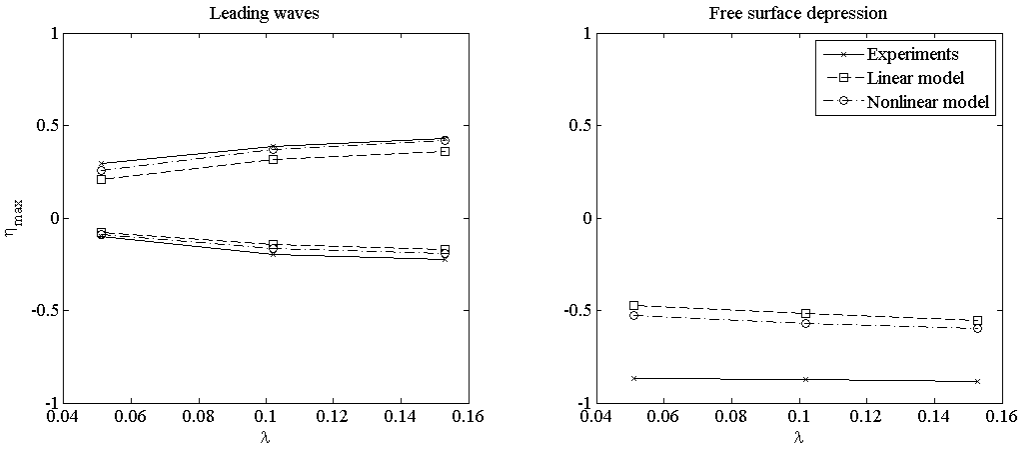

Figure 8.28: Comparisons between measured and predicted peak wave amplitudes for all experiments with $Fr = 0.500$ and $\tau = 0.35$.

the wave field appeared to be caused by the ongoing exchange of energy between the landslide and the trapped wave group, and the resulting growth of this wave group during the constant-velocity phase of motion. Thus, the linear and nonlinear models under-predicted the peak energy within the wave field by 66% and 55%, respectively.

The potential energy within the wave field continued to increase even after the landslide had ceased its motion entirely. This small period of energy increase was observed in both the predicted and measured wave fields. The motion of the landslide would initially impart kinetic energy to the fluid near the bottom boundary. It is expected that the total energy within the system would remain constant after the landslide ceased its motion, and that the short period of increasing potential energy would be accompanied by a corresponding decrease in the kinetic energy of the fluid beneath the free surface.

The potential energy within the offshore region of the wave field accounted for over 90% of the total energy within the wave field (over 96% in the case of the physical experiments). Thus, the time-dependent behaviour of the energy within the offshore region was identical to the behaviour of the total energy. The energy within the onshore region of the wave field exhibited the same time-varying behaviour as observed at lower landslide Froude numbers, since the waves within this region did not continue to interact with the landslide after their generation. The under-predictions of the initial peak in the onshore energy were 32% by the linear model, and 19% by the nonlinear model. The predicted and measured energy within the offshore and onshore regions for all experiments conducted at $Fr = 0.500$ are compared in appendix D, and the equivalent plots of total energy are provided in appendix C.

The mass transported by the onshore- and offshore-propagating waves at this Froude number also exhibited the same time-dependent behaviour as observed at the lower

landslide Froude numbers, and is not shown in this section. The plots of the directional mass transport for all experiments conducted at this Froude number are shown in appendix E. Unlike the wave amplitude and energy, the resonant behaviour of the trapped waves did not greatly impact the ability of the models to predict the mass transported by the two groups of waves at this Froude number, and the under-prediction by the linear model was 19%, compared to 11% by the nonlinear model.

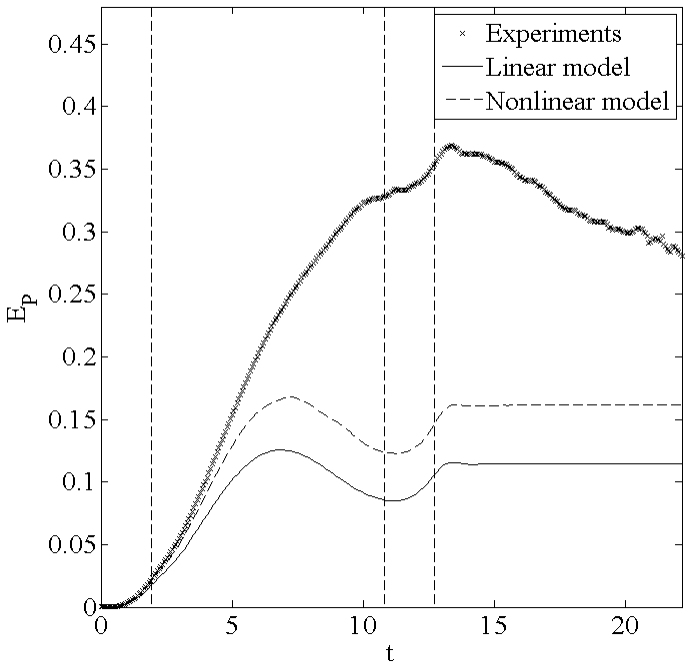

Figure 8.29: Comparisons between measured and predicted wave field potential energy for Run 24, with $\lambda = 0.153$, $Fr = 0.375$ and $\tau = 0.35$.

8.6 Viscous model comparisons

8.6.1 Viscous model resolution effects

As discussed in chapter 5, the viscous model solved the Navier-Stokes equations over an adaptive grid. Although the grid itself was dynamically refined during the simulations, it is important to determine the effect of the maximum grid resolution on the predictions of the wave field and subsurface velocity fields. Although the generated waves are of the most interest in the current study, the subsurface velocity field provides insight into the ability of the viscous model to correctly predict the turbulent wake generated by the landslide motion.

Five different maximum resolutions were tested, corresponding to maximum levels of 8, 9, 10, 11 and 12. A level is defined as the number of times one of the original

simulation boxes is divided into four smaller boxes (see chapter 5 for details). The higher resolutions are expected to perform better in their predictions of the wake formed behind the moving landslide, particularly near to the corner of the landslide itself. However the resolution is expected to have less impact on the free surface wave amplitudes predicted by the model.

Figure 8.30 compares the wave amplitudes predicted by the viscous model using the five different resolutions, at $t = 5.0$. At the coarsest grid resolution, the wave amplitudes were slightly under-predicted (this under-prediction was approximately 2% of the maximum wave amplitude). However, at the finest resolution of level 12, the solution became unstable and the free surface profile contained a large amount of noise. These instabilities were also present at level 11 to a lesser extent, but were not visible at the lower resolutions.

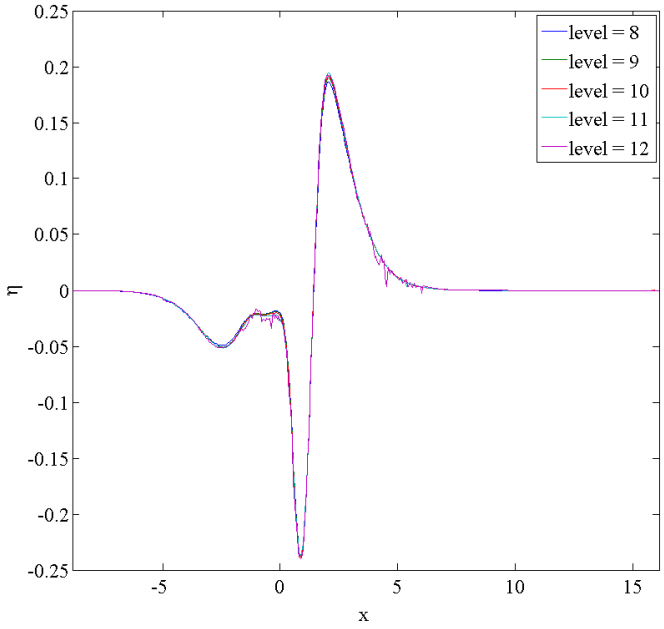

Figure 8.30: Comparisons between wave amplitude predicted by viscous model using different maximum grid resolutions.

Figures 8.31 and 8.32 compare the subsurface horizontal fluid velocities predicted by the viscous model in the vicinity of the landslide at $t = 5.0$, for maximum grid levels 8 and 12 respectively. The colour scale in both figures is modified for consistency with figure 8.33, which shows the horizontal velocity field measured during the PTV experiments at the same time. At the finer grid resolution, the horizontal fluid velocity predicted at the rear corner of the landslide (approximately $u = 12$) was much larger than the equivalent prediction at the coarser grid resolution (approximately $u = 2.5$). Both predictions were larger than the experimentally-measured values near the rear

of the landslide, although the PTV measurements were not available near the bottom boundary. The increasingly high fluid velocity appears to be linked to the instabilities on the free surface of the fluid at the finer grid resolutions. Neither the coarse or fine resolution was able to correctly predict the presence of the turbulent wake. Although a finer resolution should have been able to correctly predict this wake, the model became unstable before the wake developed. The issues with instabilities appear to have been linked to the rear corner of the landslide, and the near-vertical face of the moving solid block.

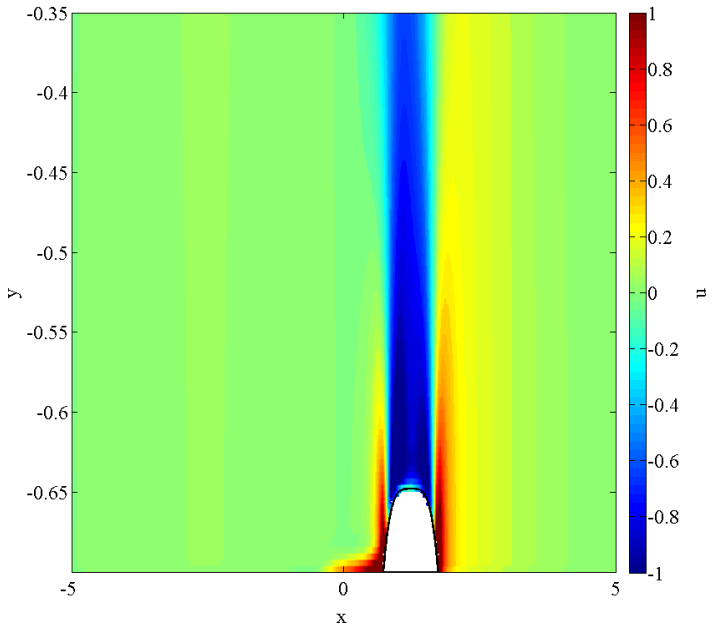

Figure 8.31: Horizontal velocity field predicted by the viscous model with a maximum grid resolution level of 8.

Since stability of the model was paramount, a relatively coarse resolution of 9 was selected for the viscous model simulations. The horizontal velocity fields shown in figures 8.31 to 8.33 show that the model would not correctly predict the presence of the turbulent wake behind the landslide. However, the grid resolution had a diminished effect on the amplitudes of the generated waves, and so the model was still able to provide free surface predictions for comparison with the physical experiments. As shown in figure 8.30, the under-prediction of the free surface at a resolution of 9 was approximately 1% (compared to the finer resolutions).

8.6.2 Viscous model predictive capabilities

As discussed in section 8.1, the viscous model provided predictions for the wave amplitudes and subsurface velocity and pressure fields generated during Run 12. The

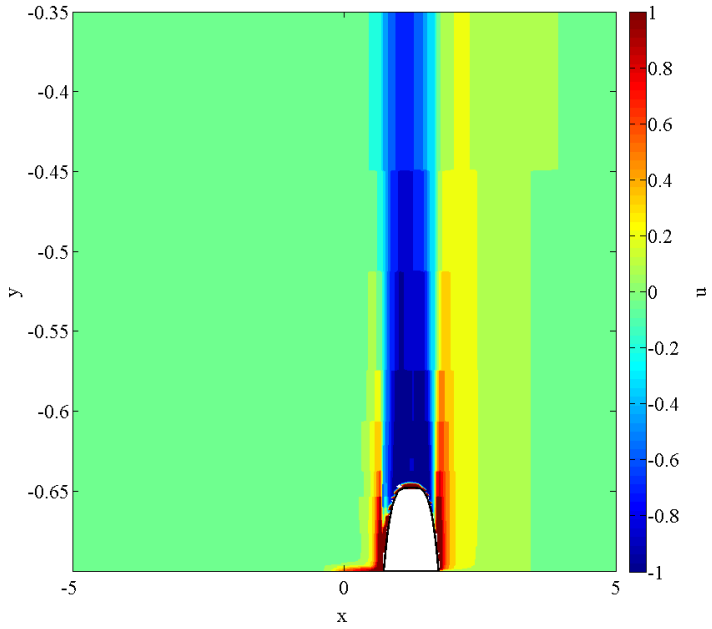

Figure 8.32: Horizontal velocity field predicted by the viscous model with a maximum grid resolution level of 12.

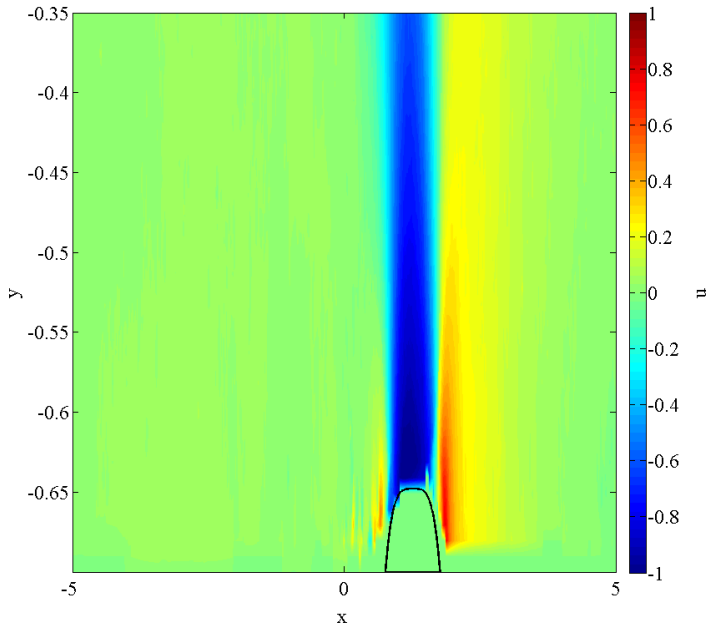

Figure 8.33: Horizontal velocity field measured during the PTV experiments.

previous section discussed the ability of the two inviscid models to correctly predict the waves generated during the experiments. The additional comparisons with the viscous model in this section allow the assessment of the validity of the inviscid-irrotational as-

sumption, and the linear assumption invoked by the inviscid models on the free surface. Figures 8.34 to 8.36 compare the predictions of the three models to the experimental measurements in a series of wave field plots.

As shown in figure 8.34, both types of models (viscous and inviscid) correctly predicted the initial evolution of the generated waves, although all of the models under-predicted the experimental wave amplitudes. At $t = 4.3$, the linear inviscid model under-predicted the amplitude of the leading crest by 19%, while the under-predictions by the nonlinear inviscid model and the viscous model were 11% and 8% respectively. The under-predictions of the free surface depression at the same time were 18%, 9% and 3% for the linear, nonlinear and viscous models. Thus, the viscous model provided more robust predictions of the initial wave amplitudes than either of the inviscid-irrotational models.

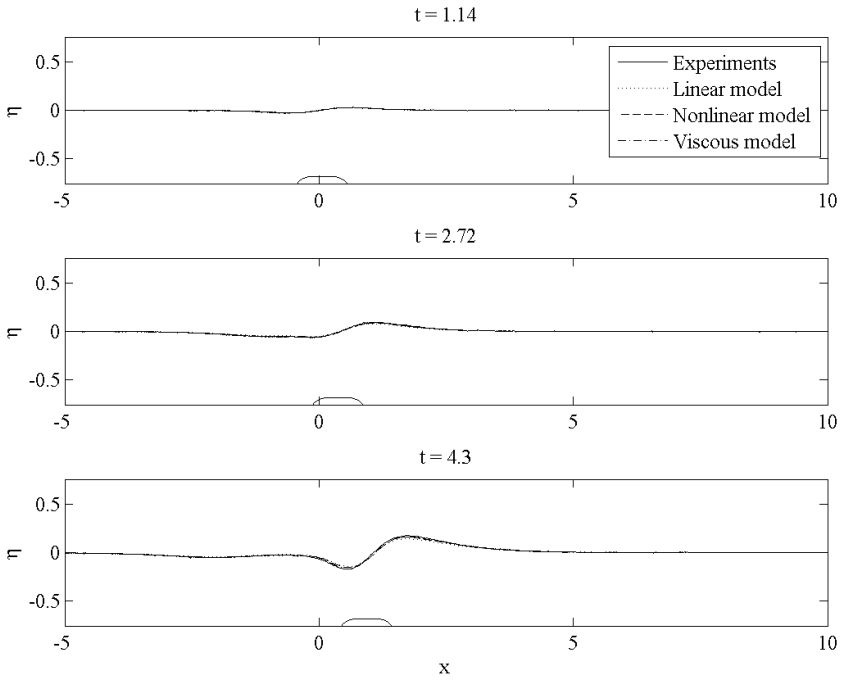

Figure 8.34: Comparisons between measured and predicted wave amplitudes in Run 12, between $t = 1.1$ and $t = 4.3$.

In figure 8.35, the inviscid models were unable to correctly predict the location or amplitude of the depression above the landslide during the constant-velocity phase of motion. As discussed in section 8.5, the inviscid models also predicted larger wave amplitudes in front of the free surface depression, but did not capture the resonant behaviour of the trapped wave group behind the depression itself. However, the viscous model predictions of the free surface depression amplitude and location were much closer to the experimental measurements. At $t = 9$, the experimentally-measured

location was 2.608, the viscous model prediction was 2.614, the linear model prediction was 2.760 and the nonlinear model prediction was 2.800. Also at $t = 9$, the under-prediction of amplitude by the viscous model was 3%, while the under-predictions by the linear and nonlinear models were 21% and 13% respectively. Thus, the inclusion of fluid viscosity and wave nonlinearity appeared to enable the numerical model to more accurately predict the interaction between the landslide and the offshore-propagating waves.

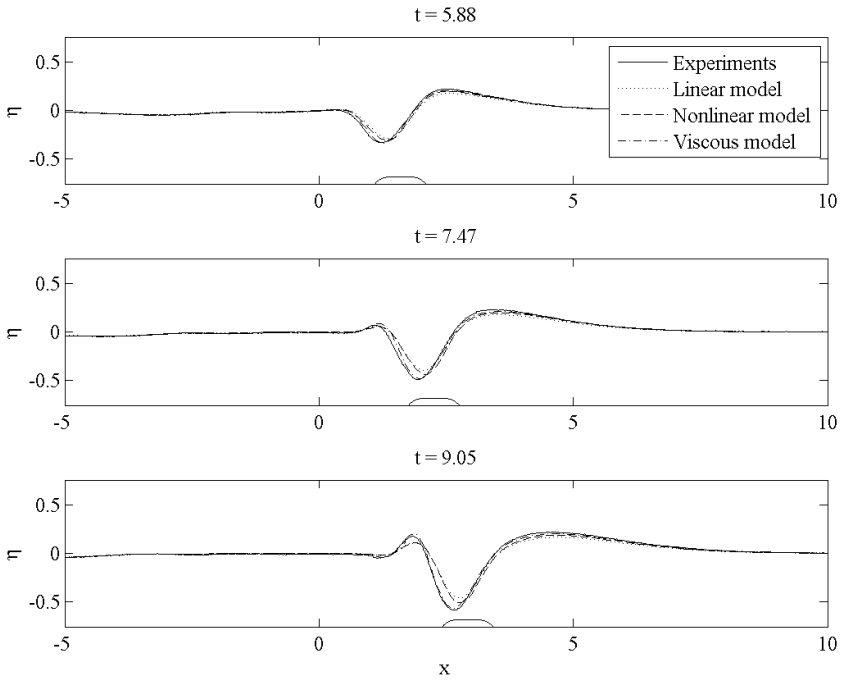

Figure 8.35: Comparisons between measured and predicted wave amplitudes in Run 12, between $t = 5.9$ and $t = 9.1$.

In the wave field plots shown in figure 8.36, the formation and resonant behaviour of the trapped wave group is evident in the experimental measurements and the viscous model predictions. The inviscid models both failed to predict this behaviour, and their predictions continued the trend of over-prediction in front of the landslide and under-prediction behind the landslide observed in figures 8.34 and 8.35. The inviscid model predictions of the offshore-propagating waves behind the landslide also became increasingly out of phase with the experimentally-measured waves during the constant-velocity phase of motion. The landslide began to decelerate at $t = 12.96$.

The viscous model predictions of the nonlinear wave behaviour during the constant-velocity phase of motion were qualitatively much closer to the experimental behaviour than either of the inviscid models. Thus, the model was able to better reflect the reduced effect of dispersion due to wave nonlinearity. However, there were still some

inconsistencies in the predictions of the amplitudes of the trapped waves. The viscous model over-predicted the amplitude of the first crest trapped behind the landslide by 12% at $t = 10.6$, and under-predicted the free surface depression amplitude by 5% at the same time. The inviscid models under-predicted the free surface depression amplitude by 26% and 17% respectively at $t = 10.6$.

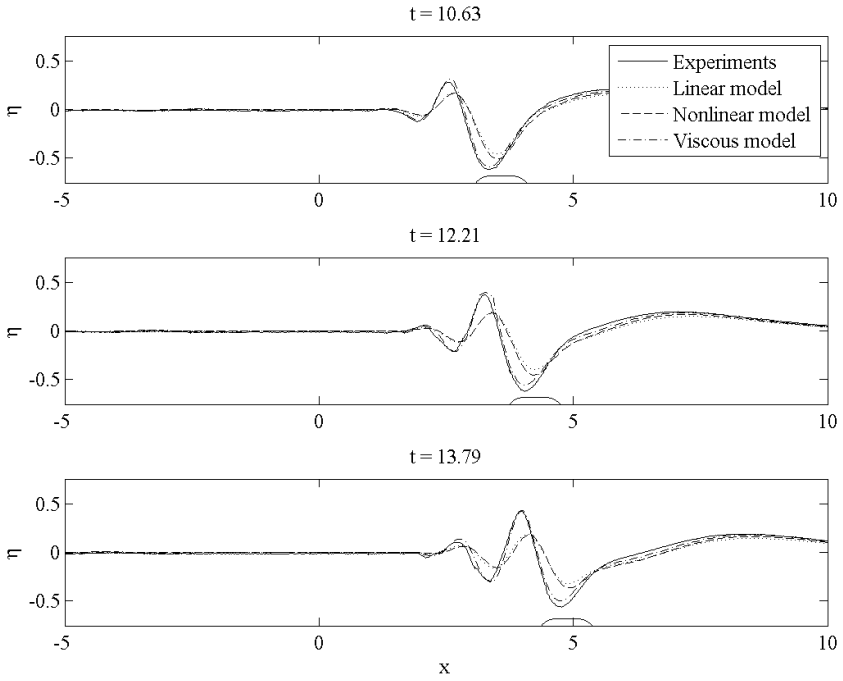

Figure 8.36: Comparisons between measured and predicted wave amplitudes in Run 12, between $t = 10.6$ and $t = 13.8$.

Figure 8.37 compares the potential energy within the wave field, as predicted by the three numerical models and calculated from the experimental measurements of wave amplitude. The linear inviscid model predicted a peak potential energy value of 0.096, occurring at a time of 10.4, the nonlinear inviscid model predicted a peak energy of 0.119, occurring at a time of 10.4, the viscous model predicted a peak energy of 0.174, occurring at a time of 12.2, while the experimental energy had a peak value of 0.204, occurring at a time of 11.8. Thus, the under-predictions of the peak potential energy within the wave field by the linear, nonlinear and viscous models were 53%, 42% and 15% respectively. The reflections of the onshore waves occurred at approximately $t = 10$, and the reflections of the offshore-propagating waves occurred at approximately $t = 18$. The reflection of the offshore-propagating waves had a much larger effect on the potential energy within the wave field, since the majority of the potential energy was contained in the offshore region during this experiment.

In summary, the viscous model still under-predicted the amplitudes of the waves

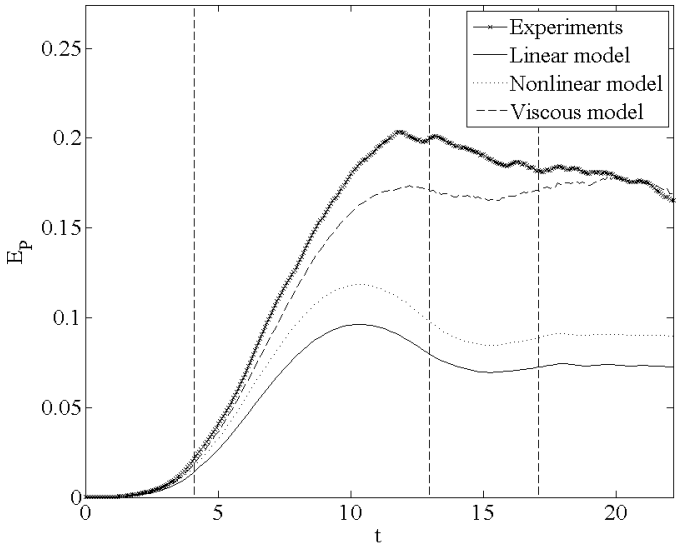

Figure 8.37: Comparisons between measured and predicted potential energy within the wave field for Run 12.

generated during the LIF experiments, and hence under-predicted the peak energy in the wave field by approximately 15%. However, the viscous model significantly improved the predictions of the interactions between the landslide and the offshore-propagating waves, due to the inclusion of nonlinearity at the free surface. The model correctly predicted the formation of the trapped wave group, and the location and amplitude of the trough above the landslide. Due to the issues discussed in section 8.6.1, the viscous model was unable to correctly resolve the turbulent wake behind the landslide, and this may be the reason for the lack of agreement with the experimental data. The effect of the fluid viscosity on the predicted subsurface velocity and pressure fields are discussed in the next section.

8.7 Subsurface predictions

The subsurface velocity field measurements obtained during the PTV experiments showed that the flow around the moving landslide was affected by the presence of the turbulent wake, and the trapped waves generated the strongest fluid motions near to the free surface. The linear inviscid-irrotational model provided predictions of the subsurface velocity and pressure fields for the same experiment (Run 12), to determine the effect of the model assumptions on its ability to predict the different features of the subsurface velocity field.

During the acceleration period, positive vertical velocities were generated at the front of the landslide, and negative vertical velocities were generated at the rear of the

landslide. The horizontal fluid velocities directly above the landslide were negative, while the positive horizontal velocities were generated at each end of the landslide. During the PTV experiments, these positive horizontal velocities were approximately equal (see chapter 7). However, the linear inviscid model predicted higher velocities at the front of the landslide than at its rear (as shown in figure 8.38, recorded at $t = 3.0$). Also, the linear inviscid model predicted higher negative vertical velocities behind the landslide than the positive vertical velocities in front of the landslide (shown in figure 8.39), while the PTV experiments showed the magnitudes to be approximately equal.

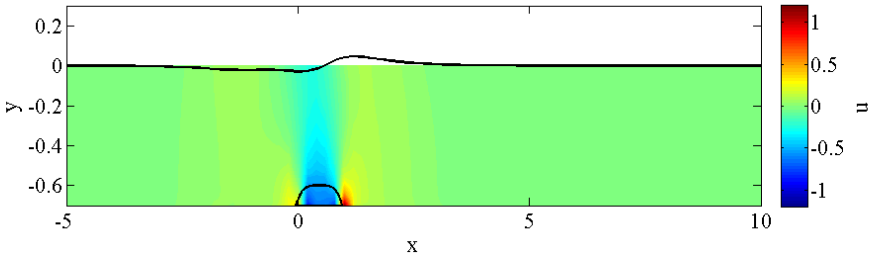

Figure 8.38: Horizontal velocity field predicted by the linear inviscid model during the acceleration of the landslide.

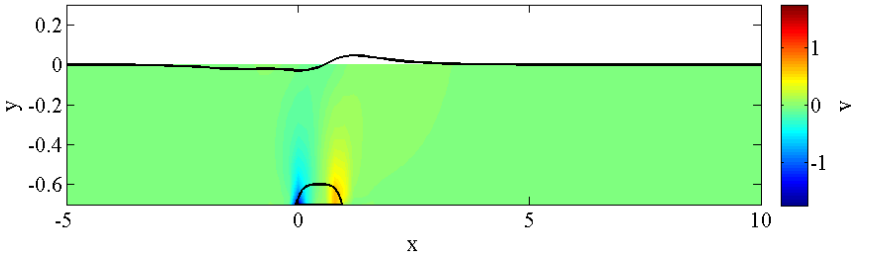

Figure 8.39: Vertical velocity field predicted by the linear inviscid model during the acceleration of the landslide.

Figures 8.40 and 8.41 show the horizontal and vertical velocity fields predicted by the linear inviscid model during the constant-velocity phase of the landslide motion, recorded at $t = 10.0$. The model predicted higher vertical velocities at the front of the landslide, but higher horizontal velocities at the rear of the landslide. However, the greatest difference between the linear inviscid model predictions and the measurements obtained during the PTV experiments is the absence of the turbulent wake in the model predictions. This turbulent wake propagated in the horizontal direction, and contained very chaotic fluid motions (see chapter 7).

The pressure field predicted by the linear inviscid model during the constant-velocity phase of motion contained the highest fluid pressures at the rear of the moving landslide. However, the presence of a turbulent wake would decrease the pressure at

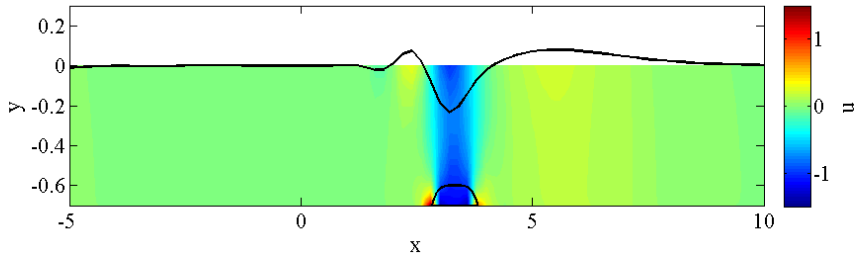

Figure 8.40: Horizontal velocity field predicted by the linear inviscid model during the constant-velocity phase of motion.

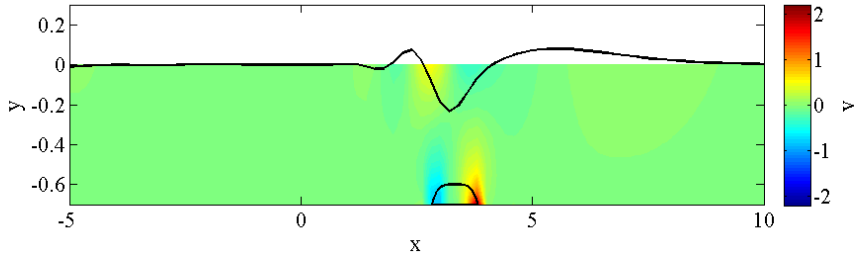

Figure 8.41: Vertical velocity field predicted by the linear inviscid model during the constant-velocity phase of motion.

this location. Along with the lack of wave nonlinearity, this high fluid pressure at the rear of the landslide has implications for the inviscid model's ability to correctly predict the wave behaviour in the vicinity of the moving landslide.

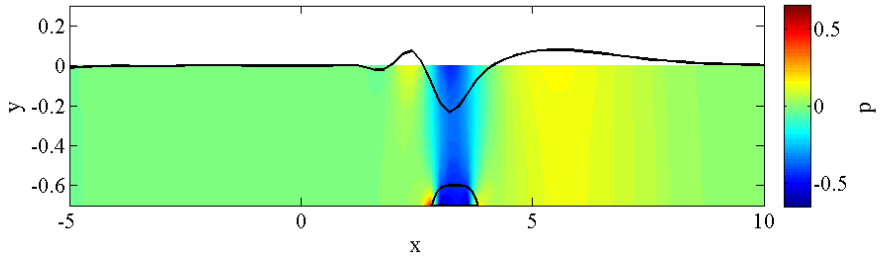

Figure 8.42: Pressure field predicted by the linear inviscid model during the constant-velocity phase of motion.

8.8 Interactions at constant landslide velocity

As discussed in the previous sections, a free surface depression was formed above the moving landslide during its constant-velocity motion. This free surface depression increased in amplitude with increasing Froude number and decreasing submergence

depth. The inviscid models under-predicted the amplitude of this free surface depression over the entire parameter space. Additionally, the inviscid models did not correctly predict the interaction between the offshore-propagating waves and the moving landslide. This was most evident at the higher landslide Froude numbers, where the inviscid models did not correctly predict the amplitudes of the group of short-wavelength waves trapped behind the landslide. This section summarises the effects of the model assumptions on their predictions of these waves.

As the landslide propagated at its terminal velocity, it input energy into the offshore-propagating waves in its vicinity. Those waves travelling with a phase velocity approximately equal to the terminal velocity of the landslide could continuously receive energy in this way, due to a Proudman-type resonance (see Vennell, 2009). Dispersive effects acted to separate these waves into their different wavelengths, and as longer-wavelength waves separated from the shorter-wavelength waves they propagated past the landslide (since their celerity was higher than the terminal velocity of the landslide).

The nonlinearity of these short-wavelength waves (which increased with the landslide Froude number) reduced the separation of the free surface disturbances over the different wavelengths. As discussed in chapter 7, the nonlinear effects were still much weaker than the effects of dispersion. However, neither of the inviscid models could predict the nonlinear steepening of the wave fronts, and therefore they only included the effects of dispersion on these waves. Hence, they under-estimated the amplitudes of the waves propagating with the landslide, and over-estimated the amplitudes of the longer-wavelength waves in front of the landslide.

The nonlinear inviscid model included the full bottom boundary condition. Although the effect of this boundary was greatest in the prediction of the leading waves by the model, the inclusion of the full boundary geometry could also slightly reduce the effects of dispersion on the waves propagating with the landslide. Considering a wave travelling with a celerity approximately equal to the landslide terminal velocity, as the wave broadened it would begin to propagate over the landslide. However, the fluid depth would reduce above the landslide, which would slightly decrease the celerity of the wave, causing it to continue propagating at the landslide velocity for a slightly longer time period. As observed in chapter 7, the short wavelengths of the trapped waves meant that they were classified as deep-water waves, and so the effects of the landslide thickness were negligible compared to the effects of wave nonlinearity. However, for very shallow submergence depths compared to the landslide length, the inclusion of the full bottom boundary nonlinearity is expected to have a greater effect on the propagation of waves past the landslide.

The inviscid models also could not predict the turbulent wake generated by the motion of the landslide. This wake would extend the length of the low-pressure region above the landslide, and decrease the depth over which the irrotational assumption

was valid. The wake may therefore have further contributed to the differences between the inviscid model predictions and experimental measurements of the free surface depression amplitude and wavelength. The effect of the turbulent wake is expected to be secondary to the effects of wave nonlinearity on the trapping of waves behind the landslide, however this could only be assessed by comparison with further simulations using an inviscid model capable of capturing the nonlinear free surface boundary conditions.

8.9 Summary

The three numerical models all provided predictions of the waves generated by the motion of the rigid block landslide along the horizontal bottom boundary. From chapter 7, the most interesting behaviour within the generated wave field occurred in the vicinity of the moving landslide during its constant-velocity motion. The interactions between the landslide and the offshore-propagating waves led to wave trapping, resonant behaviour and breaking at high Froude numbers.

During the acceleration and deceleration of the landslide, the inviscid models correctly predicted the phasing of the generated waves. Both models under-predicted the amplitudes of the generated waves, with the nonlinear model providing slightly more robust predictions than the linear model over the entire parameter space. During the constant-velocity landslide motion, both inviscid models failed to correctly predict the interaction of the offshore-propagating waves with the landslide. Generally speaking, the models predicted stronger dispersive effects than were observed during the experiments.

The performance of the inviscid models exhibited strong dependence on the landslide Froude number. As the Froude number increased, the increasing nonlinearity of waves propagating with the landslide acted to slightly reduce the dispersive separation of the offshore-propagating waves. Since the two models did not correctly predict this nonlinearity, they could not predict the reduction in dispersive effects on the waves. At the higher Froude numbers, the predictive ability of the models also exhibited dependence on the submergence depth. At lower landslide Froude numbers, the predictive ability of the models showed only small variation with the landslide acceleration and submergence depth.

The viscous model provided predictions of the generated wave field for one experiment only. This experiment was conducted at a landslide Froude number of 0.5, to determine whether the viscous model could predict the trapping and subsequent resonant behaviour of the waves behind the landslide. Although the viscous model slightly under-predicted the amplitudes of the waves over the duration of the experiment, its predictions of the interaction between the landslide and the generated waves were much closer to the experimental observations than the inviscid model predictions.

The subsurface velocity field was greatly modified by the generation of a turbulent wake during the constant-velocity motion of the landslide. The inability of the inviscid models to predict a wake behind the landslide may have further reduced their ability to correctly predict the interactions between the landslide and the offshore-propagating waves.

It should be noted that previous studies into tsunami generated by landslides moving along sloping boundaries found that the acceleration of the landslide was the most important phase of motion in terms of the wave generation (see Watts, 2000). Additionally, Sue *et al.* (2011) found that the nonlinear inviscid model (with linear free surface conditions) provided robust predictions of the waves generated during his physical experiments. The differences between his findings and those of the current study may be attributed to several factors. First, the initial acceleration occurred in the shallowest water in a sloping boundary experiment, hence this phase of motion would generate the largest waves. Additionally, a landslide moving down a sloping boundary may not reach its terminal velocity, while the current experiments enabled investigation into this phase of motion. This constant velocity motion over a horizontal boundary caused the resonant amplification of a small range of wavelengths, and the nonlinearity of these waves caused the largest discrepancies between the model predictions and experimental measurements.

Chapter 9

Preliminary three-dimensional model results

9.1 Objectives of three-dimensional numerical simulations

The majority of the physical and numerical modelling work in this project considered only wave propagation in one horizontal dimension. By modelling the problem in two dimensions (one horizontal, one vertical), these models implicitly assumed that the length of the landslide was very much smaller than its width, such that lateral dispersion could be neglected. In reality, such large aspect ratios (defined as $width : length$) are unlikely, and generated waves would propagate in both horizontal dimensions. The inclusion of a lateral dimension (and associated variation in the width of the landslide) has the capacity to change the amplitudes of the generated waves, and the behaviour of the entire wave field.

Generally speaking, the inclusion of lateral dispersion is expected to decrease the amplitudes of the generated waves. Enet & Grilli (2007) found an average reduction in the characteristic tsunami amplitudes of 0.286 when moving from 2D to 3D experiments. This reduction in amplitude also reduced the nonlinearity of the waves generated during their three-dimensional experiments. Thus, the effect of lateral dispersion may reduce the nonlinear interactions between the landslide and the offshore-propagating waves observed in the two-dimensional physical experiments.

This chapter presents the effects of an added lateral dimension on the waves predicted by the linear inviscid-irrotational model. There are several advantages associated with the use of a numerical model to investigate these effects, rather than carrying out additional physical experiments. As noted in chapter 7, one of the main difficulties in setting up physical experiments to investigate landslide-generated tsunami is the short time available before reflected waves from the ends of the flume contaminate the

generated wave field. Using (for example) a wave tank with a width of 3 m, waves generated over a depth of 0.35 m would take only approximately 1.6 s to reach the lateral boundary. Thus, only the initial generation phase could be modelled in such experiments. Additionally, the measurement of free surface variations in two horizontal dimensions would require multiple LIF cross-sections, which would greatly increase the number of experimental repetitions required to measure the full wave field.

As discussed in chapter 8, the linear inviscid model was limited in its ability to accurately predict the properties of the generated waves. The assumed linearity of the bottom boundary caused the model to under-predict the amplitudes of the waves generated by the acceleration and deceleration of the landslide. Although the dispersive nature of the generated waves was captured by the model, the assumed linearity of the free surface waves rendered the model unable to correctly predict the nonlinear behaviour of the offshore-propagating waves at the higher Froude numbers.

The main parametric study of this project investigated the dependence of the generated wave properties on the landslide acceleration, λ, the landslide Froude number, Fr, and the submergence depth, τ. Since the three-dimensional simulations were intended only to provide preliminary results relating to the effect of the landslide aspect ratio on the generated wave properties, one combination of these parameters was selected for use in this chapter, such that the landslide aspect ratio was the only parameter varied during the three-dimensional simulations. The three-dimensional numerical simulations used the parameters:

$$\tau = 0.70, \tag{9.1}$$

$$\lambda = 0.102, \tag{9.2}$$

$$Fr = 0.500. \tag{9.3}$$

Although the two-dimensional linear inviscid model did not perform well in its predictions of the experimentally-generated waves at this landslide Froude number, the inclusion of lateral dispersion is expected to decrease the nonlinearity of the offshore-propagating waves. This decreased nonlinearity will improve the applicability of the model predictions of these waves, particularly as the landslide aspect ratio decreases. The predictions of the waves generated in the onshore direction are expected to be robust, since these waves did not exhibit the same ongoing interaction with the landslide as the offshore-propagating waves (and were generally well-predicted during the two-dimensional simulations).

A total of six numerical simulations were undertaken to assess the effect of the landslide aspect ratio on the generated wave field. This aspect ratio is defined according

Table 9.1: Parameter space investigated during the three-dimensional model simulations

Run no.	**Aspect ratio, σ**
1	0.25
2	0.50
3	1.00
4	2.00
5	4.00
6	8.00

to the nondimensional parameter σ (see chapter 5). Table 9.1 lists the values of σ used in the three-dimensional model simulations.

9.2 Wave field evolution

Before discussing the effect of the landslide aspect ratio on the generated wave amplitudes and the behaviour of the wave field, Run 3 (with an aspect ratio of $\sigma = 1.00$) is used to illustrate the evolution of the generated wave field. The landslide moved in the positive x-direction only, and therefore the offshore-propagating waves continued to interact with the landslide during its motion. As such, the onshore-propagating waves had significantly smaller amplitudes than the offshore-propagating waves (following the results presented in chapter 8). The plots in this section are therefore shown separately for the onshore (negative x) and offshore (positive x) domains. Figures 9.1 to 9.3 show the evolution of the offshore-propagating waves at $t = 6.0$, 12.0 and 18.0, and figures 9.4 to 9.6 show the equivalent plots for the onshore-propagating waves.

The offshore-propagating waves followed the general behaviour of the waves generated in the two-dimensional simulations of Run 12, with a free surface depression above the moving landslide (where the landslide is shown on the contour plots as a black circle), and a series of waves becoming trapped behind the landslide. However, the added lateral dimension in the problem domain also allowed waves to propagate laterally. Thus, the landslide motion generated a series of concentric waves in the offshore direction, and the ongoing interaction between the waves and the landslide locally increased the amplitudes of these waves in the vicinity of the x-axis. The onshore-propagating waves did not interact with the landslide after its initial acceleration, and so these propagated without the local increases in amplitude near the x-axis. The maximum amplitude within the offshore-propagating wave group was approximately 60 times larger than the maximum amplitude within the onshore-propagating wave group, exhibiting the effect of the ongoing interaction with the moving landslide at this landslide Froude number.

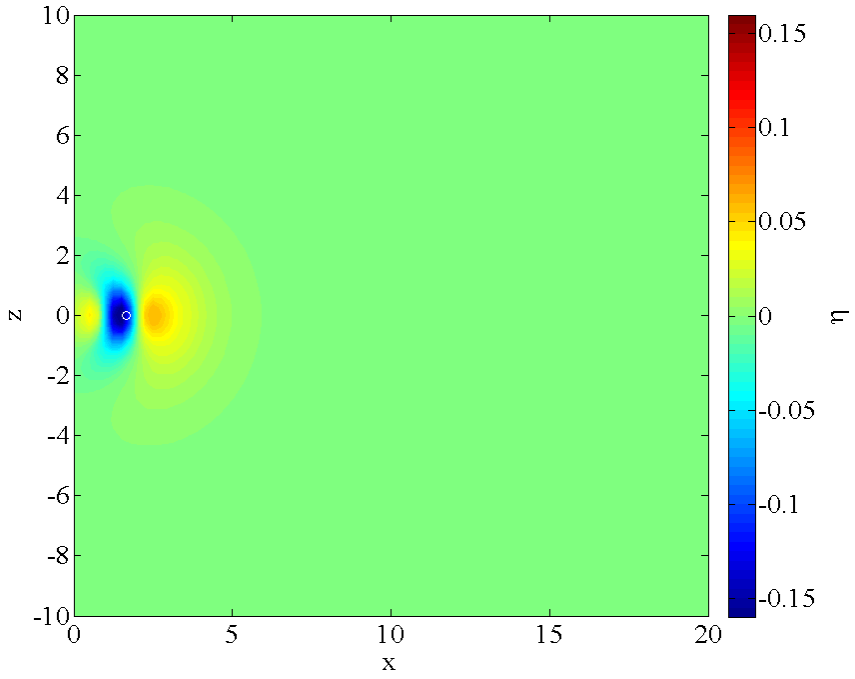

Figure 9.1: Contour plot of offshore-propagating wave amplitudes at $t = 6.0$, with landslide aspect ratio $\sigma = 1.0$.

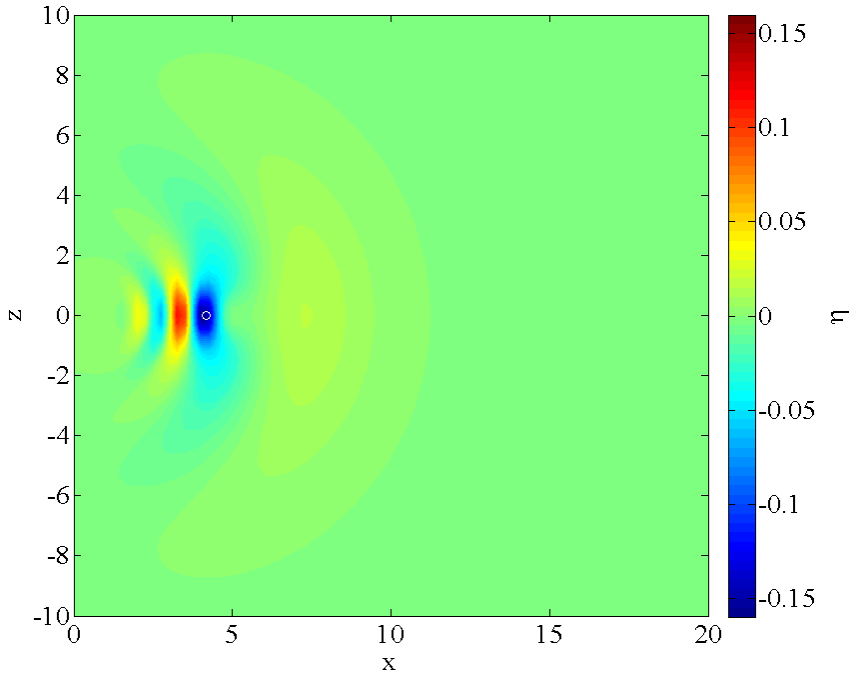

Figure 9.2: Contour plot of offshore-propagating wave amplitudes at $t = 12.0$, with landslide aspect ratio $\sigma = 1.0$.

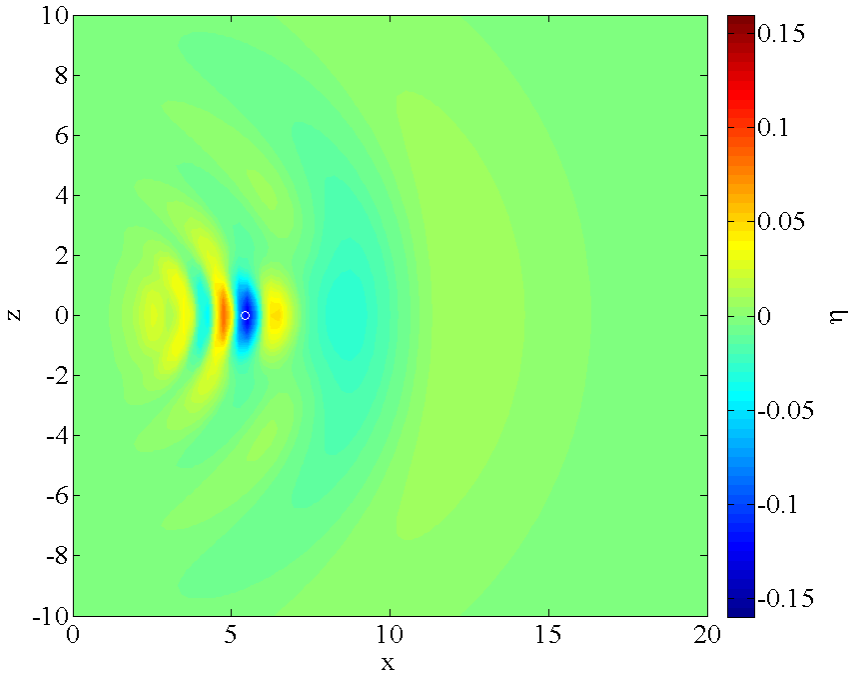

Figure 9.3: Contour plot of offshore-propagating wave amplitudes at $t = 18.0$, with landslide aspect ratio $\sigma = 1.0$.

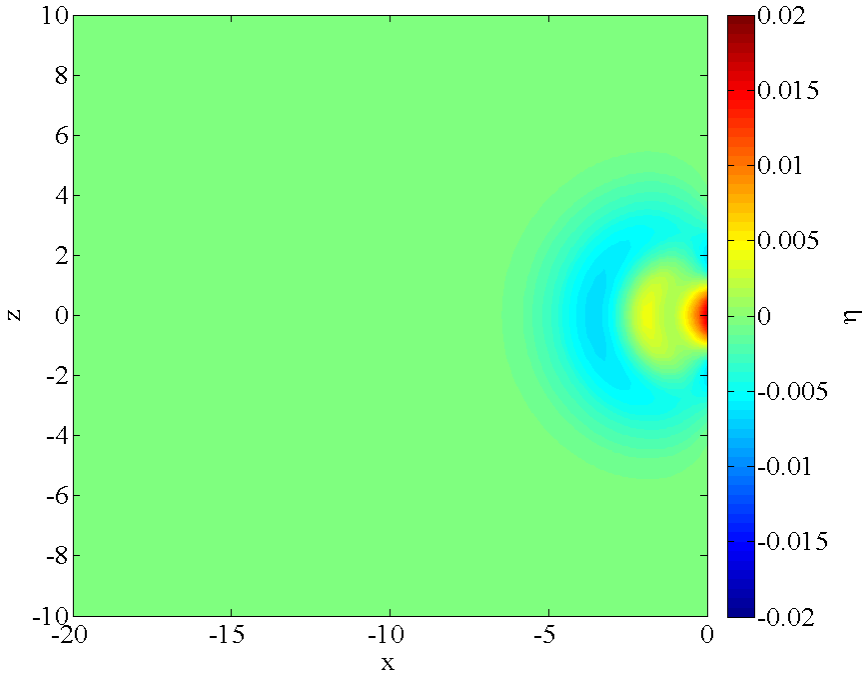

Figure 9.4: Contour plot of onshore-propagating wave amplitudes at $t = 6.0$, with landslide aspect ratio $\sigma = 1.0$.

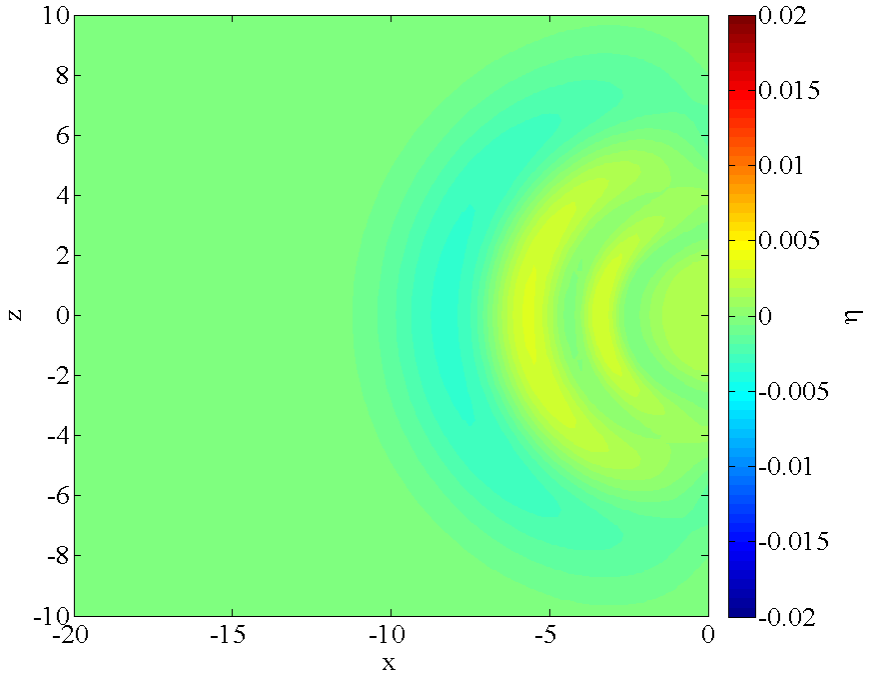

Figure 9.5: Contour plot of onshore-propagating wave amplitudes at $t = 12.0$, with landslide aspect ratio $\sigma = 1.0$.

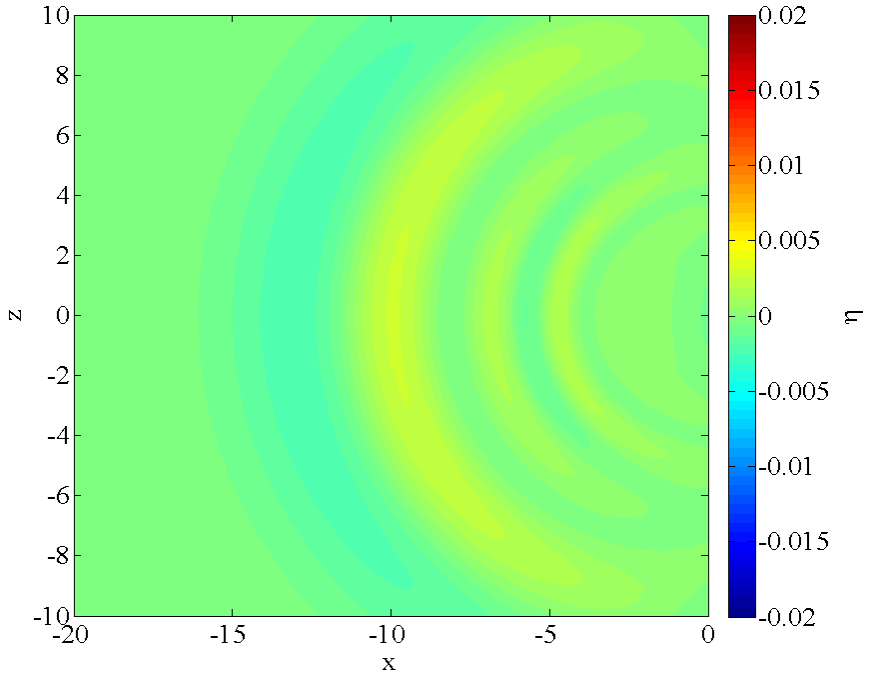

Figure 9.6: Contour plot of onshore-propagating wave amplitudes at $t = 18.0$, with landslide aspect ratio $\sigma = 1.0$.

9.3 Effect of landslide width on generated wave field

Taking into account the features of the wave field evolution for a landslide aspect ratio of 1.0, this section evaluates the changes to this evolution caused by varying the landslide aspect ratio. Figures 9.7 to 9.12 show contour plots of the wave field generated during the six different simulations, at the end of the constant-velocity phase of landslide motion ($t = t_2$). The first effect of varying the landslide aspect ratio was to change the plan-form shape of the generated waves, with the waves near the x axis becoming less curved at higher aspect ratios. Although dispersion still occurred in the z-direction, the increased landslide width caused this dispersion to occur further away from the x-axis.

The second effect of the changing aspect ratio was to change the peak amplitudes of the generated waves. An increased landslide width meant that the lateral dispersion took longer to affect the wave amplitudes along the x-axis. Thus, the ongoing interaction with the landslide caused a greater increase in the offshore-propagating wave amplitudes for those landslides with the larger σ values.

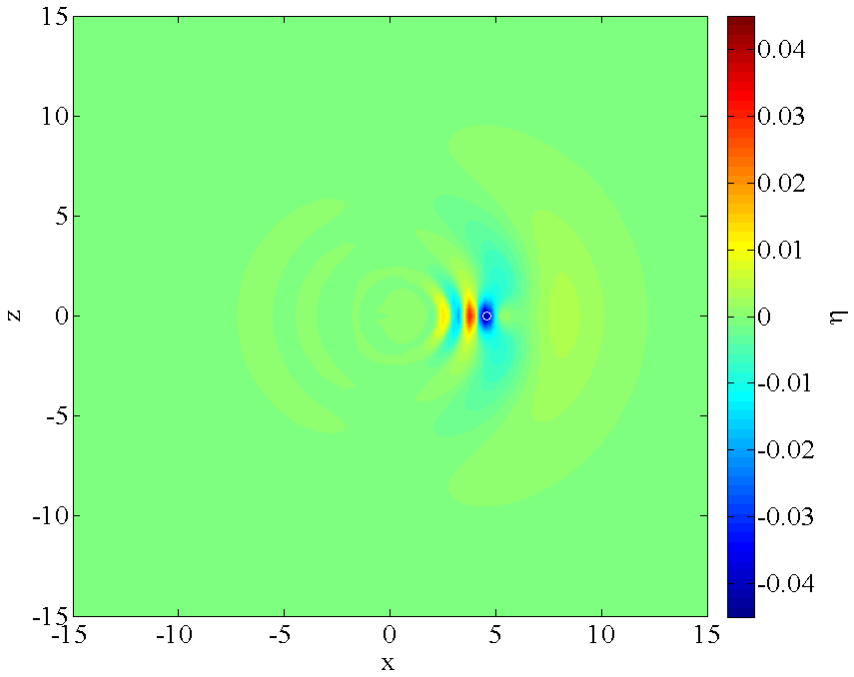

Figure 9.7: Contour plot of waves generated by a landslide with a nondimensional width $\sigma = 0.25$, shown at $t = t_2$.

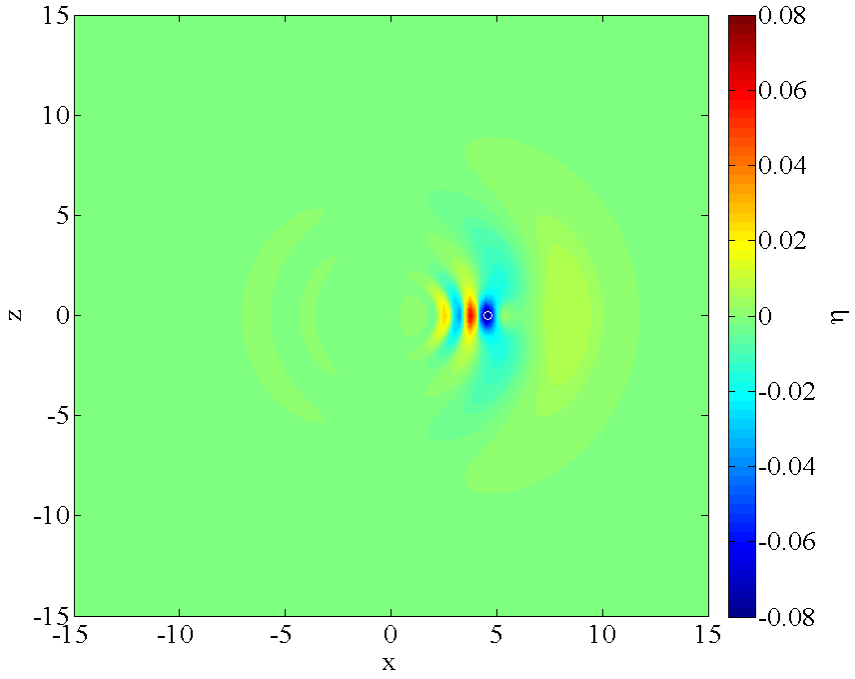

Figure 9.8: Contour plot of waves generated by a landslide with a nondimensional width $\sigma = 0.50$, shown at $t = t_2$.

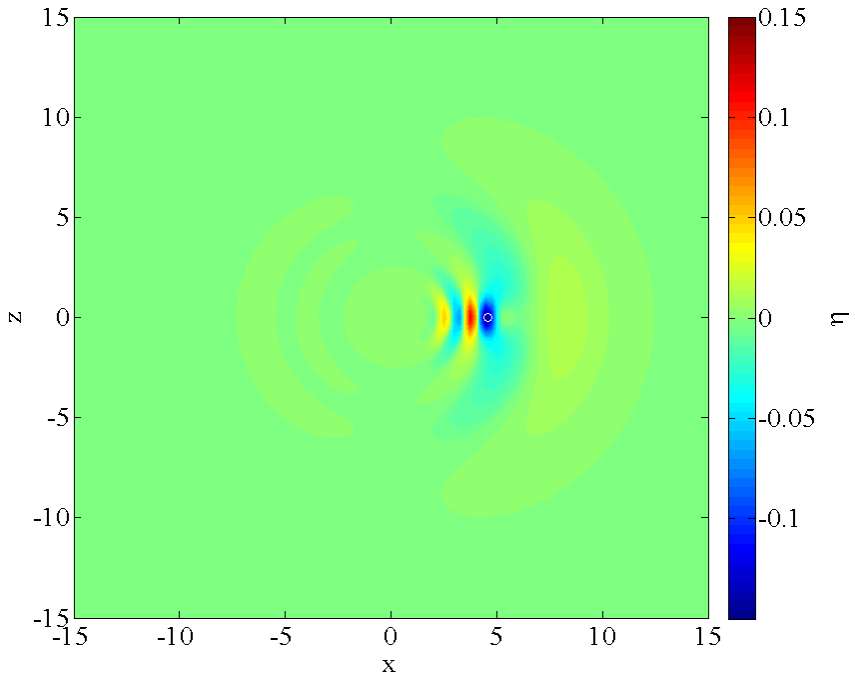

Figure 9.9: Contour plot of waves generated by a landslide with a nondimensional width $\sigma = 1.00$, shown at $t = t_2$.

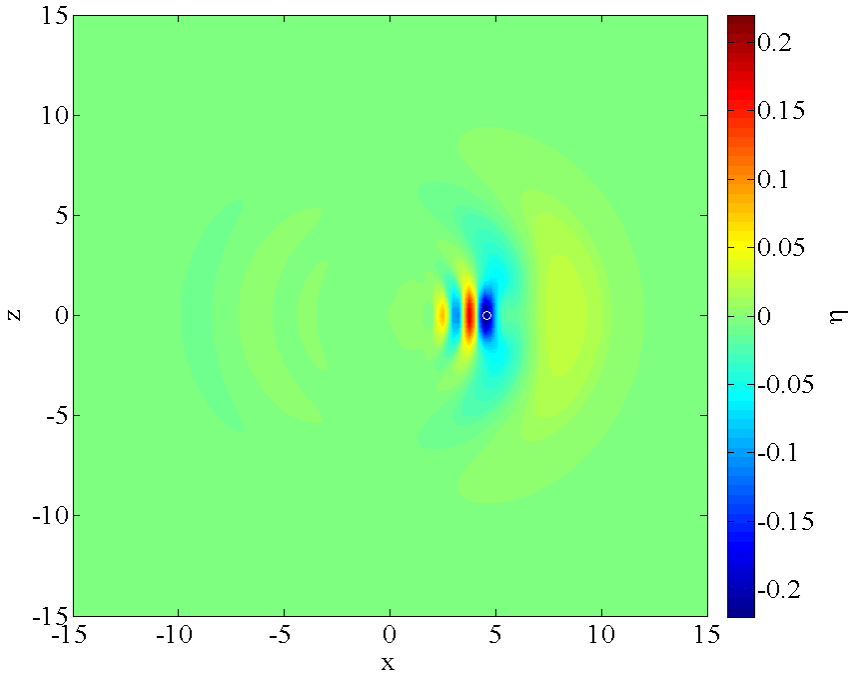

Figure 9.10: Contour plot of waves generated by a landslide with a nondimensional width $\sigma = 2.00$, shown at $t = t_2$.

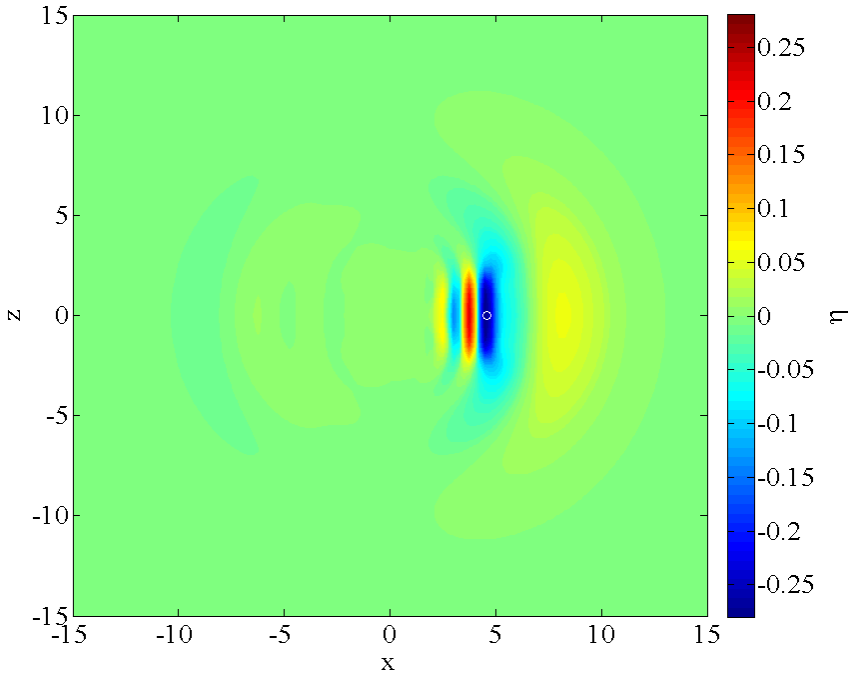

Figure 9.11: Contour plot of waves generated by a landslide with a nondimensional width $\sigma = 4.00$, shown at $t = t_2$.

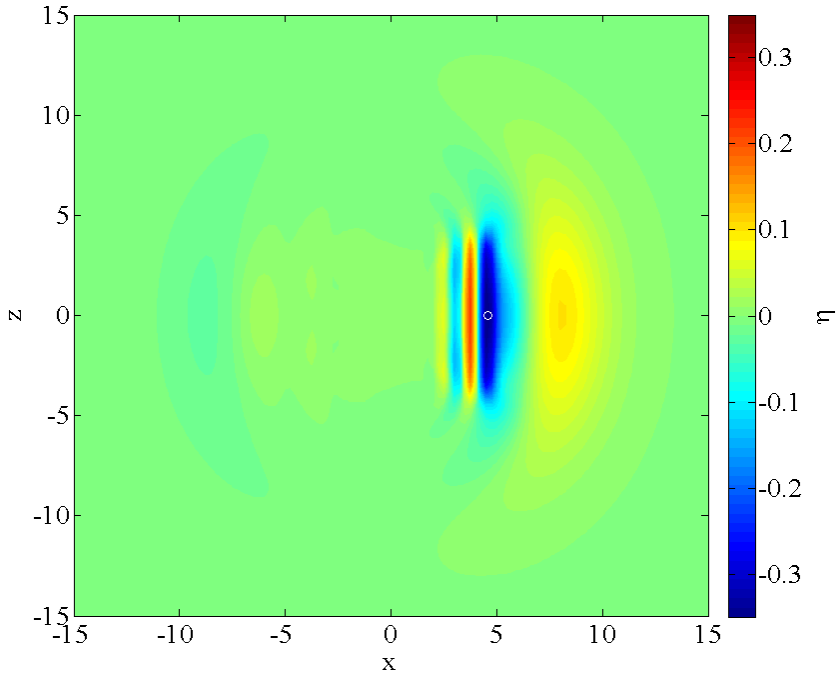

Figure 9.12: Contour plot of waves generated by a landslide with a nondimensional width $\sigma = 8.00$, shown at $t = t_2$.

9.4 Effect of landslide width on centreline wave amplitudes

Since the landslide shape was symmetric in all of the three-dimensional model simulations, the generated waves were also symmetric in the z-direction, and the largest wave amplitudes were located along the x-axis. Figure 9.13 compares the wave amplitudes along the centreline of the domain at $t = 10.0$. The larger landslide widths produced larger-amplitude waves along the x-axis, since the waves generated by these larger-width landslides were not as affected by lateral dispersion as those generated by more narrow landslides. If the landslide width were allowed to approach infinity, the wave amplitudes would approach the values predicted by the two-dimensional model simulations.

Clearly, the effect of the nondimensional parameter σ was to increase the amplitudes of the waves along the x-axis. Following the comparisons of chapters 7 and 8, figure 9.14 illustrates the dependence of the maximum leading wave amplitudes on the landslide aspect ratio over all of the three-dimensional simulations. Since these simulations were conducted at $Fr = 0.500$, the period of interaction between the landslide and the leading offshore-propagating crest was significantly longer than the period of interaction between the landslide and the leading onshore-propagating trough. Thus,

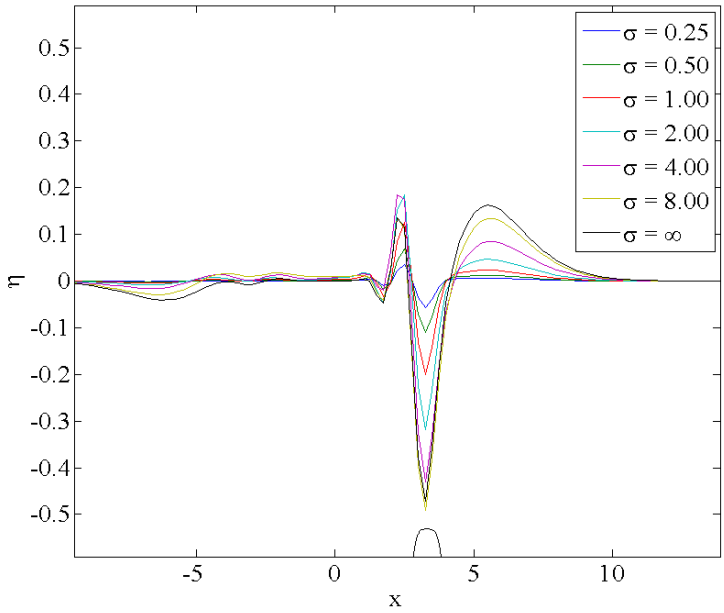

Figure 9.13: Comparison of wave amplitudes along the x-axis at $t = 10.0$.

the maximum onshore-propagating trough amplitude became relatively independent of σ above approximately $\sigma = 4.0$. The maximum leading crest amplitude within an equivalent two-dimensional simulation was approximately 0.18, while the maximum leading trough amplitude was approximately -0.05.

9.5 Energy and mass within wave field

The nondimensional energy within the generated wave fields may be calculated as

$$E_P = \frac{1}{2} \int \int \eta^2 \, dx \, dz, \tag{9.4}$$

while the nondimensional mass within the generated wave fields may be calculated as

$$m = \int \int \eta \, dx \, dz. \tag{9.5}$$

In the same manner as the two-dimensional simulations, the nondimensional mass is actually representative of the volume of fluid displaced, since the nondimensional form does not include the fluid density. The effect of the changing landslide volume (due to the different aspect ratios tested) is discussed later in this section. Since the landslide motion was in the x-direction only during the simulations, the domain was also divided into onshore (negative x) and offshore (positive x) regions. This division of the simulation domain allowed estimation of the energy and mass contained within

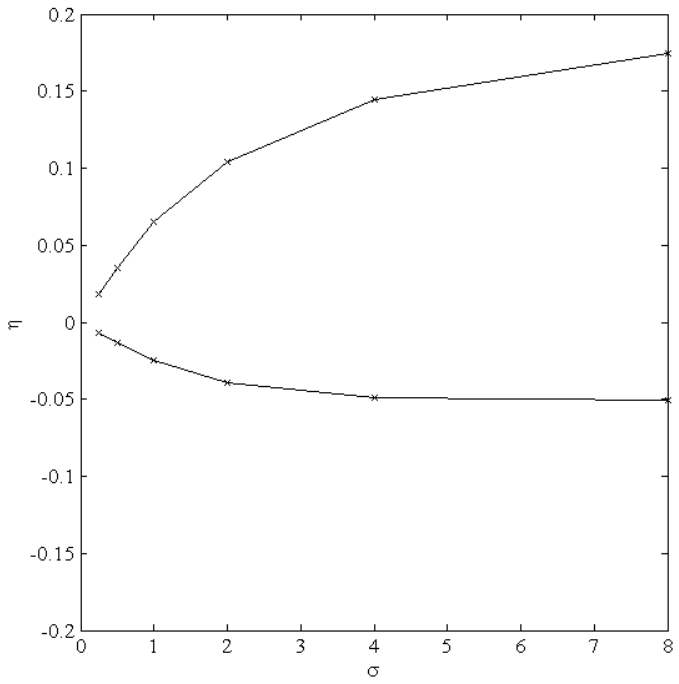

Figure 9.14: Dependence of maximum leading wave amplitudes on the landslide aspect ratio for all 3D model simulations.

the offshore and onshore regions.

Figure 9.15 shows the total energy within the wave field for all of the three-dimensional model simulations, while figure 9.16 shows the equivalent plots for the onshore and offshore regions of the domain. As with the two-dimensional simulations, the majority of the energy within the simulation domain was located within the offshore region. However, the time-dependent variation of the energy within the two regions was different to that observed in the two-dimensional simulations. The energy input in the onshore region from the deceleration-generated waves was much larger than the initial energy input from the waves generated by the landslide acceleration. Additionally, the interaction between the landslide and the offshore-propagating waves caused some fluctuations in the potential energy that were not present in the two-dimensional simulations. These fluctuations were present throughout the range of σ values tested, and appear to be caused by the interference of the onshore-propagating waves generated by the landslide deceleration and the offshore-propagating waves located behind the landslide.

Figure 9.17 shows the total mass within the wave field for all of the three-dimensional simulations. The total mass within the wave field summed to zero until waves began to leave the domain (this occurred at approximately $t = 15$). Figure 9.18 shows the mass contained within the onshore and offshore regions after scaling by the landslide aspect

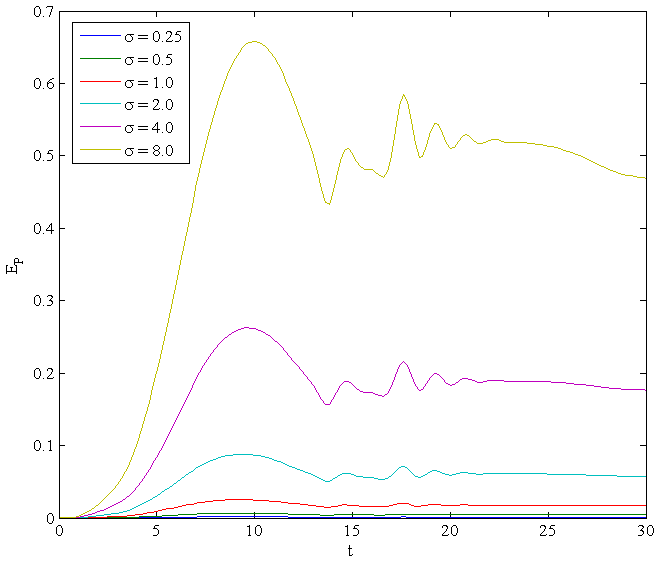

Figure 9.15: Time series of potential energy within the wave field for all of the 3D simulations.

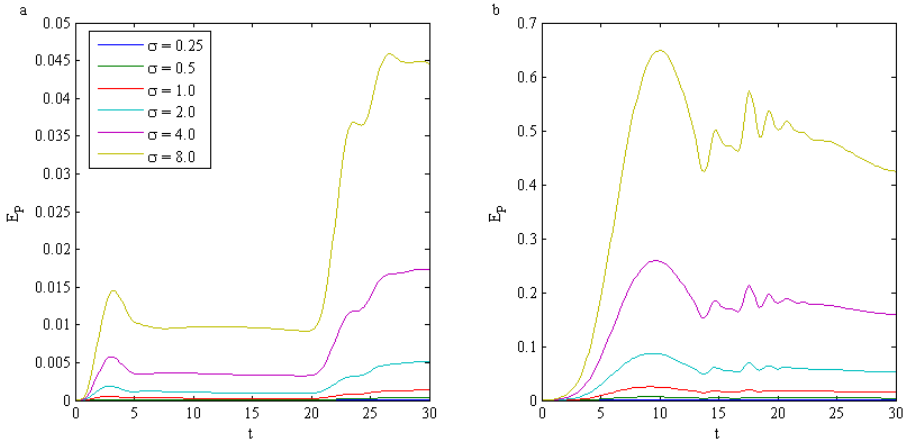

Figure 9.16: Time series of potential energy within a) the onshore region, and b) the offshore region, for all of the 3D simulations.

ratio, σ. As in the two-dimensional simulations, the waves within the onshore region contained negative mass and the waves within the offshore region contained positive mass. The mass in the two regions scaled with the landslide aspect ratio and collapsed onto a single curve until waves started to leave the simulation domain, demonstrating that the mass input into the system scaled directly with the landslide aspect ratio. Since the potential energy within the wave field depended on the integral of η^2, this quantity did not scale directly with σ, or with σ^2.

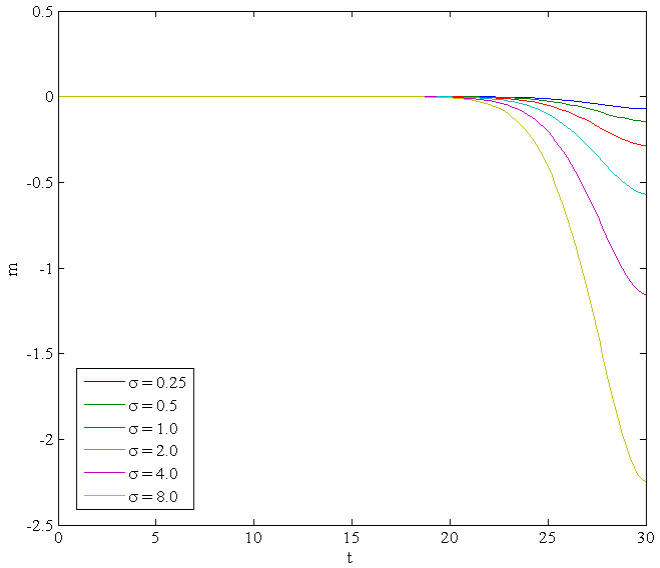

Figure 9.17: Time series of mass within the wave field for all of the 3D simulations.

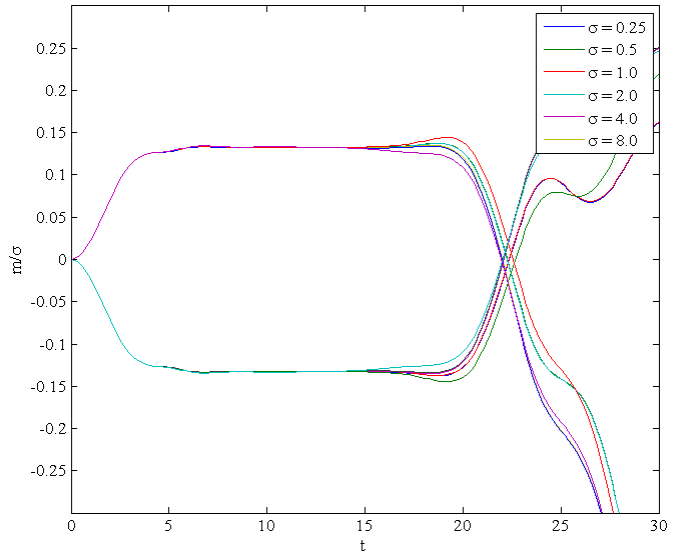

Figure 9.18: Time series of mass within the onshore and offshore regions of the wave field for all of the 3D simulations, scaled by the landslide aspect ratio.

9.6 Summary

A preliminary series of three-dimensional linear inviscid-irrotational model simulations were conducted to assess the effect of an added lateral boundary on the predictions of the waves generated by a submarine landslide. Only the landslide aspect ratio was varied during this preliminary study. As the landslide aspect ratio decreased from the

infinite value assumed in the two-dimensional linear inviscid model, lateral dispersion decreased the peak amplitudes of the generated waves.

The symmetrical landslide shape used in these simulations caused the peak amplitudes to occur along the x-axis. The maximum amplitude of the leading offshore-propagating crest exhibited a stronger dependence on the landslide aspect ratio than the maximum amplitude of the leading onshore-propagating trough. The stronger σ dependence of the amplitude of this leading wave, and of the offshore-propagating waves in general, was caused by the longer period of interaction between the landslide and the offshore-propagating wave group.

In a similar manner to the two-dimensional simulations, the onshore-propagating waves contained negative mass, while the offshore-propagating waves contained positive mass, summing to zero residual mass within the domain. The mass contained within the two regions scaled directly with the landslide aspect ratio. The energy contained within the offshore-propagating waves was one order of magnitude larger than the energy contained within the onshore-propagating waves. The potential energy within the wave field did not exhibit the same σ scaling as the mass.

Many numerical models used to predict tsunami generation and propagation consider only propagation along one horizontal dimension. Depending on the actual landslide aspect ratio, this assumption can cause significant over-prediction of the generated wave amplitudes. The over-prediction can provide conservative estimates of wave amplitude, however it is important to consider propagation in two horizontal dimensions to avoid inefficient use of resources in coastal protection measures based on model predictions. Validation of these preliminary results against the results of physical experiments would provide valuable insights into the actual effects of lateral dispersion on waves generated by submarine landslides, and whether the inviscid model was more robust at predicting the wave characteristics in this geometry than it was for two-dimensional simulations.

Chapter 10

Conclusions

10.1 Conclusions

In sloping submarine environments with substantial rates of sediment deposition, slope failure may generate a tsunami with the potential to inundate nearby communities with very little warning time. Tsunami generated by a submarine landslide tend to have high amplitudes, short wavelengths and high propagation velocities. However, due to the localised nature of a submarine mass failure, waves generated in this way do not pose the same threat of transoceanic devastation as tsunami generated by coseismic displacement of the seafloor.

Research into landslide-generated tsunami has typically consisted of a combination of field observations, mathematical model predictions and experimental replication. Post-tsunami studies in the field have measured runup levels, established the timing of wave attack from eyewitness accounts, and in some cases evaluated the effectiveness of coastal defence infrastructure. Although warning times are limited in the case of a landslide-generated tsunami, mathematical model predictions allow estimation of the wave properties generated by a particular forcing. These models may be validated by the results of physical experiments, to test their predictive capabilities for an idealised problem geometry.

Most experimental studies into tsunami generated by submarine landslides have modelled the landslide as a solid block sliding down a sloping boundary under the influence of gravity. Although older studies measured the generated wave amplitudes using traditional wave gauges, more recent studies have used flow visualisation techniques to measure full spatial and temporal variations in the free surface elevation and the subsurface velocity field. The experimental studies have focused on the kinematics of the moving landslide, and the parametric dependence of the generated wave properties on the landslide submergence depth and the mass of the block. Three-dimensional experiments have investigated the additional variation of the wave amplitudes in the

lateral direction.

The sloping boundary used in previous experimental studies prevented the measurement of onshore-propagating wave amplitudes, as well as limiting the range of landslide motion tested. The horizontal boundary used in this project allowed measurement of the properties of waves propagating in both the onshore and offshore directions. The use of a horizontal boundary also removed the need for, and the experimental issues arising from, a transition at the base of the slope. The mechanical system used to provide the landslide motion along the horizontal boundary allowed testing of a broad range of motion, as well as the ability to isolate the behaviour of the waves during the different phases of landslide motion.

A series of preliminary particle tracking velocimetry (PTV) experiments demonstrated the ability of the mechanical system to achieve targets within a trapezoidal velocity profile. The amplitudes of the waves generated by the motion of the submerged landslide block were measured using the laser-induced fluorescence (LIF) technique, following the work of Sue (2007). This technique allowed identification of the free surface to sub-pixel accuracy. Due to the limited camera field of view, each experiment was repeated 37 times to obtain free surface measurements over the flume length. A single particle tracking velocimetry (PTV) experiment was undertaken to measure the subsurface velocity field generated by the motion of the landslide. Comparisons between the horizontal and vertical velocities recorded during repetitions of the PTV experiment demonstrated the repeatability of the velocity measurements to within ± 3.0 mm/s.

The wave amplitude measurements obtained during the physical experiments were compared to the predictions of three mathematical models. The first two models were formulated using inviscid-irrotational flow theory, and invoked the linear assumption for perturbations on the free surface of the fluid (this assumption was found to have a significant effect on the predictive abilities of the two models). The first of these models applied the linear assumption on the bottom boundary, and expressed the solution as a spectral decomposition of wave modes. This model was solved in a semi-analytical manner. The second model used a nonlinear bottom boundary, and was solved using a boundary element method (BEM) solution. The third numerical model assumed a viscous ambient fluid, and was formulated within the direct numerical simulation (DNS) solver Gerris. This model solved the Navier-Stokes equations on an adaptive grid, and tracked the free surface elevation using a volume of fluid (VOF) approach. This model was significantly more computationally expensive than the two inviscid models.

In the wave fields measured using LIF, the initial acceleration of the landslide generated a leading crest in the offshore direction, and a leading trough in the onshore direction. These leading waves were each followed by a dispersive train of waves, with

progressively lower amplitudes and wavelengths. The leading waves approached the shallow water (or long-wave) limit of wave propagation, and all trailing waves were in the intermediate or deep regimes. These wave groups continued to evolve for some time after the landslide had ceased its initial acceleration.

During the constant-velocity phase of landslide motion, the waves generated by the acceleration continued to propagate throughout the length of the flume. A free surface depression was generated above the landslide itself, and remained above the landslide during this phase of motion. The free surface depression was analogous to the depression created by a subcritical flow over a hump in an open channel, and its amplitude could hence be simply predicted using hydraulic theory. The landslide deceleration generated two additional wave packets, similar to those generated by the landslide acceleration. The onshore-propagating packet had a leading crest, and the offshore-propagating packet had a leading trough.

The full spatial and temporal resolution of the generated wave fields allowed the calculation of the time-varying potential energy within the wave field. This potential energy increased during the landslide acceleration, and reached a peak value during the constant-velocity phase of motion. The energy exhibited additional variations during the constant-velocity motion of the landslide, due to the effect of the free surface depression on the offshore-propagating wave amplitudes. An estimate of the potential energy within the onshore and offshore-propagating wave packets was made by calculating the potential energy within the onshore and offshore regions of the flume. The ongoing interaction with the moving landslide led to higher potential energy within the offshore region over the entire parameter space.

The wave packets generated by the landslide acceleration and deceleration transported mass in the offshore and onshore directions. The offshore-propagating waves generated by the landslide acceleration transported positive mass, while the onshore-propagating waves transported negative mass. The wave packets generated by the landslide deceleration balanced this mass transport.

The landslide acceleration, Froude number and submergence depth were varied during the experiments and inviscid-irrotational model simulations. As the submergence depth increased, the generated waves had smaller amplitudes and longer wavelengths (and therefore higher propagation velocities). The effect of the landslide acceleration was to increase the amplitude of the generated waves, although this effect was generally lower than the effect of the submergence depth.

Changes in the landslide Froude number affected the amplitudes of the generated waves (particularly the free surface depression above the landslide) and the behaviour of the wave field as a whole. At low Froude numbers, the wave field was dominated by the waves generated by the landslide acceleration and deceleration, and the onshore-propagating waves were approximately equal in amplitude to the offshore-propagating

waves. As the landslide Froude number increased, the offshore-propagating waves grew much larger than the onshore-propagating waves, and the constant-velocity phase of motion became more important in terms of the exchange of energy between the landslide and the waves. Previous studies using sloping boundaries found that the initial landslide acceleration was the most important parameter affecting the generated wave properties, however the importance of the acceleration in these experiments was secondary to the importance of the landslide Froude number.

At the higher Froude numbers tested, a group of short-wavelength waves propagated with the landslide during its constant-velocity motion. This group propagated as a dispersive group, with new waves generated at the back of the group, however nonlinear wave steepening slightly reduced the effects of dispersion. This nonlinearity increased as the landslide Froude number increased. At $Fr = 0.500$, the landslide velocity was equal to the phase velocity of the trapped waves, and so the packet grew over time. The first crest behind the landslide broke during the experiments carried out at $Fr = 0.625$ and 0.750.

The inviscid models under-predicted the amplitudes of the generated waves over the entire parameter space. This resulted in under-prediction of the potential energy within both the offshore and onshore regions of the wave field. However, due to some apparent attenuation in the amplitudes (and hence energy) of the experimentally-generated waves, the model predictions of a particular wave amplitude improved over the timescale of its propagation. In the model predictions of the maximum leading wave amplitudes, the inclusion of the nonlinear bottom boundary condition improved the predictions by approximately 9%. The use of the full viscous model in Run 12 further improved on the predictions of the nonlinear model by approximately 3%.

The inviscid models were unable to correctly predict the interactions between the landslide and the offshore-propagating waves during the constant-velocity phase of motion. At lower Froude numbers, this was exhibited as under-predictions of the free surface depression above the landslide, and discrepancies in the phasing of the waves in front of the landslide. At higher Froude numbers (≥ 0.375), the models under-predicted the amplitudes of the waves propagating at the landslide velocity by as much as 70%. The viscous model, which did not assume linearity of the free surface waves, was able to correctly predict the formation and resonant behaviour of the wave group propagating with the landslide at $Fr = 0.500$.

The predictions of the potential energy within the wave field by the inviscid models worsened as the Froude number increased, due to the greater importance of the constant-velocity phase of motion (and associated nonlinearity of the trapped waves) on the energy within the wave field. In Run 12 (with parameters $\lambda = 0.102$, $\tau = 0.70$ and $Fr = 0.500$), the under-predictions of the peak potential energy by the linear, nonlinear and viscous models were 53%, 42% and 15% respectively. Despite

both inviscid-irrotational models assuming linearity of the free surface waves, these models did predict the transport of mass by the onshore- and offshore-propagating wave groups. Due to the under-predictions of the wave amplitudes by the models, the amount of mass transported by the wave groups was also under-predicted.

The measurements of the subsurface velocity field from the PTV experiment showed the effect of the turbulent wake on the flow around the landslide during the constant-velocity motion of the landslide. This wake may have affected the interactions between the landslide and the generated waves, in addition to the nonlinearity of the waves themselves.

A preliminary series of three-dimensional simulations by the linear inviscid model allowed the effect of a changing landslide aspect ratio to be investigated. As the landslide width, relative to its length, increased, the generated wave field approached the limiting case of a two-dimensional model. At lower aspect ratios the waves propagated approximately radially and had lower amplitudes, due to the effect of lateral dispersion. Only symmetrical landslide shapes were tested during these preliminary simulations.

The use of a solid block landslide within a two-dimensional model limits the applicability of the experimental results to any field situations. The limited flume length in the physical experiments required the use of higher landslide accelerations than would be observed on mild continental slopes. In the same way, the landslide terminal velocities tested in these experiments were significantly higher than the terminal velocity of a submerged granular slide on the continental slope. Hence, the resonant behaviour observed during experiments is unlikely in a field tsunami. However, the combined physical and numerical modelling of this project has provided insight into the applicability of inviscid-irrotational models to problems of ongoing interaction between surface waves and a submerged forcing.

Many predictive mathematical models invoke the inviscid-irrotational assumption regarding the flow of the ambient fluid around the landslide. Some models additionally assume linearity of the free surface or bottom boundary, while those models keeping free surface nonlinearity may use the shallow water approximation. In the field, although submerged landslides may runout over distances of many kilometres, the intial length scales of the failure are likely to be small compared to the water depth. As such, the waves generated by the motion of the landslide would be dispersive in nature. Thus, the shallow water approximation may be inappropriate in the prediction of waves generated by submarine landslides. In the current project, only the leading waves generated by the landslide motion approached the shallow water limit, while all other waves exhibited dispersive properties.

The use of a nonlinear bottom boundary improved the predictions of the waves generated by the landslide acceleration and deceleration. The assumed linearity of the free surface waves prevented the inviscid-irrotational models from correctly predicting

the effects of nonlinear steepening of waves moving at the landslide terminal velocity. In the field case of a submerged tsunami moving down a sloping boundary, the initial acceleration would occur in shallower water. Thus, similar to the experimental findings of Watts (2000), the acceleration of the landslide would be the most important phase of motion in contributing to the generated wave amplitudes, and a nonlinear bottom boundary would be even more important than in the current study. Additionally, a sloping boundary would make it unlikely for waves of a particular wavelength to propagate at the terminal velocity of the landslide. Even if the landslide moved at its terminal velocity for some time (previous studies often modelled the landslide motion as a period of acceleration and a period of deceleration only), the changing water depth would cause the wavelength associated with this terminal velocity to change with time. As the landslide moved into deeper water, the effect of the landslide motion on the wave amplitudes would decrease slightly, so that the highly nonlinear waves observed in these experiments are unlikely in the field. However, waves propagating in the onshore direction (or offshore-propagating waves encountering a shoreline, as in a fjord) would move into shallower water, and nonlinear effects would become increasingly important due to wave shoaling.

This study has provided a greater insight into the mechanism of wave generation by the motion of a submarine landslide, and the ability of several mathematical models to correctly predict the properties of these generated waves. In particular, the landslide motion, and hence the interactions between the landslide and the generated waves had a significant impact on the amplitudes of the waves. The landslide motion also greatly affected the division of potential energy within the generated wave field, with longer periods of acceleration leading to significantly higher potential energy within the offshore-propagating wave group.

10.2 Novel contributions

The horizontal boundary used during the physical experiments of this project allowed the properties of both onshore- and offshore-propagating waves to be measured. Previous experimental systems have not been able to measure the amplitudes of the onshore-propagating waves. The dependences of the onshore- and offshore-propagating waves on the landslide motion were very different, and these effects have not been previously investigated.

The ability to fully control the motion of the landslide during the physical experiments has allowed isolation of the effects of the different phases of motion on the properties of the generated waves. In particular, the ability of the system to generate a long period of constant landslide velocity has enabled the investigation of the additional waves trapped by the landslide at higher Froude numbers. The resonant behaviour

of these waves at subcritical landslide Froude numbers in the experiments was the most interesting feature of the experiments, and warrants further investigation.

The standard experimental geometry allowed direct validation of the predictions of three numerical models. Although these types of models have been used to predict the properties of landslide-generated tsunami in previous studies, direct comparisons with the experimentally-measure wave fields have allowed the effects of the model assumptions on their predictive capabilities to be assessed.

10.3 Future research directions

The preliminary three-dimensional simulations carried out using the linear inviscid-irrotational model highlighted the effect of the landslide width on the amplitudes of the generated waves, and wave dispersion in the lateral direction. Although limitations in the applicability of the linear inviscid model may preclude its use in a full parametric study, the mechanical system used in the current projects could also generate landslide motion within a three-dimensional wave tank, to provide experimental validation of the model predictions.

The mechanical system used to provide landslide motion in the current experiments could be extended to a seafloor uplift tsunami source mechanism. Many numerical models assume an initial condition of a displaced free surface equal to the displacement of an underwater fault rupture. An experimental study would provide measurements to determine the validity of this assumption, although the accelerations able to be achieved by the system are unlikely to reach field values. A sediment seafloor above such a mechanical system would also lead to localised mass failures (sliding and slumping) during the seafloor uplift, and experimental investigation of these combined source mechanisms would provide valuable insights into more realistic field generation mechanisms.

The seafloor uplift scenario could also be investigated using any of the numerical models described in this project. Additionally, the effect of granular slides, or solid slides composed of porous material, on the generated waves could be investigated. Comparisons between experimental measurements and numerical predictions could also help to determine the applicability of inviscid-irrotational models (for example) in the prediction of waves generated by underwater fault rupture. Although the dispersive nature of the generated waves precludes the use of shallow water models in the prediction of the experimentally-generated waves, comparisons with a fully nonlinear potential flow model would allow the effect of wave nonlinearity on the model predictions to be determined, without the need for a full Navier-Stokes solver.

Bibliography

Adrian, Ronald J. 1991. Particle-Imaging Techniques for Experimental Fluid Mechanics. *Annual Review of Fluid Mechanics*, **23**(1), 261–304.

Altinok, Y., Tinti, S., Alpar, B., Yaliner, A., Ersoy, , Bortolucci, E., & Armigliato, A. 2001. The Tsunami of August 17, 1999 in Izmit Bay, Turkey. *Natural Hazards*, **24**, 133–146. 10.1023/A:1011863610289.

Anselmetti, Flavio S., & Bussmann, Felix. 2010. Rossberg landslide history and flood chronology as recorded in Lake Lauerz sediments (Central Switzerland). *Swiss Journal of geosciences*, **103**(1), 43–59.

Best, Garland, & Sezerman, Omur M. 1999. Shedding light on hybrid optics: A tutorial in coupling. *Optics and phonotics news*, 30–34.

Biggs, Claire, Nokes, Roger, & Vennell, Ross. 2009. Laboratory investigation of an ebb tidal jet. *In: Coasts and Ports Conference 2009*.

Bird, Deanne K., Chague-Goff, Catherine, & Gero, Anna. 2011. Human Response to Extreme Events: a review of three post-tsunami disaster case studies. *Australian Geographer*, **42**(3), 225–239.

Blasio, FabioVittorio. 2011. Subaqueous Landslides. *Pages 295–351 of: Introduction to the Physics of Landslides*. Springer Netherlands.

Carvalho, Rita Fernandes de, & Carmo, Jos Sim o Antunes do. 2007. Landslides into reservoirs and their impacts on banks. *Environmental Fluid Mechanics*, **7**(6), 481.

Crimaldi, J.P. 2008. Planar laser induced fluorescence in aqueous flows. *Experiments in Fluids*, **44**, 851–863.

Cruyningen, I., Lozano, A., & Hanson, R. K. 1990. Quantitative imaging of concentration by planar laser-induced fluorescence. *Experiments in Fluids*, **10**(1), 41–49.

Di Risio, M., De Girolamo, P., Bellotti, G., Panizzo, A., Aristodemo, F., Molfetta, M. G., & Petrillo, A. F. 2009a. Landslide-generated tsunamis runup at the coast

of a conical island: New physical model experiments. *J. Geophys. Res.*, **114**(C1), C01009.

Di Risio, Marcello, Bellotti, Giorgio, Panizzo, Andrea, & De Girolamo, Paolo. 2009b. Three-dimensional experiments on landslide generated waves at a sloping coast. *Coastal Engineering*, **56**(5-6), 659–671.

Didenkulova, I.I., Nikolkina, I.F., & Pelinovsky, E.N. 2011. Resonant amplification of tsunami waves generated by an underwater landslide. *Doklady Earth Sciences*, **436**, 66–69.

Dotsenko, S. 2005. Run-Up of a Solitary Tsunami Wave on a Sloping Coast. *Physical Oceanography*, **15**(4), 211–219.

Enet, Francois, & Grilli, Stephan T. 2007. Experimental Study of Tsunami Generation by Three-Dimensional Rigid Underwater Landslides. *Journal of Waterway, Port, Coastal, and Ocean Engineering*, **133**(6), 442–454.

Fritz, H. M., Hager, W. H., & Minor, H. E. 2003a. Landslide generated impulse waves. *Experiments in Fluids*, **35**(6), 505–519.

Fritz, H. M., Hager, W. H., & Minor, H. E. 2003b. Landslide generated impulse waves. 2. Hydrodynamic impact craters. *Experiments in Fluids*, **35**(6), 520–532.

Fritz, H. M., Hager, W. H., & Minor, H. E. 2004. Near Field Characteristics of Landslide Generated Impulse Waves. *Journal of Waterway, Port, Coastal, and Ocean Engineering*, **130**(6), 287–302.

Fritz, Hermann M., Mohammed, Fahad, & Yoo, Jeseon. 2009. Lituya Bay Landslide Impact Generated Mega-Tsunami 50 super(th) Anniversary. *Pure and Applied Geophysics*, **166**(1-2), 153–153–175.

Fuhrman, David R., & Madsen, Per A. 2009. Tsunami generation, propagation, and run-up with a high-order Boussinesq model. *Coastal Engineering*, **56**(7), 747–758.

Gisler, Galen R. 2008. Tsunami Simulations. *Annual Review of Fluid Mechanics*, **40**(1), 71–90.

Gomez-Gesteira, Moncho, Rogers, Benedict D., Dalrymple, Robert A., & Crespo, Alex J. C. 2010. State-of-the-art of classical SPH for free-surface flows. *Journal of Hydraulic Research*, **48**(sup1), 6–27.

Goto, Kazuhisa, Chagu-Goff, Catherine, Fujino, Shigehiro, Goff, James, Jaffe, Bruce, Nishimura, Yuichi, Richmond, Bruce, Sugawara, Daisuke, Szczuciaski, Witold, Tappin, David R., Witter, Robert C., & Yulianto, Eko. 2011. New insights of tsunami hazard from the 2011 Tohoku-oki event. *Marine Geology*, **290**(14), 46 – 50.

Gregg, ChrisE., Houghton, BruceF., Paton, Douglas, Johnston, DavidM., Swanson, DonaldA., & Yanagi, BrianS. 2007. Tsunami Warnings: Understanding in Hawai'i. *Natural Hazards*, **40**, 71–87.

Grilli, S. T., & Watts, P. 1999. Modeling of waves generated by a moving submerged body. Applications to underwater landslides. *Engineering Analysis with Boundary Elements*, **23**(8), 645–656.

Grilli, Stephan T., & Watts, Philip. 2005. Tsunami Generation by Submarine Mass Failure. I: Modeling, Experimental Validation, and Sensitivity Analyses. *Journal of Waterway, Port, Coastal, and Ocean Engineering*, **131**(6), 283–297.

Grilli, Stephan T., Bengston, Aaron, Watts, Philip, & Imamura, Fumihiko. 2001. Benchmark Cases for Tsunamis Generated by Underwater Landslides. *Pages 1505–1514 of: Ocean Wave Measurement and Analysis (2001).*

Grilli, Stephan T., Vogelmann, Sylvia, & Watts, Philip. 2002. Development of a 3D numerical wave tank for modeling tsunami generation by underwater landslides. *Engineering Analysis with Boundary Elements*, **26**(4), 301–313.

Guillard, F., Fritzon, R., Revstedt, J., Trgrdh, C., Aldn, M., & Fuchs, L. 1998. Mixing in a confined turbulent impinging jet using planar laser-induced fluorescence. *Experiments in Fluids*, **25**, 143–150.

Guyenne, P., & Grilli, S. T. 2006. Numerical study of three-dimensional overturning waves in shallow water. *Journal of Fluid Mechanics*, **547**(-1), 361–388.

Hampton, Monty A., Lee, Homa J., & Locat, Jacques. 1996. Submarine landslides. *Reviews of Geophysics*, **34**(1), 33–59.

Harbitz, C. B., Pedersen, G., & Gjevik, B. 1993. Numerical Simulations of Large Water Waves due to Landslides. *J. Hydraul. Eng.*, **119**, 18.

Heinrich, P. 1992. Nonlinear Water Waves Generated by Submarine and Aerial Landslides. *Journal of Waterway, Port, Coastal, and Ocean Engineering*, **118**(3), 249–266.

Heinrich, PH., Piatanesi, A., & Hbert, H. 2001. Numerical modelling of tsunami generation and propagation from submarine slumps: the 1998 Papua New Guinea event. *Geophysical Journal International*, **145**(1), 97–111.

Hishida, K., & Sakakibara, J. 2000. Combined planar laser-induced fluorescenceparticle image velocimetry technique for velocity and temperature fields. *Experiments in Fluids*, **29**, S129–S140.

Imamura, Fumihiko, & Hashi, Kazumasa. 2003. Re-examination of the Source Mechanism of the 1998 Papua New Guinea Earthquake and Tsunami. *Pure and Applied Geophysics*, **160**(10), 2071–2086.

Ioualalen, M., Migeon, S., & Sardoux, O. 2010. Landslide tsunami vulnerability in the Ligurian Sea: case study of the 1979 October 16 Nice international airport submarine landslide and of identified geological mass failures. *Geophysical Journal International*, **181**(2), 724–740.

Jiang, L., & LeBlond, P. H. 1992. The Coupling of A Submarine Slide and The Surface Waves Which It Generates. *J. Geophys. Res.*, **97**(C8), 12731–12744.

Jiang, Lin, & LeBlond, Paul H. 1993. Numerical Modeling of an Underwater Bingham Plastic Mudslide and the Waves Which It Generates. *J. Geophys. Res.*, **98**(C6), 10303–10317.

Jiang, Lin, & Leblond, Paul H. 1994. Three-Dimensional Modeling of Tsunami Generation Due to a Submarine Mudslide. *Journal of Physical Oceanography*, **24**(3), 559–572.

Klaucke, I., & Cochonat, P. 1999. Analysis of past seafloor failures on the continental slope off Nice (SE France). *Geo-Marine Letters*, **19**(4), 245–253.

Kulikov, Evgueni A., Rabinovich, Alexander B., Thomson, Richard E., & Bornhold, Brian D. 1996. The landslide tsunami of November 3, 1994, Skagway Harbor, Alaska. *J. Geophys. Res.*, **101**(C3), 6609–6615.

Kurita, Tetsushi, Ikeda, Makoto, Suzuki, Koji, & Colombage, Sisira R. N. 2007. Promotion of Community-based Disaster Reduction Activity through Hands-on Training in Sri Lanka. *Journal of Natural Disaster Science*, **29**(2), 41–51.

Law, Adrian Wing-Keung, & Wang, Hongwei. 2000. Measurement of mixing processes with combined digital particle image velocimetry and planar laser induced fluorescence. *Experimental Thermal and Fluid Science*, **22**(3-4), 213–229.

Lay, Thorne, Kanamori, Hiroo, Ammon, Charles J., Nettles, Meredith, Ward, Steven N., Aster, Richard C., Beck, Susan L., Bilek, Susan L., Brudzinski, Michael R., Butler, Rhett, DeShon, Heather R., Ekstrm, Gran, Satake, Kenji, & Sipkin, Stuart. 2005. The Great Sumatra-Andaman Earthquake of 26 December 2004. *Science*, **308**(5725), pp. 1127–1133.

Le Mehaute, A. 1976. *An introduction to hydrodynamics and water waves*. Springer-Verlag, N.Y.

Lee, H., Ryan, H., Kayen, R. E., Haeussler, P. J., Dartnell, P., & Hampton, M. A. 2006. Varieties of submarine failure morphologies of seismically-induced landslides in Alaskan fjords. *Pages 221–230 of: Norsk Geologisk Tidsskrift*, vol. 86.

Lighthill, James. 1978. *Waves in Fluids.* Cambridge University Press.

Liu, P. L. F., Wu, T. R., Raichlen, F., Synolakis, C. E., & Borrero, J. C. 2005. Runup and rundown generated by three-dimensional sliding masses. *Journal of Fluid Mechanics*, **536**(-1), 107–144.

Liu, Philip L. F., Lynett, Patrick, & Synolakis, Costas E. 2003. Analytical solutions for forced long waves on a sloping beach. *Journal of Fluid Mechanics*, **478**(-1), 101–109.

Locat, Jacques, & Lee, Homa J. 2002. Submarine landslides: Advances and challenges. *Canadian Geotechnical Journal*, **39**(1), 193–212.

Lopez-Venegas, A. M., ten Brink, U. S., & Geist, E. L. 2008. Submarine landslide as the source for the October 11, 1918 Mona Passage tsunami: Observations and modeling. *Marine Geology*, **254**(1-2), 35–46.

Lynett, Patrick, & Liu, Philip L. F. 2002. A Numerical Study of Submarine-Landslide-Generated Waves and Run-Up. *Proceedings: Mathematical, Physical and Engineering Sciences*, **458**(2028), pp. 2885–2910.

Lynett, Patrick, & Liu, Philip L. F. 2005. A numerical study of the run-up generated by three-dimensional landslides. *J. Geophys. Res.*, **110**(C3), C03006.

Lynett, Patrick J., Borrero, Jose C., Liu, Philip L. F., & Synolakis, Costas E. 2003. Field Survey and Numerical Simulations: A Review of the 1998 Papua New Guinea Tsunami. *Pure and Applied Geophysics*, **160**(10), 2119–2146.

Masson, D. G., Harbitz, C. B., Wynn, R. B., Pedersen, G., & Lvholt, F. 2006. Submarine Landslides: Processes, Triggers and Hazard Prediction. *Philosophical Transactions: Mathematical, Physical and Engineering Sciences*, **364**(1845), pp. 2009–2039.

Matsumoto, Takeshi, & Tappin, David R. 2003. Possible Coseismic Large-scale Landslide off the Northern Coast of Papua New Guinea in July 1998: Geophysical and Geological Results from SOS Cruises. *Pure and Applied Geophysics*, **160**(10), 1923–1943.

Morin, Julie, De Coster, Benjamin, Paris, Rapheal, Flohic, Francois, Le Floch, Damien, & Lavigne, Franck. 2008. Tsunami-resilient communities' development in Indonesia through educative actions: Lessons from the 26 December 2004 tsunami. *Disaster Prevention and Management*, **17**, 430–446.

Murty, T. S. 2003. Tsunami Wave Height Dependence on Landslide Volume. *Pure & Applied Geophysics*, **160**(10/11), 2147–2153.

Nokes, Roger. 2009. *Streams: System theory and design.* University of Canterbury.

Novikova, Tatyana, Huang, Bor-shouh, & Wen, Kuo-liang. 2005. Application of Analytical Modeling to the Far-field Investigation of Tsunami and Oceanic Rayleigh Waves from the 1998 Papua New Guinea Earthquake. *Pure & Applied Geophysics*, **162**(11), 2071–2093.

Oliver, C. 2012. *Near field mixing of negatively buoyant jets.* Ph.D. thesis, University of Canterbury.

Panizzo, A., De Girolamo, P., & Petaccia, A. 2005. Forecasting impulse waves generated by subaerial landslides. *J. Geophys. Res.*, **110**(C12), C12025.

Panizzo, Andrea, Bellotti, Giorgio, & De Girolamo, Paolo. 2002. Application of wavelet transform analysis to landslide generated waves. *Coastal Engineering*, **44**(4), 321–338.

Paton, Douglas, Bajek, Robert, Okada, Norio, & McIvor, David. 2010. Predicting community earthquake preparedness: a cross-cultural comparison of Japan and New Zealand. *Natural Hazards*, **54**, 765–781.

Popinet, Stephane. 2003. Gerris: a tree-based adaptive solver for the incompressible Euler equations in complex geometries. *Journal of Computational Physics*, **190**(2), 572–600.

Qiu, Liu-Chao. 2008. Two-Dimensional SPH Simulations of Landslide-Generated Water Waves. *Journal of Hydraulic Engineering*, **134**(5), 668–671.

Rabinovich, A. B., Thomson, R. E., Bornhold, B. D., Fine, I. V., & Kulikov, E. A. 2003. Numerical Modelling of Tsunamis Generated by Hypothetical Landslides in the Strait of Georgia, British Columbia. *Pure and Applied Geophysics*, **160**(7), 1273–1313.

Rabinovich, Alexander B., Thomson, Richard E., Kulikov, Evgueni A., Bornhold, Brian D., & Fine, Isaac V. 1999. The landslide generated tsunami of November 3, 1994 in Skagway Harbor, Alaska: A case study. *Geophys. Res. Lett.*, **26**(19), 3009–3012.

Reid, H.F., & Taber, S. 1919. *The Porto Rico earthquakes of October-November, 1918.* Bull. Seismol. Soc. Am.

Renzi, E., & Sammarco, P. 2010. Landslide tsunamis propagating around a conical island. *Journal of Fluid Mechanics*, **650**(-1), 251–285.

Ronan, KevinR., Crellin, Kylie, & Johnston, DavidM. 2012. Community readiness for a new tsunami warning system: quasi-experimental and benchmarking evaluation of a school education component. *Natural Hazards*, **61**, 1411–1425.

Rzadkiewicz, S. Assier, Mariotti, C., & Heinrich, P. 1997. Numerical Simulation of Submarine Landslides and Their Hydraulic Effects. *Journal of Waterway, Port, Coastal, and Ocean Engineering*, **123**(4), 149–157.

Said, Aini Mat, Ahmadun, Fakhru'l Razi, Mahmud, Ahmad Rodzi, & Abas, Fuad. 2011. Community preparedness for tsunami disaster: a case study. *Disaster Prevention and Management*, **20**, 266–280.

Sammarco, P., & Renzi, E. 2008. Landslide tsunamis propagating along a plane beach. *Journal of Fluid Mechanics*, **598**(-1), 107–119.

Satake, Kenji, & Tanioka, Yuichiro. 2003. The July 1998 Papua New Guinea earthquake; mechanism and quantification of unusual tsunami generation. *Pure and Applied Geophysics*, **160**(10-11), 2087–2087–2118.

Sue, L., Nokes, R., & Davidson, M. 2011. Tsunami generation by submarine landslides: comparison of physical and numerical models. *Environmental Fluid Mechanics*, **11**(2), 133–165.

Sue, Langford Phillip. 2007. Modelling of tsunami generated by submarine landslides. Doctor of Philosophy Publisher: University of Canterbury. Civil Engineering.

Suleimani, Elena, Hansen, Roger, & Haeussler, Peter. 2009. Numerical Study of Tsunami Generated by Multiple Submarine Slope Failures in Resurrection Bay, Alaska, during the M W 9.2 1964 Earthquake. *Pure and Applied Geophysics*, **166**(1), 131–152.

Synolakis, C., Bernard, E., Titov, V., Kanlu, U., & Gonzalez, F. 2008. Validation and Verification of Tsunami Numerical Models. *Pure and Applied Geophysics*, **165**(11), 2197–2228.

Synolakis, Costas E., Bardet, Jean-Pierre, Borrero, Jose C., Davies, Hugh L., Okal, Emile A., Silver, Eli A., Sweet, Suzanne, & Tappin, David R. 2002. The Slump Origin of the 1998 Papua New Guinea Tsunami. *Proceedings: Mathematical, Physical and Engineering Sciences*, **458**(2020), 763–789.

Tinti, S., & Bortolucci, E. 2000. Energy of Water Waves Induced by Submarine Landslides. *Pure and Applied Geophysics*, **157**(3), 281–318.

Tinti, S., Bortolucci, E., & Chiavettieri, C. 2001. Tsunami Excitation by Submarine Slides in Shallow-water Approximation. *Pure and Applied Geophysics*, **158**(4), 759–797.

Tinti, Stefano, Armigliato, Alberto, Manucci, Anna, Pagnoni, Gianluca, Zaniboni, Filippo, Yaliner, Ahmet Cevdet, & Altinok, Yildiz. 2006. The generating mechanisms of the August 17, 1999 Izmit bay (Turkey) tsunami: Regional (tectonic) and local (mass instabilities) causes. *Marine Geology*, **225**(1-4), 311–330.

Van Dyke, M. 1982. *An album of fluid motion.* Parabolic Press, Stanford California.

Vennell, R. 2009. Resonance and trapping of topographic transient ocean waves generated by a moving atmospheric disturbance. *Journal of Fluid Mechanics*, **650**, 427–442.

Watts, P., Grilli, S. T., Kirby, J. T., & Fryer, G. J. 2003. Landslide tsunami case studies using a Boussinesq model and a fully nonlinear tsunami generation model. *Natural hazards and earth system sciences*, **3**(5), 391–402.

Watts, Philip. 2000. Tsunami Features of Solid Block Underwater Landslides. *Journal of Waterway, Port, Coastal, and Ocean Engineering*, **126**(3), 144–152.

Watts, Philip, Grilli, Stephan T., Tappin, David R., & Fryer, Gerard J. 2005. Tsunami Generation by Submarine Mass Failure. II: Predictive Equations and Case Studies. *Journal of Waterway, Port, Coastal, and Ocean Engineering*, **131**(6), 298–310.

Weiss, Robert, Fritz, Hermann M., & Wannemann, Kai. 2009. Hybrid modeling of the mega-tsunami runup in Lituya Bay after half a century. *Geophys. Res. Lett.*, **36**(9), L09602.

Appendix A

Velocity and displacement plots from PTV tests on landslide motion

Table A.1 summarises the parameters tested during the landslide PTV runs. The plots in this appendix show the ability of the landslide motion control system to achieve velocity and displacement targets for all the runs tested. The velocity and acceleration errors arising from these results are discussed in section 4.4.

Table A.1: Experimental parameters tested during particle tracking velocimetry checks on achievement of motion profiles

Run	**a0** (m/s^2)	$\mathbf{u_t}$ (m/s)
1	0.5	0.164
2	0.5	0.328
3	0.5	0.655
4	1.0	0.164
5	1.0	0.328
6	1.0	0.655
7	1.5	0.164
8	1.5	0.328
9	1.5	0.500

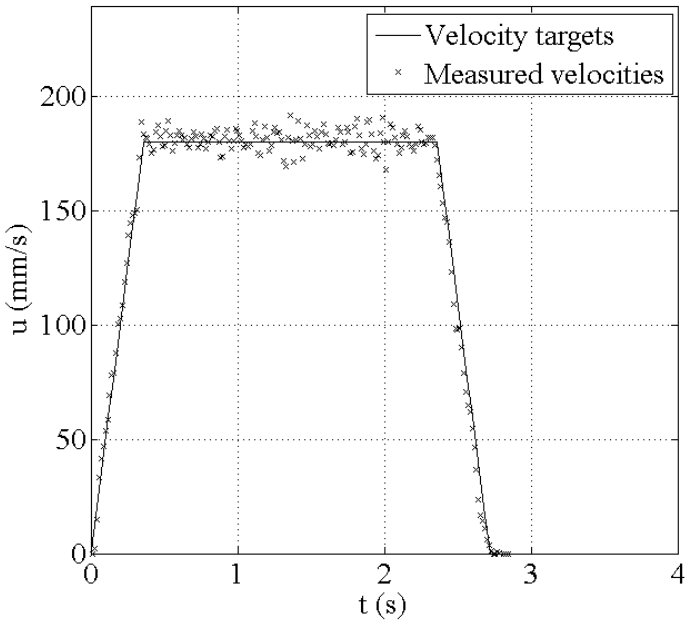

Figure A.1: Landslide target and measured velocities for Run 1 ($a0 = 0.5$ m/s^2, $u_t = 0.164$ m/s)

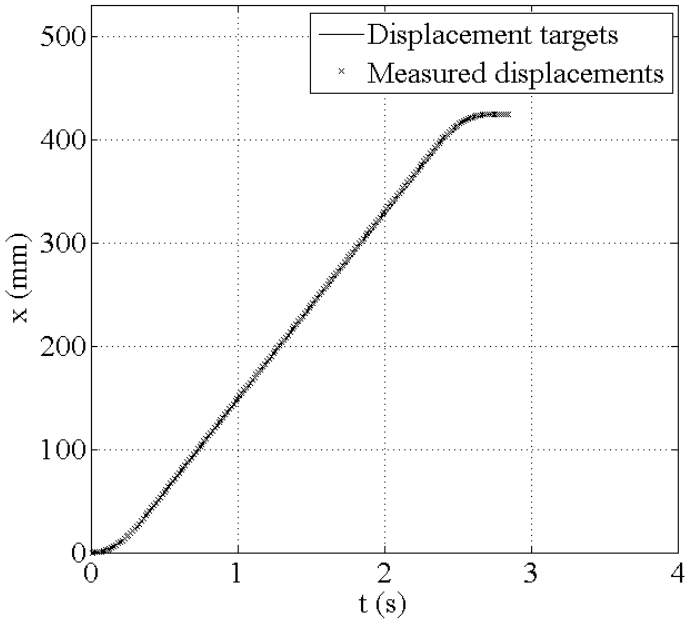

Figure A.2: Landslide target and measured displacements for Run 1 ($a0 = 0.5$ m/s^2, $u_t = 0.164$ m/s)

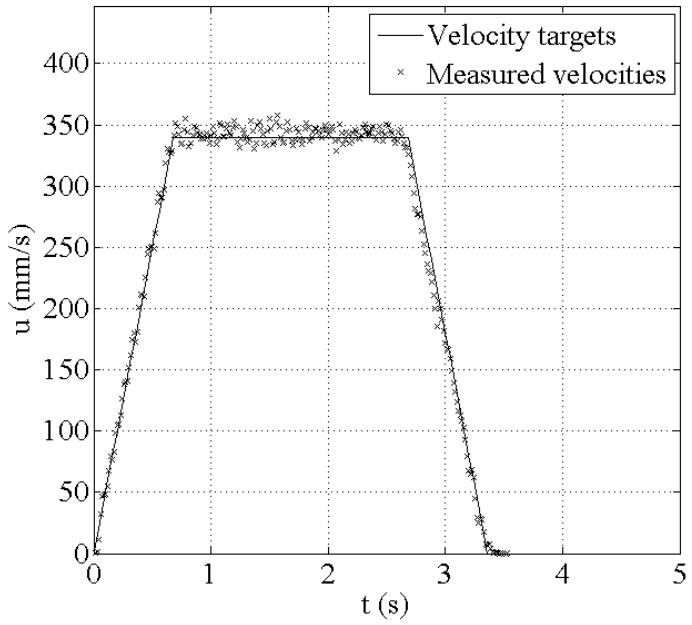

Figure A.3: Landslide target and measured velocities for Run 2 ($a0 = 0.5$ m/s^2, $u_t = 0.328$ m/s)

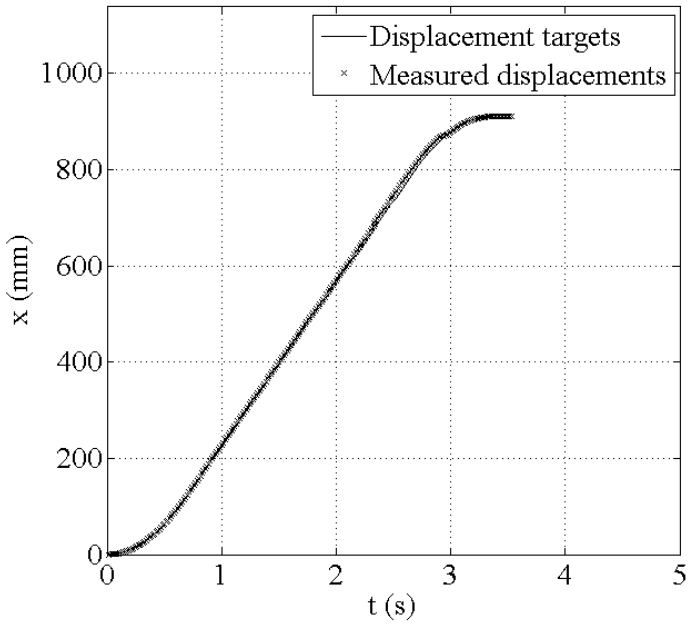

Figure A.4: Landslide target and measured displacements for Run 2 ($a0 = 0.5$ m/s^2, $u_t = 0.328$ m/s)

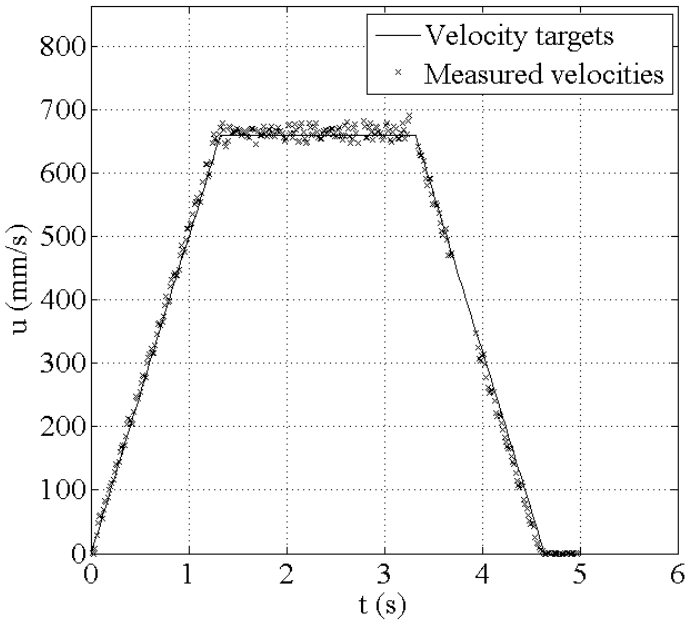

Figure A.5: Landslide target and measured velocities for Run 3 ($a0 = 0.5$ m/s^2, $u_t = 0.655$ m/s)

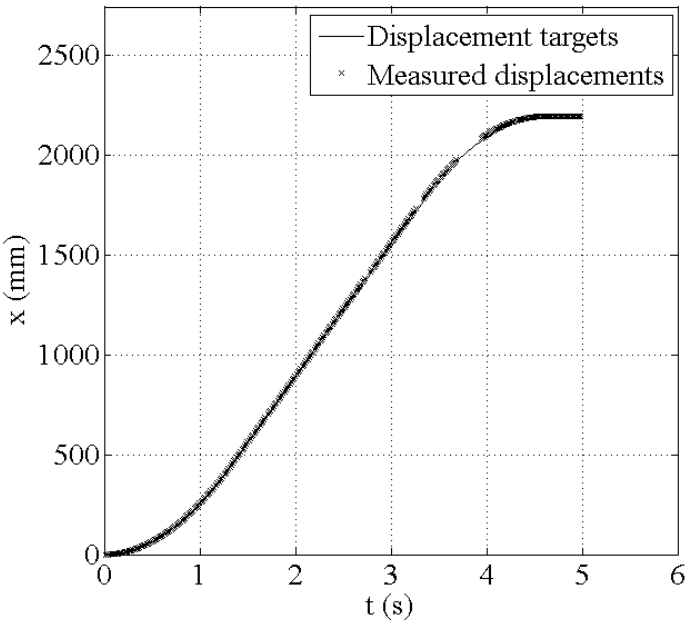

Figure A.6: Landslide target and measured displacements for Run 3 ($a0 = 0.5$ m/s^2, $u_t = 0.655$ m/s)

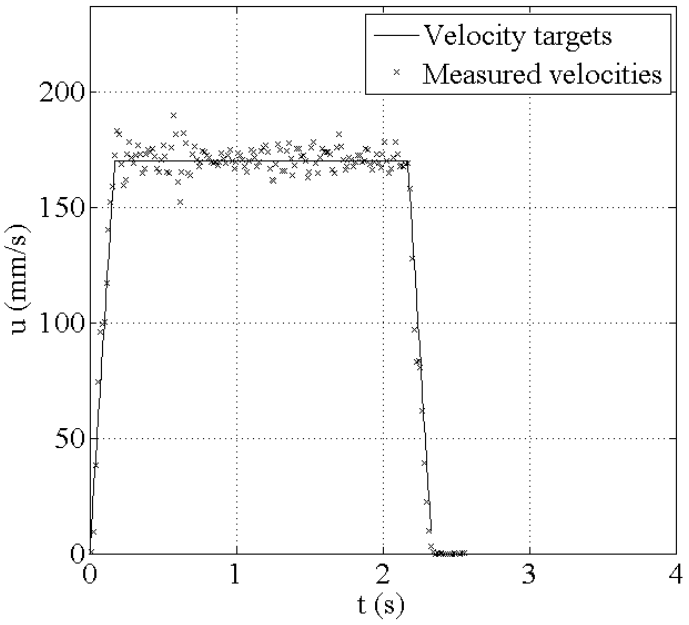

Figure A.7: Landslide target and measured velocities for Run 4 ($a0 = 1.0$ m/s^2, $u_t = 0.164$ m/s)

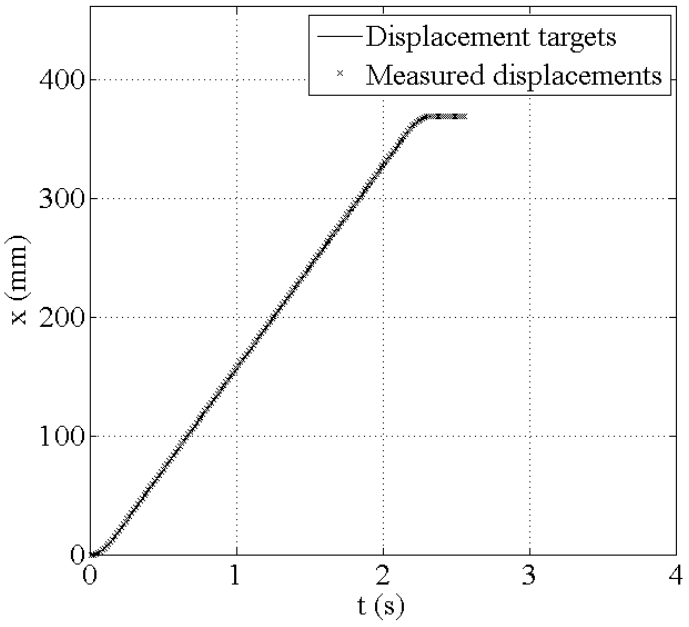

Figure A.8: Landslide target and measured displacements for Run 4 ($a0 = 1.0$ m/s^2, $u_t = 0.164$ m/s)

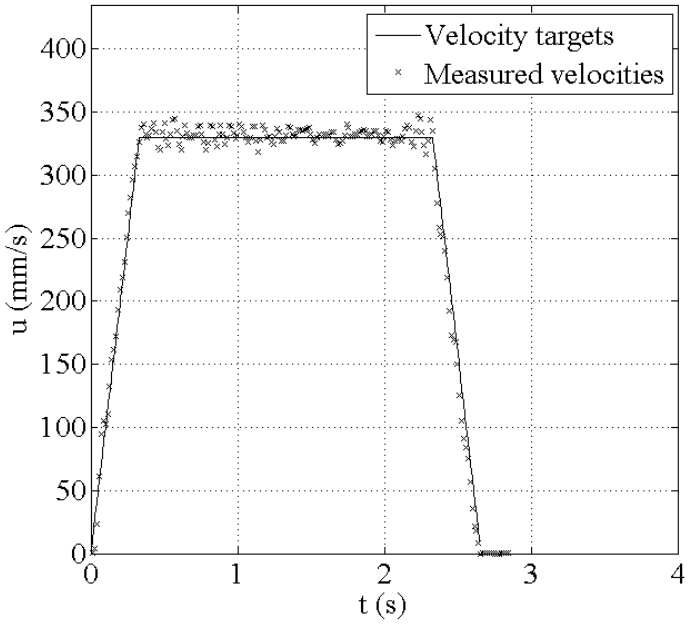

Figure A.9: Landslide target and measured velocities for Run 5 ($a0 = 1.0$ m/s^2, $u_t = 0.328$ m/s)

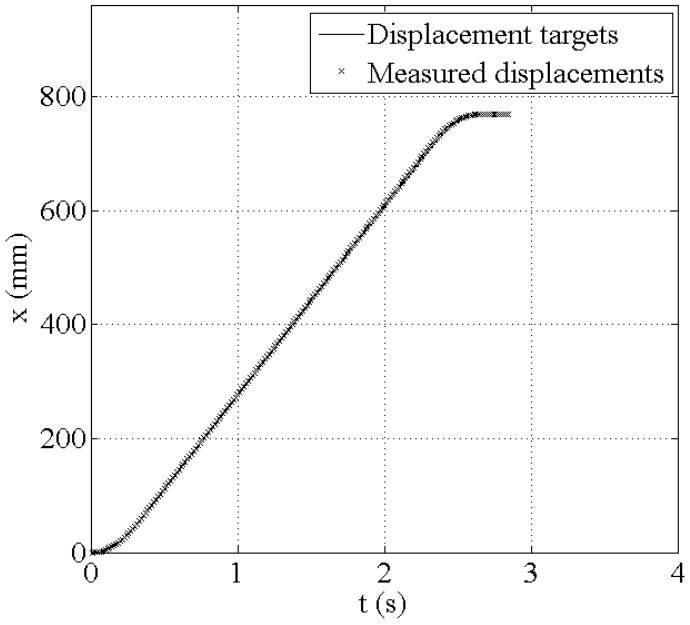

Figure A.10: Landslide target and measured displacements for Run 5 ($a0 = 1.0$ m/s^2, $u_t = 0.328$ m/s)

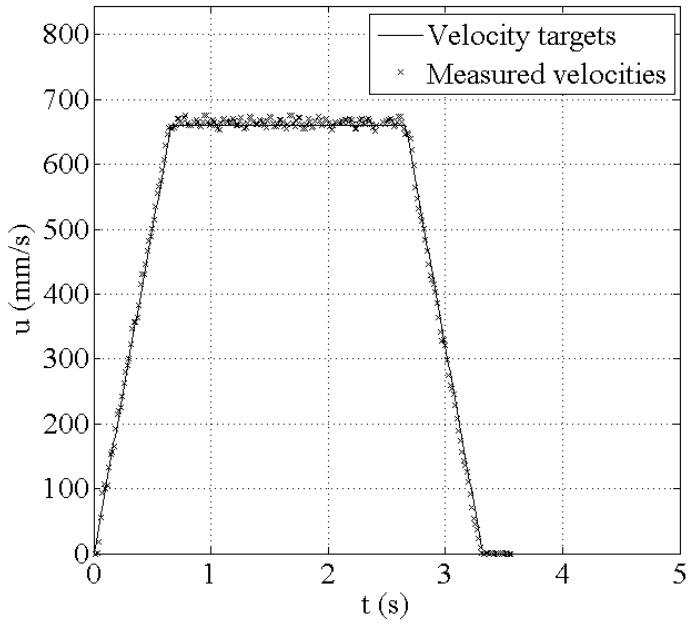

Figure A.11: Landslide target and measured velocities for Run 6 ($a0 = 1.0$ m/s^2, $u_t = 0.655$ m/s)

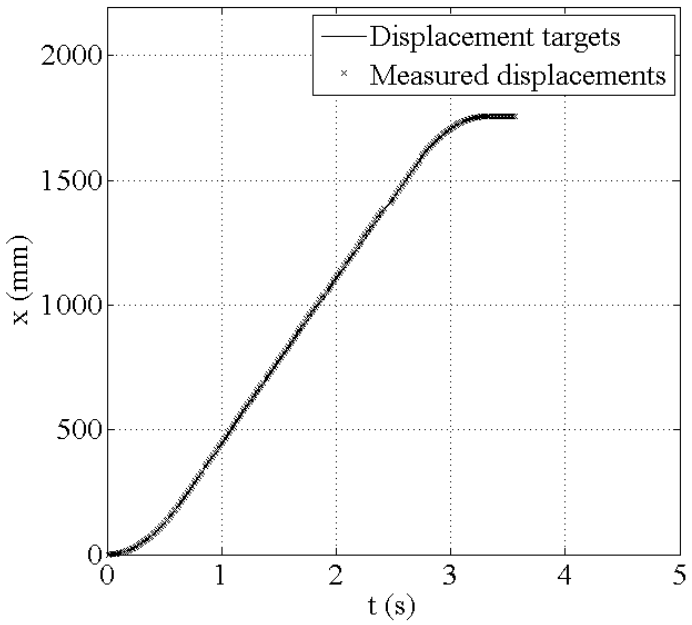

Figure A.12: Landslide target and measured displacements for Run 6 ($a0 = 1.0$ m/s^2, $u_t = 0.655$ m/s)

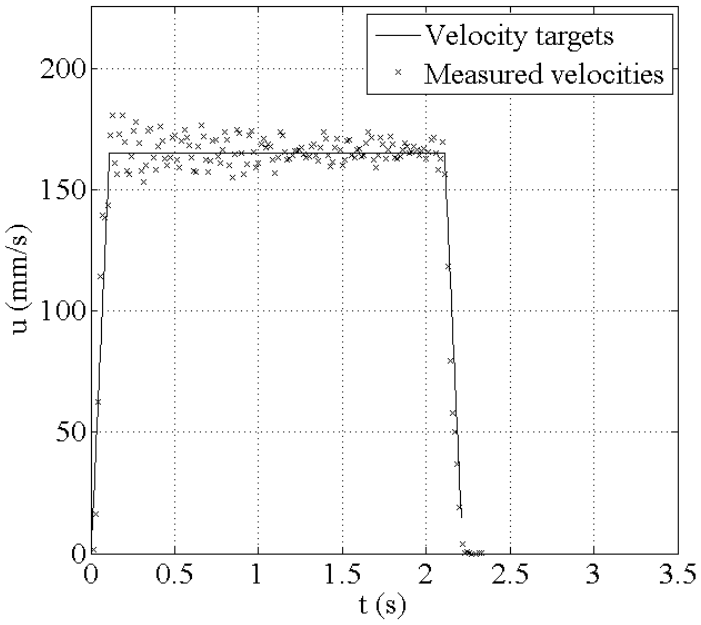

Figure A.13: Landslide target and measured velocities for Run 7 ($a0 = 1.5$ m/s^2, $u_t = 0.164$ m/s)

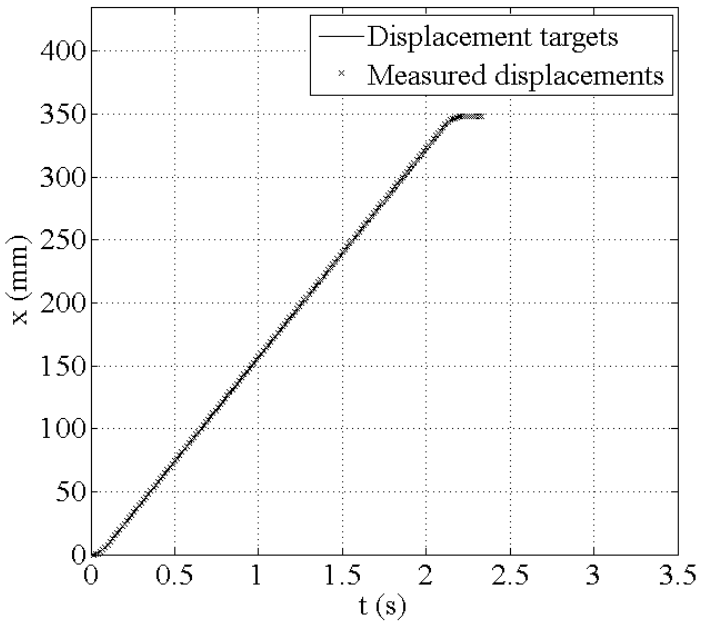

Figure A.14: Landslide target and measured displacements for Run 7 ($a0 = 1.5$ m/s^2, $u_t = 0.164$ m/s)

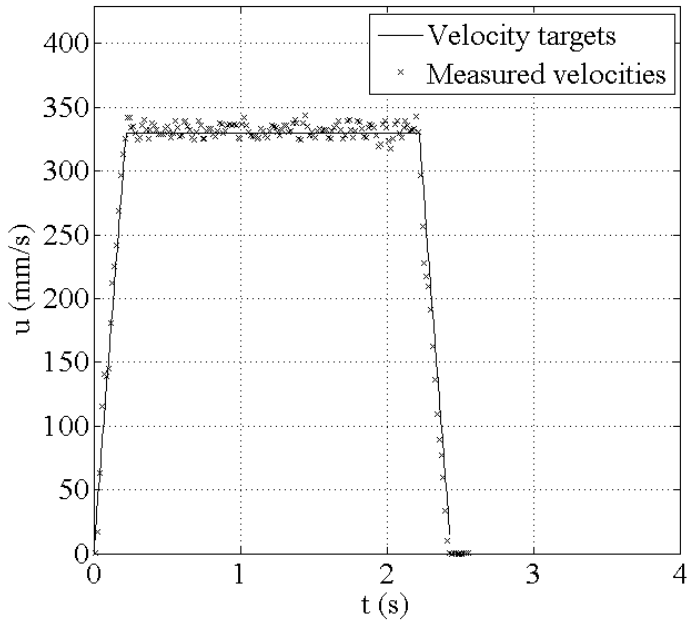

Figure A.15: Landslide target and measured velocities for Run 8 ($a0 = 1.5$ m/s^2, $u_t = 0.328$ m/s)

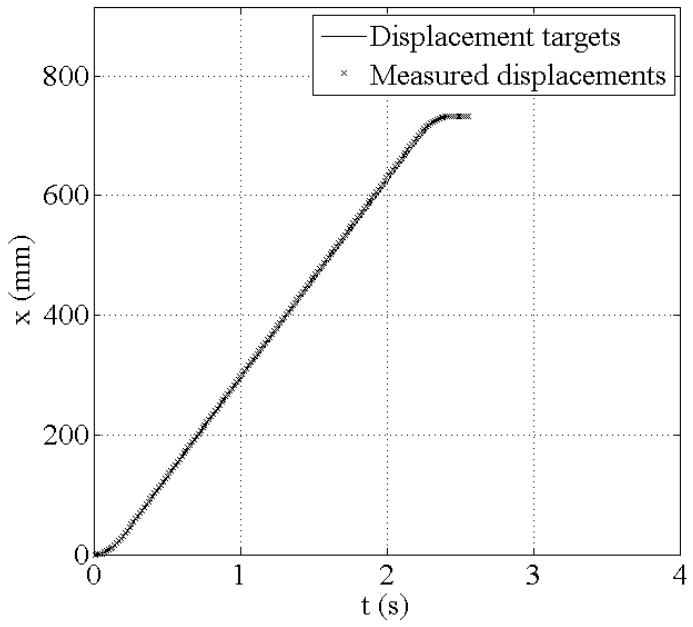

Figure A.16: Landslide target and measured displacements for Run 8 ($a0 = 1.5$ m/s^2, $u_t = 0.328$ m/s)

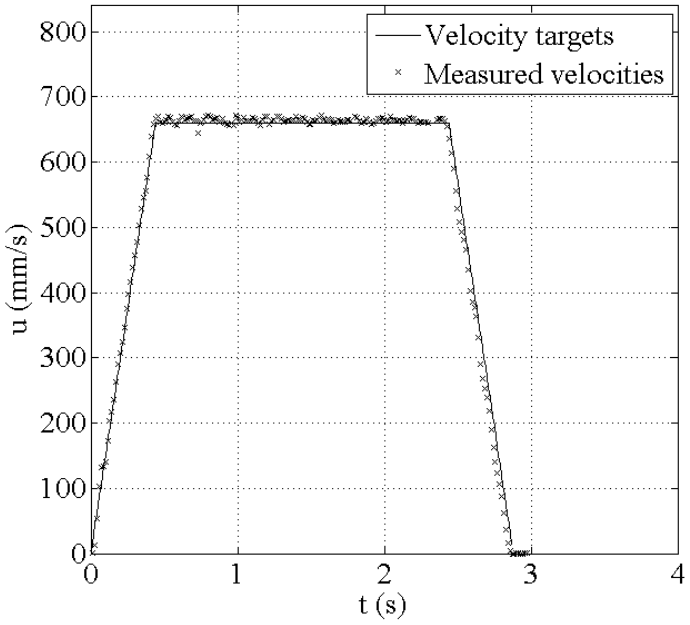

Figure A.17: Landslide target and measured velocities for Run 9 ($a0 = 1.5$ m/s^2, $u_t = 0.655$ m/s)

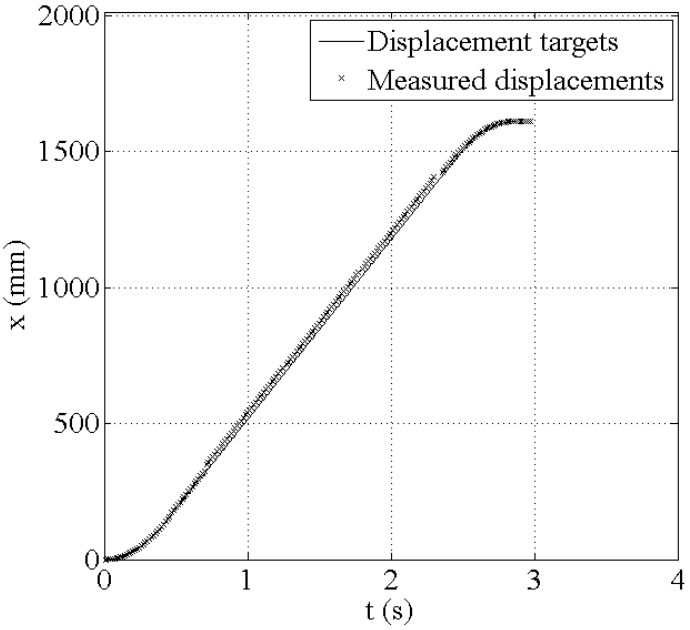

Figure A.18: Landslide target and measured displacements for Run 9 ($a0 = 1.5$ m/s^2, $u_t = 0.655$ m/s)

Appendix B

Wave field plots from LIF experiments

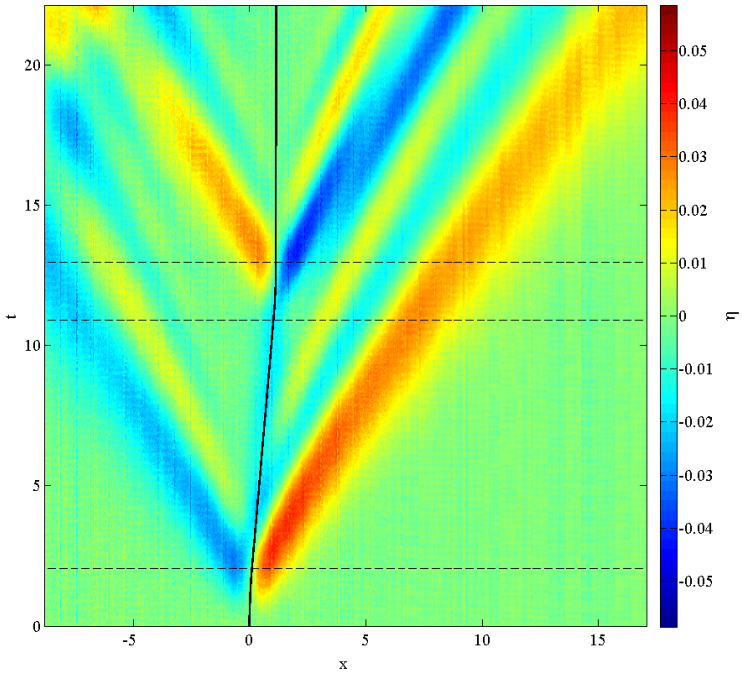

Figure B.1: Experimental wave field plot from Run 1.

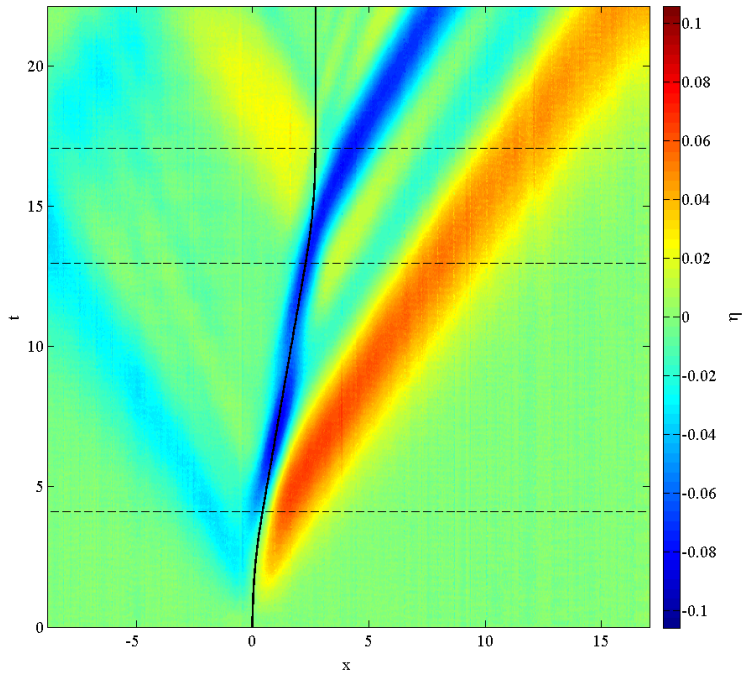

Figure B.2: Experimental wave field plot from Run 2.

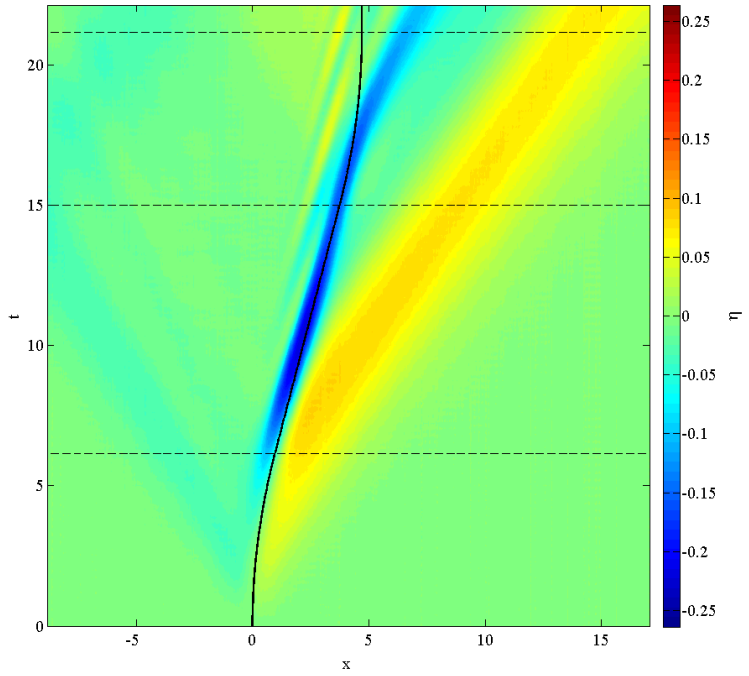

Figure B.3: Experimental wave field plot from Run 3.

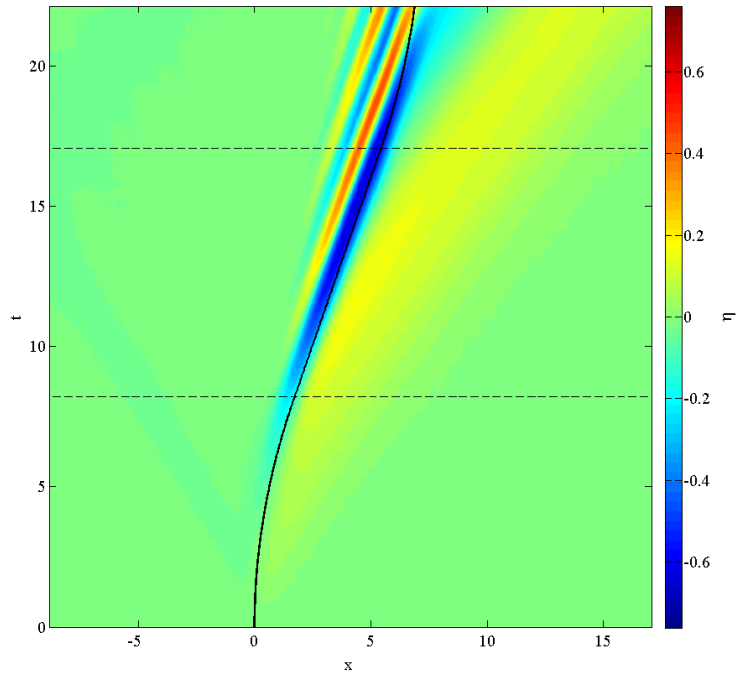

Figure B.4: Experimental wave field plot from Run 4.

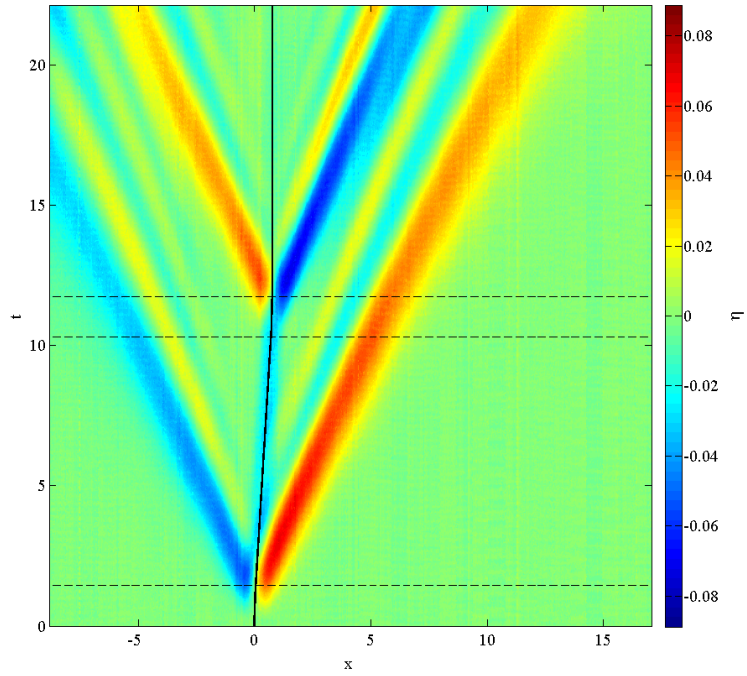

Figure B.5: Experimental wave field plot from Run 5.

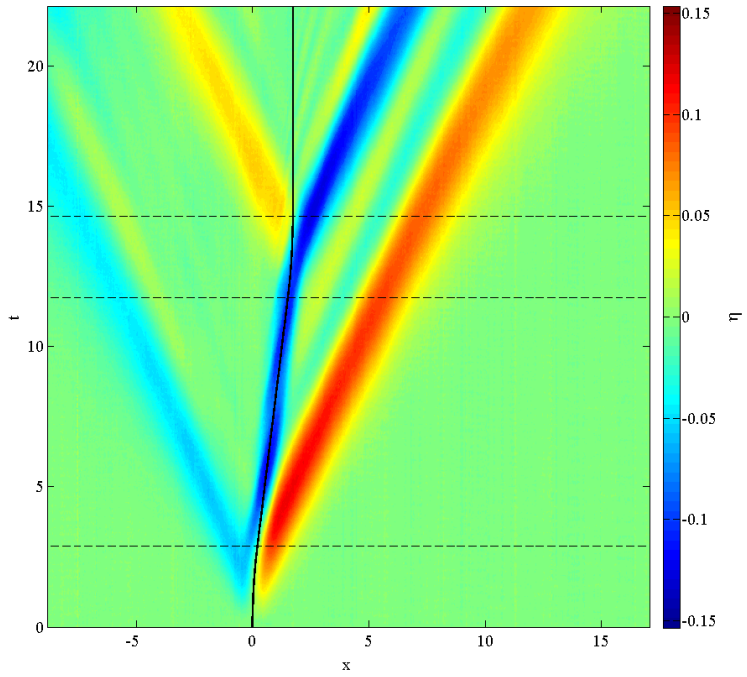

Figure B.6: Experimental wave field plot from Run 6.

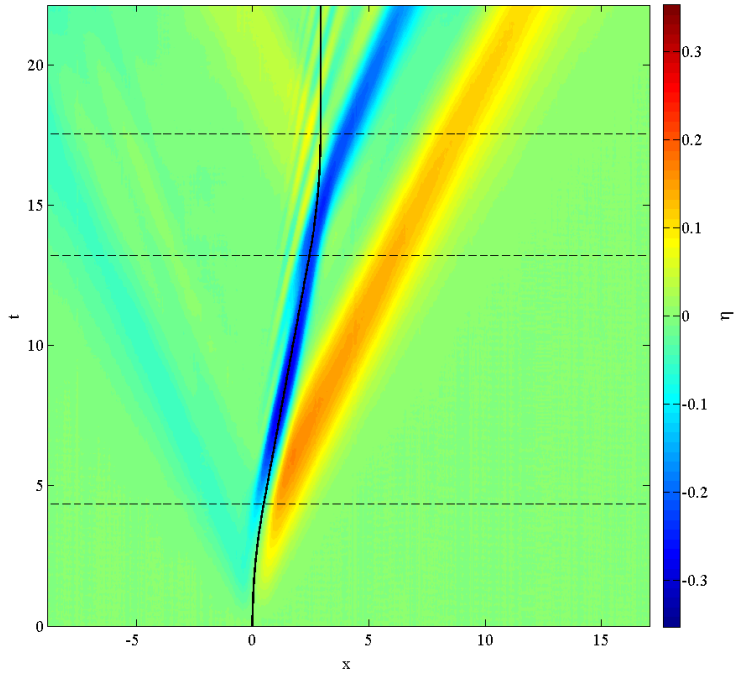

Figure B.7: Experimental wave field plot from Run 7.

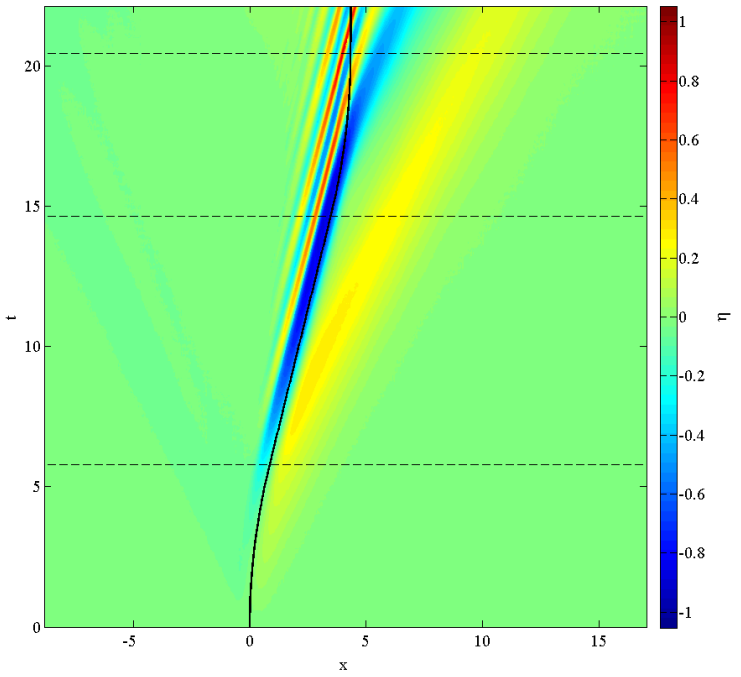

Figure B.8: Experimental wave field plot from Run 8.

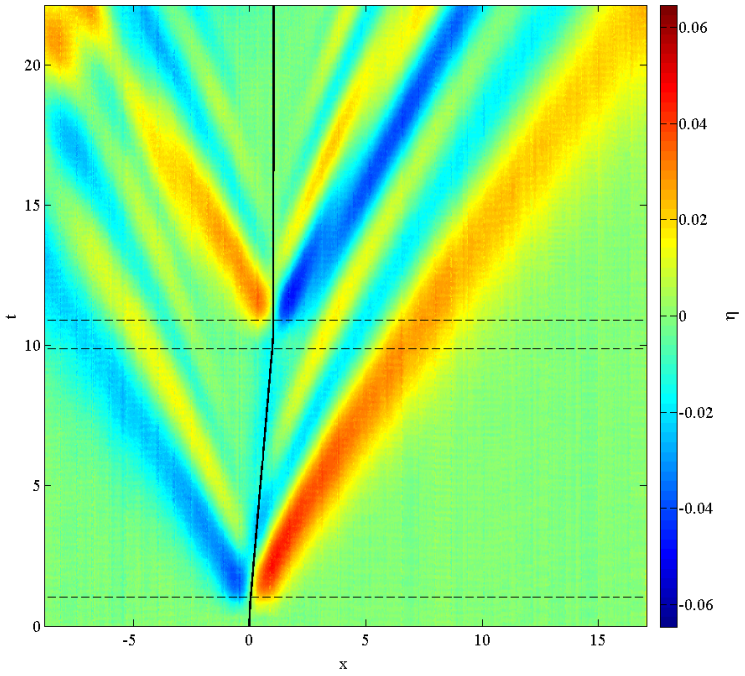

Figure B.9: Experimental wave field plot from Run 9.

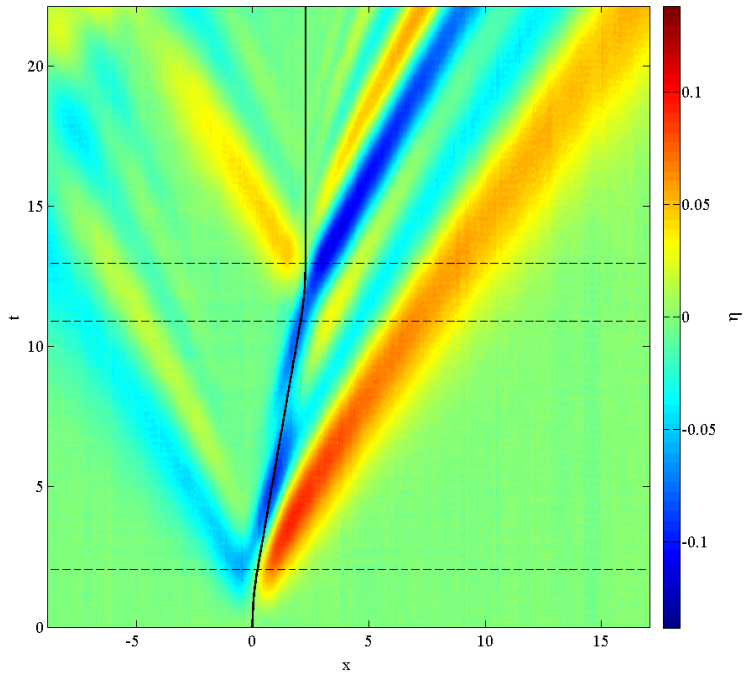

Figure B.10: Experimental wave field plot from Run 10.

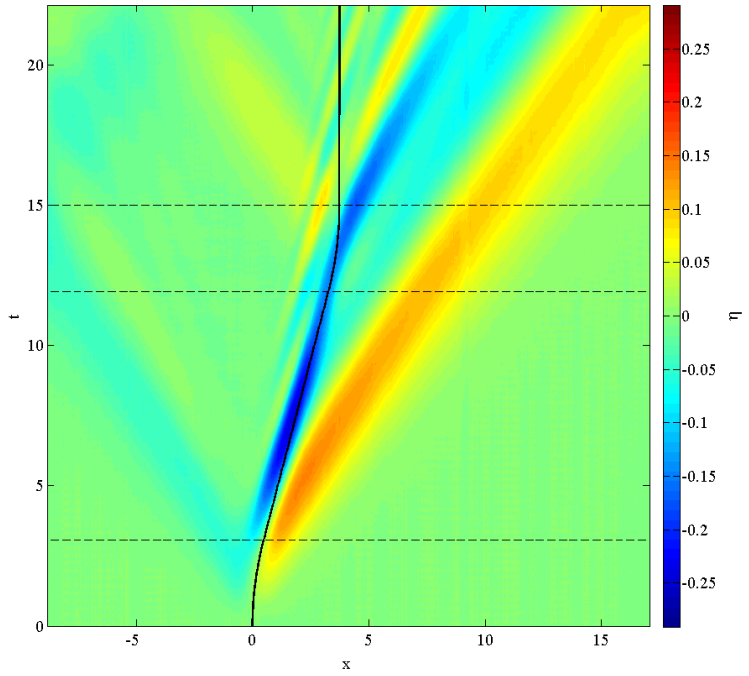

Figure B.11: Experimental wave field plot from Run 11.

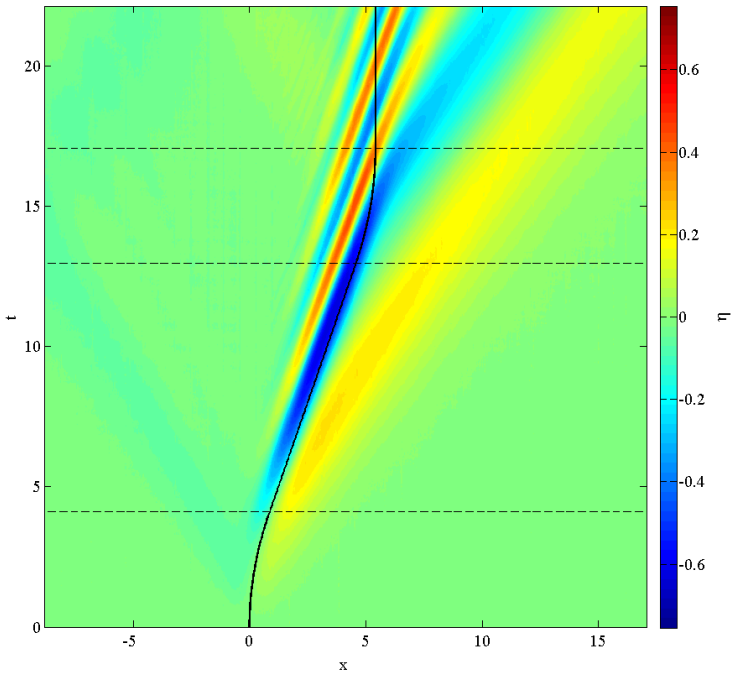

Figure B.12: Experimental wave field plot from Run 12.

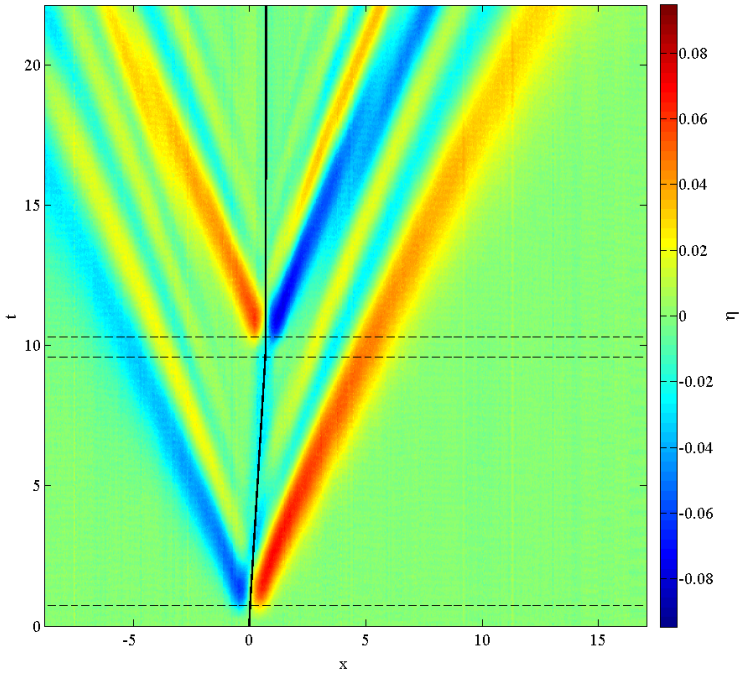

Figure B.13: Experimental wave field plot from Run 13.

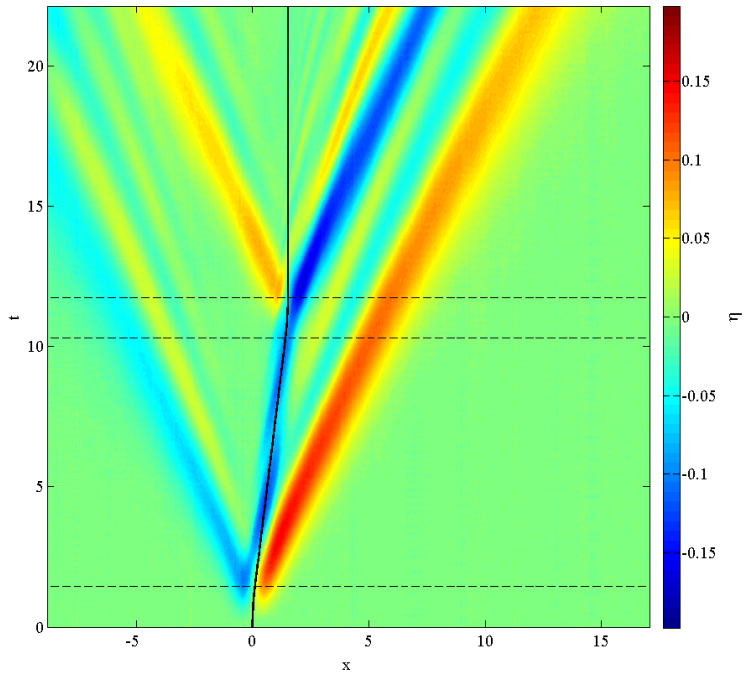

Figure B.14: Experimental wave field plot from Run 14.

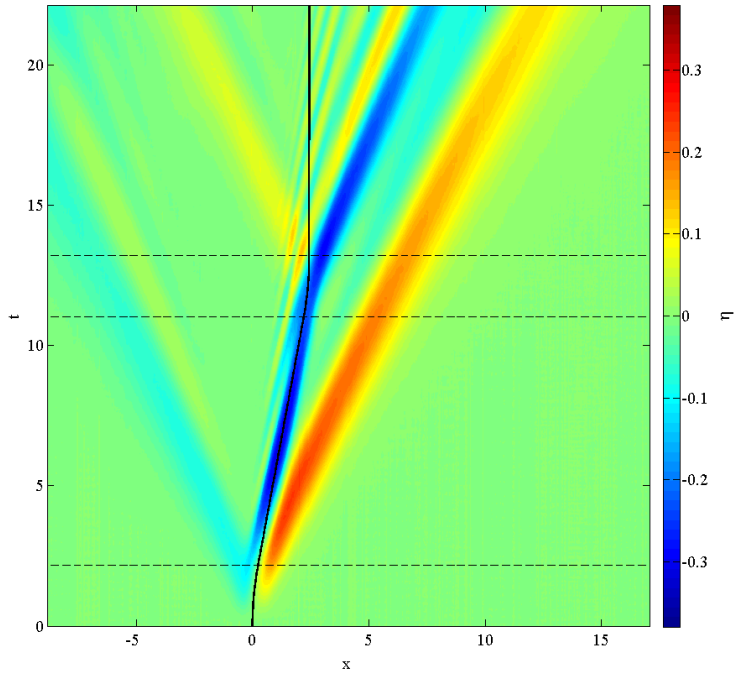

Figure B.15: Experimental wave field plot from Run 15.

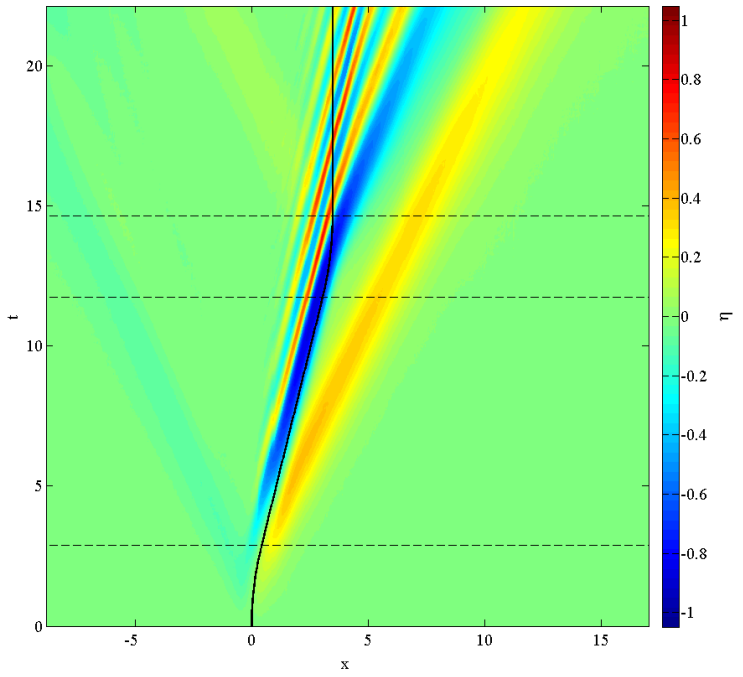

Figure B.16: Experimental wave field plot from Run 16.

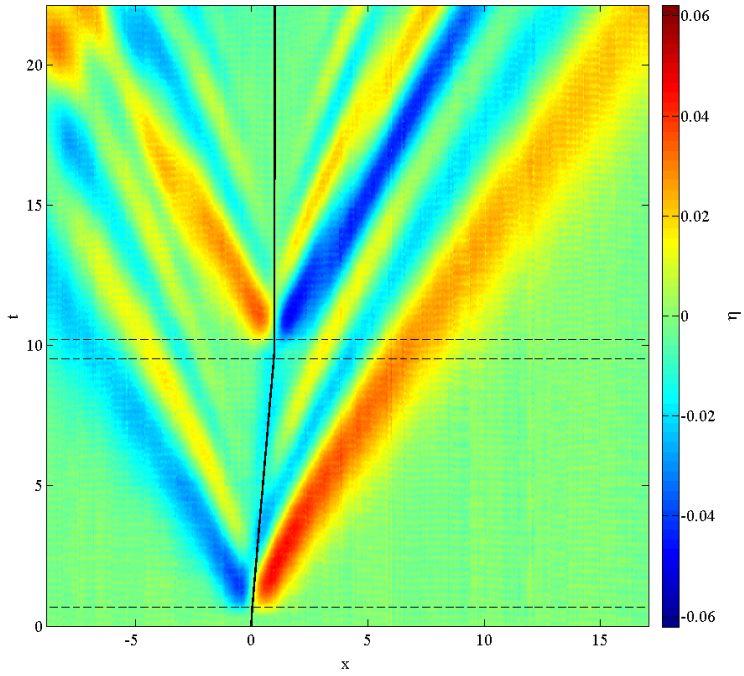

Figure B.17: Experimental wave field plot from Run 17.

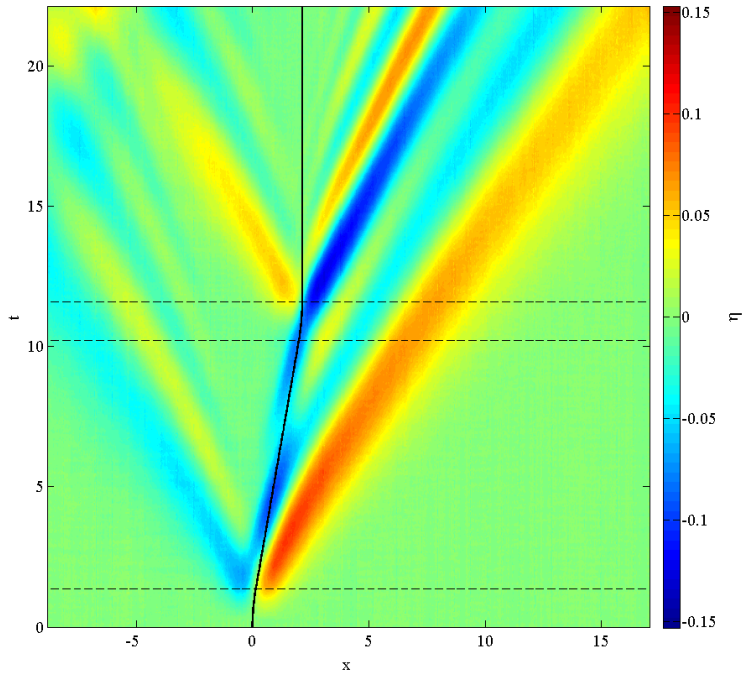

Figure B.18: Experimental wave field plot from Run 18.

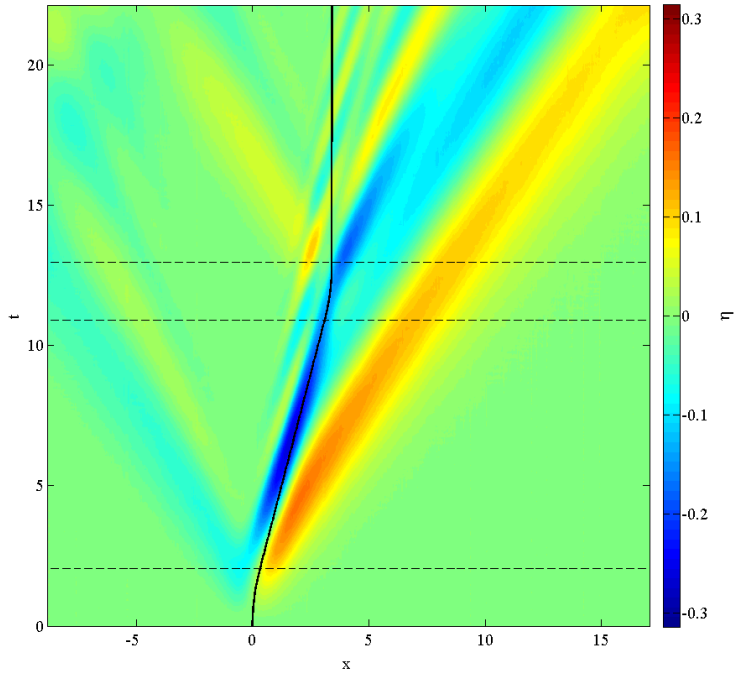

Figure B.19: Experimental wave field plot from Run 19.

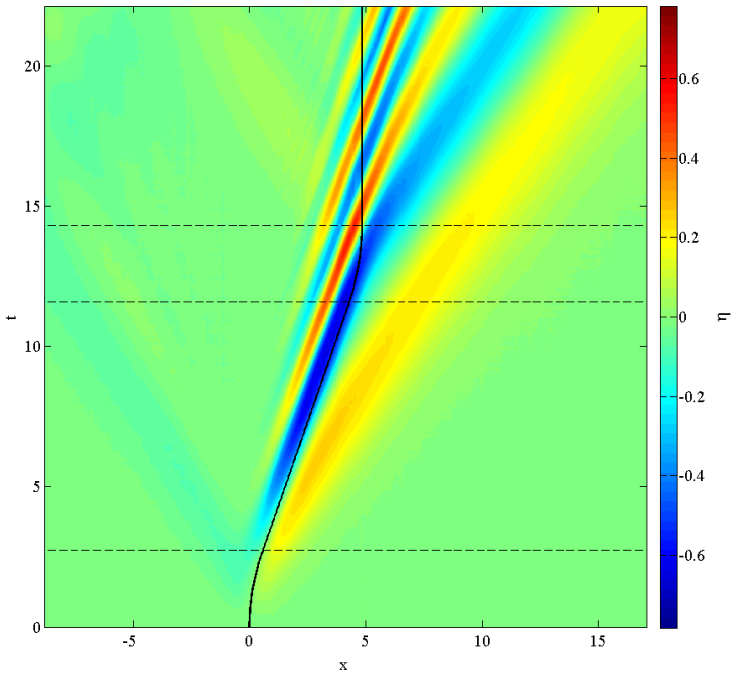

Figure B.20: Experimental wave field plot from Run 20.

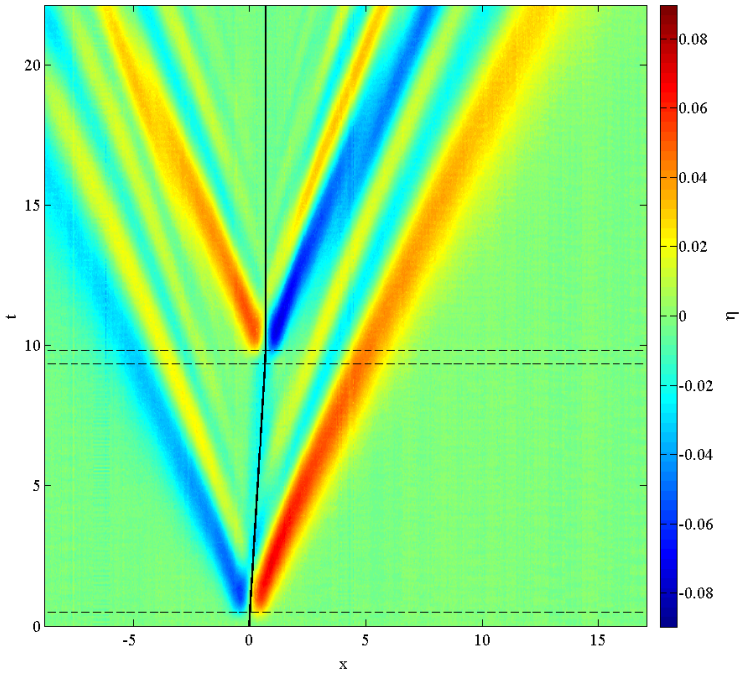

Figure B.21: Experimental wave field plot from Run 21.

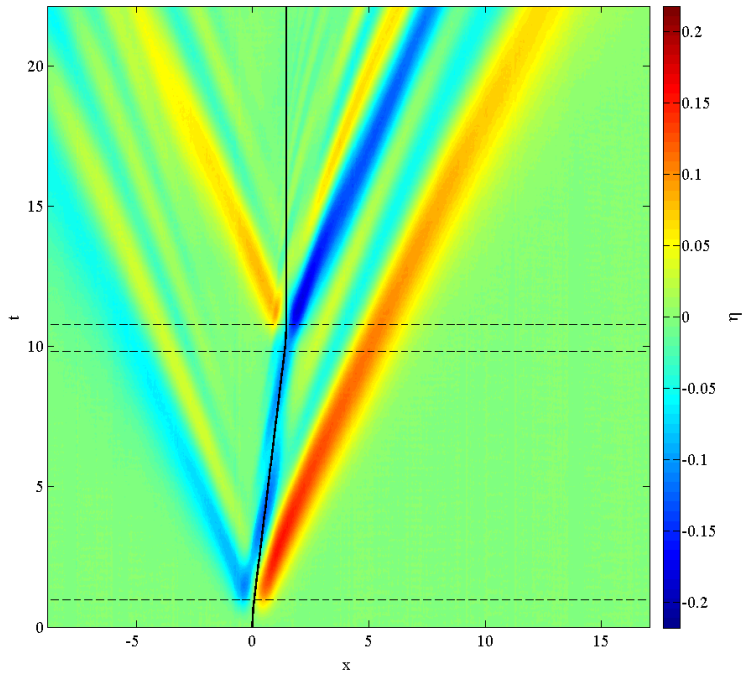

Figure B.22: Experimental wave field plot from Run 22.

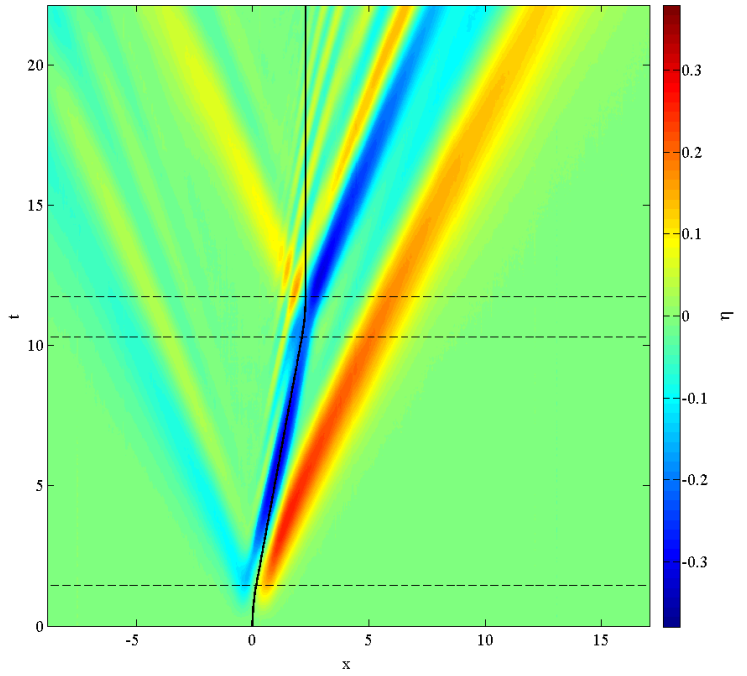

Figure B.23: Experimental wave field plot from Run 23.

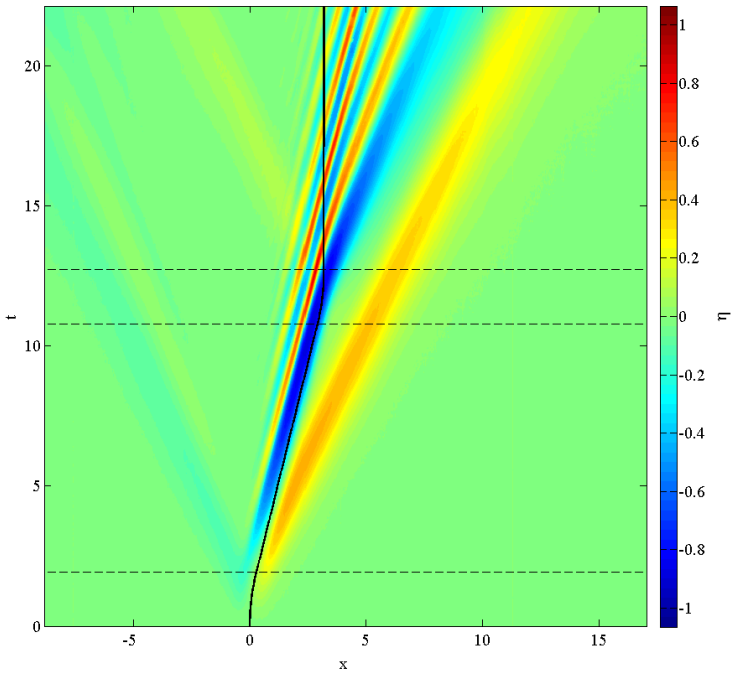

Figure B.24: Experimental wave field plot from Run 24.

Appendix C

Potential energy within wave field

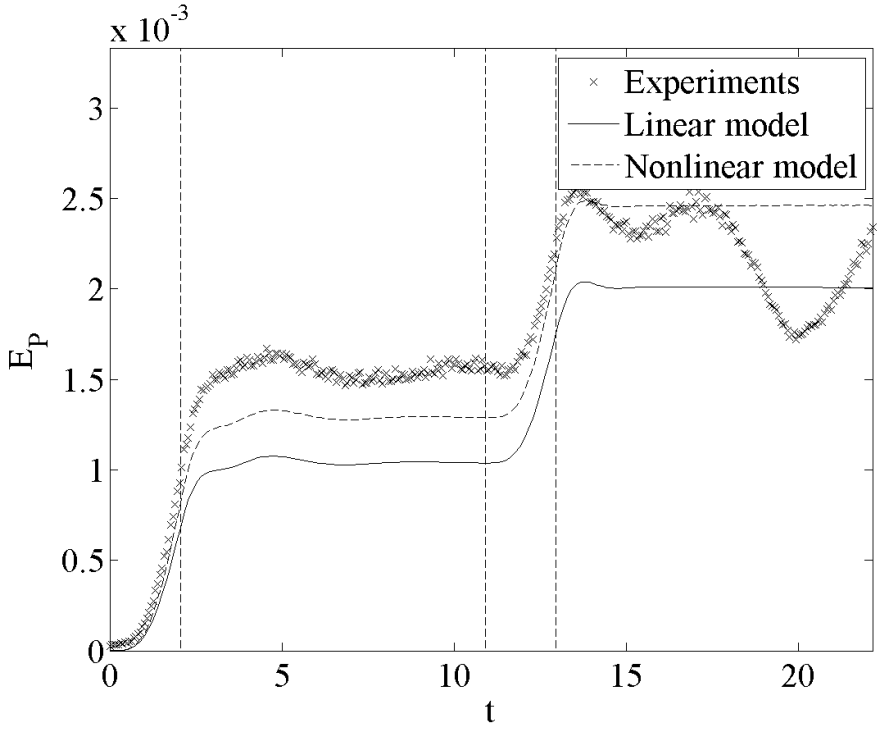

Figure C.1: Potential energy contained in the wave field for Run 1.

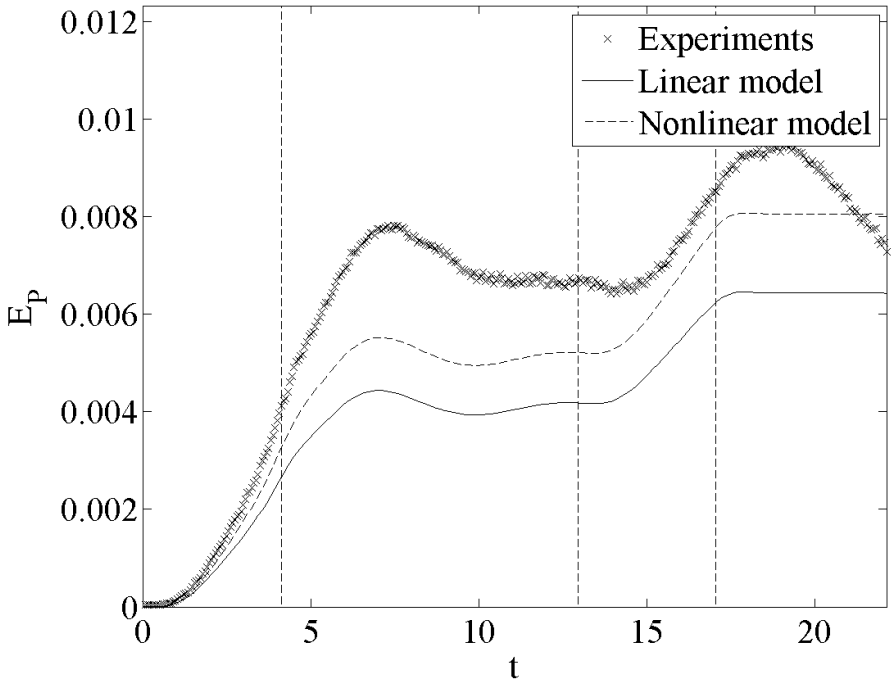

Figure C.2: Potential energy contained in the wave field for Run 2.

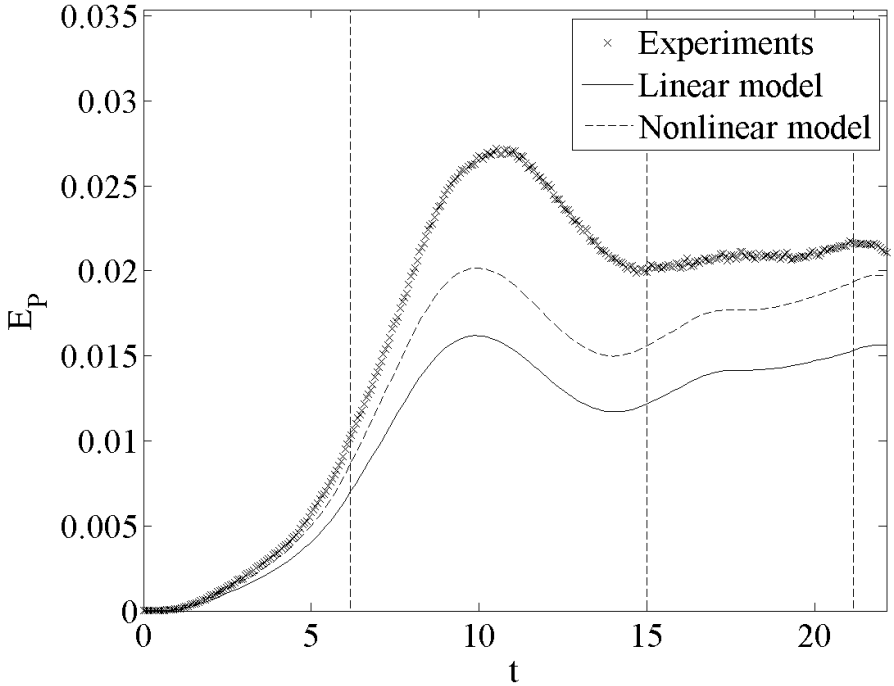

Figure C.3: Potential energy contained in the wave field for Run 3.

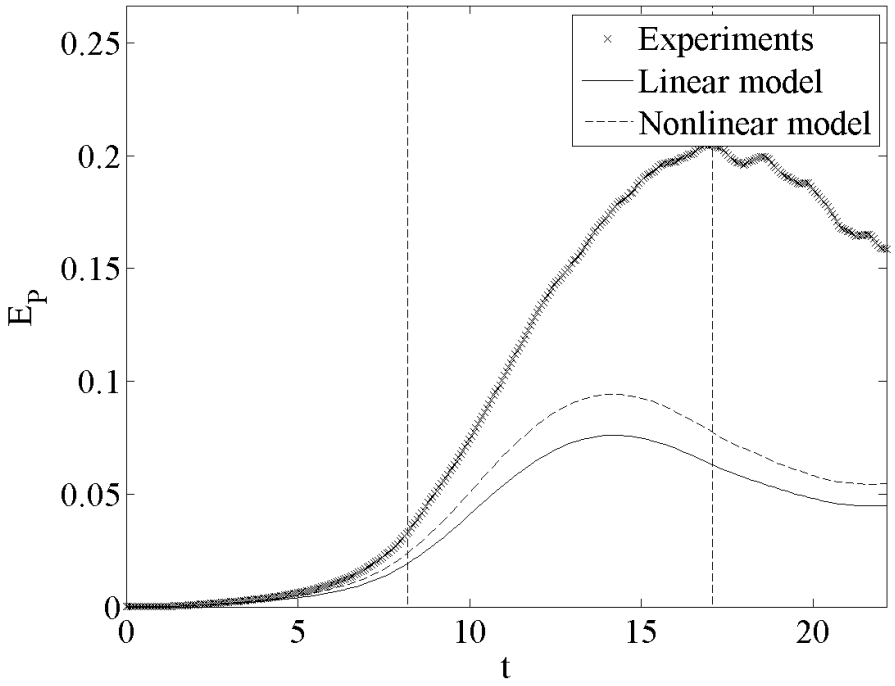

Figure C.4: Potential energy contained in the wave field for Run 4.

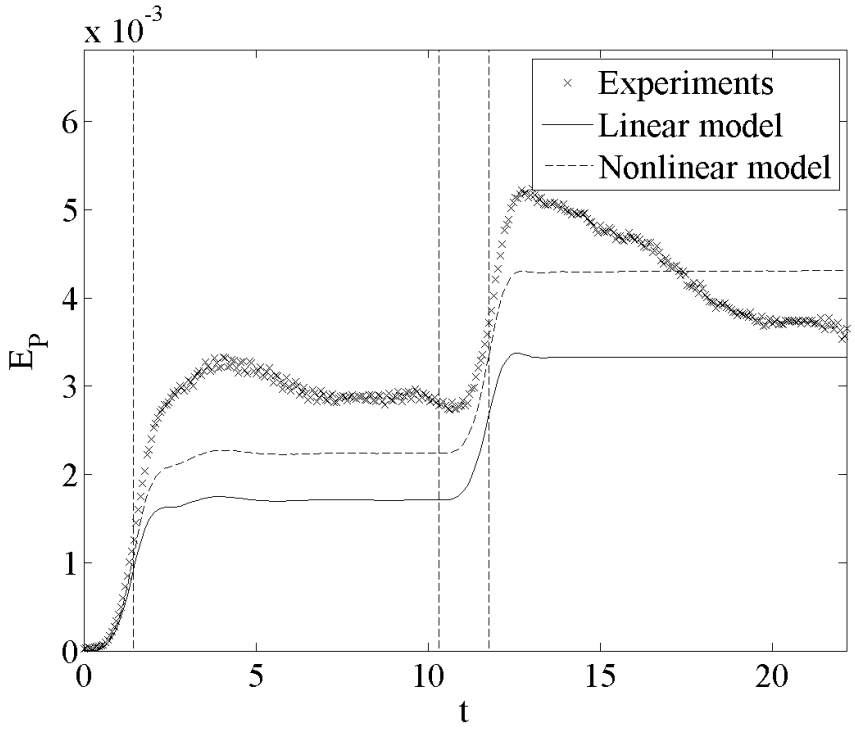

Figure C.5: Potential energy contained in the wave field for Run 5.

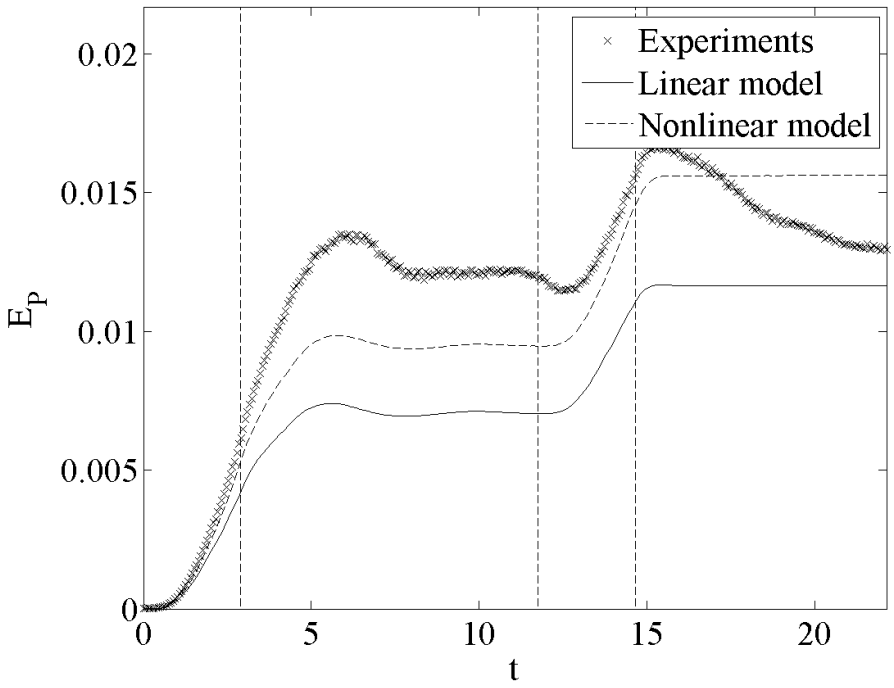

Figure C.6: Potential energy contained in the wave field for Run 6.

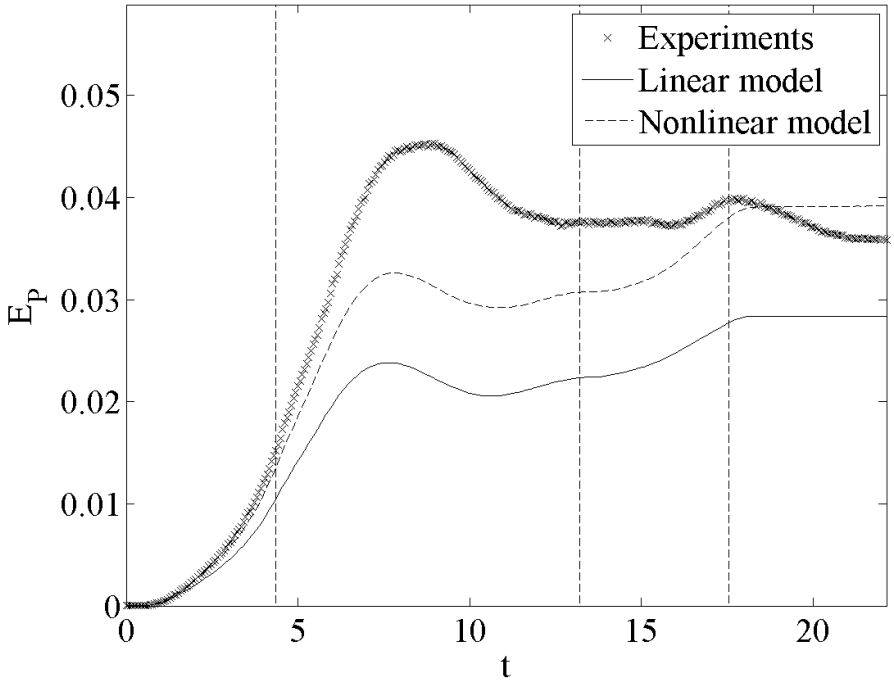

Figure C.7: Potential energy contained in the wave field for Run 7.

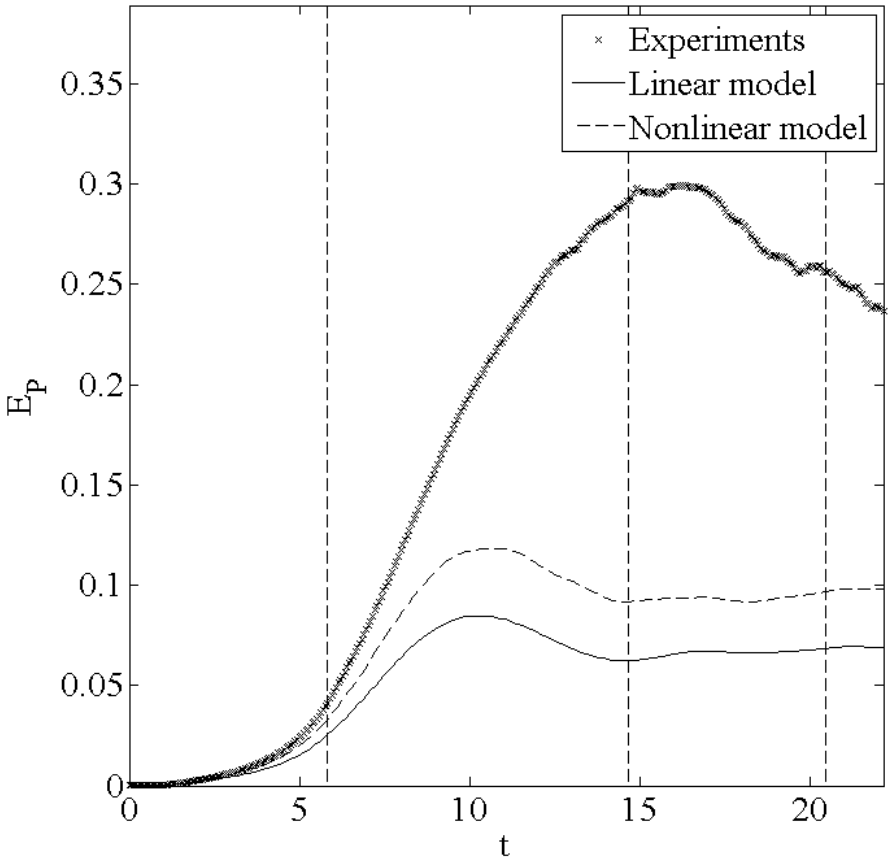

Figure C.8: Potential energy contained in the wave field for Run 8.

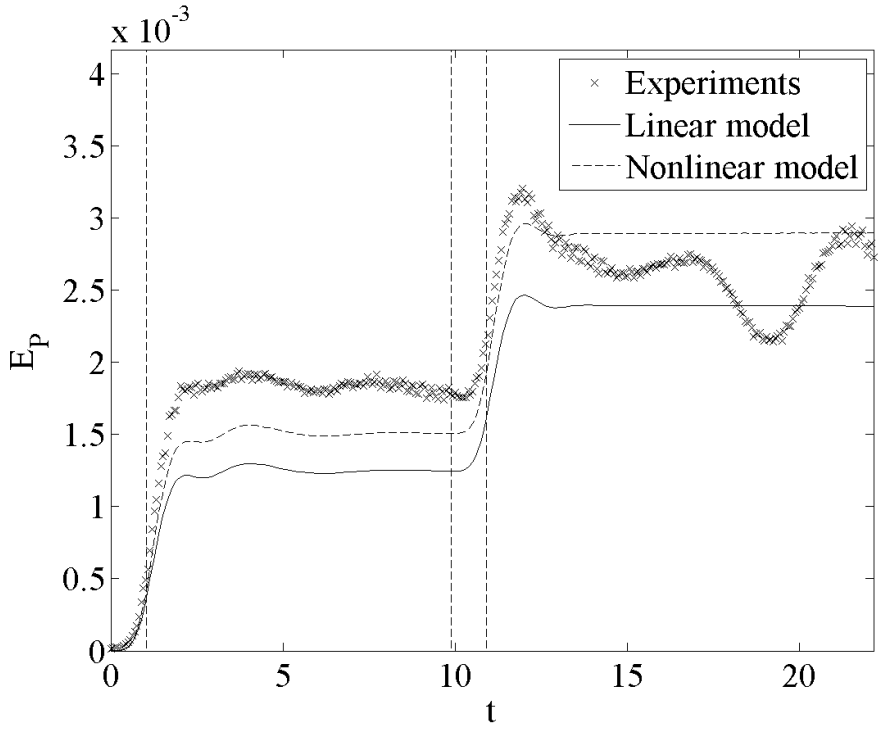

Figure C.9: Potential energy contained in the wave field for Run 9.

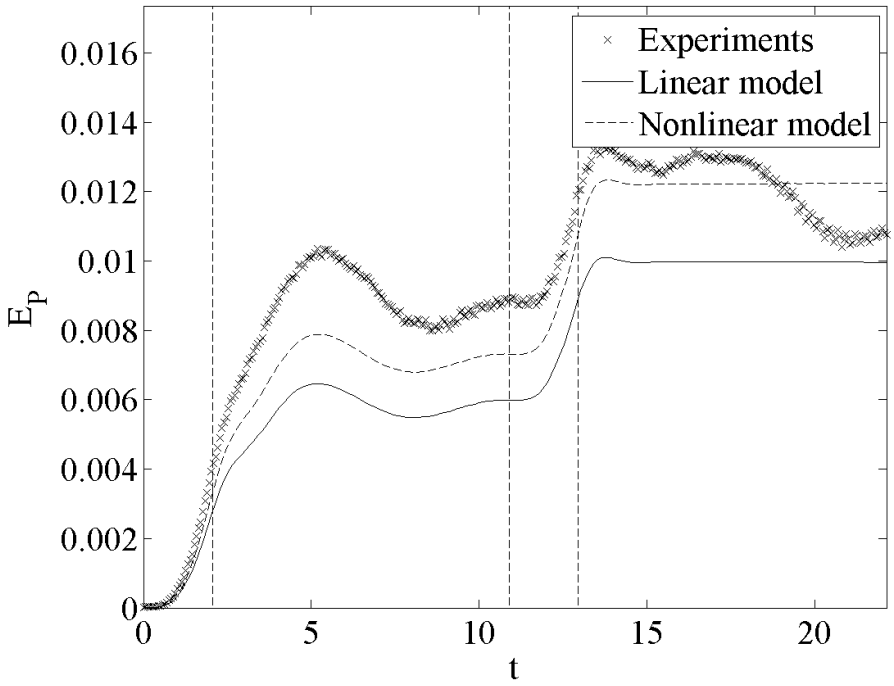

Figure C.10: Potential energy contained in the wave field for Run 10.

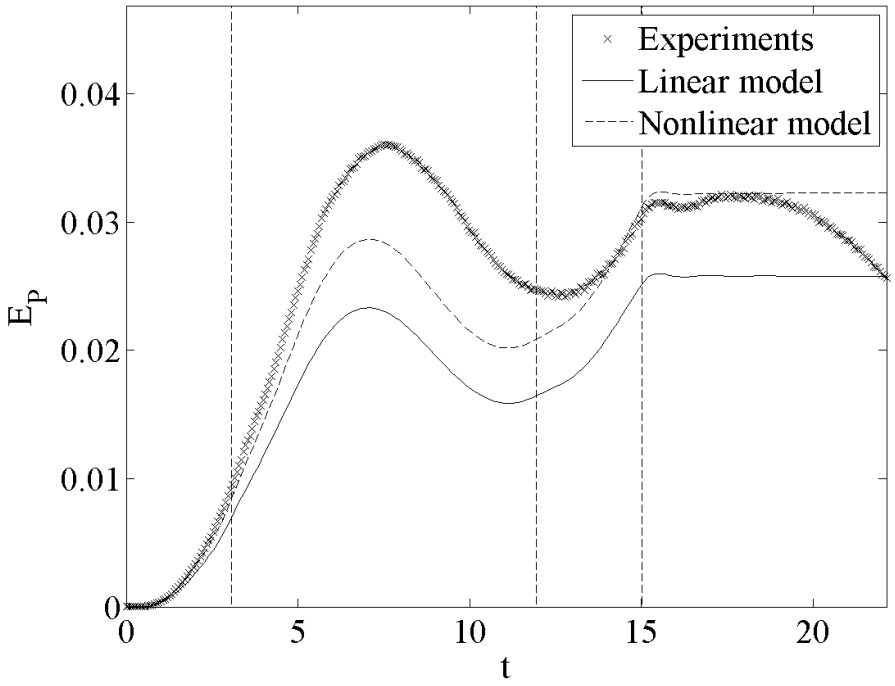

Figure C.11: Potential energy contained in the wave field for Run 11.

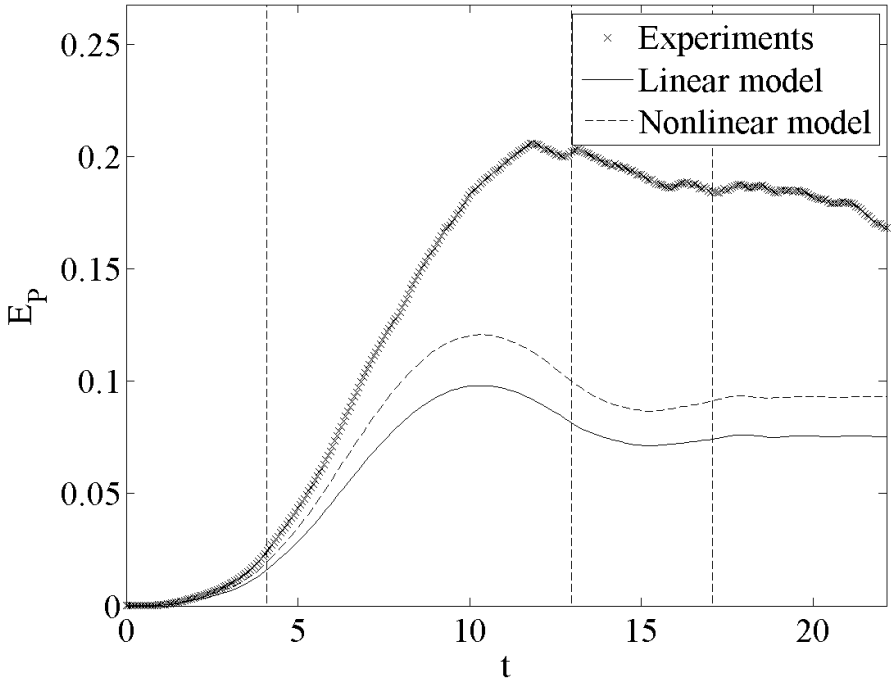

Figure C.12: Potential energy contained in the wave field for Run 12.

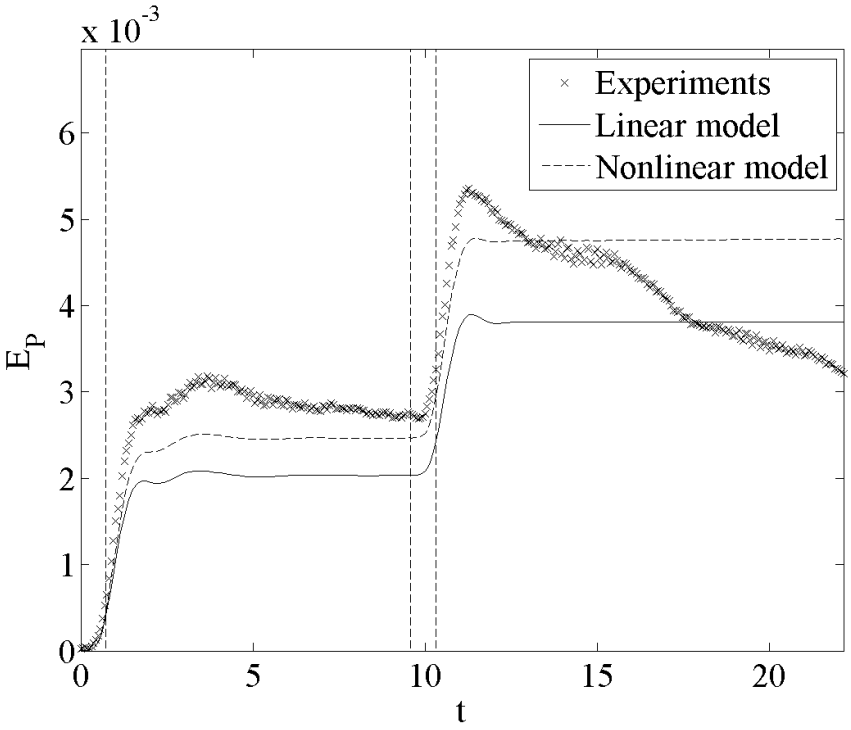

Figure C.13: Potential energy contained in the wave field for Run 13.

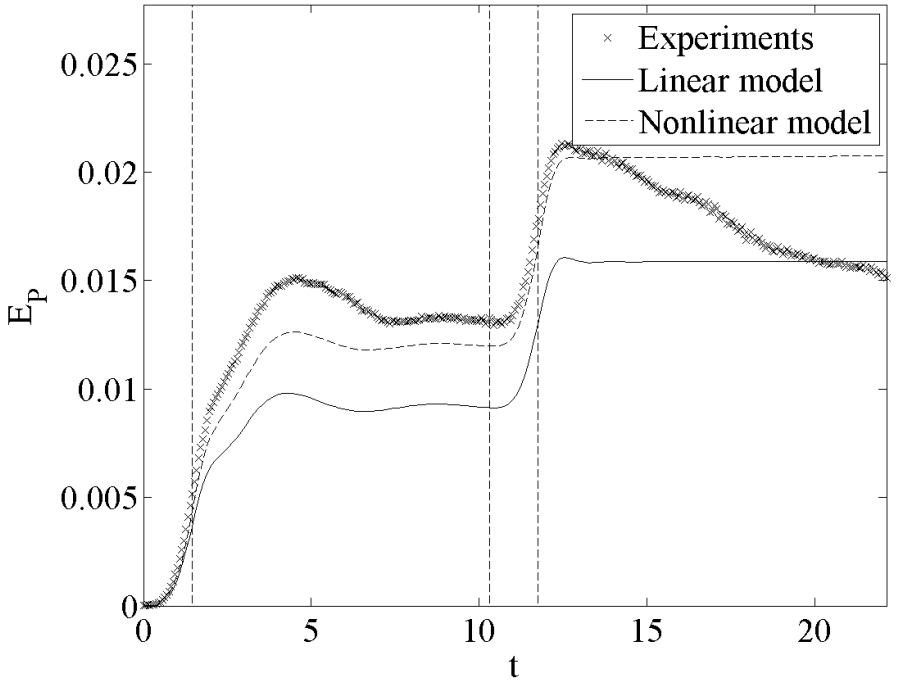

Figure C.14: Potential energy contained in the wave field for Run 14.

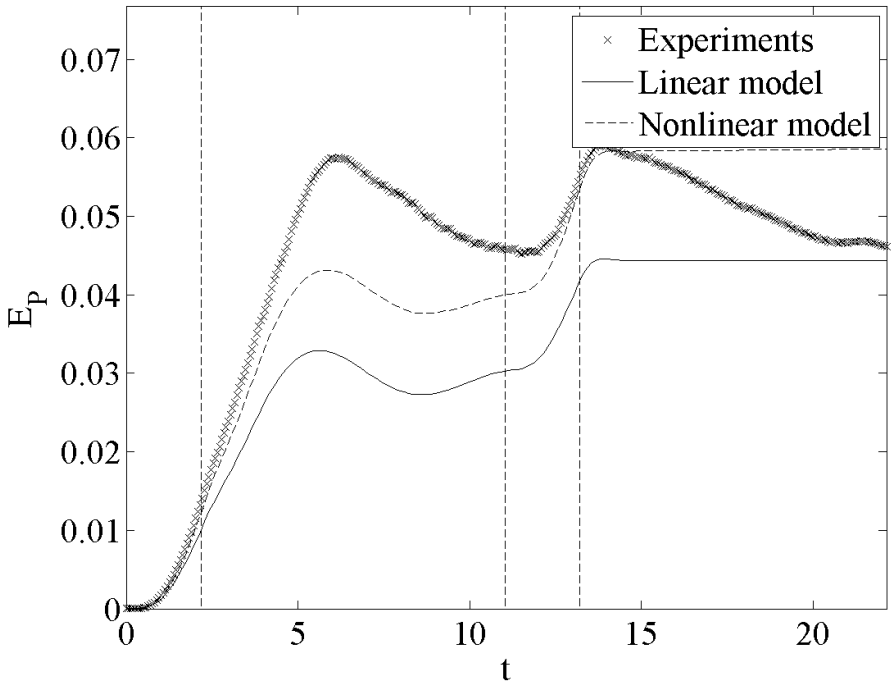

Figure C.15: Potential energy contained in the wave field for Run 15.

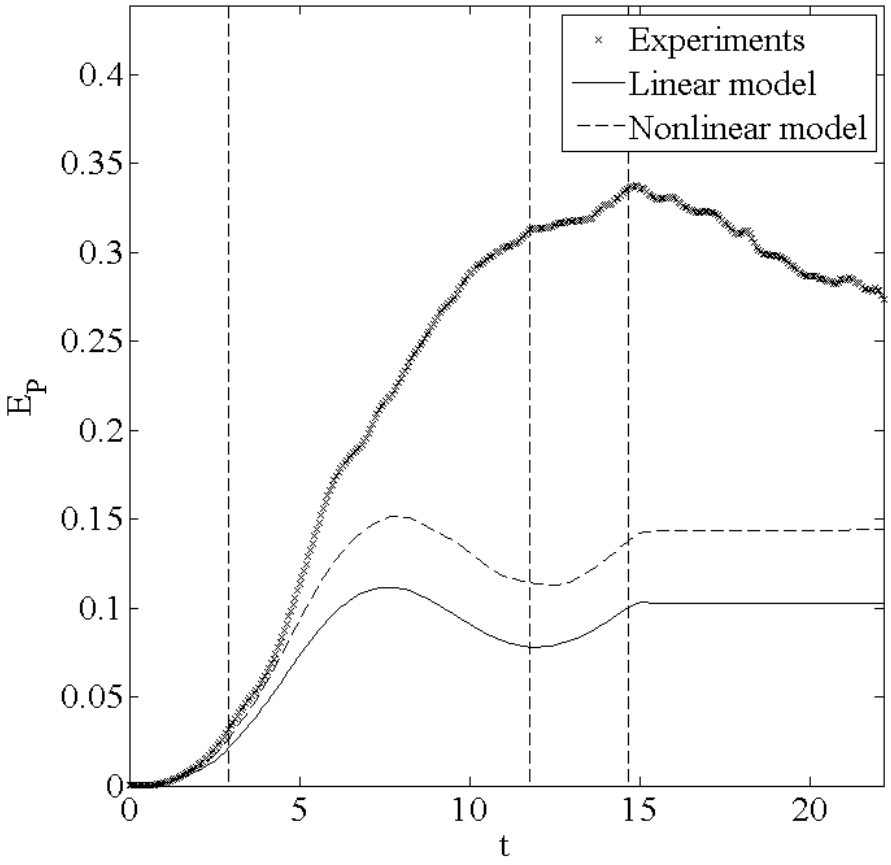

Figure C.16: Potential energy contained in the wave field for Run 16.

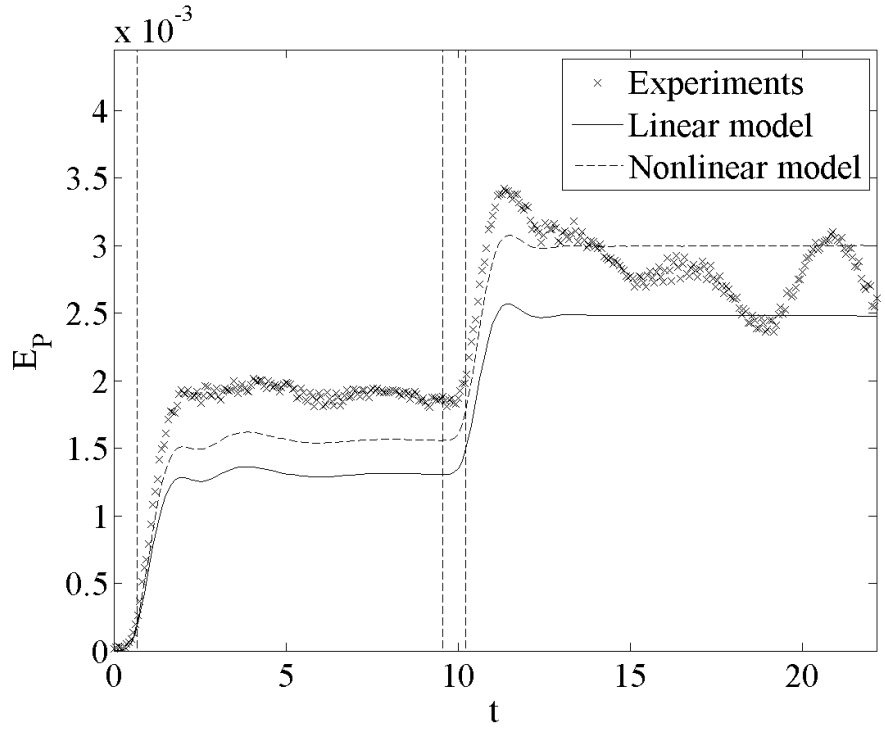

Figure C.17: Potential energy contained in the wave field for Run 17.

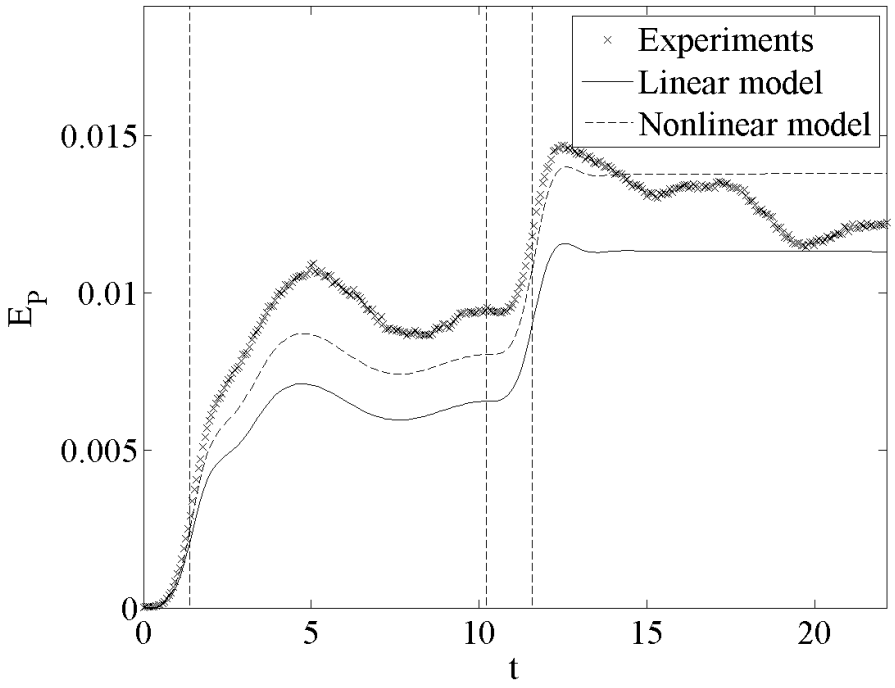

Figure C.18: Potential energy contained in the wave field for Run 18.

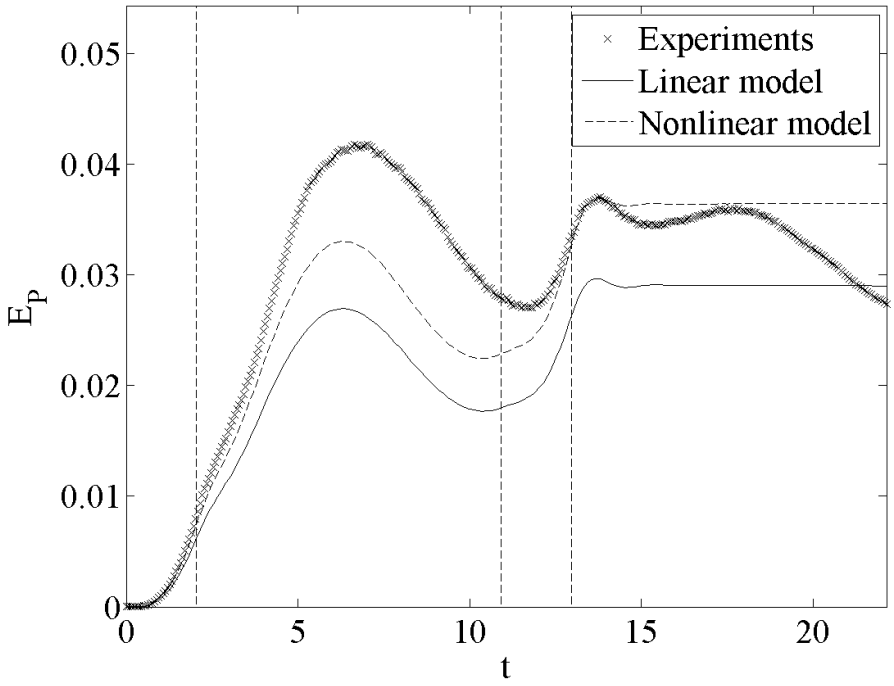

Figure C.19: Potential energy contained in the wave field for Run 19.

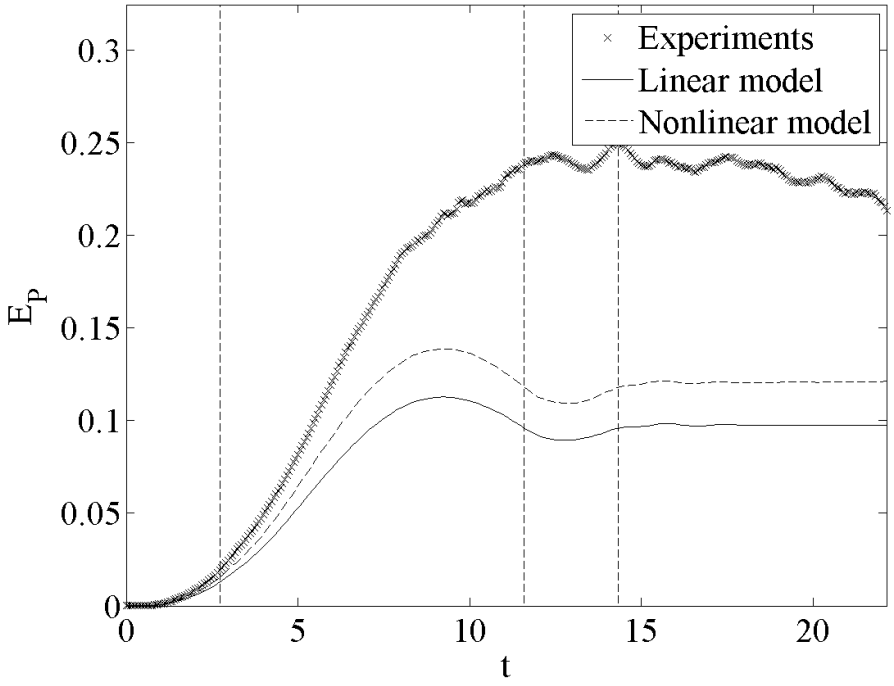

Figure C.20: Potential energy contained in the wave field for Run 20.

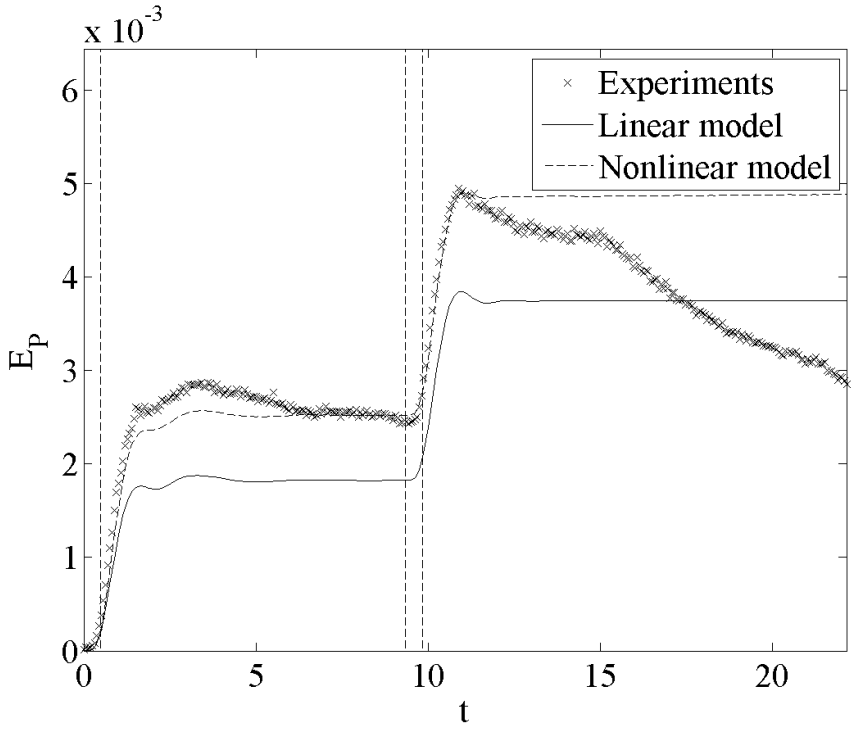

Figure C.21: Potential energy contained in the wave field for Run 21.

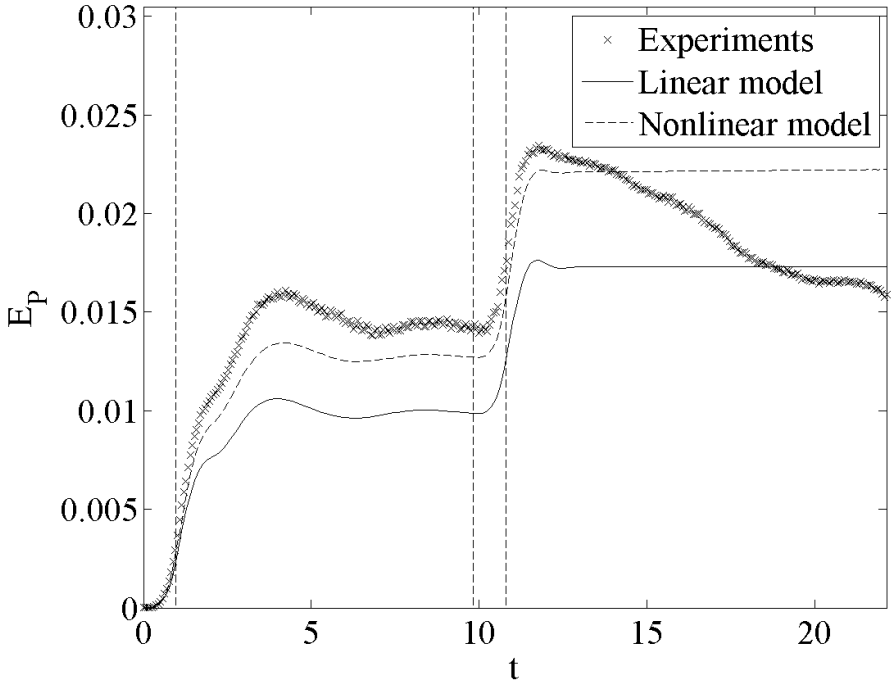

Figure C.22: Potential energy contained in the wave field for Run 22.

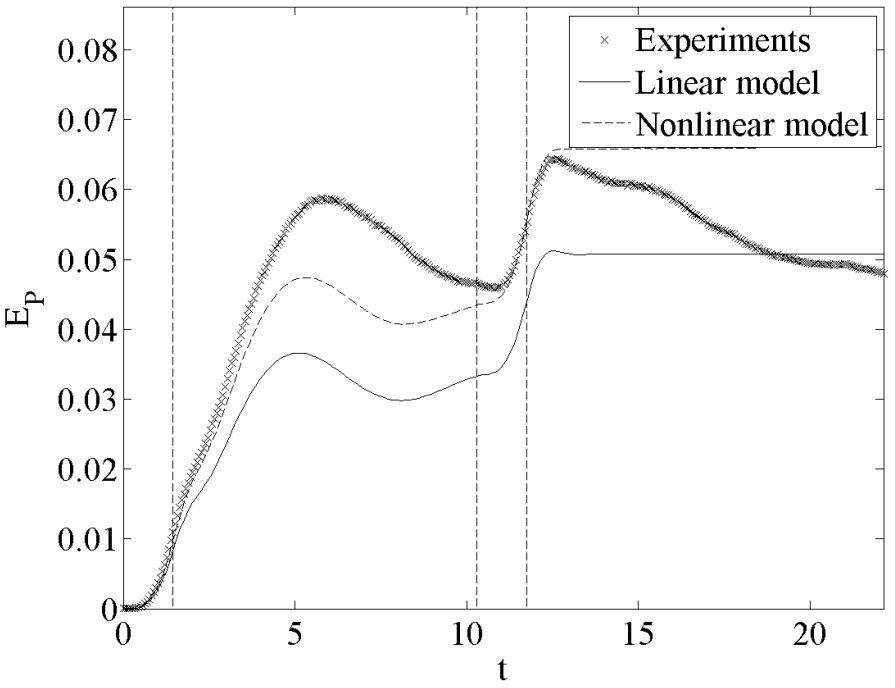

Figure C.23: Potential energy contained in the wave field for Run 23.

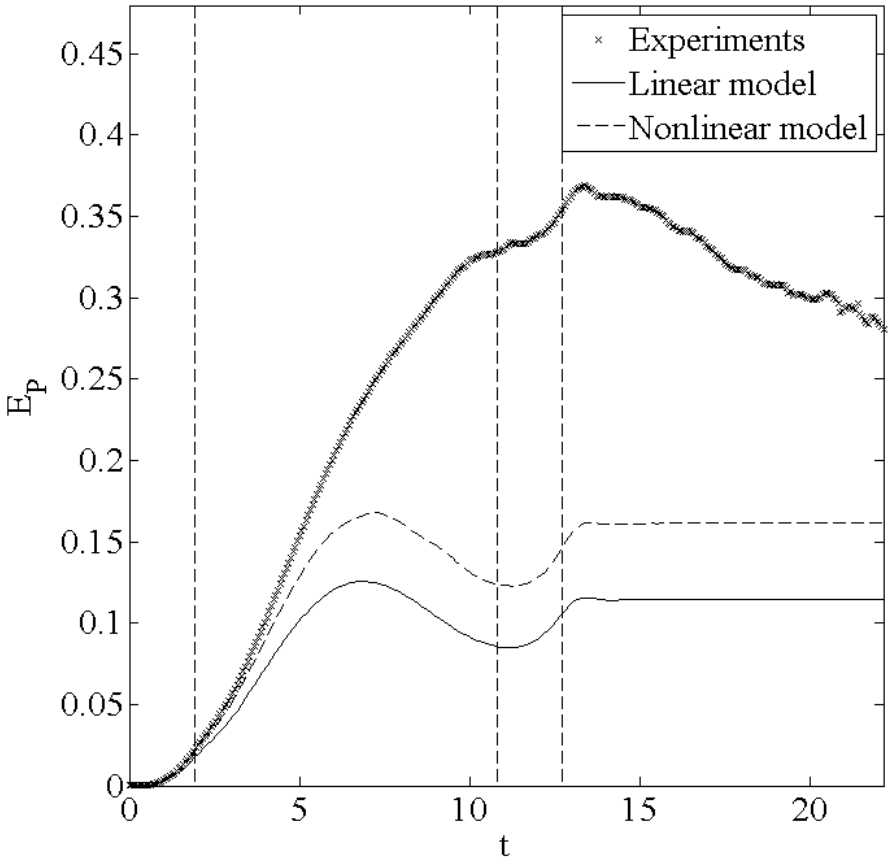

Figure C.24: Potential energy contained in the wave field for Run 24.

Appendix D

Potential energy within onshore and offshore regions

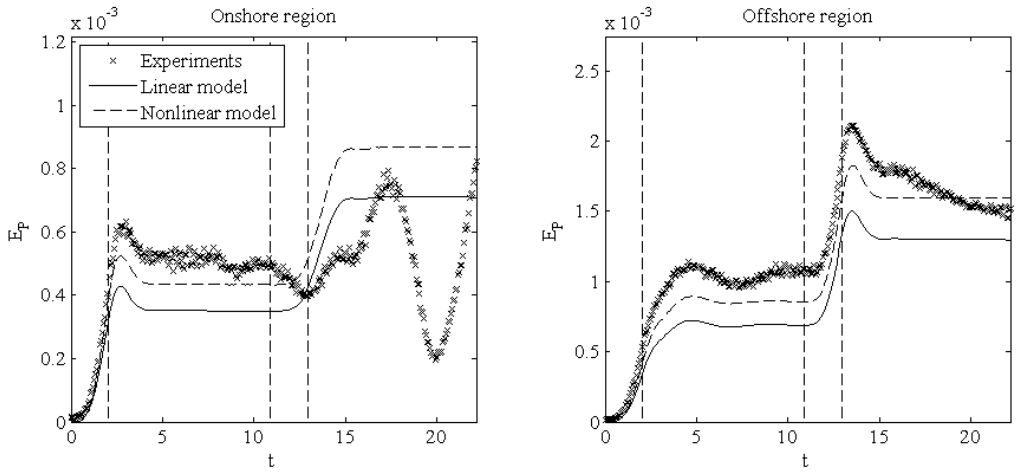

Figure D.1: Potential energy contained in the wave field for Run 1.

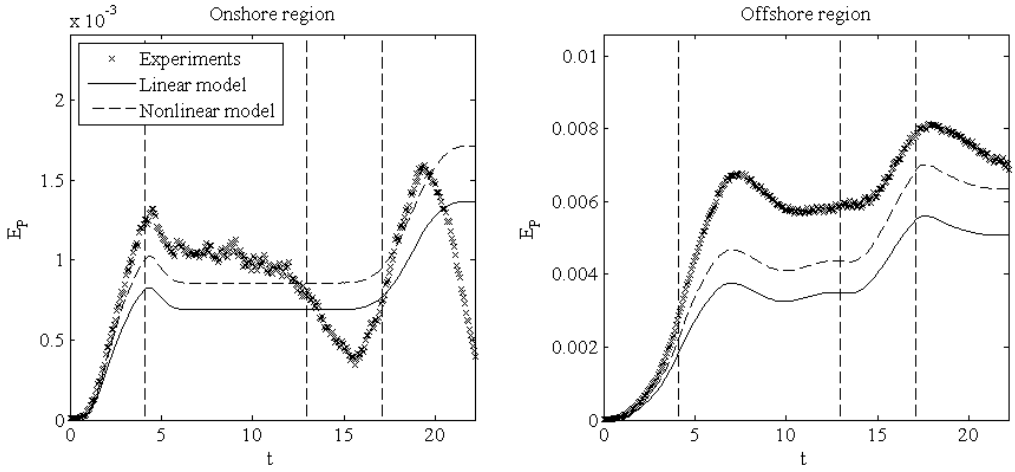

Figure D.2: Potential energy contained in the wave field for Run 2.

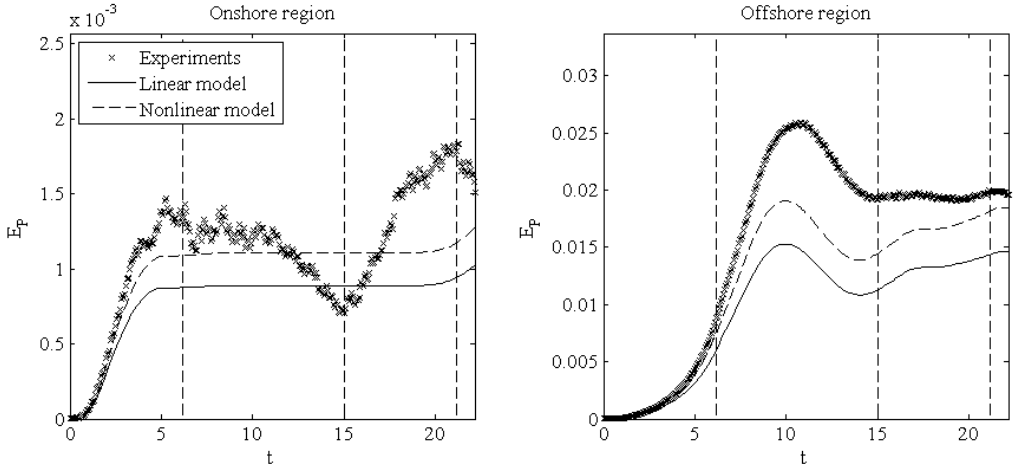

Figure D.3: Potential energy contained in the wave field for Run 3.

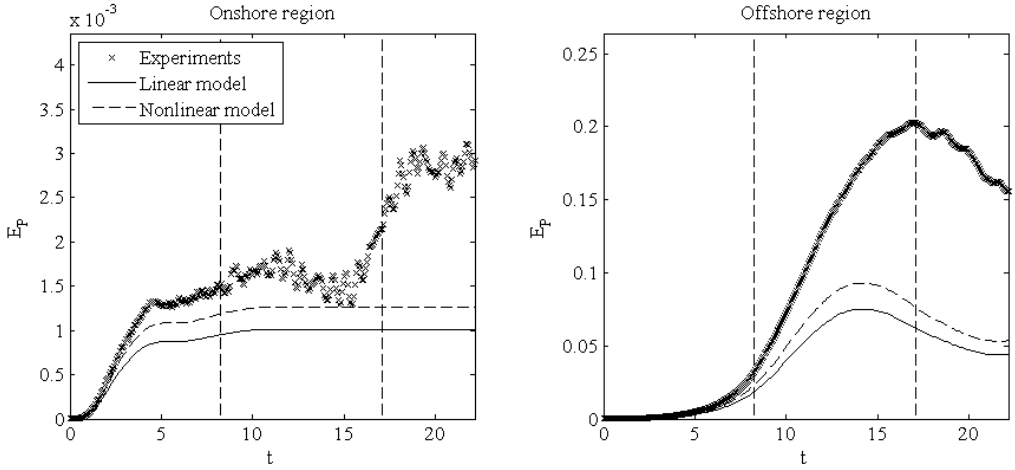

Figure D.4: Potential energy contained in the wave field for Run 4.

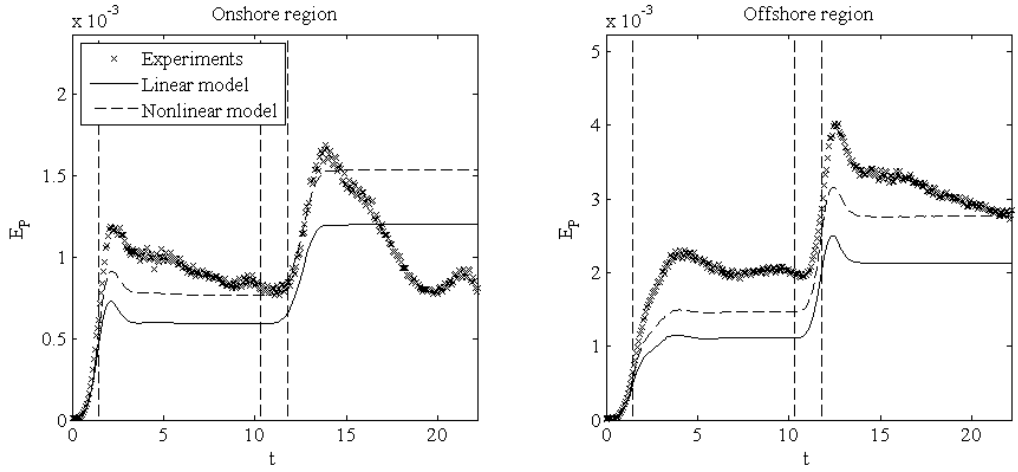

Figure D.5: Potential energy contained in the wave field for Run 5.

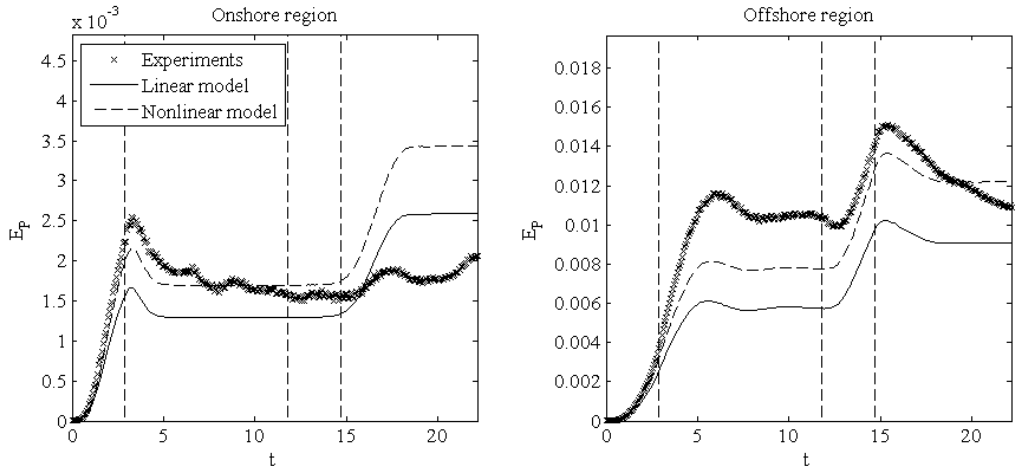

Figure D.6: Potential energy contained in the wave field for Run 6.

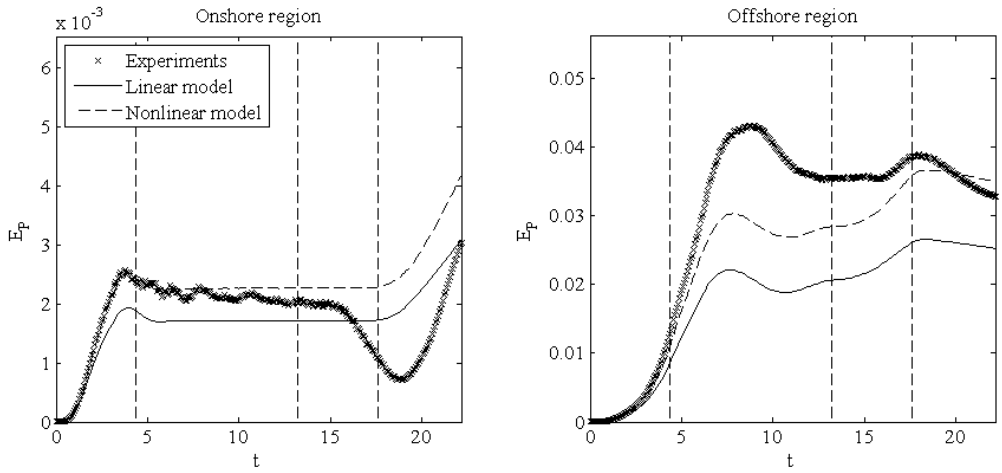

Figure D.7: Potential energy contained in the wave field for Run 7.

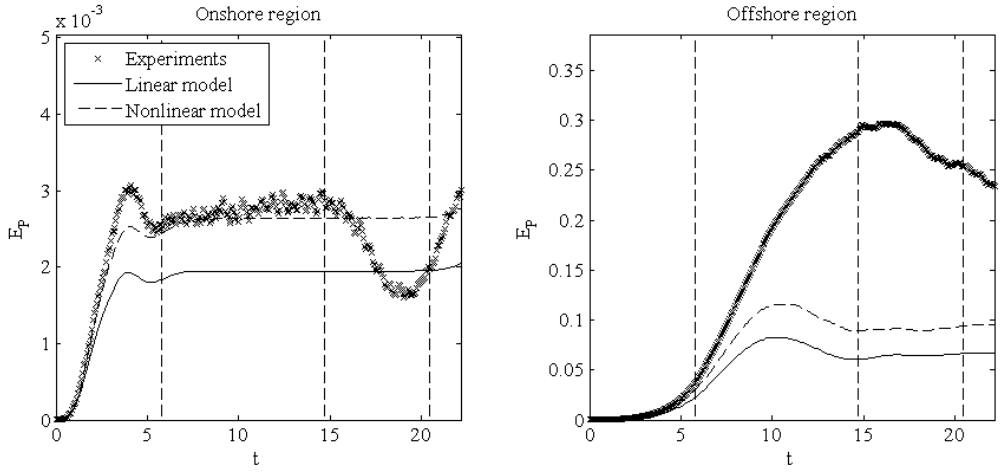

Figure D.8: Potential energy contained in the wave field for Run 8.

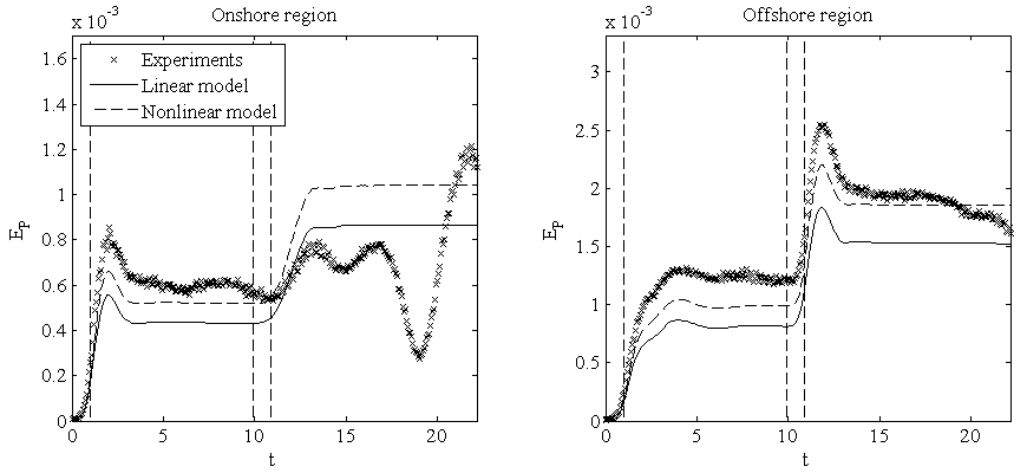

Figure D.9: Potential energy contained in the wave field for Run 9.

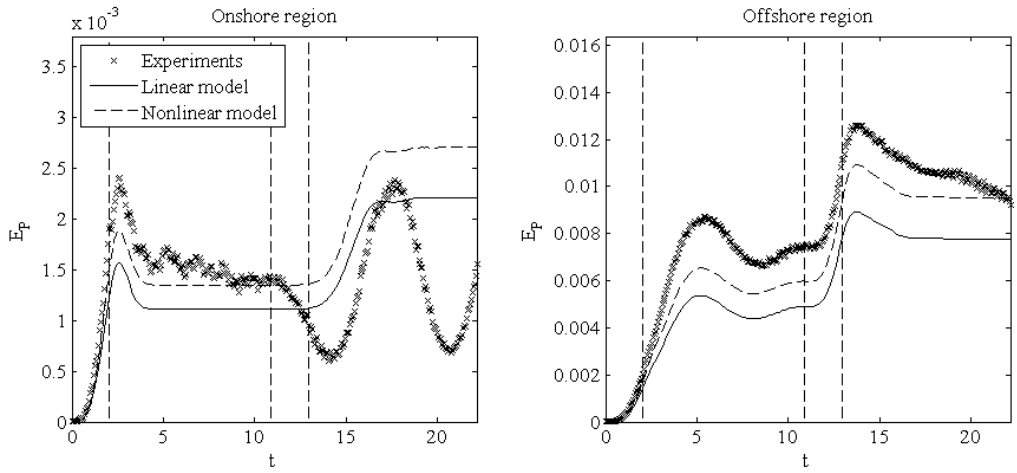

Figure D.10: Potential energy contained in the wave field for Run 10.

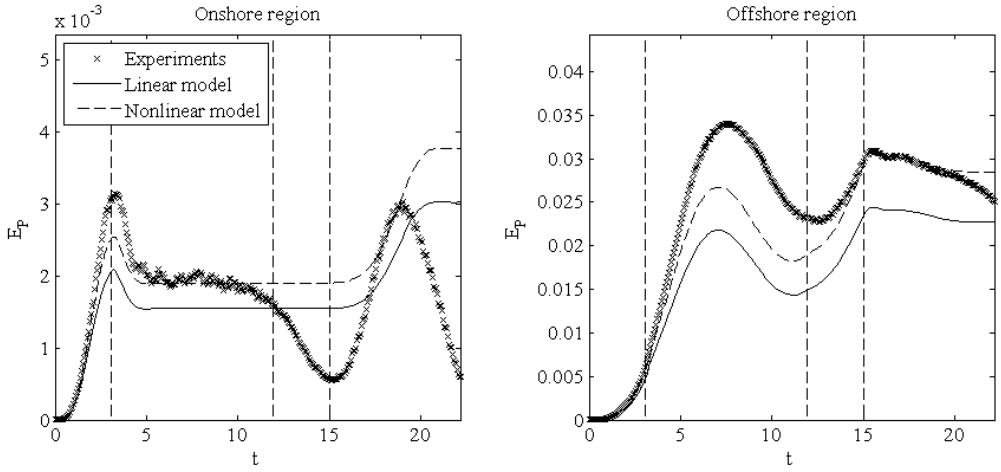

Figure D.11: Potential energy contained in the wave field for Run 11.

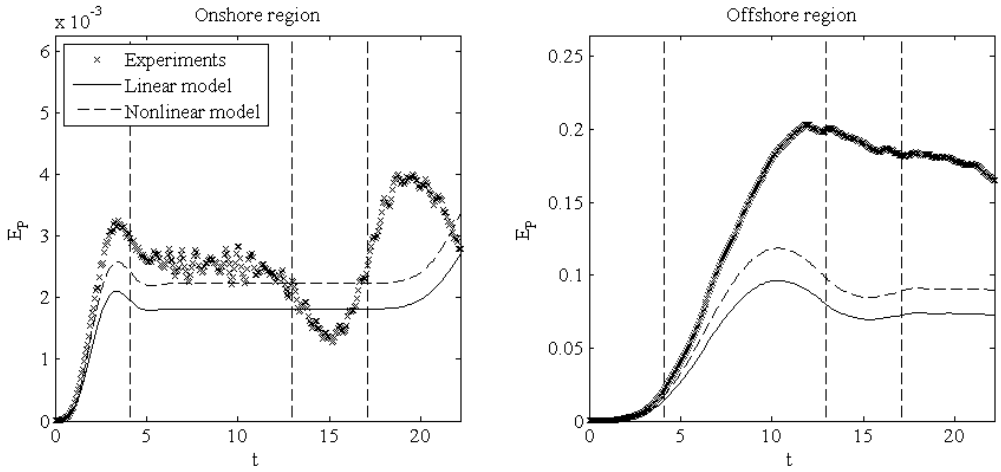

Figure D.12: Potential energy contained in the wave field for Run 12.

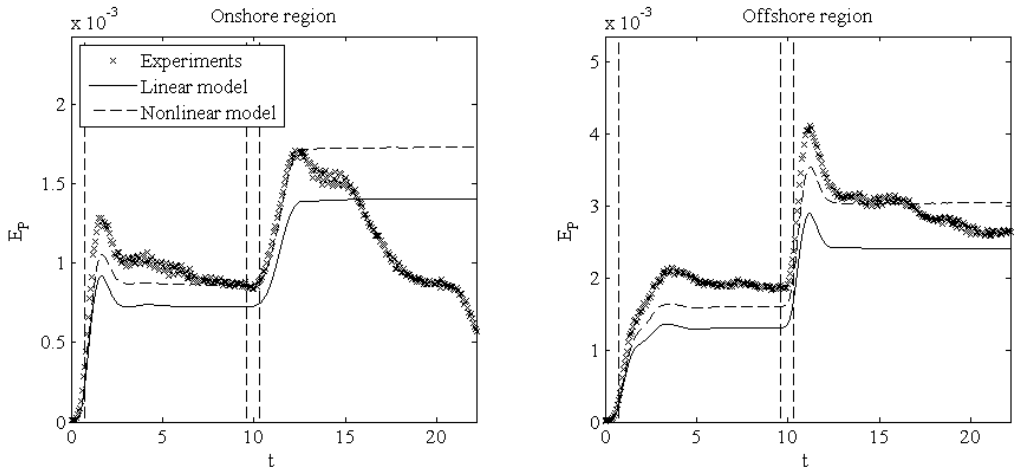

Figure D.13: Potential energy contained in the wave field for Run 13.

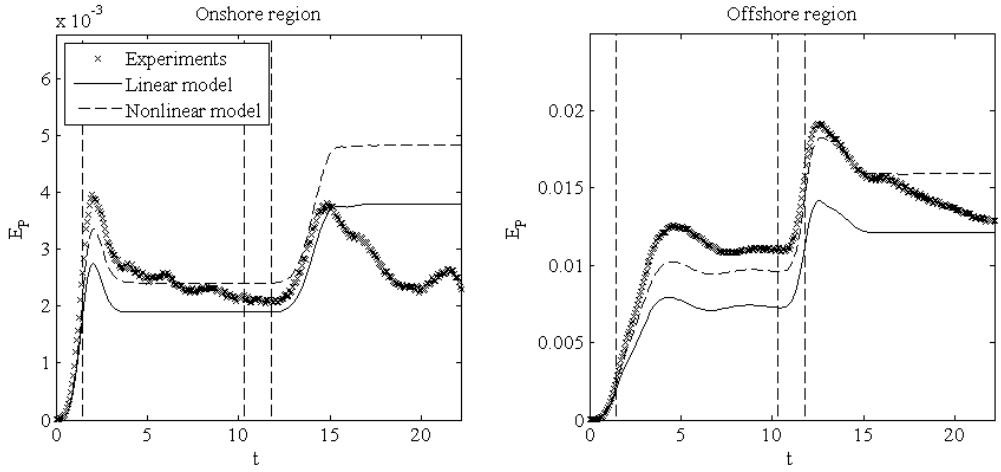

Figure D.14: Potential energy contained in the wave field for Run 14.

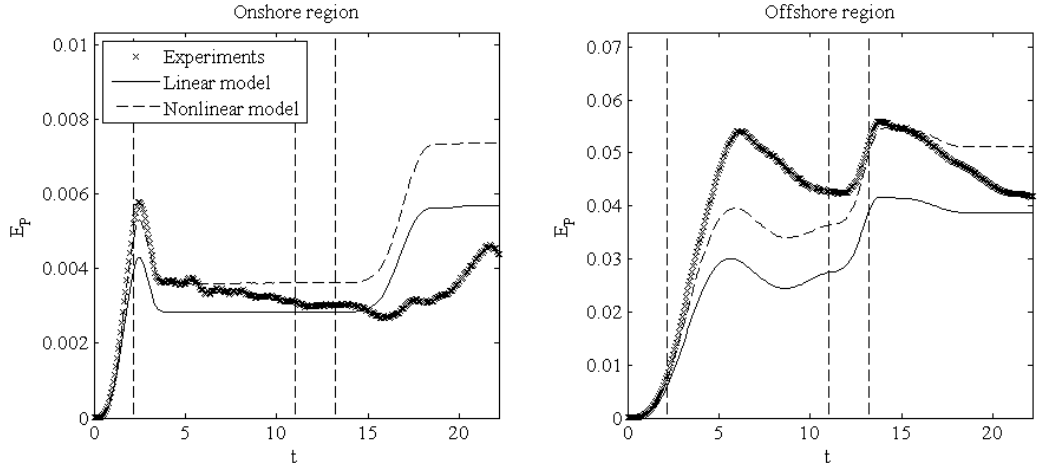

Figure D.15: Potential energy contained in the wave field for Run 15.

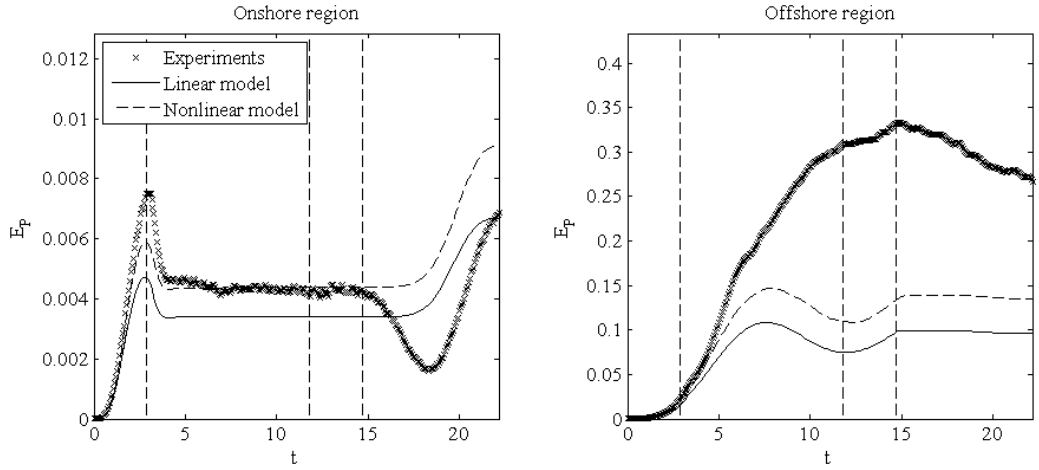

Figure D.16: Potential energy contained in the wave field for Run 16.

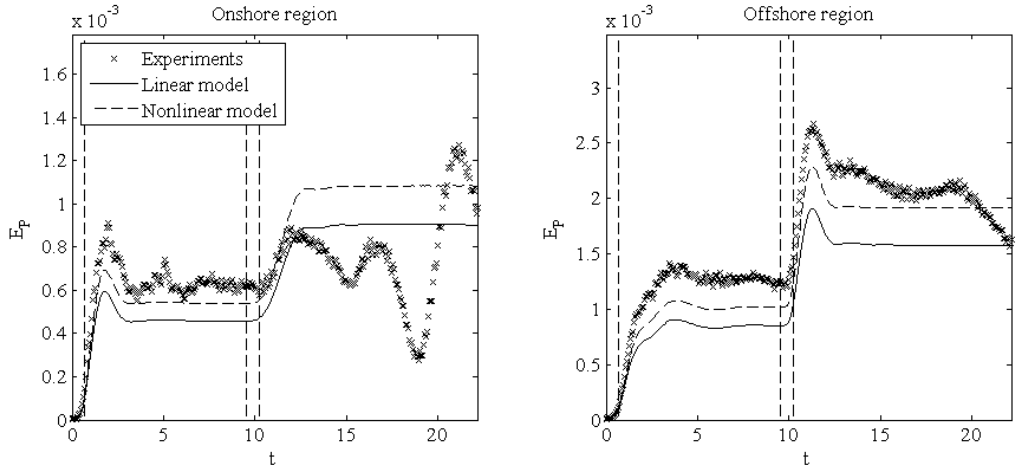

Figure D.17: Potential energy contained in the wave field for Run 17.

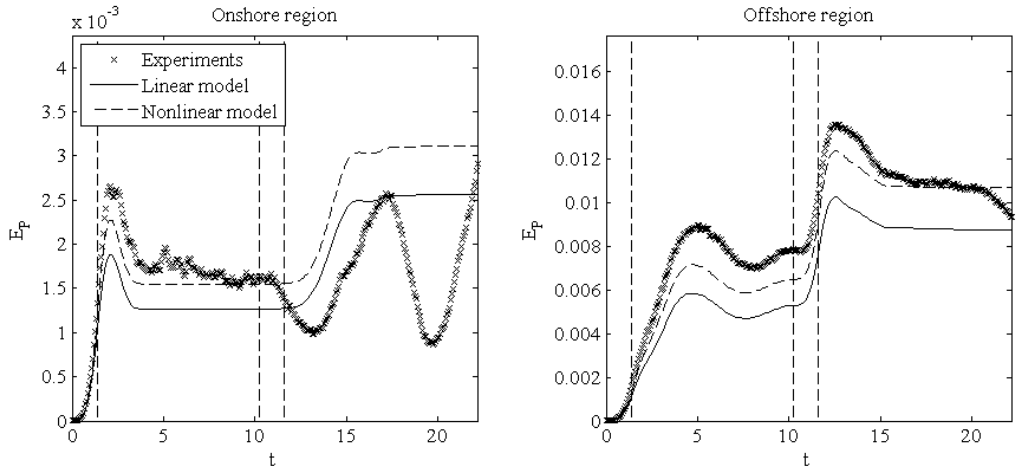

Figure D.18: Potential energy contained in the wave field for Run 18.

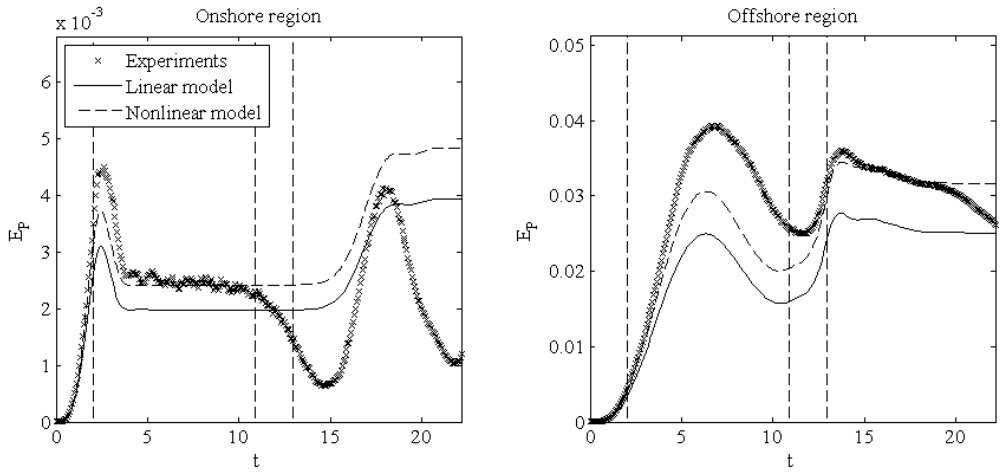

Figure D.19: Potential energy contained in the wave field for Run 19.

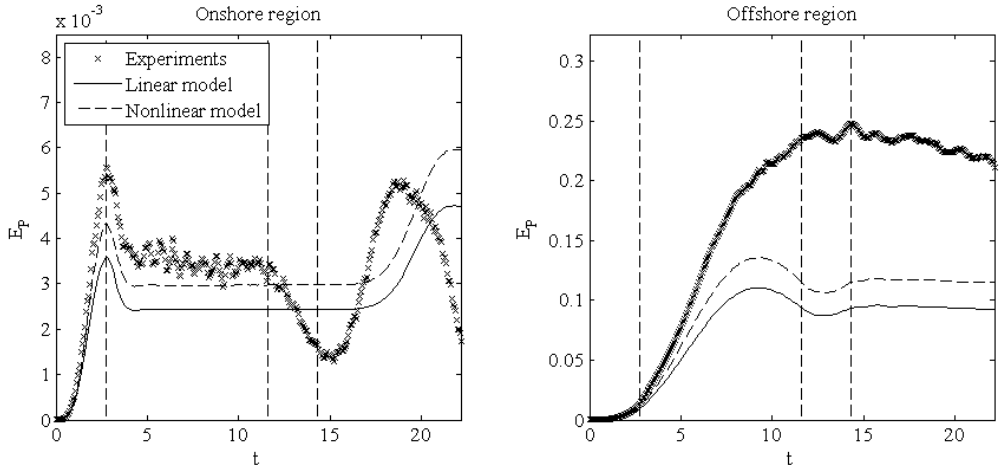

Figure D.20: Potential energy contained in the wave field for Run 20.

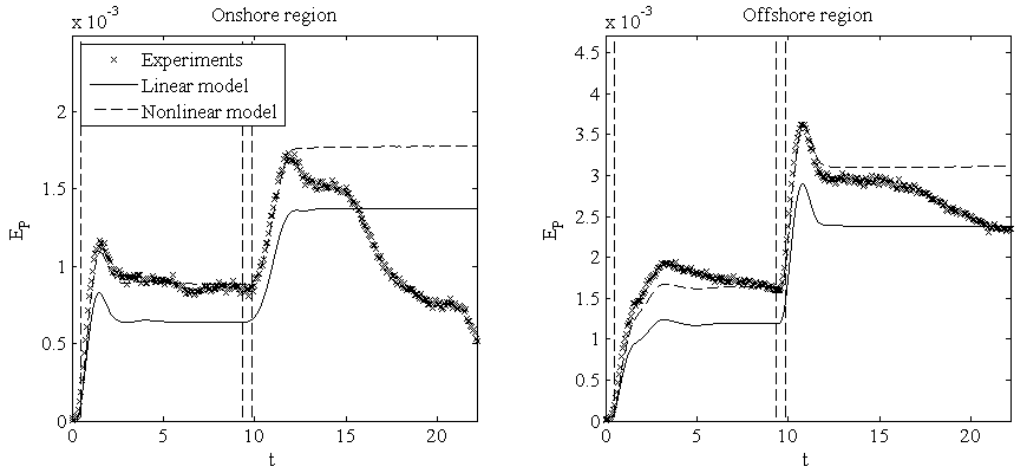

Figure D.21: Potential energy contained in the wave field for Run 21.

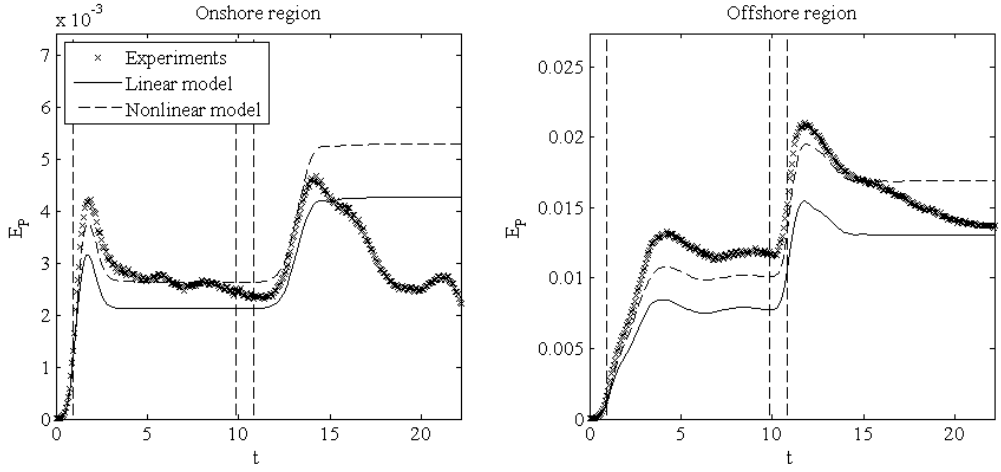

Figure D.22: Potential energy contained in the wave field for Run 22.

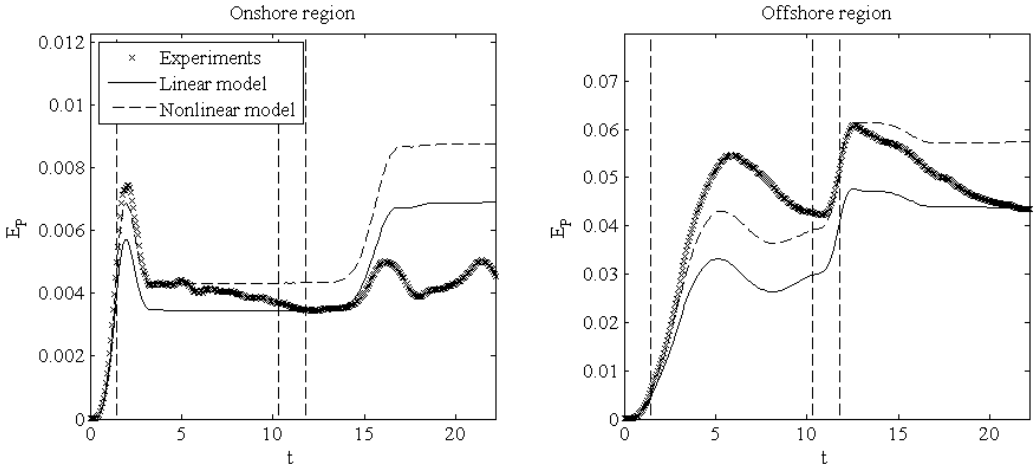

Figure D.23: Potential energy contained in the wave field for Run 23.

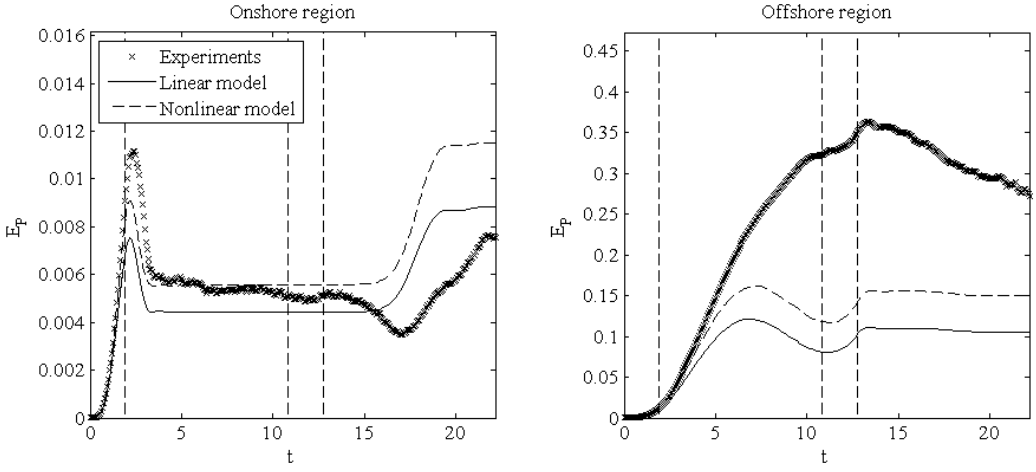

Figure D.24: Potential energy contained in the wave field for Run 24.

Appendix E

Mass within onshore and offshore regions

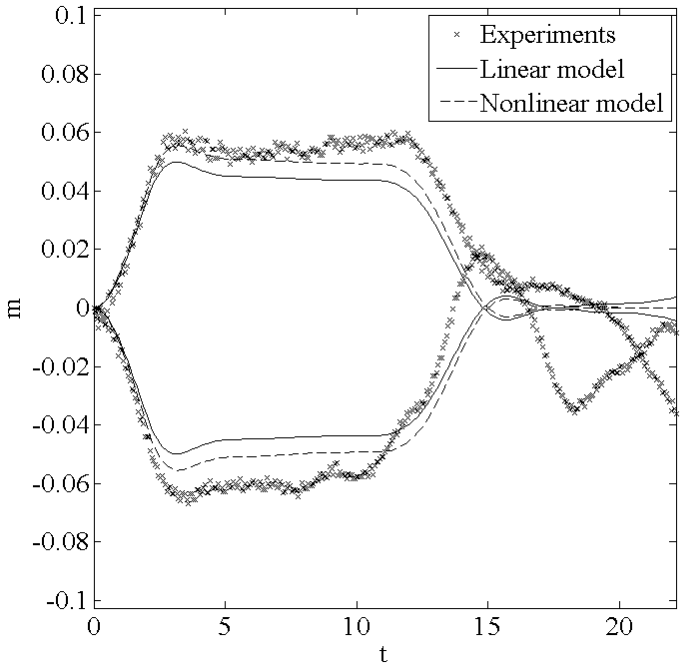

Figure E.1: Mass contained in the onshore and offshore regions of the wave field for Run 1.

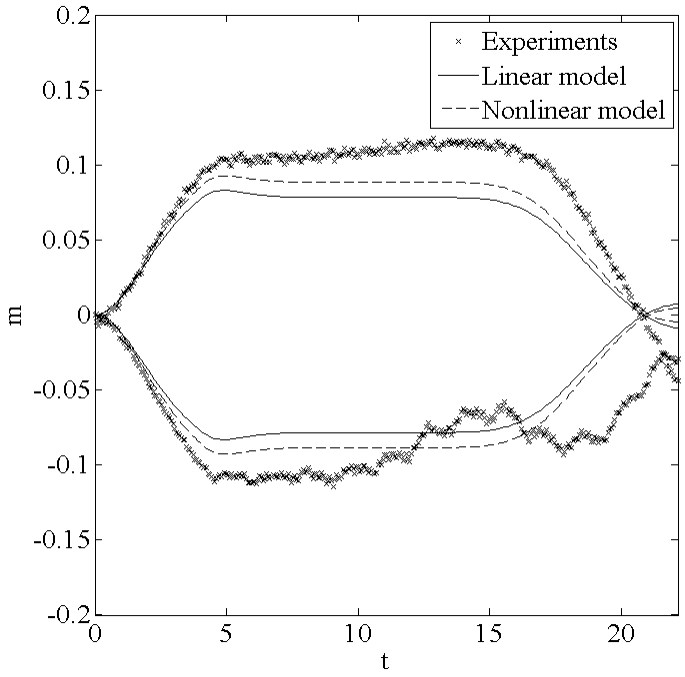

Figure E.2: Mass contained in the onshore and offshore regions of the wave field for Run 2.

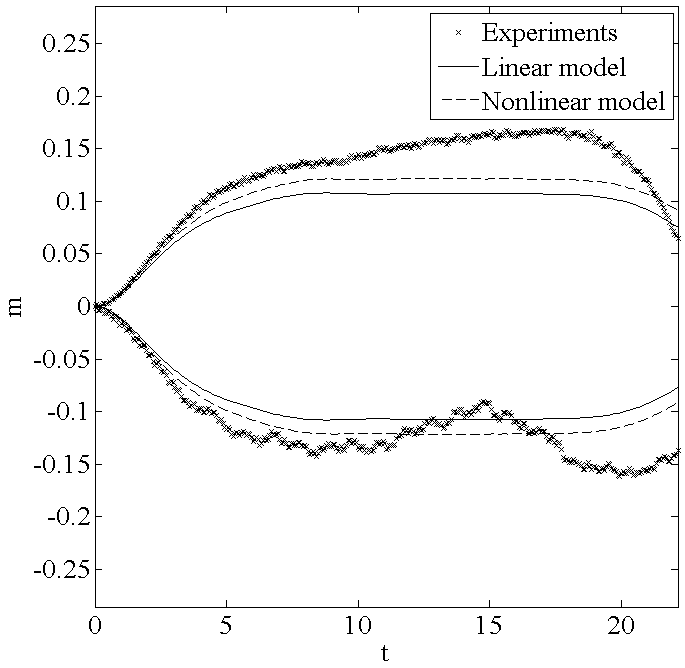

Figure E.3: Mass contained in the onshore and offshore regions of the wave field for Run 3.

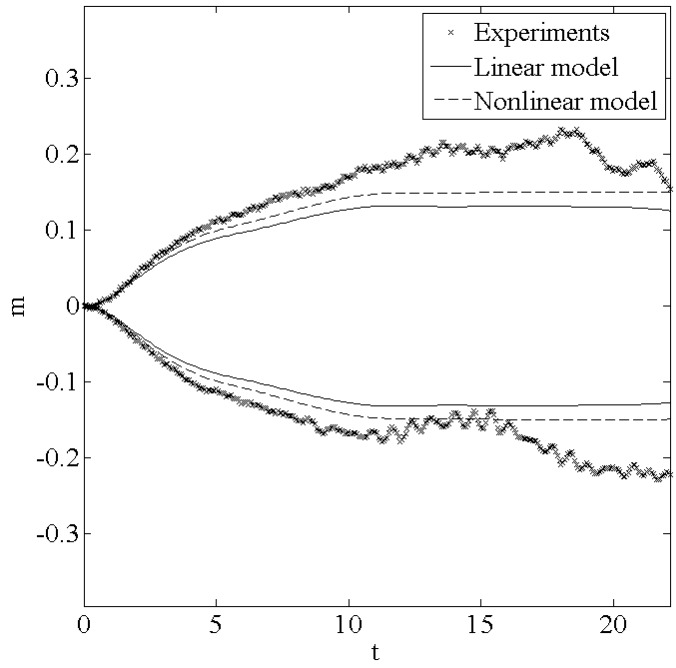

Figure E.4: Mass contained in the onshore and offshore regions of the wave field for Run 4.

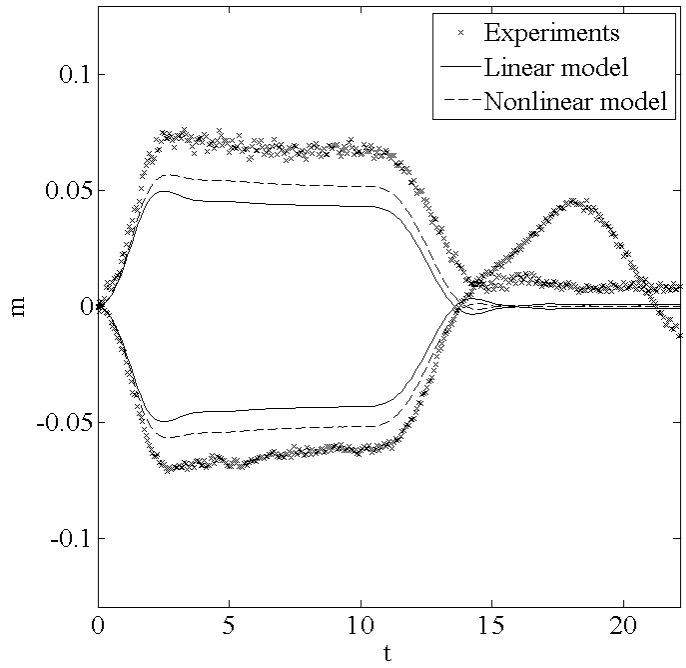

Figure E.5: Mass contained in the onshore and offshore regions of the wave field for Run 5.

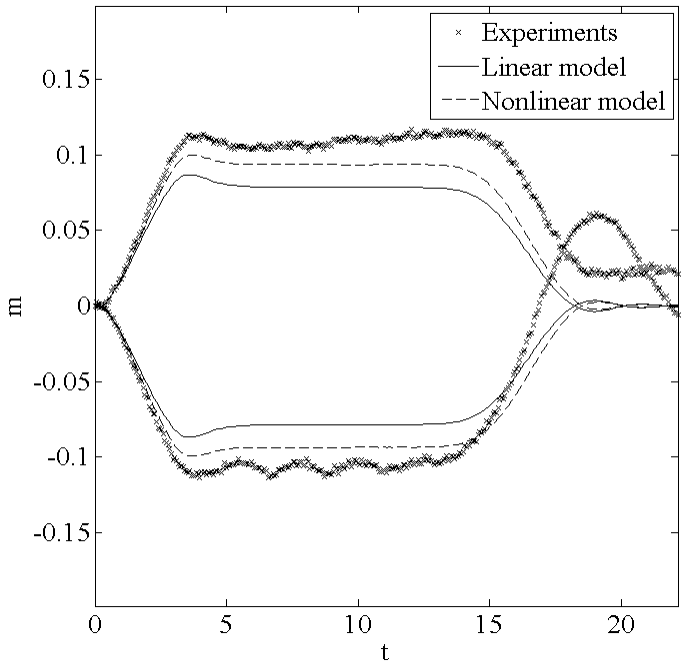

Figure E.6: Mass contained in the onshore and offshore regions of the wave field for Run 6.

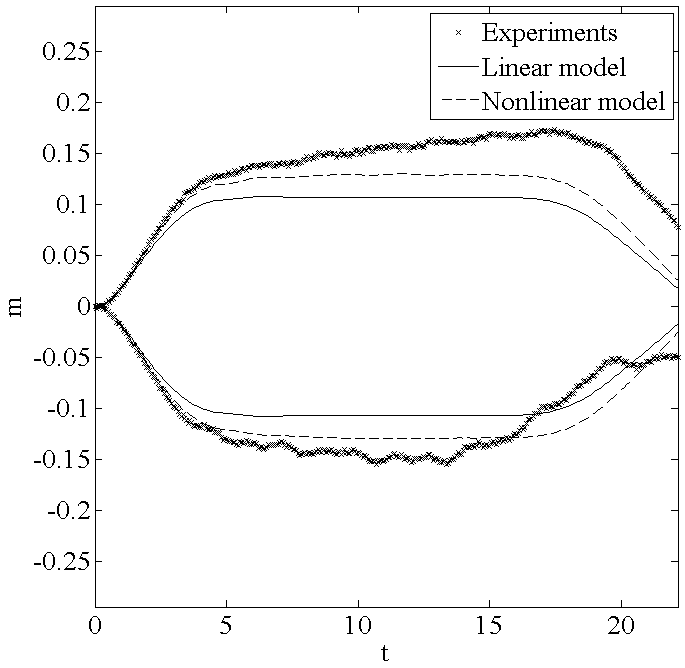

Figure E.7: Mass contained in the onshore and offshore regions of the wave field for Run 7.

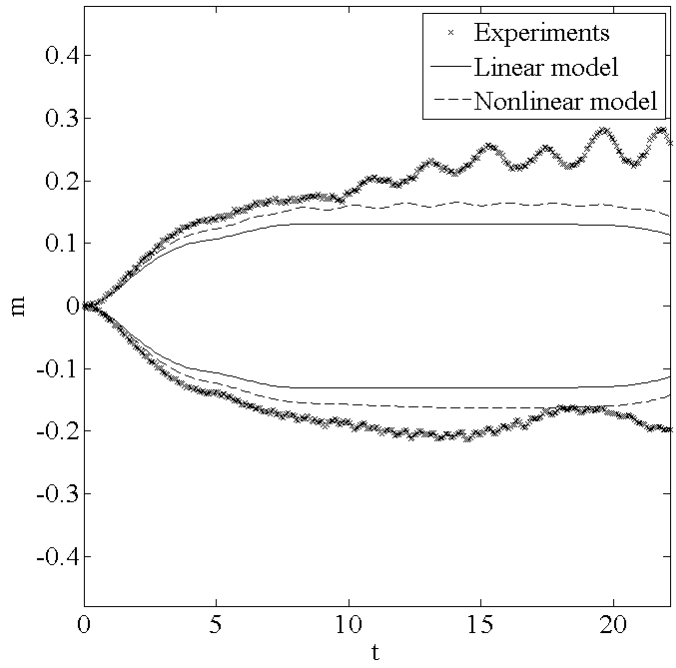

Figure E.8: Mass contained in the onshore and offshore regions of the wave field for Run 8.

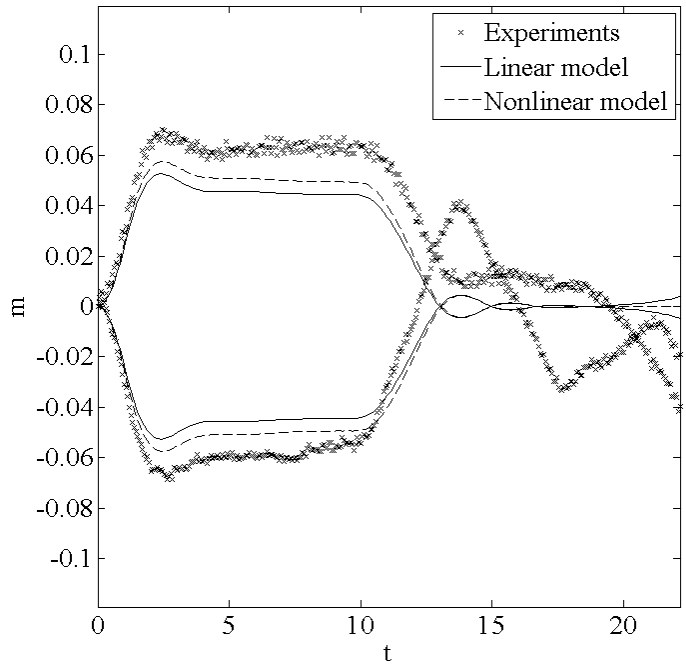

Figure E.9: Mass contained in the onshore and offshore regions of the wave field for Run 9.

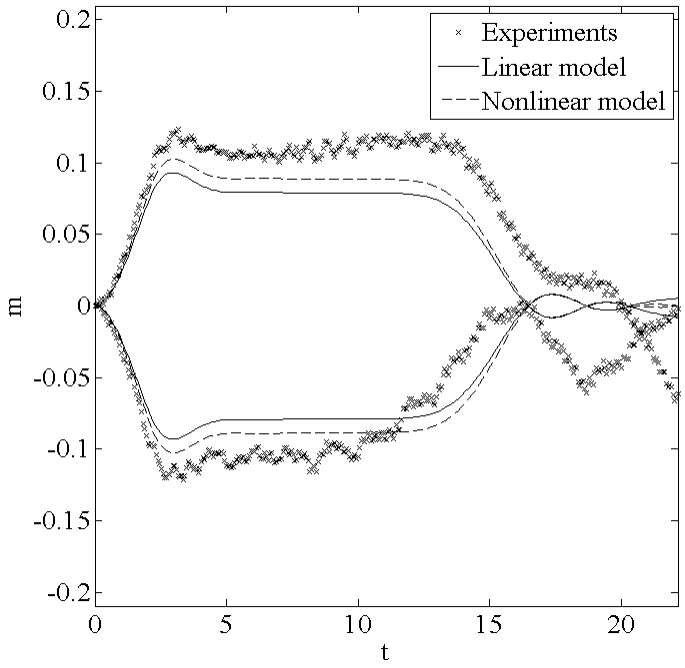

Figure E.10: Mass contained in the onshore and offshore regions of the wave field for Run 10.

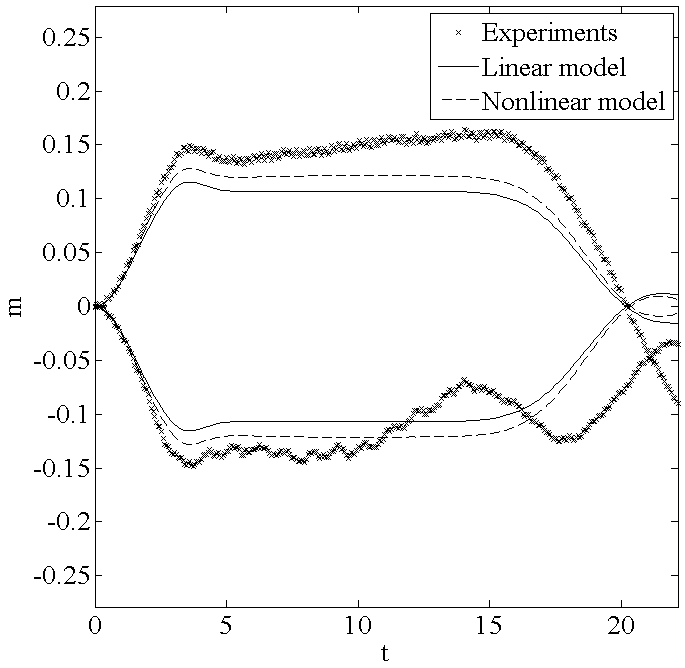

Figure E.11: Mass contained in the onshore and offshore regions of the wave field for Run 11.

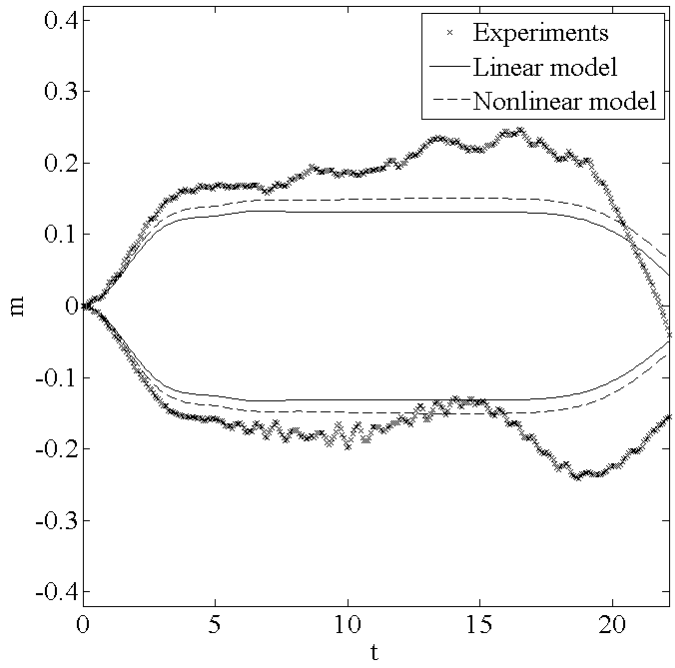

Figure E.12: Mass contained in the onshore and offshore regions of the wave field for Run 12.

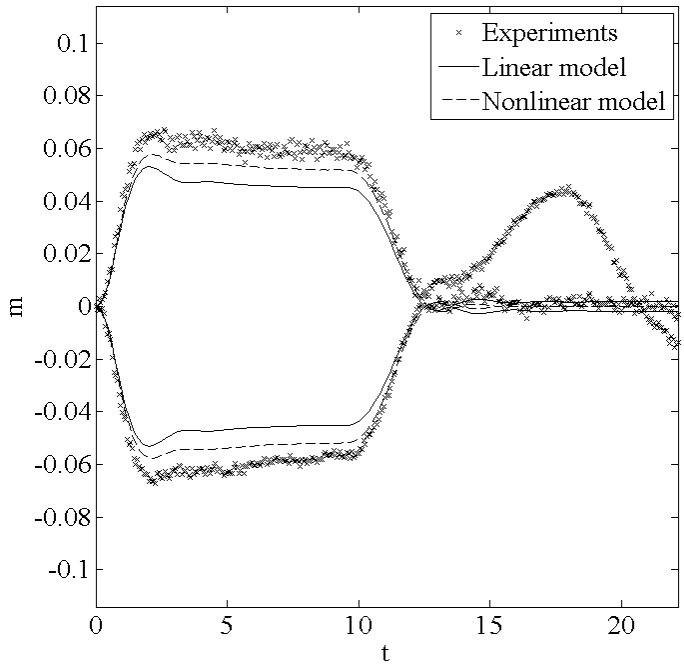

Figure E.13: Mass contained in the onshore and offshore regions of the wave field for Run 13.

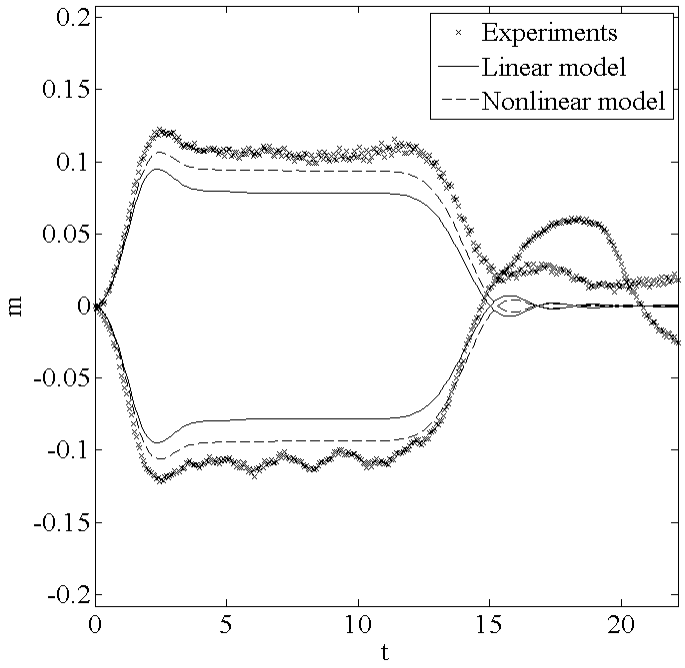

Figure E.14: Mass contained in the onshore and offshore regions of the wave field for Run 14.

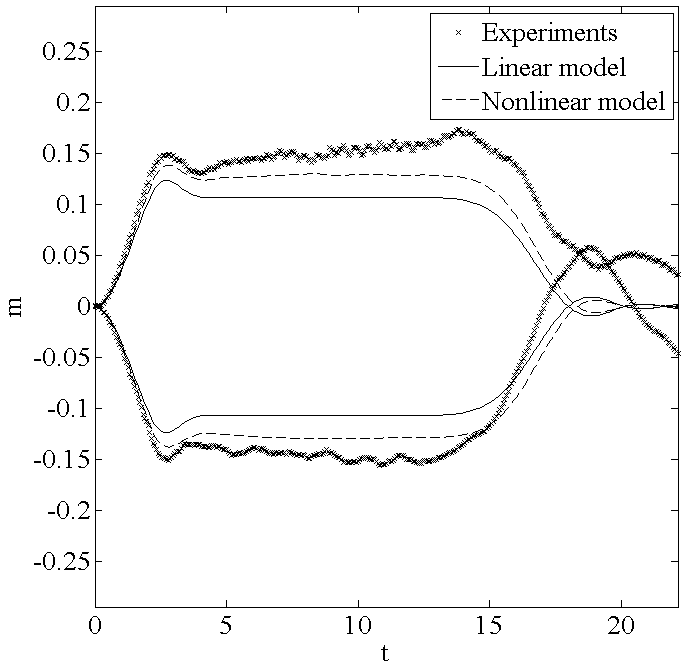

Figure E.15: Mass contained in the onshore and offshore regions of the wave field for Run 15.

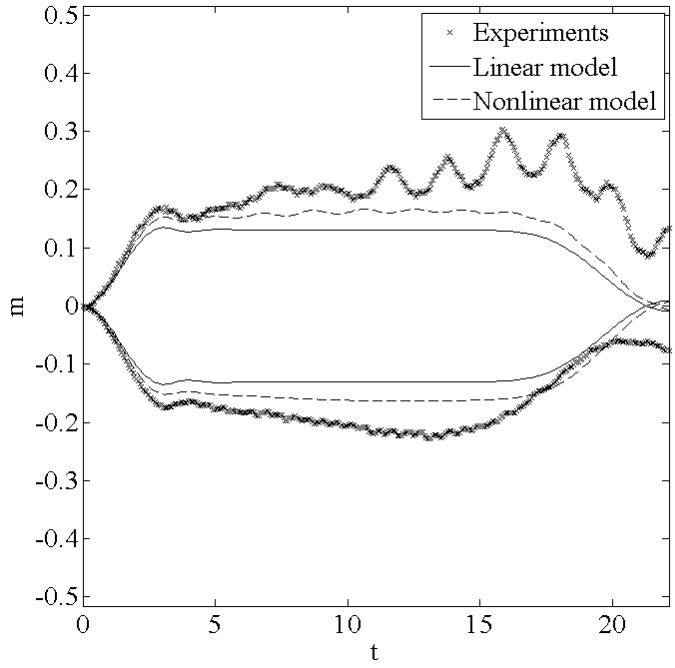

Figure E.16: Mass contained in the onshore and offshore regions of the wave field for Run 16.

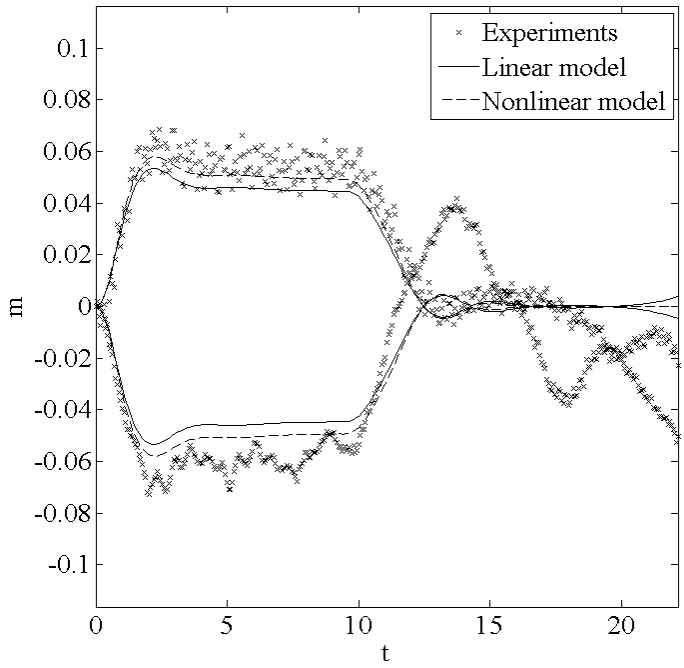

Figure E.17: Mass contained in the onshore and offshore regions of the wave field for Run 17.

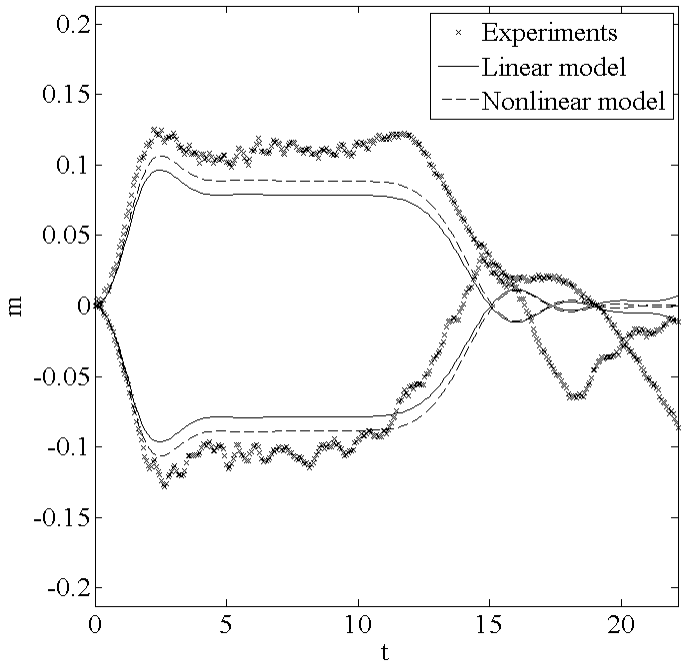

Figure E.18: Mass contained in the onshore and offshore regions of the wave field for Run 18.

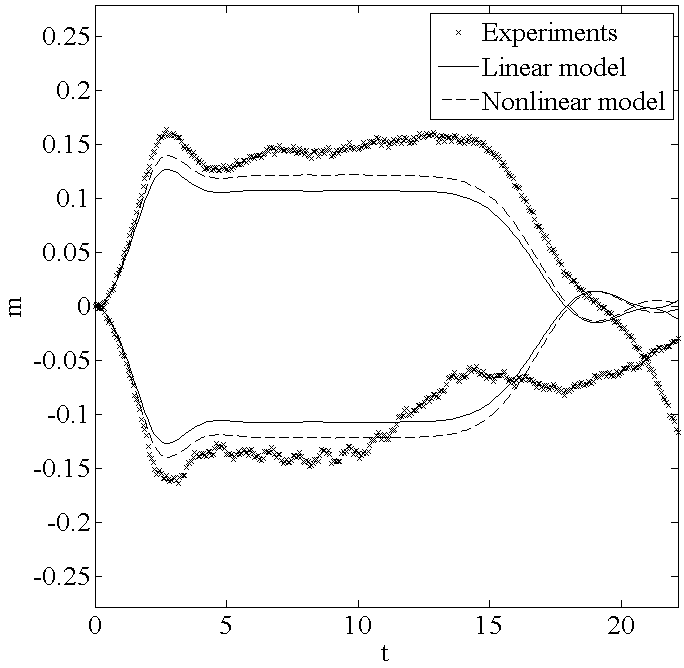

Figure E.19: Mass contained in the onshore and offshore regions of the wave field for Run 19.

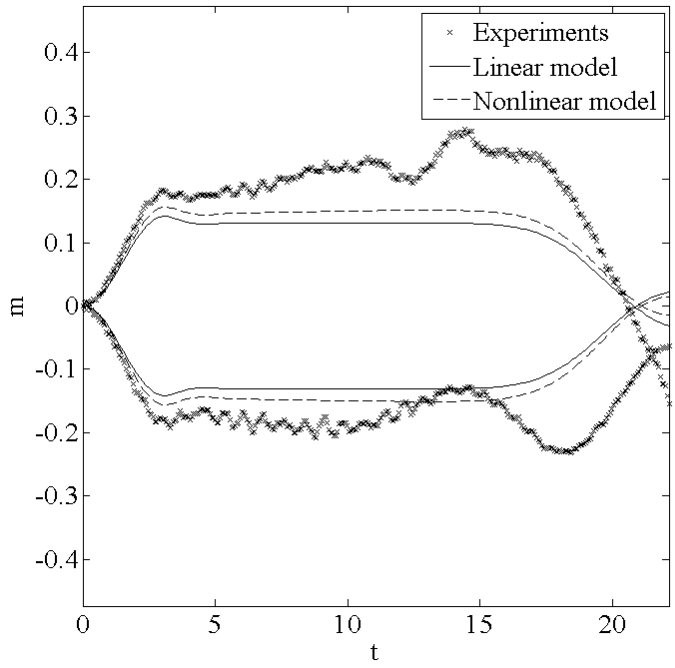

Figure E.20: Mass contained in the onshore and offshore regions of the wave field for Run 20.

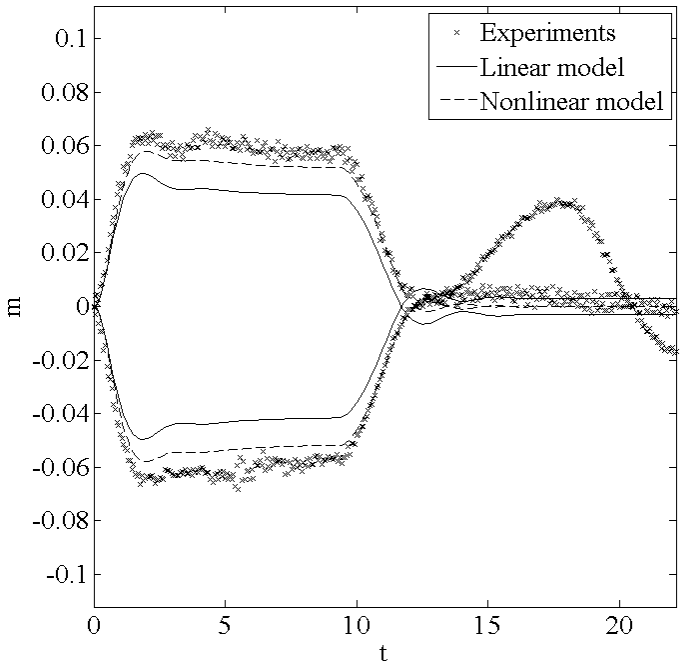

Figure E.21: Mass contained in the onshore and offshore regions of the wave field for Run 21.

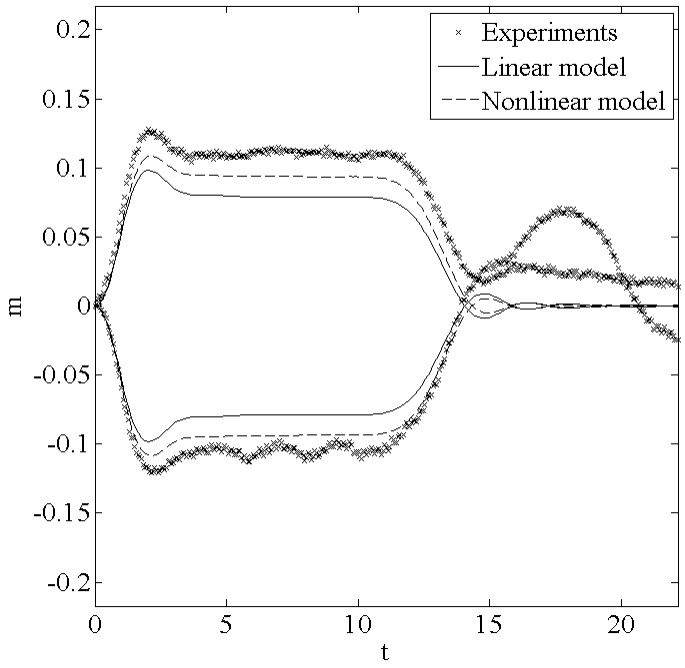

Figure E.22: Mass contained in the onshore and offshore regions of the wave field for Run 22.

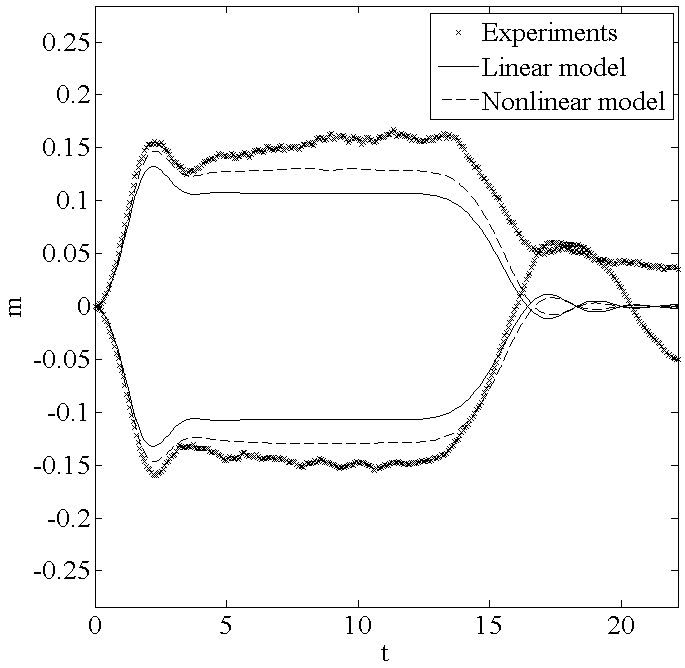

Figure E.23: Mass contained in the onshore and offshore regions of the wave field for Run 23.

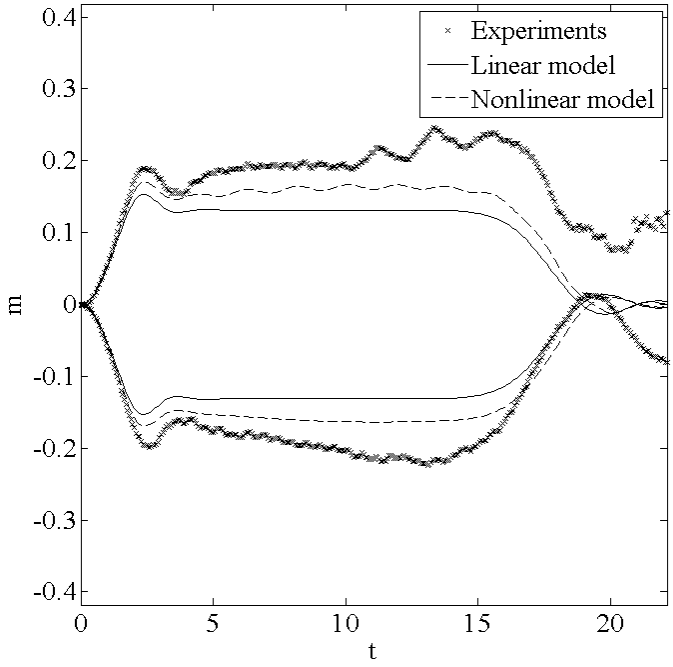

Figure E.24: Mass contained in the onshore and offshore regions of the wave field for Run 24.